UNIVERSITY OF CALIFORNIA

Santa Barbara

Expanding the Scope and Reactivity of Transition Metal Nanoclusters

A dissertation submitted in partial satisfaction of the

requirements for the degree Doctor of Philosophy

in Chemistry

by

Andrew W. Cook

Committee in charge:

Professor Trevor W. Hayton, Chair

Professor Peter C. Ford

Professor Gabriel Ménard

Professor Liming Zhang

June 2019

The dissertation of Andrew W. Cook is approved.

_____

Professor Peter C. Ford

_____

Professor Gabriel Ménard

_____

Professor Liming Zhang

_____

Professor Trevor W. Hayton, Committee Chair

May 2019

Expanding the Scope and Reactivity of Transition Metal Nanoclusters

Acknowledgements

I would first like to thank my undergraduate chemistry professors for being excellent teachers and seemingly endless sources of wisdom and guidance. I especially want to acknowledge Prof. Fred Northrup, for convincing me graduate school might be a good idea, as well as Prof. Mike "Waz" Wasielewski, who took me into his lab and showed me the life of a research scientist. I would also like to thank all the former Waz Group members, especially my mentor Dr. Patrick Hartnett, for answering every single one of my approximately ten thousand questions about chemistry, life, the universe, and pretty much everything.

Of course, I would not be anywhere close to where I am today without the patience, guidance, and support of my advisor Prof. Trevor Hayton. I arrived at UCSB fully expecting to be an organic chemist, until Trevor showed me the light of synthetic inorganic chemistry and I was hooked. My transition to this completely new field was shaky at first, but Trevor was always there to answer my now one hundred thousand questions. My committee members, Prof. Peter Ford, Prof. Gab Ménard, and Prof. Liming Zhang were always happy to lend their support and share their ideas for my various projects, and for that I am immensely grateful. I would also like to thank my various collaborators over the years, Prof. Susannah Scott and Dr. Zach Jones for their work on X-ray Absorption Spectroscopy, Prof. Ram Seshadri and Josh Bocarsly for their help with magnetometry, and Prof. Peter Hrobárik and Dr. Branislav Hvoráth for computational work and specialty NMR spectroscopy. The staff scientists at the Materials Research Lab at UCSB have also been invaluable to my research and for that I thank Dr. Rachel Behrens, Dr. Amanda Strom, Dr. Jaya Nolt, and Dr. Jerry Hu.

To all the current and former member of the Hayton group, I have no idea what I would have done without all of you. Dr. Ellie Owens, Dr. Danil Smiles, and Ed Paul were incredibly welcoming and provided excellent mentorship on how to be a successful graduate student and how to not blow up the glovebox. Working alongside me in the transition metal lab were Dr. Bi "Pouchy" Nguyen, Dr. Peter "Grouchy" Damon, and Dr. Nate "Mr. Sunshine" Hartmann. This eclectic group of nerds helped keep me sane when we were putting the pump back together for the umpteenth time and helped drive me a little insane when the days got boring. To the current Haytonians, Mikiyas Assefa, Selena Staun, Alex Touchton, Gregg Kent, Miguel Baeza, and Sheila Kulkarni: it has been an honor to see all of you grow as chemists and I wish you all the best in the future.

Finally, I would like to thank all my family and friends who have been incredibly supportive throughout this whole process. I am especially appreciative of those of you who refrained from asking "so when are you done?" too many times. Last but not least, I am eternally grateful to my fiancée Emily who has been there for the highs, lows, and everything in between.

For financial support of this work, I would like to thank the National Science Foundation (CHE 1764345). Additional funding from UCSB and the Mellichamp fellowship provided an invaluable network of collaborators and facilitated my research during the summer months. I would also like to thank UCSB Sanda Lamb Memorial Award and the ACS Division of Inorganic Chemistry for travel grants. This research made use of the SQUID Magnetometer of the Materials Research Laboratory, an NSF MRSEC (DMR 1720256), an ESI-MS supported by the MRSERC Program of the NSF under Award No. DMR 1121053, and the NMR Spectrometers of the Chemistry Department, an NIH SIG (1S10OD012077-01A1).

Vita of Andrew W. Cook

Education

University of California Santa Barbara, Santa Barbara, CA **2014-Present**

Doctor of Philosophy (Expected)
Advisor: Prof. Trevor W. Hayton

Certificate in College and University Teaching

Northwestern University – Evanston, IL **2010-2014**

Bachelor of Arts, Physical-Organic Chemistry
Minor in Environmental Policy

Professional Employment

University of California Santa Barbara **September-December 2014**

Instructor of Record, General Chemistry, Department of Chemistry

University of California Santa Barbara **2014-2018**

Teaching Assistant, Department of Chemistry

Boehringer Ingelheim **June-September 2013**

Lab Technician Intern for Parallel Synthesis of Drug Candidates
Advisor: Lana Smith

Publications

Cook, A. W.; Lewis, R. L.; Morochnik, S.; Wu, G.; Hayton, T. W.; "A New Role for the Ketimide Ligand: Stabilization of the Low-Valent Iron Nanocluster $[Fe_4(N{=}CPh_2)_6]$". *Manuscript submitted for review.*

Gladfelder, J. L.; Ghosh, S.; Cook, A. W.; Wu, G.; Hayton, T. W.; Zakarian, A.; "Enantioselective Alkylation of 2-Substituted Pyridines with Chiral Lithium Amides as Stereodirecting Auxiliaries". *Manuscript in preparation.*

Cook, A. W.; Jones, Z. R.; Wu, G.; Teat, S.; Scott, S. L.; Hayton, T. W.; "Synthesis and Characterization of "Atlas-Sphere" Copper Nanoclusters: New Insights into the Reaction of Cu^{2+} with Thiols". *Manuscript submitted for review*.

Cook, A. W.; Hrobárik, P.; Damon, P. L.; Nejera, D.; Horváth, B.; Wu, G.; Hayton, T. W.; "Homoleptic Ketimide Complexes of Palladium and Platinum: Isolation of a Hexagonal Aromatic Pd_7 Nanocluster and a Rare Two-Coordinate Pt(II) Complex". *Manuscript submitted for review.*

Cook, A. W.; Hayton, T. W.; "Case Studies in Nanocluster Synthesis and Characterization: Challenges and Opportunities". *Acc. Chem. Res.* **2018**, *51*, 2456-2464.

Cook, A. W.; Wu, G.; Hayton, T. W.; "A Re-examination of the Synthesis of Monolayer-Protected $Co_x(SCH_2CH_2Ph)_m$ Nanoclusters: Unexpected Formation of a Thiolate-Protected Co(II) T3 Supertetrahedron". *Inorg. Chem.* **2018**, *57*, 8189-8194.

Cook, A. W.; Jones, Z. R.; Wu, G.; Scott, S. L.; Hayton, T. W.; "An Organometallic Cu_{20} Nanocluster: Synthesis, Characterization, Immobilization on Silica, and 'Click' Chemistry". *J. Am. Chem. Soc.* **2018**, *140*, 394-400.

Nguyen, T.–A. D.; Cook, A. W.; Wu, G.; Hayton, T. W.; "Subnanometer-Sized Copper Clusters: A Critical Re-evaluation of the Synthesis and Characterization of $Cu_8(MPP)_4$ (HMPP = 2-Mercapto-5-*n*-propylpyrimidine)". *Inorg. Chem.* **2017**, *56*, 8390-8396.

Cook, A. W.; Nguyen, T.–A. D.; Buratto, W. R.; Wu, G.; Hayton, T. W.; "Synthesis, and Reactivity of the Group 11 Hydrido Clusters $[Ag_6H_4(dppm)_4(OAc)_2]$ and $[Cu_3H(dppm)_3(OAc)_2]$". *Inorg. Chem.* **2016**, *55*, 12435-12440.

Hartnett, P. E.; Dyar, S. M.; Margulies, E. A.; Shoer, L. E.; Cook, A. W.; Eaton, S. W.; Marks, T. J.; Wasielewski, M. R.; "Long-Lived Charge Carrier Generation in Ordered Films of a Covalent Perylenediimide–Diketopyrrolopyrrole–Perylenediimide Molecule". *Chem. Sci.* **2015**, *6*, 402-411.

Presentations

Cook, A. W.; Damon, P.; Lewis, R. A.; Wu, G.; Hayton, T. W.; "Towards organometallic nanoclusters: Ketimide-stabilized low-valent transition metal clusters" 256th ACS National Meeting Boston MA, Oral Presentation, August **2018**

Cook, A. W.; Wu, G.; Hayton, T. W.; "Transition Metal Nanoclusters: Synthesis and Applications" University of California Chemical Symposium Lake Arrowhead CA, Oral Presentation, March **2018**.

Cook, A. W.; Wu, G.; Hayton, T. W.; "Coinage Metal Nanoclusters: Synthesis and Practical Applications" Mellichamp Fellowship Student Seminar UCSB, Oral Presentation, August **2017**.

Cook, A. W.; Wu, G.; Hayton, T. W.; "A Critical Re-evaluation of Cobalt-Thiolato Nanoclusters" SoCal Organometallics, Oral Presentation, June **2017**.

Cook, A. W.; Wu, G.; Hayton, T. W.; "Coinage Metal Nanoclusters: Characterization and Catalytic Activity" 253rd ACS National Meeting San Francisco CA, Oral Presentation, April **2017**.

Cook, A. W.; Wu, G.; Hayton, T. W.; "Coinage Metal Nanoclusters: Characterization and Catalytic Activity" SoCal Organometallics, Oral Presentation, December **2017**.

Cook, A. W.; Wu, G.; Hayton, T. W.; "Group 11 Nanoclusters: Using Bite Angle to Control Morphology" SoCal Organometallics, Poster Presentation, April **2017**.

Awards

- Mellichamp Sustainability Summer Fellowship, UCSB 2017
- Outstanding Service to the Department Award, UCSB 2017
- Sandra Lamb Memorial Award, UCSB 2018
- UCCS Best Inorganic Oral Presentationn, 2018
- Mellichamp Sustainability Summer Fellowship, UCSB 2018
- ACS Division of Inorganic Chemistry Travel Grant, 2018

Field of Study

Major Field: Synthetic Inorganic Chemistry
Studies in Organometallic Cluster Chemistry and their Applications with Professor Trevor W. Hayton, University of California Santa Barbara

Abstract

Expanding the Scope and Reactivity of Transition Metal Nanoclusters

by

Andrew W. Cook

The group 11 hydride clusters $[Ag_6H_4(dppm)_4(OAc)_2]$ and $[Cu_3H(dppm)_3(OAc)_2]$ (dppm = 1,1-bis(diphenylphosphino)methane) were synthesized from the reaction of M(OAc) (M = Ag, Cu) with Ph_2SiH_2, in the presence of the bidentante phosphine ligand, dppm. $[Ag_6H_4(dppm)_4(OAc)_2]$ is the first structurally characterized homometallic polyhydrido silver cluster to be isolated. Both clusters catalyze the hydrosilylation of (α,β–unsaturated) ketones. Notably, this represents the first example of hydrosilylation with an authentic silver hydride complex. The larger copper hydride clusters $[Cu_{10}H_{10}(DBEphos)_4]$ (DBEphos = oxydi-2,1-phenylene)bis(diphenylphosphino)) and $[Cu_{14}H_{14}(DBFphos)_5]$ (DBFphos = 4,6-bis(diphenylphosphino)dibenzofuran) have also been isolated. Preliminary data suggest that there is a positive correlation between the bite angle of the bidentate phosphine and the size of the cluster generated. Finally, the copper selenoate cluster $[Cu_{13}H_{10}(SePh)_3(PPh_3)_7]$ was generated from the *in situ* reduction of Ph_2Se_2 by $[CuH(PPh_3)]_6$ and represents a facile method of selenium incorporation into copper clusters.

Further studies into Cu cluster formation is examined through the reactivity of RSH (R = CH_2CH_2Ph, *n*-Bu, *n*-$C_{12}H_{25}$) with Cu(II) under anhydrous conditions, which results in the formation of "Atlas-sphere"-type copper thiolate nanoclusters, including $[Cu_{12}(SR')_6Cl_{12}][(Cu(R'SH))_6]$ (R' = ^{n}Bu) and $[H(THF)_2]_2[Cu_{17}(SR")_6Cl_{13}(THF)_2(R"SH)_3]$ (R" = CH_2CH_2Ph). Consistent with the X-ray crystallographic data, the XANES edge energies of these clusters suggest they are constructed exclusively with Cu(I) ions. Given these results, as well as past work on Cu(II)/thiol reactivity, it is argued that Cu(0) cannot be accessed by reaction of Cu(II) with a thiol, and that previous reports of Cu(0)-containing clusters synthesized in this manner are likely erroneous.

The generation of a partially metallic Cu cluster was realized through the synthesis of the mixed-valent organometallic cluster, $[Cu_{20}(CCPh)_{12}(OAc)_6)]$, which was isolated from the reduction of Cu(OAc) with Ph_2SiH_2 in the presence of phenylacetylene. This cluster is a rare example of a two-electron copper superatom, and the first to feature a tetrahedral $[Cu_4]^{2+}$ core. $[Cu_{20}(CCPh)_{12}(OAc)_6)]$ can be readily immobilized on dry, partially-dehydroxylated silica. Both materials are effective catalysts for [3+2] cycloaddition reactions between alkynes and azides (i.e., "Click" reactions) at room temperature. Significantly, neither material requires any pre-treatment for activation toward catalysis.

To further expand the scope of first row transition metal clusters with partial metallic character, a re-examination of the synthesis and of monolayer-protected $Co_x(SCH_2CH_2Ph)_m$ nanoclusters is addressed. These clusters were reportedly formed by the reaction of $CoCl_2$ with $NaBH_4$ in the presence of $HSCH_2CH_2Ph$, and were suggested to contain between 25 and 30 Co atoms. However, there is no evidence to support the existence of these large clusters in the reaction mixture. Instead, this reaction results in the relatively clean formation of the Co(II) coordination complex $[Co_{10}(SCH_2CH_2Ph)_{16}Cl_4]$. This complex represents the first example of a thiolate-protected Co(II) T3 supertetrahedral cluster.

The ketimide ligand has been shown to stabilize high oxidation states of the transition metals, though it has recently been hypothesized that this ligand may be useful in the generation of low-valent species as well. The isolation of the Pd(0) containing, ketimide-stabilized cluster $Pd_7(N{=}C^tBu_2)_6$ reinforces this hypothesis. Similar reactivity studies with Pt results in the isolation of the Pt(II) complex, $Pt(N{=}C^tBu_2)_2$. Additionally, the low-valent Fe-ketimide cluster, $[Fe_4(N{=}CPh_2)_6]$, is isolated. These complexes have been previously reported by former Hayton group members, though their syntheses and characterization have been significantly improved. $Pt(N{=}C^tBu_2)_2$ exhibits exceptionally short Pt-N distances (av. Pt-N = 1.815 Å) and an unusually deshielded ^{195}Pt chemcial shift (δ_{Pt} = -629 ppm) with a large $^1J_{PtN}$ coupling constant (537 Hz). $Pd_7(N{=}C^tBu_2)_6$ features a mixed-valent, hexagonal planar $[Pd_7]^{6+}$ core stabilized by six ketimide ligands. Finally, $[Fe_4(N{=}CPh_2)_6]$ displays fully delocalized metal bonding electrons, which gives rise to a ground spin-state of S = 7 and single molecule magnet behavior.

Table of Contents

List of Figures

List of Schemes

List of Tables

Let’s think the unthinkable, let’s do the undoable.

Let us prepare to grapple with the ineffable itself, and see if we may not eff it after all.

-Douglas Adams

Chapter 1. Introduction

1.1 Transition Metal Nanoparticles and Nanoclusters

The observation of gold particles "of very minute dimension" by Michael Faraday has served as the foundation for nanoscience for over 150 years.[1-2] Over this time, nanoparticles have garnered particular interest for a variety of applications as their high surface area to volume ratio is particularly desirable for catalysis. As such, a significant effort has been made to fully understand the nature of the metal-metal bonding within these particles, the nature of their surface chemistry, and to what extent the size and morphology of these materials can be tailored.

1.1.1 Synthesis and Characterization of Nanoparticles

While the syntheses of nanoparticles are numerous and varied, solution phase techniques are relatively common and typically involve the controlled generation of M(0) atoms, which nucleate and grow until their size is arrested by a capping ligand.[3-6] These capping ligands often contain long alkyl chains, which act as surfactants and play an important role in determining the morphology of the resultant nanoparticle.[7] Significant improvements have been made to these synthetic procedures over the past two decades to increase the homogeneity of the nanoparticles, such as the Trukevich-Frens and Brust-Schiffrin methods for gold nanoparticle synthesis, however it is inevitable that a mixture of various sizes and morphologies arises during their formation.[5, 8-11] Additionally, these nanoparticles often co-precipitate with excess ligand, unreacted starting materials, and unwanted side products. The polydispersity and potential for impurities hampers the characterization of these materials and casts doubt onto the resulting structure function relationships.

One common characterization technique that can be used to characterize nanoparticles is electron microscopy, which allows for the detailed imaging of the metal centers of the

material.[12] While this technique offers insight into the size, morphology, and dispersity of the particles, there is no structural information gleaned about the capping ligands nor the interaction of those ligands with the metal surface. Additionally, electron microscopy exposes the sample to high energy radiation, which can damage small particles, further obfuscating the nature of the material.[13] Because the catalytic active sites are often at the metal-ligand interface, it is imperative to have a clear understanding of the nanoparticle surface chemistry moving forward.

1.1.2 A Transition from Nanoparticles to Nanoclusters

To better understand the surface chemistry of these nanomaterials, ultrasmall (< 2 nm, ~10 – 300 atoms) nanoparticles, which are perfectly monodisperse and can be resolved with atomic precision, have been synthesized. This new class of materials are collectively known as nanoclusters.[14-15] To differentiate these small nanoclusters from simple coordination clusters, two conditions must be met: (1) the cluster must possesses some M(0) character, and (2) there should be a significant amount of metal-metal bonding. These criteria are met through the partial reduction of metal salt precursors in the presence of a stabilizing ligand, similar to the synthesis of nanoparticles, albeit with a few key differences. First, nanoclusters contain a precise number of metal atoms with a reduced, M(0) core encapsulated by a M^{n+} shell, surrounded by a well-defined ligand surface, whereas nanoparticles often have an ambiguous quantity of metal atoms and, as mentioned previously, ill-defined capping ligand environements. Second, the long-chain alkane surfactant/stabilizing ligands have been replaced by more traditional organometallic ligands, which render nanoclusters much easier to crystallize. This newfound crystallizability has allowed for single crystals of these materials to be isolated, which, by necessity, are perfectly monodisperse and can be easily separated

from impurities. These single crystals can then be investigated by X-ray diffractometry (XRD) to determine, with atomic precision, the location and identity of not only the metal centers, as was the case with nanoparticles, but also of the capping ligands. This new class of materials bridges the gap between molecular complexes and traditional nanoparticles, combining the solubility and atomic precision of metal complexes with the intriguing properties of nanoparticles (Figure 1.1).

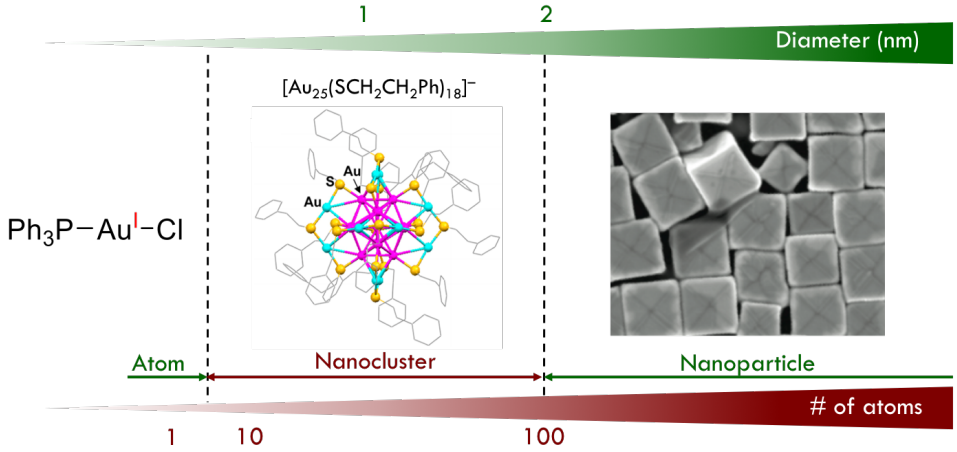

Figure 1.1. Nanoclusters bridge the gap between molecular complexes and nanoparticles. Figure adapted from ref. 15.

By far the most well studied class of nanoclusters are those of group 11, especially of gold.[14] This is due to the relatively stability of gold(0) compared to silver(0) and copper(0), as revealed by the standard redox potentials versus the standard hydrogen electrode.[16] That is, the M(I) salt precursors used in the synthesis of nanoclusters are much easier to reduce for gold (1.83 V) than silver (0.80 V) or copper (0.52 V), and once reduced, Au(0) tends to resist oxidation better than Ag(0) and Cu (0).[16] What follows will be a discussion of the synthesis and isolation of group 11 nanoclusters, as well as a brief survey of particularly groundbreaking or interesting examples. For a more complete review of the state of group 11 nanocluster literature through 2016, please see the recent Chemical Review article by Jin and co-

workers.[14] Beginning in the 1960s, Malatesta and co-workers isolated tertiary phosphine protected gold clusters of Au_6, Au_9, and Au_{11} via reduction of Au(I)-phosphine precursor complexes.[17] This work was followed up by Mingos and co-workers in the 1970s which culminated in the synthesis of a Au_{13} nanocluster, as well as a description of the electronic structure of these materials.[18] Schmid and co-workers pushed this cluster chemistry even further in 1981 when they isolated the gold-phosphine cluster Au_{55}, though a crystal structure could not be obtained.[19] Finally, in 1992, Teo and co-workers were able to generate a Au_{39} cluster, the largest to be structurally characterized at the time.[20] This chemistry languished somewhat for the next 15 years, in part because the synthetic procedures were unpredictable and not generalizable.[18] However, in 2007 Kornberg and co-workers modified the Brust-Schiffrin method of nanoparticle synthesis to yield the first group 11-thiolate nanocluster structurally characterized, $[Au_{102}(p\text{-MBA})_{44}]$ (*p*-MBAH = *p*-mercaptobenzoic acid).[21]

In the decade since this seminal result, much of the research on gold nanoclusters utilized the gold-thiolate motif, in part, because the synthetic procedure proved general to a variety of thiolates, though there are examples of other capping ligands, such as phosphines, acetylides, and selenoates.[14] Of particular importance is the $[Au_{25}(SR)_{18}]^n$ (q = -1, 0, 1; R = glutathione, CH_2CH_2Ph, $CH_2C_6H_4$-*p*-^{t}Bu, *etc.*) cluster, which features a Au_{13} icosahedral core that has been frequently observed in subsequent clusters and can be considered one of the basic structural motifs of gold nanoclusters.[22-24] Recently, there has been a quest to generate ever larger clusters, with more metallic character, which have properties similar to perfectly monodisperse nanoparticles. In 2018, Wu and co-workers structurally characterized the gold cluster $[Au_{144}(SCH_2Ph)_{60}]$, which had eluded researchers for nearly a decade.[25] A larger gold cluster $[Au_{246}(SC_6H_4\text{-}p\text{-}CH_3)_{80}]$ has also been characterized by Jin and co-workers, and is

thought to represent the largest cluster to not have primarily metallic character.[26] In late 2018 Dass and co-workers and Jin and co-workers simultaneously published the structure of $[Au_{279}(SC_6H_4\text{-}p\text{-}^tBu)_{84}]$, which was observed to have surface plasmon resonance, previously unreported for gold nanoclusters and indicative of the overwhelming metallic character of the cluster.[27-28] Finally, while much less well studied, acetylide ligands are beginning to gain traction within the gold nanocluster community and Wang and co-workers have reported a few elegant structures recently, such as $[Au_{19}(CCPh)_9(Hdppa)_3][SbF_6]_2$ (Hdppa = N,N-bis(diphenylphosphino)amine), $[Au_{24}(CCPh)_{14}(PPh_3)_4][SbF_6]_2$.[29]

Structures of silver-thiolate nanocluster structures are much rarer as these materials do not seem to possess the same stability as their gold counterparts. The first published crystal structure appeared in 2013 when Bigioni and co-workers and Zheng and co-workers simultaneously reported the synthesis and characterization of $[Ag_{44}(SR)_{30}]^{4-}$ (R = C_6H_4-*p*-COOH, C_6H_4-*p*-CF_3).[30-31] Two years later, Bakr and co-workers synthesized $[Ag_{25}(SC_6H_3\text{-}2,4\text{-}Me_2)_{18}]^-$, which is isostructural to its gold nanocluster counterpart.[32] The largest silver-thiolate cluster known to date is $[Ag_{146}Br_2(SC_6H_4\text{-}p\text{-}^iPr)_{80}]$, while smaller than the largest gold clusters, is still an impressive accomplishment.[33] Much like their gold analogs, silver nanoclusters usually feature thiolates as supporting ligands , though Liu and co-workers have synthesized a series of dichalcogenate-supported clusters, while Wang and co-workers have extended their gold-acetylide chemistry to silver, as well.[29, 34]

Copper nanoclusters, however, remain woefully underexplored. There are a few examples of heterobimetallic Au/Cu core/shell type clusters, including $[Au_{12}Cu_{32}(SPh\text{-}p\text{-}CF_3)_{30}]^{4-}$ and $[Au_{19}Cu_{30}(CC\text{-}3\text{-}SC_4H_3)_{22}(PPh_3)_6Cl_2]^{3+}$, however these examples are few and far between.[35-36] To the best of my knowledge, at the start of my project there were only three structurally

characterized copper only nanoclusters, two of which were reported by the Hayton group at UCSB by Dr. Thuy-Ai (Bi) Nguyen, $[Cu_{25}H_{22}(PPh_3)_{12}]^+$ and $[Cu_{29}Cl_4H_{22}(Ph_2Phen)_{12}]^+$ (Ph_2Phen = 4,7-diphenyl-1,10-phenanthroline), both of which utilize hydride as the supporting ligand.[37-38] The third cluster, reported by Liu and co-workers in 2016, has the formula $[Cu_{13}\{S_2CN^nBu_2\}_6(CCR)_4]^+$ (R = C(O)OMe, *m*-C_6H_4F) and is ligated by a mix of dithiocarbamates and acetylides. Conspicuously absent are copper-thiolate nanoclusters. While there have been many attempts to synthesize these materials, most of these materials were poorly characterized, and in one case a reported Cu_8 nanocluster was shown to be a simple coordination complex instead.[39] Clearly there is a need to develop this chemical space further, especially in developing new supporting ligands, and acetylides appear to be that promising new ligand.

1.1.3 Superatom Theory as it Relates to Nanoclusters

As mentioned previously, nanoclusters often have significant M(0) character, extensive metal-metal bonding, and tend to have well-defined speciation. To help explain these characteristics, cluster chemists utilize what is known as superatom theory.[40] According to this theory of electronic structure, the metal-metal bonding electrons are fully delocalized in the M(0) core of the nanocluster. These electrons occupy molecular orbitals (MOs) that are derived from the metal valence s-orbitals, which follow the same aufbau principle as atomic orbitals, though the ordering of the energy levels is different, as follows: $1S^21P^61D^{10}2S^21F^{14}2P^61G^{18}2D^{10}3S^21H^{22}$… etc., where S, P, D, F, G, and H are the angular momentum quantum numbers of the orbitals.[40] As these orbitals are filled and closed shell electronic configurations are generated, the nanocluster equivalent of a noble gas configuration is formed, which helps explain the speciation of these materials. That is, clusters

with these closed shell configurations, i.e., those that have achieved a "magic number" configuration, can be viewed as occupying a local thermodynamic minimum. However, the relative energies of these clusters are often similar and the thermodynamic barrier to cluster conversion can be small.[40] As a result, several "magic number" gold nanoclusters are generated at short reaction times, which converge to a more stable product(s) as the reaction progresses, which was confirmed by Dass and co-workers who monitored the speciation of gold nanoclusters by mass spectrometry over the course of several days.[41]

To determine the magic number (N^*) of a nanocluster, the simple equation $N^* = N_{vA} - M - z$ is used, where N is the number of metal atoms in the cluster, v_A is the number of valence electrons of those metal atoms (for example, Au has $v_A = 1$ from the $6s^1$ orbital, Al would have $v_A = 3$ from the $2s^2 2p^1$ configuration, *etc*.), M is the number of singly charged anionic ligands (thiolates count for one, sulfides count for two, and PPh_3 counts for zero), and z is the overall charge on the cluster. For example, $[Cu_{25}H_{22}(PPh_3)_{12}]^+$ would have a closed shell $N^* = 2$ from $N = 25$, $v_A = 1$, $M = 22$, and $z = 1$. According to this theory, clusters with a wide range of N^* (2, 8, 18, 20, 34, 58…) should be isolable, though these closed shell configurations are only applicable to spherical clusters as oblate or prolate cluster follow different electron counting rules.[42]

1.2 Expanding the Nanocluster Scope to Other Transition Metals

To date, the research on transition metal nanoclusters outside of group 11 remains sparse (Figure 1.2). Though metal-carbonyl clusters have been well-documented,[43] their classification as nanoclusters is tenuous. These complexes are typically small in size (<8 metal centers) and of uncertain oxidation state, which makes the assignment of M(0) character to these species nearly impossible. There are a handful of example of nickel and cobalt carbonyl

clusters that are relatively large and mixed-valent, though these complexes act as cage compounds to interstitial phosphides and carbides, respectively.[44-45] Outside of the transition metals, Andreas Schnepf, Hangeorg Schnöckel, and others have reported extensive studies on clusters of Zn and various metalloids, such as $[Li(THF)_2]_3[Ge_{14}\{Ge(SiMe_3)_3\}_5]$, $Si@Al_{56}[N\{(2,6\text{-}^{i}Pr_2C_6H_3)(SiMe_3)\}]_{12}$, $[Ga_{19}\{(C(SiMe_{3)6}\}]^-$, and others.[46-52]

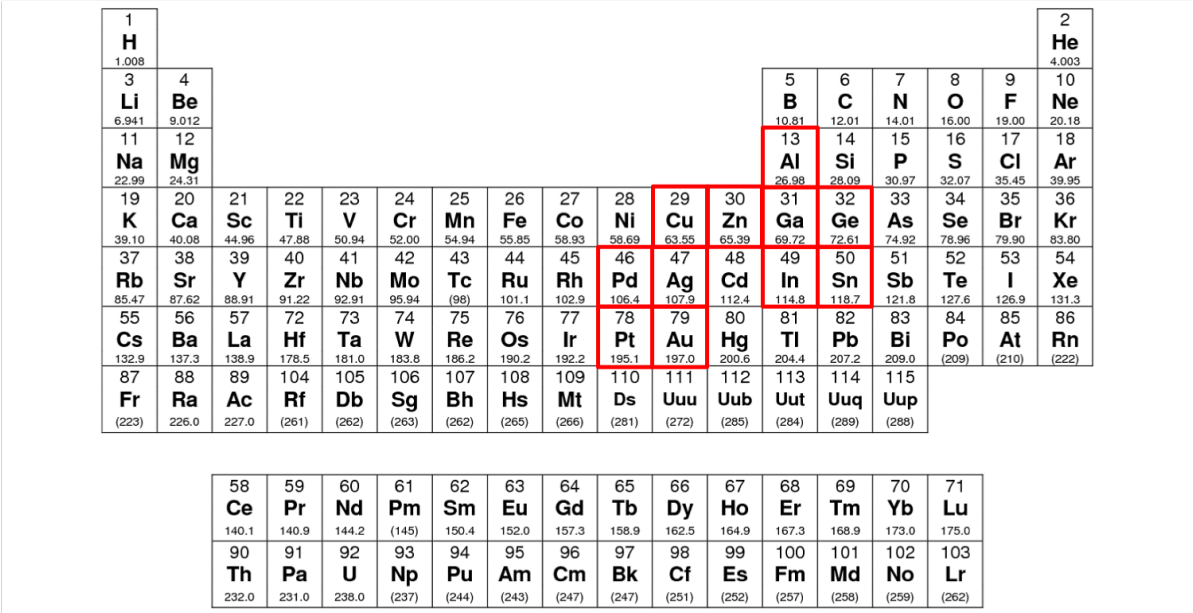

Figure 1.2. Periodic table showing the elements with known nanoclusters, highlighted in red.

1.2.1 Clusters of Palladium and Platinum

One approach in which palladium and platinum nanoclusters have been synthesized is through the reduction of metal salt precursors in the presence of carbon monoxide and phosphine ligands.[53] In this manner, the $Pd_{10}(CO)_{12}(PR_3)_6$ (R = ^{n}Bu, Et) cluster can be isolated in excellent yield. This cluster is only stable under an atmosphere of CO and will readily convert to $Pd_{23}(CO)_{20}(PEt_3)_{10}$ after exposure to inert gas.[54] This targeted decomposition approach can be refined to give the giant palladium clusters $Pd_{50}(CO)_{20}(P^{i}Pr_3)_{12}$ and $Pd_{145}(CO)_{60}(PEt_3)_{30}$.[55-56] A similar approach has been utilized to synthesize $[Pt_{33}(CO)_{38}]^{2-}$ and $[Pt_{40}(CO)_{40}]^{4-}$ from the Chini cluster, $[Pt_3(CO)_6]^{2-}$.[57]

Several attempts have been made to synthesize thiolate-protected nanoclusters of palladium and platinum through the reduction of metal salts by $NaBH_4$ in the presence of a thiol, as described above.[58] However, these materials were never characterized by XRD and their formulae were assigned solely on the basis of mass spectrometry. Without full structural characterization, there is significant doubt as to the chemical composition of these materials. It would appear that, like copper, generation of palladium and platinum nanoclusters must be accomplished via an alternate synthetic route. Given that phosphines and carbon monoxide are able to stabilize clusters of these metals,[53-57] strongly π-accepting ligands, such as ketimides, may be necessary to isolate nanoclusters of metals other than Au and Ag. The ability for these ligands to accept electron density should facilitate the formation and stabilization of a highly reduced, M(0) core.

1.2.2 Attempted Syntheses of Nickel and Iron Clusters

The synthesis of nickel and iron nanoclusters represents a significant challenge, as any low-valent complex of these metals will be highly sensitive to oxidation.[16] However, there have been a few attempts to isolate metal-thiolate nanoclusters for nickel, for example. [59-63] These reactions again follow the basic protocol of attempted reduction of a metal salt precursor in the presence of thiol; unfortunately in every case the only isolated products characterized by XRD are the Ni(II)-thiolate oligomers $[Ni(SCH_2CH_2Ph)_2]_x$ (x = 4, 6).[60-62] Though these reactions (nor the examples with copper, palladium, and palladium) did not produce the desired nanoclusters, they do provide insight into cluster formation. That is, it appears that the metal-thiolate coordination-clusters generated are thermodynamically stable and cannot be reduced by $NaBH_4$. Therefore, I hypothesize that it is not viable to simply transpose the synthetic techniques that are able to generate nanoclusters for gold and silver to

other metals, and that new methods of reducing the metal centers or generating less thermodynamically stable intermediates will be crucial moving forward.

To the best of my knowledge, there have been no reports of Fe(0)-containing nanoclusters to date, though recently, several groups have explored the synthesis of mixed-valent Fe(II)/Fe(I) clusters. In one case, an Fe(III) salt was reduced by RMgBr (R = Me, Ph) to generate the low-valent clusters $[MgCl(THF)_5][Fe_8Me_{12}]$ (Figure 1.3a) and $[Fe_4Ph_6(THF)_4]$ (Figure 1.3b).[64-65] Other examples of partially reduced Fe_3, Fe_4, Fe_6, and Fe_8 clusters have been synthesized through chemical reduction of the all-ferrous parent clusters with alkali metals.[66-71] Finally, both a Fe_4 arene/silylamide, as well as a Fe_7 hydride/silylamide clusters (Figure 1.3c) were isolated following the reduction of $Fe(N(SiMe_3)_2)_2$ with pinacolborane.[72-73] While none of these clusters have metallic Fe(0) character, their synthesis does highlight the need to move away from thiolate ligands and that stronger reducing agents will be required to isolate nanoclusters of these more recalcitrant metals.

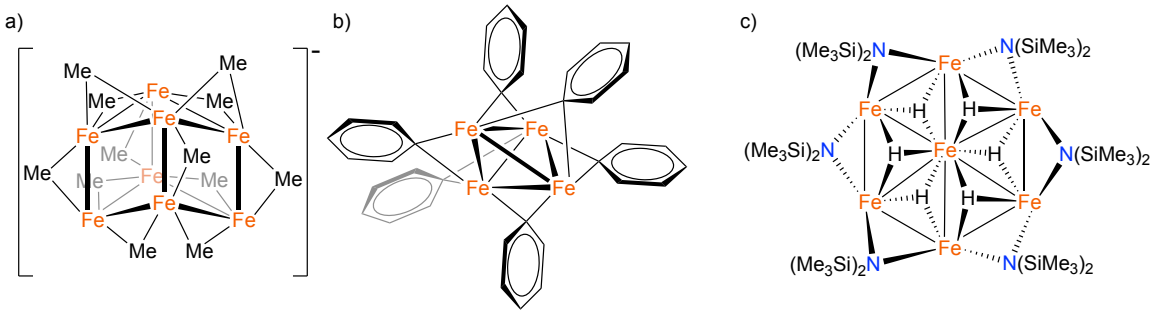

Figure 1.3. Structures of the mixed-valent Fe clusters, $[MgCl(THF)_5][Fe_8Me_{12}]$ (a, $MgCl^+$ counterion and THF molecules omitted for clarity, ref. 64); $[Fe_4Ph_6(THF)_4]$ (b, THF molecules omitted for clarity, ref. 65); and $[Fe_7H_6\{N(SiMe_3)_2\}_6]$ (c, ref 73).

1.3 Applications of Nanomaterials

The applications of these nanomaterials have been extensively studied and encompass a broad range of utilization.[12] Of particular interest to the Hayton group is the catalytic activity

of these compounds, which has been the subject of intense research for the last 50 years.[12] These materials have been shown to be effective catalysts for a variety of chemical transformations, including cycloadditions, cross-coupling, reduction, oxidation, electrocatalysis, and photocatalysis.[4, 6, 74] By far the most widely studied group of nanoparticles are those of the noble metals (Ag, Au, Pd, Pt, Ru, and Rh) due to their impressive catalytic activity as well as high stability to a variety of reaction conditions. Haruta and co-workers were among the first to observe that gold nanoparticles deposited onto metal-oxide surfaces were able to catalyze the oxidation of H_2 and CO.[75] Their catalyst was active even at low temperatures or high humidity, and remained active for up to 7 days. These catalytic oxidation reactions have been expanded to organic substrates. Moreover, the current industrial catalyst for ethylene epoxidation consists of silver nanoparticles;[76] additionally, platinum group and gold nanomaterials can perform the selective oxidations of alcohols.[77-78] On the reductive side, platinum nanoparticles in the presence of H_2 are efficient hydrogenation catalysts for alkyl, aryl, aromatic, and cyclic substrates.[74, 79-81]

Copper based nanomaterials have also received a great deal of attention for their use as catalysts in organic reactions, lignin depolymerization, as well as in the reduction of CO_2.[6] For example, Varma and co-workers demonstrated the ability for chitosan immobilized copper nanoparticles to efficiently catalyze the ubiquitous Huisgen [3+2] cycloaddition of azides and alkynes (colloquially known as "Click" chemistry), as well as recycle their catalyst.[82] Additionally, Ford and co-workers developed the "UCSB process" in which a copper-doped porous metal oxide catalyst in supercritical methanol quantitatively transformed woody biomass (sawdust) into liquid fuels.[83] Subsequent reports by the Ford group have improved the selectivity of this reaction to give aromatic hydrocarbon compounds.[84-86] Copper

nanoparticles are also unique in their ability to promote C-C bond formation via electrocatalytic reduction of CO_2.[6] Yeo and co-workers have successfully converted CO_2 to ethylene electrocatalytically using copper nanoparticles embedded in a Cu_2O film and Nilsson and co-workers have shown similar reactivity for copper nanocubes.[87-88] Unfortunately, these materials required large overpotentials and generally had low faradaic efficiencies. However, the Hayton group reported that a copper-hydride cluster, $[Cu_{14}H_{12}(phen)_6][Cl]_2$, was able to stoichiometrically convert CO_2 to formate, suggesting catalytic reduction may be possible.[89] Copper-hydride nanoclusters have also been shown to catalyze a wide range of organic transformations.[90] While it remains unclear if these materials maintain their nuclearity during catalysis, such metal-metal cooperativity could completely alter the mechanism or regioselectivity of the reaction.

Iron and cobalt nanocatalysts have been less extensively studied as their instability in air renders them difficult to work with and limits the scope of their reactivity.[4, 76] However, small iron particles have been implicated as the reactive species in ammonia formation through the Haber-Bosch process.[91] Similarly, iron and cobalt nanoparticles have been utilized in the Fischer-Tropsch process to generate long-chain hydrocarbons from CO and H_2.[92-94] Significantly, these materials showed efficiencies approaching conventional rhodium catalysts.

Unsurprisingly, many of the properties of these nanoparticles are controlled not only by their chemical composition, but also their morphology and size.[3, 7, 74] For example, Tsukuda and co-workers demonstrated that the rate of oxidation of 4-hydroxy-benzyl alcohol is highly dependent on the size of the gold nanocatalyst, with smaller particles exhibiting much faster normalized rates (Figure 1.4).[15, 95] Understanding the precise relationship between particle

size/morphology and reactivity is therefore critically important in the development of new, better materials.

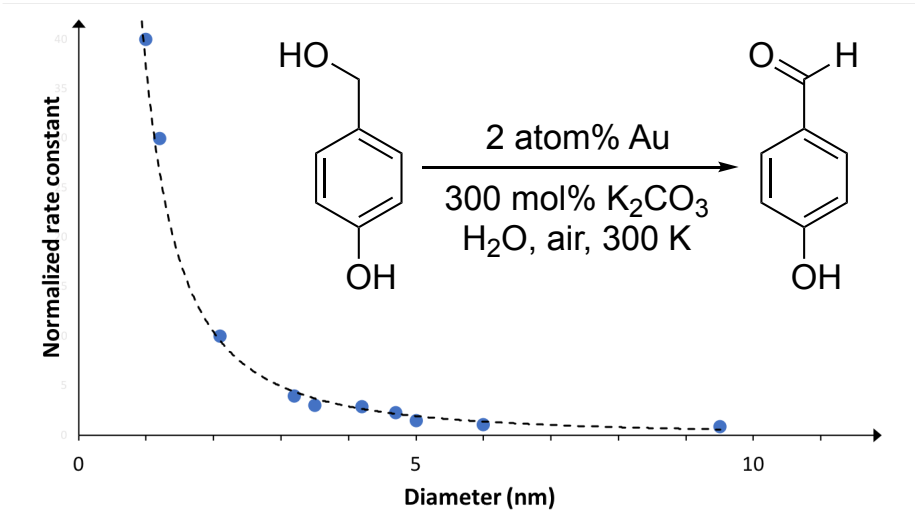

Figure 1.4. Dependence of catalytic activity on the size of gold nanoparticle. From ref. 95.

However, the polydispersity and ill-defined surface chemistry of nanoparticles prevents any correlation to be drawn between structure and function. While metal-thiolate nanoclusters have the benefit of being perfectly monodisperse and atomically precise, they often require harsh pretreatment (heating to >100 ºC under an O_2 atmosphere) to partially remove their thiolate ligands before they become active catalysts.[14, 96] Therefore, while these nanomaterials show promising activity, the reaction mechanisms and active species remain unclear. The development of nanocatalysts which are highly reactive in their own regard, or are protected by reactive ligands such as acetylides and hydrides, will be necessary moving forward.

1.4 General Remarks

The research described herein represents an effort to develop new synthetic procedures for the generation of transition metal nanoclusters, as well as explore the use of new stabilizing ligands, such as ketimides and acetylides. The research also explores the potential applications of these new and exciting materials, such as catalysis and magnetism. Group 11 clusters were

the initial targets of this research, though strides have also been made to more fully understand Pd and Pt clusters as well as to develop synthetic protocols for Co and Fe clusters.

Chapter 2 describes the synthesis, characterization, and reactivity of new group 11 hydride clusters. Using a bidentate phosphine ligand, the first silver polyhydride cluster, Ag_6, as well as a trimetallic copper hydride complex, Cu_3, were synthesized. The effect of bite angle of the bidentate phosphine and size of the Cu cluster generated was also explored. The reactivity of $[CuH(PPh_3)]_6$ and Ph_2Se_2 was determined which yielded a Cu_{13}-selenoate cluster. Notably, the Ag_6 and Cu_3 clusters were able to catalyze the 1,4- and 1,2-hydrosilylation of (α,β-unsaturated) ketones.

Chapter 3 explores the reduction of Cu(II) salts with thiols in an effort to synthesize Cu-thiolate clusters. Literature precedent suggested reduction to low-valent Cu(0) was possible under these conditions, however through X-ray crystallography, NMR spectroscopy, mass spectrometry, and X-ray absorption spectroscopy, it was determined that the Cu(I) coordination clusters Cu_{17} and Cu_{18} were the only products from these reactions. Both of the clusters feature a $[Cu_{12}S_6]$ "Atlas-sphere" core structure and display orange luminescence in the solid-state. An argument for more thorough characterization of nanoclusters, especially for those with potential applications, is made.

Chapter 4 details the synthesis and characterization of a Cu_{20} superatom, with $N^* = 2$, bearing acetylide ligands. This complex was investigated with a combination of X-ray crystallography, NMR spectroscopy, mass spectrometry, and X-ray absorption spectroscopy. Notably, the acetylide moieties have been activated and the Cu_{20} cluster acts as a competent catalyst for "Click" chemistry. Cu_{20} can be deposited on a silica support and was shown to

perform heterogeneous catalysis, as well. The deposited cluster was recovered with full reactivity and little to no degradation or deformation of cluster, as demonstrated by EXAFS.

Chapter 5 highlights a re-examination of the reported preparation of mixed-valent Co-thiolate clusters. Attempts to replicate the published procedure led to the isolation of a Co_{10} coordination complex with no Co(0) character or Co-Co bonds. This cluster was then synthesized rationally and characterized via X-ray crystallography, NMR spectroscopy, and mass spectrometry. Experiments to utilize Co_{10} as a seed for cluster growth were also conducted. Additionally, exposure of Co_{10} to air and water resulted in the formation of a product with remarkably similar physical properties to the originally reported material. This result prompted a discussion on the importance of the rigorous exclusion of air in nanocluster synthesis.

Chapter 6 investigates the ability of ketimide ligands to stabilize low-valent Pd, Pt, and Fe clusters. Previous research in the Hayton group indicated that low-valent Pd_7 and Fe_4 species were isolable, though their initial characterization was sparse. The syntheses of these materials, as well as various Pt(II) ketimide complexes, has been improved and their characterization completed. Additionally, the mechanism of formation of the Pd and Pt complexes was probed using *in situ* NMR spectroscopy. The oxidation state and magnetization of the Fe_4 complex was also probed through Mössbauer spectroscopy and SQUID magnetometry. Significantly, the complex was found to have a mixed-valent Fe(II)/Fe(I) oxidation state and $S = 7$ room temperature spin ground-state.

1.5 References

(1) Faraday, M., X. The Bakerian Lecture. — Experimental relations of gold (and other metals) to light. *Philos. Trans. R. Soc. London* **1857**, *147*, 145.

(2) Edwards, P. P.; Thomas, J. M., Gold in a Metallic Divided State—From Faraday to Present-Day Nanoscience. *Angew. Chem., Int. Ed.* **2007**, *46*, 5480-5486.

(3) Burda, C.; Chen, X.; Narayanan, R.; El-Sayed, M. A., Chemistry and Properties of Nanocrystals of Different Shapes. *Chem. Rev.* **2005**, *105*, 1025-1102.

(4) Huber, D. L., Synthesis, Properties, and Applications of Iron Nanoparticles. *Small* **2005**, *1*, 482-501.

(5) Zhao, P.; Li, N.; Astruc, D., State of the art in gold nanoparticle synthesis. *Coord. Chem. Rev.* **2013**, *257*, 638-665.

(6) Gawande, M. B.; Goswami, A.; Felpin, F.-X.; Asefa, T.; Huang, X.; Silva, R.; Zou, X.; Zboril, R.; Varma, R. S., Cu and Cu-Based Nanoparticles: Synthesis and Applications in Catalysis. *Chem. Rev.* **2016**, *116*, 3722-3811.

(7) Xia, Y.; Xiong, Y.; Lim, B.; Skrabalak, S. E., Shape-Controlled Synthesis of Metal Nanocrystals: Simple Chemistry Meets Complex Physics? *Angew. Chem., Int. Ed.* **2009**, *48*, 60-103.

(8) Turkevich, J.; Stevenson, P. C.; Hillier, J., A study of the nucleation and growth processes in the synthesis of colloidal gold. *Faraday Discuss.* **1951**, *11*, 55-75.

(9) Frens, G., Controlled Nucleation for the Regulation of the Particle Size in Monodisperse Gold Suspensions. *Nat.-Phys. Sci.* **1973**, *241*, 20.

(10) Brust, M.; Walker, M.; Bethell, D.; Schiffrin, D. J.; Whyman, R., Synthesis of thiol-derivatised gold nanoparticles in a two-phase Liquid–Liquid system. *J. Chem. Soc., Chem. Commun.* **1994**, 801-802.

(11) Daniel, M.-C.; Astruc, D., Gold Nanoparticles: Assembly, Supramolecular Chemistry, Quantum-Size-Related Properties, and Applications toward Biology, Catalysis, and Nanotechnology. *Chem. Rev.* **2004**, *104*, 293-346.

(12) Deepak, F. L.; Anumol, E. A.; Li, J., Advanced Electron Microscopy Techniques Toward the Understanding of Metal Nanoparticles and Clusters. In *Metal Nanoparticles and Clusters: Advances in Synthesis, Properties and Applications*, Deepak, F. L., Ed. Springer International Publishing: Cham, 2018; pp 219-287.

(13) Azcárate, J. C.; Fonticelli, M. H.; Zelaya, E., Radiation Damage Mechanisms of Monolayer-Protected Nanoparticles via TEM Analysis. *J. Phys. Chem. C* **2017**, *121*, 26108-26116.

(14) Jin, R.; Zeng, C.; Zhou, M.; Chen, Y., Atomically Precise Colloidal Metal Nanoclusters and Nanoparticles: Fundamentals and Opportunities. *Chem. Rev.* **2016**, *116*, 10346-10413.

(15) Yamazoe, S.; Koyasu, K.; Tsukuda, T., Nonscalable Oxidation Catalysis of Gold Clusters. *Acc. Chem. Res.* **2014**, *47*, 816-824.

(16) Bratsch, S. G., Standard Electrode Potentials and Temperature Coefficients in Water at 298.15 K. *J. Phys. Chem. Ref. Data* **1989**, *18*, 1-21.

(17) Malatesta, L., Cluster compounds of gold. *Gold Bull.* **1975**, *8*, 48-52.

(18) Mingos, D. M. P., Gold cluster compounds. *Gold Bull.* **1984**, *17*, 5-12.

(19) Schmid, G.; Pfeil, R.; Boese, R.; Bandermann, F.; Meyer, S.; Calis, G. H. M.; van der Velden, J. W. A., $Au_{55}[P(C_6H_5)_3]_{12}Cl_6$ — ein Goldcluster ungewöhnlicher Größe. *Chem. Ber.* **1981**, *114*, 3634-3642.
(20) Teo, B. K.; Shi, X.; Zhang, H., Pure gold cluster of 1:9:9:1:9:9:1 layered structure: a novel 39-metal-atom cluster $[(Ph_3P)_{14}Au_{39}Cl_6]Cl_2$ with an interstitial gold atom in a hexagonal antiprismatic cage. *J. Am. Chem. Soc.* **1992**, *114*, 2743-2745.
(21) Jadzinsky, P. D.; Calero, G.; Ackerson, C. J.; Bushnell, D. A.; Kornberg, R. D., Structure of a Thiol Monolayer-Protected Gold Nanoparticle at 1.1 Å Resolution. *Science* **2007**, *318*, 430-433.
(22) Heaven, M. W.; Dass, A.; White, P. S.; Holt, K. M.; Murray, R. W., Crystal Structure of the Gold Nanoparticle $[N(C_8H_{17})_4][Au_{25}(SCH_2CH_2Ph)_{18}]$. *J. Am. Chem. Soc.* **2008**, *130*, 3754-3755.
(23) Zhu, M.; Aikens, C. M.; Hollander, F. J.; Schatz, G. C.; Jin, R., Correlating the Crystal Structure of A Thiol-Protected Au_{25} Cluster and Optical Properties. *J. Am. Chem. Soc.* **2008**, *130*, 5883-5885.
(24) Dainese, T.; Antonello, S.; Gascón, J. A.; Pan, F.; Perera, N. V.; Ruzzi, M.; Venzo, A.; Zoleo, A.; Rissanen, K.; Maran, F., $Au_{25}(SEt)_{18}$, a Nearly Naked Thiolate-Protected Au_{25} Cluster: Structural Analysis by Single Crystal X-ray Crystallography and Electron Nuclear Double Resonance. *ACS Nano* **2014**, *8*, 3904-3912.
(25) Yan, N.; Xia, N.; Liao, L.; Zhu, M.; Jin, F.; Jin, R.; Wu, Z., Unraveling the long-pursued Au_{144} structure by x-ray crystallography. *Sci. Adv.* **2018**, *4*, eaat7259.
(26) Zeng, C.; Chen, Y.; Kirschbaum, K.; Lambright, K. J.; Jin, R., Emergence of hierarchical structural complexities in nanoparticles and their assembly. *Science* **2016**, *354*, 1580-1584.
(27) Higaki, T.; Zhou, M.; Lambright, K. J.; Kirschbaum, K.; Sfeir, M. Y.; Jin, R., Sharp Transition from Nonmetallic Au_{246} to Metallic Au_{279} with Nascent Surface Plasmon Resonance. *J. Am. Chem. Soc.* **2018**, *140*, 5691-5695.
(28) Sakthivel, N. A.; Stener, M.; Sementa, L.; Fortunelli, A.; Ramakrishna, G.; Dass, A., $Au_{279}(SR)_{84}$: The Smallest Gold Thiolate Nanocrystal That Is Metallic and the Birth of Plasmon. *J. Phys. Chem. Lett.* **2018**, *9*, 1295-1300.
(29) Lei, Z.; Wan, X.-K.; Yuan, S.-F.; Guan, Z.-J.; Wang, Q.-M., Alkynyl Approach toward the Protection of Metal Nanoclusters. *Acc. Chem. Res.* **2018**, *51*, 2465-2474.
(30) Desireddy, A.; Conn, B. E.; Guo, J.; Yoon, B.; Barnett, R. N.; Monahan, B. M.; Kirschbaum, K.; Griffith, W. P.; Whetten, R. L.; Landman, U.; Bigioni, T. P., Ultrastable silver nanoparticles. *Nature* **2013**, *501*, 399.
(31) Yang, H.; Wang, Y.; Huang, H.; Gell, L.; Lehtovaara, L.; Malola, S.; Häkkinen, H.; Zheng, N., All-thiol-stabilized Ag_{44} and $Au_{12}Ag_{32}$ nanoparticles with single-crystal structures. *Nat. Commun.* **2013**, *4*, 2422.
(32) Joshi, C. P.; Bootharaju, M. S.; Alhilaly, M. J.; Bakr, O. M., $[Ag_{25}(SR)_{18}]^-$: The "Golden" Silver Nanoparticle. *J. Am. Chem. Soc.* **2015**, *137*, 11578-11581.
(33) Song, Y.; Lambright, K.; Zhou, M.; Kirschbaum, K.; Xiang, J.; Xia, A.; Zhu, M.; Jin, R., Large-Scale Synthesis, Crystal Structure, and Optical Properties of the $Ag_{146}Br_2(SR)_{80}$ Nanocluster. *ACS Nano* **2018**, *12*, 9318-9325.

(34) Sharma, S.; Chakrahari, K. K.; Saillard, J.-Y.; Liu, C. W., Structurally Precise Dichalcogenolate-Protected Copper and Silver Superatomic Nanoclusters and Their Alloys. *Acc. Chem. Res.* **2018**, *51*, 2475-2483.
(35) Yang, H.; Wang, Y.; Yan, J.; Chen, X.; Zhang, X.; Häkkinen, H.; Zheng, N., Structural Evolution of Atomically Precise Thiolated Bimetallic $[Au_{12+n}Cu_{32}(SR)_{30+n}]^{4-}$ (n = 0, 2, 4, 6) Nanoclusters. *J. Am. Chem. Soc.* **2014**, *136*, 7197-7200.
(36) Wan, X.-K.; Cheng, X.-L.; Tang, Q.; Han, Y.-Z.; Hu, G.; Jiang, D.-e.; Wang, Q.-M., Atomically Precise Bimetallic $Au_{19}Cu_{30}$ Nanocluster with an Icosidodecahedral Cu_{30} Shell and an Alkynyl–Cu Interface. *J. Am. Chem. Soc.* **2017**, *139*, 9451-9454.
(37) Nguyen, T.-A. D.; Jones, Z. R.; Goldsmith, B. R.; Buratto, W. R.; Wu, G.; Scott, S. L.; Hayton, T. W., A Cu_{25} Nanocluster with Partial Cu(0) Character. *J. Am. Chem. Soc.* **2015**, *137*, 13319-13324.
(38) Nguyen, T.-A. D.; Jones, Z. R.; Leto, D. F.; Wu, G.; Scott, S. L.; Hayton, T. W., Ligand-Exchange-Induced Growth of an Atomically Precise Cu_{29} Nanocluster from a Smaller Cluster. *Chem. Mater.* **2016**, *28*, 8385-8390.
(39) Nguyen, T.-A. D.; Cook, A. W.; Wu, G.; Hayton, T. W., Subnanometer-Sized Copper Clusters: A Critical Re-evaluation of the Synthesis and Characterization of $Cu_8(MPP)_4$ (HMPP = 2-Mercapto-5-*n*-propylpyrimidine). *Inorg. Chem.* **2017**, *56*, 8390-8396.
(40) Walter, M.; Akola, J.; Lopez-Acevedo, O.; Jadzinsky, P. D.; Calero, G.; Ackerson, C. J.; Whetten, R. L.; Grönbeck, H.; Häkkinen, H., A unified view of ligand-protected gold clusters as superatom complexes. *Proc. Natl. Acad. Sci.* **2008**, *105*, 9157.
(41) Dharmaratne, A. C.; Krick, T.; Dass, A., Nanocluster Size Evolution Studied by Mass Spectrometry in Room Temperature $Au_{25}(SR)_{18}$ Synthesis. *J. Am. Chem. Soc.* **2009**, *131*, 13604-13605.
(42) Mingos, D. M. P., Structural and bonding patterns in gold clusters. *Dalton Trans.* **2015**, *44*, 6680-6695.
(43) Dyson, P. J.; McIndoe, J. S., *Transition Metal Carbonyl Cluster Chemistry*. Gordon and Breach Science Publishers: Imperial College, London, United Kingdom, 2000.
(44) Ciabatti, I.; Femoni, C.; Gaboardi, M.; Iapalucci, M. C.; Longoni, G.; Pontiroli, D.; Riccò, M.; Zacchini, S., Structural rearrangements induced by acid–base reactions in metal carbonyl clusters: the case of $[H_{3-n}Co_{15}Pd_9C_3(CO)_{38}]^{n-}$ (n = 0–3). *Dalton Trans.* **2014**, *43*, 4388-4399.
(45) Capacci, C.; Ciabatti, I.; Femoni, C.; Iapalucci, M. C.; Funaioli, T.; Zacchini, S.; Zanotti, V., Molecular Nickel Phosphide Carbonyl Nanoclusters: Synthesis, Structure, and Electrochemistry of $[Ni_{11}P(CO)_{18}]^{3-}$ and $[H_{6-n}Ni_{31}P_4(CO)_{39}]^{n-}$ (n = 4 and 5). *Inorg. Chem.* **2018**, *57*, 1136-1147.
(46) Schnepf, A., Metalloid group 14 cluster compounds: An introduction and perspectives to this novel group of cluster compounds. *Chem. Soc. Rev.* **2007**, *36*, 745-758.
(47) Huber, M.; Schnepf, A.; Anson, C. E.; Schnöckel, H., $Si@Al_{56}[N(2,6\text{-}{}^{i}Pr_2C_6H_3)SiMe_3]_{12}$: The Largest Neutral Metalloid Aluminum Cluster, a Molecular Model for a Silicon-Poor Aluminum–Silicon Alloy? *Angew. Chem., Int. Ed.* **2008**, *47*, 8201-8206.

(48) Schnockel, H., Formation, structure and bonding of metalloid Al and Ga clusters. A challenge for chemical efforts in nanosciences. *Dalton Trans.* **2008**, 4344-4362.
(49) Schnepf, A., Metalloid cluster compounds of germanium: novel structural motives on the way to elemental germanium! *New J. Chem.* **2010**, *34*, 2079-2092.
(50) Scharfe, S.; Kraus, F.; Stegmaier, S.; Schier, A.; Fässler, T. F., Zintl Ions, Cage Compounds, and Intermetalloid Clusters of Group 14 and Group 15 Elements. *Angew. Chem., Int. Ed.* **2011**, *50*, 3630-3670.
(51) Kysliak, O.; Schrenk, C.; Schnepf, A., The Largest Metalloid Group 14 Cluster, $Ge_{18}[Si(SiMe_3)_3]_6$: An Intermediate on the Way to Elemental Germanium. *Angew. Chem., Int. Ed.* **2016**, *55*, 3216-3219.
(52) Heider, Y.; Scheschkewitz, D., Stable unsaturated silicon clusters (siliconoids). *Dalton Trans.* **2018**, *47*, 7104-7112.
(53) Mednikov, E. G.; Dahl, L. F., Syntheses, structures and properties of primarily nanosized homo/heterometallic palladium CO/PR_3-ligated clusters. *Philos. Trans. Royal Soc. A* **2010**, *368*, 1301-1332.
(54) Mednikov, E. G.; Wittayakun, J.; Dahl, L. F., Synthesis and Stereochemical/Electrochemical Analyses of Cuboctahedral-Based $Pd_{23}(CO)_x(PR_3)_{10}$ Clusters (x=20 with $R_3=Bu^n_3$, Me_2Ph; x=20, 21, 22 with $R_3=Et_3$): Geometrically Analogous $Pd_{23}(PEt_3)_{10}$ Fragments with Variable Carbonyl Ligations and Resulting Implications. *J. Cluster Sci.* **2005**, *16*, 429-454.
(55) Mednikov, E. G.; Jewell, M. C.; Dahl, L. F., Nanosized (μ_{12}-Pt)$Pd_{164-x}Pt_x(CO)_{72}(PPh_3)_{20}$ ($x \approx 7$) Containing Pt-Centered Four-Shell 165-Atom Pd−Pt Core with Unprecedented Intershell Bridging Carbonyl Ligands: Comparative Analysis of Icosahedral Shell-Growth Patterns with Geometrically Related $Pd_{145}(CO)_x(PEt_3)_{30}$ ($x \approx 60$) Containing Capped Three-Shell Pd_{145} Core. *J. Am. Chem. Soc.* **2007**, *129*, 11619-11630.
(56) Erickson, J. D.; Mednikov, E. G.; Ivanov, S. A.; Dahl, L. F., Isolation and Structural Characterization of a Mackay 55-Metal-Atom Two-Shell Icosahedron of Pseudo-I_h Symmetry, $Pd_{55}L_{12}(\mu_3\text{-}CO)_{20}$ (L = PR_3, R = Isopropyl): Comparative Analysis with Interior Two-Shell Icosahedral Geometries in Capped Three-Shell Pd_{145}, Pt-Centered Four-Shell Pd–Pt M_{165}, and Four-Shell Au_{133} Nanoclusters. *J. Am. Chem. Soc.* **2016**, *138*, 1502-1505.
(57) Cattabriga, E.; Ciabatti, I.; Femoni, C.; Funaioli, T.; Iapalucci, M. C.; Zacchini, S., Syntheses, Structures, and Electrochemistry of the Defective ccp $[Pt_{33}(CO)_{38}]^{2-}$ and the bcc $[Pt_{40}(CO)_{40}]^{6-}$ Molecular Nanoclusters. *Inorg. Chem.* **2016**, *55*, 6068-6079.
(58) Chakraborty, I.; Pradeep, T., Atomically Precise Clusters of Noble Metals: Emerging Link between Atoms and Nanoparticles. *Chem. Rev.* **2017**, *117*, 8208-8271.
(59) Ji, J.; Wang, G.; Wang, T.; You, X.; Xu, X., Thiolate-protected Ni_{39} and Ni_{41} nanoclusters: synthesis, self-assembly and magnetic properties. *Nanoscale* **2014**, *6*, 9185-9191.
(60) Kagalwala, H. N.; Gottlieb, E.; Li, G.; Li, T.; Jin, R.; Bernhard, S., Photocatalytic Hydrogen Generation System Using a Nickel-Thiolate Hexameric Cluster. *Inorg. Chem.* **2013**, *52*, 9094-9101.
(61) Zhu, M.; Zhou, S.; Yao, C.; Liao, L.; Wu, Z., Reduction-resistant and reduction-catalytic double-crown nickel nanoclusters. *Nanoscale* **2014**, *6*, 14195-14199.

(62) Joya, K. S.; Sinatra, L.; AbdulHalim, L. G.; Joshi, C. P.; Hedhili, M. N.; Bakr, O. M.; Hussain, I., Atomically monodisperse nickel nanoclusters as highly active electrocatalysts for water oxidation. *Nanoscale* **2016**, *8*, 9695-9703.
(63) Pollitt, S.; Pittenauer, E.; Rameshan, C.; Schachinger, T.; Safonova, O. V.; Truttmann, V.; Bera, A.; Allmaier, G.; Barrabés, N.; Rupprechter, G., Synthesis and Properties of Monolayer-Protected $Co_x(SC_2H_4Ph)_m$ Nanoclusters. *J. Phys. Chem. C* **2017**, *121*, 10948-10956.
(64) Muñoz III, S. B.; Daifuku, S. L.; Brennessel, W. W.; Neidig, M. L., Isolation, Characterization, and Reactivity of $Fe_8Me_{12}^-$: Kochi's S = 1/2 Species in Iron-Catalyzed Cross-Couplings with MeMgBr and Ferric Salts. *J. Am. Chem. Soc.* **2016**, *138*, 7492-7495.
(65) Carpenter, S. H.; Baker, T. M.; Muñoz, S. B.; Brennessel, W. W.; Neidig, M. L., Multinuclear iron–phenyl species in reactions of simple iron salts with PhMgBr: identification of $Fe_4(\mu\text{-}Ph)_6(THF)_4$ as a key reactive species for cross-coupling catalysis. *Chem. Sci.* **2018**, *9*, 7931-7939.
(66) Zhao, Q.; Harris, T. D.; Betley, T. A., $[(^{H}L)_2Fe_6(NCMe)_m]^{n+}$ (m = 0, 2, 4, 6; n = −1, 0, 1, 2, 3, 4, 6): An Electron-Transfer Series Featuring Octahedral Fe_6 Clusters Supported by a Hexaamide Ligand Platform. *J. Am. Chem. Soc.* **2011**, *133*, 8293-8306.
(67) Hernández Sánchez, R.; Betley, T. A., Meta-Atom Behavior in Clusters Revealing Large Spin Ground States. *J. Am. Chem. Soc.* **2015**, *137*, 13949-13956.
(68) Hernández Sánchez, R.; Zheng, S.-L.; Betley, T. A., Ligand Field Strength Mediates Electron Delocalization in Octahedral $[(^{H}L)_2Fe_6(L')_m]^{n+}$ Clusters. *J. Am. Chem. Soc.* **2015**, *137*, 11126-11143.
(69) Lichtenberg, C.; Garcia Rubio, I.; Viciu, L.; Adelhardt, M.; Meyer, K.; Jeschke, G.; Grützmacher, H., A Low-Valent Iron Imido Heterocubane Cluster: Reversible Electron Transfer and Catalysis of Selective C–C Couplings. *Angew. Chem., Int. Ed.* **2015**, *54*, 13012-13017.
(70) Sánchez, R. H.; Willis, A. M.; Zheng, S.-L.; Betley, T. A., Synthesis of Well-Defined Bicapped Octahedral Iron Clusters $[(trenL)_2Fe_8(PMe_2Ph)_2]^n$ (n = 0, −1). *Angew. Chem., Int. Ed.* **2015**, *54*, 12009-12013.
(71) Sánchez, R. H.; Betley, T. A., Thermally Persistent High-Spin Ground States in Octahedral Iron Clusters. *J. Am. Chem. Soc.* **2018**, *140*, 16792-16806.
(72) Araake, R.; Sakadani, K.; Tada, M.; Sakai, Y.; Ohki, Y., $[Fe_4]$ and $[Fe_6]$ Hydride Clusters Supported by Phosphines: Synthesis, Characterization, and Application in N_2 Reduction. *J. Am. Chem. Soc.* **2017**, *139*, 5596-5606.
(73) Gieshoff, T. N.; Chakraborty, U.; Villa, M.; Jacobi von Wangelin, A., Alkene Hydrogenations by Soluble Iron Nanocluster Catalysts. *Angew. Chem., Int. Ed.* **2017**, *56*, 3585-3589.
(74) Liu, L.; Corma, A., Metal Catalysts for Heterogeneous Catalysis: From Single Atoms to Nanoclusters and Nanoparticles. *Chem. Rev.* **2018**,
(75) Haruta, M.; Yamada, N.; Kobayashi, T.; Iijima, S., Gold catalysts prepared by coprecipitation for low-temperature oxidation of hydrogen and of carbon monoxide. *J. Catal.* **1989**, *115*, 301-309.
(76) Ramirez, A.; Hueso, J. L.; Suarez, H.; Mallada, R.; Ibarra, A.; Irusta, S.; Santamaria, J., A Nanoarchitecture Based on Silver and Copper Oxide with an

Exceptional Response in the Chlorine-Promoted Epoxidation of Ethylene. *Angew. Chem., Int. Ed.* **2016**, *55*, 11158-11161.
(77) Mallat, T.; Baiker, A., Oxidation of Alcohols with Molecular Oxygen on Solid Catalysts. *Chem. Rev.* **2004**, *104*, 3037-3058.
(78) Abad, A.; Concepción, P.; Corma, A.; García, H., A Collaborative Effect between Gold and a Support Induces the Selective Oxidation of Alcohols. *Angew. Chem., Int. Ed.* **2005**, *44*, 4066-4069.
(79) Song, H.; Rioux, R. M.; Hoefelmeyer, J. D.; Komor, R.; Niesz, K.; Grass, M.; Yang, P.; Somorjai, G. A., Hydrothermal Growth of Mesoporous SBA-15 Silica in the Presence of PVP-Stabilized Pt Nanoparticles: Synthesis, Characterization, and Catalytic Properties. *J. Am. Chem. Soc.* **2006**, *128*, 3027-3037.
(80) Kliewer, C. J.; Aliaga, C.; Bieri, M.; Huang, W.; Tsung, C.-K.; Wood, J. B.; Komvopoulos, K.; Somorjai, G. A., Furan Hydrogenation over Pt(111) and Pt(100) Single-Crystal Surfaces and Pt Nanoparticles from 1 to 7 nm: A Kinetic and Sum Frequency Generation Vibrational Spectroscopy Study. *J. Am. Chem. Soc.* **2010**, *132*, 13088-13095.
(81) Pushkarev, V. V.; Musselwhite, N.; An, K.; Alayoglu, S.; Somorjai, G. A., High Structure Sensitivity of Vapor-Phase Furfural Decarbonylation/Hydrogenation Reaction Network as a Function of Size and Shape of Pt Nanoparticles. *Nano Lett.* **2012**, *12*, 5196-5201.
(82) Baig, R. B. N.; Varma, R. S., Copper on chitosan: a recyclable heterogeneous catalyst for azide–alkyne cycloaddition reactions in water. *Green Chem.* **2013**, *15*, 1839-1843.
(83) Matson, T. D.; Barta, K.; Iretskii, A. V.; Ford, P. C., One-Pot Catalytic Conversion of Cellulose and of Woody Biomass Solids to Liquid Fuels. *J. Am. Chem. Soc.* **2011**, *133*, 14090-14097.
(84) Barrett, J. A.; Gao, Y.; Bernt, C. M.; Chui, M.; Tran, A. T.; Foston, M. B.; Ford, P. C., Enhancing Aromatic Production from Reductive Lignin Disassembly: *in Situ* O-Methylation of Phenolic Intermediates. *ACS Sustain. Chem. Eng.* **2016**, *4*, 6877-6886.
(85) Bernt, C. M.; Bottari, G.; Barrett, J. A.; Scott, S. L.; Barta, K.; Ford, P. C., Mapping reactivities of aromatic models with a lignin disassembly catalyst. Steps toward controlling product selectivity. *Catal. Sci. Technol.* **2016**, *6*, 2984-2994.
(86) Chui, M.; Metzker, G.; Bernt, C. M.; Tran, A. T.; Burtoloso, A. C. B.; Ford, P. C., Probing the Lignin Disassembly Pathways with Modified Catalysts Based on Cu-Doped Porous Metal Oxides. *ACS Sustain. Chem. Eng.* **2017**, *5*, 3158-3169.
(87) Ren, D.; Deng, Y.; Handoko, A. D.; Chen, C. S.; Malkhandi, S.; Yeo, B. S., Selective Electrochemical Reduction of Carbon Dioxide to Ethylene and Ethanol on Copper(I) Oxide Catalysts. *ACS Catalysis* **2015**, *5*, 2814-2821.
(88) Roberts, F. S.; Kuhl, K. P.; Nilsson, A., High Selectivity for Ethylene from Carbon Dioxide Reduction over Copper Nanocube Electrocatalysts. *Angew. Chem., Int. Ed.* **2015**, *54*, 5179-5182.
(89) Nguyen, T.-A. D.; Goldsmith, B. R.; Zaman, H. T.; Wu, G.; Peters, B.; Hayton, T. W., Synthesis and Characterization of a Cu_{14} Hydride Cluster Supported by Neutral Donor Ligands. *Chem. Eur. J.* **2015**, *21*, 5341-5344.

(90) Jordan, A. J.; Lalic, G.; Sadighi, J. P., Coinage Metal Hydrides: Synthesis, Characterization, and Reactivity. *Chem. Rev.* **2016**, *116*, 8318-8372.
(91) Dumesic, J. A.; Topsøe, H.; Khammouma, S.; Boudart, M., Surface, catalytic and magnetic properties of small iron particles: II. Structure sensitivity of ammonia synthesis. *J. Catal.* **1975**, *37*, 503-512.
(92) Suslick, K. S.; Hyeon, T.; Fang, M., Nanostructured Materials Generated by High-Intensity Ultrasound: Sonochemical Synthesis and Catalytic Studies. *Chem. Mater.* **1996**, *8*, 2172-2179.
(93) Iglesia, E., Design, synthesis, and use of cobalt-based Fischer-Tropsch synthesis catalysts. *Appl. Catal., A* **1997**, *161*, 59-78.
(94) Bezemer, G. L.; Bitter, J. H.; Kuipers, H. P. C. E.; Oosterbeek, H.; Holewijn, J. E.; Xu, X.; Kapteijn, F.; van Dillen, A. J.; de Jong, K. P., Cobalt Particle Size Effects in the Fischer−Tropsch Reaction Studied with Carbon Nanofiber Supported Catalysts. *J. Am. Chem. Soc.* **2006**, *128*, 3956-3964.
(95) Tsunoyama, H.; Ichikuni, N.; Sakurai, H.; Tsukuda, T., Effect of Electronic Structures of Au Clusters Stabilized by Poly(N-vinyl-2-pyrrolidone) on Aerobic Oxidation Catalysis. *J. Am. Chem. Soc.* **2009**, *131*, 7086-7093.
(96) Li, G.; Jin, R., Atomically Precise Gold Nanoclusters as New Model Catalysts. *Acc. Chem. Res.* **2013**, *46*, 1749-1758.

Chapter 2. Synthesis, Characterization, and Reactivity of the Group 11 Hydrido Clusters, $[Ag_6H_4(dppm)_4(OAc)_2]$, $[Cu_3H(dppm)_3(OAc)_2]$, $[Cu_{10}H_{10}(DPEphos)_4]$, $[Cu_{14}H_{14}(DBFphos)_5]$, and $[Cu_{13}H_{10}(SePh)_3(PPh_3)_7]$

Portions of this work were published in:

Andrew W. Cook, Thuy-Ai D. Nguyen, William R. Buratto, Guang Wu, and Trevor W. Hayton. Synthesis, Characterization, and Reactivity of the Group 11 Hydrido Clusters, $[Ag_6H_4(dppm)_4(OAc)_2]$ and $[Cu_3H(dppm)_3(OAc)_2]$. *Inorg. Chem.* **2016**, *55*, 12435-12440.

Table of Contents

2.1 Introduction

Copper hydrides have proven to be potent catalysts for the hydrogenation and hydrosilylation of α,β–unsaturated ketones, carbon-carbon multiple bonds, and CO_2.[1-14] In contrast, only a handful of examples of silver-catalyzed hydrogenation and hydrosilylation are known.[15-20] For example, AgOTf has been shown to catalyze the hydrosilylation of aryl aldehydes in the presence of Me_2PhSiH and PEt_3.[16] Similarly, the semi-hydrogenation of alkynes by a heterobimetallic Ag/Ru catalyst has been reported.[19] In both cases, catalysis is thought to proceed via a Ag-H intermediate, but this hypothesis has yet to be confirmed, though recently a silver hydride dimer, $[\{(SIDipp)Ag\}_2(\mu\text{-}H)]X$ (SIDipp = 1,3-bis(2,6-diiso-propylphenyl)imidazolin-2-ylidene; X^- = OTf^- or BF_4^-) (Figure 2.1A), was shown to stoichiometrically reduce CO_2 to formate.[21]

This limited understanding of Ag-H reactivity is due, in part, to the difficulty in generating stable silver hydride complexes; a consequence of this metal's relatively high M(I)/M(0) half-cell potential (0.80 V).[22] Because of this property, Ag^I-H complexes more easily decompose to yield Ag^0 and H_2 versus their Cu counterparts. Consequently, Ag^I-H complexes have proven to be relatively rare.[21, 23-40] Moreover, the examples isolated thus far are either homometallic monohydrides, e.g., $[Ag_7H\{Se_2P(O^iPr)_2\}_6]$[31] (Figure 2.1B), heterometallic polyhydrides, e.g., $[Ag(\mu\text{-}H)_4\{Re_2(\mu\text{-}H)(CO)_8\}_2]^-$,[33] or polyhydrides observed via electrospray ionization mass spectrometry, (e.g., $[Ag_{10}H_8(dppm)_6]^{2+}$)[34] (dppm = 1,1-bis(diphenylphosphino)methane) or NMR spectroscopy (e.g., $[Ag_{18}H_{16}(Ph_3P)_{10}]^{2+}$).[41] In the research reported herein, I describe the synthesis and characterization of the first structurally characterized homometallic silver polyhydrido cluster, $[Ag_6H_4(dppm)_4(OAc)_2]$ (**2.1**) as well as the copper hydride cluster $[Cu_3H(dppm)_3(OAc)_2]$ (**2.2**). In addition, I have examined the ability of each of these clusters

to catalyze the 1,4- and 1,2-hydrosilylations of (α,β–unsaturated) ketones. I also determined the ability of other bidentate phosphines to generate Cu^{I}-H clusters and have isolated the copper polyhydrido clusters $[Cu_{10}H_{10}(DPEphos)_4]$ (DPEphos = (oxydi-2,1-phenylene)bis(diphenylphosphino, **2.8**) and $[Cu_{14}H_{14}(DPEphos)_5]$ (DBFphos = 4,6-bis(diphenylphosphino)dibenzofuran, **2.9**). Finally, I explored the reactivity of $[CuH(PPh_3)]_6$[42] towards diphenyldiselenide (Ph_2Se_2) to generate the copper selenoate cluster $[Cu_{13}H_{10}(SePh)_3PPh_3)_7]$ (**2.9**).

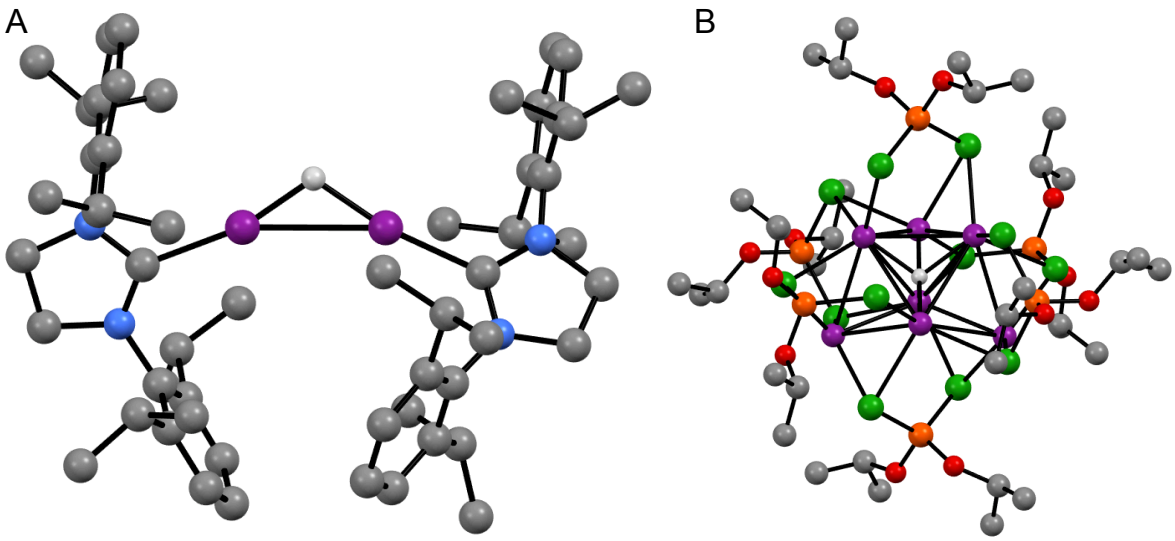

Figure 2.1. Ball and stick diagram of the homometallic silver hydrides $[\{(SIDipp)Ag\}_2(\mu\text{-}H)]X$ (SIDipp = 1,3-bis(2,6-diiso-propylphenyl)imidazolin-2-ylidene; $X^- = OTf^-$ or BF_4^-) (A, ref. 21) and $[Ag_7H\{Se_2P(O^iPr)_2\}_6]$ (B, ref. 31).

2.2 Results and Discussion

2.2.1 Synthesis and Characterization of $[Ag_6H_4(dppm)_4(OAc)_2]$ (2.1)

Addition of 1 equiv of dppm and 0.5 equiv of diphenylsilane (Ph_2SiH_2) to a slurry of Ag(OAc) in benzene resulted in a rapid color change from white to dark red-brown. Work-up of the solution after stirring at room temperature for 15 h resulted in the isolation of the first

silver polyhydrido cluster, $[Ag_6H_4(dppm)_4(OAc)_2]$ (**2.1**), as a colorless, crystalline solid in 47% yield (Scheme 2.1).

Scheme 2.1. Syntheses of complexes 2.1 and 2.2

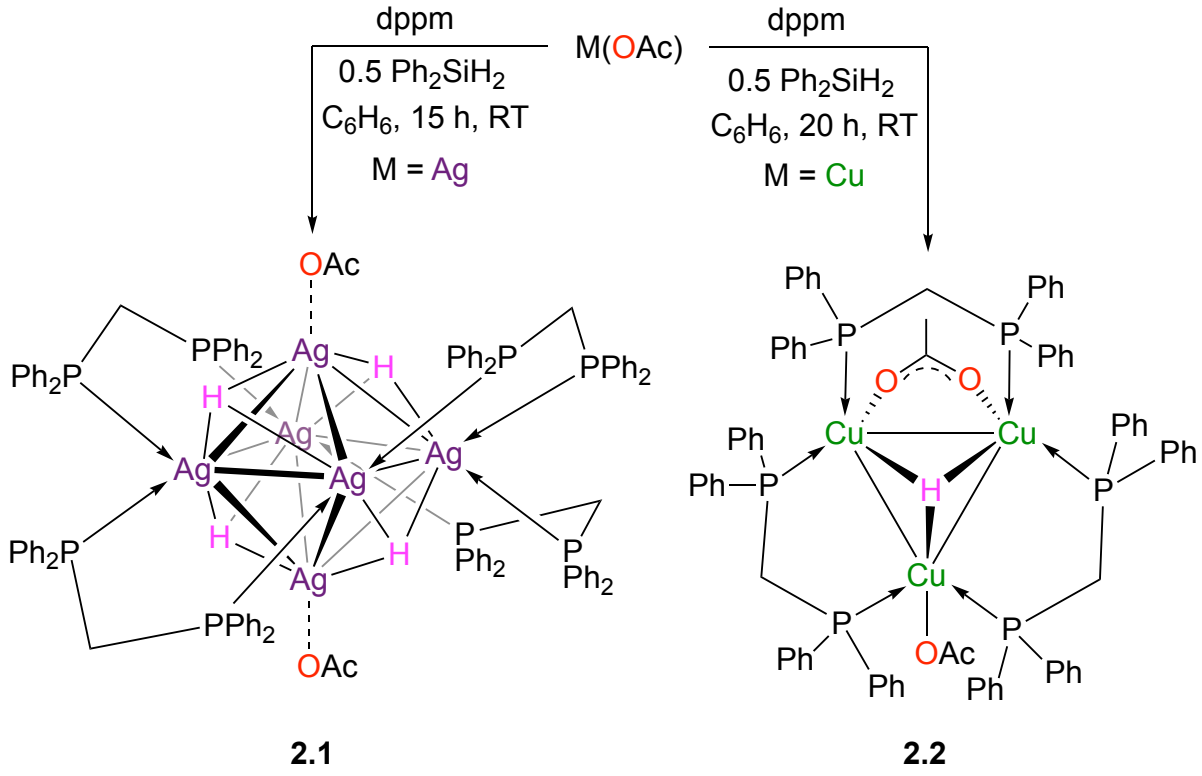

Complex **2.1** crystallizes in the triclinic space group $P\bar{1}$ as the benzene solvate **2.1**·2.5C_6H_6 (Figure 2.2). In the solid state, the Ag atoms of the $[Ag_6]^{6+}$ core are arranged in an octahedron. The four dppm ligands coordinate to an equatorial belt formed by four Ag atoms. Each dppm ligand is deflected out of the $[Ag_4]^{4+}$ plane, with two arranged above the plane and two below the plane in an alternating fashion. While the four hydride ligands were not located in the difference Fourier map, the arrangement of the dppm ligands likely requires that the hydride ligands occupy the four trigonal faces that are opposite a dppm moiety with a μ_3-binding mode. Lastly, the two acetate counterions are bound to Ag atoms at axial positions of the $[Ag_6]^{6+}$ core, via κ^1 and κ^2 binding modes.

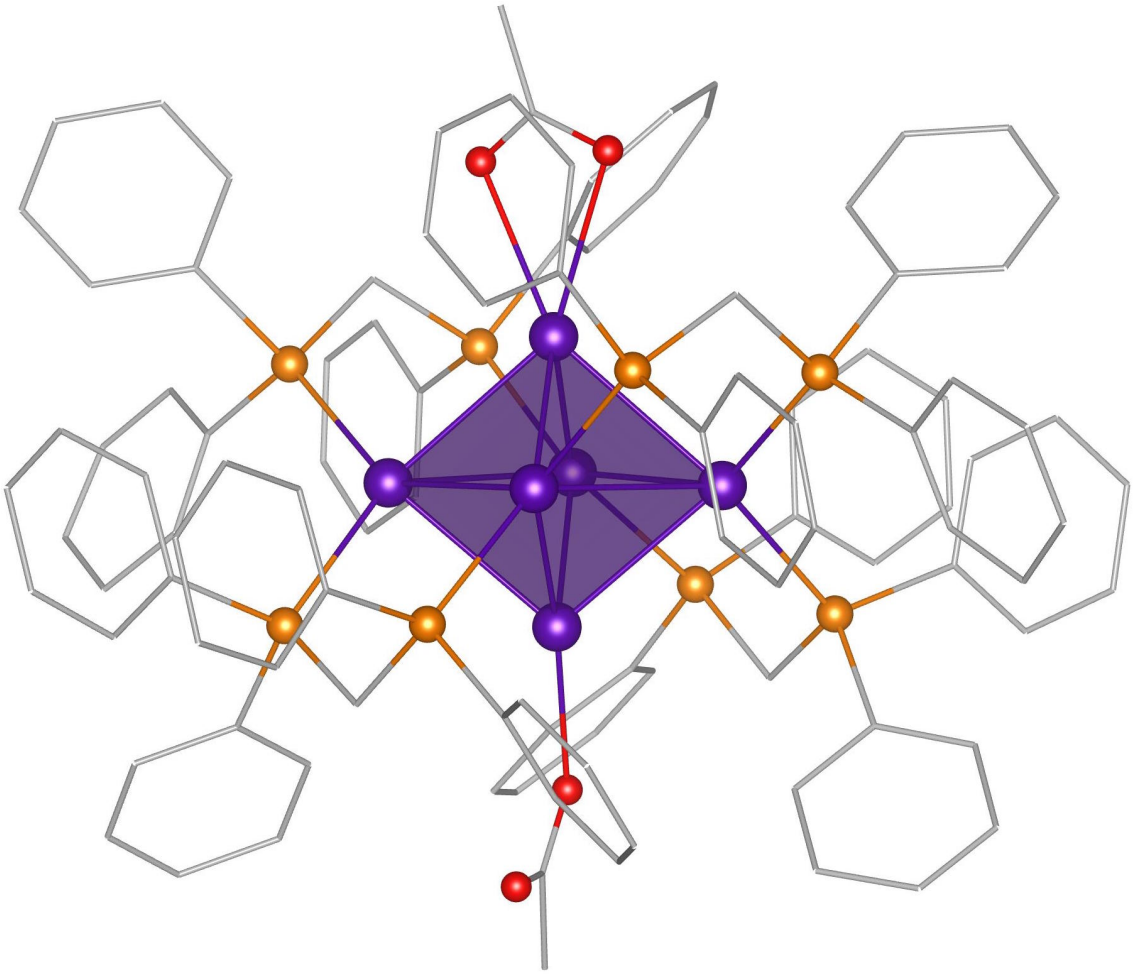

Figure 2.2. Ball and stick diagram of **2.1**. All hydrogen atoms and solvent molecules have been omitted for clarity. Color legend: Ag = purple; P = yellow-orange; O = red; C = grey wireframe.

The average Ag–Ag bond length within the $[Ag_4]^{4+}$ belt is 3.08 Å, which is longer than the average Ag_{cap}–Ag_{belt} bond length of 2.88 Å. The Ag_{cap}–Ag_{belt} interaction is within the covalent radius for Ag,[43] and the Ag_{belt}–Ag_{belt} interaction lies well within twice the van der Waals radius for Ag (1.72 Å),[44] suggestive of considerable argentophilic interactions within the $[Ag_6]^{6+}$ core. These values are also similar to those reported for other Ag^I-H clusters[21, 28-32, 35, 37-38] and Ag_6 octahedra.[45-51] Finally, the average Ag–P distance (2.51 Å) is typical of Ag–P bonds.[32, 35, 38, 52-57]

The ^{1}H NMR spectrum of complex **2.1** in C_6D_6 (Figure 2.3) shows a single acetate resonance at 2.92 ppm, while the diastereotopic methylene protons of the dppm ligand appears at 3.02 ppm and 5.44 ppm. Most notably, a complicated multiplet, centered at 5.82 ppm and integrating for 4H, is assignable to the four equivalent hydride moieties.

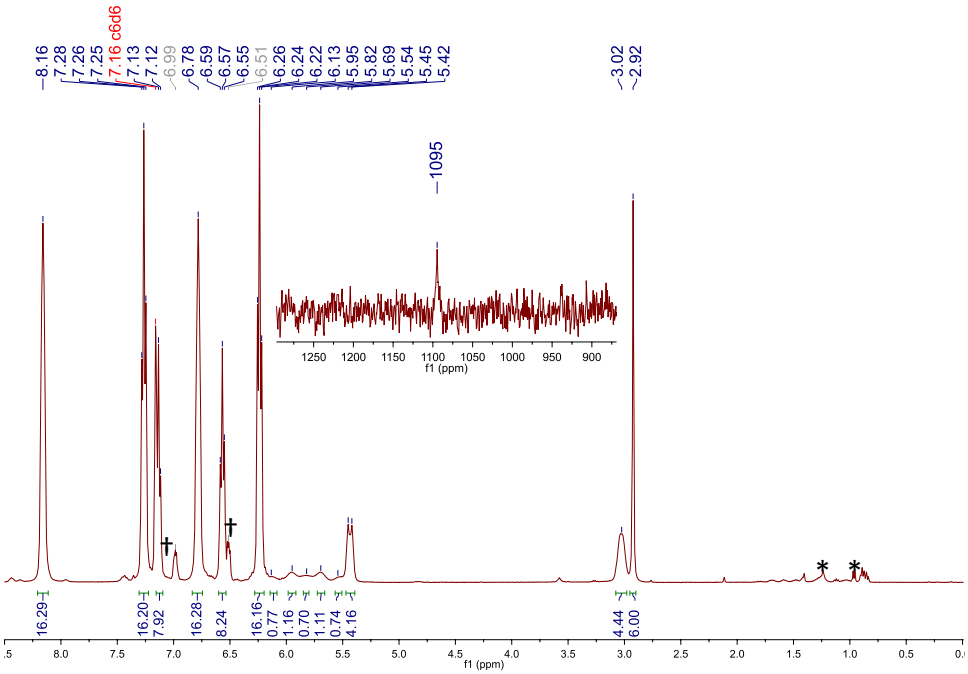

Figure 2.3. ^{1}H NMR spectrum of **2.1** in C_6D_6. (*) denotes the presence of hexanes. (†) denotes the presence of 1,2-dichlorobenzene. Inset shows the ^{109}Ag{^{1}H} INEPT NMR spectrum of **2.1** in 1,2-dichlorobenzene:1,2-$C_6D_4Cl_2$ (2:1, v:v).

The ^{2}H NMR spectrum (Figure A2.6) of the isotopically labeled analogue, **2.1-*d*$_4$**, features a resonance at 5.76 ppm in 1,2-$C_6H_4Cl_2$:C_6D_6 (99:1, v/v), confirming the assignment of this feature as a hydride resonance. The ^{109}Ag NMR spectrum (Figure 2.3, inset) of **2.1** in 1,2-$C_6D_4Cl_2$, recorded using an INEPT pulse sequence,[58] features a single resonance at 1095 ppm. This chemical shift is in good agreement with the ^{109}Ag signals observed for the Ag^{I}-H dichalcogenatophosphate clusters reported by Liu and co-workers.[28-31] However, only one resonance was observed in the spectrum, despite the presence of two unique Ag environments

in this complex, which may be a consequence of poor signal-to-noise due to its low solubility. In agreement with the high symmetry of complex **2.1** in the solid state, its $^{31}P\{^{1}H\}$ NMR spectrum features a single ^{31}P resonance at 8.06 ppm in C_6D_6 (Figure A2.2). This resonance features a complicated *J*-coupling pattern, due to one- and two-bond coupling to the ^{107}Ag and ^{109}Ag nuclei in the $[Ag_6]^{6+}$ core.

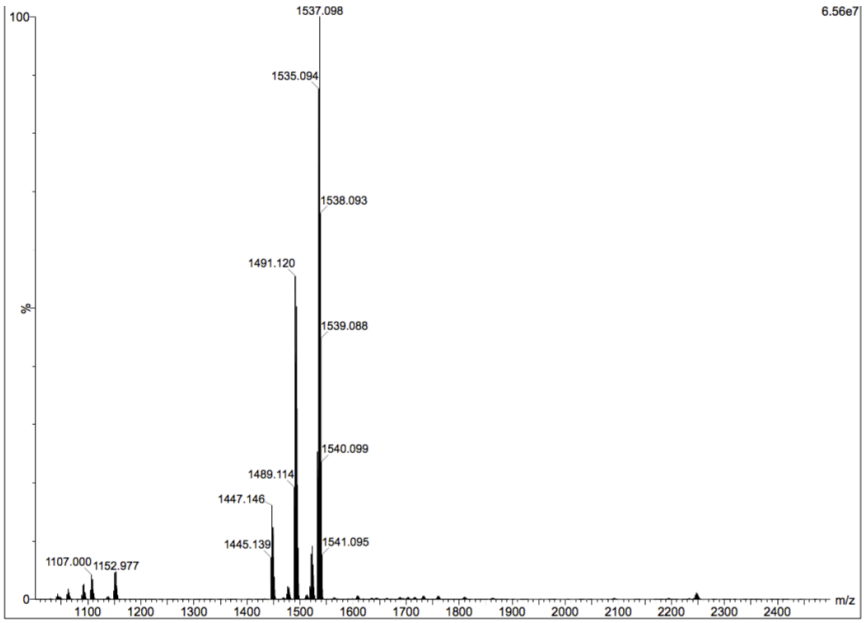

Figure 2.4. ESI-MS (positive mode) of $[Ag_6H_4(dppm)_4(OAc)_2]$ (**2.1**).

Finally, the electrospray ionization (ESI) mass spectrum (Figure 2.4) of **2.1** features a signal at 2246.942 *m/z* corresponding to $[M\text{-}OAc]^+$ (calculated *m/z* 2246.954). For comparison, the ESI mass spectrum of **2.1-*d*$_4$** (Figure A2.41) gave rise to a signal at 2250.978 *m/z* (calculated *m/z* 2250.979), a shift of 4 *m/z* versus **2.1**, as anticipated for a tetra-hydrido complex. Interestingly, the ESI mass spectrum of **2.1** contained another major feature at 1537.098 *m/z* (calculated *m/z* 1537.095), which is assignable to the $[Ag_3(dppm)_3H(OAc)]^+$ fragmentation product, consistent with O'Hair's observation that the $Ag_3(\mu_3\text{-}H)$ core is especially stable.[32, 34-36, 38] The facile formation of this fragment ion may also indicate a

plausible mechanism for cluster assembly, as dimerization of $[Ag_3(dppm)_3H(OAc)]^+$, concomitant with dppm dissociation, would generate the observed Ag_6 core.

I also briefly explored the chemical properties of **2.1**. Complex **2.1** is modestly soluble in C_6H_6 and THF, insoluble in MeCN, Et_2O, and non-polar solvents, and reasonably soluble in 1,2-dichlorobenzene. Complex **2.1** exhibits only modest thermal stability. On standing overnight at 25 ºC in C_6D_6, it partially decomposes to H_2 and silver metal, amongst other products (Figure A2.19). An ESI mass spectrum of this sample suggests that a mixture of larger silver nanoclusters is generated (Figure A2.44-A2.46); however, their identities remain unknown. Complex **2.1** also reacts slowly with excess H_2O (10 equiv) in C_6D_6, forming Ag^0, as well as other products.

To better understand the formation of **2.1** I recorded ^1H and ^{31}P NMR spectra of the crude reaction mixture (Figures A2.17 and A2.18). These spectra reveales the presence of free dppm, complex **2.1**, and an unidentified silver hydride cluster, as indicated by broad hydride ligand resonances at 2.40 and 3.60 ppm in the ^1H NMR spectrum. Accordingly, I speculate that the modest yield of **2.1** is due to the competing formation of these by-products, as well as the gradual decomposition of complex **2.1** over the course of the 15 h reaction time. The formation of these other Ag clusters also likely accounts for the dark brown color of the reaction mixture. Interestingly, if the reaction is performed using a Ag to dppm ratio that corresponds to the molecular formula (6:4), the yield of **2.1** drops precipitously. I suggest that the Ag to dppm ratio shown in Scheme 2.1 (i.e., 1:1) results in higher concentrations of dppm, which helps to stabilize transient "Ag^I-H" monomers, and reduces the probability of decomposition.

2.2.2 Synthesis and Characterization of $[Cu_3H(dppm)_3(OAc)_2]$ (2.2)

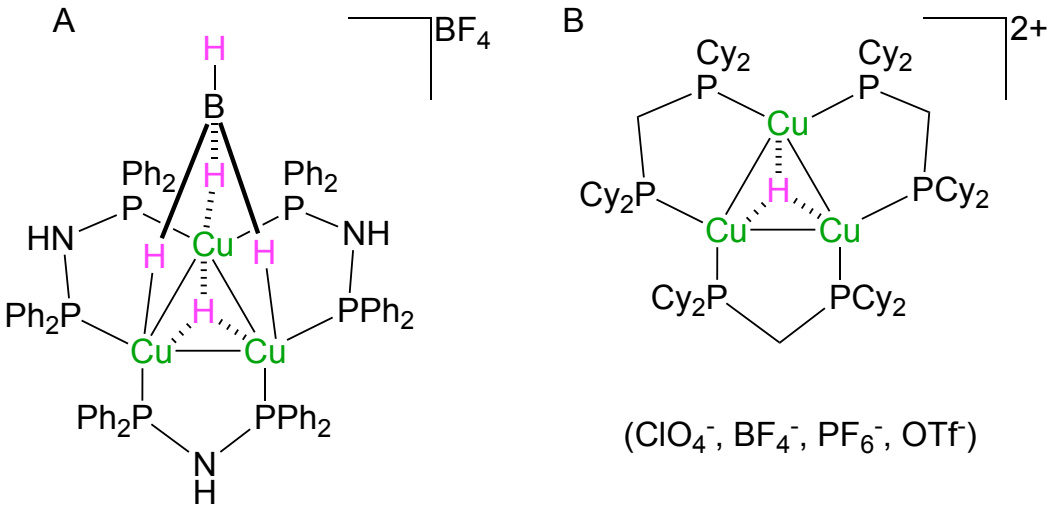

Figure 2.5. Previously reported complexes with the $[Cu_3H]^{2+}$ structure: $[Cu_3H(dcpm)_3]^{2+}$ (dcpm = 1,1-bis(dicyclohexylphosphino)methane) (A, ref. 57) and $[Cu_3(BH_4)H(dppa)_3]^{+}$ (dppa = bis(diphenylphosphino)amine) (B, ref. 58).

For further comparison, I endeavored to synthesize the Cu congener of **2.1**. Previous attempts to make a dppm Cu-H cluster ended with decomposition because of the high basicity of the $[Cu(O^tBu)]_4$ starting material coupled to the acidity of dppm.[59] However, the combined use of Cu(OAc) and Ph_2SiH_2 to generate the Cu^I-H moiety obviates the use of an alkoxide precursor. Thus, addition of 1 equiv of dppm and 0.5 equiv of Ph_2SiH_2 to a slurry of Cu(OAc) in benzene resulted in the gradual color change from pale green to yellow. Work-up of the solution after 20 h afforded the copper hydride cluster $[Cu_3H(dppm)_3(OAc)_2]$ (**2.2**), as colorless crystals in 83% yield (Scheme 2.1). Complex **2.2** is closely related to the known Cu^I-H clusters, $[Cu_3H(dcpm)_3]^{2+}$ (dcpm = 1,1-bis(dicyclohexylphosphino)methane) and $[Cu_3(BH_4)H(dppa)_3]^{+}$ (dppa = bis(diphenylphosphino)amine) (Figure 2.5).[60-61]

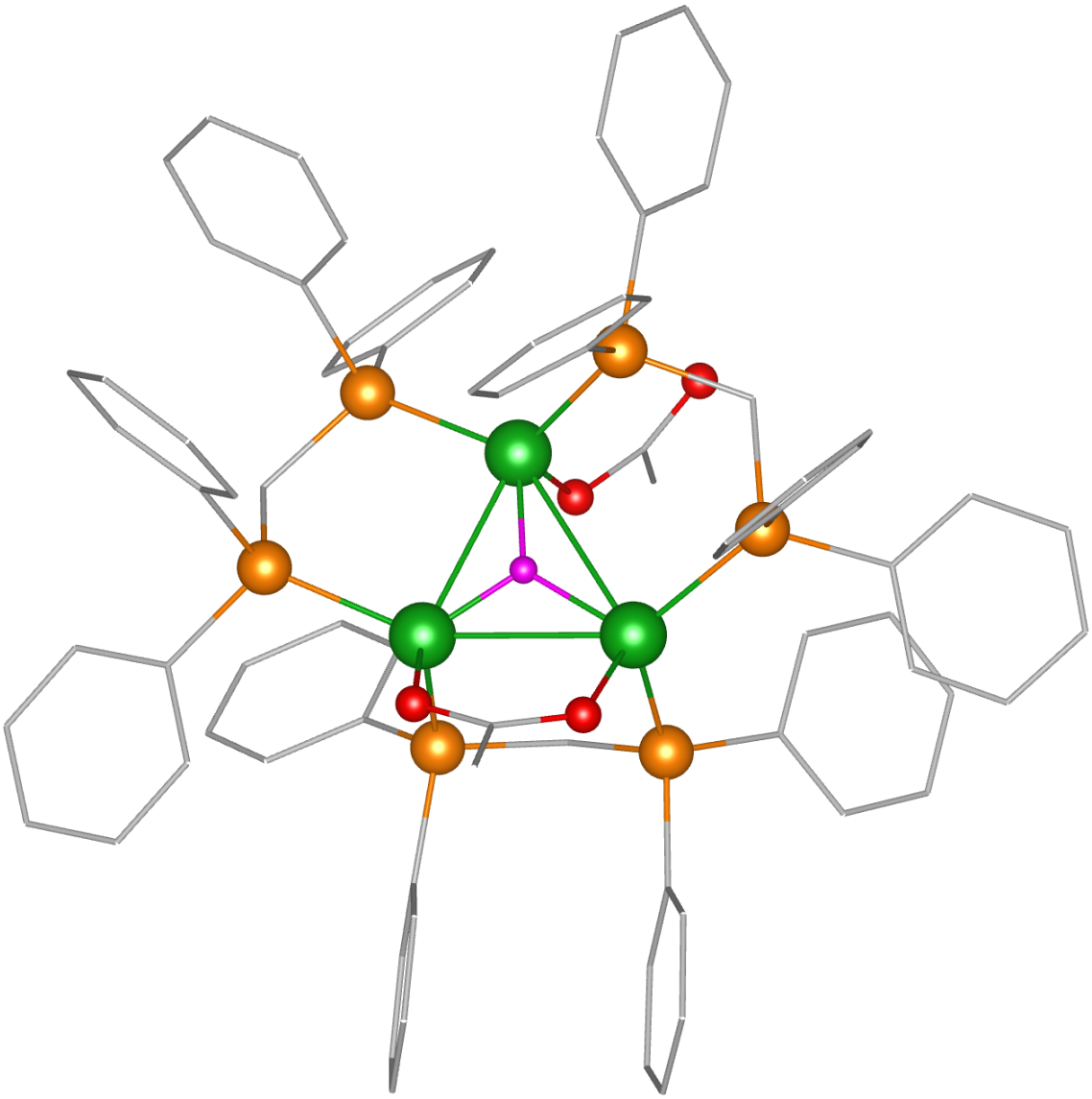

Figure 2.6. Ball and stick diagram of **2.2**. All hydrogen atoms (except the hydride ligand) and solvent molecules have been omitted for clarity. Color legend: Cu = green; H = magenta; P = yellow-orange; O = red; C = grey wireframe.

Complex **2.2** crystallizes as the benzene solvate, **2.2**·$2C_6H_6$ (Figure 2.6), in the monoclinic space group $P2_1/n$. In the solid state, complex **2.2** contains a triangular $[Cu_3]^{3+}$ core with an average Cu–Cu distance of 2.91 Å. This distance is comparable to the average Cu–Cu distance of 2.882(1) Å reported for $[Cu_3H(dcpm)_3]^{2+}$.[60] The average Cu–P distance in **2.2** (2.28 Å) is consistent with Cu–P bonds in other phosphine-supported Cu^I-H clusters.[13, 42,

[59-60, 62-66] The hydride ligand was located in the difference Fourier map, and was found to display a μ_3 binding mode. Lastly, the two acetate counterions both bind to the Cu_3 core, via κ^1 and κ^2 binding modes.

While complex **2.2** appears to have C_s symmetry in the solid state, there is only one resonance observed in its $^{31}P\{^1H\}$ NMR spectrum (Figure A2.12), at -6.66 ppm, in MeCN-d_3. Likewise, complex **2.2** exhibits a sharp singlet at 1.91 ppm in its ^1H NMR spectrum (Figure 2.7), assignable to the methyl group of a single acetate environment.

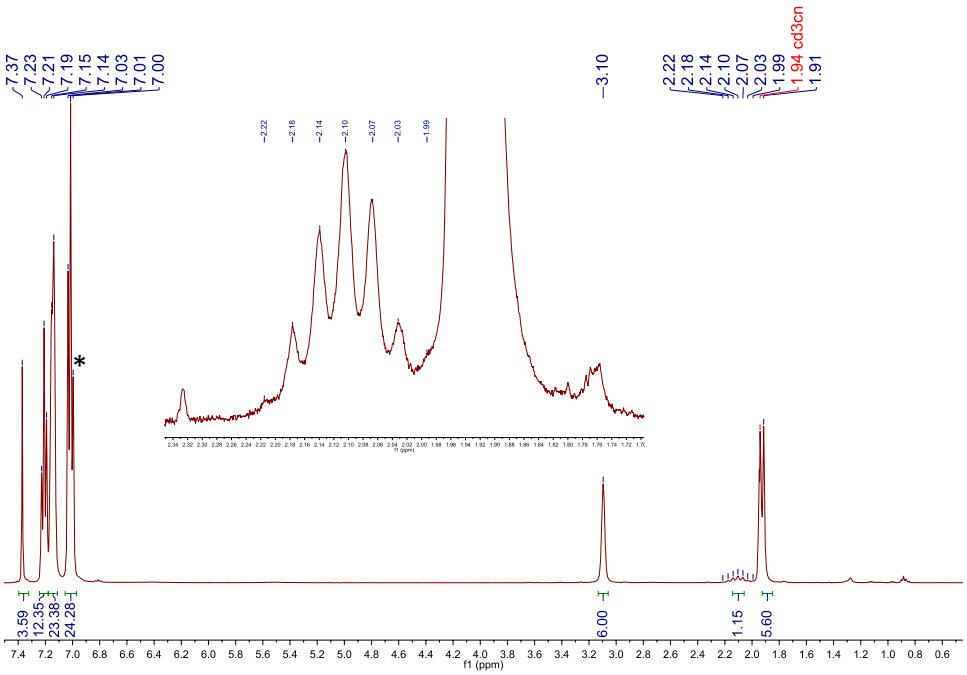

Figure 2.7. ^1H NMR spectrum of **2.2** in MeCN-d_3. (*) denotes the presence of benzene. Inset shows an expanded view of the hydride region.

Overall, these data are consistent with fast exchange of the acetate moieties at room temperature, which results in a higher effective symmetry in solution than observed in the solid-state. A septet centered at 2.10 ppm in the ^1H NMR spectrum ($^2J_{PH}$ = 14.4 Hz) is assignable to the lone hydride moiety (Figure 2.7, inset). This signal collapses to a singlet upon ^{31}P decoupling (Figure A2.11). To further confirm the presence of a single hydride

ligand, I synthesized the isotopically labeled complex, **2.2-*d*$_1$**. Gratifyingly, complex **2.2-*d*$_1$** features a singlet at 1.74 ppm in the ^{2}H NMR spectrum in C_6H_6:C_6D_6 (9:1, v:v), assignable to the deuteride ligand.

Finally, complex **2.2** produced a signal at 1379.120 *m/z* in the ESI mass spectrum (Figure 2.8), corresponding to the $[Cu_3H(dppm)_3Cl]^+$ ion (calculated *m/z* 1379.125). For comparison, complex **2.2-*d*$_1$** features a signal at 1380.123 *m/z* in its ESI mass spectrum (Figure A2.50), corresponding to the $[Cu_3D(dppm)_3Cl]^+$ ion (calculated *m/z* 1380.131), a shift of 1 *m/z*. A parent peak for **2.2** was not found in the mass spectrum, likely due to facile exchange of acetate for Cl^- during the ESI-MS ionization process.

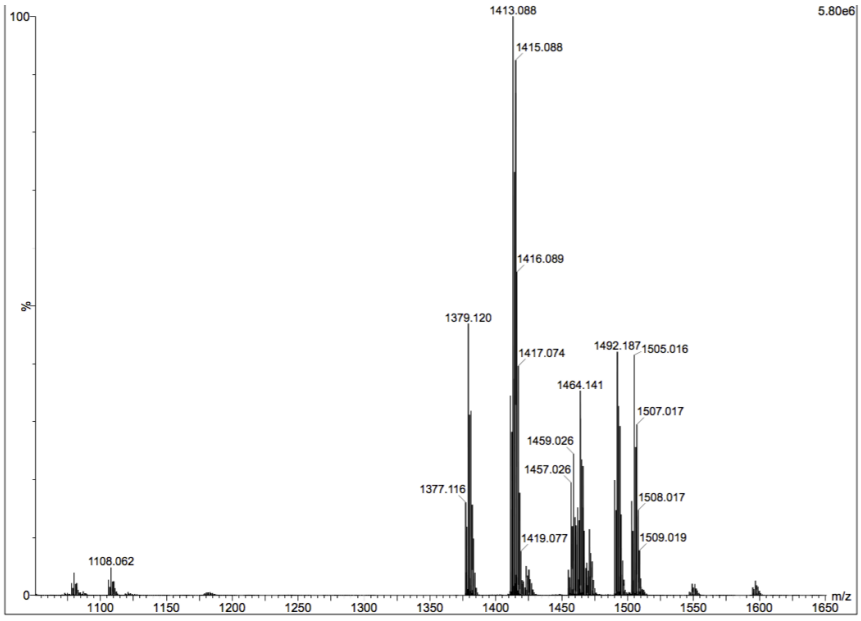

Figure 2.8. ESI-MS (positive mode) of $[Cu_3H(dppm)_3(OAc)_2]$ (**2.2**).

I also explored the chemical properties of **2.2**. Complex **2.2** is soluble in MeCN, partially soluble in C_6H_6 and THF, and insoluble in Et_2O and non-polar solvents. It is stable in MeCN for at least 3d, showing no signs of decomposition over this time. In contrast to complex **2.1**, complex **2.2** does not appear to react with excess H_2O, even over the course of 24 h.

2.2.3 Hydrosilylation Catalysis Using Clusters 2.1 and 2.2

Group 11 hydrides are known to catalyze both 1,4- and 1,2-hydrosilylations of (α,β–unsaturated) ketones, in the presence of a silane.[6-7, 16, 67-68] Given this precedent, I screened the ability of complex **2.1** to catalyze the 1,4-hydrosilylation of 2-cyclohexen-1-one (**2.3**). Thus, addition of Ph_2SiH_2 (1.5 equiv) to **2.3**, in the presence of **2.1** (0.05 H^- equivalents), in C_6D_6 results in 76% conversion to the corresponding silyl enol **2.4a** after 24 h (Table 2.1). Also formed in small amounts is the 1,2-hydrosilylation product, **2.4c**.[69] To the best of my knowledge, this transformation represents the first example of hydrosilylation with an authentic silver hydride complex.[70] Complex **2.2** is also an effective pre-catalyst for the 1,4-hydrosilylation of **2.3**, achieving 96% total conversion after 24 h using a similar catalyst loading. However, this pre-catalyst features somewhat lower selectivity for the 1,4-hydrosilylation reaction. Surprisingly, in the absence of silane, neither **2.1** nor **2.2** can perform the stoichiometric reduction of **2.3** (Figures A2.24 and A2.25). A similar observation has been reported for other copper hydrides,[70-71] and can be rationalized by assuming that formation of the copper enolate intermediate is reversible, but its equilibrium concentration is very low. As a result, the presence of silane is required to trap the enolate and drive the reaction to completion.[70, 72] For comparison, I also monitored the ability of $[CuH(PPh_3)]_6$ to catalyze 1,4-hydrosilylation of **2.3** under similar conditions. Of the three complexes tested, this reagent proved the most effective, reaching >99% conversion in only 15 min.

Table 2.1. 1,4-hydrosilylation of 2-cyclohexen-1-one catalyzed by **2.1**, **2.2**, and $[CuH(PPh_3)]_6$.

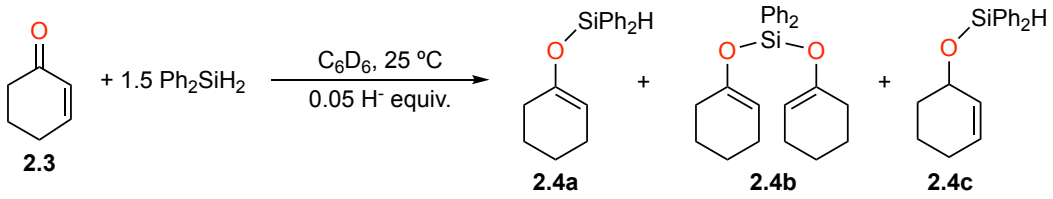

2.3 **2.4a** **2.4b** **2.4c**

catalyst[a]	reaction time (h)	conversion (%)[b]	2.4a:2.4b:2.4c
2.1	24	79	76:0:3
2.2	24	96	57:29:10
$[CuH(PPh_3)]_6$	<0.25	>99	79:21:0

[a]For experimental details see section 2.4. [b]Total conversion to **2.4abc** determined by ^1H NMR integration with long pulse delay (d_1 = 60 s) against an internal standard of hexamethyldisiloxane.

I also screened the ability of **2.1**, **2.2**, and $[CuH(PPh_3)]_6$ to catalyze the 1,2-hydrosilylation of cyclohexanone (**2.5**). Thus, addition of Ph_2SiH_2 (1.3 equiv) to **2.5**, in the presence of **2.1** (0.10 H^- equivalents), in C_6D_6 resulted in 42% conversion to the silyl ether **2.6** after 24h (Table 2.2). Complex **2.2** is an even better pre-catalyst for the 1,2-hydrosilylation of **2.5**, achieving >99% conversion after just 2 h, using a similar catalyst loading. Surprisingly, $[CuH(PPh_3)]_6$ was the least effective pre-catalyst for this reaction, achieving only 26% conversion after 24 h. It is not readily apparent why complex **2.2** is a more effective pre-catalyst relative to **2.1** or $[CuH(PPh_3)]_6$; however, the changes in efficacy, relative to the results observed for the 1,4-hydrosilylation (Table 2.1), could indicate a change in the reaction mechanism.[73]

Table 2.2. 1,2-hydrosilylation of cyclohexanone catalyzed by **2.1**, **2.2**, and $[CuH(PPh_3)]_6$.

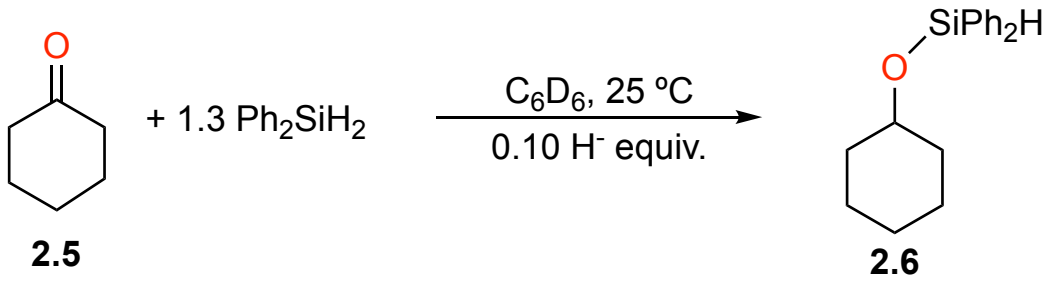

2.5 **2.6**

catalyst[a]	reaction time (h)	conversion (%)[b]
2.1	24	42
2.2	2	>99
$[CuH(PPh_3)]_6$	24	26

[a]For experimental details see section 2.4. [b]Total conversion to **2.6** determined by 1H NMR integration with long pulse delay (d_1 = 60 s) against an internal standard of hexamethyldisiloxane.

2.2.4 Synthesis and Solid State Molecular Structures of $[Cu_{10}H_{10}(DPEphos)_4]$ (2.7) and $[Cu_{14}H_{14}(DBFphos)_5]$ (2.8)

In general, nanocluster syntheses are unpredictable with no discernible correlation between ligand identity and cluster morphology.[60, 64-65, 70, 74-78] For example, gold nanoclusters supported by phenylethanethiolate can have core structures of Au_{25}, Au_{38}, Au_{40}, Au_{130}, and Au_{144}, depending on reaction time and stoichiometry.[75] Establishing predictability would be a useful tool for synthetic chemists looking to isolate a particular morphology for specific applications.[70] Therefore, I endeavored to explore the effect of the bite angle of the bidentate phosphine ligand on the copper cluster speciation.[79] I hypothesized that the greater the bite angle of the phosphine, the larger the cluster that can be formed. Some evidence has been published that supports this claim. For example, the use of small bite angle bidentate

phosphines, such as dppm (bite angle ≈ 71º), generates planar clusters with three Cu centers akin to complex **2.2**.[36, 76] Using a bidentate phosphine with a larger bite angle, Caulton and co-workers employed dppp (1,3-bis(diphenylphosphino)propane, bite angle ≈ 91º) to synthesize the cluster $[Cu_8H_8(dppp)_4]$.[79-80] To investigate this trend further, I attempted the synthesis of Cu-hydride clusters using the bidentate phosphine ligands DPEphos (DPEphos = (oxydi-2,1-phenylene)bis(diphenylphosphino), bite angle ≈ 102º) and DBFphos (DBFphos = 4,6-bis(diphenylphosphino)dibenzofuran, bite angle ≈ 131º) (Figure 2.9). The Cu nanocluster syntheses using these bidentate phosphine ligands (Scheme 2.2) always resulted in complicated mixtures of products rendering isolation of pure material impossible. However, two new Cu^I-H clusters have been identified: $[Cu_{10}H_{10}(DPEphos)_4]$ and $[Cu_{14}H_{14}(DBFphos)_5$. What follows is a brief discussion of their solid-state structures.

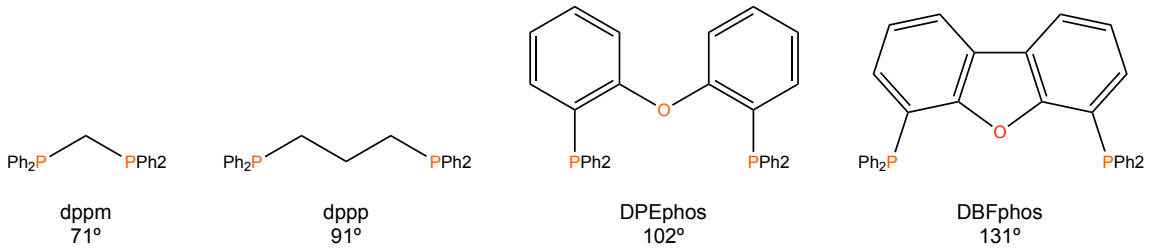

Figure 2.9. Ligands used in this study in order of increasing bite angle.

Thus, addition of DPEphos (1 equiv) and Ph_2SiH_2 (0.5 equiv) to a slurry of Cu(OAc) in benzene resulted in the formation of a bright orange solution. Work up of the reaction mixture after 20 h results in the formation of a small amount of orange crystals of $[Cu_{10}H_{10}(DPEphos)_4]$ (**2.7**) in approximately 14% yield, though this product is always isolated as a mixture of products (Scheme 2.2).

Scheme 2.2. Syntheses of complexes 2.7 and 2.8

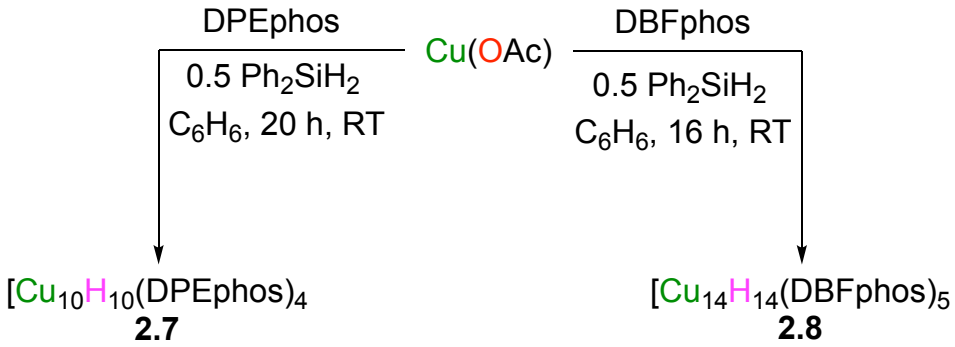

Complex **2.7** crystallizes as the ether solvate, **2.7**·$3C_4H_{10}O$, in the orthorhombic space group $P2_12_12$ (Figure 2.10) with approximate C_2 symmetry. In the solid state, the copper core of complex **2.7** appears as a distorted, bi-capped square antiprism. The Cu–Cu distances range from 2.374(4) to 2.930(4) Å, consistent with other reported Cu(I)-H clusters.[42, 59] As observed in complexes **2.1** and **2.2**, the four DPEphos ligands are bridging across two metal centers with the Cu–P distances average 2.25 Å, which is slightly shorter than other reported Cu–P distances for Cu(I)-DPEphos complexes.[81-83] While the proposed hydride ligands were not located in the Fourier difference map, I believe that complex **2.7** consists entirely of Cu(I) and therefore should have 10 hydrides. Interestingly, two Cu atoms in complex **2.7** are "bare", in that they are not ligated to P and are held in the cluster solely through Cu–H and Cu–Cu bonds. Consistent with my hypothesis, the Cu(I)-H cluster generated with DPEphos has greater nuclearity than the cluster synthesized with dppp. Comparing cluster size versus bite angle for complex **2.1**, $[Cu_8H_8(dppp)_4]$, and complex **2.7**, there is a steady increase of approximately one Cu atom per 5º increase in bite angle. To investigate this trend, I endeavored to synthesize a Cu(I)-H cluster using DBFphos as the supporting ligand.

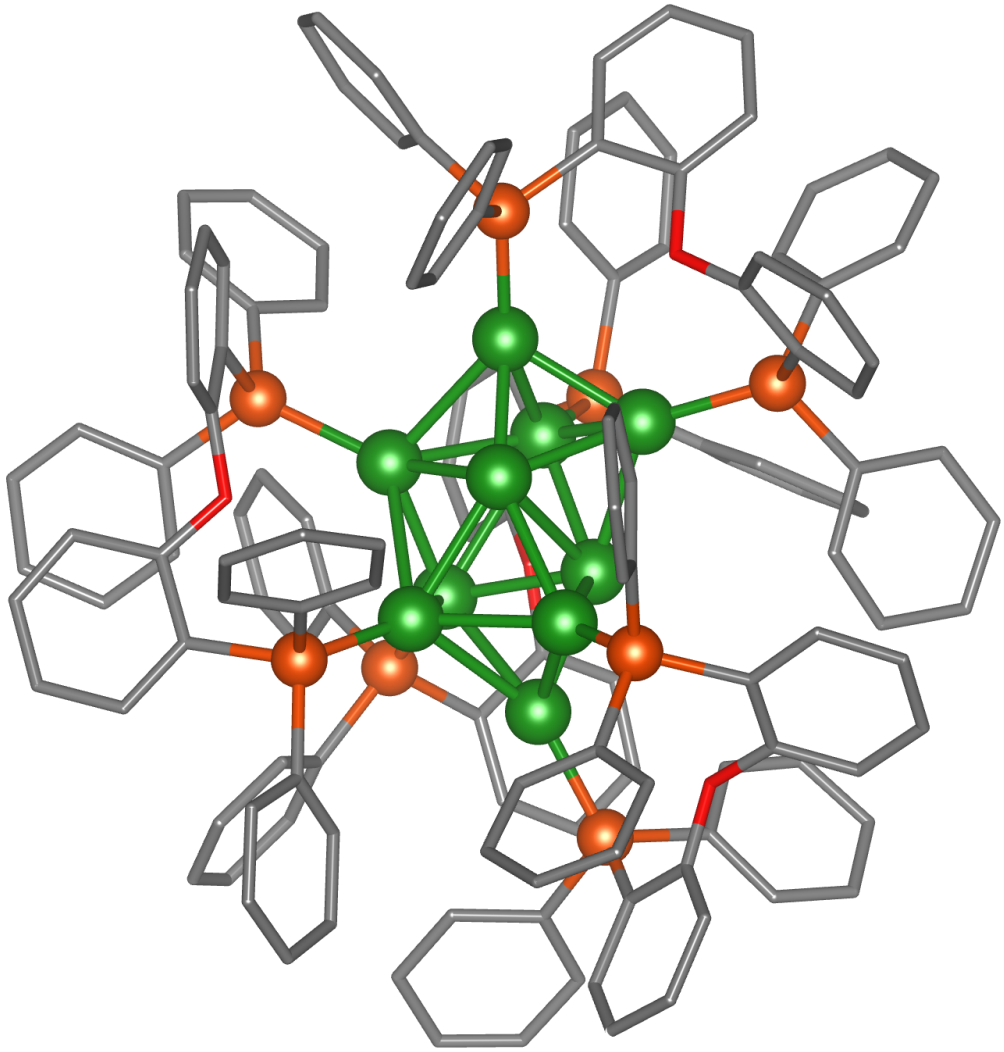

Figure 2.10. Ball and stick diagram of **2.7**·$3C_4H_{10}O$. All hydrogen atoms and solvent molecules have been omitted for clarity. Color legend: Cu = green; P = yellow-orange; O = red wireframe; C = grey wireframe.

Thus, addition of DBFphos (1 equiv) and Ph_2SiH_2 (0.5 equiv) to a slurry of Cu(OAc) in benzene resulted in the formation of a red-orange solution. Work up of the reaction mixture after 15 h results in the formation of a small amount of orange crystals of $[Cu_{14}H_{14}(DBFphos)_5]$ (**2.8**) in approximately 11% yield, though this product can only be isolated as a mixture as well (Scheme 2.2). Gratifyingly, the complex **2.8** saw an increase in

nuclearity; however, there were two fewer Cu atoms than expected based on the 5º per Cu atom rule mentioned previously.

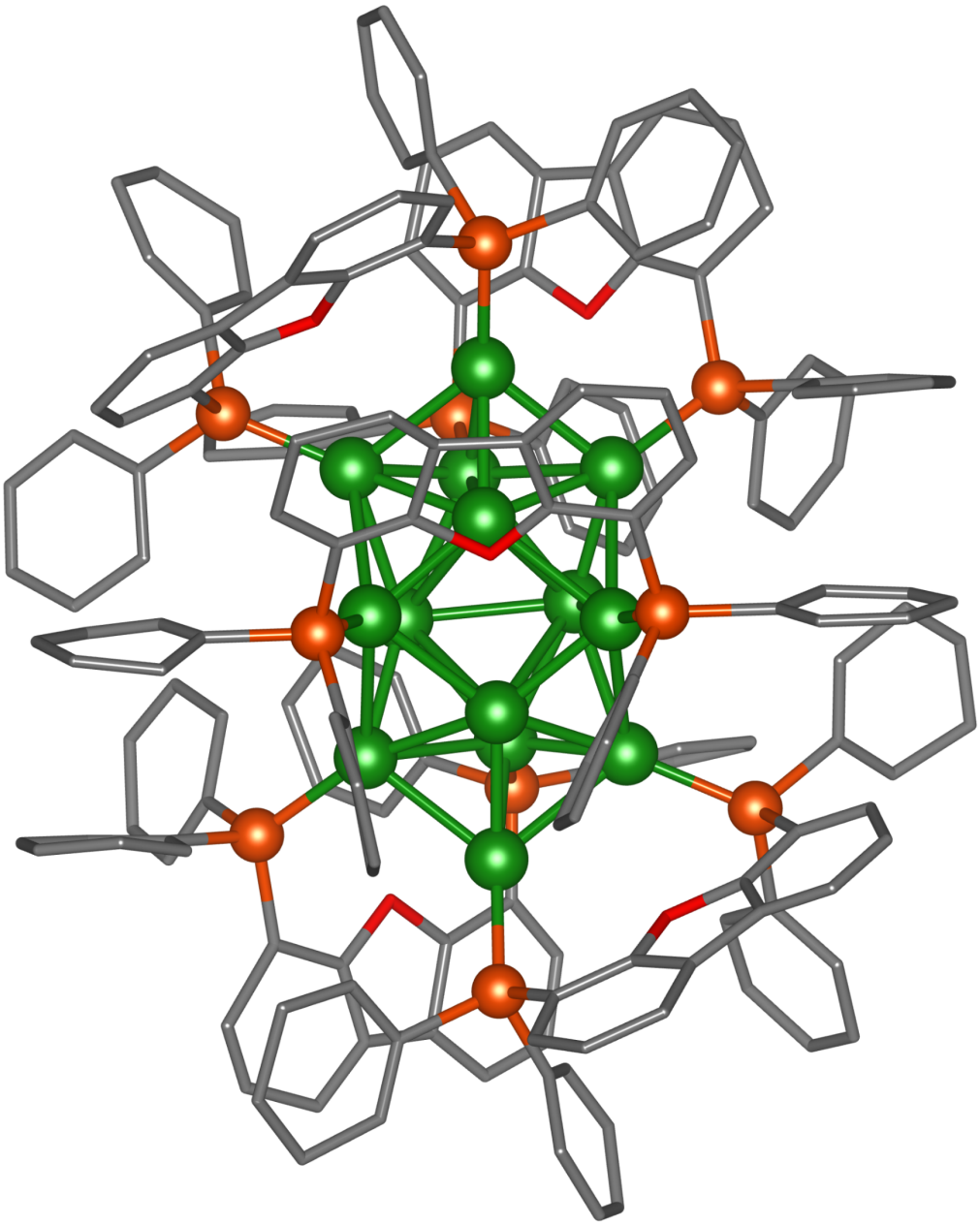

Figure 2.11. Ball and stick diagram of **2.8**. All hydrogen atoms have been omitted for clarity. Color legend: Cu = green; P = yellow-orange; O = red wireframe; C = grey wireframe.

Complex **2.8** crystallizes in the monoclinic space group $P2\frac{1}{n}$ (Figure 2.11) also with approximate C_2 symmetry. In the solid state, the copper core of complex **2.8** appears as a

distorted, rhombic dodecahedron. The Cu–Cu distances range from 2.427(6) to 2.858(6) Å, a slightly narrower distribution than in complex **2.7** and consistent with other reported Cu(I)-H clusters.[42, 59] While the hydride moieties could not be located on the Fourier difference map, I propose that there are likely 14 hydride ligands, to balance the charge on the cluster as complex **2.8** likely does not have partial Cu(0) character. Consistent with my observations for complexes **2.1**, **2.2**, and **2.7**, the four DBFphos ligands are again bridging across two metal centers with the Cu–P distances average 2.27 Å, which is slightly longer than the Cu–P distances for complex **2.7** and for only other structurally characterized Cu(I)-DBFphos complex.[84] Similar to complex **2.7**, there are now four "bare" Cu atoms in complex **2.8**.

Unfortunately, neither complex **2.7** nor complex **2.8** can be isolated cleanly. All attempts at modification of the reaction conditions only produce intractable mixtures. These preliminary data suggest a correlation between the bite angle of a bidentate phosphine supporting ligand and the nuclearity of the corresponding Cu(I)-H cluster generated. However, until the syntheses can be improved, no conclusive statements can be made about this supposed trend. Also, in the time since the inception of this research, three new Cu(I)-H clusters supported by small bite angle bidentate phosphine ligands have been published: $[Cu_8H_6(dppm)_5]^{2+}$, $[Cu_{16}H_{14}(dppa)_6]^{2+}$, and $[Cu_{18}H_{16}(dppe)_6]^{2+}$ (dppe = 1,2-bis(diphenylphosphino)ethane).[85-86] These clusters were isolated using a substoichiometric amount of ligand, which induced larger cluster formation. Clearly, there are more factors than just bite angle at work during cluster synthesis to determine the resultant speciation.

2.2.5 Synthesis and Solid State Molecular Structure of $[Cu_{13}H_{10}(SePh)_3(PPh_3)_7]$ (2.9)

Since its characterization in 1971 by Osborn and co-workers, the hexameric Cu(I)-H cluster $[CuH(PPh_3)]_6$ has garnered immense interest for its reactivity with organic substrates.[42, 70, 87] However, investigation into the potential for this hexameric cluster to act a seed for larger nanocluster growth has remained relatively underexplored.[13, 63-64, 85, 88] Recently, the Hayton group has demonstrated that reaction of $[CuH(PPh_3)]_6$ with phenanthroline (phen) in dichloromethane generates the new Cu(I)-H cluster $[Cu_{14}H_{12}(phen)_6(PPh_3)_4][Cl]_2$.[13] Similarly, Tanase and co-workers isolated the octameric cluster $[Cu_8H_6(dppm)_5](PF_6)_2$ through reaction of $[CuH(PPh_3)]_6$ with dppm in the presence of $[Cu(NCCH_3)_4]PF_6$.[85] Surprisingly, to the best of my knowledge, the reactivity of $[CuH(PPh_3)]_6$ towards chalcogenides and chalcogenoates has yet to be explored.

That said, copper chalcogenide/chalcogenoate clusters have been studied extensively due to their unusual semi-conductor properties.[89-90] Synthesis of these materials often employs simple Cu(I) salts as precursors and the composition of the clusters is governed by the reaction stoichiometry, though this synthetic procedure remains imprecise and ill-defined cluster speciation remains a problem.[89-94] Additionally, the source of the selenium or tellurium in these clusters is often the highly noxious selenol or tellurol reagents and introduction of a synthetic pathway that obviates the need for those reagents would be beneficial. Thus, I endeavored to synthesize a new copper selenoate cluster using $[CuH(PPh_3)]_6$ as a nucleation point. In this regard, I have isolated the Cu(I)-selenoate cluster $[Cu_{13}H_{10}(SePh)_3(PPh_3)_7]$ (**2.9**) from the *in situ* reduction of the Se-Se bond of Ph_2Se_2 by the hydride ligands of $[CuH(PPh_3)]_6$.

Addition of a yellow C_6H_6 solution of Ph_2Se_2 (1.5 equiv) to a stirring, red C_6H_6 solution of $[CuH(PPh_3)]_6$ at room temperature results in rapid effervescence of H_2 and a color change to bright orange. Work-up of the reaction mixture after 2 h results in the isolation of the Cu(I)-selenoate cluster $[Cu_{13}H_{10}(SePh)_3(PPh_3)_7]$ (**2.9**) in 12% yield (Scheme 2.3). The modest yield of this product is partially due to the formation of three by-products – a second hydride-containing product (which has thus far eluded characterization), PPh_3, as well as the known bimetallic Cu(I)-selenoate complex $[Cu_2(SePh)_2(PPh_3)_3]$[91] (Figure A2.30-A2.32) and the separation of those by-products. Briefly, the isolation of complex **2.9** begins with the recrystallization of the filtered reaction mixture in C_6H_6 layered with hexanes to remove PPh_3. The resultant mixture of red-orange crystals of **2.9**, orange crystalline powder of the second cluster, and a yellow powder of $[Cu_2(SePh)_2(PPh_3)_3]$ was then washed in a minimal amount of THF to remove the orange and yellow powder. However, complex **2.9** is also soluble in THF and care must be taken to use as little solvent as possible in this wash step. The red-orange crystals can then be dissolved in CH_2Cl_2 and layered with hexanes to give pure **2.9** in 12% yield. Pure complex **2.9** is soluble in CH_2Cl_2 and THF, sparingly soluble in toluene and C_6H_6, and insoluble in pentane, hexanes and diethyl ether.

Scheme 2.3. Synthesis of 2.9

$$2[CuH(PPh_3)]_6 + 3Ph_2Se_2 \xrightarrow[-H_2]{C_6H_6,\ 25\ ^\circ C} [Cu_{13}H_{10}(SePh)_3(PPh_3)_7] + [Cu_2(SePh)_2(PPh_3)_3] + PPh_3 + \text{other products}$$

Mechanistically, two of the hydride moieties on $[CuH(PPh_3)]_6$ act as reducing agents to cleave the Se-Se bond in Ph_2Se_2 to generate the observed H_2 gas (*vide infra*) and phenylselenoate, $[PhSe]^-$. This new anionic ligand then rapidly reacts with any Cu-containing materials in the reaction mixture and through a self-assembly process generates complex **2.9**

and the aforementioned by-products. Interestingly, the Cu:P ratio has dropped significantly, from 1:1 in $[CuH(PPh_3)]_6$ to nearly 2:1 in complex **2.9**. Typically, with these metal to ligand ratios, larger, low-valent Cu clusters can be formed.[65, 95] However, I speculate that the presence of free PPh_3 in the reaction mixture inhibits cluster growth.

Complex **2.9** crystallizes as the THF solvate, **2.9**·3THF, in the trigonal space group $R\bar{3}c$ with approximate C_{3v} symmetry (Figure 2.12B). The Cu_9 core of **2.9** consists of a distorted, triangular cupola with Cu_{cupola}-Cu_{cupola} distances ranging from 2.393(3) to 2.903(3) Å. The hexagonal face of the cupola is capped with a single Cu atom, Cu_{apical}, with Cu_{cupola}-Cu_{apical} bond distances ranging between 2.554(4) and 3.069(3) Å. Finally, each of the three, square faces of the cupola are capped by an additional Cu atom, Cu_{cap}, with Cu_{cupola}-Cu_{cap} distances ranging from 2.492(3) to 3.255(5) Å. These bond lengths, and their large ranges, are typical of Cu(I)-H clusters.[42, 59] While the hydride moieties could not be located in the Fourier difference map, there are likely 10 to balance the charge of the cluster as I do not believe that complex **2.9** is low-valent.

Each of Cu_{apical} and Cu_{cap}, and three of the core Cu atoms on the hexagonal face are bonded to a PPh_3 ligand (Figure 2.12A), with Cu-P bond distances of 2.258(8), 2.228(9), and 2.231(9) Å, respectively, within range of Cu-P distances for Cu(I)-H clusters.[42, 59] Finally, the three SePh ligands are bridging μ_2 between a Cu atom on the trigonal face of the cupola and a C_{cap} with a Cu_{cupola}-Se distance of 2.379(3) Å and Cu_{cap}-Se distance of 2.403(4) Å, within range of other μ_2 Cu-Se bond distances in Cu-selenoate clusters.[89, 91, 93] As was seen in complexes **2.7** and **2.8**, three Cu atoms in **2.9** remain "bare" and are likely held within the cluster through Cu-H and Cu-Cu bonds.

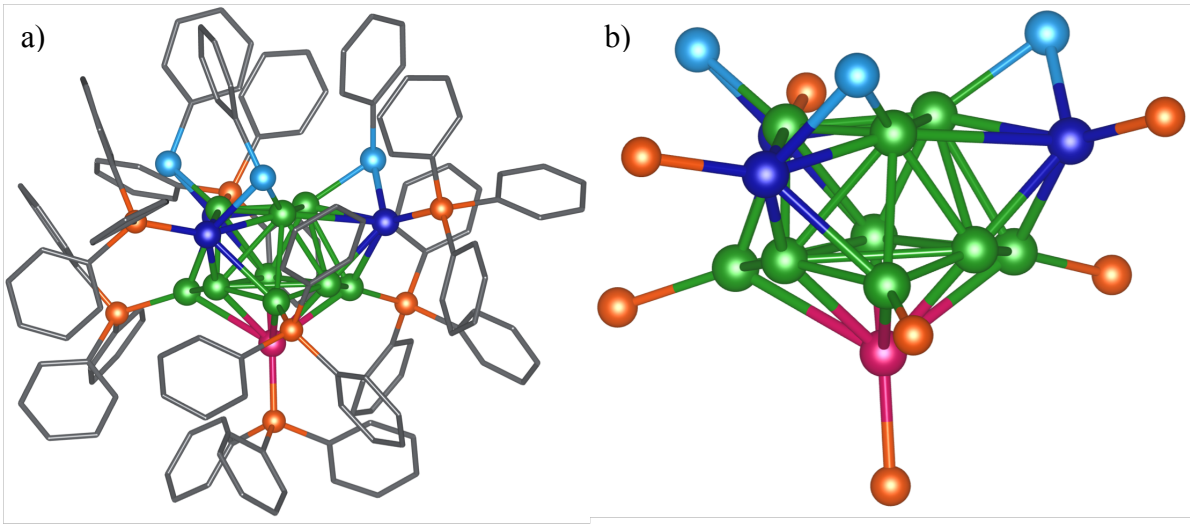

Figure 2.12. Ball and stick diagram showing a) the full structure and b) the $[Cu_{13}P_7Se_3]$ core of complex **2.9**. All hydrogen atoms have been omitted for clarity. Color legend: Cu_{cupola} = green; Cu_{apical} = magenta; Cu_{cap} = dark blue P = yellow-orange; Se = light blue; C = grey wireframe.

A ^{1}H NMR spectrum (Figure 2.13) of **2.9** taken in CD_2Cl_2 reveals the presence of three hydride environments at 2.73, 2.97, and 3.12 ppm, suggesting that the C_{3v} symmetry is maintained in solution. Overall, these resonances integrate for 10, consistent with my proposed formula. The presence of three environments indicates that there are three unique hydride environments, each with three hydrides. The signal for the fourth hydride environment, consisting of a single hydride, likely overlaps with one of these resonances, though isolation of the deuterated cluster **2.9-*d*$_{10}$** and subsequent ^{2}H NMR spectroscopy would confirm this hypothesis. The relatively upfield shift of these hydride environments indicates these ligands are likely on the surface of the cluster, not in an interstitial site.[13] The aryl region of the spectrum contains 9 magnetically unique environments, which is fewer than the expected 12, however integration of the multiplet at 6.97 ppm for 39H indicates that four of the environments are overlapping. Overall, the resonances in the ^{1}H spectrum integrate for

130H, consistent with my proposed formulation. The $^{1}H\{^{31}P\}$ NMR spectrum (Figure 2A.29) essentially the same as the ^{1}H NMR spectrum; the only notable difference is that the resonances centered at 7.38 and 7.89 ppm change from triplets to doublets, indicating they arise from the PPh_3 ligands. The ^{31}P NMR spectrum (Figure 2.13, inset) curiously only features two resonances at -3.38 and 3.62 ppm in a 4:3 ratio. The resonance at -3.38 ppm is tentatively assigned to the overlapping PPh_3 ligands on Cu_{apical} and Cu_{cupola} as the proximity to the selenoate likely shifts the resonance for the PPh_3 moiety bonded to Cu_{cap} downfield.

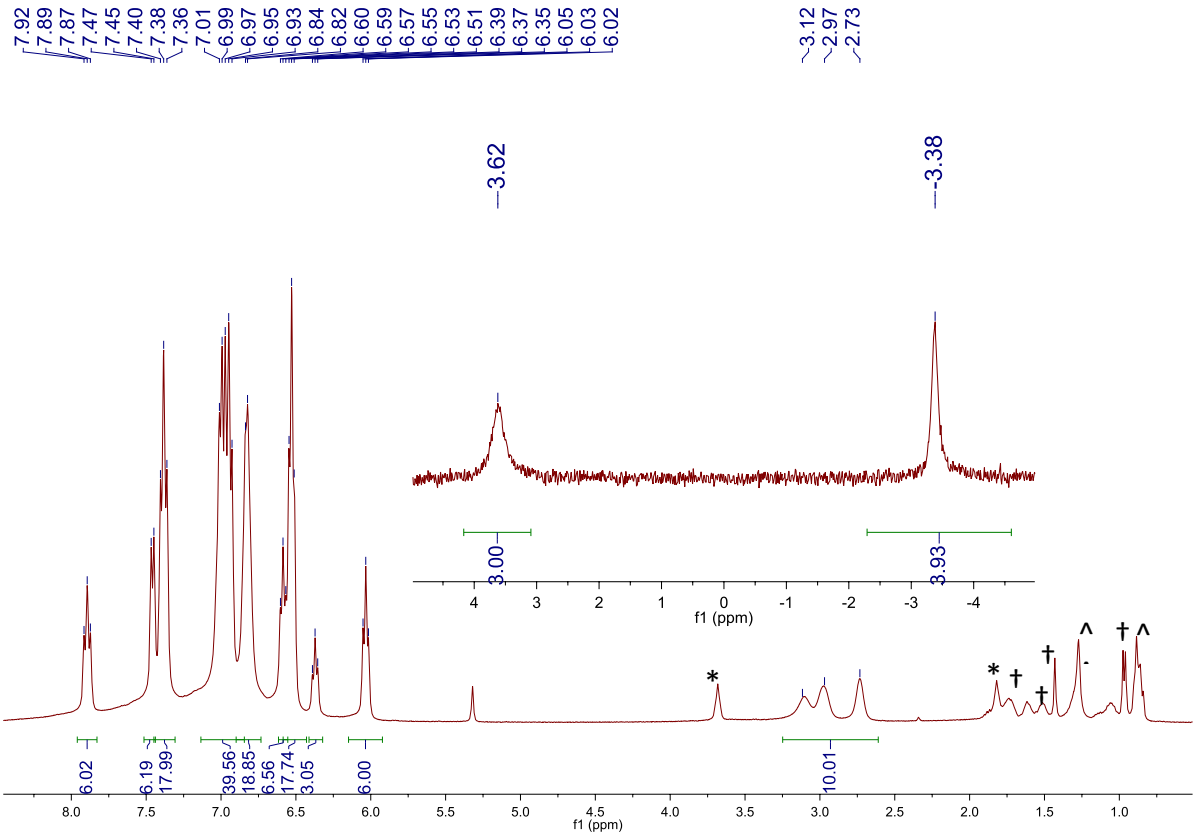

Figure 2.13. ^{1}H and ^{31}P (inset) NMR spectra of $[Cu_{13}H_{10}(SePh)_3(PPh_3)_7]$ (**2.9**) in CD_2Cl_2. (*) indicates a resonance assignable to THF, (^) indicates a resonance assignable to hexanes, and (†) indicates a resonance assignable to an unidentified impurity.

To better understand the mechanism by which **2.9** forms, I followed the reaction of $[CuH(PPh_3)]_6$ with Ph_2Se_2 (1.5 equiv) in C_6D_6 over the course of 2 h (Figure A2.33-A2.35).

Upon addition of Ph_2Se_2 to $[CuH(PPh_3)]_6$ the reaction mixture changed color from red to orange with release of H_2. The ^{31}P NMR spectra (Figure A2.35) reveal resonances assignable to complex **2.9** at 1.50 and -3.90 ppm, PPh_3 at -5.41ppm, and the bimetallic complex $[Cu_2(SePh)_2(PPh_3)_3]$[91] at 4.31 and -2.56 ppm. There is another small resonance at -6.32 ppm, as well as a shoulder on the resonance at -2.56 ppm, which may be assignable to the second Cu(I)-hydride complex. Interestingly, after 20 min, no resonances assignable to $[CuH(PPh_3)]_6$ are present, indicating that this reaction may occur nearly instantaneously. The ^1H NMR spectra show a small resonance at 4.47 ppm, which confirms that H_2 is being released as the reaction progresses. Also present is a doublet centered at 8.41 ppm, which is diagnostic for the other Cu cluster that is generated during the course of this reaction. These spectra also reveal hydride environments assignable to complex **2.9** at 3.53, 3.43, and 3.15 ppm. Notably, there is a second set of hydride resonances at 5.52, 3.38 and 3.20 ppm, which are present in ^1H NMR spectrum of a crude mixture **2.9**, the second cluster, and $[Cu_2(SePh)_2(PPh_3)_3]$ and likely correspond to the hydride environments of that second cluster.

To confirm the hydride assignments from the *in situ* ^1H NMR spectra, I repeated the above experiment with $[CuD(PPh_3)]_6$ instead. Gratifyingly, the ^1H and ^{31}P NMR spectra (Figure A2.36-A2.38) are virtually identical to those from the experiment with $[CuH(PPh_3)]_6$ suggesting that similar products are forming. The ^1H NMR spectrum tellingly does not feature any broad resonances between 3 and 6 ppm, confirming their previous assignment as hydrides/deuterides. Unfortunately, **2.9-*d*$_{10}$** was not isolated, nor a ^2H NMR spectrum collected for the *in situ* experiment. In an effort to ascertain the identity of the second cluster, as well as confirm the presence of 10 hydride ligands in complex **2.9**, an ESI-MS was recorded on a crude mixture of **2.9**, the second cluster, and $[Cu_2(SePh)_2(PPh_3)_3]$ in CH_2Cl_2 (Figure

A2.54). Unfortunately, the parent ion [**2.9**]$^{+}$, with *m/z* = 3139.6680, was not found in this spectrum. However, a signal was observed at *m/z* = 3096.5630 which is flanked by several species related to this feature by ±PPh_3. While this *m/z* is a poor match for [**2.9**]$^{+}$, it may arise from a slight rearrangement of the complex. It is also possible that this feature is related to the unidentified product, though my attempts at modelling the exact formula and isotope pattern have been unsuccessful. Clearly, more work must be done to determine the chemical formula of the second cluster, as well as verify the number of hydride ligands in **2.9**.

2.3 Summary

In summary, I have isolated and characterized the diphosphine ligated clusters, $[Ag_6H_4(dppm)_4(OAc)_2]$ (**2.1**) and $[Cu_3H(dppm)_3(OAc)_2]$ (**2.2**). Complex **2.1** is the first homometallic silver polyhydrido cluster to be structurally characterized. Interestingly, both **2.1** and **2.2** are the products of incomplete reduction; each cluster features the incorporation of two acetate moieties. While the cause of this is not certain, I posit that the $[Cu_3H]^{2+}$ and $[Ag_6H_4]^{2+}$ cores are unusually stable, and a more powerful hydride source would be required to drive the reduction to completion. Both **2.1** and **2.2** are effective pre-catalysts for the hydrosilylation of (α,β–unsaturated) ketones. Most notably, these results represent the first example of catalysis with an authentic, isolable silver hydride, expanding the scope of catalytic reactivity known for the group 11 hydrides. Attempts at generating larger Cu(I)-H clusters through manipulation of the supporting bidentate ligand bite angle results in the formation of the new clusters, $[Cu_{10}H_{10}(DPEphos)_4]$ (**2.7**) and $[Cu_{14}H_{14}(DBFphos)_5]$ (**2.8**). Neither cluster can be isolated cleanly, therefore the observed correlation between bite angle and cluster nuclearity remains hypothetical. Finally, I have explored the reactivity of $[CuH(PPh_3)]_6$ with Ph_2Se_2 to generate the new Cu(I)-H cluster $[Cu_{13}H_{10}(SePh)_3(PPh_3)_7]$ (**2.9**).

This cluster is formed in conjunction with at least one other Cu(I)-H cluster that has yet to be identified, along with the Cu-selenoate complex, $[Cu_2(SePh)_2(PPh_3)_3]$. Notably, the selenium source for complex **2.9** is Ph_2Se_2, which can be readily reduced by hydride to $[PhSe]^-$ obviating the need for noxious reagents, such as selenols. While further investigation into this reaction is required, it represents a new avenue to generate Cu(I)-H clusters with selenoate co-ligands using $[CuH(PPh_3)]_6$ as a seed and Ph_2Se_2 as a vehicle for selenide incorporation.

2.4 Experimental

2.4.1 General Procedures

All reactions and subsequent manipulations were performed under anaerobic and anhydrous conditions under an atmosphere of nitrogen. Hexanes, diethyl ether, and tetrahydrofuran (THF) were dried using a Vacuum Atmospheres DRI-SOLV Solvent Purification system and stored over 3Å sieves for 24 h prior to use. Benzene, acetonitrile, and dichloromethane were degassed and dried over 3Å molecular sieves for 72 h prior to use. Acetonitrile-d_3 (MeCN-d_3), benzene-d_6 (C_6D_6), 1,2-dichlorobenzene, 1,2-dichlorobenzene-d_4 ($1,2\text{-}C_6D_4Cl_2$), dichloromethane-d_2 (CD_2Cl_2), diphenylsilane, and diphenylsilane-d_2 (Sigma-Aldrich, 97 atom% D), were dried over 3Å molecular sieves for 24 h prior to use. All other reagents were purchased from commercial suppliers and used as received. $[CuH(PPh_3)]_6$ and DBFphos were prepared according to their respective literature procedures.[13, 96]

^1H NMR spectra were recorded on an Agilent Technologies 400-MR DD2 spectrometer. $^{13}C\{^1H\}$ and variable temperature NMR spectra were recorded on a Varian Unity Inova 500 MHz spectrometer. $^{31}P\{^1H\}$ and ^2H NMR spectra were recorded on an Agilent Technologies 400-MR DD2 spectrometer. $^{109}Ag\{^1H\}$ NMR spectra were recorded on a Bruker Avance 500 MHz spectrometer. To increase the sensitivity of the ^{109}Ag acquisition an INEPT pulse

sequence was used.[58] The parameters employed were: 90 degree pulses of 23 and 12 μs for ^{1}H and ^{109}Ag, respectively; J_{AgH} = 100 Hz; acquisition time of 1.3 s; relaxation delay of 15 s; total scans = 10,088. The chemical shifts of all nuclei were referenced indirectly with the ^{1}H resonance of $SiMe_4$ at 0 ppm, according to IUPAC standard,[97-98] or by using the residual solvent peaks (^{1}H and ^{2}H NMR experiments) or the characteristic resonances of the solvent nuclei as internal standards ($^{13}C\{^{1}H\}$ NMR experiments). $^{109}Ag\{^{1}H\}$ NMR spectra were referenced indirectly with the ^{109}Ag resonance of $Ag(NO_3)$ (4M in D_2O) at 31.7 ppm.[99] IR spectra were recorded on a Nicolet 6700 FT-IR spectrometer with a NXR FT Raman Module. Mass spectra were collected at the Materials Research Laboratory Shared Experimental Facilities at UCSB, using an electrospray ion (ESI) source on positive ion mode with a Waters Xevo G2-XS TOF Time-of-Flight mass spectrometer. Mass spectra were smoothed 3 times using the Savitzky-Golay algorithm with a smooth window of 2 channels. Elemental analyses were performed by the Micro-Mass Facility at the University of California, Berkeley.

2.4.2 Synthesis of $[Ag_6H_4(dppm)_4(OAc)_2]$ (2.1)

To a stirring, white suspension of Ag(OAc) (100.0 mg, 0.599 mmol) in benzene (1 mL) was added dropwise a solution containing 1,1-bis(diphenylphosphino)methane (233.3 mg, 0.606 mmol) and diphenylsilane (60.0 μL, 0.323 mmol) in benzene (2 mL). This resulted in a rapid color change to dark red-brown, concomitant with the deposition of an off-white solid. After stirring at room temperature for 15 h, the reaction mixture was concentrated to 1.5 mL *in vacuo*. The mixture was then filtered through a medium porosity frit, and the collected solid was rinsed with diethyl ether (2 × 4 mL), benzene (1 × 1.5 mL), tetrahydrofuran (1 × 0.5 mL), and again with diethyl ether (1 × 4 mL). The washings were then discarded. The resulting pale grey powder was dissolved in 1,2-dichlorobenzene (3 mL) and filtered through a Celite

column (0.5 cm × 2.0 cm) supported on glass wool. To the resulting pale-yellow solution was added benzene (1 mL). This solution was then layered with diethyl ether (8 mL). The solution was stored at –25 °C for 2 d, which resulted in the deposition of colorless crystals. The crystals were isolated by decanting the supernatant, washed with diethyl ether (3 × 2 mL), and dried *in vacuo* to yield **2.1** (107.9 mg, 47% yield). Anal. Calcd for $C_{104}H_{98}Ag_6O_4P_8$: C, 54.14; H, 4.28. Found: C, 53.87; H, 4.09. ^{1}H NMR (400 MHz, 25 °C, C_6D_6): δ 2.92 (s, 6H, OAc), 3.02 (br s, 4H, C*H*H), 5.44 (br m, 4H, C*H*H), 5.82 (br m, 4H, μ_3-H), 6.24 (t, J_{HH} = 7.5 Hz, 16H, *m*-Ph), 6.57 (t, J_{HH} = 7.3 Hz, 8H, *p*-Ph), 6.78 (br s, 16H, *o*-Ph), 7.13 (t, J_{HH} = 7.2 Hz, 8H, *p*-Ph), 7.26 (t, J_{HH} = 7.5 Hz, 16H, *m*-Ph), 8.16 (br s, 16H, *o*-Ph). ^{1}H{^{31}P} NMR (400 MHz, 25 °C, C_6D_6): δ 2.92 (s, 6H, OAc), 3.03 (br m, 4H, C*H*H), 5.44 (d, J_{HH} = 13.4 Hz, 4H, C*H*H), 5.83 (br m, 4H, μ_3-H), 6.24 (t, J_{HH} = 7.6 Hz, 16H, *m*-Ph), 6.57 (d, J_{HH} = 7.4 Hz, 8H, *p*-Ph), 6.78 (d, J_{HH} = 7.5 Hz, 16H, *o*-Ph), 7.13 (t, J_{HH} = 7.3 Hz, 8H, *p*-Ph), 7.26 (t, J_{HH} = 7.6 Hz, 16H, *m*-Ph), 8.16 (d, J_{HH} = 7.7 Hz, 16H, *o*-Ph). ^{31}P{^{1}H} NMR (162 MHz, 25 °C, C_6D_6): δ 8.06 (br m). ^{109}Ag{^{1}H} NMR (23.30 MHz, 25 °C, 1,2-$C_6D_4Cl_2$: 1,2-$C_6H_4Cl_2$, 1:2, v:v): δ 1095 (br s). ESI-MS: *m/z* 2246.942 $[M\text{-}OAc]^+$ (Calcd *m/z* 2246.954), 1537.098 $[Ag_3H(dppm)_3(OAc)]^+$ (Calcd *m/z* 1537.095). IR (KBr pellet, cm^{-1}): 436 (w), 473 (m), 513 (m), 615 (w), 644 (w), 691 (s), 713 (m), 736 (s), 784 (m), 846 (w), 914 (w), 999 (m), 1026 (m), 1096 (m), 1156 (w), 1184 (w), 1261 (w), 1307 (w), 1326 (w), 1389 (s), 1434 (s), 1456 (w), 1481 (m), 1561 (s), 1573 (s), 1652 (w), 1771 (w), 1810 (w), 1888 (w), 1954 (w), 2870 (w), 2925 (w), 2961 (w), 3048 (m).

2.4.3 Synthesis of $[Ag_6D_4(dppm)_4(OAc)_2]$ (2.1-d_4)

To a stirring, white suspension of Ag(OAc) (105.0 mg, 0.629 mmol) in benzene (1 mL) was added dropwise a solution containing 1,1-bis(diphenylphosphino)methane (249.3 mg, 0.649 mmol) and diphenylsilane-d_2 (60.0 μL, 0.323 mmol) in benzene (2 mL). This resulted

in a rapid color change to dark red-brown, concomitant with the deposition of an off-white solid. After stirring at room temperature for 15 h, the reaction mixture was concentrated to 1.5 mL *in vacuo*. The mixture was then filtered through a medium porosity frit, and the collected solid was rinsed with diethyl ether (2 × 4 mL), benzene (1 × 1.5 mL), tetrahydrofuran (1 × 1 mL), and again with diethyl ether (1 × 4 mL). The washings were then discarded. The resulting pale grey powder was dissolved in 1,2-dichlorobenzene (3 mL) and filtered through a Celite column (0.5 cm × 2.0 cm) supported on glass wool. To the resulting pale-yellow solution was added benzene (1 mL). This solution was then layered with diethyl ether (8 mL), and the solution was stored at ⁻25 °C for 2 d, which resulted in the deposition of colorless crystals. The crystals were isolated by decanting the supernatant, washed with diethyl ether (3 × 2 mL), and dried *in vacuo* to yield **2.1-*d*$_4$** (81.8 mg, 34% yield). ^{1}H NMR (400 MHz, 25 °C, C_6D_6): δ 2.93 (s, 6H, OAc), 3.02 (br s, 4H, C*H*H), 5.44 (br m, 4H, CH*H*), 6.23 (t, J_{HH} = 8.0 Hz, 16H, *m*-Ph), 6.57 (t, J_{HH} = 6.0 Hz, 8H, *p*-Ph), 6.78 (br s, 16H, *o*-Ph), 7.13 (t, J_{HH} = 8.0 Hz, 8H, *p*-Ph), 7.26 (t, J_{HH} = 8.0 Hz, 16H, *m*-Ph), 8.16 (br s, 16H, *o*-Ph). ^{1}H{^{31}P} NMR (400 MHz, 25 °C, C_6D_6): δ 2.93 (s, 6H, OAc), 3.03 (br m, 4H, CH*H*), 5.44 (d, J_{HH} = 13.3 Hz, 4H, CH*H*), 6.23 (t, J_{HH} = 8 Hz, 16H, *m*-Ph), 6.57 (t, J_{HH} = 6.0 Hz, 8H, *p*-Ph), 6.78 (d, J_{HH} = 8.0 Hz, 16H, *o*-Ph), 7.13 (t, J_{HH} = 8.0 Hz, 8H, *p*-Ph), 7.26 (t, J_{HH} = 8.0 Hz, 16H, *m*-Ph), 8.16 (d, J_{HH} = 8.0 Hz, 16H, *o*-Ph). ^{31}P{^{1}H} NMR (162 MHz, 25 °C, C_6D_6): δ 8.09 (br m). ^{2}H NMR (61 MHz, 25 °C, 1,2-$C_6D_4Cl_2$ with 1% C_6D_6): δ 5.76 (br m). ESI-MS: *m/z* 2250.978 $[M\text{-}OAc]^+$ (Calcd *m/z* 2250.979), 1538.109 $[Ag_3D(dppm)_3(OAc)]^+$ (Calcd *m/z* 1538.102). IR (KBr pellet, cm^{-1}): 439 (w), 473 (m), 481 (m), 501 (m), 513 (m), 616 (w), 647 (w), 692 (s), 714 (m), 737 (s), 783 (m), 848 (w), 916 (w), 971 (vw), 999 (m), 1027 (m), 1069 (vw), 1097 (m), 1156 (w), 1185 (w), 1275 (w), 1308 (w), 1327 (m), 1391 (s), 1434 (s), 1481 (m), 1574 (s), 1653 (w), 1813

(w), 1891 (w), 1955 (w), 2278 (w), 2869 (w), 2926 (w), 2983 (vw), 2961 (vw), 3017 (w), 3049 (m).

2.4.4 Synthesis of $[Cu_3H(dppm)_3(OAc)_2]$ (2.2)

To a stirring, pale green suspension of Cu(OAc) (150.0 mg, 1.22 mmol) and 1,1-bis(diphenylphosphino)methane (475.0 mg, 1.24 mmol) in benzene (6 mL) was added diphenylsilane (115 μL, 0.620 mmol) via syringe. After 10 min of stirring, a significant portion of the green solid had dissolved and the solution became pale-yellow in color, concomitant with the deposition of a fine white solid. The yellow solution was stirred for 20 h at room temperature, whereupon the reaction mixture was filtered through a Celite column (0.5 cm × 2.0 cm) supported on glass wool. The pale-yellow filtrate was concentrated *in vacuo* to ca. 3 mL, and layered with hexanes (4 mL). Storage of this solution at room temperature for 36 h resulted in the deposition of colorless crystals. The supernatant was decanted, the solid was washed with hexanes (3 × 1.5 mL) until the washings were colorless, and then subsequently dried *in vacuo* to yield **2.2** (492.1 mg, 83% yield). Anal. Calcd for $C_{79}H_{73}Cu_3O_4P_6 \cdot 2C_6H_6$: C, 67.50; H, 5.29. Found: C, 67.70; H, 5.10. ^{1}H NMR (400 MHz, 25 °C, C_6D_6): δ 1.71 (br s, 1H, μ_3-H), 2.44 (s, 6H, OAc), 3.35 (br s, 6H, CH_2), 6.83-6.88 (m, 36H, *m*-Ph overlapping *p*-Ph), 7.52 (d, J_{HH} = 8.0 Hz, 24H, *o*-Ph). ^{1}H NMR (400 MHz, 25 °C, MeCN-d_3): δ 1.91 (br s, 6H, OAc), 2.10 (sept, J_{PH} = 14.4 Hz, 1H, μ_3-H), 3.10 (br s, 6H, CH_2), 7.01 (t, J_{HH} = 7.5 Hz, 24H, *m*-Ph), 7.15 (d, J_{HH} = 6.2 Hz, 24H, *o*-Ph), 7.21 (t, J_{HH} = 7.4 Hz, 12H, *p*-Ph). ^{1}H{^{31}P} NMR (400 MHz, 25 °C, C_6D_6): δ 1.70 (br s, 1H, μ_3-H), 2.44 (s, 6H, OAc), 3.35 (s, 6H, CH_2), 6.82-6.88 (m, 36H, *m*-Ph overlapping *p*-Ph), 7.51 (d, J_{HH} = 8.0 Hz, 24H, *o*-Ph). ^{1}H{^{31}P} NMR (400 MHz, 25 °C, MeCN-d_3): δ 1.91 (s, 6H, OAc), 2.10 (s, 1H, μ_3-H), 3.09 (s, 6H, CH_2), 7.01 (t, J_{HH} = 7.6 Hz, 24H, *m*-Ph), 7.15 (d, J_{HH} = 7.4 Hz, 24H, *o*-Ph), 7.21 (t, J_{HH} = 7.4 Hz, 12H, *p*-

Ph). $^{31}P\{^{1}H\}$ NMR (162 MHz, 25 °C, C_6D_6): δ -10.21 (br s). $^{31}P\{^{1}H\}$ NMR (162 MHz, 25 °C, MeCN-d_3): δ -6.66 (br s). $^{13}C\{^{1}H\}$ NMR (101 MHz, 25 °C, C_6D_6): δ 26.17 (s, CH_3), 29.49 (t, J_{PC} = 4.6 Hz, CH_2), 128.48 (s, *m*-Ph), 128.59 (s, *p*-Ph), 133.88 (br s, *o*-Ph), 136.80 (br m, *ipso*-C), 176.21 (s, O_2CMe). ESI-MS: *m/z* 1379.120 $[Cu_3H(dppm)_3Cl]^+$ (Calcd *m/z* 1379.125), 1413.088 $[Cu_3(dppm)_3Cl_2]^+$ (Calcd *m/z* 1413.086), 1505.016 $[Cu_3(dppm)_3ICl]^+$ (Calcd *m/z* 1505.021). IR (KBr pellet, cm^{-1}): 442 (w), 471 (m), 484 (m), 515 (s), 616 (w), 678 (s), 692 (s), 714 (s), 737 (s), 789 (s), 848 (w), 908 (w), 970 (w), 1000 (m), 1027 (m), 1069 (m), 1095 (s), 1156 (m), 1187 (m), 1276 (m), 1321 (m), 1380 (s), 1405 (s), 1433 (s), 1480 (s), 1565 (s), 1577 (s), 1594 (s), 1653 (w), 1772 (w), 1813 (w), 1890 (w), 1958 (w), 2879 (w), 2912 (w), 2960 (w), 2984 (w), 3050 (m).

2.4.5 Synthesis of $[Cu_3D(dppm)_3(OAc)_2]$ (2.2-d_1)

To a stirring, pale-green suspension of Cu(OAc) (30.0 mg, 0.245 mmol) and 1,1-bis(diphenylphosphino)methane (95.0 mg, 0.247mmol) in benzene (4 mL) was added diphenylsilane-d_2 (24.0 μL, 0.129 mmol) via microsyringe. After 10 min of stirring, a significant portion of the green solid had dissolved and the solution became pale-yellow in color, concomitant with the deposition of a fine white solid. The yellow solution was stirred for 20 h at room temperature, whereupon the reaction mixture was filtered through a Celite column (0.5 cm × 2.0 cm) supported on glass wool. The pale-yellow filtrate was concentrated *in vacuo* to ca. 2 mL, and layered with hexanes (4 mL). Storage of this solution at room temperature for 36 h resulted in the deposition of colorless crystals. The supernatant was decanted, the solid was washed with hexanes (3 × 1.5 mL) until the washings were colorless, and then subsequently dried *in vacuo* to yield **2.2-d_1** (47.6 mg, 40% yield). ^{1}H NMR (400 MHz, 25 °C, C_6D_6): δ 2.44 (s, 6H, OAc), 3.33 (br s, 6H, CH_2), 6.83-6.85 (m, 36H, *m*-Ph

overlapping *p*-Ph), 7.51 (br s, 24H, *o*-Ph). $^{1}H\{^{31}P\}$ NMR (400 MHz, 25 °C, C_6D_6): δ 2.44 (s, 6H, OAc), 3.34 (s, 6H, CH_2), 6.84-6.87 (m, 36, *m*-Ph overlapping *p*-Ph), 7.52 (d, J_{HH} = 7.3 Hz, 24H, *o*-Ph). $^{31}P\{^{1}H\}$ NMR (162 MHz, 25 °C, C_6D_6): δ -9.99 (br s). ^{2}H NMR (61 MHz, 25 °C, C_6H_6:C_6D_6, 9:1, v:v): δ 1.74 (br s). ESI-MS: *m/z* 1380.123 $[Cu_3D(dppm)_3Cl]^+$ (Calcd *m/z* 1380.131), 1413.088 $[Cu_3(dppm)_3Cl_2]^+$ (Calcd *m/z* 1413.086), 1505.016 $[Cu_3(dppm)_3ICl]^+$ (Calcd *m/z* 1505.021). IR (KBr pellet, cm^{-1}): 442 (w), 472 (m), 482 (m), 515 (m), 616 (w), 657 (m), 692 (s), 714 (m), 736 (s), 788 (m), 847 (w), 917 (w), 1026 (m), 1095 (s), 1156 (w), 1186 (w), 1261 (m), 1321 (m), 1378 (s), 1403 (s), 1433 (s), 1481 (s), 1563 (s), 1576 (m), 1669 (w), 1811 (w), 1889 (w), 1957 (w), 2918 (w), 2961 (w), 2983 (w), 3048 (m).

2.4.6 Catalytic Hydrosilylation of 1-Cyclohexen-1-one (2.3)

2.4.6.1 Using 2.1 as the Catalyst

A J. Young NMR tube was charged with 2-Cyclohexen-1-one (**2.3**) (10.0 μL, 0.103 mmol), Ph_2SiH_2 (29.0 μL, 0.155 mmol), and C_6D_6 (1.5 mL). Hexamethyldisiloxane (2.5 μL, 0.046 mmol) was then added as an internal standard. To this solution was added complex **2.1** as a solid (3.0 mg, 0.0013 mmol, 0.05 H^- equivalents). The reaction mixture was then allowed to stand at room temperature. After 24 h, a ^{1}H NMR spectrum was recorded, which revealed the presence of **2.4a** and **2.4c**. The formation of (cyclohex-1-en-1-yloxy)diphenylsilane (**2.4a**) and (cyclohex-2-en-1-yloxy)diphenylsilane (**2.4c**) was confirmed by comparison with previously published NMR data.[69, 100] The % conversion to **2.4a** and **2.4c** was determined by integration of the resonance assigned to the vinylic hydrogen (5.17 ppm for **2.4a**); or the resonance assigned to silane hydrogen (5.78 ppm for **2.4c**) vs. the internal standard.

2.4a, *(cyclohexyl-1-en-1-yloxy)diphenylsilane*: 76% conversion. ^{1}H NMR (C_6D_6, 400 MHz): δ 1.31 (m, 2H), 1.46 (m, 2H), 1.86 (m, 2H), 2.14 (m, 2H), 5.18 (t, J_{HH} = 4.0 Hz, 1H), 5.88 (s, 1H, Si*H*), 7.19-7.13 (m, 6H), 7.72 (m, 4H).

2.4c, *(cyclohexyl-2-en-1-yloxy)diphenylsilane*: 3% conversion. ^{1}H NMR (C_6D_6, 400 MHz): δ 1.64 (m, 3H), 1.76 (m, 3H), 4.44 (m, 1H), 5.63 (m ,1H), 5.78 (s, 1H, Si*H*), 7.11-7.84 (m, 10H).

2.4.6.2 Using 2.2 as the Catalyst

A J. Young NMR tube was charged with 2-Cyclohexen-1-one (**2.3**) (10.0 μL, 0.103 mmol), Ph_2SiH_2 (29.0 μL, 0.155 mmol), and C_6D_6 (1.5 mL). Hexamethyldisiloxane (1.25 μL, 0.023 mmol) was then added as an internal standard. To this solution was added complex **2.2** as a solid (7.5 mg, 0.005 mmol, 0.05 H^- equivalents). The reaction mixture was then allowed to stand at room temperature. After 24 h, a ^{1}H NMR spectrum was recorded, which revealed the presence of **2.4a**, **2.4b**, and **2.4c**. The formation of (cyclohex-1-en-1-yloxy)diphenylsilane (**2.4a**), bis(cyclohex-1-en-1-yloxy)diphenylsilane (**2.4b**) and (cyclohex-2-en-1-yloxy)diphenylsilane (**2.4c**) was confirmed by comparison with previously published NMR data.[69, 100-101] The % conversion to **2.4a**, **2.4b** and **2.4c** was determined by integration of the resonance assigned to the vinylic hydrogen (5.17 ppm for **2.4a**; 5.37 ppm for **2.4b**) or the resonance assigned to silane hydrogen (5.78 ppm for **2.4c**) vs. the internal standard.

2.4a, *(cyclohexyl-1-en-1-yloxy)diphenylsilane*: 57% conversion. ^{1}H NMR (C_6D_6, 400 MHz): δ 1.31 (m, 2H), 1.46 (m, 2H), 1.86 (m, 2H), 2.14 (m, 2H), 5.18 (t, J_{HH} = 4.0 Hz, 1H), 5.88 (s, 1H, Si*H*), 7.19-7.13 (m, 6H), 7.72 (m, 4H).

2.4b, *Bis(cyclohexyl-1-en-1-yloxy)diphenylsilane*: 29% conversion. ^{1}H NMR (C_6D_6, 400 MHz): δ 1.31 (m, 4H), 1.46 (m, 4H), 1.85 (m, 4H), 2.19 (m, 4H), 5.37 (t, J_{HH} = 4.0 Hz, 2H), 7.17-7.10 (m, 6H), 7.92 (m, 4H).

2.4c, *(cyclohexyl-2-en-1-yloxy)diphenylsilane*: 10% conversion. ^{1}H NMR (C_6D_6, 400 MHz): δ 1.64 (m, 3H), 1.76 (m, 3H), 4.44 (m, 1H), 5.63 (m ,1H), 5.78 (s, 1H, Si*H*), 7.11-7.84 (m, 10H).

2.4.6.3 Using $[CuH(PPh_3)]_6$ as the Catalyst

A J. Young NMR tube was charged with 2-Cyclohexen-1-one (**2.3**) (20.0 μL, 0.206 mmol), Ph_2SiH_2 (58.0 μL, 0.310 mmol), and C_6D_6 (1.5 mL). Hexamethyldisiloxane (5.0 μL, 0.092 mmol) was then added as an internal standard. To this solution was added $[CuH(PPh_3)]_6$ as a solid (3.3 mg, 0.0083 mmol, 0.05 H^- equivalents). The reaction mixture was then allowed to stand at room temperature. After 15, a ^{1}H NMR spectrum was recorded, which revealed the presence of **2.4a**, and **2.4b**. The formation of (cyclohex-1-en-1-yloxy)diphenylsilane (**2.4a**) and bis(cyclohex-1-en-1-yloxy)diphenylsilane (**2.4b**) was confirmed by comparison with previously published NMR data.[100-101] The % conversion to **2.4a** and **2.4b** was determined by integration of the resonance assigned to the vinylic hydrogen (5.17 ppm for **2.4a**; 5.37 ppm for **2.4b**) vs. the internal standard.

2.4a, *(cyclohexyl-1-en-1-yloxy)diphenylsilane*: 79% conversion. ^{1}H NMR (C_6D_6, 400 MHz): δ 1.31 (m, 2H), 1.46 (m, 2H), 1.86 (m, 2H), 2.14 (m, 2H), 5.18 (t, J_{HH} = 4.0 Hz, 1H), 5.88 (s, 1H, Si*H*), 7.19-7.13 (m, 6H), 7.72 (m, 4H).

2.4b, *Bis(cyclohexyl-1-en-1-yloxy)diphenylsilane*: 21% conversion. ^{1}H NMR (C_6D_6, 400 MHz): δ 1.31 (m, 4H), 1.46 (m, 4H), 1.85 (m, 4H), 2.19 (m, 4H), 5.37 (t, J_{HH} = 4.0 Hz, 2H), 7.17-7.10 (m, 6H), 7.92 (m, 4H).

2.4.7 Catalytic Hydrosilylation of Cyclohexanone (2.5)

2.4.7.1 Using 2.1 as the Catalyst

A J. Young NMR tube was charged with Cyclohexanone (**2.5**) (10.0 μL, 0.097 mmol), Ph_2SiH_2 (24.0 μL, 0.129 mmol), and C_6D_6 (1.7 mL). Hexamethyldisiloxane (1.2 μL, 0.0056 mmol) was then added as an internal standard. To this solution was added complex **2.1** as a solid (5.6 mg, 0.0024 mmol, 0.10 H^- equivalents). The reaction mixture was then allowed to stand at room temperature. After 24 h, a ^1H NMR spectrum was recorded, which revealed the presence of unreacted **2.5**, as well as **2.6**. The formation of (cyclohexyloxy)diphenylsilane (**2.6**) was confirmed by comparison with previously published NMR data.[102] The % conversion to **2.6** was determined by integration of the resonance at 3.85 ppm (C*H*OSiHPh$_2$) vs. the internal standard.

2.6, *(cyclohexyloxy)diphenylsilane*: 42% conversion. ^1H NMR (C_6D_6, 400 MHz): δ 1.05 (m, 3H), 1.27 (m, 1H), 1.49 (m, 2H), 1.60 (m, 2H), 1.81 (m, 2H), 3.85 (m, 1H, C*H*OSi), 5.77 (s, 1H, Si*H*), 7.19-7.12 (m, 6H), 7.73 (m, 4H).

2.4.7.2 Using 2.2 as the Catalyst

A J. Young NMR tube was charged with Cyclohexanone (**2.5**) (10.0 μL, 0.097 mmol), Ph_2SiH_2 (24.0 μL, 0.129 mmol), and C_6D_6 (1.7 mL). Hexamethyldisiloxane (1.2 μL, 0.0056 mmol) was then added as an internal standard. To this solution was added complex **2.2** as a solid (14.2 mg, 0.0097 mmol, 0.10 H^- equivalents). The reaction mixture was then allowed to stand at room temperature. After 2 h, a ^1H NMR spectrum was recorded, which revealed the presence of **2.6**. The formation of (cyclohexyloxy)diphenylsilane (**2.6**) was confirmed by comparison with previously published NMR data.[102] The % conversion to **2.6** was determined by integration of the resonance at 3.85 ppm (C*H*OSiHPh$_2$) vs. the internal standard.

2.6, *(cyclohexyloxy)diphenylsilane*: 99% conversion. ^{1}H NMR (C_6D_6, 400 MHz): δ 1.05 (m, 3H), 1.27 (m, 1H), 1.49 (m, 2H), 1.60 (m, 2H), 1.81 (m, 2H), 3.85 (m, 1H, C*H*OSi), 5.77 (s, 1H, Si*H*), 7.19-7.12 (m, 6H), 7.73 (m, 4H).

2.4.7.3 Using $[CuH(PPh_3)]_6$ as the Catalyst

A J. Young NMR tube was charged with Cyclohexanone (**2.5**) (10.0 μL, 0.097 mmol), Ph_2SiH_2 (24.0 μL, 0.129 mmol), and C_6D_6 (1.7 mL). Hexamethyldisiloxane (1.2 μL, 0.0056 mmol) was then added as an internal standard. To this solution was added complex **2.1** as a solid (3.2 mg, 0.0016 mmol, 0.10 H^- equivalents). The reaction mixture was then allowed to stand at room temperature. After 24 h, a ^{1}H NMR spectrum was recorded, which revealed the presence of unreacted **2.5**, as well as **2.6**. The formation of (cyclohexyloxy)diphenylsilane (**2.6**) was confirmed by comparison with previously published NMR data.[102] The % conversion to **2.6** was determined by integration of the resonance at 3.85 ppm (C*H*OSiHPh_2) vs. the internal standard.

2.6, *(cyclohexyloxy)diphenylsilane*: 26% conversion. ^{1}H NMR (C_6D_6, 400 MHz): δ 1.05 (m, 3H), 1.27 (m, 1H), 1.49 (m, 2H), 1.60 (m, 2H), 1.81 (m, 2H), 3.85 (m, 1H, C*H*OSi), 5.77 (s, 1H, Si*H*), 7.19-7.12 (m, 6H), 7.73 (m, 4H).

2.4.8 Synthesis of $[Cu_{10}H_{10}(DPEphos)_4]$ (2.7)

To a stirring, pale green-white suspension of Cu(OAc) (30.0 mg, 0.245 mmol) and (oxydi-2,1-phenylene)bis(diphenylphosphino) (132.0 mg, 0.245 mmol) in THF (3 mL) was added diphenylsilane (25.0 μL, 0.135 mmol) via microsyringe. The reaction mixture slowly turned bright orange over the course of 30 min, which darkened to red-orange over 5 h, concomitant with the deposition of a fine orange powder. The red-orange solution was stirred for 20 h at room temperature, whereupon the volatiles were removed *in vacuo* to give a dark red-orange

oil. The oil was dissolved in diethyl ether (2 mL) and was filtered through a Celite column (0.5 cm × 2.0 cm) supported on glass wool. The filter was rinsed with diethyl ether until the washings were colorless (2 × 1 mL). The washings were added to the filtrate. The red-orange filtrate was concentrated *in vacuo* to ca. 2 mL, and layered with hexanes (4 mL). Storage of this solution at -25 ºC for 24 h resulted in the deposition of orange crystals of **2.7** and a red-orange powder (10.0 mg, 14%).

2.4.9 Synthesis of $[Cu_{14}H_{14}(DBFphos)_5]$ (2.8)

To a stirring, pale green-white suspension of Cu(OAc) (50.0 mg, 0.408 mmol) and 4,6-bis(diphenylphosphino)dibenzofuran (110.0 mg, 0.205 mmol) in benzene (6 mL) was added diphenylsilane (40.0 μL, 0.216 mmol) via microsyringe. The reaction mixture slowly turned yellow over the course of 30 min, which darkened to red-orange over 5 h, concomitant with the deposition of a fine yellow powder. The red-orange solution was stirred for 16 h at room temperature, whereupon the volatiles were removed *in vacuo* to give a dark red-orange oil. The oil was dissolved in dichloromethane (2 mL) and was filtered through a Celite column (0.5 cm × 2.0 cm) supported on glass wool. The filter was rinsed with dichloromethane until the washings were colorless (2 × 1 mL). The washings were added to the filtrate. The red-orange filtrate was layered with hexanes (8 mL). Storage of this solution at -25 ºC for 48 h resulted in the deposition of orange crystals of **2.8** and an orange-yellow powder (12.0 mg, 11%).

2.4.10 Synthesis of $[Cu_{13}H_{10}(PPh_3)_7(SePh)_3]$ (2.9)

To a stirring, red solution of $[CuH(PPh_3)]_6$ (200.0 mg, 0.101 mmol) in C_6H_6 (4 mL) was added dropwise a yellow solution of Ph_2Se_2 (48.0 mg, 0.154 mmol) in C_6H_6 (2 mL). Immediately upon addition, bubbles of H_2 rapidly formed and the solution became orange.

The reaction mixture was allowed to stir at room temperature for 2 h, over which time the solution became a brighter orange color. The solution was then filtered through a Celite column (0.5 cm × 2.0 cm) supported on glass wool. The filter was rinsed with C_6H_6 until the washings were colorless (2 × 1 mL) and a very small amount of light brown powder remained on the filter pad. The washings were added to the filtrate. The orange filtrate was layered with hexanes (10 mL). Storage of this solution at room temperature for 48 h resulted in the deposition of a mixture large orange block crystals, yellow microcrystalline solids, and a pale-yellow powder. This mixture of solids was subsequently rinsed with THF to remove the yellow products, as well as some of the orange crystals. The remaining orange solids were rinsed with dichloromethane (3 mL) and filtered through a Celite column (0.5 cm × 1.0 cm) supported on glass wool. The bright orange filtrate was then layered with hexanes (9 mL) and allowed to stand at -25 ºC for 24 h, which resulted in the deposition of orange crystals of **2.9** (17.0 mg, 12%). ^{1}H NMR (400 MHz, 25 °C, C_6D_6): δ 2.73 (br s, H$^-$), 2.97 (br s, H$^-$), 3.12 (br s, H$^-$), 6.03 (t, J_{HH} = 6 Hz, 6H, *m*-SePh), 6.37 (t, J_{HH} = 8 Hz, 3H, *p*-SePh), 6.53 (t, J_{HH} = 8 Hz, 18H, *m*-PPh_3), 6.59 (t J_{HH} = 8 Hz, 6H, apical *m*-Ph), 6.83 (m, 18H, *m*-PPh_3), 6.97 (m, 39H, overlapping apical *p*-PPh_3, two *p*-PPh_3 environments, and *o*-PPh_3), 7.38 (t, J_{HH} = 8 Hz, 18H, *o*-PPh_3), 7.46 (d, J_{HH} = 8 Hz, 6H, *o*-SePh), 7.89 (t, J_{HH} = 10 Hz, 6H, apical *o*-PPh_3). ^{1}H{^{31}P} NMR (400 MHz, 25 °C, C_6D_6): δ 2.73 (br s, H$^-$), 2.97 (br s, H$^-$), 3.09 (br s, H$^-$), 6.03 (t, J_{HH} = 6 Hz, 6H, *m*-SePh), 6.37 (t, J_{HH} = 8 Hz, 3H, *p*-SePh), 6.53 (t, J_{HH} = 8 Hz, 18H, *m*-PPh_3), 6.58 (t J_{HH} = 6 Hz, 6H, apical *m*-Ph), 6.83 (m, 18H, *m*-PPh_3), 6.98 (m, 39H, overlapping apical *p*-PPh_3, two *p*-PPh_3 environments, and *o*-PPh_3), 7.38 (d, J_{HH} = 8 Hz, 18H, *o*-PPh_3), 7.46 (d, J_{HH} = 8 Hz, 6H, *o*-SePh), 7.89 (d, J_{HH} = 8 Hz, 6H, apical *o*-PPh_3). ^{31}P{^{1}H} NMR (162 MHz, 25 °C, C_6D_6): δ -3.38 (s, 4P, two overlapping P environments), 3.62 (br s, 3P).

2.4.11 X-ray Crystallography

Data for **2.1**·2.5C_6H_6, **2.2**·2C_6H_6, **2.7**·3$C_4H_{10}O$, **2.8**, and **2.9**·3THF were collected on a Bruker KAPPA APEX II diffractometer equipped with an APEX II CCD detector using a TRIUMPH monochromater with a MoKα X-ray source (α = 0.71073 Å). Crystals were mounted on a cryoloop under Paratone-N oil, and all data were collected at 103(2) K for complex **2.1** and 100(2) K for complex **2.2** using an Oxford nitrogen gas cryostream system. X-ray data for **2.1**·2.5C_6H_6, **2.2**·2C_6H_6, **2.8**, and **2.9**·3THF were collected utilizing frame exposures of 10 s X-ray data for **2.7**·3$C_4H_{10}O$ was collected utilizing frame exposures of 15 s. Data collection and cell parameter determination were conducted using the SMART program.[103] Integration of the data frames and final cell parameter refinement were performed using SAINT software.[104] Absorption correction of the data was carried out using the multi-scan method SADABS.[105] Subsequent calculations were carried out using SHELXTL.[106] Structure determination was done using direct methods and difference Fourier techniques. All hydrogen atom positions were idealized, and rode on the atom of attachment, with the exception of the hydride moiety in complex **2.2** and two of the disordered diethyl ether solvates in **2.7**. Structure solution, refinement, graphics, and creation of publication materials were performed using SHELXTL.[106]

The μ_3-hydride ligand (H200) in **2.2**·2C_6H_6 was located in the difference Fourier map, and its position was refined isotropically. In contrast, the four μ_3-hydride ligands in **2.1**·2.5C_6H_6 were not located in the difference Fourier map, likely due to the high electron density around the hexametallic core. Complex **2.1**·2.5C_6H_6 contains positional disorder on one of the phenyl groups of the dppm ligand. The positional order was addressed by modeling the phenyl ring over 2 positions, each with half occupancy. Hydrogen atoms were not assigned

to this phenyl ring. The C–C bonds within this ring were fixed with the DFIX command, and the ring was constrained with the FLAT command. Additionally, for complex **2.2**·2C_6H_6, the C–C bond lengths in one of the benzene solvate molecules were fixed using the DFIX command. Complex **2.7**·3$C_4H_{10}O$, contains positional disorder on two of the diethyl ether solvates (O7 and O8). This positional disorder was addressed by modeling the diethyl ether solvates over two positions, each with half occupancy and using the DFIX and FLAT commands to fix the C–C and C–O bond lengths. Complex **2.8** contains positional disorder in six phenyl rings (C67, C73, C93, C147, C171, C177) and one phenyl ring of a dibenzylfuran (C67). The C–C bond lengths and flat geometry of these rings were constrained using the DFIX and FLAT commands, respectively. Complex **2.9**·3THF contains some thermal disorder, which was addressed using the SADI command.

Further crystallographic details can be found in Table 2.3 and Table 2.4.

Table 2.3. X-ray Crystallographic Data for **2.1**·2.5C_6H_6 and **2.2**·2C_6H_6.

	2.1·2.5C_6H_6	**2.2**·2C_6H_6
empirical formula	$C_{119}H_{113}Ag_6O_4P_8$	$C_{91}H_{85}Cu_3O_4P_6$
crystal habit, color	block, colorless	block, colorless
crystal size (mm)	0.15 × 0.1 × 0.1	0.2 × 0.05 × 0.05
crystal system	triclinic	monoclinic
space group	$P\bar{1}$	$P2\frac{1}{n}$
volume (Å^3)	5302.0(16)	7794(3)
a (Å)	15.918(3)	13.493(3)
b (Å)	17.571(3)	43.365(9)
c (Å)	19.574(3)	13.796(4)
α (deg)	86.263(4)	90
β (deg)	80.463(5)	105.106(7)
γ (deg)	79.321(5)	90
Z	2	4
formula weight (g/mol)	2502.07	1619.02
density (calculated) (Mg/m^3)	1.567	1.380
absorption coefficient (mm^{-1})	1.260	0.987
F_{000}	2522	3360
total no. reflections	26245	16382
unique reflections	17801	10152
final R indices [I>2σ(I)]	R_1 = 0.0745	R_1 = 0.0538
	wR_2 = 0.1173	wR_2 = 0.1101
largest diff. peak and hole (e$^-$A^{-3})	2.879 and -1.786	1.247 and -0.510
GOF	1.099	0.988

Table 2.4. X-ray Crystallographic Data for **2.7**·$3C_4H_{10}O$, **2.8**, and **2.9**·3THF

	2.7·$3C_4H_{10}O$	**2.8**	**2.9**·3THF
empirical formula	$C_{156}H_{152}Cu_{10}O_7P_8$	$C_{180}H_{144}Cu_{14}O_5P_{10}$	$C_{156}H_{154}Cu_{13}P_7Se_3O_3$
crystal habit, color	plate, orange	plate, orange	block, orange
crystal size (mm)	0.2 × 0.2 × 0.04	0.1 × 0.1 × 0.04	0.4 × 0.4 × 0.3
crystal system	orthorhombic	monoclinic	trigonal
space group	$P2_12_12$	$P2\frac{1}{n}$	$R\bar{3}c$
volume ($Å^3$)	7379(9)	20625(3)	49122(26)
a (Å)	17.704(12)	21.884(2)	28.024(5)
b (Å)	25.983(17)	31.103(3)	28.024(5)
c (Å)	16.041(11)	30.306(3)	72.21(2)
α (deg)	90	90	90
β (deg)	90	91.007(6)	90
γ (deg)	90	90	120
Z	4	4	6
formula weight (g/mol)	3022.12	3586.44	3356.68
density (calculated) (Mg/m^3)	1.361	1.155	1.362
absorption coefficient (mm^{-1})	1.260	1.531	2.442
F_{000}	3092	7224	22644
total no. reflections	13094	29970	5231
unique reflections	6428	4184	2906
final R indices [I>2σ(I)]	R_1 = 0.1033	R_1 = 0.1292	R_1 = 0.0709
	wR_2 = 0.2343	wR_2 = 0.3350	wR_2 = 0.1586
largest diff. peak and hole (e^-A^{-3})	1.923 and -0.857	2.210 and -0.960	1.667 and -0.772
GOF	1.338	0.803	1.091

2.5 Appendix

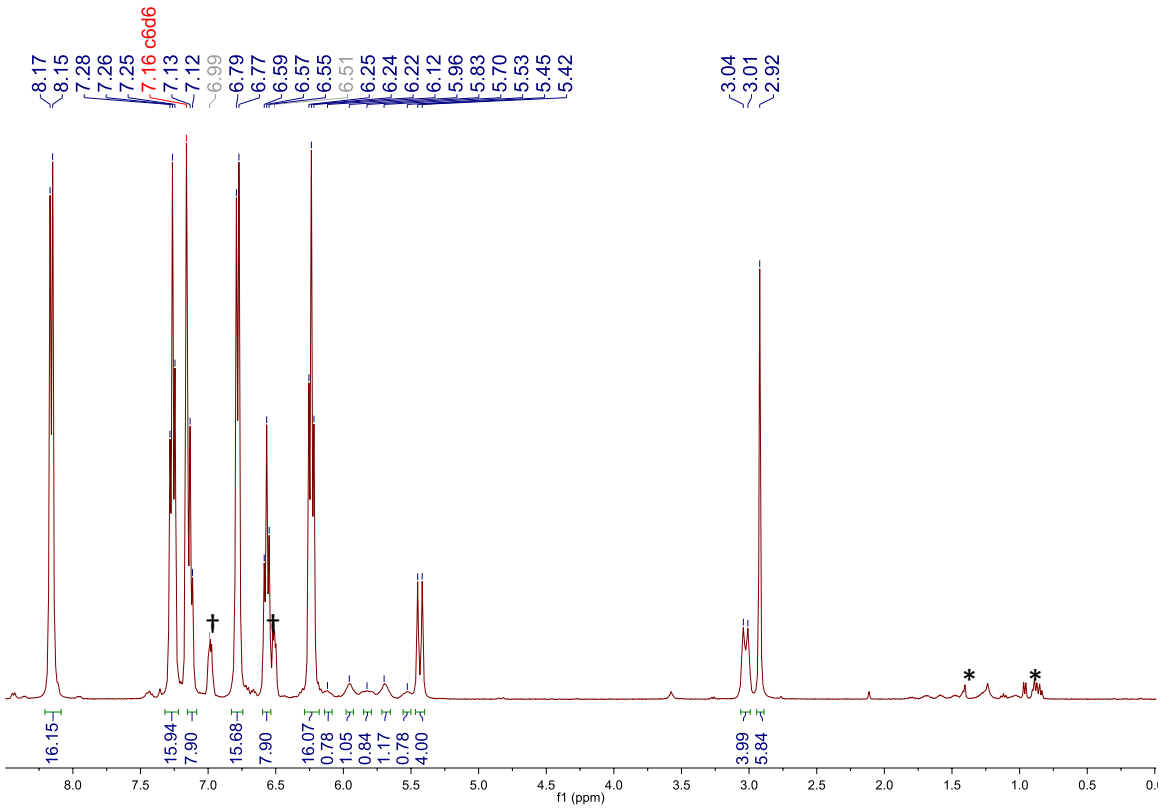

Figure A2.1. $^{1}H\{^{31}P\}$ NMR spectrum of **2.1** in C_6D_6. (*) denotes the presence of hexanes. (†) denotes the presence of 1,2-dichlorobenzene.

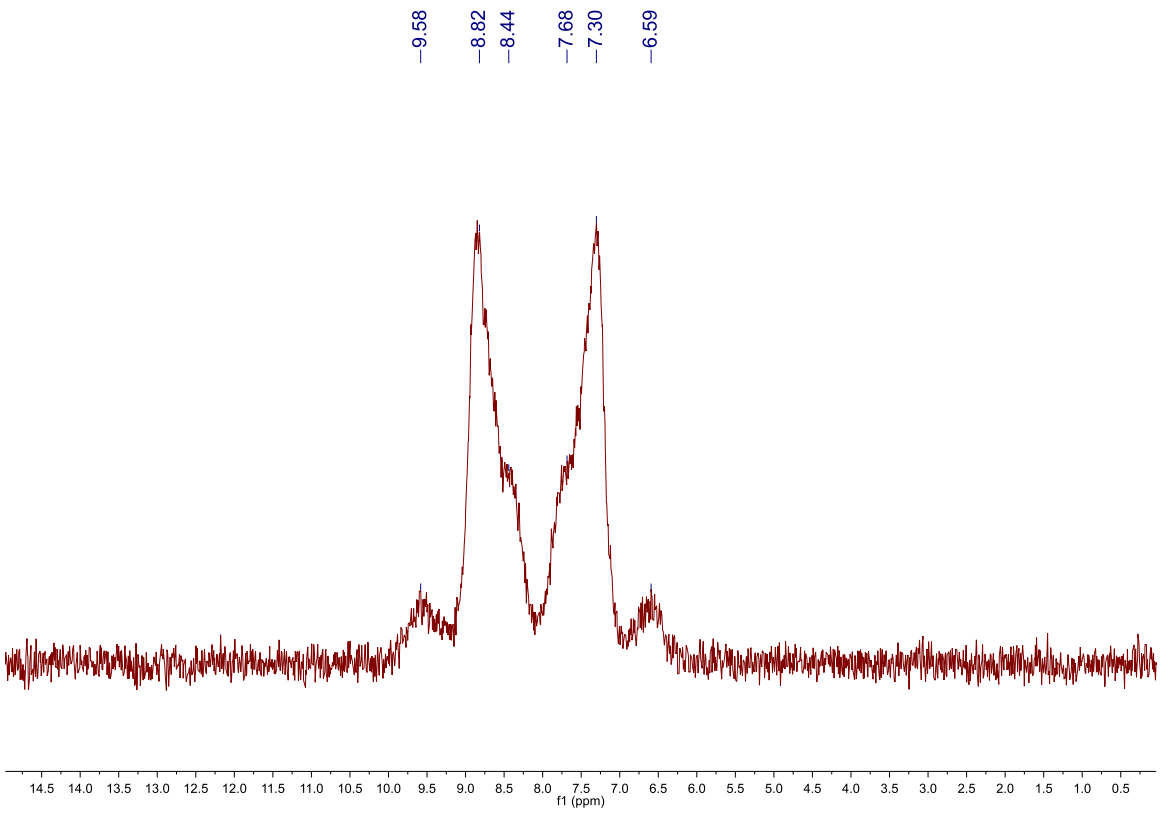

Figure A2.2. $^{31}P\{^{1}H\}$ NMR spectrum of **2.1** in C_6D_6.

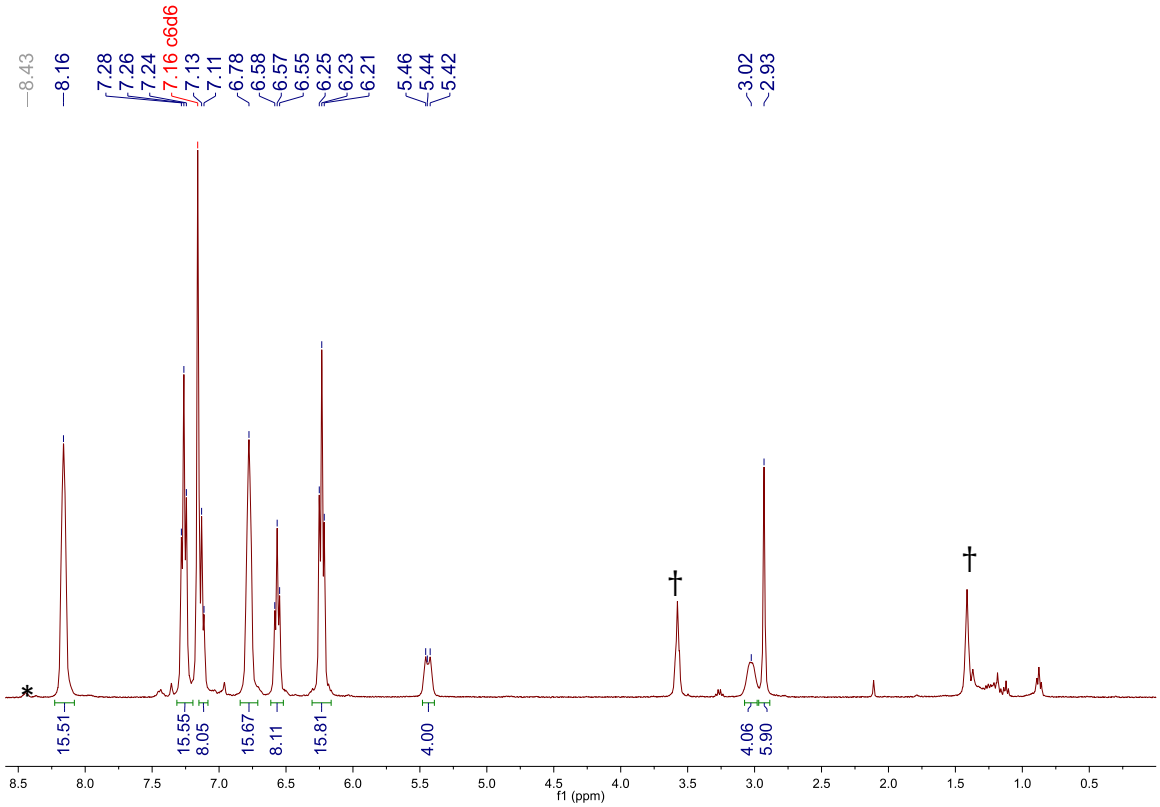

Figure A2.3. ^{1}H NMR spectrum of **2.1-*d*$_4$** in C_6D_6. (*) denotes the presence of a decomposition product of the cluster. (†) denotes the presence of tetrahydrofuran.

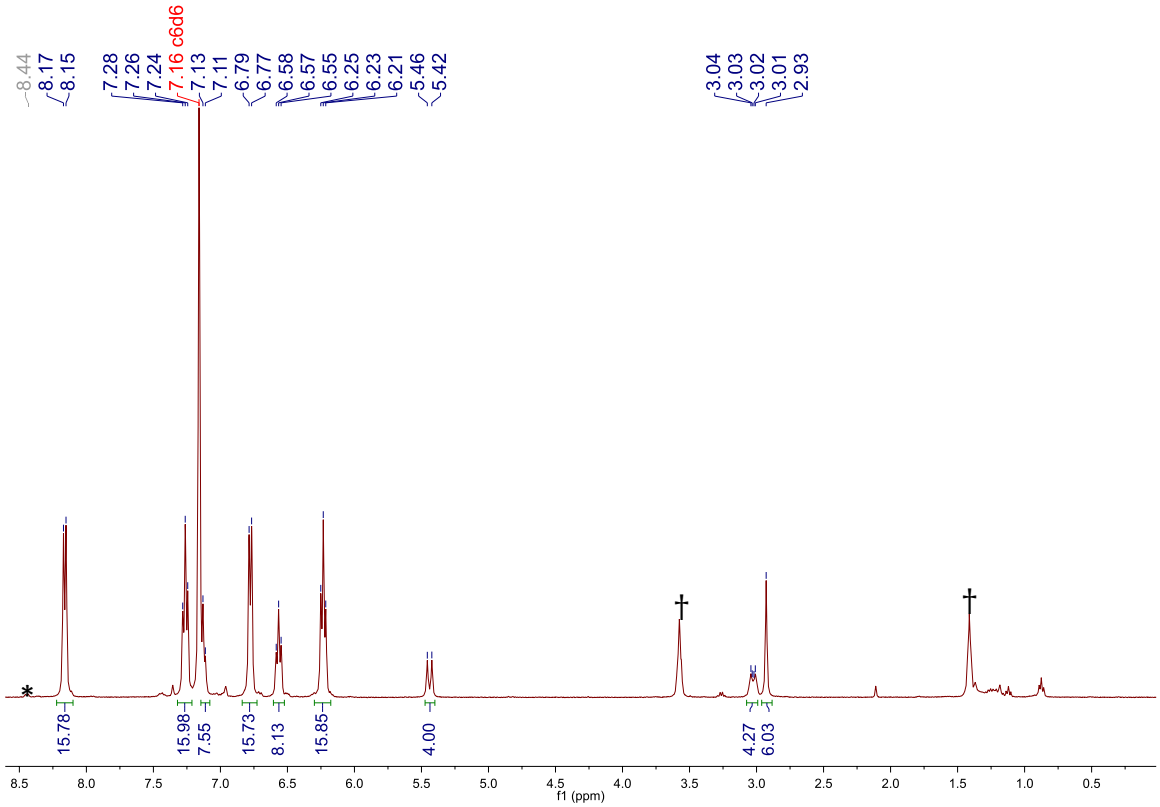

Figure A2.4. $^{1}H\{^{31}P\}$ NMR spectrum of **2.1-*d*$_4$** in C_6D_6. (*) denotes the presence of a decomposition product of the cluster. (†) denotes the presence of tetrahydrofuran.

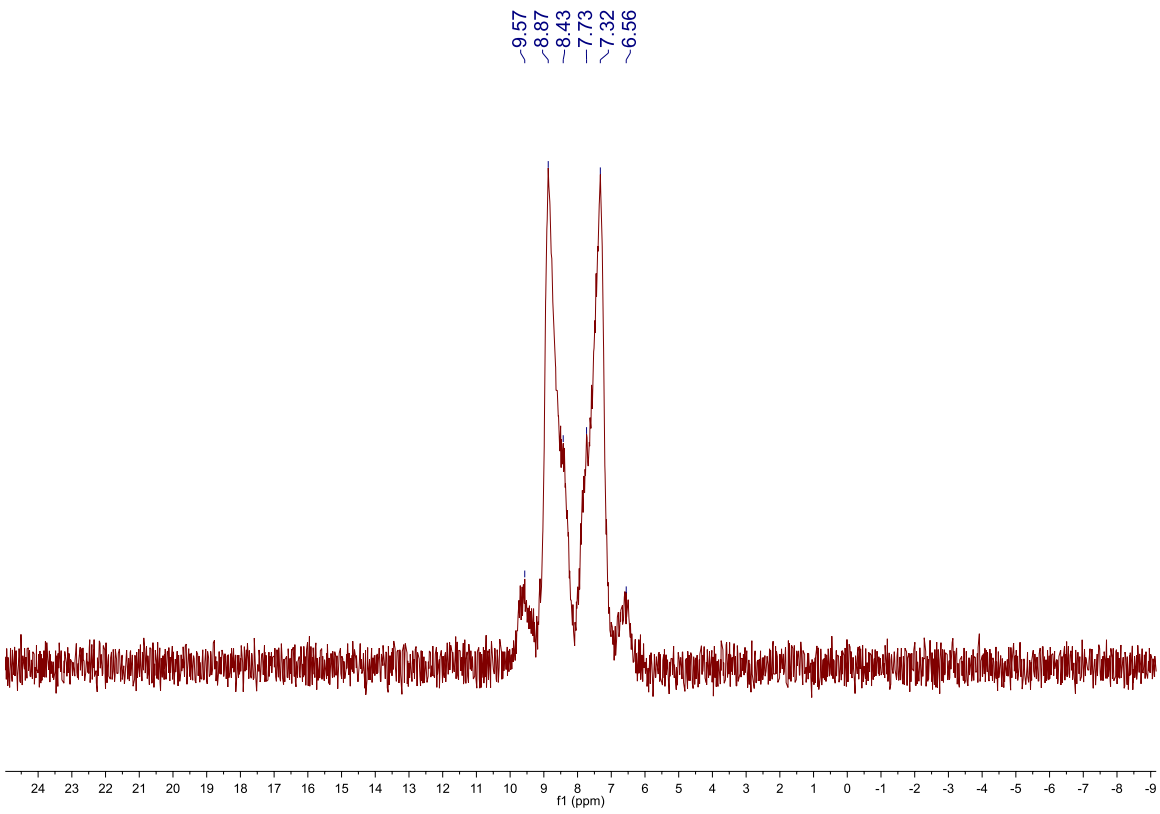

Figure A2.5. $^{31}P\{^{1}H\}$ NMR spectrum of **2.1-*d*$_4$** in C_6D_6.

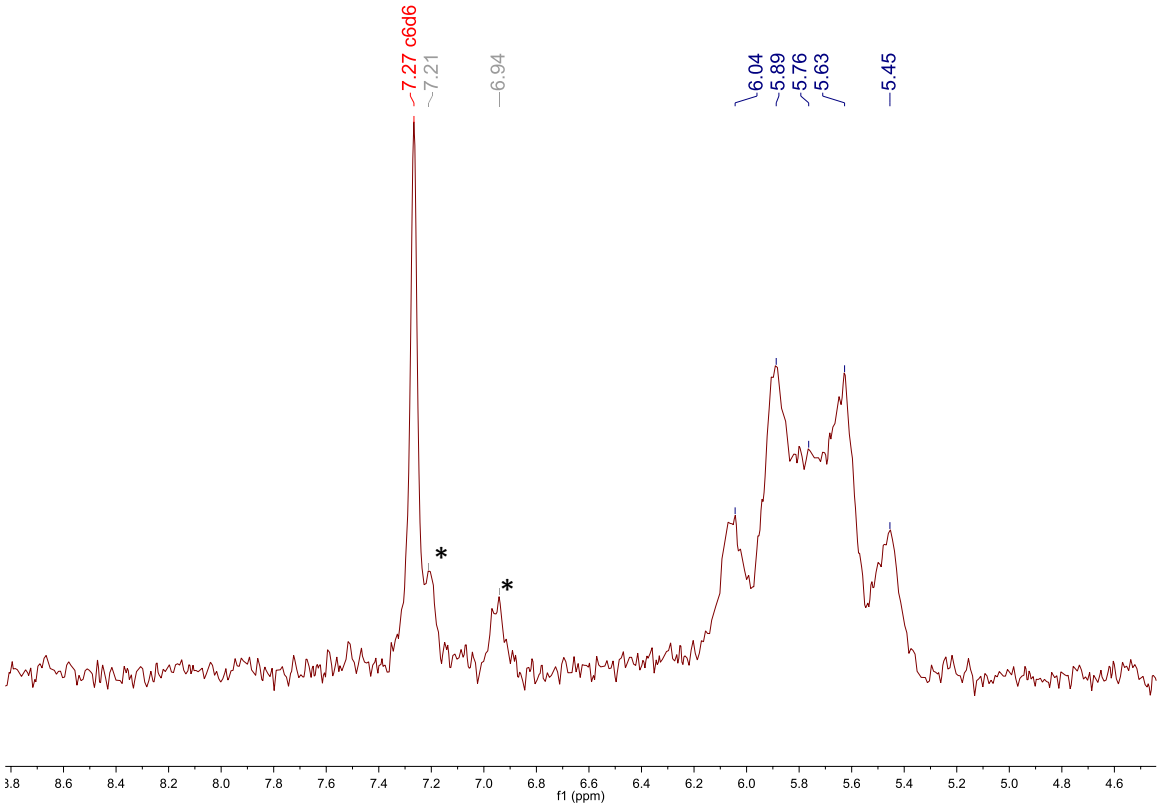

Figure A2.6. ^{2}H NMR spectrum of **2.1-*d*$_4$** in 1,2-dichlorobenzene with 1% by volume C_6D_6 for lock. (*) denotes the presence of 1,2-$C_6D_4Cl_2$.

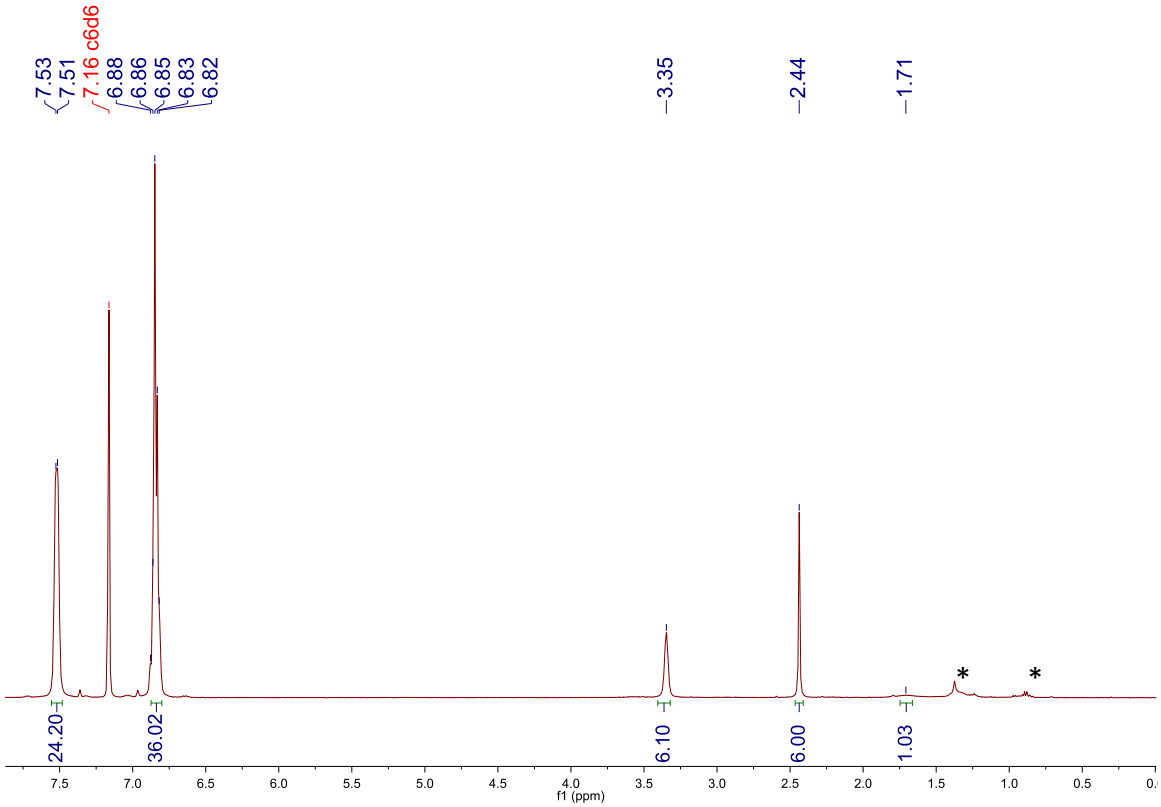

Figure A2.7. ^{1}H NMR spectrum of $[Cu_3H(dppm)_3(OAc)_2]$ (**2.2**) in C_6D_6. (*) denotes the presence of hexanes.

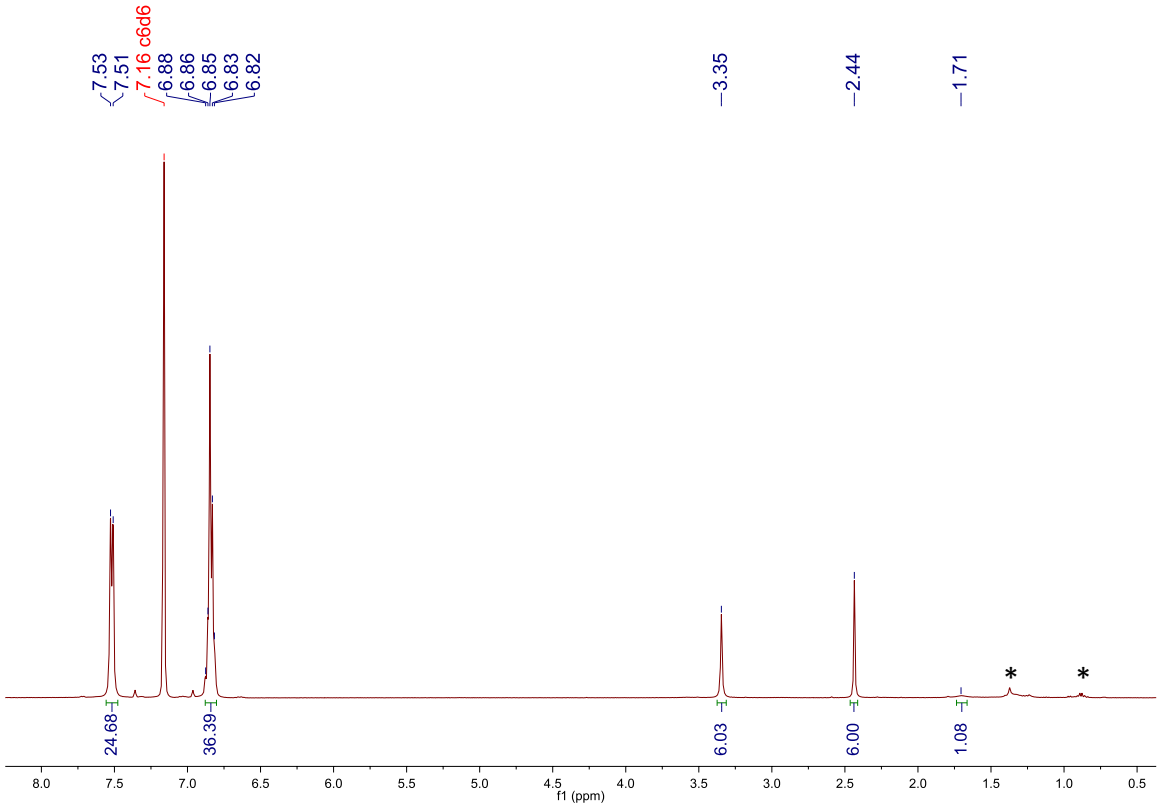

Figure A2.8. $^{1}H\{^{31}P\}$ NMR spectrum of $[Cu_3H(dppm)_3(OAc)_2]$ (**2.2**) in C_6D_6. (*) denotes the presence of hexanes.

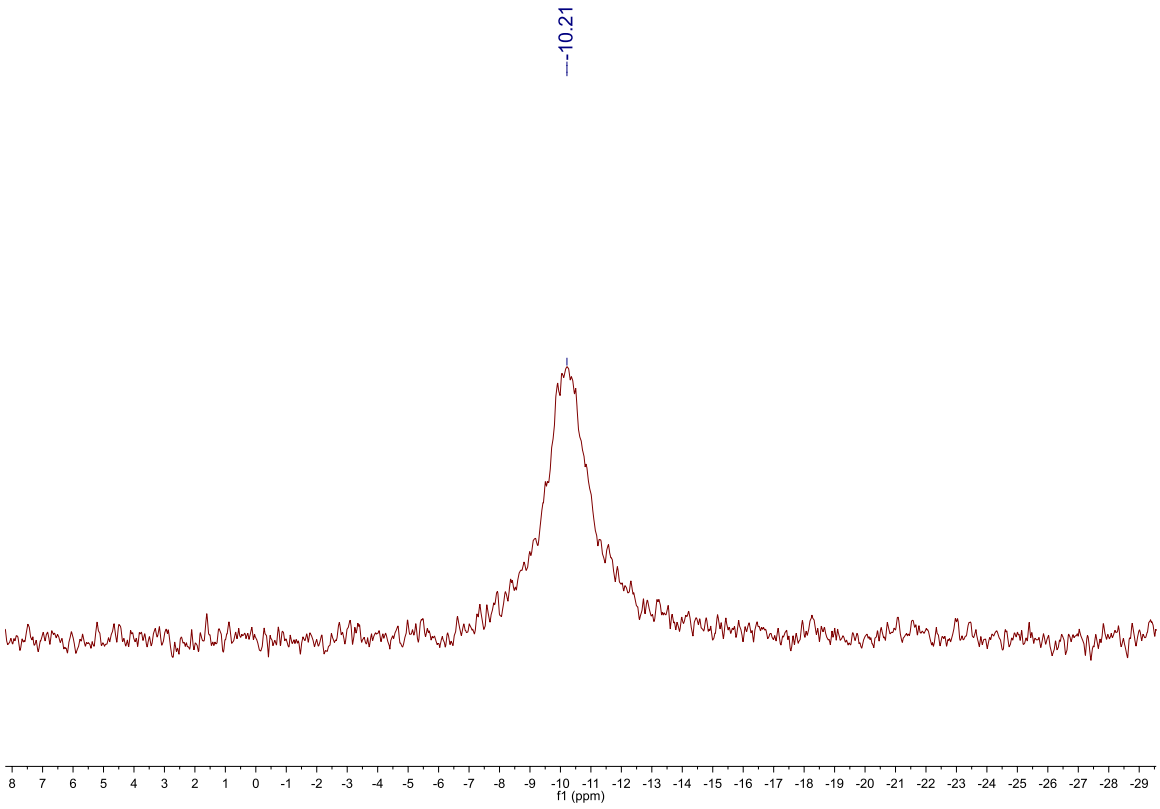

Figure A2.9. $^{31}P\{^{1}H\}$ NMR spectrum of **2.2** in C_6D_6.

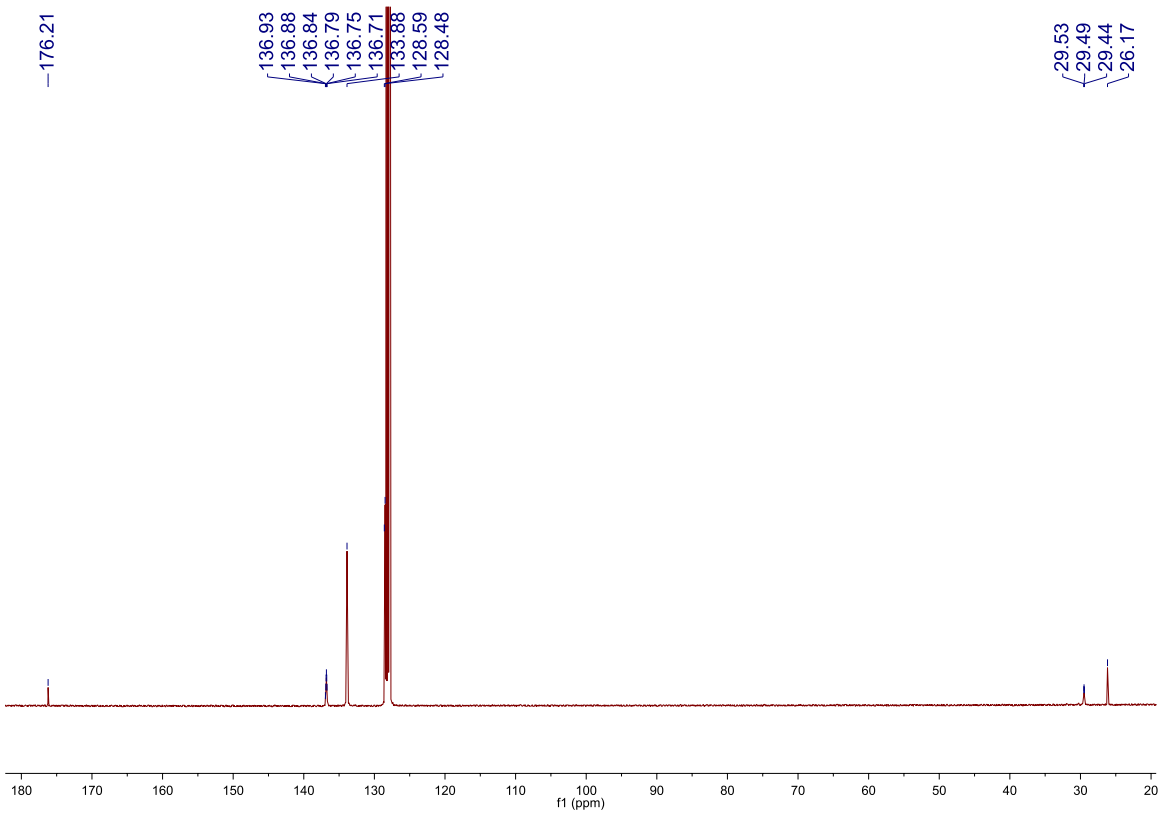

Figure A2.10. $^{13}C\{^{1}H\}$ NMR spectrum of **2.2** in C_6D_6.

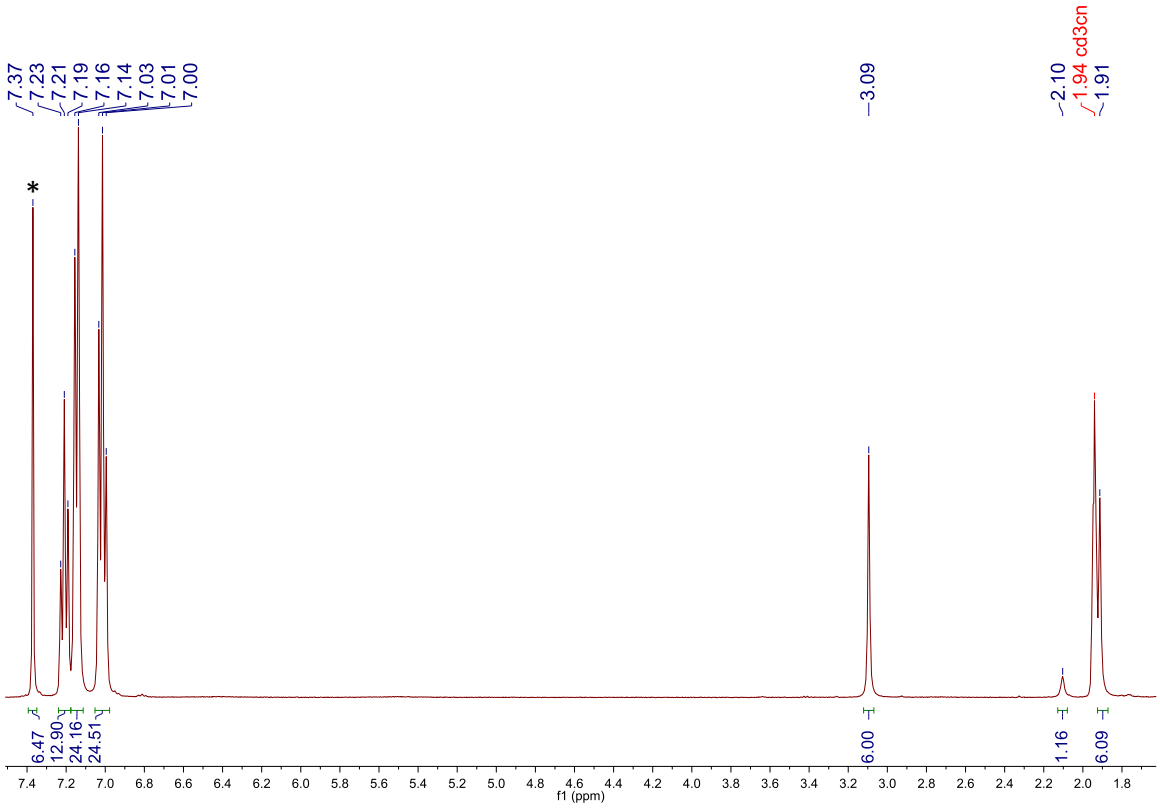

Figure A2.11. $^{1}H\{^{31}P\}$ NMR spectrum of **2.2** in MeCN-d_3. (*) denotes the presence of benzene. The resonance at 2.10 ppm collapses to a singlet upon ^{31}P decoupling.

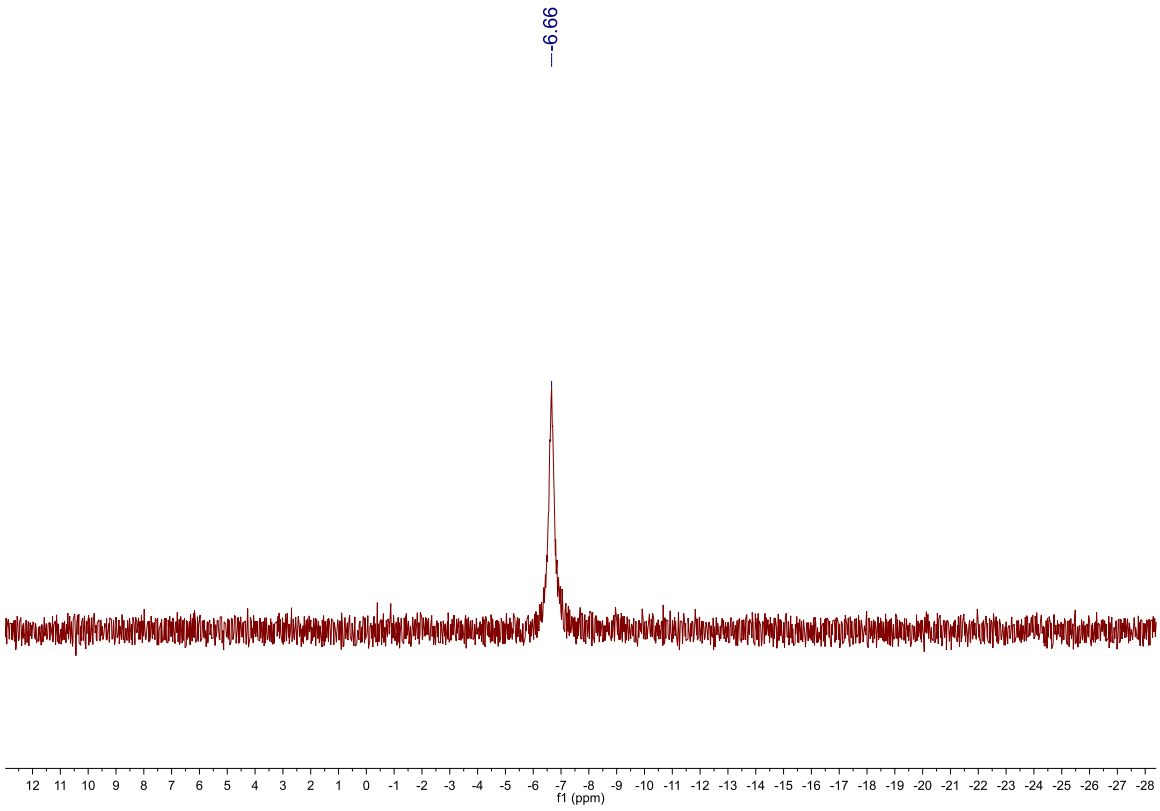

Figure A2.12. $^{31}P\{^{1}H\}$ NMR spectrum of **2.2** in MeCN-d_3.

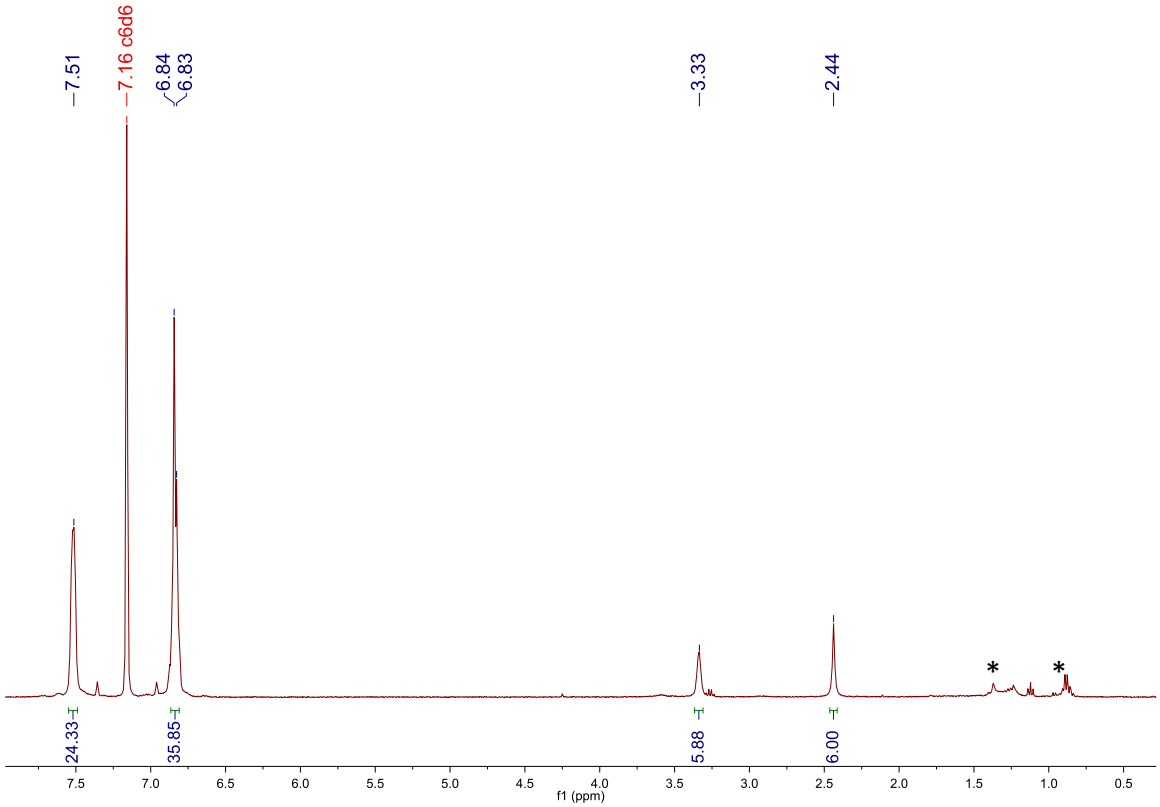

Figure A2.13. ^{1}H NMR spectrum of **2.2-*d*$_1$** in C_6D_6. (*) denotes the presence of hexanes.

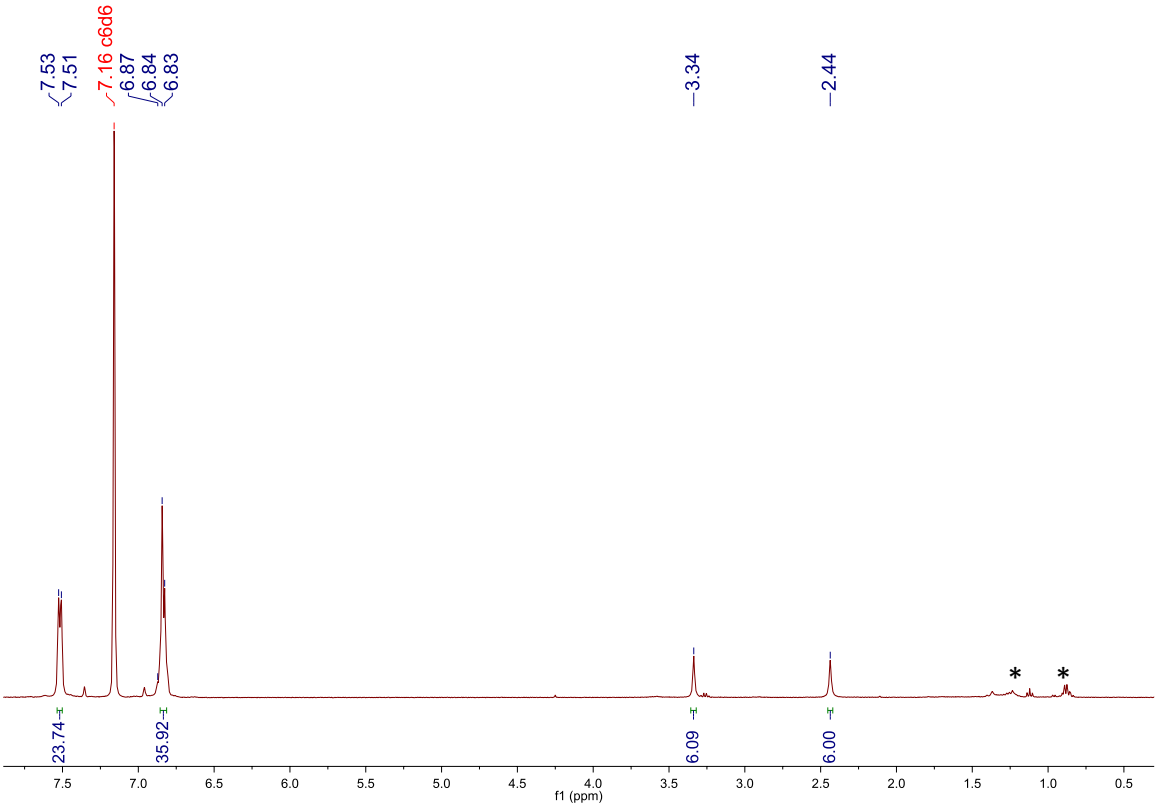

Figure A2.14. $^{1}H\{^{31}P\}$ NMR spectrum of **2.2-*d*$_1$** in C_6D_6. (*) denotes the presence of hexanes.

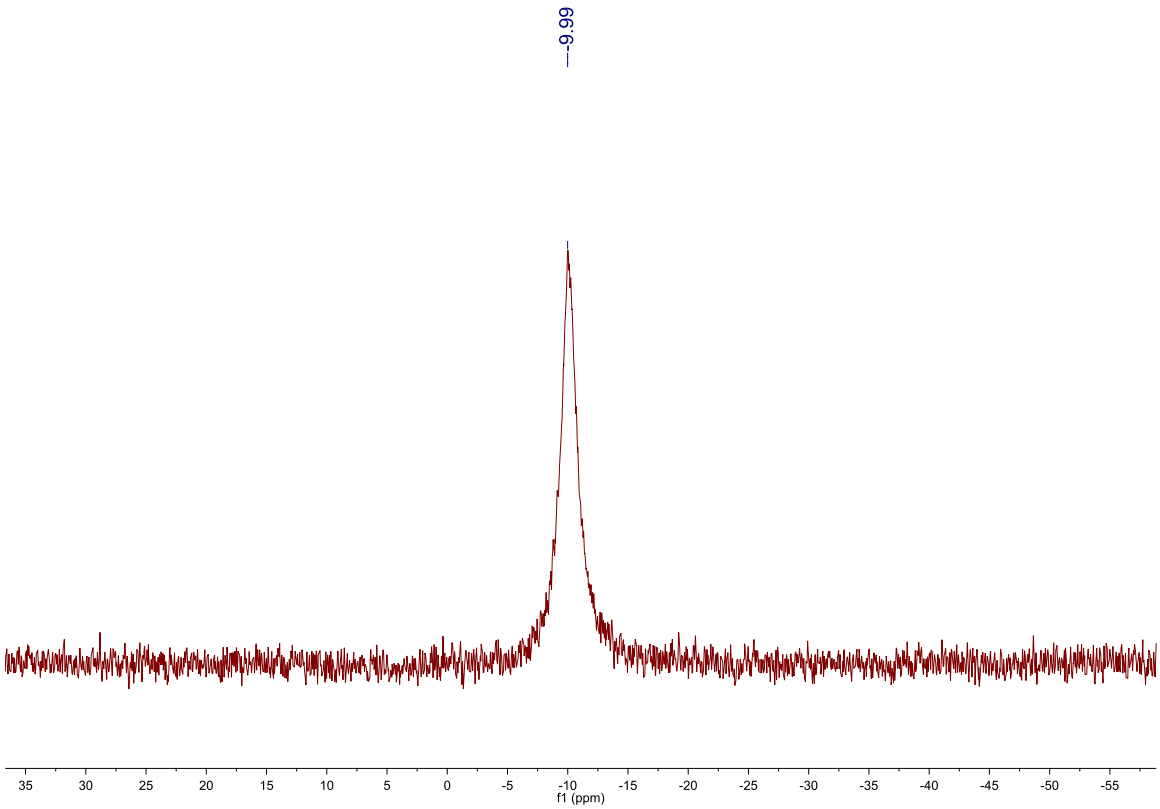

Figure A2.15. $^{31}P\{^{1}H\}$ NMR spectrum of **2.2-*d*$_1$** in C_6D_6.

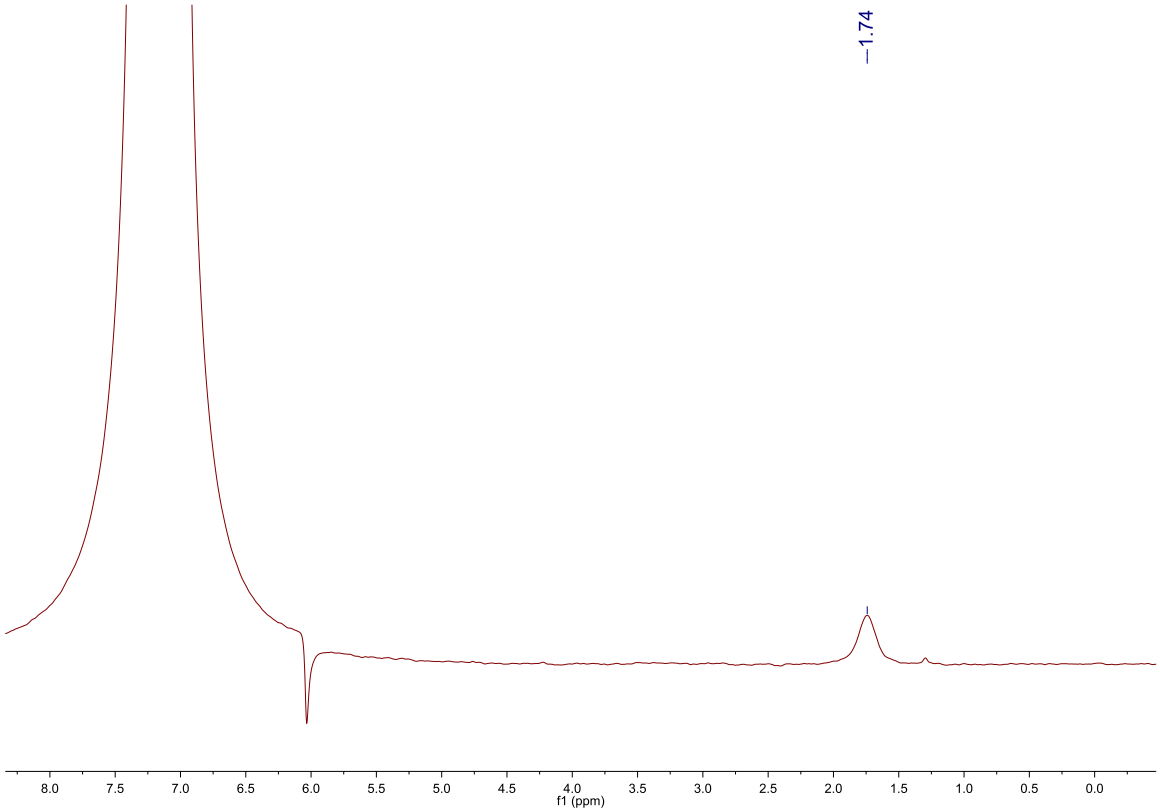

Figure A2.16. ^{2}H NMR spectrum of **2.2-*d*$_1$** in C_6H_6:C_6D_6 (9:1, v:v).

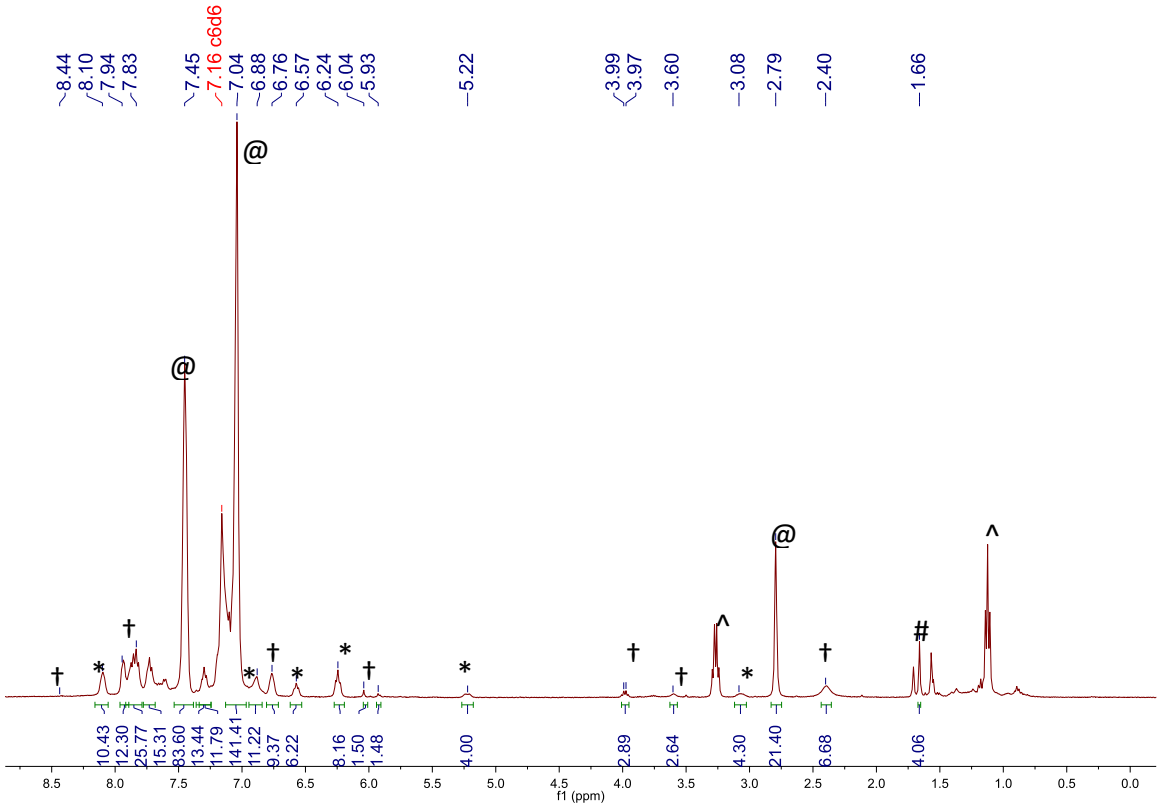

Figure A2.17. ^{1}H NMR spectrum of the crude reaction mixture to form **2.1** after 15 h. (*) denotes the presence of **2.1**, (†) denotes the presence of other AgH clusters, (#) denotes the presence of a silylated side product, $Ph_2Si(OAc)_2$, (@) denotes the presence of free dppm, and (^) denotes the presence of Et_2O.

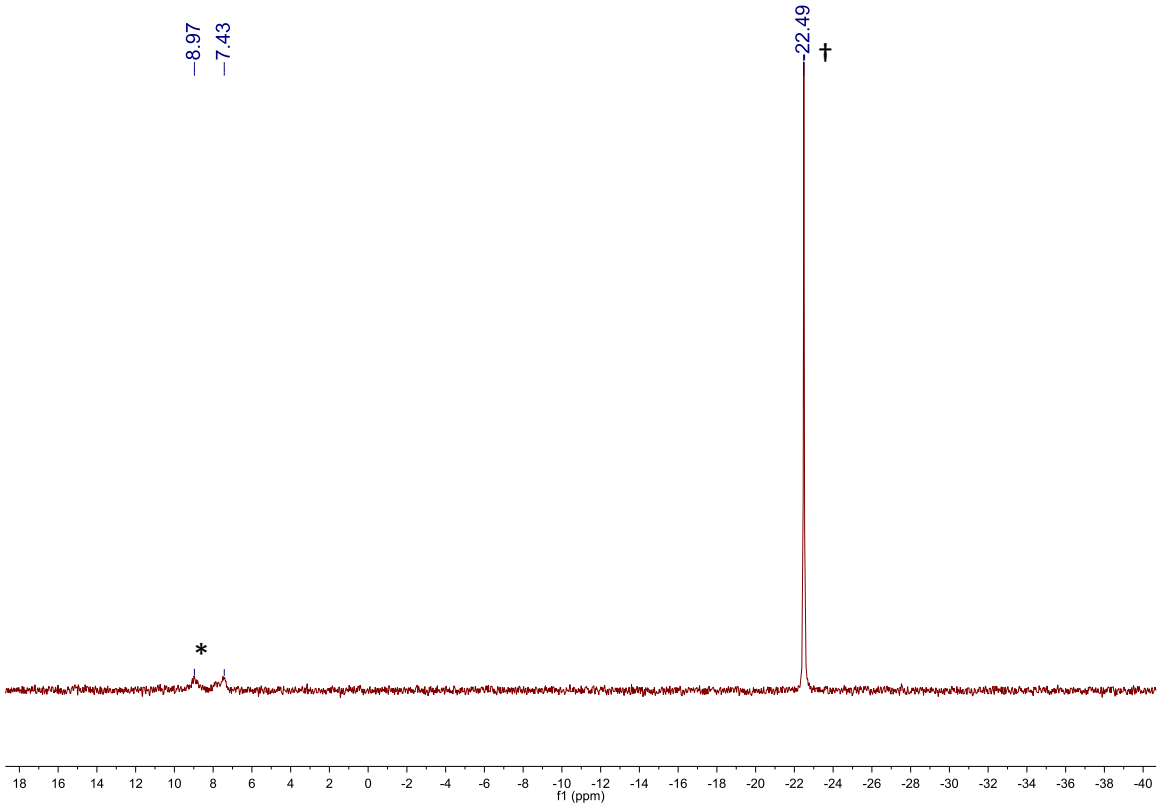

Figure A2.18. $^{31}P\{^{1}H\}$ NMR spectrum of the crude reaction mixture to form **2.1** after 15 hr. (*) denotes the presence of **2.1**, (†) denotes the presence of free dppm.

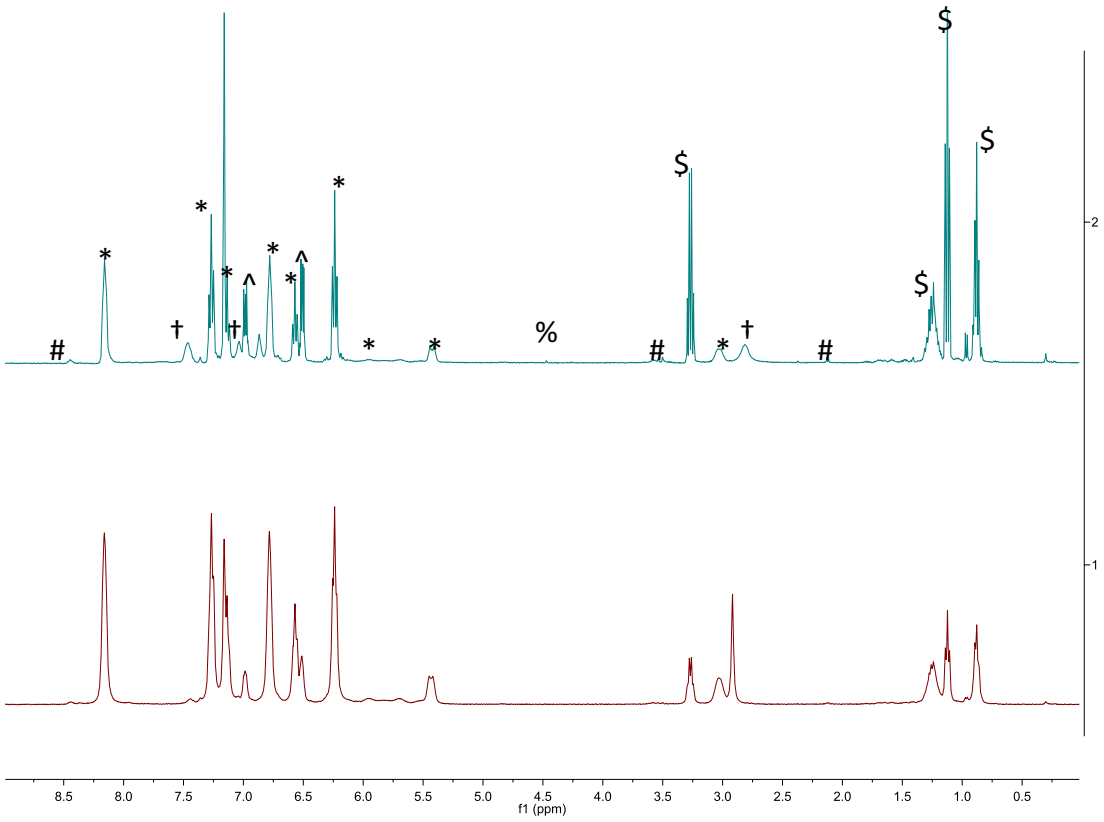

Figure A2.19. ^{1}H NMR spectra of **2.1** in C_6D_6 t = 0 (bottom) and after 15 hr at 25 °C (top). (*) denotes the presence of **2.1**, (†) denotes the presence of dppm, (#) denotes the presence of unidentified AgH clusters, (%) indicates the presence of H_2, (^) indicates the presence of 2,2-$C_6H_4Cl_2$, and ($) indicates the presence of diethyl ether and hexanes.

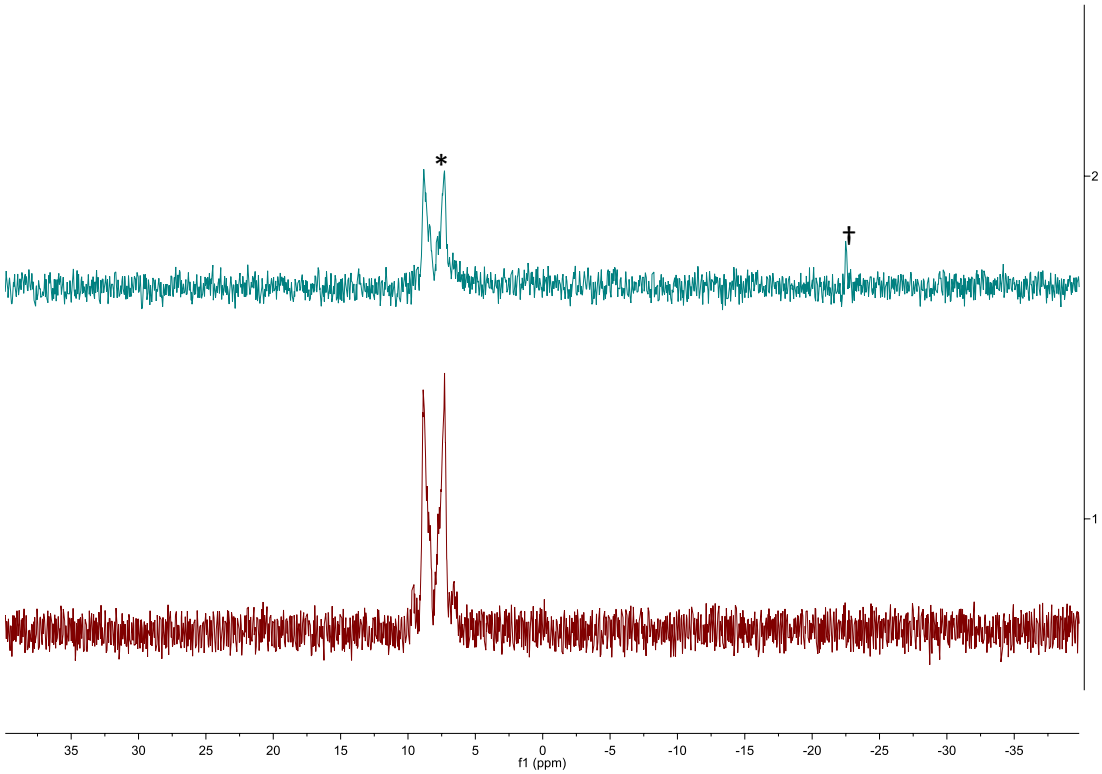

Figure A2.20. $^{31}P\{^{1}H\}$ NMR spectra of **2.1** in C_6D_6 t = 0 (bottom) and after t = 15 hr at 25 °C (top). (*) denotes the presence of **2.1**, and (†) denotes the presence of dppm.

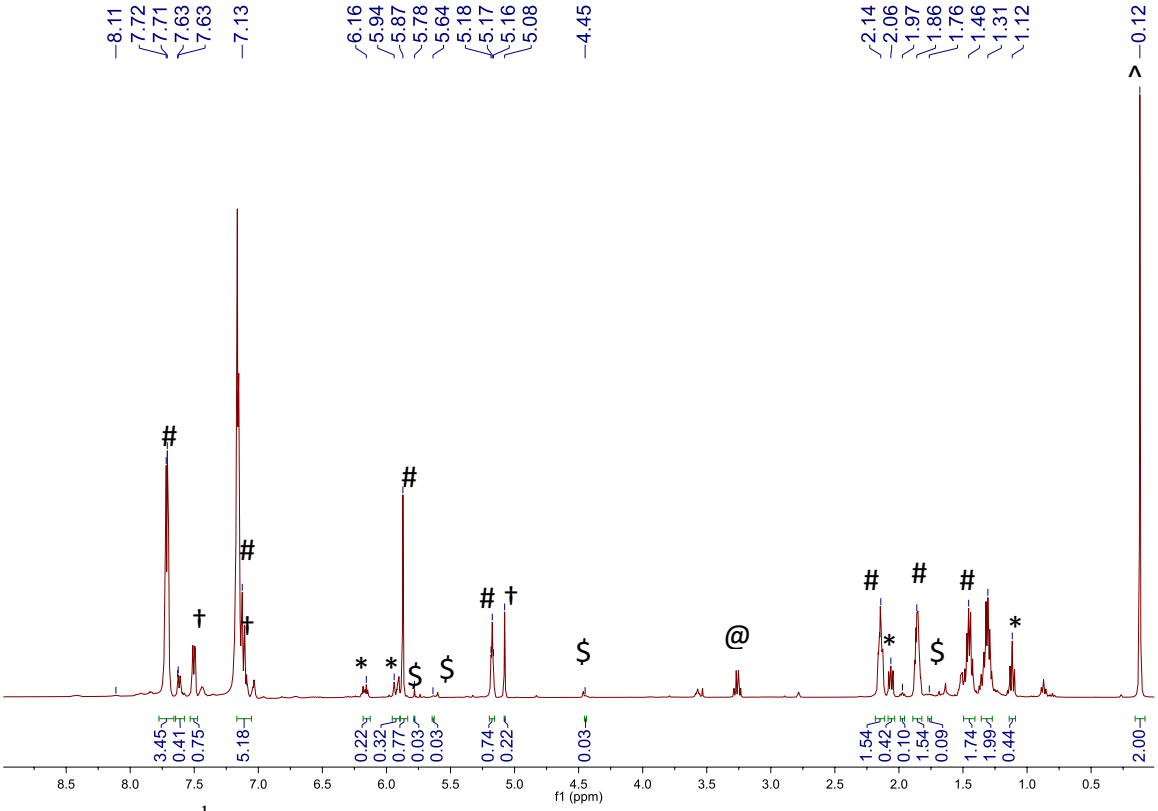

Figure A2.21. ^{1}H NMR spectrum in C_6D_6 of the reaction of 2-cyclohexen-1-one (**2.3**) and Ph_2SiH_2 with **2.1** (0.05 equiv H^-) after 24 h. (*) indicates the presence of 2-cyclohexen-1-one (**2.3**), (†) indicates the presence of Ph_2SiH_2, (#) indicates the presence of (cyclohex-1-en-1-yloxy)diphenylsilane (**2.4a**),[100] ($) indicates the presence of (cyclohex-2-en-1-yloxy)diphenylsilane (**2.4c**),[69] (^) indicates the presence of hexamethyldisiloxane, and (@) indicates the presence of diethyl ether.

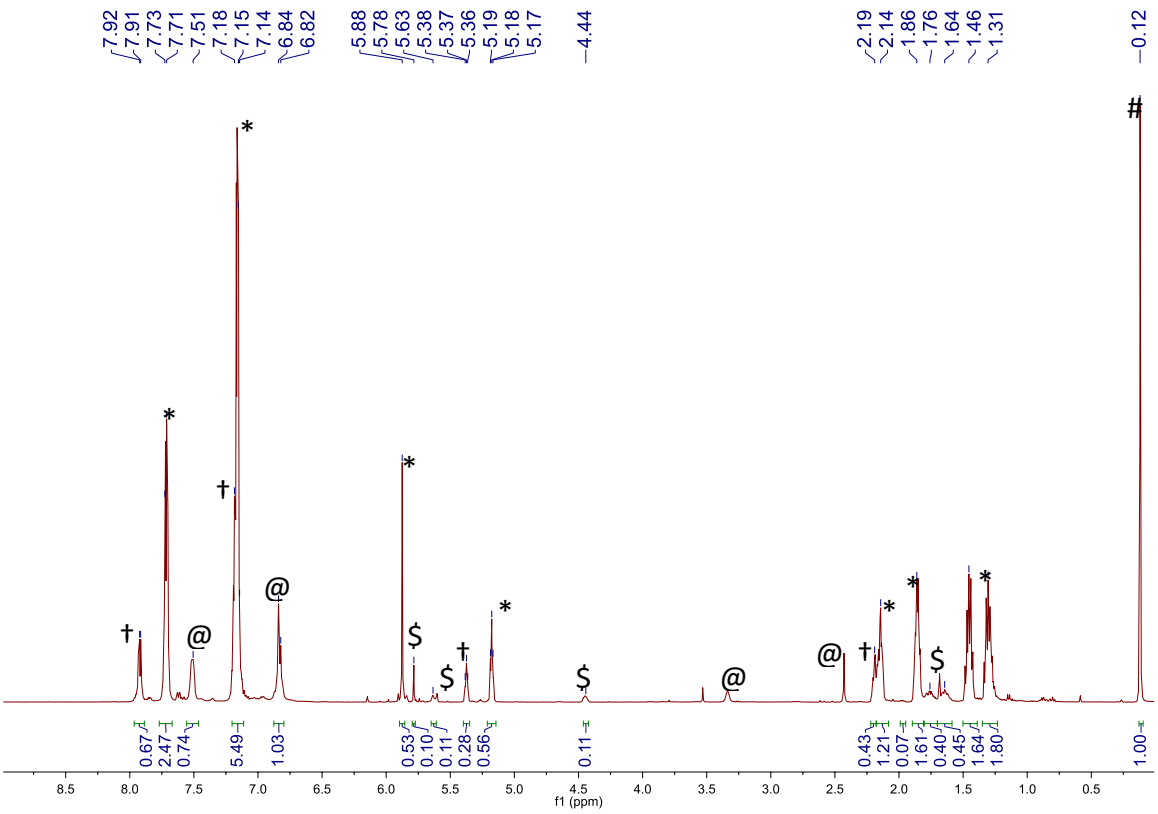

Figure A2.22. ^{1}H NMR spectrum in C_6D_6 of the reaction of 2-cyclohexen-1-one (**2.3**) and Ph_2SiH_2 with **2.2** (0.05 equiv H^-) after 24 h. (*) indicates the presence of (cyclohex-1-en-1-yloxy)diphenylsilane (**2.4a**),[100] (†) indicates the presence of bis(cyclohex-1-en-1-yloxy)diphenylsilane (**2.4b**),[101] ($) indicates the presence of (cyclohex-2-en-1-yloxy)diphenylsilane (**2.4c**),[69] (#) indicates the presence of hexamethyldisiloxane, and (@) indicates the presence of complex **2**.

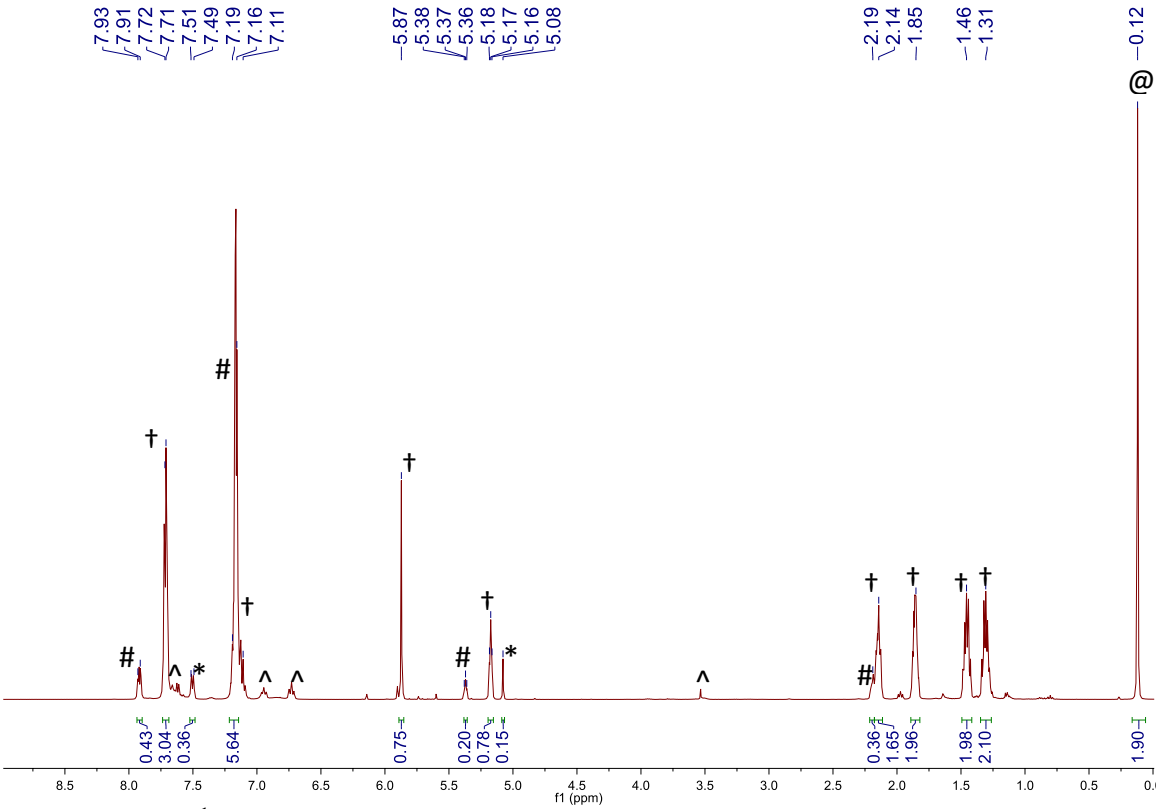

Figure A2.23. ^{1}H NMR spectrum in C_6D_6 of the reaction of 2-cyclohexen-1-one (**2.3**) and Ph_2SiH_2 with $[CuH(PPh_3)]_6$ (0.05 equiv H^-) after 15 min. (*) indicates the presence of Ph_2SiH_2, (†) indicates the presence of (cyclohex-1-en-1-yloxy)diphenylsilane (**2.4a**),[100] (#) indicates the presence of bis(cyclohex-1-en-1-yloxy)diphenylsilane(**2.4b**),[101] (@) indicates the presence of hexamethyldisiloxane, and (^) indicates the presence of $[CuH(PPh_3)]_6$.

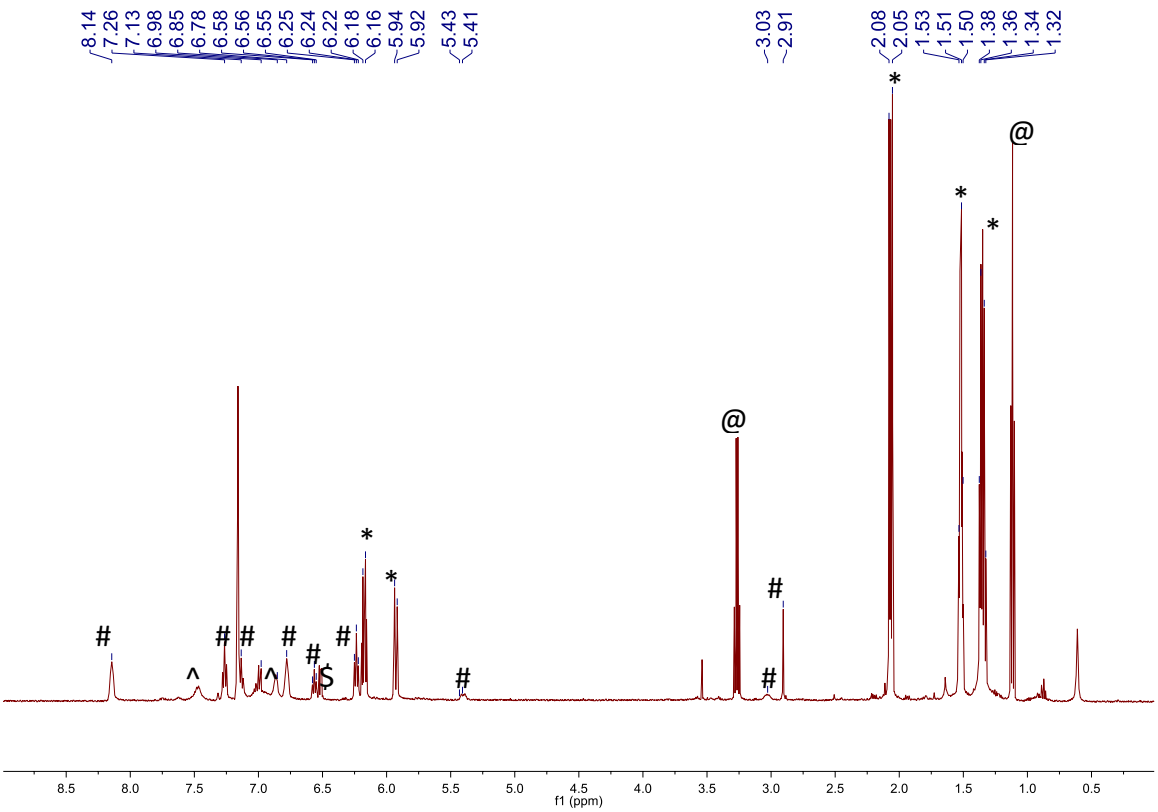

Figure A2.24. ^{1}H NMR spectrum in C_6D_6 of the reaction of 2-cyclohexen-1-one (**2.3**) with complex **2.1** after 24 h. (#) indicates the presence of **2.1**, (^) indicates the presence of free dppm, (*) indicates the presence of 2-cyclohexen-1-one (**2.3**), (@) indicates the presence of Et_2O, and ($) indicates the presence of 1,2-$C_6H_4Cl_2$. **Experimental Details:** Complex **2.1** (10 mg, 0.0043 mmol) was dissolved in C_6D_6 (1.5 mL) and transfered to a J. Young NMR tube. To this solution was added **2.3** (1.4 µL, 0.0155 mmol), and the reaction mixture was allowed to stand at room temperature for 24 h.

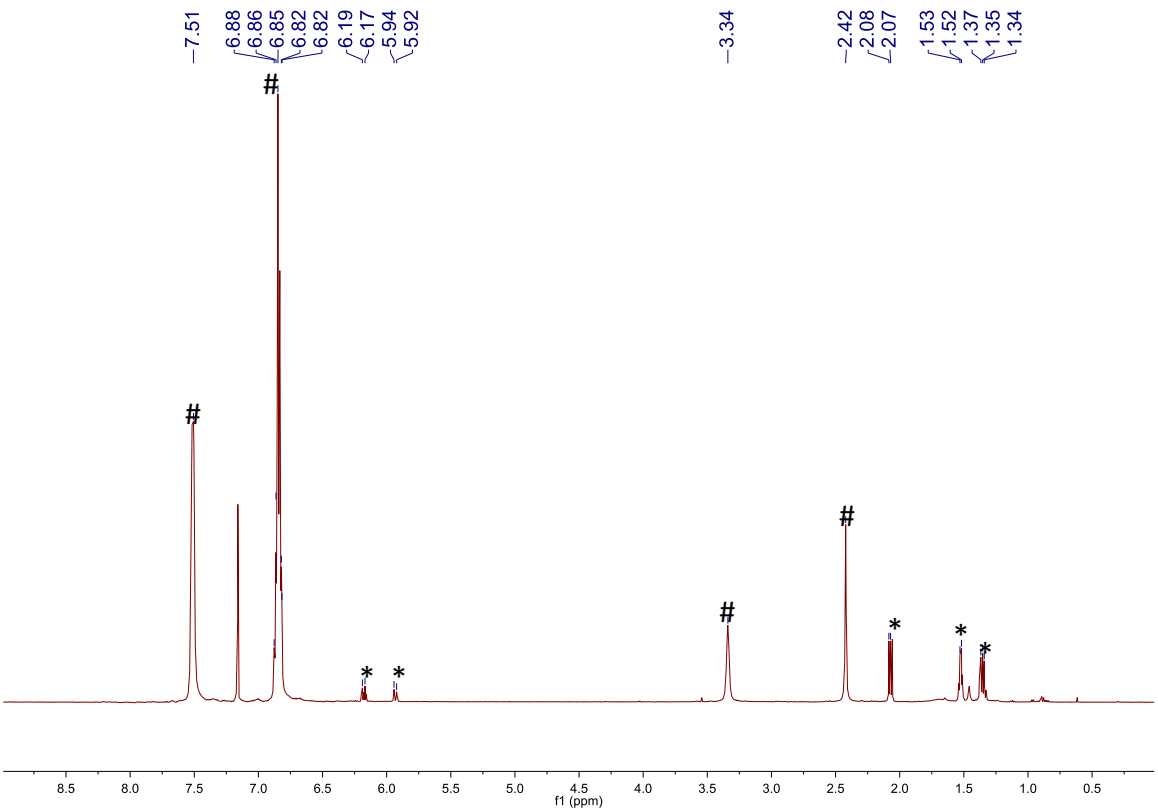

Figure A2.25. ^{1}H NMR spectrum in C_6D_6 of the reaction of 2-cyclohexen-1-one (**2.3**) with complex **2.2** after 24 h. (#) indicates the presence of **2.2**, (*) indicates the presence of 2-cyclohexen-1-one (**2.3**). **Experimental Details:** Complex **2.2** (15 mg, 0.0102 mmol) was dissolved in C_6D_6 (1.5 mL) and transfered to a J. Young NMR tube. To this solution was added **2.3** (1.0 μL, 0.0103 mmol), and the reaction mixture was allowed to stand at room temperature for 24 h.

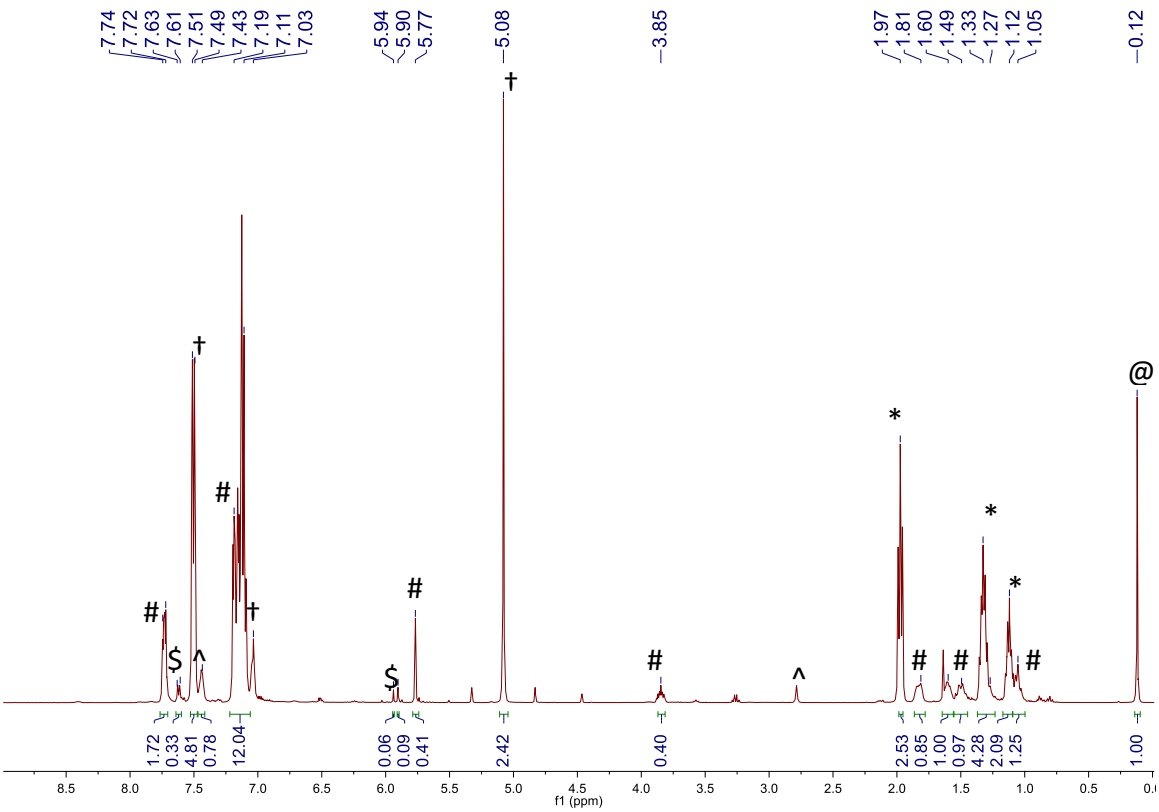

Figure A2.26. ^{1}H NMR spectrum in C_6D_6 of the reaction of cyclohexanone (**2.5**) and Ph_2SiH_2 with **2.1** (0.10 equiv H^-) after 24 h. (*) indicates the presence of cyclohexanone (**2.5**), (†) indicates the presence of Ph_2SiH_2, (#) indicates the presence of (cyclohexyloxy)diphenylsilane (**2.6**),[102] (@) indicates the presence of hexamethyldisiloxane, (^) indicates the presence of free dppm, and ($) indicates the presence of $(Ph_2SiH)_2O$.[107]

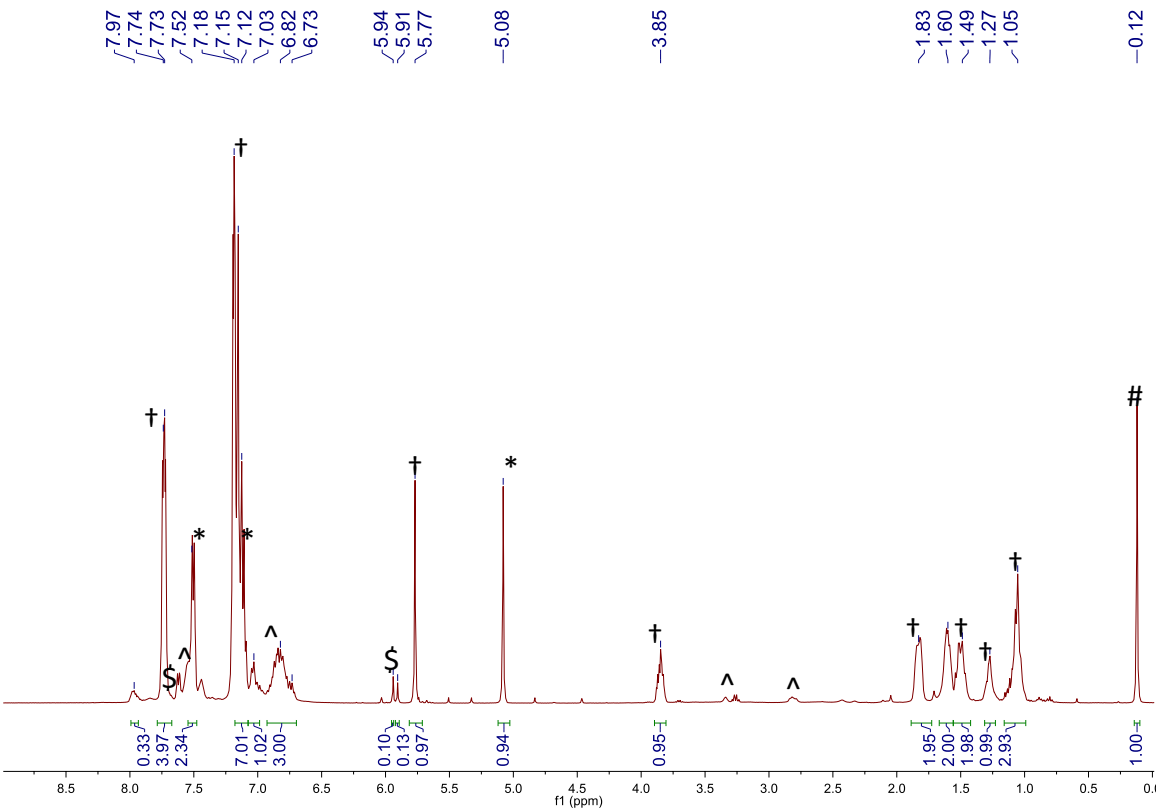

Figure A2.27. ^{1}H NMR spectrum in C_6D_6 of the reaction of cyclohexanone (**2.5**) and Ph_2SiH_2 with **2.2** (0.10 equiv H^-) after 2 h. (*) indicates the presence of Ph_2SiH_2, (†) indicates the presence of (cyclohexyloxy)diphenylsilane (**2.6**),[102] (#) indicates the presence of hexamethyldisiloxane, (^) indicates the presence of complex **2.2**, and ($) indicates the presence of $(Ph_2SiH)_2O$.[107]

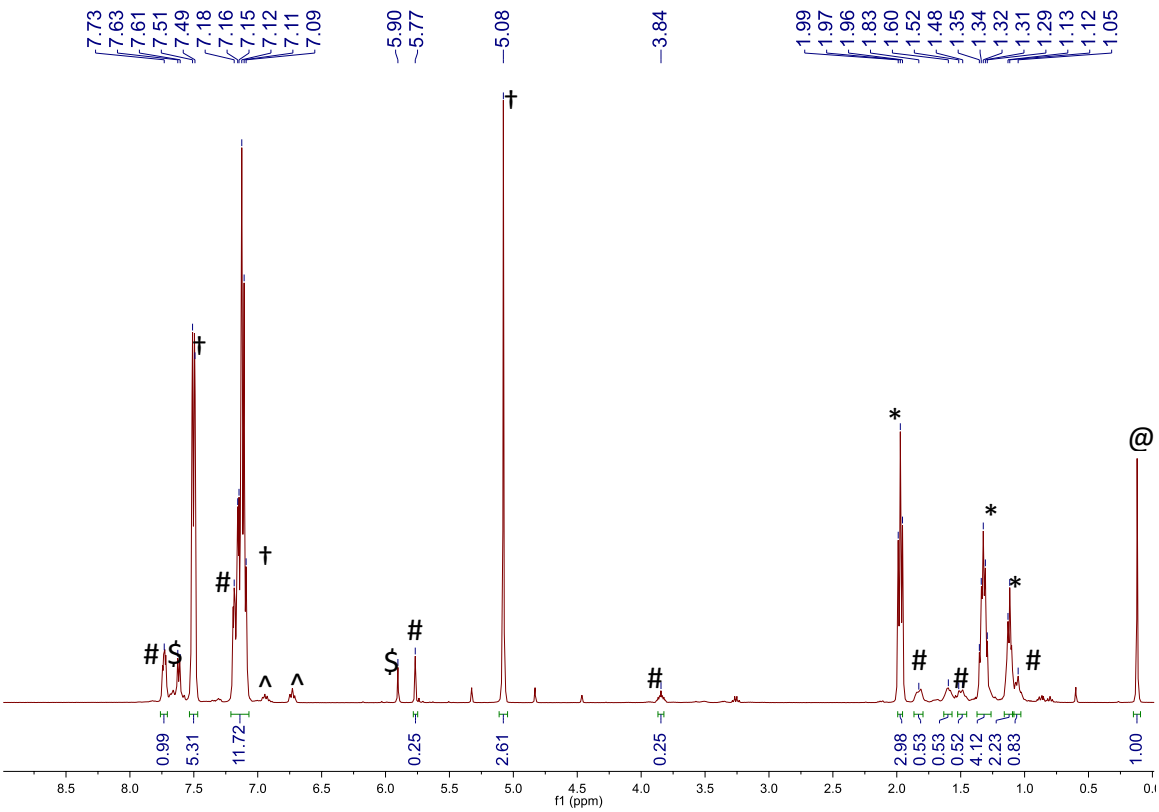

Figure A2.28. ^{1}H NMR spectrum in C_6D_6 of the reaction of cyclohexanone (**2.5**) and Ph_2SiH_2 with $[CuH(PPh_3)]_6$ (0.10 equiv H^-) after 24 h. (*) indicates the presence of cyclohexanone (**2.5**), (†) indicates the presence of Ph_2SiH_2, (#) indicates the presence of (cyclohexyloxy)diphenylsilane (**2.6**),[102] (@) indicates the presence of hexamethyldisiloxane, (^) indicates the presence of $[CuH(PPh_3)]_6$, and ($) indicates the presence of $(Ph_2SiH)_2O$.[107]

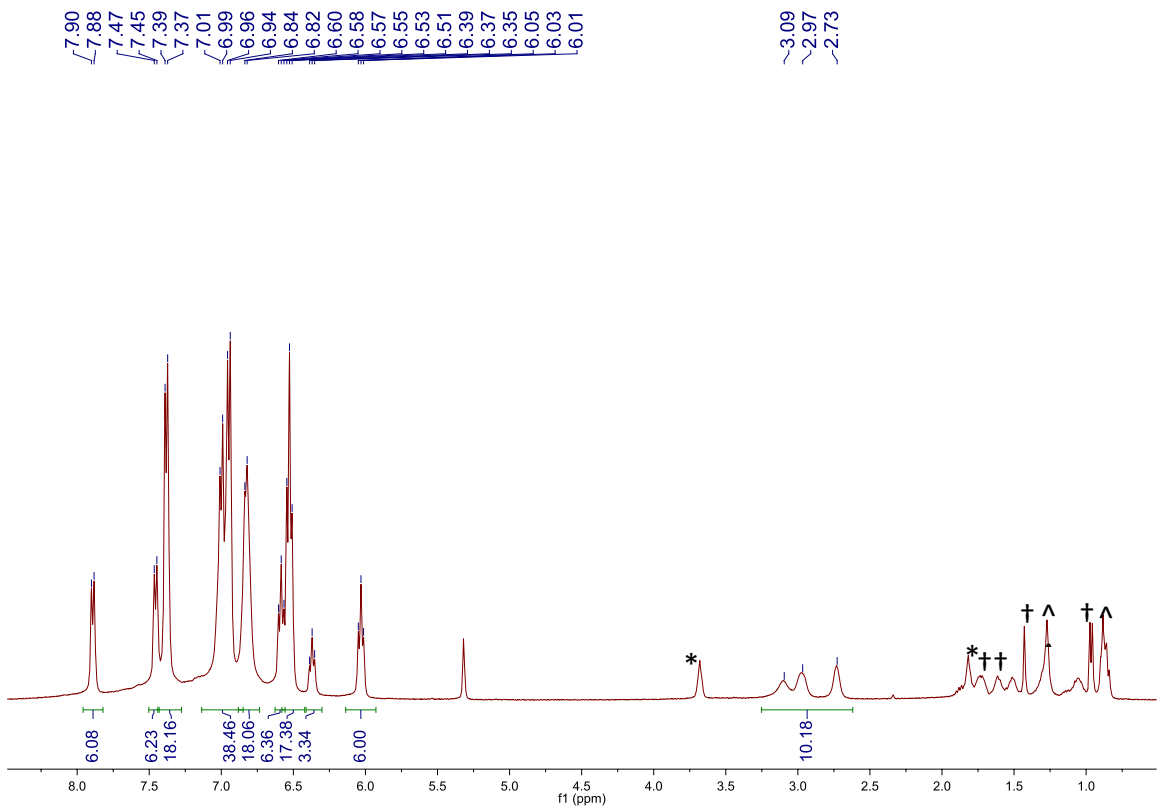

Figure A2.29. $^{1}H\{^{31}P\}$ NMR spectrum of $[Cu_{13}H_{10}(SePh)_3(PPh_3)_7]$ (**2.9**) in CD_2Cl_2. (*) indicates a resonance assignable to THF, (^) indicates a resonance assignable to hexanes, and (†) indicates a resonance assignable to an unidentified impurity.

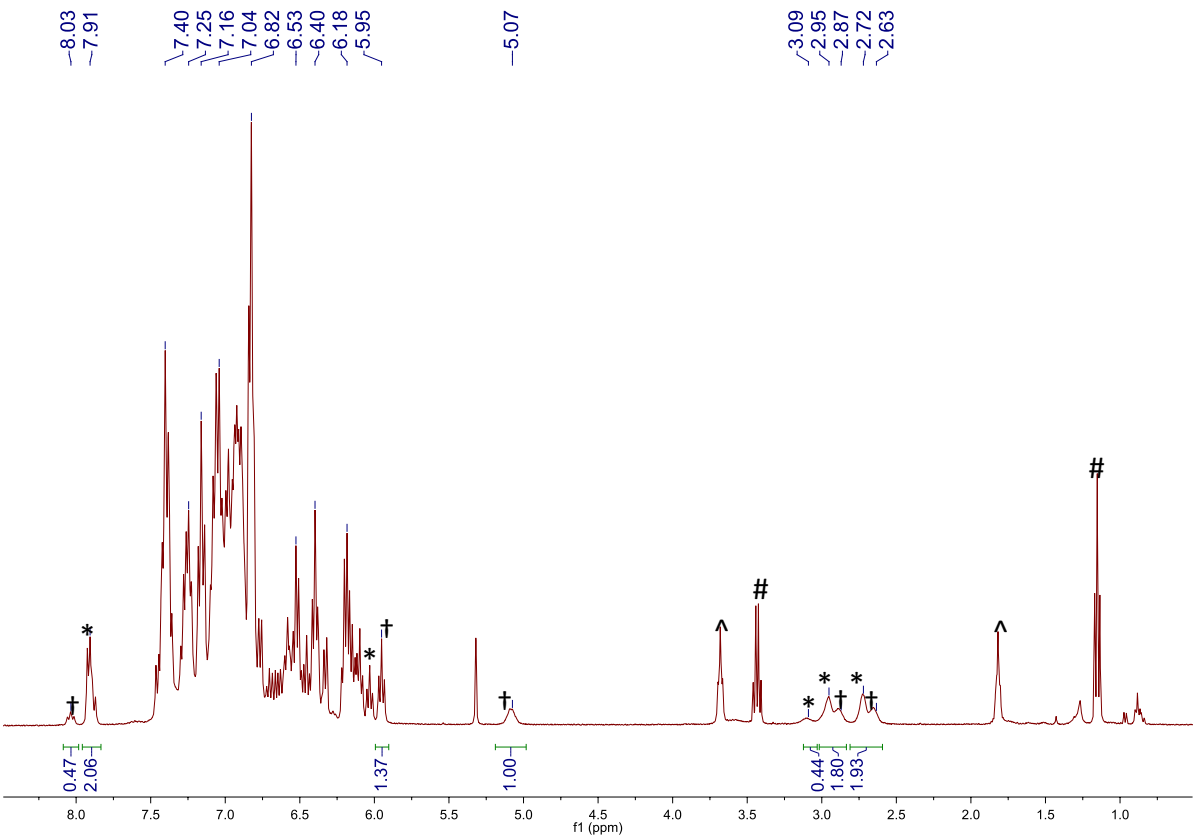

Figure A2.30. ^{1}H NMR spectrum in CD_2Cl_2 of the crude solids from the reaction to generate **2.9**. (*) indicates a resonance assignable to **2.9**, (†) indicates a resonance tentatively assignable to another Cu-H cluster, (^) indicates a resonance assignable to THF, and (#) indicates a resonance assignable to Et_2O. All other resonances are thus far unassigned.

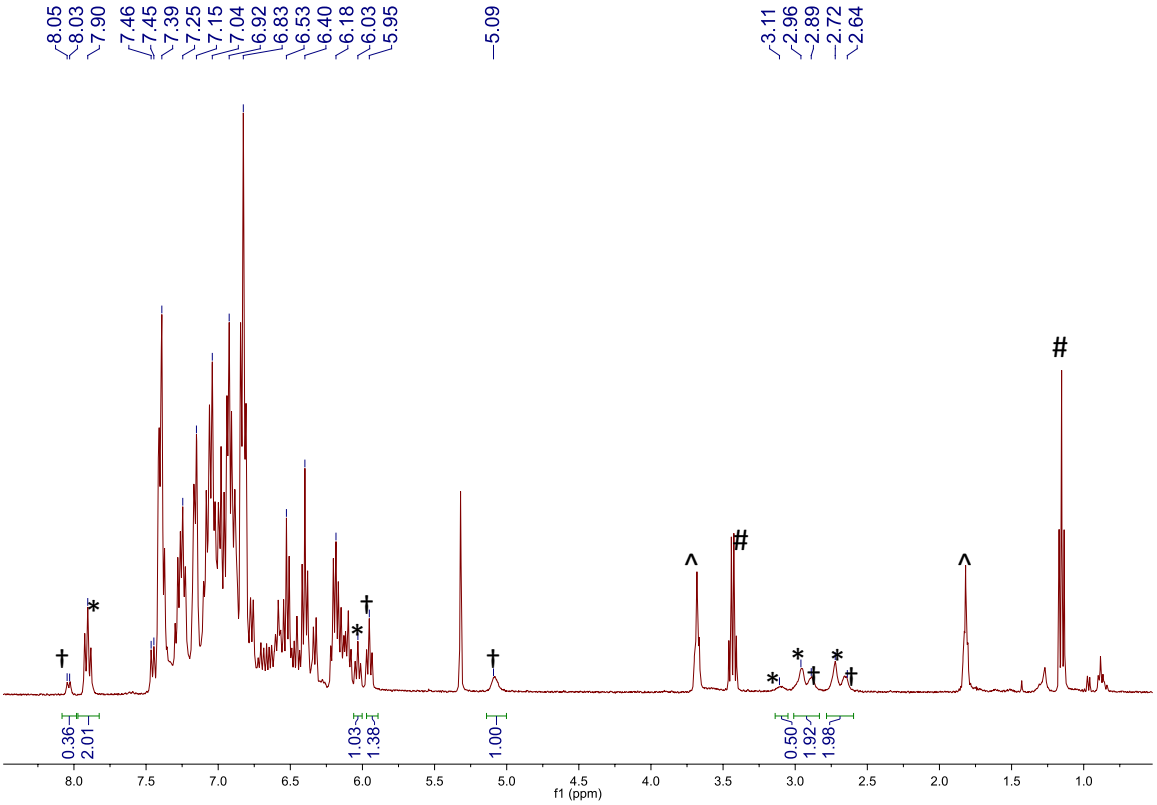

Figure A2.31. $^{1}H\{^{31}P\}$ NMR spectrum in CD_2Cl_2 of the crude solids from the reaction to generate **2.9**. (*) indicates a resonance assignable to **2.9**, (†) indicates a resonance tentatively assignable to another Cu-H cluster, (^) indicates a resonance assignable to THF, and (#) indicates a resonance assignable to Et_2O. All other resonances are thus far unassigned.

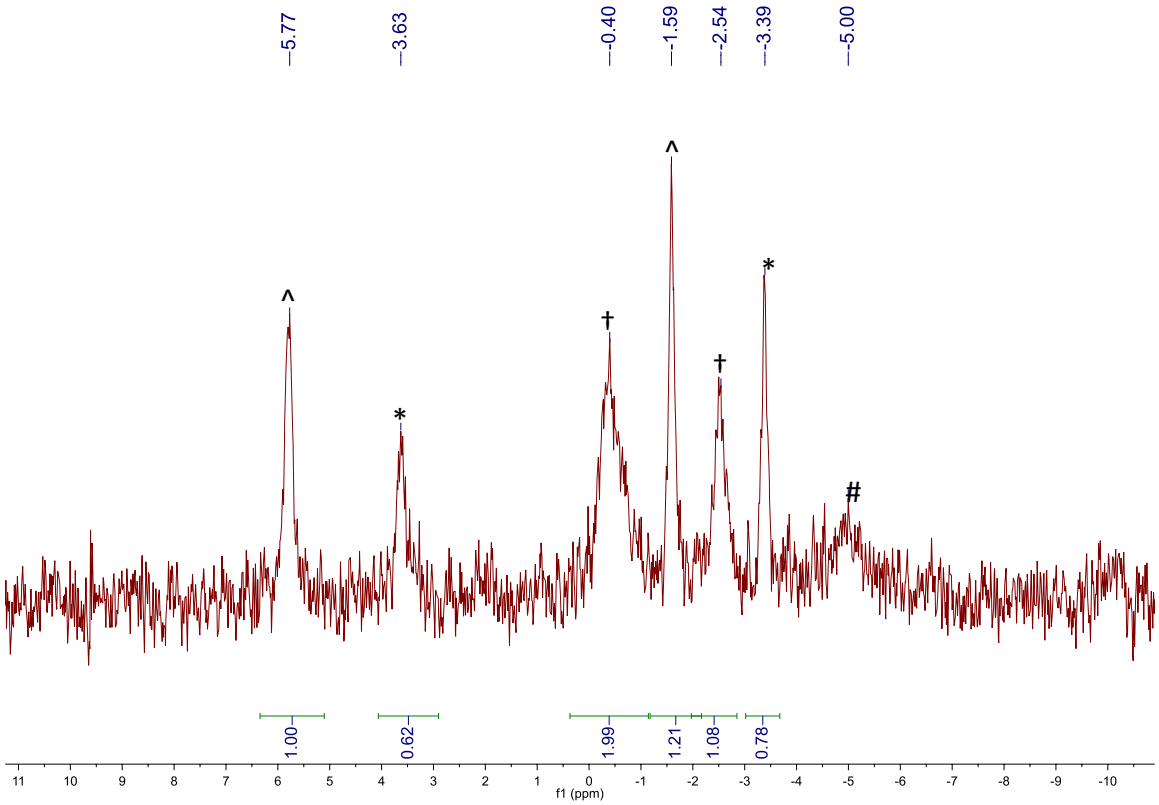

Figure A2.32. $^{1}H\{^{31}P\}$ NMR spectrum in CD_2Cl_2 of the crude soluble solids from the reaction to generate **2.9**. (*) indicates a resonance assignable to **2.9**, (†) indicates a resonance tentatively assignable to another Cu-H cluster, (^) indicates a resonance tentatively assignable to the known dimer $[Cu_2(SePh)_2(PPh_3)_3]$[91], and (#) indicates a resonance assignable to PPh_3.

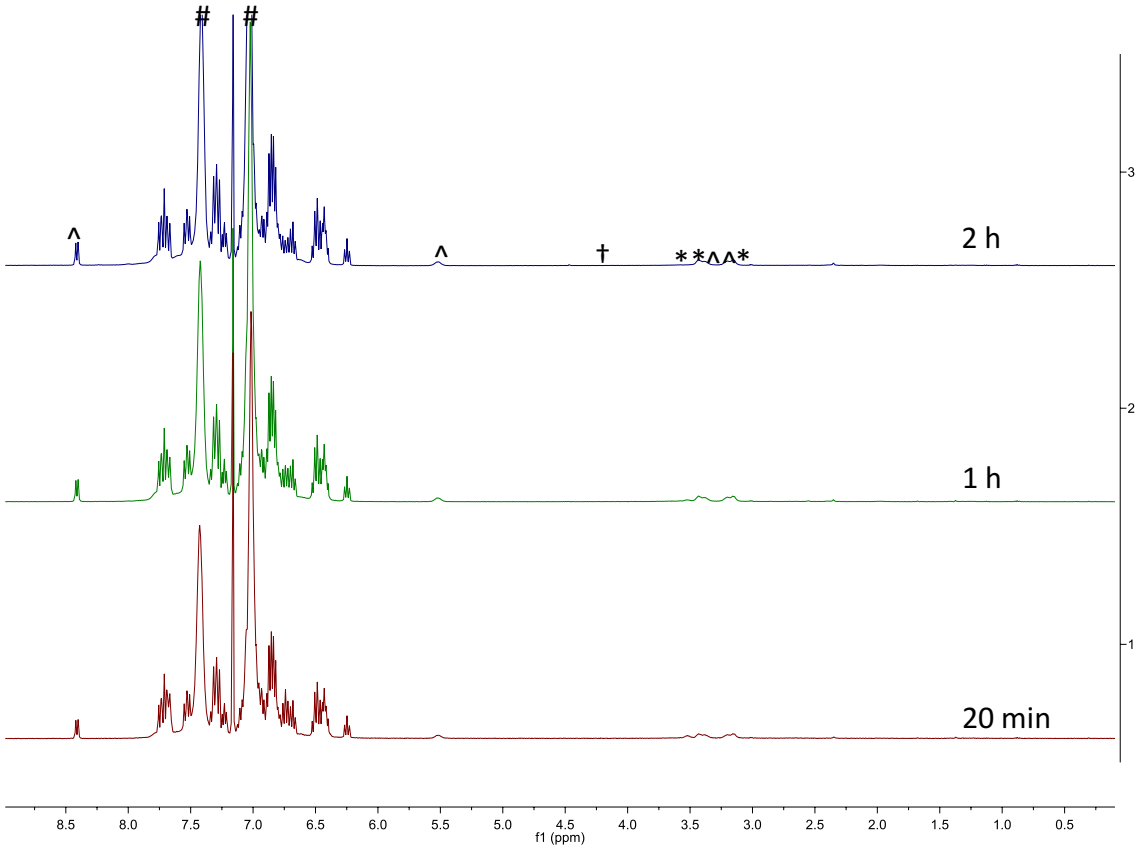

Figure A2.33. ^{1}H NMR spectra in C_6D_6 of the reaction of $[CuH(PPh_3)]_6$ and Ph_2Se_2 (1.5 equiv). **Experimental details:** $[CuH(PPh_3)]_6$ (15.0 mg, 7.53 μmol) and Ph_2Se_2 (3.6 mg, 11.5 μmol) were added to a J. Young NMR tube equipped with a Teflon rotoflow valve and dissolved in C_6D_6. The solution immediately turned orange with bubbling, which subsided after 10 min. The reaction mixture was allowed to stand at room temperature for 2 h and was monitored intermittently by ^{1}H NMR spectroscopy. (*) indicates a resonance assignable to **2.9**, (^) indicates a resonance assignable to a secondary Cu(I)-H cluster, (†) indicates a resonance assignable to H_2, and (#) indicates a resonance assignable to PPh_3. All other resonances are thus far unassigned.

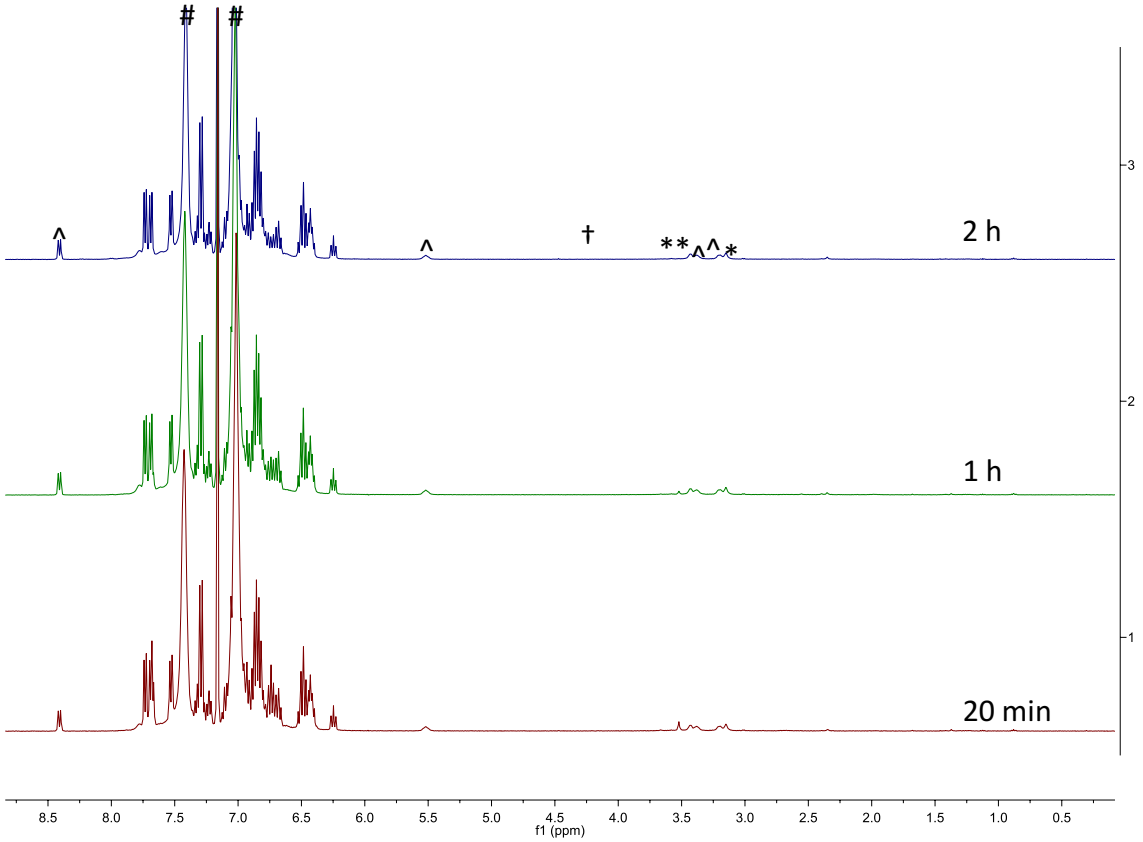

Figure A2.34. $^{1}H\{^{31}P\}$ NMR spectra in C_6D_6 of the reaction of $[CuH(PPh_3)]_6$ and Ph_2Se_2 (1.5 equiv). (*) indicates a resonance assignable to **2.9**, (^) indicates a resonance assignable to a secondary Cu(I)-H cluster, (†) indicates a resonance assignable to H_2, and (#) indicates a resonance assignable to PPh_3. All other resonances are thus far unassigned.

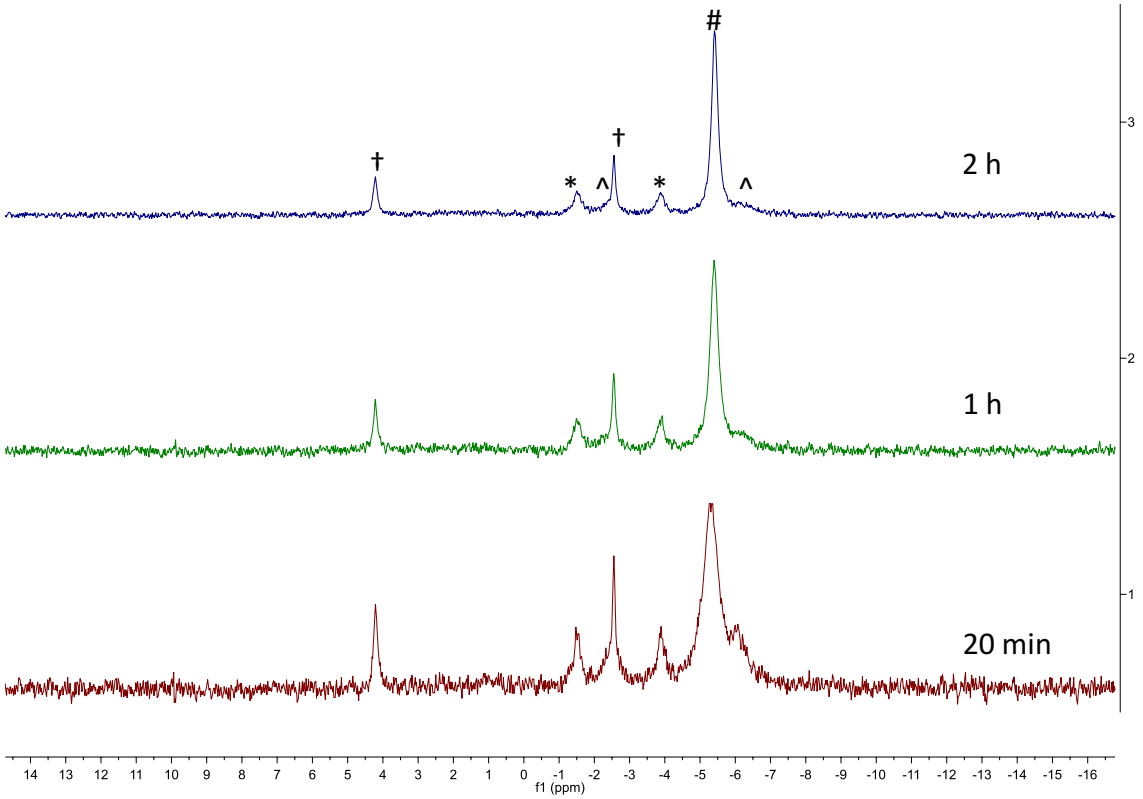

Figure A2.35. $^{31}P\{^{1}H\}$ NMR spectra in C_6D_6 of the reaction of $[CuH(PPh_3)]_6$ and Ph_2Se_2 (1.5 equiv). (*) indicates a resonance assignable to **2.9**, (^) indicates a resonance tentatively assignable to a secondary Cu(I)-H cluster, (†) indicates a resonance tentatively assignable to $[Cu_2(SePh)_2(PPh_3)_3]$, and (#) indicates a resonance assignable to PPh_3. All other resonances are thus far unassigned.

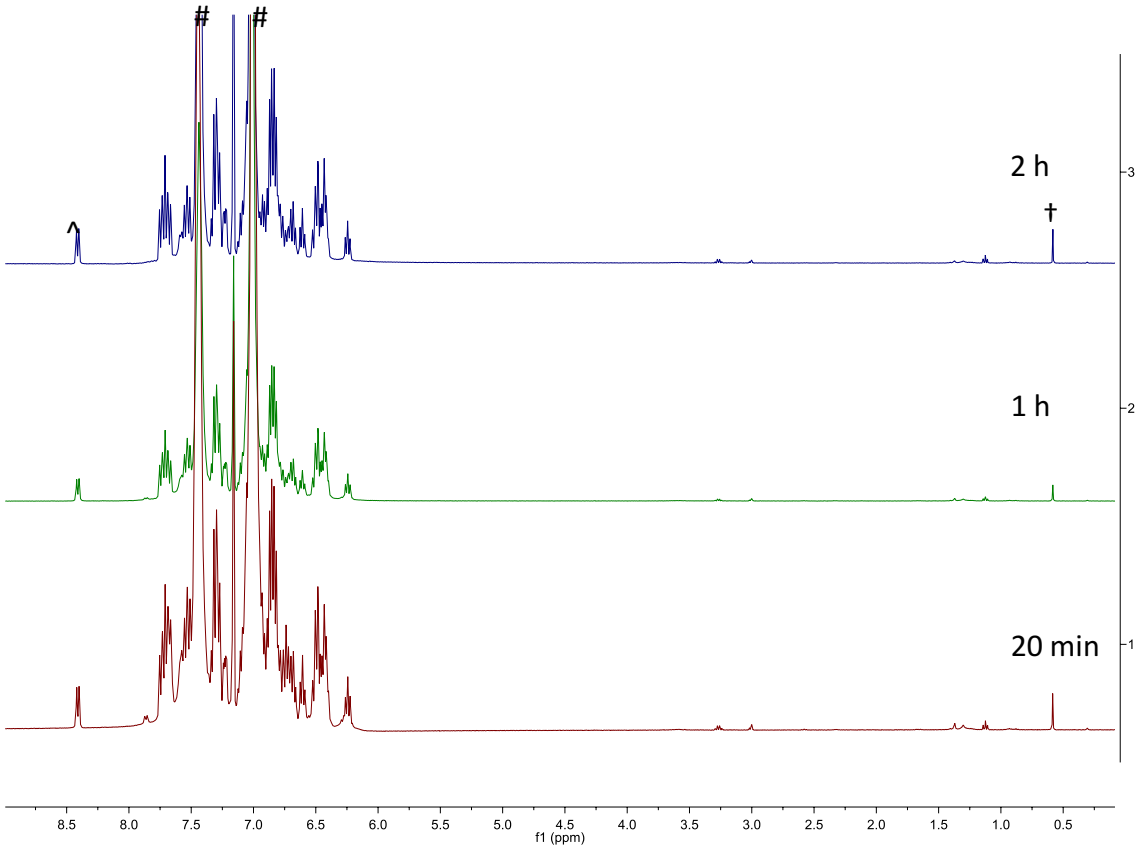

Figure A2.36. ^{1}H NMR spectra in C_6D_6 of the reaction of $[CuD(PPh_3)]_6$ and Ph_2Se_2 (1.5 equiv). **Experimental details:** $[CuD(PPh_3)]_6$ (17.0 mg, 8.51 μmol) and Ph_2Se_2 (4.0 mg, 12.8 μmol) were added to a J. Young NMR tube equipped with a Teflon rotoflow valve and dissolved in C_6D_6. The solution immediately turned orange with bubbling, which subsided after 10 min. The reaction mixture was allowed to stand at room temperature for 2 h and was monitored intermittently by ^{1}H NMR spectroscopy. (^) indicates a resonance assignable to a secondary Cu(I)-D cluster, (†) indicates resonance assignable to an unknown impurity, and (#) indicates a resonance assignable to PPh_3. All other resonances are thus far unassigned.

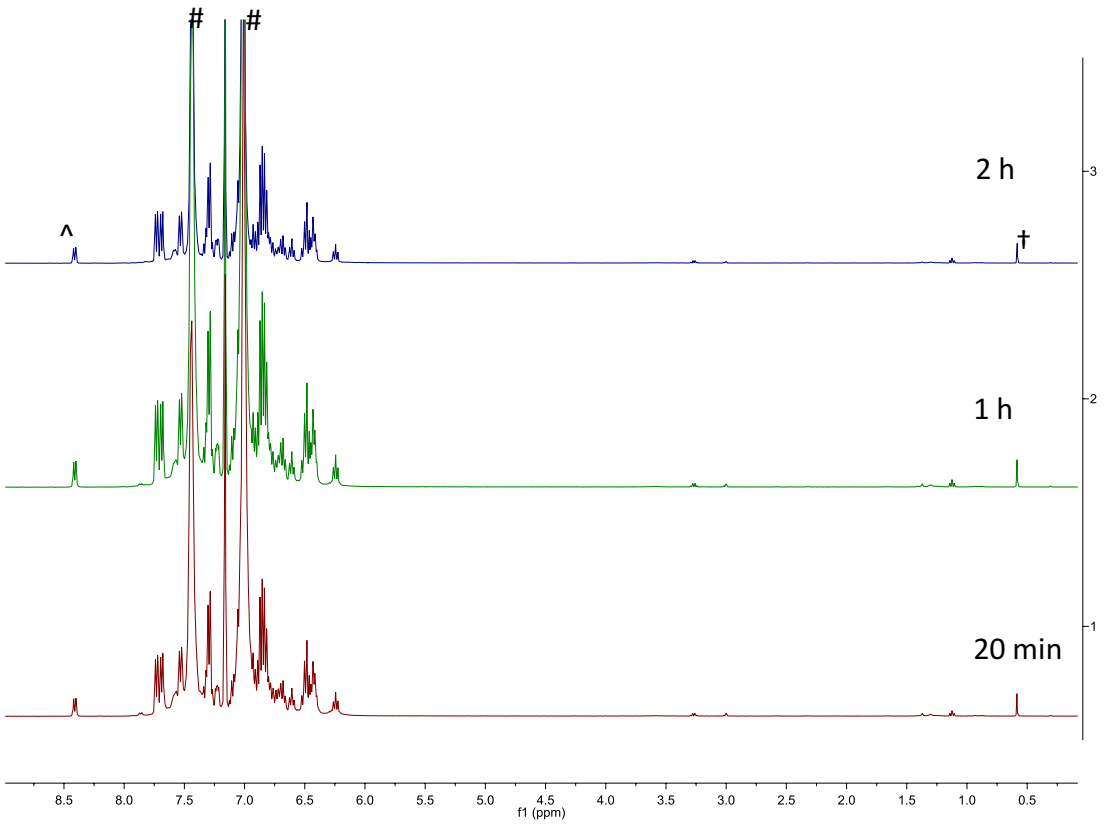

Figure A2.37. $^{1}H\{^{31}P\}$ NMR spectra in C_6D_6 of the reaction of $[CuD(PPh_3)]_6$ and Ph_2Se_2 (1.5 equiv). (^) indicates a resonance assignable to a secondary Cu(I)-D cluster, (†) indicates resonance assignable to an unknown impurity, and (#) indicates a resonance assignable to PPh_3. All other resonances are thus far unassigned.

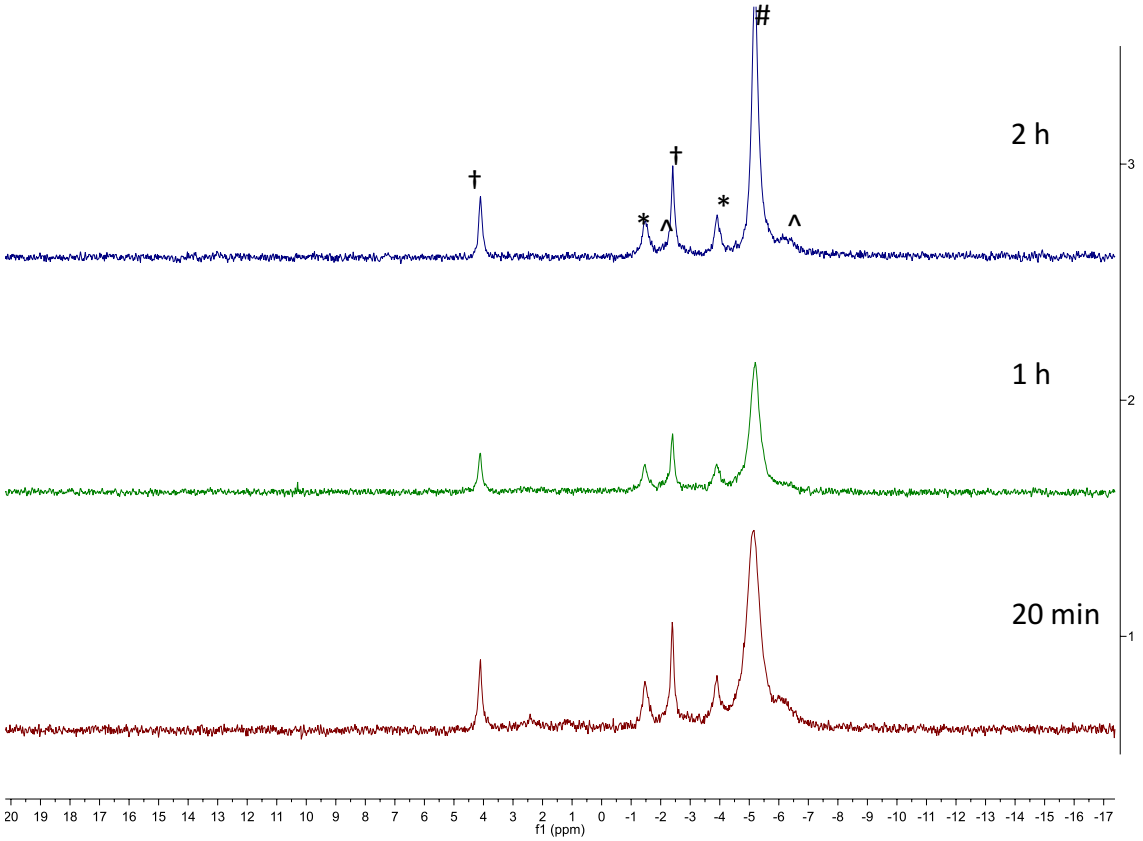

Figure A2.38. $^{31}P\{^{1}H\}$ NMR spectra in C_6D_6 of the reaction of $[CuD(PPh_3)]_6$ and Ph_2Se_2 (1.5 equiv). (*) indicates a resonance assignable to **2.9**, (^) indicates a resonance tentatively assignable to a secondary Cu(I)-D cluster, (†) indicates a resonance tentatively assignable to $[Cu_2(SePh)_2(PPh_3)_3]$, and (#) indicates a resonance assignable to PPh_3. All other resonances are thus far unassigned.

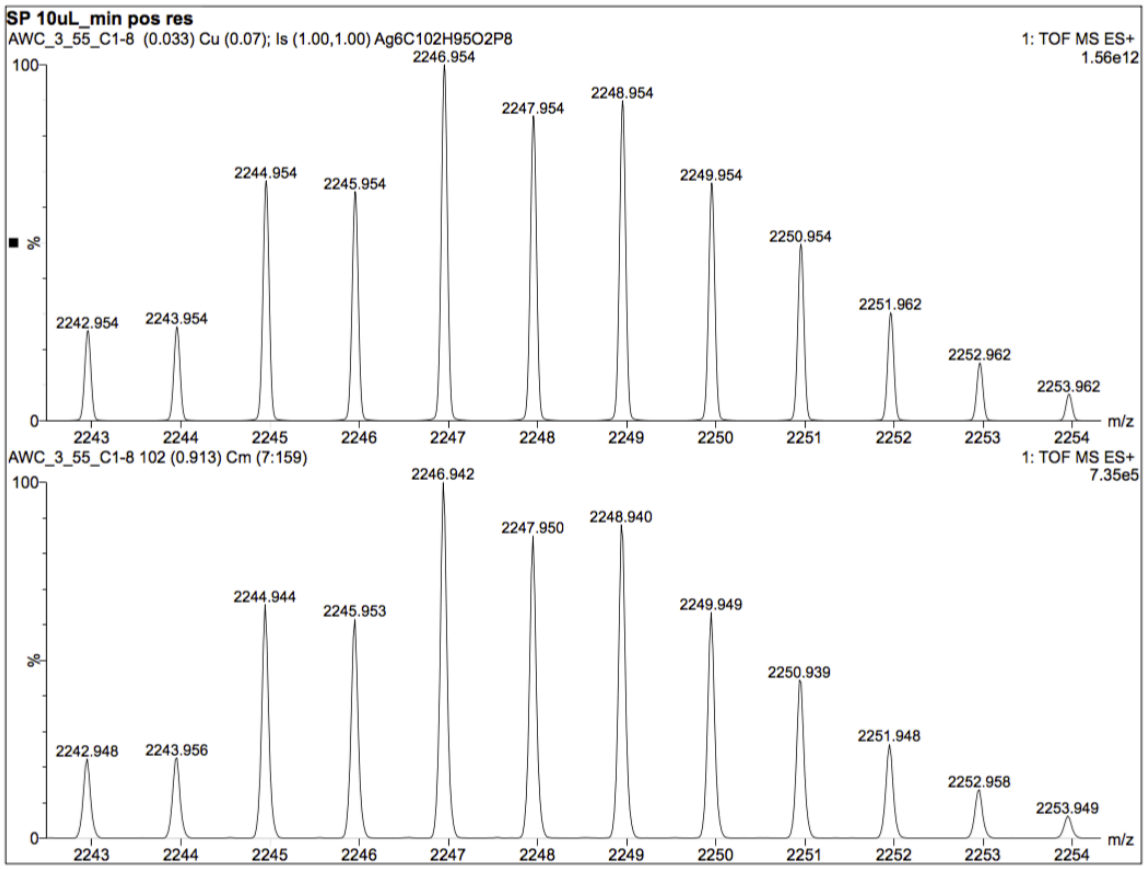

Figure A2.39. Partial ESI-MS (positive mode) of $[Ag_6H_4(dppm)_4(OAc)_2]$ (**2.1**). The experimental (bottom) and calculated (top) peaks assignable to the $[M\text{-}OAc]^+$ ion are shown.

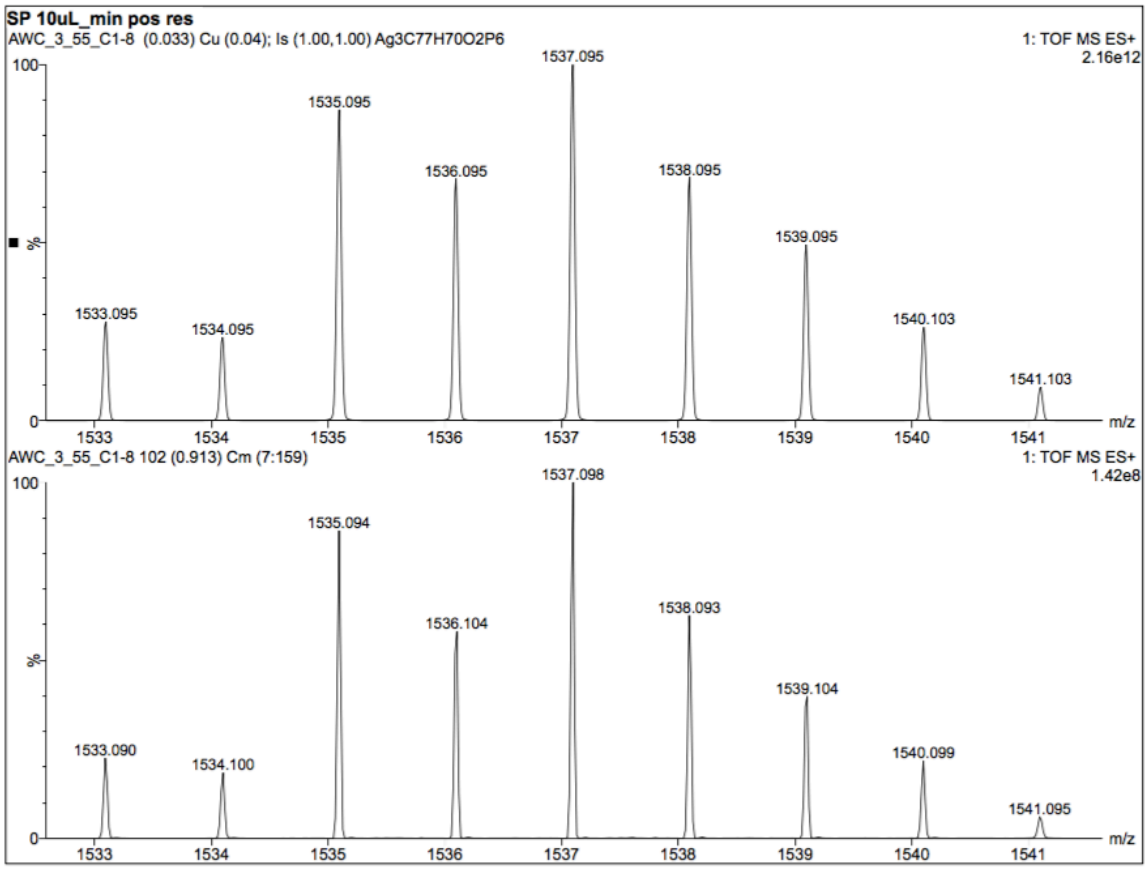

Figure A2.40. Partial ESI-MS (positive mode) of $[Ag_6H_4(dppm)_4(OAc)_2]$ (**2.1**). The experimental (bottom) and calculated (top) peaks assignable to the $[Ag_3H(dppm)_3(OAc)]^+$ ion are shown.[35]

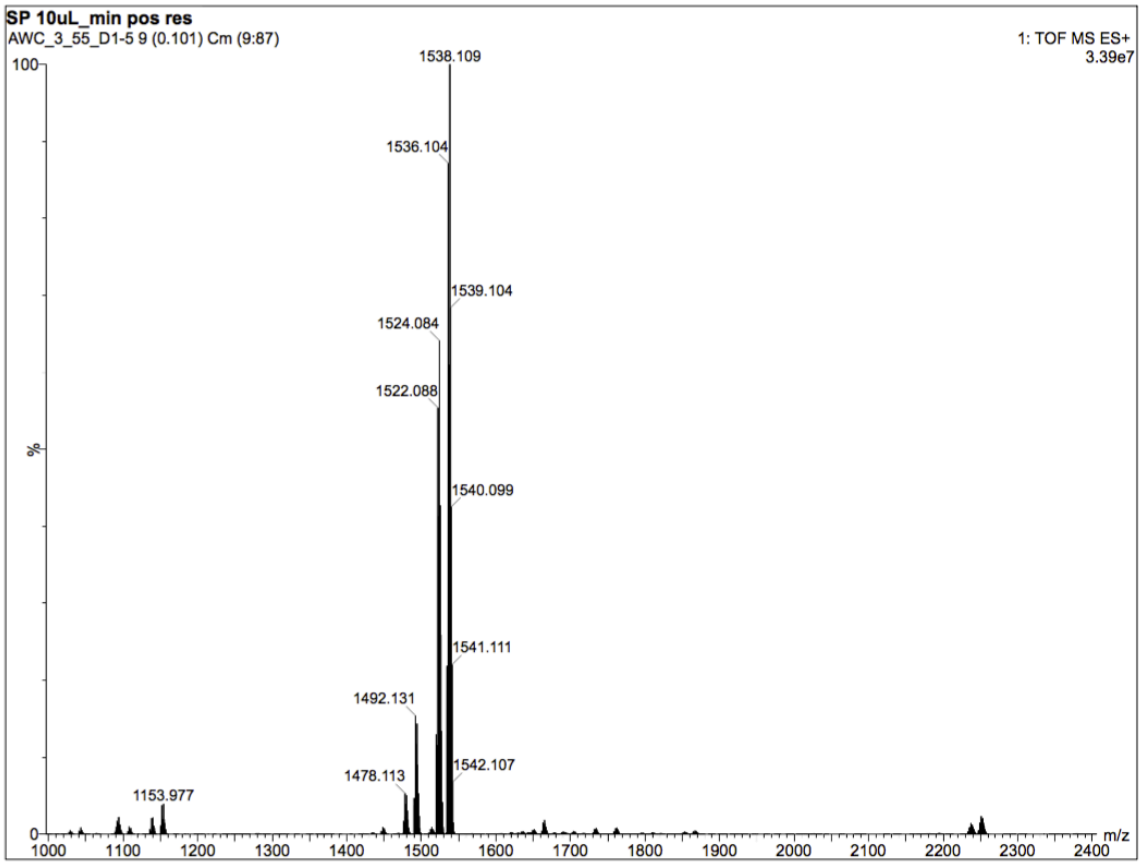

Figure A2.41. ESI-MS (positive mode) of $[Ag_6D_4(dppm)_4(OAc)_2]$ (**2.1-*d*$_4$**).

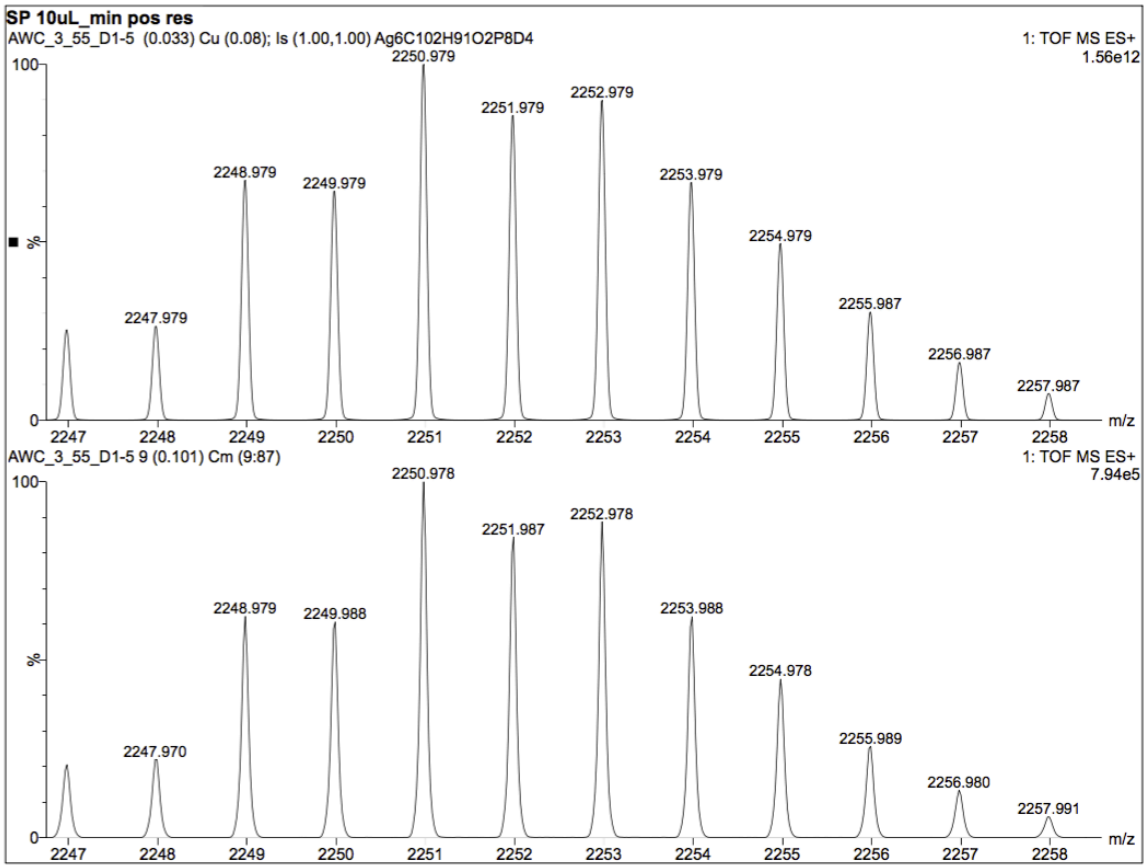

Figure A2.42. Partial ESI-MS (positive mode) of $[Ag_6D_4(dppm)_4(OAc)_2]$ (**2.1-*d*$_4$**). The experimental (bottom) and calculated (top) peaks assignable to the $[M\text{-}OAc]^+$ ion are shown.

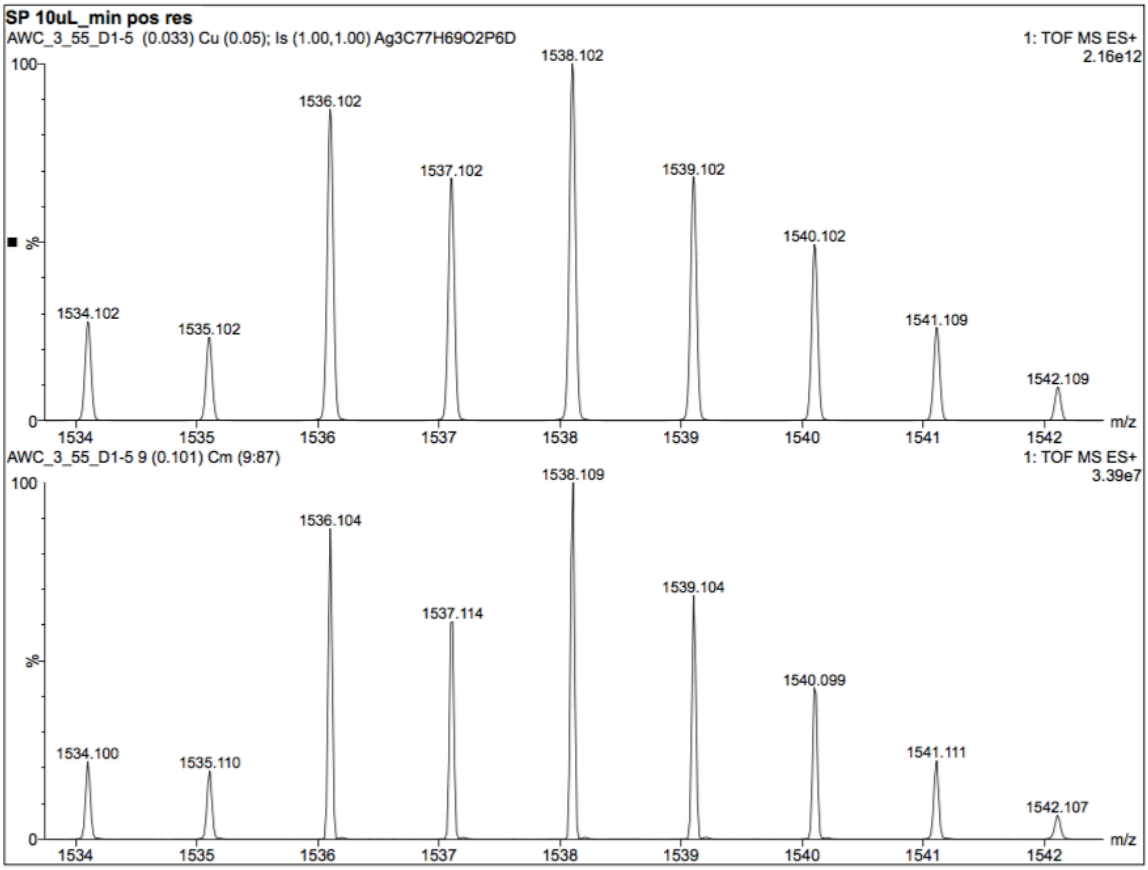

Figure A2.43. Partial ESI-MS (positive mode) of $[Ag_6D_4(dppm)_4(OAc)_2]$ (**2.1-*d*$_4$**). The experimental (bottom) and calculated (top) peaks assignable to the $[Ag_3D(dppm)_3(OAc)]^+$ ion are shown.

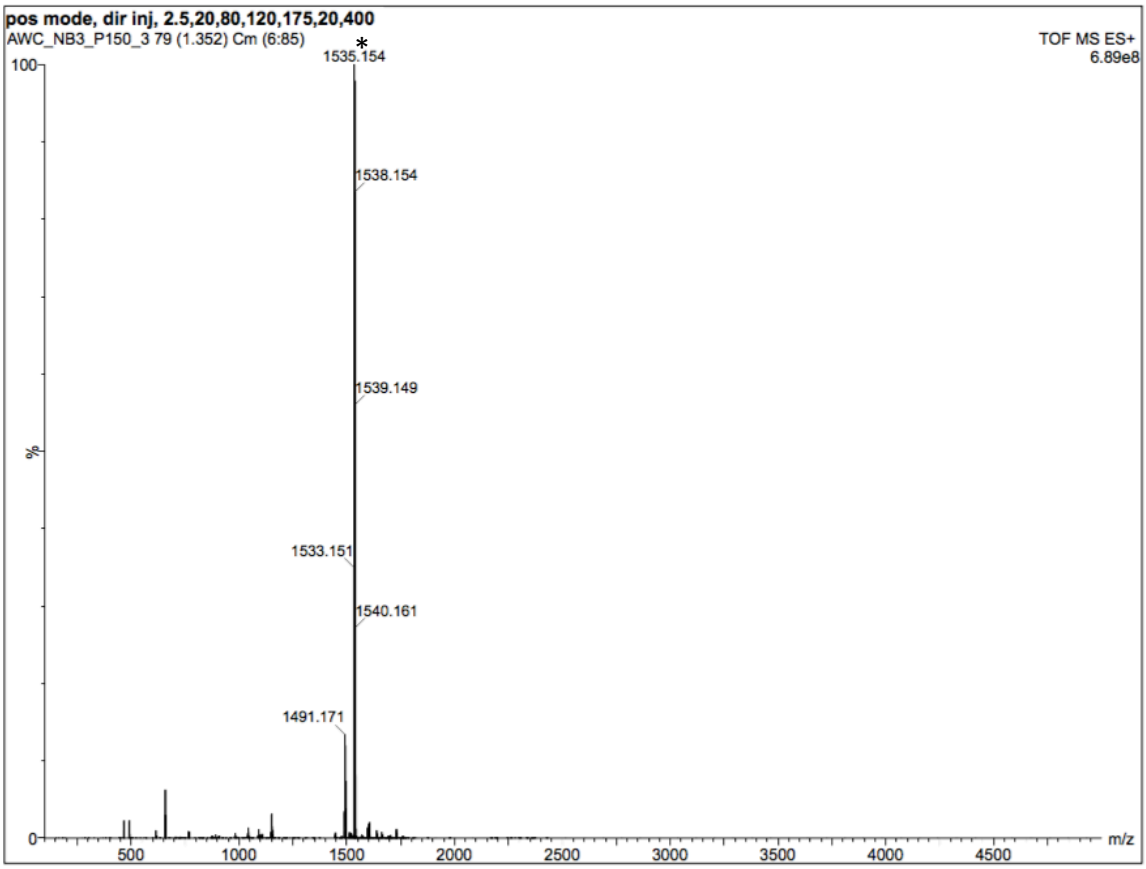

Figure A2.44. ESI-MS (positive mode) of the mixture formed upon partial decomposition of $[Ag_6H_4(dppm)_4(OAc)_2]$ (**2.1**) in benzene after 15 h. (*) denotes the $[Ag_3H(dppm)_3(OAc)]^+$ ion.

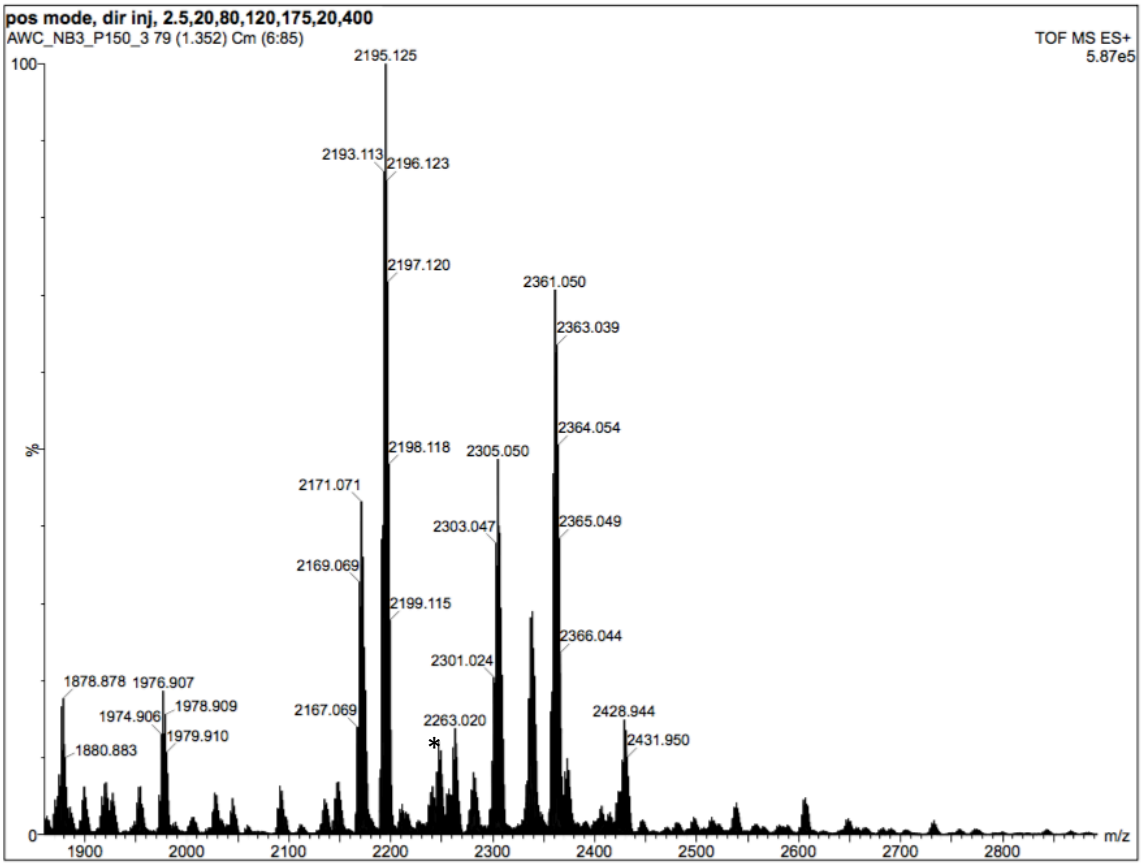

Figure A2.45. Partial ESI-MS (positive mode) of the mixture formed upon partial decomposition of $[Ag_6H_4(dppm)_4(OAc)_2]$ (**2.1**) in benzene after 15 h. (*) denotes the $[M\text{-}OAc]^+$ ion.

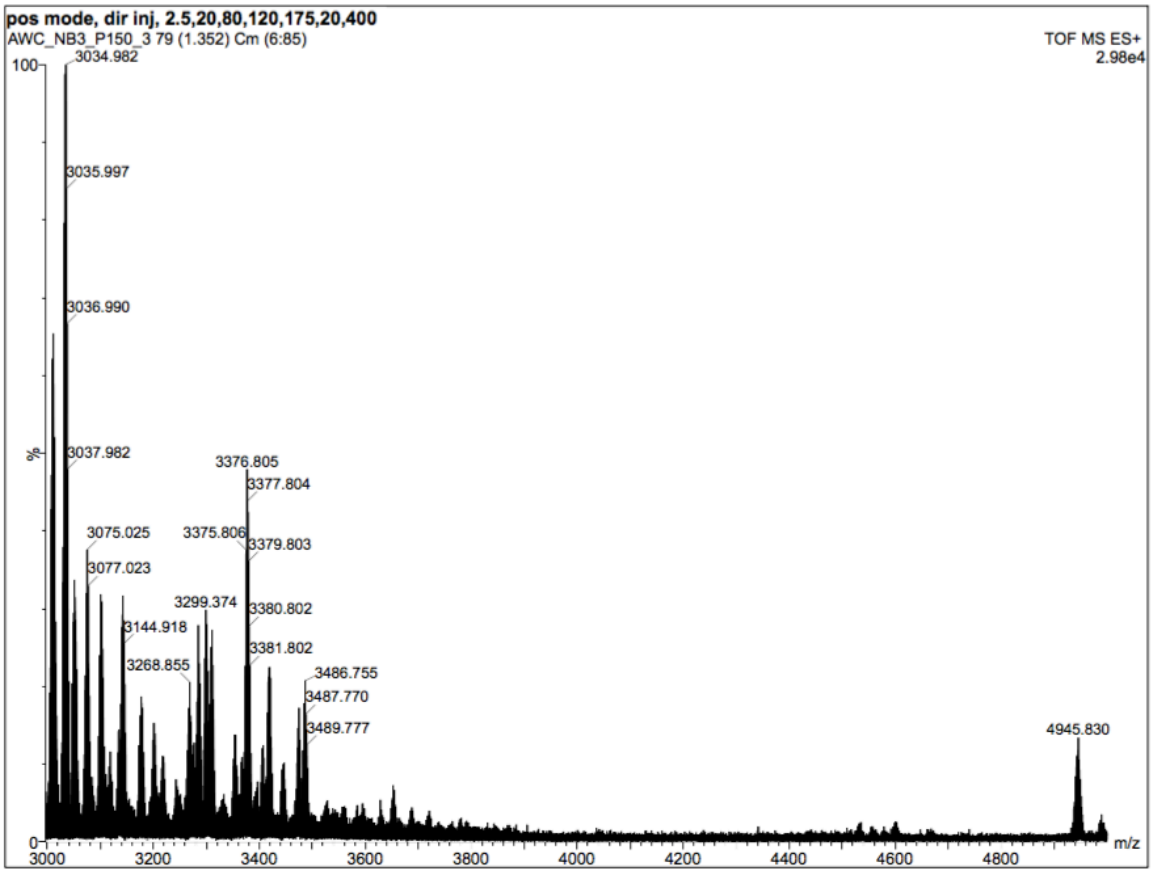

Figure A2.46. Partial ESI-MS (positive mode) of the mixture formed upon partial decomposition of $[Ag_6H_4(dppm)_4(OAc)_2]$ (**2.1**) in benzene after 15 h. The featured centered at 4945.830 *m/z* represents a new cluster with greater than 10 Ag atoms.

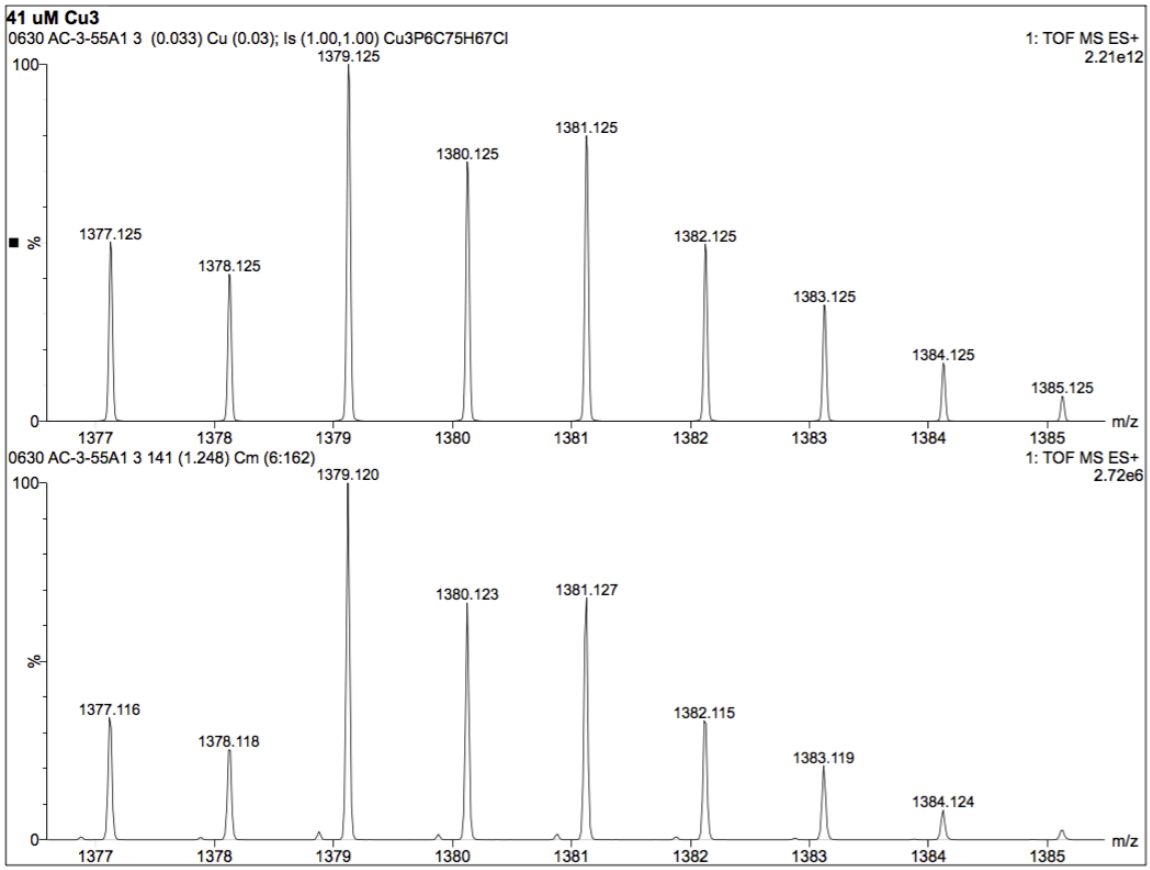

Figure A2.47. Partial ESI-MS (positive mode) of $[Cu_3H(dppm)_3(OAc)_2]$ (**2.2**). The experimental (bottom) and calculated (top) peaks assignable to the $[Cu_3H(dppm)_3Cl]^+$ ion are shown.

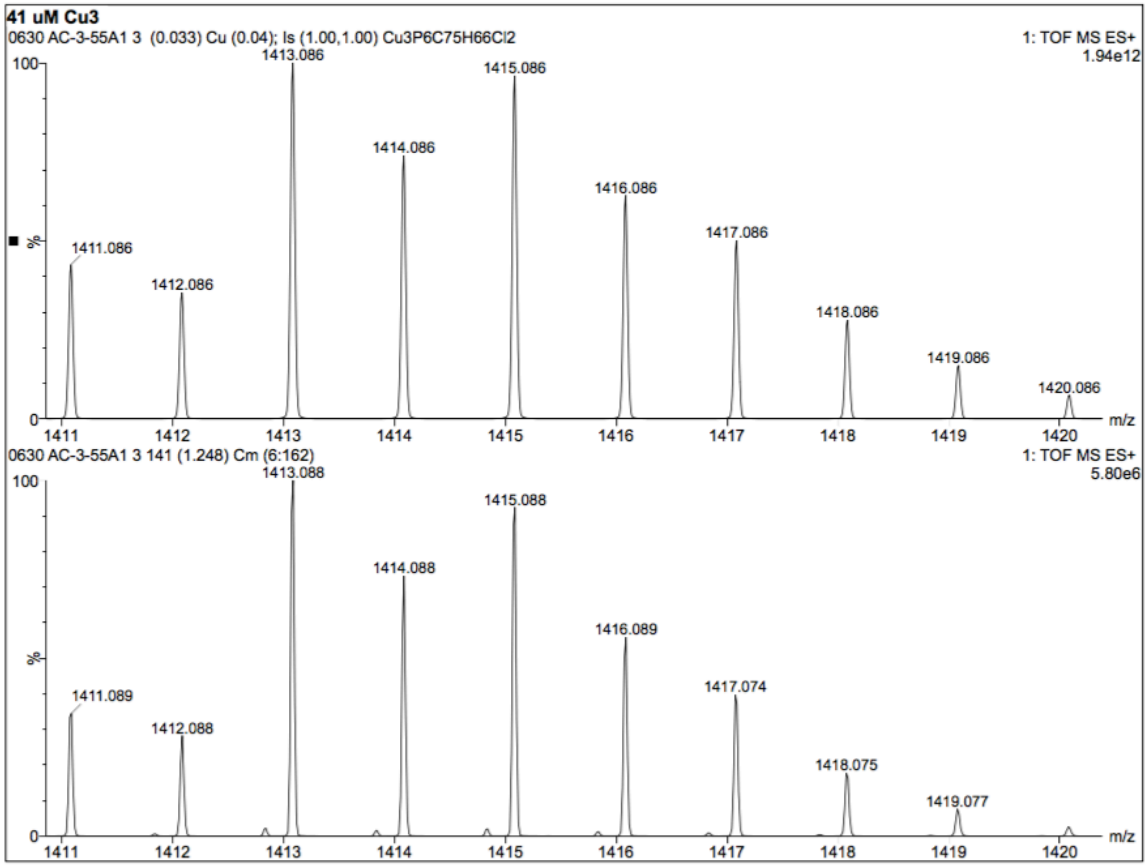

Figure A2.48. Partial ESI-MS (positive mode) of $[Cu_3H(dppm)_3(OAc)_2]$ (**2.2**). The experimental (bottom) and calculated (top) peaks assignable to the $[Cu_3(dppm)_3Cl_2]^+$ ion are shown.

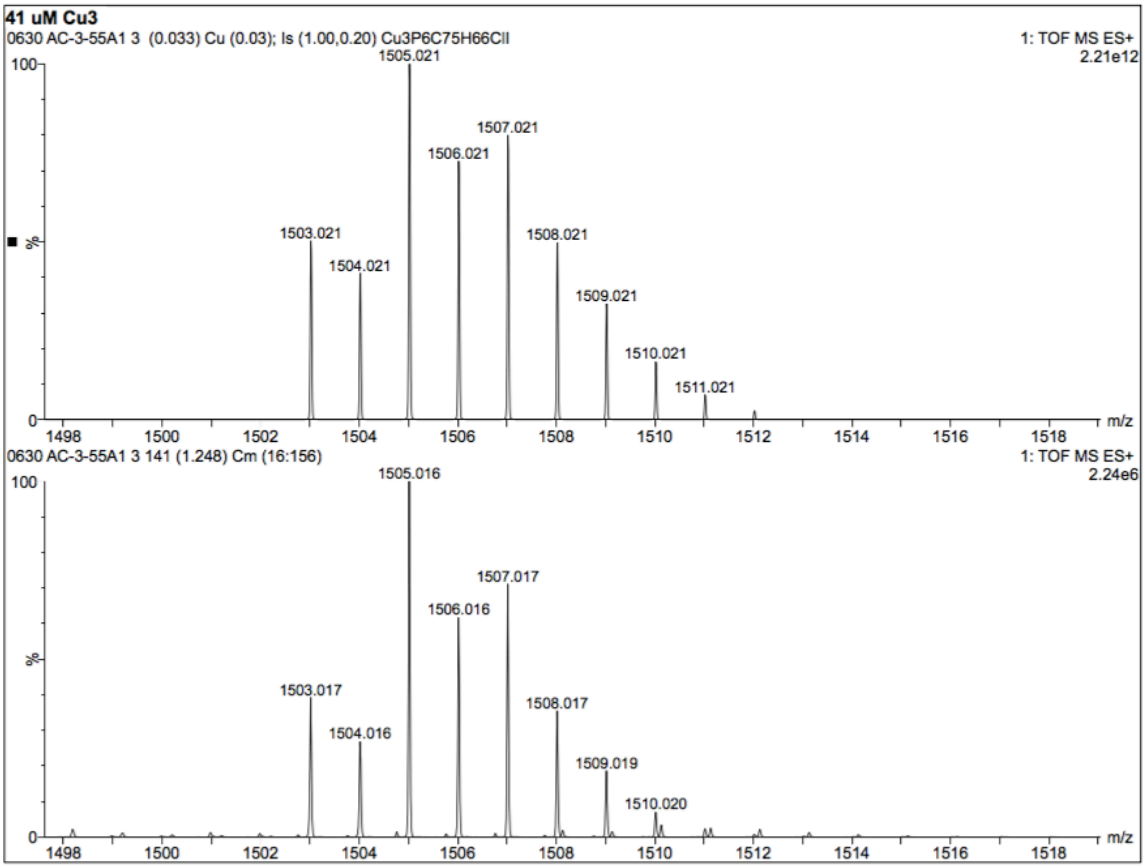

Figure A2.49. Partial ESI-MS (positive mode) of $[Cu_3H(dppm)_3(OAc)_2]$ (**2.2**). The experimental (bottom) and calculated (top) peaks assignable to the $[Cu_3(dppm)_3ICl]^+$ ion are shown.

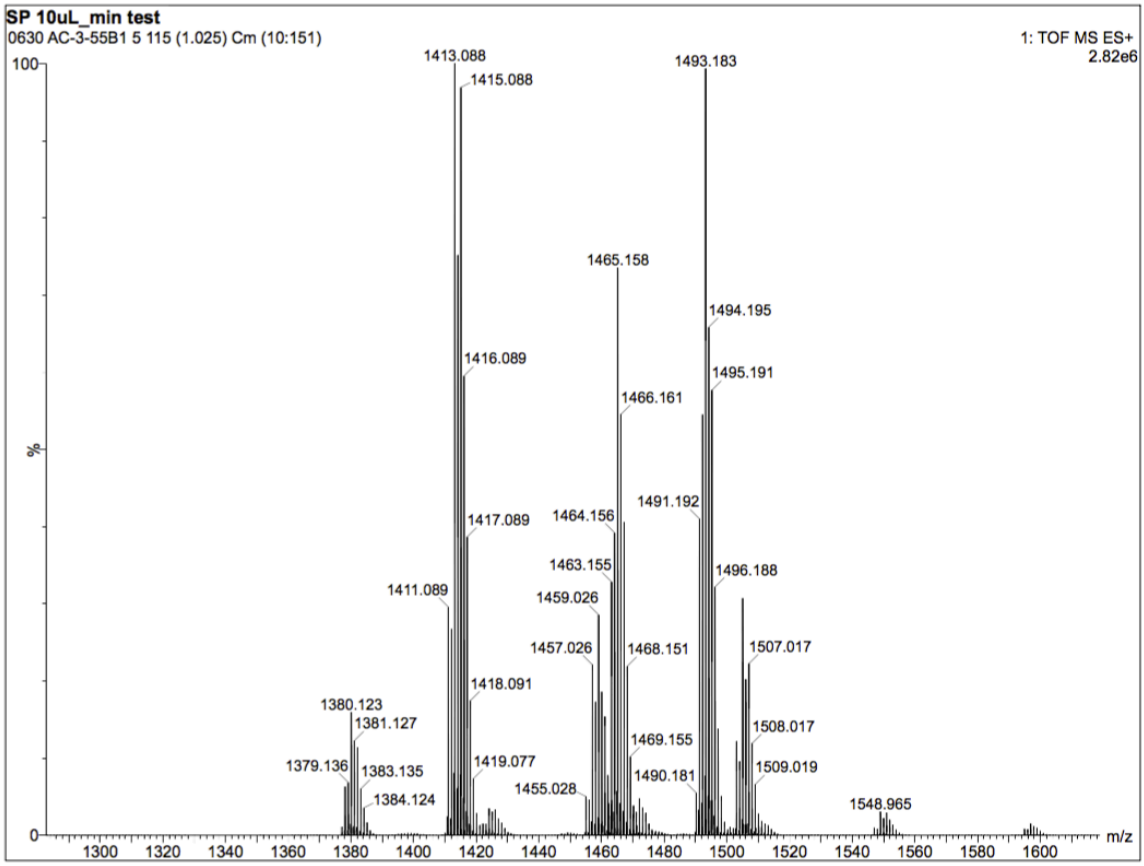

Figure A2.50. ESI-MS (positive mode) of $[Cu_3D(dppm)_3(OAc)_2]$ (**2.2-*d*$_1$**).

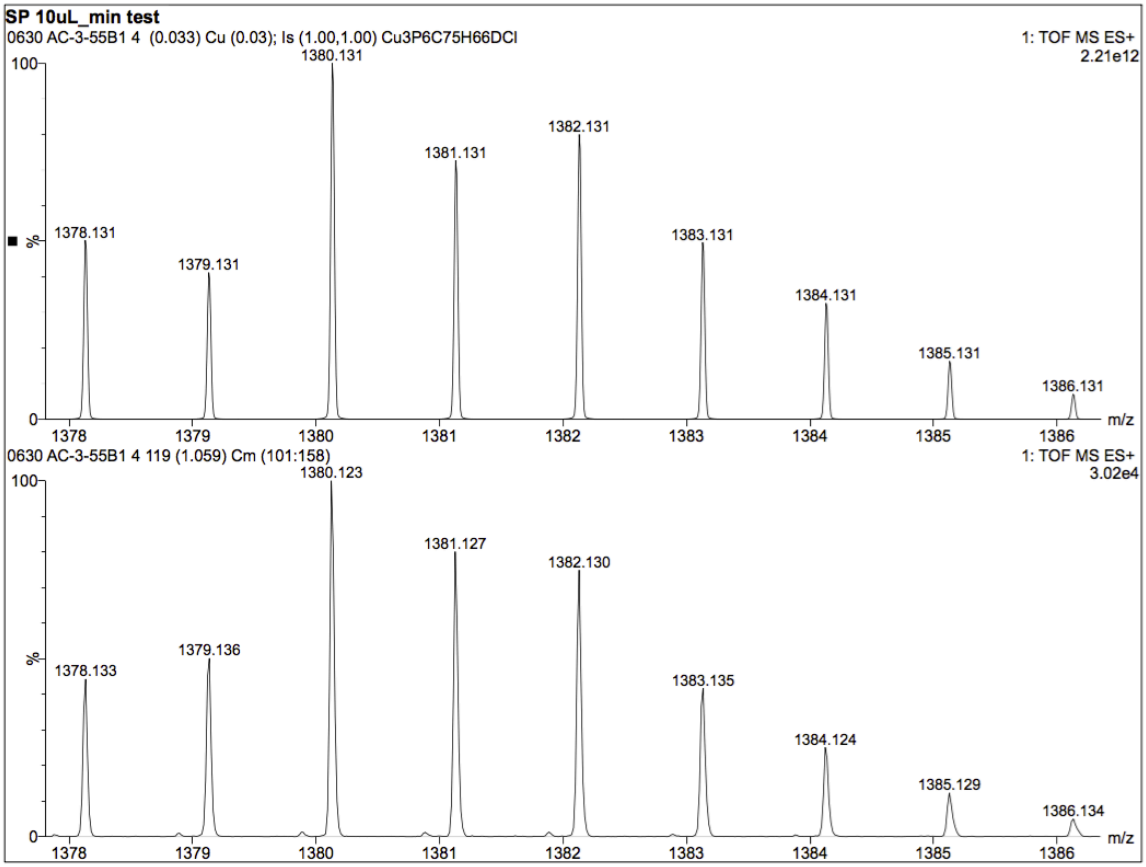

Figure A2.51. Partial ESI-MS (positive mode) of $[Cu_3D(dppm)_3(OAc)_2]$ (**2.2-*d*$_1$**). The experimental (bottom) and calculated (top) peaks assignable to the $[Cu_3D(dppm)_3Cl]^+$ ion are shown.

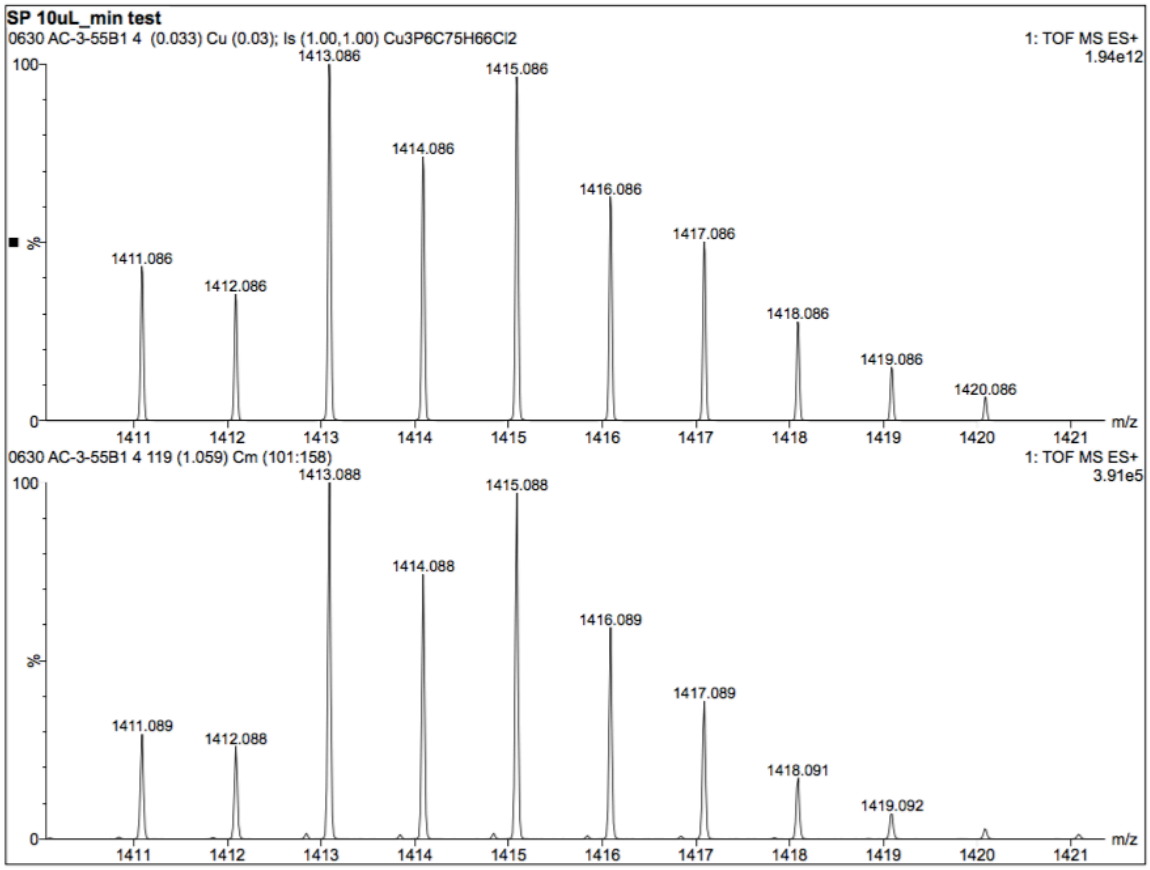

Figure A2.52. Partial ESI-MS (positive mode) of $[Cu_3D(dppm)_3(OAc)_2]$ (**2.2-*d*$_1$**). The experimental (bottom) and calculated (top) peaks assignable to the $[Cu_3(dppm)_3Cl_2]^+$ ion are shown.

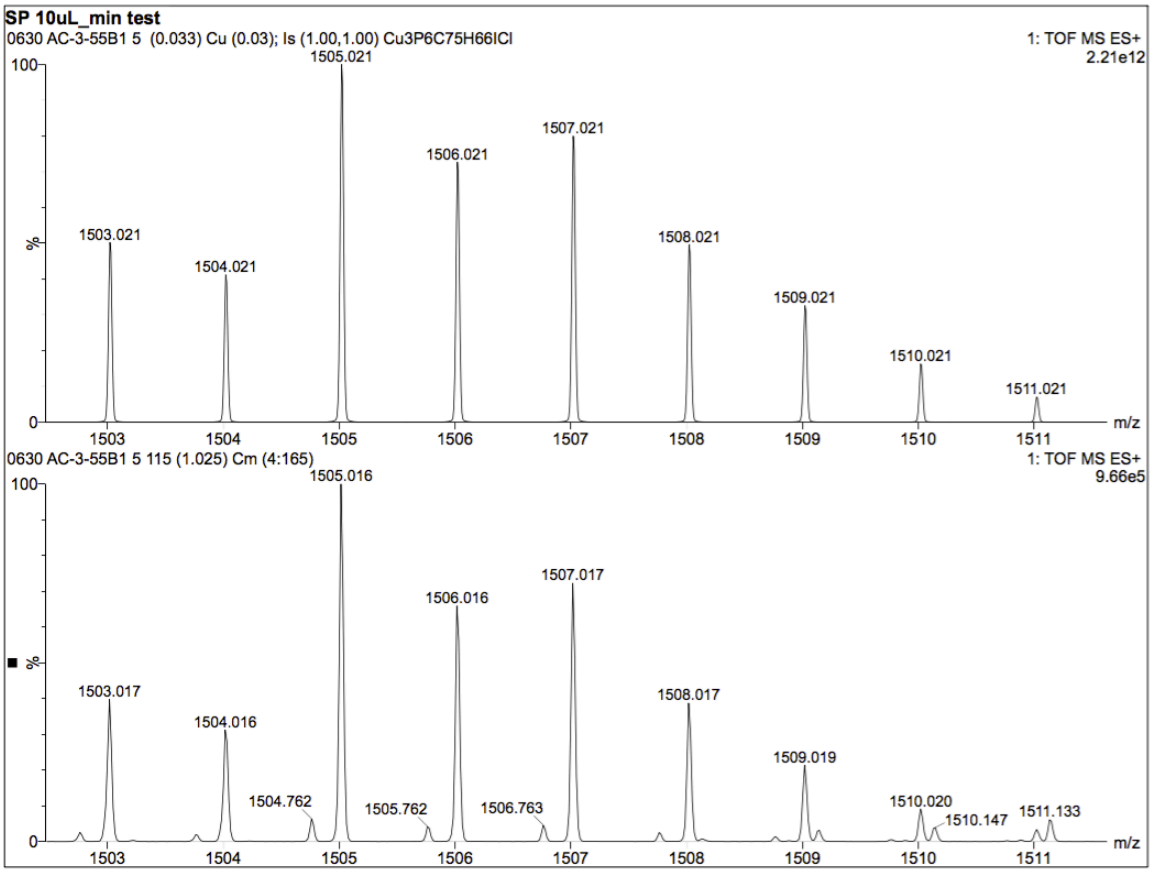

Figure A2.53. Partial ESI-MS (positive mode) of $[Cu_3D(dppm)_3(OAc)_2]$ (**2.2-*d*$_1$**). The experimental (bottom) and calculated (top) peaks assignable to the $[Cu_3(dppm)_3ICl]^+$ ion are shown.

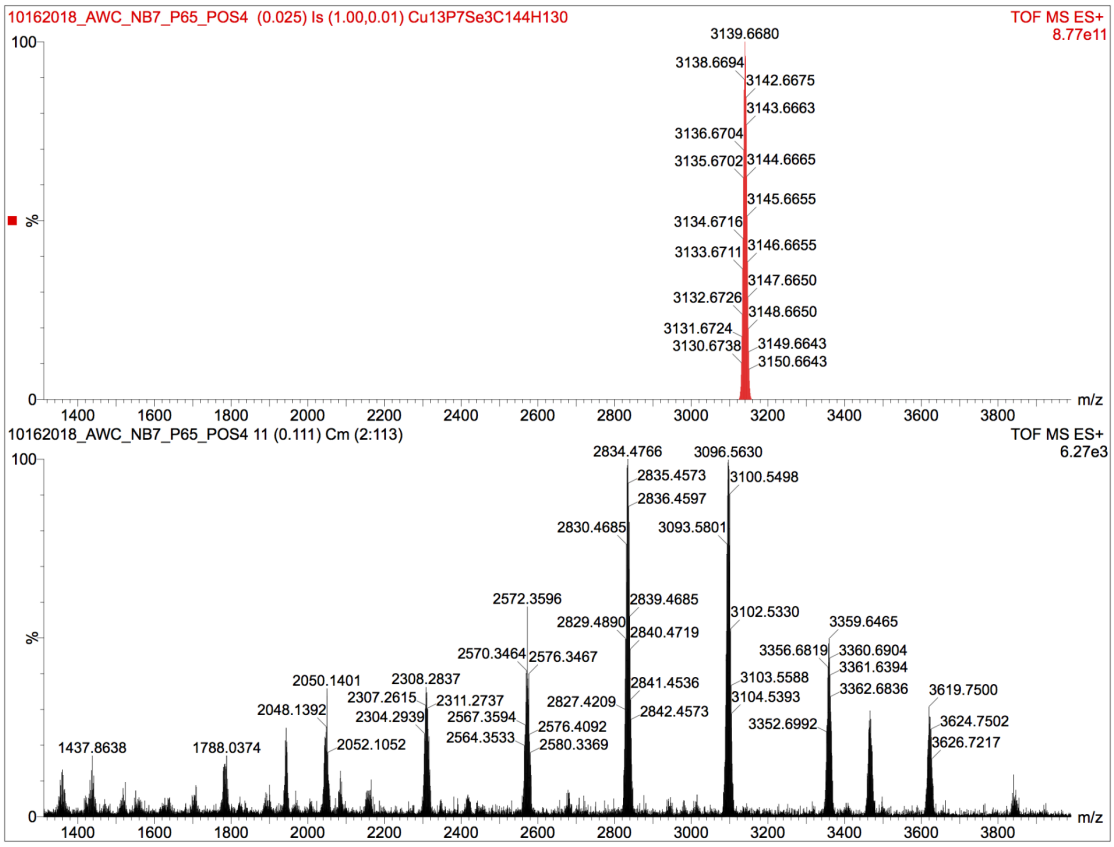

Figure A2.54. Partial ESI-MS (positive mode) of $[Cu_{13}H_{10}(SePh)_3(PPh_3)_7]$ (**2.9**). The experimental (bottom) and calculated (top) peaks for $[\mathbf{2.9}]^+$ ion are shown.

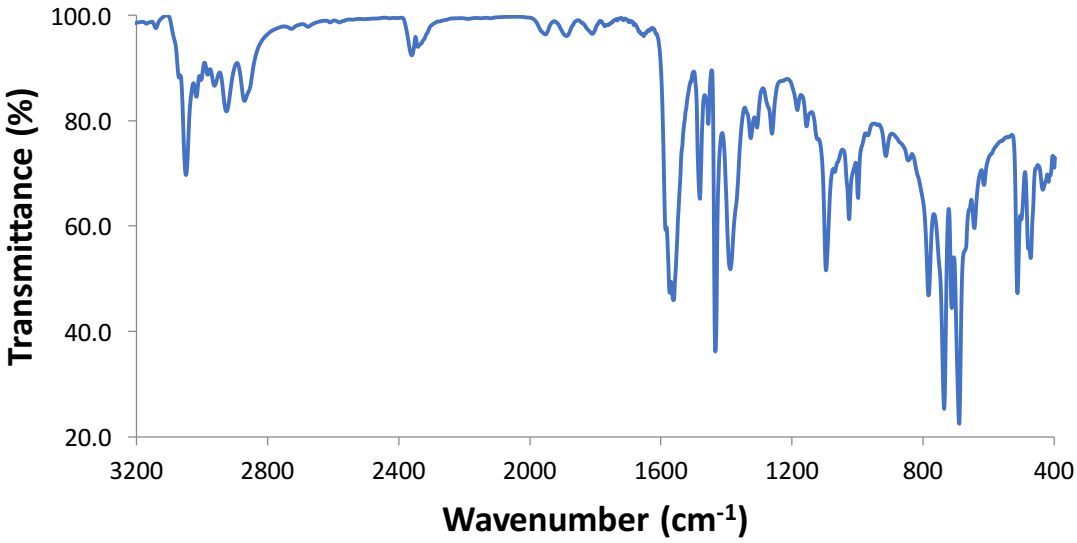

Figure A2.55. Partial IR spectrum of **2.1** (KBr pellet).

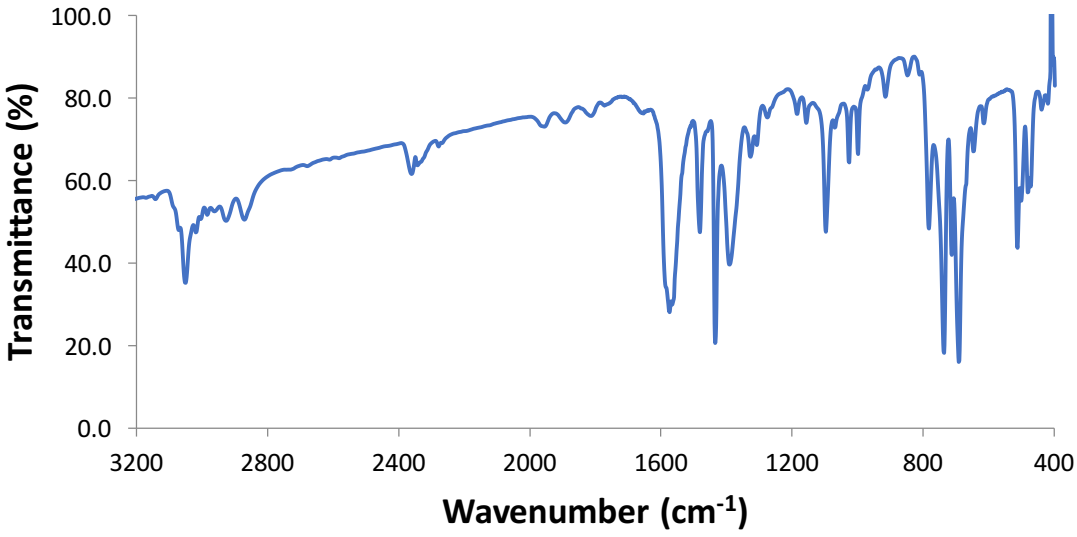

Figure A2.56. Partial IR spectrum of **2.1-*d*$_4$** (KBr pellet).

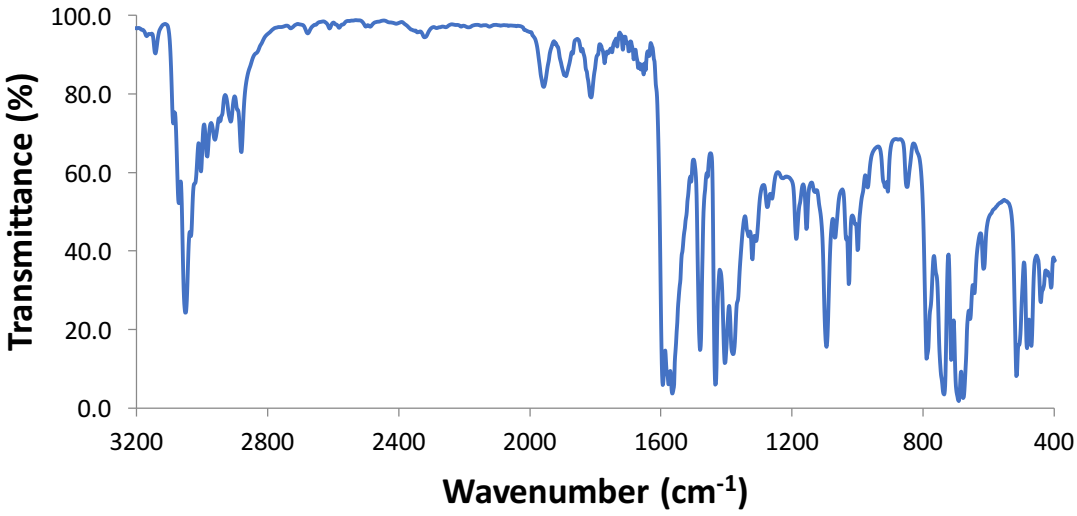

Figure A2.57. Partial IR spectrum of **2.2** (KBr pellet).

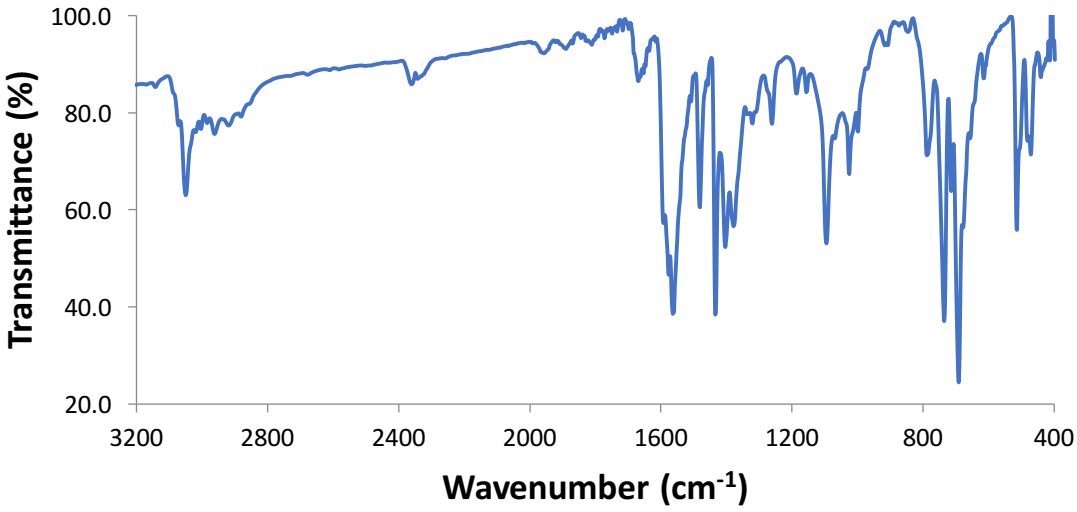

Figure A2.58. Partial IR spectrum of **2.2-*d*$_1$** (KBr pellet).

2.6 References

(1) Osborn, M. E.; Pegues, J. F.; Paquette, L. A., Reduction of α,β-Unsaturated Nitriles with a Copper Hydride Complex. *J. Org. Chem.* **1980**, *45*, 167-168.

(2) Goeden, G. V.; Caulton, K. G., Soluble Copper Hydrides: Solution Behavior and Reactions Related to Carbon Monoxide Hydrogenation. *J. Am. Chem. Soc.* **1981**, *103*, 7354-7355.

(3) Mahoney, W. S.; Brestensky, D. M.; Stryker, J. M., Selective Hydride-Mediated Conjugate Reduction of α,β-Unsaturated Carbonyl Compounds Using $[(Ph_3P)CuH]_6$. *J. Am. Chem. Soc.* **1988**, *110*, 291-293.

(4) Daeuble, J. F.; McGettigan, C.; Stryker, J. M., Selective Reduction of Alkynes to Cis-Alkenes by Hydrometallation Using $[(Ph_3P)CuH]_6$. *Tetrahedron Lett.* **1990**, *31*, 2397-2400.

(5) Lautens, M.; Ren, Y., Transition Metal Catalyzed Stereospecific Intramolecular [3 + 2] Cycloadditions of Methylenecyclopropanes with Alkynes. *J. Am. Chem. Soc.* **1996**, *118*, 9597-9605.

(6) Lipshutz, B. H.; Keith, J.; Papa, P.; Vivian, R., A Convenient, Efficient Method for Conjugate Reductions Using Catalytic Quantities of Cu(I). *Tetrahedron Lett.* **1998**, *39*, 4627-4630.

(7) Lipshutz, B. H.; Chrisman, W.; Noson, K., Hydrosilylation of aldehydes and ketones catalyzed by $[Ph_3P(CuH)]_6$. *J. Organomet. Chem.* **2001**, *624*, 367-371.

(8) Ren, Y.; Xu, X.; Sun, K.; Xu, J., A new and effective method for providing optically active monosubstituted malononitriles: selective reduction of α,β-unsaturated dinitriles catalyzed by copper hydride complexes. *Tetrahedron: Asymmetry* **2005**, *16*, 4010-4014.

(9) Yun, J.; Kim, D.; Yun, H., A new alternative to Stryker's reagent in hydrosilylation: synthesis, structure, and reactivity of a well-defined carbene-copper(II) acetate complex. *Chem. Commun.* **2005**, 5181-5183.

(10) Baker, B. A.; Bošković, Ž. V.; Lipshutz, B. H., (BDP)CuH: A "Hot" Stryker's Reagent for Use in Achiral Conjugate Reductions. *Org. Lett.* **2008**, *10*, 289-292.

(11) Zhang, L.; Cheng, J.; Hou, Z., Highly efficient catalytic hydrosilylation of carbon dioxide by an N-heterocyclic carbene copper catalyst. *Chem. Commun.* **2013**, *49*, 4782-4784.

(12) Zhang, L.; Hou, Z., N-Heterocyclic carbene (NHC)-copper-catalysed transformations of carbon dioxide. *Chem. Sci.* **2013**, *4*, 3395-3403.

(13) Nguyen, T.-A. D.; Goldsmith, B. R.; Zaman, H. T.; Wu, G.; Peters, B.; Hayton, T. W., Synthesis and Characterization of a Cu_{14} Hydride Cluster Supported by Neutral Donor Ligands. *Chem. – Eur. J.* **2015**, *21*, 5341-5344.

(14) Zall, C. M.; Linehan, J. C.; Appel, A. M., Triphosphine-Ligated Copper Hydrides for CO_2 Hydrogenation: Structure, Reactivity, and Thermodynamic Studies. *J. Am. Chem. Soc.* **2016**, *138*, 9968-9977.

(15) Halpern, J.; Czapski, G.; Jortner, J.; Stein, G., Mechanism of the Oxidation and Reduction of Metal Ions by Hydrogen Atoms. *Nature* **1960**, *186*, 629-630.

(16) Wile, B. M.; Stradiotto, M., Silver-catalyzed hydrosilylation of aldehydes. *Chem. Commun.* **2006**, 4104-4106.

(17) Jia, Z.; Liu, M.; Li, X.; Chan, A. S. C.; Li, C.-J., Highly Efficient Reduction of Aldehydes with Silanes in Water Catalyzed by Silver. *Synlett* **2013**, *24*, 2049-2056.
(18) Jia, Z.; Zhou, F.; Liu, M.; Li, X.; Chan, A. S. C.; Li, C.-J., Silver-Catalyzed Hydrogenation of Aldehydes in Water. *Angew. Chem., Int. Ed.* **2013**, *52*, 11871-11874.
(19) Karunananda, M. K.; Mankad, N. P., E-Selective Semi-Hydrogenation of Alkynes by Heterobimetallic Catalysis. *J. Am. Chem. Soc.* **2015**, *137*, 14598-14601.
(20) Zavras, A.; Khairallah, G. N.; Krstić, M.; Girod, M.; Daly, S.; Antoine, R.; Maitre, P.; Mulder, R. J.; Alexander, S.-A.; Bonačić-Koutecký, V.; Dugourd, P.; O'Hair, R. A. J., Ligand-induced substrate steering and reshaping of $[Ag_2(H)]^+$ scaffold for selective CO_2 extrusion from formic acid. *Nat. Commun.* **2016**, *7*, 11746.
(21) Tate, B. K.; Wyss, C. M.; Bacsa, J.; Kluge, K.; Gelbaum, L.; Sadighi, J. P., A dinuclear silver hydride and an umpolung reaction of CO_2. *Chem. Sci.* **2013**, *4*, 3068-3074.
(22) Bratsch, S. G., Standard Electrode Potentials and Temperature Coefficients in Water at 298.15 K. *J. Phys. Chem. Ref. Data* **1989**, *18*, 1-21.
(23) Brown, S. S. D.; Salter, I. D.; Sik, V.; Colquhoun, I. J.; McFarlane, W.; Bates, P. A.; Hursthouse, M. B.; Murray, M., The heteronuclear cluster chemistry of the group 1B metals. Part 9. Stereochemical non-rigidity of the metal skeletons of cluster compounds in solution. ^{109}Ag-{^{1}H} INEPT nuclear magnetic resonance studies on $[Ag_2Ru_4(\mu_3\text{-}H)_2\{\mu\text{-}Ph_2P(CH_2)PPh_2\}(CO)_{12}]$(n= 1, 2, or 4) and X-ray crystal structure of $[Ag_2Ru_4(\mu_3\text{-}H)_2(\mu\text{-}Ph_2PCH_2PPh_2)(CO)_{12}]$. *J. Chem. Soc., Dalton Trans.* **1988**, 2177-2185.
(24) Albinati, A.; Chaloupka, S.; Demartin, F.; Koetzle, T. F.; Ruegger, H.; Venanzi, L. M.; Wolfer, M. K., Complexes with platinum-hydrogen-silver bonds. *J. Am. Chem. Soc.* **1993**, *115*, 169-175.
(25) Brunner, H.; Mijolovic, D.; Wrackmeyer, B.; Nuber, B., NMR analysis of trinuclear silver(I) complexes with μ_2-H bridged group VI metallocene hydrides as ligands and X-ray structure analysis of $\{[(\eta^5\text{-}MeC_5H_4)_2Mo(\mu_2\text{-}H)_2]_2Ag\}PF_6$. *J. Organomet. Chem.* **1999**, *579*, 298-303.
(26) Gorol, M.; Mosch-Zanetti, N. C.; Roesky, H. W.; Noltemeyer, M.; Schmidt, H.-G., Unprecedented stabilisation of the Ag_2^{2+}-ion by two hydrido-iridium(III) complexes. *Chem. Commun.* **2003**, 46-47.
(27) Bruce, M. I.; Low, P. J.; Nicholson, B. K.; Skelton, B. W.; Zaitseva, N. N.; Zhao, X.-l., Preparation and molecular structures of the decanuclear diynyl-ruthenium-silver and -copper complexes $[M_6\{\mu_3\text{-}CCCC[Ru(dppe)Cp^*]\}_4(\mu\text{-}dppm)_2](BF_4)_2$ (M = Ag, Cu). *J. Organomet. Chem.* **2010**, *695*, 1569-1575.
(28) Liu, C. W.; Chang, H.-W.; Sarkar, B.; Saillard, J.-Y.; Kahlal, S.; Wu, Y.-Y., Stable Silver(I) Hydride Complexes Supported by Diselenophosphate Ligands. *Inorg. Chem.* **2010**, *49*, 468-475.
(29) Liao, P.-K.; Liu, K.-G.; Fang, C.-S.; Liu, C. W.; Fackler, J. P.; Wu, Y.-Y., A Copper(I) Homocubane Collapses to a Tetracapped Tetrahedron Upon Hydride Insertion. *Inorg. Chem.* **2011**, *50*, 8410-8417.
(30) Liu, C. W.; Liao, P.-K.; Fang, C.-S.; Saillard, J.-Y.; Kahlal, S.; Wang, J.-C., An eleven-vertex deltahedron with hexacapped trigonal bipyramidal geometry. *Chem. Commun.* **2011**, *47*, 5831-5833.

(31) Liu, C. W.; Lin, Y.-R.; Fang, C.-S.; Latouche, C.; Kahlal, S.; Saillard, J.-Y., $[Ag_7(H)\{E_2P(OR)_2\}_6]$ (E = Se, S): Precursors for the Fabrication of Silver Nanoparticles. *Inorg. Chem.* **2013**, *52*, 2070-2077.
(32) Zavras, A.; Khairallah, G. N.; Connell, T. U.; White, J. M.; Edwards, A. J.; Donnelly, P. S.; O'Hair, R. A. J., Synthesis, Structure and Gas-Phase Reactivity of a Silver Hydride Complex $[Ag_3\{(PPh_2)_2CH_2\}_3(\mu_3\text{-}H)(\mu_3\text{-}Cl)]BF_4$. *Angew. Chem., Int. Ed.* **2013**, *52*, 8391-8394.
(33) Donghi, D.; Maggioni, D.; D'Alfonso, G.; Beringhelli, T., Rhenium–silver bicyclic "spiro" hydrido-carbonyl clusters: NMR investigation of their formation and reversible fragmentation. *J. Organomet. Chem.* **2014**, *751*, 462-470.
(34) Girod, M.; Krstić, M.; Antoine, R.; MacAleese, L.; Lemoine, J.; Zavras, A.; Khairallah, G. N.; Bonačić-Koutecký, V.; Dugourd, P.; O'Hair, R. A. J., Formation and Characterisation of the Silver Hydride Nanocluster Cation $[Ag_3H_2((Ph_2P)_2CH_2)]^+$ and Its Release of Hydrogen. *Chem. – Eur. J.* **2014**, *20*, 16626-16633.
(35) Zavras, A.; Khairallah, G. N.; Connell, T. U.; White, J. M.; Edwards, A. J.; Mulder, R. J.; Donnelly, P. S.; O'Hair, R. A. J., Synthesis, Structural Characterization, and Gas-Phase Unimolecular Reactivity of the Silver Hydride Nanocluster $[Ag_3((PPh_2)_2CH_2)_3(\mu_3\text{-}H)](BF_4)_2$. *Inorg. Chem.* **2014**, *53*, 7429-7437.
(36) Daly, S.; Krstic, M.; Giuliani, A.; Antoine, R.; Nahon, L.; Zavras, A.; Khairallah, G. N.; Bonacic-Koutecky, V.; Dugourd, P.; O'Hair, R. A. J., Gas-phase VUV photoionisation and photofragmentation of the silver deuteride nanocluster $[Ag_{10}D_8L_6]^{2+}$ (L = bis(diphenylphosphino)methane). A joint experimental and theoretical study. *Phys. Chem. Chem. Phys.* **2015**, *17*, 25772-25777.
(37) Tate, B. K.; Nguyen, J. T.; Bacsa, J.; Sadighi, J. P., Heterolysis of Dihydrogen by Silver Alkoxides and Fluorides. *Chem. – Eur. J.* **2015**, *21*, 10160-10169.
(38) Zavras, A.; Ariafard, A.; Khairallah, G. N.; White, J. M.; Mulder, R. J.; Canty, A. J.; O'Hair, R. A. J., Synthesis, structure and gas-phase reactivity of the mixed silver hydride borohydride nanocluster $[Ag_3(\mu_3\text{-}H)(\mu_3\text{-}BH_4)LPh_3]BF_4$ (LPh = bis(diphenylphosphino)methane). *Nanoscale* **2015**, *7*, 18129-18137.
(39) Romero, E. A.; Olsen, P. M.; Jazzar, R.; Soleilhavoup, M.; Gembicky, M.; Bertrand, G., Spectroscopic Evidence for a Monomeric Copper(I) Hydride and Crystallographic Characterization of a Monomeric Silver(I) Hydride. *Angew. Chem. Int. Ed.* **2017**, *56*, 4024-4027.
(40) Ma, H. Z.; White, J. M.; Mulder, R. J.; Reid, G. E.; Canty, A. J.; O'Hair, R. A. J., Synthesis, structure, and condensed-phase reactivity of $[Ag_3(\mu_3\text{-}H)(\mu_3\text{-}BH_4)L(Ph)_3](BF_4)$ (L(Ph) = bis(diphenylphosphino)amine) with CS_2. *Dalton Trans.* **2018**, *47*, 14713-14725.
(41) Bootharaju, M. S.; Dey, R.; Gevers, L. E.; Hedhili, M. N.; Basset, J.-M.; Bakr, O. M., A New Class of Atomically Precise, Hydride-Rich Silver Nanoclusters Co-Protected by Phosphines. *J. Am. Chem. Soc.* **2016**, *138*, 13770-13773.
(42) Bezman, S. A.; Churchill, M. R.; Osborn, J. A.; Wormald, J., Preparation and crystallographic characterization of a hexameric triphenylphosphinecopper hydride cluster. *J. Am. Chem. Soc.* **1971**, *93*, 2063-2065.

(43) Cordero, B.; Gomez, V.; Platero-Prats, A. E.; Reves, M.; Echeverria, J.; Cremades, E.; Barragan, F.; Alvarez, S., Covalent radii revisited. *Dalton Trans.* **2008**, 2832-2838.
(44) Bondi, A., van der Waals Volumes and Radii. *J. Chem. Phys.* **1964**, *68*, 441-451.
(45) Wei, Q.-H.; Zhang, L.-Y.; Shi, L.-X.; Chen, Z.-N., Octahedral hexanuclear silver(I) and copper(I) ferrocenylacetylide complexes. *Inorg. Chem. Commun.* **2004**, *7*, 286-288.
(46) Yue, C.; Yan, C.; Feng, R.; Wu, M.; Chen, L.; Jiang, F.; Hong, M., A Polynuclear d^{10}–d^{10} Metal Complex with Unusual Near-Infrared Luminescence and High Thermal Stability. *Inorg. Chem.* **2009**, *48*, 2873-2879.
(47) Sun, D.; Luo, G.-G.; Zhang, N.; Huang, R.-B.; Zheng, L.-S., Simultaneous self-assembly of a cage-like silver(I) complex encapsulating an Ag_6 neutral cluster core and carbon dioxide fixation. *Chem. Commun.* **2011**, *47*, 1461-1463.
(48) Kikukawa, Y.; Kuroda, Y.; Suzuki, K.; Hibino, M.; Yamaguchi, K.; Mizuno, N., A discrete octahedrally shaped $[Ag_6]^{4+}$ cluster encapsulated within silicotungstate ligands. *Chem. Commun.* **2013**, *49*, 376-378.
(49) Yang, H.; Lei, J.; Wu, B.; Wang, Y.; Zhou, M.; Xia, A.; Zheng, L.; Zheng, N., Crystal structure of a luminescent thiolated Ag nanocluster with an octahedral Ag_6^{4+} core. *Chem. Commun.* **2013**, *49*, 300-302.
(50) Lane, A. C.; Vollmer, M. V.; Laber, C. H.; Melgarejo, D. Y.; Chiarella, G. M.; Fackler, J. P.; Yang, X.; Baker, G. A.; Walensky, J. R., Multinuclear Copper(I) and Silver(I) Amidinate Complexes: Synthesis, Luminescence, and CS_2 Insertion Reactivity. *Inorg. Chem.* **2014**, *53*, 11357-11366.
(51) Rajput, G.; Yadav, M. K.; Drew, M. G. B.; Singh, N., Impact of Ligand Framework on the Crystal Structures and Luminescent Properties of Cu(I) and Ag(I) Clusters and a Coordination Polymer Derived from Thiolate/Iodide/dppm Ligands. *Inorg. Chem.* **2015**, *54*, 2572-2579.
(52) Ho, D. M.; Bau, R., Preparation and Structural Characterization of $[Ag_2(dpm)_2(NO_3)_2]$ and $[Ag_4(dpm)_4(NO_3)_2]^{2+}[PF_6]^-_2$: Conformational Flexibility in the M_2P_4 Core Structure of Bis(diphenylphosphino)methane Complexes. *Inorg. Chem.* **1983**, *22*, 4073-4079.
(53) Neo, S. P.; Zhou, Z.-Y.; Mak, T. C. W.; Hor, T. S. A., Solid-State Tetramer vs. Solution-State Dimer. Reinvestigation of $[Ag_2(OAc)_2(dppm)]_2$ and Its dppm Addition Product $[Ag(OAc)(dppm)]_2$ (dppm = $Ph_2PCH_2PPh_2$). *Inorg. Chem.* **1995**, *34*, 520-523.
(54) Deivaraj, T. C.; Vittal, J. J., Synthesis, structures and ^{31}P NMR studies of bis(diphenylphosphino)methane adducts of copper and silver thiocarboxylates. *J. Chem. Soc., Dalton Trans.* **2001**, 322-328.
(55) Djordjevic, B.; Schuster, O.; Schmidbaur, H., A Cyclic Hexamer of Silver Trifluoroacetate Supported by Four Triphenylphosphine Sulfide Template Molecules. *Inorg. Chem.* **2005**, *44*, 673-676.
(56) Partyka, D. V.; Deligonul, N., Phosphine- and Carbene-Ligated Silver Acetate: Easily-Accessed Synthons for Reactions with Silylated Nucleophiles. *Inorg. Chem.* **2009**, *48*, 9463-9475.

(57) Kaeser, A.; Delavaux-Nicot, B.; Duhayon, C.; Coppel, Y.; Nierengarten, J.-F., Heteroleptic Silver(I) Complexes Prepared from Phenanthroline and Bis-phosphine Ligands. *Inorg. Chem.* **2013**, *52*, 14343-14354.
(58) Brevard, C.; Van Stein, G. C.; Van Koten, G., ^{109}Ag and ^{103}Rh NMR Spectroscopy with Proton Polarization Transfer. *J. Am. Chem. Soc.* **1981**, *103*, 6746-6748.
(59) Lemmen, T. H.; Folting, K.; Huffman, J. C.; Caulton, K. G., Copper Polyhydrides. *J. Am. Chem. Soc.* **1985**, *107*, 7774-7775.
(60) Mao, Z.; Huang, J.-S.; Che, C.-M.; Zhu, N.; Leung, S. K.-Y.; Zhou, Z.-Y., Unexpected Reactivities of Cu_2(diphosphine)$_2$ Complexes in Alcohol: Isolation, X-ray Crystal Structure, and Photoluminescent Properties of a Remarkably Stable $[Cu_3(\text{diphosphine})_3(\mu_3\text{-H})]^{2+}$ Hydride Complex. *J. Am. Chem. Soc.* **2005**, *127*, 4562-4563.
(61) Li, J.; White, J. M.; Mulder, R. J.; Reid, G. E.; Donnelly, P. S.; O'Hair, R. A. J., Synthesis, Structural Characterization, and Gas-Phase Unimolecular Reactivity of Bis(diphenylphosphino)amino Copper Hydride Nanoclusters $[Cu_3(X)(\mu_3\text{-H})((PPh_2)_2NH)_3](BF_4)$, Where X = μ_2-Cl and μ_3-BH_4. *Inorg. Chem.* **2016**, *55*, 9858-9868.
(62) Goeden, G. V.; Huffman, J. C.; Caulton, K. G., A Cu-(μ-H) Bond Can Be Stronger Than an Intramolecular P → Cu Bond. Synthesis and Structure of $Cu_2(\mu\text{-H})_2[\eta^2\text{-}CH_3C(CH_2PPh_2)_3]_2$. *Inorg. Chem.* **1986**, *25*, 2484-2485.
(63) Albert, C. F.; Healy, P. C.; Kildea, J. D.; Raston, C. L.; Skelton, B. W.; White, A. H., Lewis-base adducts of Group 11 metal(I) compounds. 49. Structural characterization of hexameric and pentameric (triphenylphosphine)copper(I) hydrides. *Inorg. Chem.* **1989**, *28*, 1300-1306.
(64) Eberhart, M. S.; Norton, J. R.; Zuzek, A.; Sattler, W.; Ruccolo, S., Electron Transfer from Hexameric Copper Hydrides. *J. Am. Chem. Soc.* **2013**, *135*, 17262-17265.
(65) Nguyen, T.-A. D.; Jones, Z. R.; Goldsmith, B. R.; Buratto, W. R.; Wu, G.; Scott, S. L.; Hayton, T. W., A Cu_{25} Nanocluster with Partial Cu(0) Character. *J. Am. Chem. Soc.* **2015**, *137*, 13319-13324.
(66) Nakamae, K.; Kure, B.; Nakajima, T.; Ura, Y.; Tanase, T., Facile Insertion of Carbon Dioxide into Cu_2(μ-H) Dinuclear Units Supported by Tetraphosphine Ligands. *Chem. – Asian J.* **2014**, *9*, 3106-3110.
(67) Chen, J.-X.; Daeuble, J. F.; Brestensky, D. M.; Stryker, J. M., Highly Chemoselective Catalytic Hydrogenation of Unsaturated Ketones and Aldehydes to Unsaturated Alcohols Using Phosphine-Stabilized Copper(I) Hydride Complexes. *Tetrahedron* **2000**, *56*, 2153-2166.
(68) Lipshutz, B. H.; Caires, C. C.; Kuipers, P.; Chrisman, W., Tweaking Copper Hydride (CuH) for Synthetic Gain. A Practical, One-Pot Conversion of Dialkyl Ketones to Reduced Trialkylsilyl Ether Derivatives. *Org. Lett.* **2003**, *5*, 3085-3088.
(69) Ojima, I.; Donovan, R. J.; Clos, N., Rhodium and Cobalt Carbonyl Clusters $Rh_4(CO)_{12}$, $Co_2Rh_2(CO)_{12}$, and $Co_3Rh(CO)_{12}$ As Effective Catalysts For Hydrosilylation of Isoprene, Cyclohexanone, and Cyclohexenone. *Organometallics* **1991**, *10*, 2606-2610.
(70) Jordan, A. J.; Lalic, G.; Sadighi, J. P., Coinage Metal Hydrides: Synthesis, Characterization, and Reactivity. *Chem. Rev.* **2016**, *116*, 8318-8372.

(71) Lipshutz, B. H.; Noson, K.; Chrisman, W.; Lower, A., Asymmetric Hydrosilylation of Aryl Ketones Catalyzed by Copper Hydride Complexed by Nonracemic Biphenyl Bis-phosphine Ligands. *J. Am. Chem. Soc.* **2003**, *125*, 8779-8789.
(72) Issenhuth, J.-T.; Notter, F.-P.; Dagorne, S.; Dedieu, A.; Bellemin-Laponnaz, S., Mechanistic Studies on the Copper-Catalyzed Hydrosilylation of Ketones. *Eur. J. Inorg. Chem.* **2010**, *2010*, 529-541.
(73) Shirobokov, O. G.; Kuzmina, L. G.; Nikonov, G. I., Nonhydride Mechanism of Metal-Catalyzed Hydrosilylation. *J. Am. Chem. Soc.* **2011**, *133*, 6487-6489.
(74) Dhayal, R. S.; van Zyl, W. E.; Liu, C. W., Polyhydrido Copper Clusters: Synthetic Advances, Structural Diversity, and Nanocluster-to-Nanoparticle Conversion. *Acc. Chem. Res.* **2016**, *49*, 86-95.
(75) Jin, R.; Zeng, C.; Zhou, M.; Chen, Y., Atomically Precise Colloidal Metal Nanoclusters and Nanoparticles: Fundamentals and Opportunities. *Chem. Rev.* **2016**, *116*, 10346-10413.
(76) Li, J.; White, J. M.; Mulder, R. J.; Reid, G. E.; Donnelly, P. S.; O'Hair, R. A. J., Synthesis, Structural Characterization, and Gas-Phase Unimolecular Reactivity of Bis(diphenylphosphino)amino Copper Hydride Nanoclusters $[Cu_3(X)(\mu_3\text{-}H)((PPh_2)_2NH)_3](BF_4)$, Where X = μ_2-Cl and μ_3-BH_4. *Inorg. Chem.* **2016**, DOI: 10.1021/acs.inorgchem.6b01696.
(77) Nguyen, T.-A. D.; Jones, Z. R.; Leto, D. F.; Wu, G.; Scott, S. L.; Hayton, T. W., Ligand-Exchange-Induced Growth of an Atomically Precise Cu29 Nanocluster from a Smaller Cluster. *Chem. Mater.* **2016**, *28*, 8385-8390.
(78) Nakajima, T.; Kamiryo, Y.; Hachiken, K.; Nakamae, K.; Ura, Y.; Tanase, T., Tri- and Tetranuclear Copper Hydride Complexes Supported by Tetradentate Phosphine Ligands. *Inorg. Chem.* **2018**, *57*, 11005-11018.
(79) Dierkes, P.; W. N. M. van Leeuwen, P., The bite angle makes the difference: a practical ligand parameter for diphosphine ligands. *J. Chem. Soc., Dalton Trans.* **1999**, 1519-1530.
(80) Rhodes, L. F.; Huffman, J. C.; Caulton, K. G., Multiple Mixed-Metal Condensation Leading to the Trigonal Bipyramidal Iridium Copper Hexahydride $Ir_2Cu_3H_6(MeCN)_3(PMe_2Ph)_6^{3+}$. *J. Am. Chem. Soc.* **1985**, *107*, 1759-1760.
(81) Venkateswaran, R.; Balakrishna, M. S.; Mobin, S. M.; Tuononen, H. M., Copper(I) Complexes of Bis(2-(diphenylphosphino)phenyl) Ether: Synthesis, Reactivity, and Theoretical Calculations. *Inorg. Chem.* **2007**, *46*, 6535-6541.
(82) Czerwieniec, R.; Yu, J.; Yersin, H., Blue-Light Emission of Cu(I) Complexes and Singlet Harvesting. *Inorg. Chem.* **2011**, *50*, 8293-8301.
(83) Sun, Y.; Lemaur, V.; Beltrán, J. I.; Cornil, J.; Huang, J.; Zhu, J.; Wang, Y.; Fröhlich, R.; Wang, H.; Jiang, L.; Zou, G., Neutral Mononuclear Copper(I) Complexes: Synthesis, Crystal Structures, and Photophysical Properties. *Inorg. Chem.* **2016**, *55*, 5845-5852.
(84) Xie, M.; Han, C.; Zhang, J.; Xie, G.; Xu, H., White Electroluminescent Phosphine-Chelated Copper Iodide Nanoclusters. *Chem. Mater.* **2017**, *29*, 6606-6610.
(85) Nakamae, K.; Tanaka, M.; Kure, B.; Nakajima, T.; Ura, Y.; Tanase, T., A Fluxional Cu_8H_6 Cluster Supported by Bis(diphenylphosphino)methane and its Facile Reaction with CO_2. *Chem. – Eur. J.* **2017**, *23*, 9457-9461.

(86) Li, J.; Ma, H. Z.; Reid, G. E.; Edwards, A. J.; Hong, Y.; White, J. M.; Mulder, R. J.; O'Hair, R. A. J., Synthesis and X-Ray Crystallographic Characterisation of Frustum-Shaped Ligated $[Cu_{18}H_{16}(DPPE)_6]^{2+}$ and $[Cu_{16}H_{14}(DPPA)_6]^{2+}$ Nanoclusters and Studies on Their H_2 Evolution Reactions. *Chem. – Eur. J.* **2018**, *24*, 2070-2074.
(87) Deutsch, C.; Krause, N.; Lipshutz, B. H., CuH-Catalyzed Reactions. *Chem. Rev.* **2008**, *108*, 2916-2927.
(88) Liu, S.; Eberhart, M. S.; Norton, J. R.; Yin, X.; Neary, M. C.; Paley, D. W., Cationic Copper Hydride Clusters Arising from Oxidation of $(Ph_3P)_6Cu_6H_6$. *J. Am. Chem. Soc.* **2017**, *139*, 7685-7688.
(89) Fuhr, O.; Dehnen, S.; Fenske, D., Chalcogenide clusters of copper and silver from silylated chalcogenide sources. *Chem. Soc. Rev.* **2013**, *42*, 1871-1906.
(90) Coughlan, C.; Ibáñez, M.; Dobrozhan, O.; Singh, A.; Cabot, A.; Ryan, K. M., Compound Copper Chalcogenide Nanocrystals. *Chem. Rev.* **2017**, *117*, 5865-6109.
(91) Kampf, J.; Kumar, R.; Oliver, J. P., Electrochemical Synthesis and the Molecular Structure of a Benzeneselenolato Complex of Copper, $Ph_3PCu(\mu\text{-}SePh)_2Cu(PPh_3)_2 \cdot CH_3CN$, Containing Both Three- and Four-Coordinate Copper. *Inorg. Chem.* **1992**, *31*, 3626-3629.
(92) DeGroot, M. W.; Cockburn, M. W.; Workentin, M. S.; Corrigan, J. F., Trialkylphosphine-Stabilized Copper−Phenyltellurolate Complexes: From Small Molecules to Nanoclusters via Condensation Reactions. *Inorg. Chem.* **2001**, *40*, 4678-4685.
(93) Kluge, O.; Grummt, K.; Biedermann, R.; Krautscheid, H., Trialkylphosphine-Stabilized Copper(I) Phenylchalcogenolate Complexes - Crystal Structures and Copper–Chalcogenolate Bonding. *Inorg. Chem.* **2011**, *50*, 4742-4752.
(94) Cabral, B. N.; Zawatski, L. E.; Abram, U.; Lang, E. S., Synthesis and Structural Characterization of Copper(I) Phenylselenolate Complexes Stabilized by N, N′-Donor Ligands. *Z. Anorg. Allg. Chem.* **2015**, *641*, 739-743.
(95) Nguyen, T.-A. D. Synthesis and Characterization of Atomically Precise Copper Nanoclusters. University of California, Santa Barbara, Santa Barbara, CA, 2017.
(96) Kranenburg, M.; van der Burgt, Y. E. M.; Kamer, P. C. J.; van Leeuwen, P. W. N. M.; Goubitz, K.; Fraanje, J., New Diphosphine Ligands Based on Heterocyclic Aromatics Inducing Very High Regioselectivity in Rhodium-Catalyzed Hydroformylation: Effect of the Bite Angle. *Organometallics* **1995**, *14*, 3081-3089.
(97) Harris, R. K.; Becker, E. D.; Cabral de Menezes, S. M.; Goodfellow, R.; Granger, P., NMR nomenclature. Nuclear spin properties and conventions for chemical shifts (IUPAC Recommendations 2001). *Pure Appl. Chem.* **2001**, *73*, 1795-1818.
(98) Harris, R. K.; Becker, E. D.; Cabral de Menezes, S. M.; Granger, P.; Hoffman, R. E.; Zilm, K. W., Further conventions for NMR shielding and chemical shifts (IUPAC Recommendations 2008). *Pure Appl. Chem.* **2008**, *80*, 59.
(99) Burges, C.-W.; Koschmieder, R.; Sahm, W.; Schwenk, A., ^{107}Ag and ^{109}Ag Nuclear Magnetic Resonance Studies on Ag^+ Ions in Aqueous Solutions. *Z. Naturforsch* **1973**, *28a*, 1753-1758.
(100) Steiman, T. J.; Uyeda, C., Reversible Substrate Activation and Catalysis at an Intact Metal–Metal Bond Using a Redox-Active Supporting Ligand. *J. Am. Chem. Soc.* **2015**, *137*, 6104-6110.

(101) Avetta, C. T.; Konkol, L. C.; Taylor, C. N.; Dugan, K. C.; Stern, C. L.; Thomson, R. J., Diastereoselective Oxidative Carbon−Carbon Bond Formation via Silyl Bisenol Ethers. *Org. Lett.* **2008**, *10*, 5621-5624.
(102) Yang, J.; Tilley, T. D., Efficient Hydrosilylation of Carbonyl Compounds with the Simple Amide Catalyst [Fe{N(SiMe$_3$)$_2$}$_2$]. *Angew. Chem., Int. Ed.* **2010**, *49*, 10186-10188.
(103) *SMART Apex II, Version 2.1*. Bruker AXS Inc.: Madison, WI, 2005.
(104) *SAINT Software User's Guide, Version 7.34a*. Bruker AXS Inc.: Madison, WI, 2005.
(105) Sheldrick, G. M., *SADABS*. University of Göttingen: Göttingen, Germany, 2005.
(106) *SHELXTL PC, Version 6.12*. Bruker AXS Inc.: Madison, WI, 2005.
(107) Matsuo, T.; Kawaguchi, H., From Carbon Dioxide to Methane: Homogeneous Reduction of Carbon Dioxide with Hydrosilanes Catalyzed by Zirconium−Borane Complexes. *J. Am. Chem. Soc.* **2006**, *128*, 12362-12363.

Chapter 3. Synthesis and Characterization of the "Atlas-sphere" Copper Nanoclusters $[Cu_{12}(SR')_6Cl_{12}][(Cu(R'SH))_6]$ (R' = ^{n}Bu) and $[H(THF)_2]_2[Cu_{17}(SR'')_6Cl_{13}(THF)_2(R''SH)_3]$ (R'' = CH_2CH_2Ph): New Insights into the Reaction of Cu^{2+} with Thiols

Table of Contents

3.1 Introduction

The past decade has seen a dramatic increase in the number of known atomically precise nanoclusters (APNCs) of gold and silver.[1] Many of these APNCs have been characterized by X-ray crystallography, giving researchers an level of detail that is not available for traditional nanoparticles. For Ag and Au, the most common capping ligands are thiolates (RS^-) (R = alkyl, aryl). For example, one of the first structurally characterized Au APNCs, $[Au_{25}(SCH_2CH_2Ph)_{18}]^-$, features eighteen phenylethylthiolate capping ligands.[2-3] Other notable thiolate-stabilized Au APNCs include $[Au_{38}(SCH_2CH_2Ph)_{24}]$, $[Au_{144}(SCH_2CH_2Ph)_{60}]$, $[Au_{246}(SC_6H_4\text{-}p\text{-}Me)_{80}]$, and $Au_{279}(SC_6H_4\text{-}p\text{-}^tBu)_{84}$.[4-7] Similarly, many of the first structurally characterized Ag APNCs also feature thiolate ligands, including $[Ag_{44}(p\text{-}MBA)_{30}]^{4-}$ (*p*-MBA = *para*-mercaptobenzoic acid) and $[Ag_{25}(SCH_2CH_2Ph)_{18}]^-$.[8-10] As seen in these aforementioned examples, both alkyl and aryl thiolates are effective at stabilizing Ag and Au ANPCs. The ubiquitous use of thiolates for this purpose is likely related the strength of the M-S bond,[11] which protects these APNCs against agglomeration and unwanted reactivity. As a result, these materials have been proposed for a variety of applications for which high stability is desired, including *in vivo* chemical sensing and drug delivery.[1]

Given this context, it is surprising that low-valent, thiolate-stabilized Cu APNCs are essentially unknown, and of the few Cu APNCs that have been reported, most have only been partially characterized.[12-14] For example, Mukherjee and co-workers synthesized a glutathione-stabilized Cu APNC with the formula $[Cu_{15}(GSH)_4]$.[15] This material was characterized by TEM, MALDI-TOF mass spectrometry, and UV-vis spectroscopy, but a single crystal X-ray structure was not forthcoming. Similarly, Chang and co-workers reported the synthesis of mercaptobenzoic acid-stabilized Cu nanoclusters, but a mass spectral analysis

suggested that these NCs were not monodisperse. Not surprisingly, given their polydispersity, these materials were not structurally characterized.[16] In contrast, structurally-characterized mercaptobenzoic acid-stabilized ANPCs of both Ag and Au are known.[1] Cu APNCs of aryl thiolates have also been reported, such as $[Cu_9(SC_6H_4\text{-}p\text{-}F)_7]$ and $[Cu_9(SC_6H_4\text{-}p\text{-}Br)_6]$, but again structural characterization by X-ray crystallography has remained elusive.[17] Finally, it is worth noting that a 2011 report of a Cu_8 nanocluster, $[Cu_8(MPP)_4]$ (HMPP = 2-mercapto-5-*n*-propylpyrimidine), was recently proved to be erroneous.[18-19]

Recently, Zhang and co-workers reported the synthesis of a mixed-valent Cu-thiolate APNC $Cu_{14}(SR)_{10}$ ($R = C_{12}H_{25}$), which was formed by reaction of $CuCl_2$ with excess RSH in dibenzyl ether.[20] Under these conditions the thiol acts as both the capping ligand and the reductant. $Cu_{14}(SR)_{10}$ was characterized by UV-Vis and fluorescence spectroscopies, and powder X-ray diffraction. While its exact structure could not be verified by single crystal X-ray diffraction, the authors use MALDI mass spectrometry and DFT analysis to support their proposed formulation. Significantly, this Cu APNC was reported to have attractive photo-physical properties,[21-23] prompting speculation that it could be incorporated into light emitting diodes and displays.[17]

$Cu_{14}(SR)_{10}$ is especially appealing to us, given the Hayton group's long-standing interest in Cu nanocluster chemistry,[19, 24-27] and because it represents an atypical example of Cu nanocluster with partial Cu(0) character. Only a handful of low-valent Cu(0)-containing nanoclusters have been reported, including $[Cu_{25}H_{22}(PPh_3)_{12}]Cl$, $[Cu_{29}Cl_4H_{22}(Ph_2phen)_{12}]Cl$, $[Cu_{13}\{S_2CN^nBu_2\}_6(CCR)_4][PF_6]$ (R = C(O)OMe, C_6H_4F), $[Cu_{20}(CCPh)_{12}(OAc)_6]$, $[Cp^*_{12}Cu_{43}Al_{12}]$, and $[Cu_{53}(CF_3CO_2)_{10}(CC^tBu)_{20}Cl_2H_{18}]^+$.[24, 26-30] $Cu_{14}(SR)_{10}$ would also be an exceptionally rare example of a copper superatom with $N^* = 4$, which is not a magic number.[20]

While non-magic number copper superatoms are known, such as $[Cp^*_{12}Cu_{43}Al_{12}]$, they are still unusual.[1, 19, 29]

Herein, I attempted to remake the Cu APNC $Cu_{14}(SR_{10})$, as well explore copper-thiolate clusters more generally. Specifically, I found that the reaction of $CuCl_2$ with RSH ($R = C_{12}H_{25}$) does not result in a Cu APNC with Cu(0) character. Instead, the product is most likely a Cu(I)-containing "Atlas-sphere"-type copper-thiolate nanocluster. This conclusion is supported by a comparative synthetic and spectroscopic study, which includes analysis by XANES and EXAFS. During the course of this work, I also the synthesized and structurally characterized two other Cu(I) thiolate-containing clusters, $[Cu_{12}(SR')_6Cl_{12}][(Cu(R'SH))_6]$ ($R' = {}^nBu$) (**3.2**) and $[H(THF)_2]_2[Cu_{17}(SR'')_6Cl_{13}(THF)_2(R''SH)_3]$ ($R'' = CH_2CH_2Ph$) (**3.3**) using similar conditions reported by Zhang and co-workers.[20]

3.2 Results and Discussion

3.2.1 Attempted Synthesis of $Cu_{14}(SR)_{10}$ ($R = C_{12}H_{25}$)

$Cu_{14}(SR)_{10}$ was reportedly formed by reaction of $CuCl_2 \cdot 2H_2O$ (1 equiv), which was dissolved in dibenzyl ether (6 mL) after 10 min of ultrasonication at room temperature. 1-dodecanethiol (22 equiv) was then added, and the reaction mixture was stirred at 0 ºC for 5 min (Scheme 3.1). Addition of chloroform and acetone resulted in precipitation of solid material, which was then collected via centrifugation. A yield was not reported and the color of the material was not described, but photographs provided in the Supporting Information show that the solid is a pale-yellow powder.[20-21] Zhang and co-workers characterized this material through a variety of methods, including UV-vis and emission spectroscopies, as well as electrospray ionization (ESI) mass spectrometry. The $Cu_{14}(SR)_{10}$ formulation was proposed primarily on the basis of the ESI-MS data, however neither an exact mass match nor an

analysis of the isotope pattern was provided.[20-21] The UV-vis data of the material isolated by Zhang and co-workers revealed the presence of two absorption bands at 275 and 358 nm. The fluorescence spectrum (λ_{ex} = 365 nm) showed a weak emission at approximately 380 nm.

Scheme 3.1. Original Synthetic Procedure Used to Prepare "$Cu_{14}(SR)_{10}$"

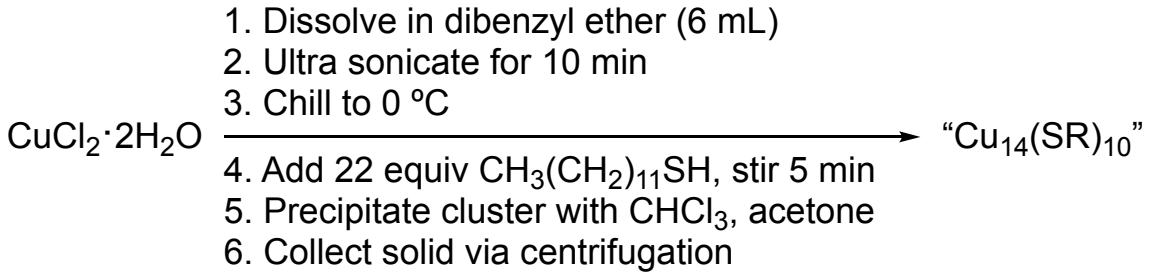

I attempted to repeat the synthesis of $Cu_{14}(SR)_{10}$, using the originally reported procedure with a few minor modifications. In particular, I used anhydrous $CuCl_2$ in place of $CuCl_2 \cdot 2H_2O$, I did not sonicate the $CuCl_2$ suspension, and I performed the reaction at room temperature. I believe that these minor changes should not affect the product speciation; however, they could affect the rate of reaction by modifying the solubility and grain size of the $CuCl_2$ starting material. The reaction generally proceeded as originally described (Scheme 3.1). Thus, addition of $CuCl_2$ (1 equiv) to dibenzyl ether (2 mL) at room temperature resulted in formation of a brown slurry. Addition of 1-dodecanethiol (4 equiv) to this suspension resulted in dissolution of the brown solid over the course of 20 min, concomitant with the deposition of a very pale gray solid, which is similar in appearance to the material reported by Zhang and co-workers.[20] The solid was then collected on a fritted glass filter, and rinsed with hexanes to give **3.1** as an off-white solid (Figure A3.23). I also performed the reaction in THF. In this solvent, addition of 1-dodecanethiol to the slurry of $CuCl_2$ in dibenzyl ether initially resulted in dissolution of all the solid over the course of 2 min, concomitant with formation of a clear, pale-yellow solution. However, upon further stirring very pale yellow powder began to

precipitate from the solution (Figure A3.24). After 20 min of stirring, this solid was collected on a fritted glass filter and rinsed with several portions of hexanes to give **3.1** and a colorless filtrate. Whether prepared from dibenzyl ether or THF, complex **3.1** is insoluble in alkanes, diethyl ether, benzene, toluene, THF, CH_2Cl_2, chloroform, MeCN, DMSO, DMF, MeOH, EtOH, and water. While complex **3.1** is also insoluble in pyridine, it does appear to very slowly react with this solvent.

To better ascertain the reaction stoichiometry, I collected the filtrate and removed the volatiles *in vacuo* to yield a colorless oil. A ^{1}H NMR spectrum of this colorless oil, in CD_2Cl_2 (Figure A3.8), reveals the presence of unreacted 1-dodecanthiol thiol, as well as di(1-dodecane)disulfide.[31] These observations are consistent with the proposed reaction stoichiometry of Zhang and co-workers who also noted the reduction of the Cu(II) ions via thiol oxidation.

A diffuse reflectance spectrum of complex **3.1** as a solid features the onset of an absorption band at ca. 425 nm (Figure 3.1, black trace). A fluorescence spectrum of solid **3.1** excited at 365 nm reveals a very broad emission centered at 510 nm (Figure 3.1, red trace). These data are broadly consistent with the spectra reported by Zhang and co-workers. For example, $Cu_{14}(SR)_{10}$ was reported to have an absorption band centered at 368 nm,[20] along with emission peaks centered between 490 and 550 nm (after annealing). Overall, the similarity of these spectroscopic results with those previously reported by Zhang, along with the similar physical descriptions of the two materials, leads us to believe that I am making the same material.

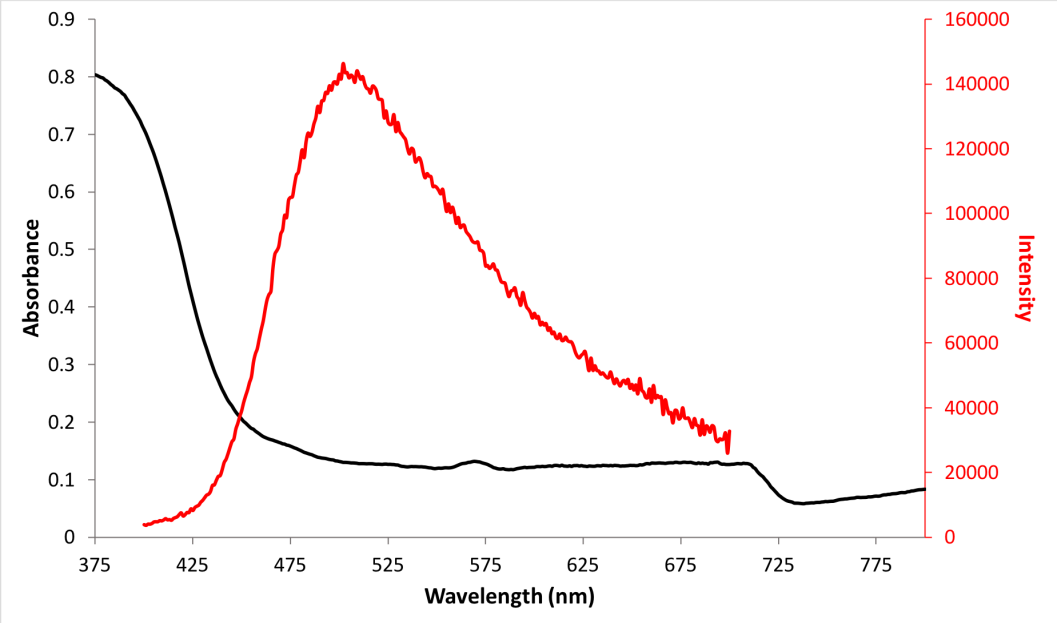

Figure 3.1. Solid-state absorbance (black) and emission (red, λ_{ex} = 365 nm) spectra for complex **3.1**, synthesized from THF.

Finally, I recorded an X-ray photoelectron spectrum (Figure 3.2) of complex **3.1** to confirm the Cu oxidation state and determine its elemental composition. Specifically, the spectrum features two prominent peaks at 932.70 and 952.70 eV, which are attributable to the Cu $2p_{3/2}$ and Cu $2p_{1/2}$ binding energies, respectively (Figure A3.16). These values are similar to the binding energies reported for other Cu(I)-containing materials.[24, 32] Unfortunately, however, given the similarity of the Cu(I) and Cu(0) binding energies,[33] it is generally difficult to discriminate between these two states, and so I cannot rule out the presence or absence of Cu(0) in this sample. Nonetheless, the absence of satellite peaks in this region of the spectrum is consistent with absence of Cu(II). Moreover, the Cu LMM transitions for **3.1** appear at 918.3, 915.5, and 911.6 eV (Figure A3.17). These values are also consistent with the presence of Cu(I), in multiple chemical environments. As with the Cu $2p_{3/2}$ data, it is difficult to use the Cu LMM data to discriminate between the Cu(0) and Cu(I) states. That said, the Cu LMM

data closely matches that originally reported for $Cu_{14}(SR)_{10}$, which exhibits Cu LMM transitions at ca. 918 and 915 eV.[20]

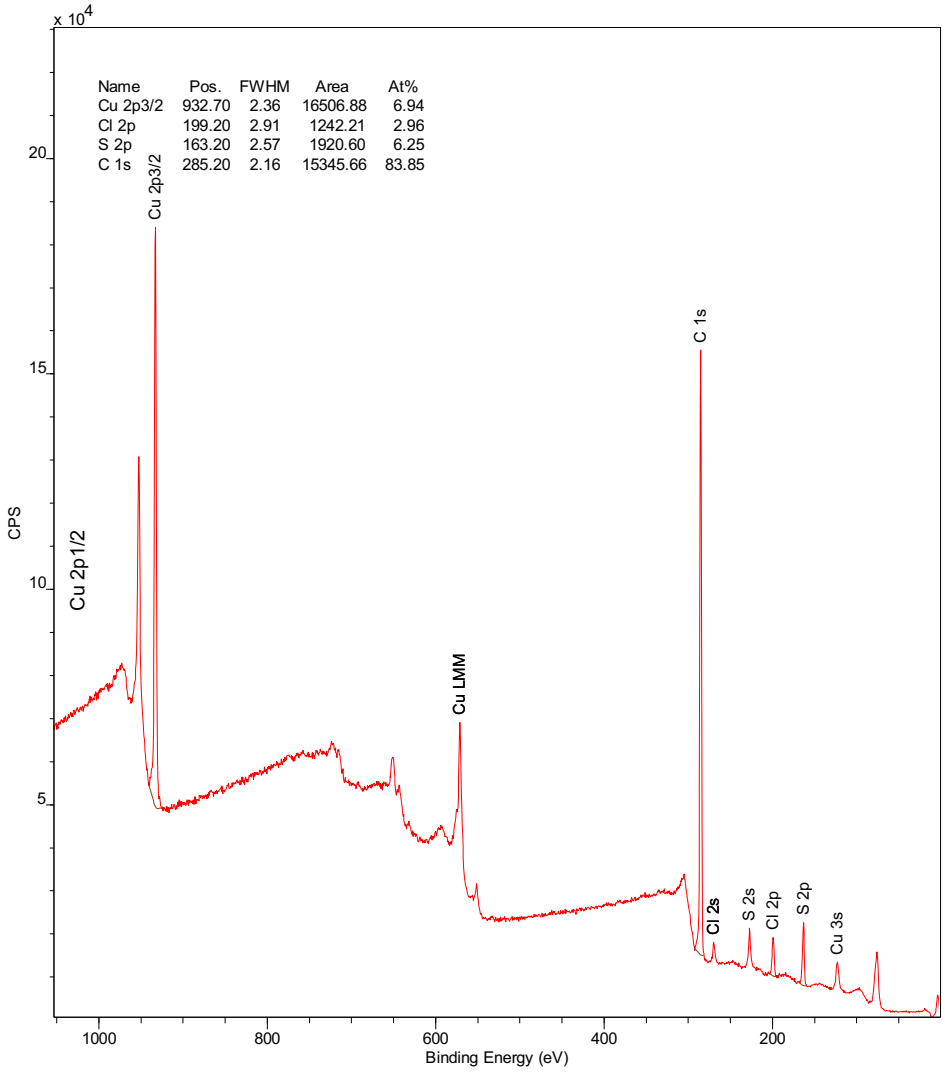

Figure 3.2. XPS spectrum of **3.1** synthesized from THF indicating a Cu:S:Cl ratio of approximately 2:2:1.

Curiously, the XPS spectrum also reveals the presence of Cl, as revealed by the Cl 2s and Cl $2p_{3/2}$ peaks at 269.7 and 199.2 eV (Figure A3.19).[33] According to XPS data, the Cu:S:Cl ratio is approx. 2:2:1. Significantly, these data are not consistent with the original $Cu_{14}(SR)_{10}$ formulation, which should not contain Cl^-, but are in-line with my findings from a comparative synthetic study using different thiols (*vide infra*). Therefore, on the basis of these results, I

believe that complex **3.1** is not a partially-metallic, mixed-valent Cu nanocluster, as initially described by Zhang and co-workers. Instead, I believe that this material is likely closely related to an "Atlas-sphere" $[Cu_{12}(SR)_6]^{6+}$-type cluster. That is, it does not contain any Cu(0) character but instead exclusively contains Cu(I). The evidence to support this conclusion are outlined in the next sections.

3.2.2 Synthesis of $[Cu_{12}(SR')_6Cl_{12}][(Cu(R'SH))_6]$ (R' = ^{n}Bu) (3.2)

The insolubility of **3.1** greatly limited my ability to confirm its formulation. Therefore, I attempted to generate a more tractable material by substituting the 1-dodecanethiol ligand for an aliphatic thiol that was more amenable to crystallization, yet similar in structure and donor ability (Scheme 3.2). Thus, reaction of a slurry of $CuCl_2$ (1 equiv) in THF (2 mL) with *n*-butylthiol (5 equiv) at room temperature immediately results in dissolution of the $CuCl_2$, concomitant with the generation of a bright yellow solution. Work-up of the reaction mixture after 20 min resulted in the isolation of pale-yellow crystals of the Cu(I) nanocluster, $[Cu_{12}(SR')_6Cl_{12}][(Cu(R'SH))_6]$ (**3.2**, R' = ^{n}Bu) in 90% yield.

Scheme 3.2. Synthesis of 3.2.

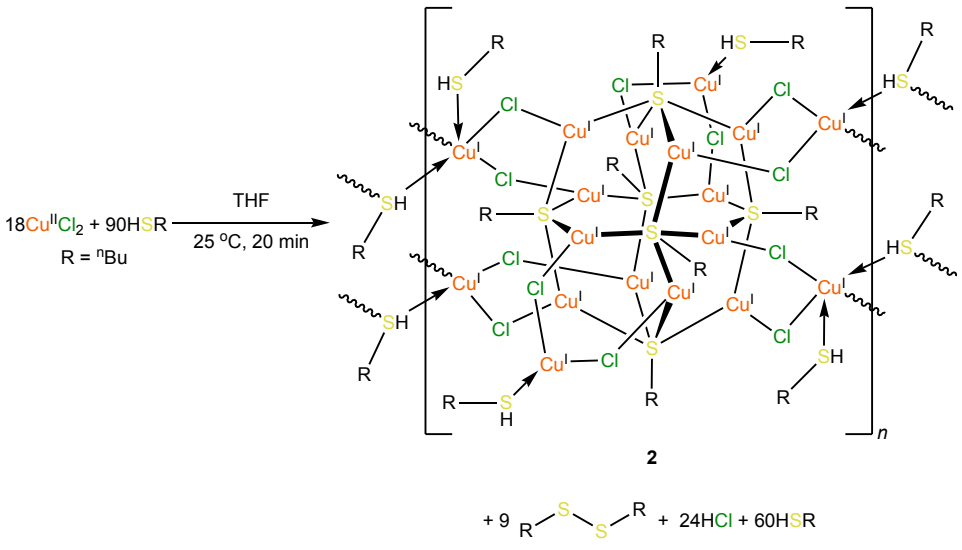

Complex **3.2** crystallizes in the triclinic space group $P\bar{1}$ (Figure 3.3b). It features a $[Cu_{12}(SR')_6]^{6+}$ "Atlas-sphere" core (Figure 3.3a), which has been observed for several other Cu(I) thiolate clusters.[12, 34-37] Within the $Cu_{12}S_6$ core, each Cu occupies the vertex of a regular cuboctahedron, while each thiolate ligand is bound in a μ_4 fashion and occupies one of the six square faces of the cuboctahedron. The Cu–Cu distances range from 2.6524(7) to 3.7110(8) Å, while the Cu-SR' distances range from 2.225(2) to 2.276(1) Å. Both of these ranges are comparable to those seen in other $[Cu_{12}(SR')_6]^{6+}$-containing clusters.[12, 34-37] Each of the 12 Cu atoms in the "Atlas-sphere" core is also coordinated to a Cl^- ligand. Six additional Cu^+ ions are bound to the outer surface of the cluster, via bridging interactions with two of the 12 Cl^- ions. Two of these outer Cu^+ ions re each coordinated to a single thiol ligand, while the remaining four Cu^+ ions are each coordinated to two thiol ligands, four of which originate from an adjacent cluster. These bridging interactions give rise to a ladder-type coordination polymer bridging through two μ_2-HSR linkages (Figure 3.3c).[36] The average Cu-S_{thiol} distance is 2.30 Å (range: 2.257(1) – 2.346(2) Å), which is slightly longer than the Cu-thiolate distance, as expected.

A ^{1}H NMR spectrum of **3.2** in THF-d_8 (Figure A3.1) features resonances at 3.26 and 2.53 ppm, which are assignable to α-CH_2 resonances of the six μ_4-S^{n}Bu ligands and the six ^{n}BuSH ligands, respectively. These resonances are present in a 1:1 ratio, which is consistent with the solid-state structure. Also present in this spectrum is a broad singlet at 1.85 ppm, which is assignable to the SH proton of the six ^{n}BuSH ligands.

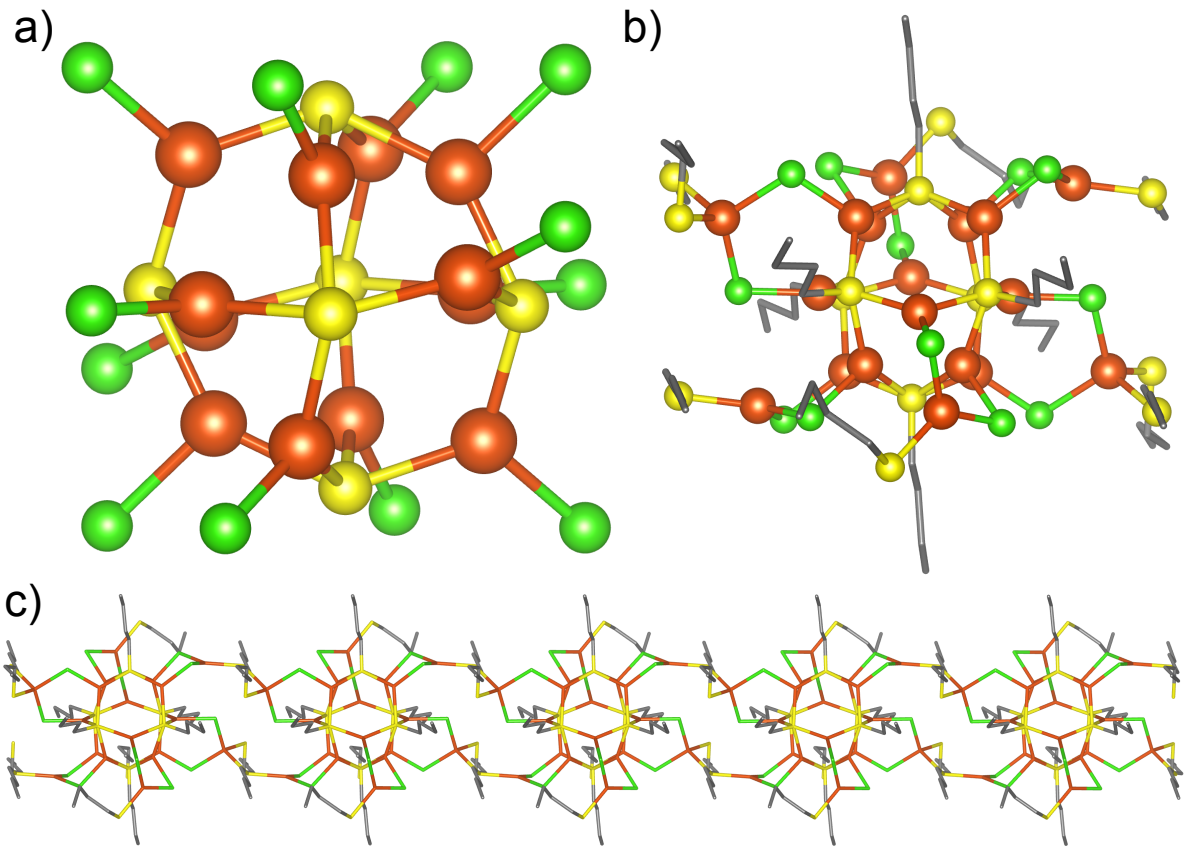

Figure 3.3. Ball-and-stick diagram showing a) the $[Cu_{12}(SR)_6Cl_{12}]^{6-}$ core, b) the structure of the monomeric unit, and c) the polymeric structure of **3.2** (hydrogen atoms omitted for clarity). Color legend: orange, Cu; yellow, S; green, Cl; gray wireframe, C.

ESI-MS of **3.2**, recorded in THF in negative ion mode, features a major peak at *m/z* = 2039.9023, which corresponds to the fragment $[Cu_{17}(SR')_6Cl_{12}]^-$ (calcd *m/z* = 2039.6666) (Figure 3.4). In addition to this peak, several other peaks are present. For example, a peak at *m/z* = 2139.7942 corresponds to $[Cu_{18}(SR')_6Cl_{13}]^-$ (calcd *m/z* = 2139.5649), a peak at *m/z* = 1940.9977 corresponds to $[Cu_{16}(SR')_6Cl_{11}]^-$ (calcd *m/z* = 1940.7682), a peak at *m/z* = 1842.0930 corresponds to $[Cu_{15}(SR')_6Cl_{10}]^-$ (calcd *m/z* = 1841.8719), and a peak at *m/z* = 1744.175 corresponds to $[Cu_{14}(SR')_6Cl_9]^-$ (calcd *m/z* = 1743.9734). Each of these peaks is related to the parent ion by loss/gain of CuCl (*m/z* = 99). These data suggest that the $[Cu_{12}(SR')_6Cl_{12}]^{6-}$ core is relatively stable, and that the six outer Cu^+ ions and coordinated

thiol ligands are quite labile. Interestingly, a ESI-MS signal for **3.2** was only observed upon addition of $[NEt_4][Cl]$ to the ESI-MS sample. It has been previously observed that addition of salts to a nanocluster sample can facilitate the transfer of material into the gas phase.[38]

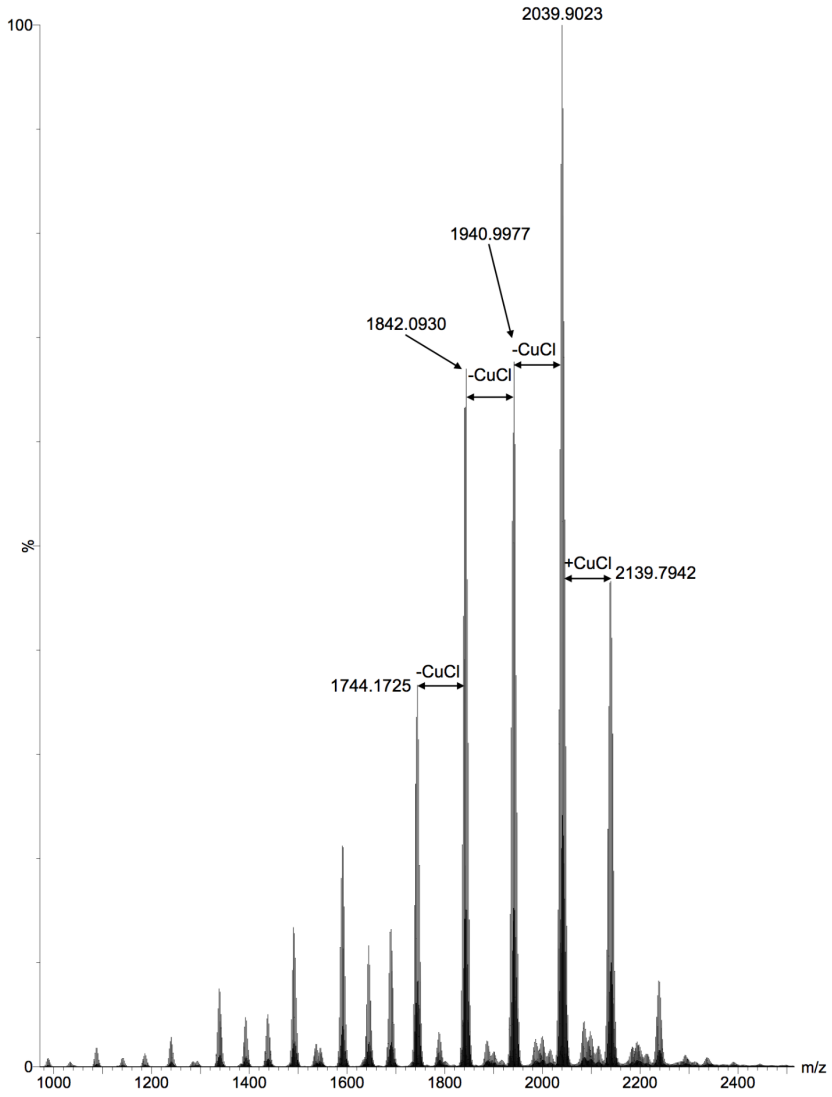

Figure 3.4. Partial ESI-MS of complex **3.2** in negative ion mode.

Finally, a UV-Vis spectrum of **3.2** in THF (Figure 3.5, black trace) reveals the presence of an absorption band at 370 nm, along with a shoulder at 274 nm. The spectrum is qualitatively similar to the spectrum recorded for $Cu_{14}(SR)_{10}$,[20] proving further support that

that material and **3.2** are structurally similar. The fluorescence spectrum of solid **3.2** (λ_{ex} = 365 nm) reveals a broad peak at 585 nm (Figure 3.5, red trace), which is orange (Figure 3.5, inset).

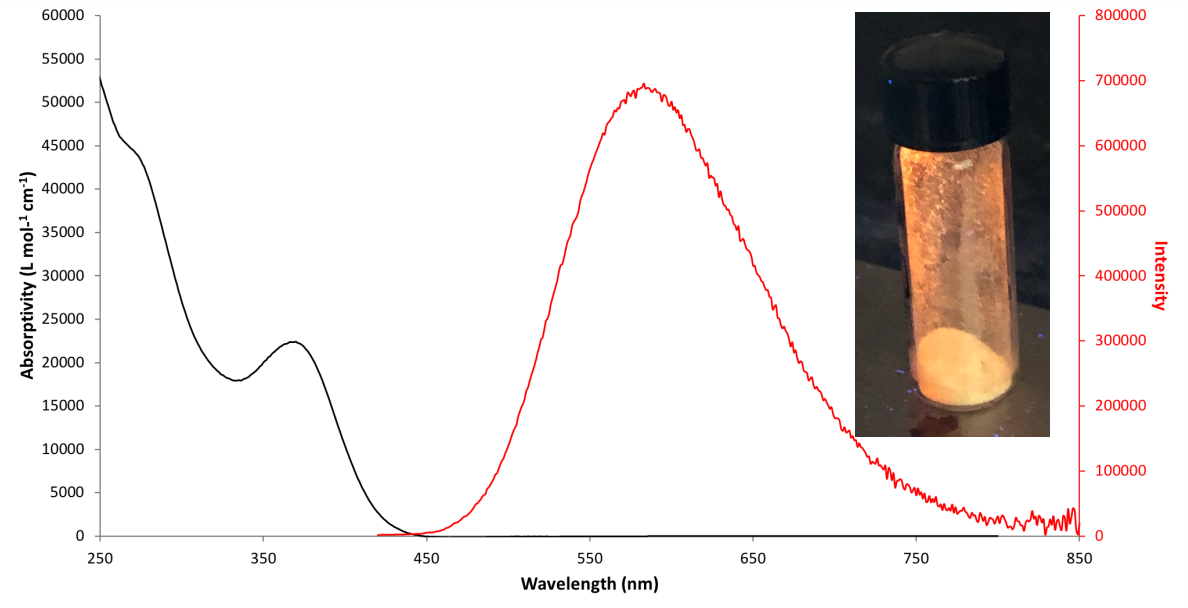

Figure 3.5. UV-Vis in THF (21.2 μM) (black) and solid-state emission (red) spectra for complex **3.2** (λ_{ex} = 365 nm). Inset: photograph of the solid-state fluorescence of **3.2**.

In an effort to better understand the stoichiometry of the transformation, the reaction of $CuCl_2$ with ^{n}BuSH (5 equiv) in THF-d_8 was monitored by ^{1}H NMR spectroscopy (Figure A3.4). Addition of thiol to a THF-d_8 slurry of $CuCl_2$ results in the rapid dissolution of all solids and the formation of a bright yellow solution. After 20 minutes, the ^{1}H NMR spectrum of this solution revealed the presence a resonance at 3.24 ppm, which is assignable to the α-CH_2 resonance of the six μ_4-S^{n}Bu ligands in **3.2**, a resonance at 2.68 ppm, which is assignable to the α-CH_2 resonance of di-*n*-butyl disulfide, and a broad resonance at 8.56 ppm, which is assignable to HCl. Integration of these methylene resonances against an internal standard (hexamethyldisiloxane) indicated that **3.2** is formed in 99% yield, while only 0.5 equiv of di-*n*-butyl disulfide is generated per $CuCl_2$. Similarly, integration of the HCl resonance indicates

that 1.3 equiv of HCl is formed per starting $CuCl_2$. Importantly, this amount of disulfide and HCl production is only consistent with the reduction of Cu(II) to Cu(I) and formation of **3.2**. If $Cu_{14}(SR)_{10}$ was being formed in this transformation, I would instead expect the formation of 0.64 equiv of di-*n*-butyl disulfide and 2.0 equiv of HCl.

I also briefly examined the chemical properties of complex **3.2**. Complex **3.2** is insoluble in alkanes, Et_2O, benzene, toluene, CH_2Cl_2, and MeCN. It is soluble in THF, though it partially decomposes if left in solution at room temperature, as evidenced by the gradual bleaching of the pale-yellow color in conjunction with the deposition of copious amounts of white powder, which is presumably CuCl. This process occurs over the course of 24 h. Finally, complex **3.2** immediately reacts with pyridine, upon dissolution in that solvent, to form $[CuCl(pyridine)_3]$ (**3.4**) as the only isolable product. This complex can be isolated in 68% yield (based on Cl^-) after work-up.[39] The isolation of **3.4** from this reaction mixture demonstrates that, under the appropriate conditions, the "Atlas-sphere" core is susceptible to disassembly.

3.2.3 Synthesis of $[H(THF)_2]_2[Cu_{17}(SR")_6Cl_{13}(THF)_2(R"SH)_3]$ (R" = CH_2CH_2Ph). (3.3)

To further understand the reactivity of Cu(II) with thiols, I explored the reaction of $CuCl_2$ with 2-phenylethanethiol. This specific thiol was chosen because it is widely used in the synthesis of Ag and Au APNCs,[1] but a 2-phenylethylthioate-containing Cu APNC has so far remained elusive. Thus, reaction of a slurry of $CuCl_2$ (1 equiv) in THF with 2-phenylethanethiol (4 equiv) at room temperature immediately generates a bright yellow solution concomitant with the dissolution of the $CuCl_2$. Work-up of the reaction mixture after 20 min resulted in the isolation of pale-yellow crystals of the Cu(I) nanocluster

$[H(THF)_2]_2[Cu_{17}(SR")_6Cl_{13}(THF)_2(R"SH)_3]$ (R" = CH_2CH_2Ph, **3.3**) in 93% yield (Scheme 3.3).

Scheme 3.3. Synthesis of 3.3.

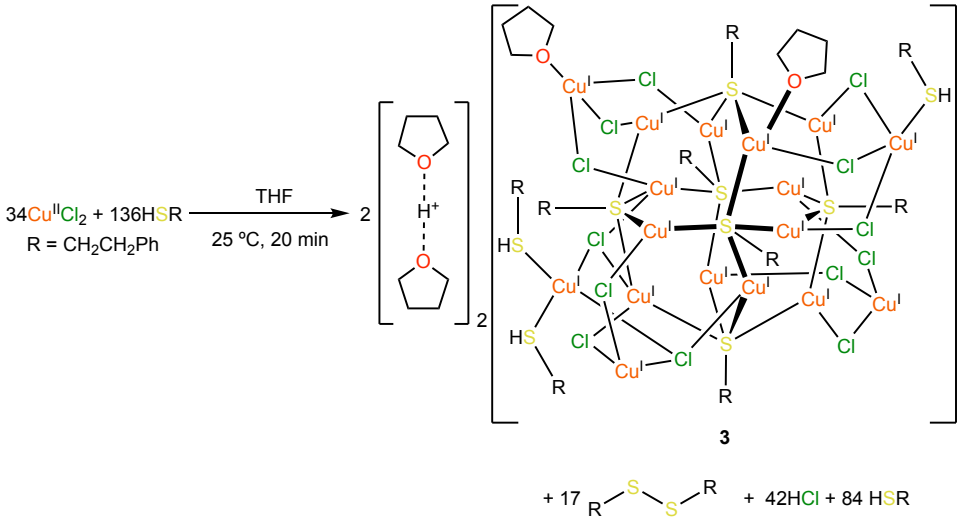

Complex **3.3** crystallizes in the triclinic space group $P\bar{1}$ as a THF solvate, **3.3**·1.5THF (Figure 3.6b). Like **3.2**, complex **3.3** features a $[Cu_{12}(SR")_6]^{6+}$ "Atlas-sphere" core (Figure 3.6a). Within the core, the Cu–Cu distances range from 2.685(3) to 3.678(4) Å, while the average Cu–SR distance is 2.28 Å. These values are similar to those observed for **3.2**. Each of the 12 Cu atoms in the $[Cu_{12}(SR")_6]^{6+}$ core is coordinated to one Cl^- ligand. These Cl^- ions are grouped into four groups of three. Each group of Cl^- ions forms a trigonal planar bonding pocket, which is filled with a Cu^+ ion. A thirteenth Cl^- ligand (Cl13) is also bound to the $[Cu_{12}(SR")_6]^{6+}$ core, in an μ_2 interaction with Cu6 and Cu7. One of the outer Cu^+ ions (Cu11) is bound by an RSH ligand, while another (Cu5) is bound by a THF ligand. Additionally, complex **3.3** features a $[Cu(HSR")_2]$ fragment appended to its outer surface via dative interactions with two Cl^- ligands (Cl12 and Cl13). One of the "core" Cu atoms (Cu10) is also bound by a THF ligand. It is likely that this peripheral fragment, along with the peripheral

THF and RSH ligands are extremely labile. Not surprisingly, its ^{1}H NMR spectrum (*vide infra*) in THF-d_8 reveals a highly symmetric cluster, with only one magnetically unique thiolate ligand.

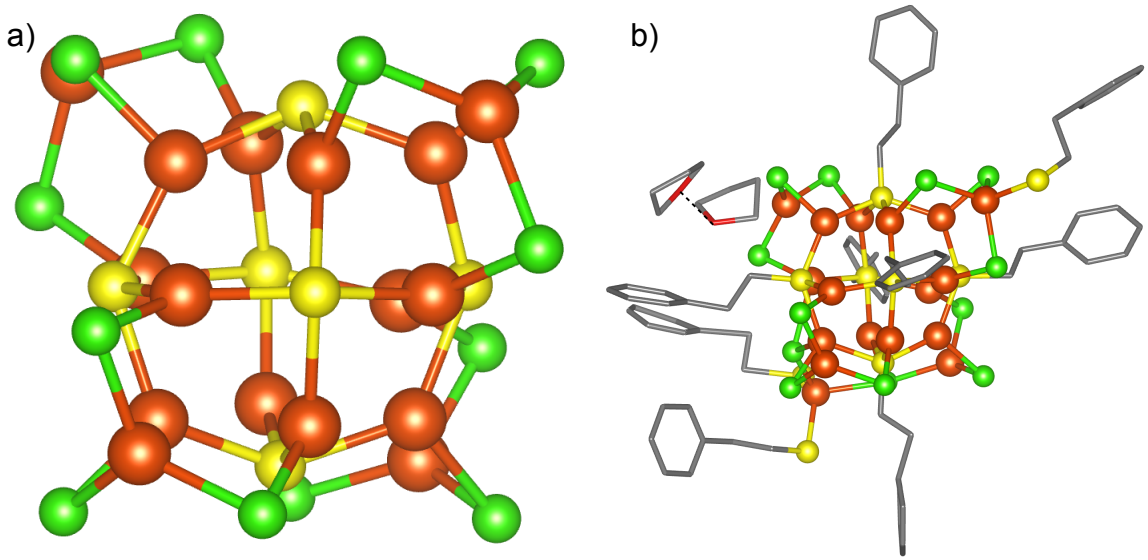

Figure 3.6. Ball-and-stick diagram showing a) the $[Cu_{16}(SR)_6Cl_{12}]^{2-}$ core, b) the full structure of **3.3**·1.5THF, including one $[H(THF)_2]^+$ cation (hydrogen atoms, THF ligand, and THF solvate molecules omitted for clarity). Color legend: orange, Cu; yellow, S; green, Cl; red wireframe, O; gray wireframe, C.

Finally, the overall cluster charge is balanced by the presence of two $[H(THF)_2]^+$ cations. While the H-bonded protons in these cations were not located in the difference Fourier map, their presence is supported by the close approach of two sets of THF molecules. Specifically, the distances between O3 and O4 (2.47(2) Å) and O8 and O8* (2.36(1) Å) are similar to the O-O distances in other $[H(THF)_2]^+$ and $[H(Et_2O)_2]^+$ cations.[40-47]

The ^{1}H NMR spectrum of **3.3** in THF-d_8 (Figure A3.6) reveals resonances at 3.47 and 3.37 ppm, which are assignable to CH_2 resonances of the six μ_4-SCH_2CH_2Ph ligands. Likewise, resonances at 2.88 and 2.77 ppm are assignable to the CH_2 resonances of the thiol ligands. Also present is the thiol SH proton at 1.95 ppm. I also observe a very broad resonance

at 8.82 ppm, which I have assigned to the O-H-O proton of the $[H(THF)_2]^+$ counterion.[43, 46-47] For comparison, the O-H-O proton of the $[H(THF)_2]^+$ counterion in $[H(THF)_2][Al\{OC(CF_3)_3\}_4]$ is reported to appear at ca. 8 ppm.[43] The presence of the thiolate and thiol environments in a 6:4 ratio, instead of the expected 6:3 ratio, suggests that a small amount of excess of thiol is present in the final product, which I have been unable to remove.

ESI-MS data were collected for a THF solution of **3.3**, run in negative ion mode. The major feature of the spectrum was observed at *m/z* = 2129.8726, which corresponds to the fragment $[Cu_{15}(SR")_6Cl_{10}]^-$ (calcd *m/z* = 2129.8718) (Figure 3.7). In addition to this peak, several other peaks are also observed. For example, a peak at *m/z* = 2527.6428 corresponds to $[Cu_{19}(SR")_6Cl_{14}]^-$ (calcd *m/z* = 2527.4636), a peak at *m/z* = 2431.7378 corresponds to $[Cu_{18}(SR")_6Cl_{13}]^-$ (calcd *m/z* = 2431.5574), a peak at *m/z* = 2327.6748 corresponds to $[Cu_{17}(SR")_6Cl_{12}]^-$ (calcd *m/z* = 2327.6667), a peak at *m/z* = 2229.7747 corresponds to $[Cu_{16}(SR")_6Cl_{11}]^-$ (calcd *m/z* = 2229.7683), a peak at *m/z* = 2031.9645 corresponds to $[Cu_{14}(SR")_6Cl_9]^-$ (calcd *m/z* = 2031.9734), a peak at *m/z* = 1932.0714 corresponds to $[Cu_{13}(SR")_6Cl_8]^-$ (calcd *m/z* = 1932.0750), and a peak a *m/z* = 1831.0859 corresponds to $[Cu_{12}(SR")_6Cl_7]^-$ (calcd *m/z* = 1831.1843). Each of these peaks is related to the parent ion by the loss/gain of CuCl (*m/z* = 99). These data suggest that the $[Cu_{12}(SR")_6]^{6+}$ core of **3.3** is relatively stable, but that the outer Cl^- anions, Cu^+ cations, and thiols ligands are more labile. Once again, I only observed a signal after addition of $[NEt_4][Cl]$ to the ESI-MS sample.

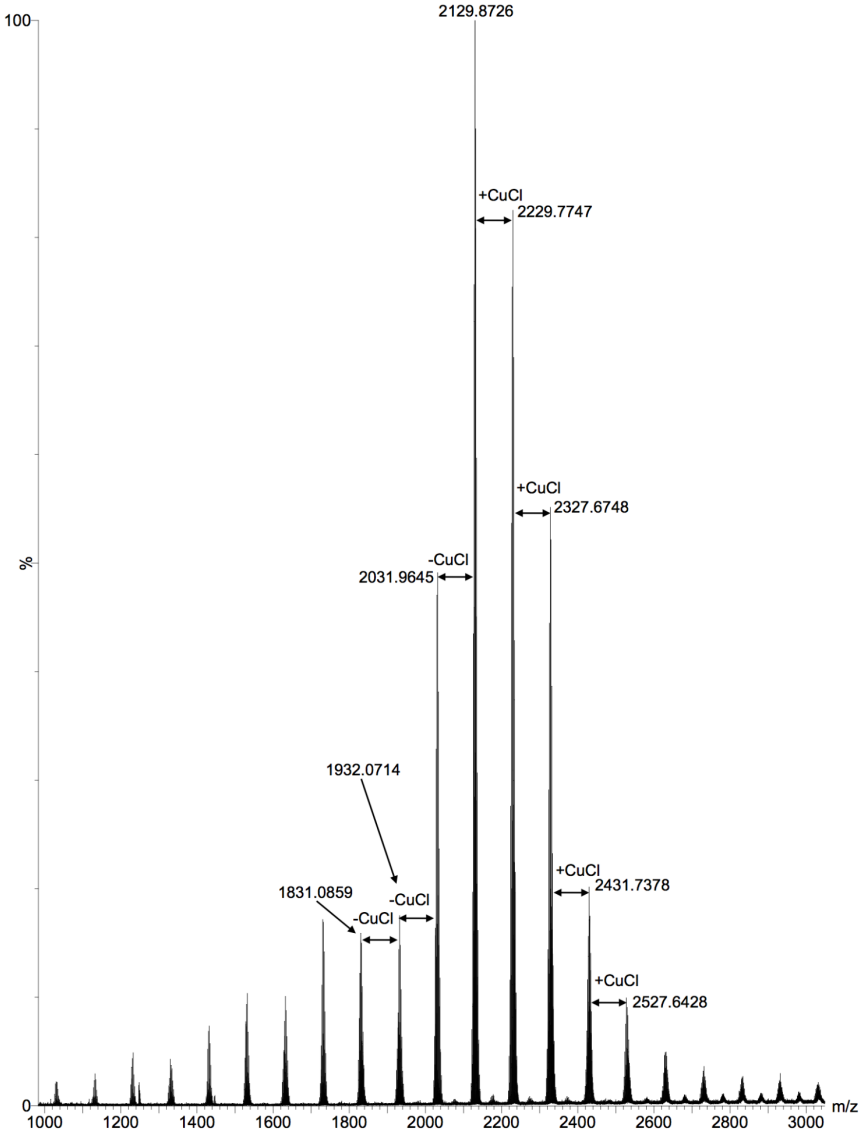

Figure 3.7. Partial ESI-MS of **3.3** in negative ion mode.

A UV-Vis spectrum of **3.3** in THF and features a broad absorption band at 355 nm (Figure 3.8, black trace), in good agreement with the spectrum observed for **3.2**. The fluorescence spectrum of **3.3**, recorded as a solid and excited at 365 nm, reveals a broad peak at 650 nm (Figure 3.8, red trace), which, similar to complex **3.2**, is orange (Figure 3.8, inset).

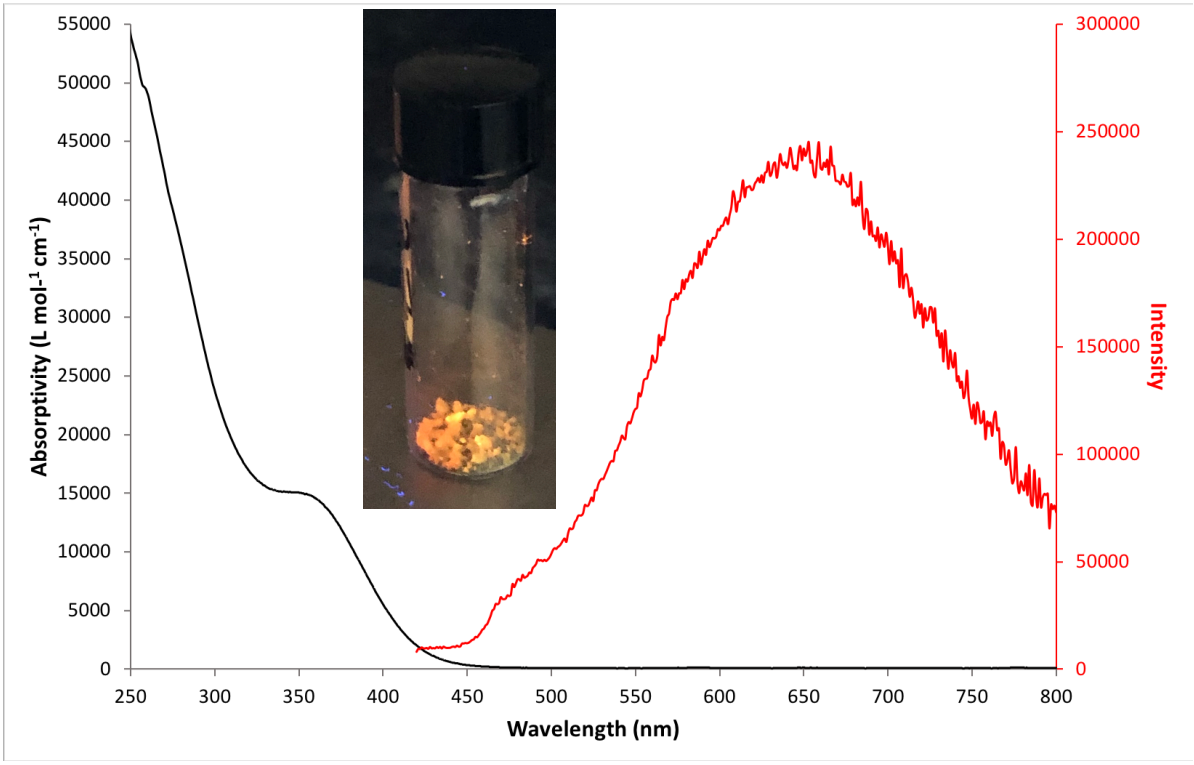

Figure 3.8. UV-Vis in THF (24.4 μM) (black) and solid-state emission (red) spectra for complex **3.3** (λ_{ex} = 365 nm). Inset: photograph of the solid-state fluorescence of **3.3**.

I also briefly examined the chemical properties of complexes **3.3**. Similar to complex **3.2**, it is insoluble in alkanes, Et_2O, benzene, toluene, CH_2Cl_2, and MeCN. It is soluble in THF, although the cluster appears to partially decompose in that solvent upon standing at room temperature for 5 h, as evidenced by the deposition of a white powder and loss of the yellow color. Complex **3.3** also reacts with pyridine to form **3.4**, which can be isolated in 95% yield after work-up.[39]

3.2.4 X-ray Absorption Spectroscopy of 3.1, 3.2, and 3.3

Samples of **3.1**, **3.2**, and **3.3** were given to Dr. Zach Jones, formerly of Scott group at UCSB, for X-ray absorption spectroscopy (XAS) and subsequent data processing. Previously, the Hayton group has shown that XAS is a valuable tool for the structural characterization of copper nanoclusters.[24, 26-27] Building on this past work, I measured the Cu K-edge XANES

and EXAFS of nanoclusters **3.1**, **3.2**, and **3.3**. Importantly, I have shown that the XANES edge energy is highly sensitive to the average Cu oxidation state in Cu nanoclusters.[24, 26-27] The XANES spectra of nanoclusters **3.1**, **3.2**, and **3.3** feature edge positions at 8980.7, 8981.1, and 8980.5 eV (Figure A3.21), respectively. These values are essentially identical to those measured for the Cu(I) coordination complexes $[CuCl(PPh_3)]_4$ (8080.9 eV) and CuCl (8981.9 eV).[24, 26] and corroborate the assignment of **3.2** and **3.3** as Cu(I)-containing nanoclusters. Moreover, these data suggest that complex **3.1** is also a Cu(I)-containing nanocluster with no Cu(0) character. If **3.1**, **3.2**, and **3.3** did contain some Cu(0) character, I would expect to observe edge positions at lower energies (e.g., 8979.6 eV for $[Cu_{25}H_{22}(PPh_3)_{12}][Cl]$ and 8987.0 eV for Cu foil).[24, 26-27]

The EXAFS spectra for nanoclusters **3.1**, **3.2**, and **3.3** show similar features (Figure 3.9). Specifically, there are two major peaks at ca. 1.8 and 2.3 Å in *R*-space. The first peak represents scattering from the light atoms (Cl and S) coordinated directly to Cu, while the second peak represents Cu-Cu scattering. Both features are more intense for **3.1**, whose EXAFS also contains a prominent long-range path at ca. 3.8 Å. For all three nanoclusters, scattering involving nearest-neighbor Cu-Cl, Cu-S and Cu-Cu paths was simulated using the "Atlas-sphere" $[Cu_{12}(SR)_6Cl_{12}]^{6-}$ core present in clusters **3.2** and **3.3**. For the ligand-based paths, the expected coordination numbers are *N*(Cu-Cl) = 1.0 and *N*(Cu-S) = 0.5, which have nearly identical average distances of 2.27 and 2.28 Å, respectively. These similar pathlengths led us to combine the scattering paths for all ligands into a single Cu-L path in the EXAFS fit. The expected nearest-neighbor coordination number *N*(Cu-Cu) is 2.0, at an average distance of 2.76 Å; however, there is a large range in the crystallographically-determined Cu-Cu distances (see above). To account for this variation, EXAFS data were fitted with two

difference Cu-Cu path, following a previous successful approach.[26-27] The FEEF model also predicts significant contribution from a variety of single-scattering paths at ca. 4.0 Å, which was modelled using a long Cu-Cu path. The results of the fits are shown in Table 3.1.

Satisfactory fits were achieved for all three nanoclusters. For example, for nanocluster **3.2**, the curve fit gives a Cu-L path length of 2.240(2) Å (N = 1.2(2)), while the combined N(Cu-Cu) is 1.9(6). These parameters are in good agreement with the FEFF-predicted paths for the "Atlas-sphere" core, $[Cu_{12}(SR)_6Cl_{12}]^{6-}$. A similarly good fit was achieved for nanocluster **3.3**. For nanocluster **3.1**, the curve fit gives a Cu-L path length of 2.246(6) Å (N = 1.8(3)), while the combined N(Cu-Cu) is 2.0(5). Most significantly, these parameters are in good agreement with those determined for **3.2** and **3.3**, and demonstrate that a single "Atlas-sphere" structural model can be used to describe the EXAFS of all three nanoclusters, albeit with slight differences in EXAFS intensity, which likely arises from perturbations of the core due to the different outer surface environments. These findings further buttress the hypothesis that nanocluster **3.1** is an "Atlas-sphere"-type cluster, and not a low-valent, Cu(0)-containing nanocluster as originally surmised.

Table 3.1. Comparison of average FEFF-predicted paths for the "Atlas-sphere" core $[Cu_{12}(SR)_6Cl_{12}]^{6-}$, with EXAFS curvefit parameters for nanoclusters **3.1**, **3.2**, and **3.3**.

Cluster	Path	N	R (Å)	$10^3\ \sigma^2$ (Å^2)	ΔE^0
$[Cu_{12}(SR)_6Cl_{12}]^{6-}$	Cu-L1	1.5	2.278	n.a.	
	Cu-Cu1	1.33	2.718		
	Cu-Cu2	0.67	2.944		
	Cu-Cu3	2.87	4.03		
3.1 [a]	Cu-L	1.8(3)	2.249(6)	3.9(3)	5.7(5)
	Cu-Cu1	1.6(3)	2.796(9)	4.6(2)[b]	
	Cu-Cu2	0.4(2)	2.983(9)	4.6(2)[b]	
	Cu-Cu3	2.4(4)	4.047(2)	8.9(5)	
3.2 [b]	Cu-L	1.2(2)	2.240(2)	3.0(9)	5.7(2)
	Cu-Cu1	1.5(4)	2.77(4)	11(4)[d]	
	Cu-Cu2	0.4(2)	2.982(1)	11(4)[d]	
3.3 [c]	Cu-L	1.5(3)	2.298(6)	4.1(3)	4.7(5)
	Cu-Cu1	1.6(5)	2.71(1)	12(4)[f]	
	Cu-Cu2	0.7(3)	2.92(2)	12(4)[f]	

[a] N_{idp} = 23, ΔR = 1.0 – 4.5 Å, Δk = 3.0 – 13.5 Å^{-1}. [b] Constrained to the same value. [c] N_{idp} =15, ΔR = 1.0 – 3.0 Å, Δk = 3.0 – 14.5 Å^{-1}. [d] Constrained to the same value. [e] N_{idp} =13, ΔR = 1.0 – 3.0 Å, Δk = 3.0 – 13.3 Å^{-1}. [f] Constrained to the same value. In all fits, the value of S_o^2 was fixed at 0.8, in accordance with previous analyses of Cu(I) standards and Cu-based clusters,[26-27] and ΔE_0 was refined as a global fit parameter. Uncertainties are shown in parentheses; values without uncertainties were fixed during curvefitting.

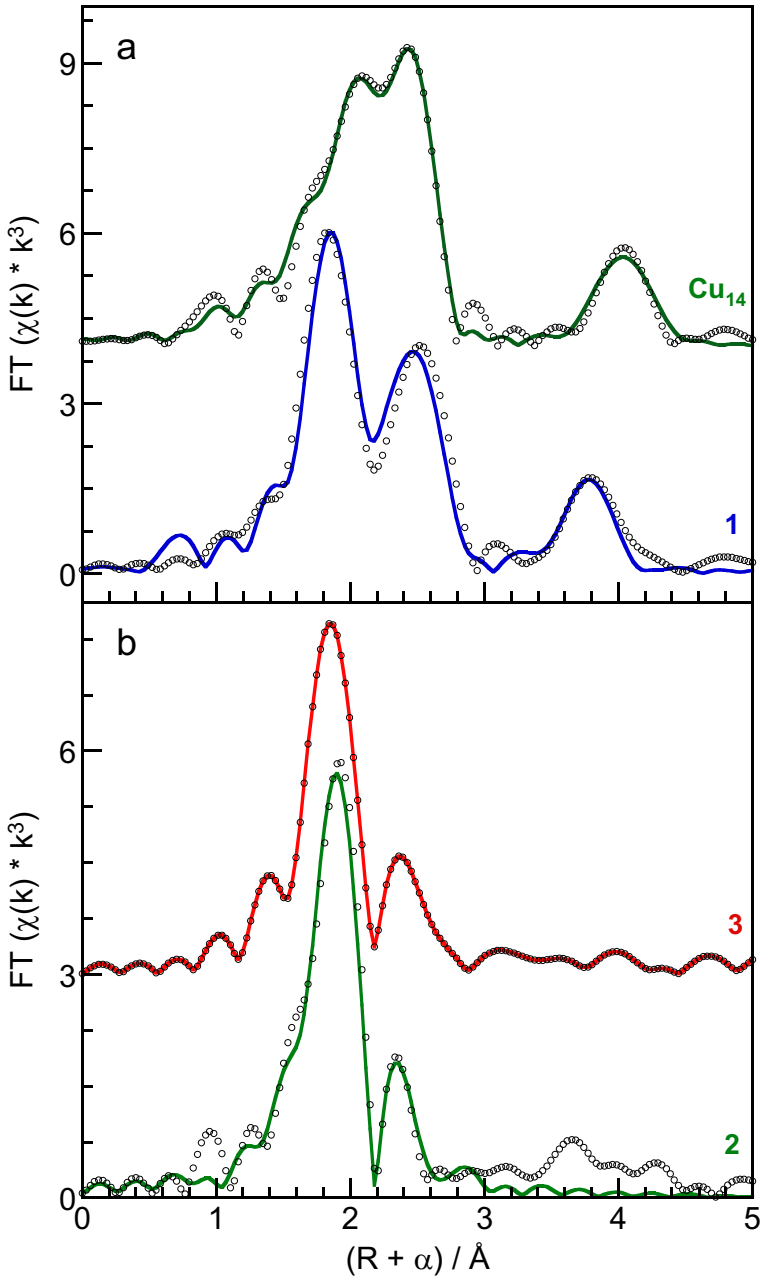

Figure 3.9. Comparison of Cu K-edge EXAFS for (a) $[Cu_{14}H_{12}(phen)_6(PPh_3)_4][Cl]_2$ and **3.1**; and (b) **3.2** and **3.3**. All spectra are shown as FT magnitudes in non-phase corrected *R*-space (points). Parameters for the curvefits (solid lines) are shown in Tables 3.1 and 3.5. Spectra are offset vertically for clarity.

For further comparison, the EXAFS data for an authentic Cu_{14} cluster, $[Cu_{14}H_{12}(phen)_6(PPh_3)_4][Cl]_2$, which Dr. Bi Nguyen synthesized and structurally

characterized in 2015, was also recorded.[48] In the solid state, $[Cu_{14}H_{12}(phen)_6(PPh_3)_4][Cl]_2$ features a significantly shorter average Cu-Cu distance than that found in either **3.2** or **3.3**, making it a good model for a low-valent, Cu(0)-containing nanocluster. Its EXAFS spectrum contains a broad signal with multiple, overlapping components centered at ca. 2 Å (Figure 3.9). These were fit using contributions from Cu-L (L = N, P) scattering, as well as a three distinct Cu-Cu single-scattering paths (Table 3.5). In particular, the curve fit gives a Cu-N and Cu-P path lengths of 2.07(1) and 2.30(1) Å, respectively, while the combined *N*(Cu-Cu) is 4.1(5). These parameters are in good agreement with those extracted from the X-ray crystallographic analysis. More importantly, though, the *N*-weighted average Cu-Cu EXAFS pathlength is 2.60 Å, which is close to the value of 2.55 Å found for bulk Cu metal,[24] and much different from the Cu-Cu pathlengths measured for nanocluster **3.1**. Finally, the prominent feature at ca. 4 Å in the EXAFS of $[Cu_{14}H_{12}(phen)_6(PPh_3)_4][Cl]_2$ is reproduced well by a near-collinear multiple-scattering path (Cu-Cu-Cu, $N = 6$, $\angle$ 160.1°). Overall, the data for Cu_{14} exemplify the EXAFS curves expected for a low-valent Cu(0) nanocluster with strong Cu-Cu bonding, and are much different from that observed for **3.1**, **3.2**, and **3.3**, solidifying the conclusion about the structure of **3.1**.

3.2.5 Comparison to Other Reported Copper Thiolate Nanoclusters

As mentioned in the introduction, several thiolate-protected Cu APNCs with partial Cu(0) character have been reported in the past few years, including $[Cu_{15}(GSH)_4]$, $[Cu_9(SC_6H_4\text{-}p\text{-}F)_7]$, and $[Cu_9(SC_6H_4\text{-}p\text{-}Br)_6]$.[15, 17] Many of these low-valent nanoclusters were reportedly formed by direct reaction of a Cu(II) salt with an alkyl or aryl thiol, which acts as both reducing agent and capping ligand. On the basis of the reactivity I have reported herein, I now believe that that these previous reactions do not result in the formation of low-valent Cu

APNCs. Instead, I suspect that these reactions result in the formation of Cu(I)-containing thiolate clusters, similar in formulation and structure to complexes **3.1**, **3.2**, and **3.3**. Given the apparent thermodynamic stability of the "Atlas-sphere" structure type, as revealed by the structures of **3.2** and **3.3**, as well as the structures of $[Cu_{12}(SR)_6X_{12}][CuX]$ (X = Cl, Br; R = $CH_2CH_2NH_3$), $[Cu_{12}(SR)_6Cl_{12}][CuCl]_5$, $[Cu_{12}(SMe)_6(CN)_6]$, and $[Cu_{12}E_6L_8]$ (E = S, Se; L = phosphine),[35-36, 49-52] it is likely that many of these complexes also feature an $[Cu_{12}(SR)_6]^{6+}$ core. That said, other core structures are also possible, including $[Cu_4(SR)_4]$ (R = 2,6-$(Me_3Si)_2C_6H_3$, 2,4,6-$^iPr_3$-C_6H_2),[53-54] $[Cu_4(SR)_6]^{2-}$ (R = Me, Et, ^{i}Pr, Ph, *p*-Cl-C_6H_4, *o*-^{t}Bu-C_6H_4),[55-62] $[Cu_5(SR)_6]^-$ (R = ^{t}Bu, 2,6-Me_2-C_6H_3, 1-adamantyl),[61, 63-65] $[Cu_5(SR)_7]^{2-}$ (R = Me, Ph),[59, 66-67] $[Cu_6(SR)_6(\mu_6\text{-Br})]$ (R = 1-(thiolato)triptycene),[68] $[Cu_8(SR)_8]$ (R = 2,4,6-$^iPr_3$-C_6H_2),[54, 69] $[Cu_8(SR)_6Cl_6]^{2+}$ (R = $CH_2CH_2NH_3$),[52] and $[Cu_{12}(SR)_{12})]$ (R = 2-$(Me_3Si)C_6H_4$).[70]

The reactivity of Cu(I) and Cu(II) salts with thiols and thiolates is actually well explored.[71] Despite this long history, there is no crystallographically authenticated example of this reaction resulting in formation of a mixed-valent Cu(I)/Cu(0)-containing product. For example, Kroneck and co-workers monitored the reaction of $[Cu(MeCN)_4][ClO_4]$ with a variety of thiols in $MeCN/H_2O$. These reactions exclusively produce thiolate-containing Cu(I) coordination polymers.[72] In no cases do they observe reduction of Cu(I) to Cu(0). Similarly, reaction of $[Cu(MeCN)_4][PF_6]$ with HSC_6H_4-*o*-$SiMe_3$ results in formation of the Cu(I) nanocluster, $[Cu(SC_6H_4\text{-}o\text{-}SiMe_3)]_{12}$.[70] More recently, Donahue and co-workers found that reaction of CuCl with [*n*-Bu_4N][Cl] and NaSR (R = 1-(thiolato)triptycene) results in formation of the monometallic Cu(I) "ate" complex, $[Cu(SR)_2]^-$.[68] It is also useful to survey the reactivity of Ag and Au salts with thiols. For instance, reaction of $Ag(NO_3)$ with RSH/NEt_3 in MeCN resulted in formation of $[Ag(SR)]_n$ oligomers.[73-74] The reaction conditions are similar to those

used in this study, yet no reduction to Ag(0) was observed, despite the fact that Ag(I) is a much stronger oxidant than Cu^{+}.[75] Similarly, reaction of $Ag(NO_3)$ with PhSH/$[NMe_4][Cl]$ in MeOH/MeCN yields a series of $Ag^{I}(SPh)$ "ate" complexes.[76] Again, no reduction to Ag(0) is observed. With respect to Au(III), which is a stronger oxidant than either Ag(I) or Cu(I),[75] reaction of $H[AuCl_4]$ with excess RSH in water results in formation of $[Au^{I}(SR)]_n$ in excellent yields,[77] although in this case, reduction to metallic gold can be observed if the reaction mixture gets too hot. Similarly, reaction of $Na[AuCl_4]$ with 3 equiv of RSH in EtOH also results in formation of $[Au^{I}(SR)]_n$.[78] This procedure is compatible with a wide variety of R groups, including ^{n}Bu and $C_{12}H_{25}$, which were also employed in the current study.

The well-known photochemical properties of Cu(I) clusters further buttresses the argument that the material isolated by Zhang and co-workers is structurally similar to a Cu(I)-containing "Atlas-sphere" nanocluster, and not the mixed valent nanocluster, $Cu_{14}(SR)_{10}$ that was original proposed. For example, the "Atlas-sphere" clusters, $[Cu_{12}E_6L_8]$ (E = S, Se; L = phosphine), are strongly luminescent, with measured PL quantum yields of up to 90%.[49-51] In fact, many Cu(I)-containing clusters are known to be photoluminescent,[13, 79-86] including many Cu(I)-thiolate and Cu(I)-thiolate/halide clusters .[13, 80, 84-86] For example, $[Cu(SR)]_n$ (n = 2, 4, 7; R = p-S-C_6H_4-NMe_2)[13] features an emission peak between 480 and 560 nm, depending on its nuclearity, while $[(Cu(S^{t}Bu))_4(dppe)]_n$ (dppe = bis(diphenylphosphino)ethane) and $[(CuS^{t}Bu)_6(bix)]_n$ (bix = 1,4-bis(imidazole-1-ylmethyl)benzene) emit at 603 and 629 nm, respectively.[85]

3.3 Summary

I have examined the reactions of $CuCl_2$ with a variety of thiols (RSH) under anhydrous conditions. In the cases where R = n-Bu and R = CH_2CH_2Ph, I isolate "Atlas-sphere"-type

nanoclusters in good yields. Both nanoclusters are built around identical $[Cu_{12}(SR)_6]^{6+}$ core structures and both contain Cu(I) ions exclusively. Neither cluster features any Cu(0) character. In the case where R = *n*-$C_{12}H_{25}$, I generate an insoluble Cu(I)-containing thiolate nanocluster. The insolubility of this material has prevented us from growing X-ray quality crystals. However, I believe this cluster also features an "Atlas-sphere" core on the basis of a comparative XANES and EXAFS analysis. My conclusion concerning the nature of this material is further buttressed by the XPS characterization data, as well as the observation that the "Atlas-sphere" structure type is a conserved across a variety of thiolate ligands. Contrary to previous reports. I do not believe that this material is a mixed valent, Cu(0)-containing nanocluster.

This conclusion concerning the nature of **3.1** also better aligned with previously reported group 11 thiolate chemistry, which has been extensively studied. In particular, this past work suggests that the M(0) state is not accessible without addition of stronger reducing agents, such as $NaBH_4$. To the best of my knowledge, all previous reactions of the Cu salts with thiols only result in formation of Cu(I)-containing products. Put differently, thiols alone cannot reduce Cu(II) or Cu(I) to Cu(0). Perhaps most importantly, it is apparent that the synthesis of thiolate-stabilized, Cu(0)-containing APNCs is an unsolved synthetic problem. Their isolation would represent an important synthetic advance, but these materials remain elusive, which contrasts greatly with the plethora of known thiolate-stabilized Au(0) and Ag(0) APNCs. Going forward, I will continue to pursue the synthesis of Cu(0)-containing thiolate-stabilized APNCs. However, their successful isolation will likely require the development of new ligands and new synthetic procedures.

3.4 Experimental

3.4.1 General Procedures

All reactions and subsequent manipulations were performed under anaerobic and anhydrous conditions under an atmosphere of nitrogen. Hexanes were dried using a Vacuum Atmospheres DRI-SOLV Solvent Purification system and stored over 3Å sieves for 24 h prior to use. Tetrahydrofuran (THF) was dried by two-step distillation over calcium hydride (CaH_2) followed by sodium benzophenone ketyl. Dichloromethane (CH_2Cl_2) and pentane were dried on an MBraun solvent purification system. Dibenzyl ether and pyridine were degassed and dried over 3Å molecular sieves for 72 h prior to use. THF-d_8, C_5D_5N (py-d_5), CD_2Cl_2, hexamethyldisiloxane (HMDSO), 1-butanethiol, 2-phenylethanethiol, and 1-dodecanethiol were dried over 3Å molecular sieves for 24 h prior to use. Na(S^nBu) and $[Cu_{14}H_{12}(phen)_6(PPh_3)_4][Cl]_2$ were prepared according to the literature procedure.[48, 87] All other reagents were purchased from commercial suppliers and used as received.

All NMR spectra were collected at room temperature. ^1H NMR spectra were recorded on an Agilent Technologies 400-MR DD2 400 MHz spectrometer or a Varian Unity Inova 500 MHz spectrometer. The chemical shifts of all nuclei were referenced by using the residual solvent peaks. IR spectra were recorded on a Nicolet 6700 FT-IR spectrometer with a NXR FT Raman Module. Electronic absorption spectra were recorded on a UV-2401 PC Shimadzu UV-NIR spectrophotometer. The diffuse reflectance spectrum was recorded on a UV-3600 Shimadzu UV-NIR spectrophotometer equipped with an integrating sphere using a powder sample of **3.1**. Fluorescence spectra were recorded on a Horiba FluoroMax 4 spectrometer equipped with a 420 nm colored glass pass filter. Electrospray ionization (ESI) mass spectra were collected in THF at the Materials Research Laboratory Shared Experimental Facilities

at UCSB, using an ESI source in negative ion mode with a Waters Xevo G2-XS TOF mass spectrometer. A 0.25 mM THF solution of NEt_4Cl was added to the mass spectra samples to enhance the ionization of the dissolved species. GC mass spectra were collected in CH_2Cl_2 at the Mass Spectrometry Facility in the Department of Chemistry and Biochemistry at UCSB on an HP 5970 mass spectrometer equipped with a J&W DB-5ms 30m GC column, with 0.25 mm ID and 0.25 μm film thickness. Mass spectra were smoothed 3 times using the mean algorithm with a smooth window of 2 channels. The XPS spectrum of a solid sample of **1** was recorded on a Kratos Axis Ultra DLD X-ray Photoelectron Spectroscopy system equipped with a monochromated Al-k alpha source (1486 eV). Survey and high-resolution scans were recorded at 160 and 20 eV pass energies, respectively. A low-energy electron flood was used for charge neutralization, and peak positions were calibrated against the aliphatic C 1s peak (285.0 eV).

3.4.2 X-ray Absorption Spectroscopy

X-ray absorption near-edge spectra (XANES) and extended X-ray absorption fine structure (EXAFS) were recorded with the help of Dr. Zach Jones, formerly of the Scott group at UCSB. The X-ray absorption spectra (XAS) were collected at the Stanford Synchrotron Radiation Lightsource (SSRL, 3-GeV ring with a current of 500mA) on station 7-3 with a Si(220) $\phi = 90^o$ crystal. Samples of complexes **3.1** and **3.2** used for the XAS analysis were synthesized using dibenzyl ether as the solvent, while complex **3.3** was synthesized using THF as the solvent. Each sample was collected at 10 K under a LHe cryostat. Six individual scans were collected and aligned with an *in situ* Cu metal calibration foil and averaged with the Athena software package. Linear pre-edge subtraction and normalization by edge jumps were applied to the averaged scans. Then the extended fine structure (EXAFS), $\chi(k)$, function was

isolated by subtracting a smooth, third-order polynomial approximating the absorption background of an isolated atom. The spectra are presented in k^3-weighted and were Fourier transformed prior to non-linear curvefitting. The energy phase shift parameter (ΔE_o) was refined as a global parameter and then fixed for the remainder of the curvefitting analysis. The amplitude reduction factor, S_o^2, was fixed at 0.8 in accordance with previous analyses of Cu(I) standards and Cu-based clusters.[26-27] The scattering paths were simulated using FEFF8 calculations and the Artemis software.[88] The number of Cu-Cu interactions were reduced to one, two or three paths, due to the high number of Cu absorbing atoms in the cluster. The paths that occurred at distances with the highest frequency as predicted from the FEFF calculations were selected to represent the overall Cu-Cu bonding. The coordination number, *N*, path length, *R*, and mean-squared displacements, σ^2, were used as variables. The values of R and σ^2 were initially refined before being held while *N* was refined.

3.4.3 Attempted Synthesis of 1-Dodecanethiol-Protected Copper Nanoclusters[20]

To $CuCl_2$ (93.0 mg, 0.692 mmol) in a 20 mL scintillation vial equipped with a magnetic stir bar was added dibenzyl ether (2 mL) at 25 °C to give a brown slurry. 1-dodecanethiol (0.65 mL, 2.71 mmol) was then added to this slurry with a syringe. The resulting mixture was stirred for 20 min, which resulted in the dissolution of the brown solid concomitant with the deposition of a very pale fine gray solid. The reaction mixture was then filtered through a medium porosity frit, the collected solids were rinsed with hexanes (2 × 4 mL), and the colorless filtrate was discarded. The gray powder was then dried *in vacuo* to yield **3.1** (148 mg).

3.4.4 Attempted Synthesis of Dodecanethiol-Protected Copper Nanoclusters in THF

To $CuCl_2$ (90.0 mg, 0.669 mmol) in a 20 mL scintillation vial equipped with a magnetic stir bar was added THF (2 mL) at 25 °C to give a brown slurry. 1-dodecanethiol (0.65 mL, 2.71 mmol) was added to this slurry with a syringe which resulted in the rapid dissolution of the brown solid over the course of 2 min to give a pale-yellow solution. The reaction mixture was then allowed to stir for 20 min, whereupon a very pale-yellow powder was deposited in the vial. The reaction mixture was then filtered through a medium porosity frit and the collected solids were rinsed with hexanes (2 × 4 mL). The resulting pale-yellow powder was then dried *in vacuo* to yield **3.1** (116 mg). Diffuse Reflectance UV/vis: 361 nm (sh). Fluorescence (λ_{ex} = 365 nm): 510 nm (FWHM = 130 nm). IR (KBr pellet, cm^{-1}): 716 (s), 728 (m), 736 (m), 752 (m), 827 (w), 889 (w), 1029 (m), 1069 (m), 1188 (m), 1214 (m), 1241 (m), 1270 (m), 1297 (m), 1324 (w), 1345 (w), 1383 (m), 1427 (m), 1471 (s), 1618 (w), 2635 (w), 2850 (s), 2918 (s), 2956 (s). The colorless filtrate was then transferred to a 20 mL scintillation vial and the volatiles were removed *in vacuo* to yield a colorless oil (402 mg). The oil was analyzed via ^{1}H NMR spectroscopy, which revealed the presence of unreacted 1-docdecanethiol and di(1-dodecane)disulfide (Figure A3.8). ^{1}H NMR (400 MHz, 25 °C, CD_2Cl_2): δ 2.68 (t, J_{HH} = 6 Hz, di(1-dodecane)disulfide, α-CH_2), 2.51 (m, 1-dodecanethiol, α-CH_2), 1.66 (m, di(1-dodecane)disulfide, β-CH_2), 1.59 (m, 1-dodecanethiol, β-CH_2), 1.37 (br m, overlapping CH_2 of di(1-dodecane)disulfide and 1-dodecanethiol), 1.27 (br m, overlapping CH_2 of di(1-dodecane)disulfide and 1-dodecanethiol), 0.88 (t, J_{HH} = 6 Hz, overlapping CH_3 of di(1-dodecane)disulfide and 1-dodecanethiol).

3.4.5 Synthesis of $[Cu_{12}(SR')_6Cl_{12}][(Cu(HSR'))_6]$ (R' = ^{n}Bu) (3.2)

To a stirring slurry of $CuCl_2$ (100.0 mg, 0.744 mmol) in THF (2 mL) was added 1-butanethiol (0.40 mL, 3.71 mmol) via syringe. The brown powder quickly dissolved over the course of 30 s to give a bright yellow solution. The reaction mixture was allowed to stir for 20 min, whereupon it was filtered through a Celite column supported on glass wool (0.5 × 1 cm). The column was washed with THF (1 mL) And the washings were added to the filtrate. The filtrate was then layered with pentane (12 mL) and stored at -25 °C for 2 d, which resulted in the deposition of pale-yellow crystals. The crystals were isolated by decanting the supernatant and then dried *in vacuo* to yield **3.2** (104 mg, 90% yield). Anal. Calcd for $C_{48}H_{114}Cl_{12}Cu_{18}S_{12}$: C, 21.79; H, 4.34. Found C, 23.12; H 4.72. ^{1}H NMR (500 MHz, 25 °C, THF-d_8): δ 3.26 (br s, 12H, $SCH_2CH_2CH_2CH_3$), 2.53, (br s, 12H, $HSCH_2CH_2CH_2CH_3$), 1.98 (br s, 12H, $SCH_2CH_2CH_2CH_3$), 1.85 (br s, 6H, $HSCH_2CH_2CH_2CH_3$), 1.58 (m, 12H, $HSCH_2CH_2CH_2CH_3$), 1.41 (m, 24H, $SCH_2CH_2CH_2CH_3$, overlapping with $HSCH_2CH_2CH_2CH_3$), 0.92 (m, 36H, $SCH_2CH_2CH_2CH_3$, overlapping with $HSCH_2CH_2CH_2CH_3$). ESI-MS: *m/z* = 2139.7942 $[Cu_{18}(SR')_6Cl_{13}]^-$ (Calcd *m/z* = 2139.5649) *m/z* = 2039.9023 $[Cu_{17}(SR')_6Cl_{12}]^-$ (Calcd *m/z* = 2039.6666), *m/z* = 1940.9977 $[Cu_{16}(SR')_6Cl_{11}]^-$ (calcd *m/z* = 1940.7682), *m/z* = 1842.0930 $[Cu_{15}(SR')_6Cl_{10}]^-$ (calcd *m/z* = 1841.8719), *m/z* = 1744.175 $[Cu_{14}(SR')_6Cl_9]^-$ (calcd *m/z* = 1743.9734). UV-Vis / NIR (THF, 21.2 μM, 25 °C, $L \cdot mol^{-1} \cdot cm^{-1}$): 274 nm (sh, ε = 44000), 370 nm (ε = 22000). Fluorescence (λ_{ex} = 365 nm): 585 nm (FWHM = 140 nm). IR (KBr pellet, cm^{-1}): 649 (w), 705 (m), 728 (m), 780 (w), 914 (m), 1052 (m), 1068 (m), 1222 (s), 1270 (m), 1298 (m), 1337 (w), 1353 (w), 1379 (m), 1429 (m), 1463 (s), 1618 (w), 2502 (w), 2646 (w), 2731 (w), 2872 (s), 2928 (s),

2957 (s). Complex **3.2** could also be prepared in similar yields by using dibenzyl ether as the solvent.

3.4.6 Synthesis of di-*n*-butyl disulfide

To a stirring slurry of colorless NaS^nBu (69 mg, 0.615 mmol) in THF (5 mL) was added dropwise a THF solution (2mL) of I_2 (78 mg, 0.307 mmol) over the course of 10 min. The reaction mixture was allowed stir for 20 h, whereupon. the volatiles were removed *in vacuo* and the resulting colorless oil was triturated with pentane (3 × 2 mL) to remove any remaining THF. The volatiles were then removed *in vacuo* to give di-*n*-butyl disulfide as a colorless oil (48 mg, 87% yield). ^{1}H NMR (500 MHz, 25 °C, CD_2Cl_2): δ 2.69 (t, J_{HH} = 5 Hz, 4H, $SCH_2CH_2CH_2CH_3$), 1.65 (m, 4H, $SCH_2CH_2CH_2CH_3$), 1.41 (m, 4H, $SCH_2CH_2CH_2CH_3$), 0.92 (t, J_{HH} = 7 Hz, 6H, $SCH_2CH_2CH_2CH_3$). ^{13}C NMR (125 MHz, 25 °C, CD_2Cl_2): δ 39.28 ($SCH_2CH_2CH_2CH_3$), 31.76 ($SCH_2CH_2CH_2CH_3$), 22.08 ($SCH_2CH_2CH_2CH_3$), 13.89 ($SCH_2CH_2CH_2CH_3$). GC-MS: *m/z* = 178.07 $[M]^+$ (Calcd *m/z* = 178.08). These NMR spectral data are similar to those previously reported for di-*n*-butyl disulfide in $CDCl_3$.[89]

3.4.7 Reaction of 3.2 with pyridine

A 20 mL scintillation vial was charged with a magnetic stir bar, complex **3.2** (17.7 mg, 6.69 μmol), and pyridine (2.0 mL, 25 mmol). The pale-yellow solid quickly dissolved to give a bright yellow solution. The solution was allowed to stir for 20 min, whereupon a small amount of white powder deposited from solution. The reaction mixture was then filtered through a Celite column supported on glass wool (0.5 × 1 cm). The column was washed with pyridine (1 mL) and the washings were added to the filtrate. The filtrate was then layered with diethyl ether (12 mL) and stored at room temperature for 2 d, which resulted in the deposition of yellow needles. The crystals were isolated by decanting the supernatant and then dried *in*

vacuo to yield [CuCl(py)$_3$] (18.3 mg, 68% yield based on Cl^-). The identity of the crystals was confirmed by a comparison of the unit cell parameters with the literature values.[39] Unit cell parameters: a = 14.353(2) Å, b = 9.833(2) Å, 11.710 (2) Å; α= 90.00°, β = 90.00°, γ = 90.00°.

3.4.8 Synthesis of $[H(THF)_2]_2[Cu_{17}(SR")_6Cl_{13}(THF)_2(HSR")_3]]$ (R" = CH_2CH_2Ph) (3.3)

To a stirring slurry of $CuCl_2$ (90.0 mg, 0.692 mmol) in THF (2 mL) was added 2-phenylethanethiol (0.36 mL, 2.69 mmol) via syringe. The brown powder quickly dissolved over the course of 30 s to give a bright yellow solution. The reaction mixture was allowed to stir for 20 min, whereupon it was filtered through a Celite column supported on glass wool (0.5 × 1 cm). The column was washed with THF (1 mL) and the washings were added to the filtrate. The filtrate was then layered with pentane (12 mL) and stored at -25 °C for 2 d, which resulted in the deposition of pale-yellow crystals. The crystals were isolated by decanting the supernatant and then dried *in vacuo* to yield **3.3** (113 mg, 94%). Anal. Calcd for $C_{96}H_{136}Cl_{13}Cu_{17}O_6S_9$: C, 35.86; H, 4.26. Found C, 37.93; H 4.60. ^{1}H NMR (400 MHz, 25 °C, THF-d_8): δ 8.82 (br s, 2H, $[H(THF)_2]^+$), 7.31-7.15 (m, 45H, overlapping phenyl regions of SCH_2CH_2Ph and $HSCH_2CH_2Ph$), 3.47 (m, 12H, SCH_2CH_2Ph), 3.37 (m, 12H, SCH_2CH_2Ph), 2.88 (m, 6H, $HSCH_2CH_2Ph$), 2.77 (m, 6H, $HSCH_2CH_2Ph$), 1.95 (br s, 3H, $HSCH_2CH_2Ph$). ESI-MS: *m/z* = 2527.6428 $[Cu_{19}(SR")_6Cl_{14}]^-$ (Calcd *m/z* = 2527.4636), *m/z* = 2431.7378 $[Cu_{18}(SR")_6Cl_{13}]^-$ (Calcd *m/z* = 2431.5574), *m/z* = 2327.6748 $[Cu_{17}(SR")_6Cl_{12}]^-$ (calcd *m/z* = 2327.6667), *m/z* = 2229.7747 $[Cu_{16}(SR")_6Cl_{11}]^-$ (Calcd *m/z* = 2229.7683), *m/z* = 2129.8726 $[Cu_{15}(SR")_6Cl_{10}]^-$ (Calcd *m/z* = 2129.8718), *m/z* = 2031.9645 $[Cu_{14}(SR")_6Cl_9]^-$ (Calcd *m/z* = 2031.9734), *m/z* = 1932.0714 $[Cu_{13}(SR")_6Cl_8]^-$ (Calcd *m/z* = 1932.0750), *m/z* = 1831.0859 $[Cu_{12}(SR")_6Cl_7]^-$ (Calcd *m/z* = 1831.1843). UV-Vis / NIR (THF, 24.4 μM, 25 °C, $L \cdot mol^{-1} \cdot cm^-$

^{1}): 260 nm (sh, ε = 49000), 355 nm (ε = 15000). Fluorescence (λ_{ex} = 365 nm): 650 nm (FWHM = 190 nm). IR (KBr pellet, cm^{-1}): 493 (m), 565 (m), 647 (w), 706 (s), 756 (s), 846 (w), 909 (w), 969 (m), 1029 (m), 1070 (m), 1222 (m), 1266 (w), 1312 (m), 1417 (m), 1453 (s), 1496 (s), 1583 (w), 1602 (m), 1808 (w), 1878 (w), 1949 (w), 2524 (w), 2632 (w), 2870 (m), 2928 (s), 2026 (s), 3060 (m).

3.4.9 Reaction of 3.3 with pyridine

A 20 mL scintillation vial was charged with a magnetic stir bar, complex **3.3** (20.6 mg, 6.41 μmol), and pyridine (2.0 mL, 25 mmol). The pale-yellow solid quickly dissolved to give a bright yellow solution. The solution was allowed to stir for 20 min. The reaction mixture was then filtered through a Celite column supported on glass wool (0.5 × 1 cm). The column was washed with pyridine (1 mL) and the washings were added to the filtrate. The filtrate was then layered with diethyl ether (14 mL) and stored at room temperature for 2 d, which resulted in the deposition of yellow needles. The crystals were isolated by decanting the supernatant and then dried *in vacuo* to yield [$CuCl(py)_3$] (26.5 mg, 95% yield based on Cl^-). The identity of the crystals was confirmed by a comparison of the unit cell parameters with the literature values.[39] a = 14.340(2) Å, b = 9.828(2) Å, 11.692 (2) Å; α= 90.00°, β = 90.00°, γ = 90.00°.

3.4.10 X-ray Crystallography

Data for **3.2** were collected on a Bruker APEX 3 D8 diffractometer equipped with a PHOTON II CPAD detector on Beamline 12.2.1 at the Lawrence Berkeley National Laboratory Advanced Light Source (ALS) Synchrotron X-ray source (α = 0.7288 Å), which operates at 1.9 GeV with a ring current of 500 mA. X-rays were monochromatized using reflection from a Si(111) monochrometer. Data for **3.3**·1.5THF were collected on a Bruker KAPPA APEX II diffractometer equipped with an APEX II CCD detector using a TRIUMPH

monochromater with a MoKα X-ray source (α = 0.71073 Å). Crystals were mounted on a cryoloop under Paratone-N oil, and all data were collected at 100(2) K using an Oxford nitrogen gas cryostream system.

X-ray data for **3.2** and **3.3**·1.5THF were collected utilizing frame exposures of 10 s. Data collection and cell parameter determination was conducted using the SMART program.[90] Integration of the data frames and final cell parameter refinement were performed using SAINT software.[91] Absorption correction of the data was carried out using the multi-scan method SADABS.[92] Subsequent calculations were carried out using SHELXTL.[93] Structure determination was done using direct methods and difference Fourier techniques. All hydrogen atom positions on the ligands were idealized, and rode on the atom of attachment. Structure solution, refinement, graphics, and creation of publication materials were performed using SHELXTL.[93]

For complexes **3.2** and **3.3**, hydrogen atoms were not assigned to the thiol (i.e. RSH) sulfur atoms. Additionally, for complex **3.3**, the H^+ counterions could not be located in the Fourier difference map and were not assigned. Due to unresolved positional disorder, the EADP command was applied to some of the carbon atoms of three thiolate (S2, S3, S4) ligands and one thiol (S8) ligand in **3.3**. Similarly, the FLAT and DFIX commands were used to constrain the phenyl ring of one thiol ligand in **3.3**, due to unresolved positional disorder. One THF solvate (O7) was constrained using the DFIX, SADI, and FREE commands. One THF solvate (O6) was modelled with 50% occupancy.

Further crystallographic details can be found in Table 3.2.

Table 3.2. X-ray Crystallographic Data for **3.2** and **3.3**·1.5THF.

	3.2	**3.3**·1.5THF
empirical formula	$C_{48}H_{114}Cl_{12}Cu_{18}S_{12}$	$C_{102}H_{148}Cl_{13}Cu_{17}O_{7.5}S_9$
crystal habit, color	needle, pale-yellow	block, pale-yellow
crystal size (mm)	0.050 × 0.015 × 0.005	0.2 × 0.2 × 0.15
crystal system	triclinic	triclinic
space group	$P\bar{1}$	$P\bar{1}$
volume ($Å^3$)	2185.8(4)	6439(12)
a (Å)	12.5832(13)	15.268(15)
b (Å)	13.4715(13)	15.916(18)
c (Å)	14.9134(14)	29.58(3)
α (deg)	60.640(4)	91.56(2)
β (deg)	86.533(5)	101.67(2)
γ (deg)	73.574(4)	111.83(2)
Z	1	2
formula weight (g/mol)	2645.23	3323.77
density (calculated) (Mg/m^3)	2.010	1.700
absorption coefficient (mm^{-1})	5.306	3.178
F_{000}	1320	3356
total no. reflections	11797	25756
unique reflections	8613	12659
final R indices [I>2σ(I)]	R_1 = 0.0525	R_1 = 0.0849
	wR_2 = 0.1133	wR_2 = 0.2046
largest diff. peak and hole (e^-A^{-3})	1.915 and -1.717	2.343 and -1.524
GOF	1.390	1.224

3.5 Appendix

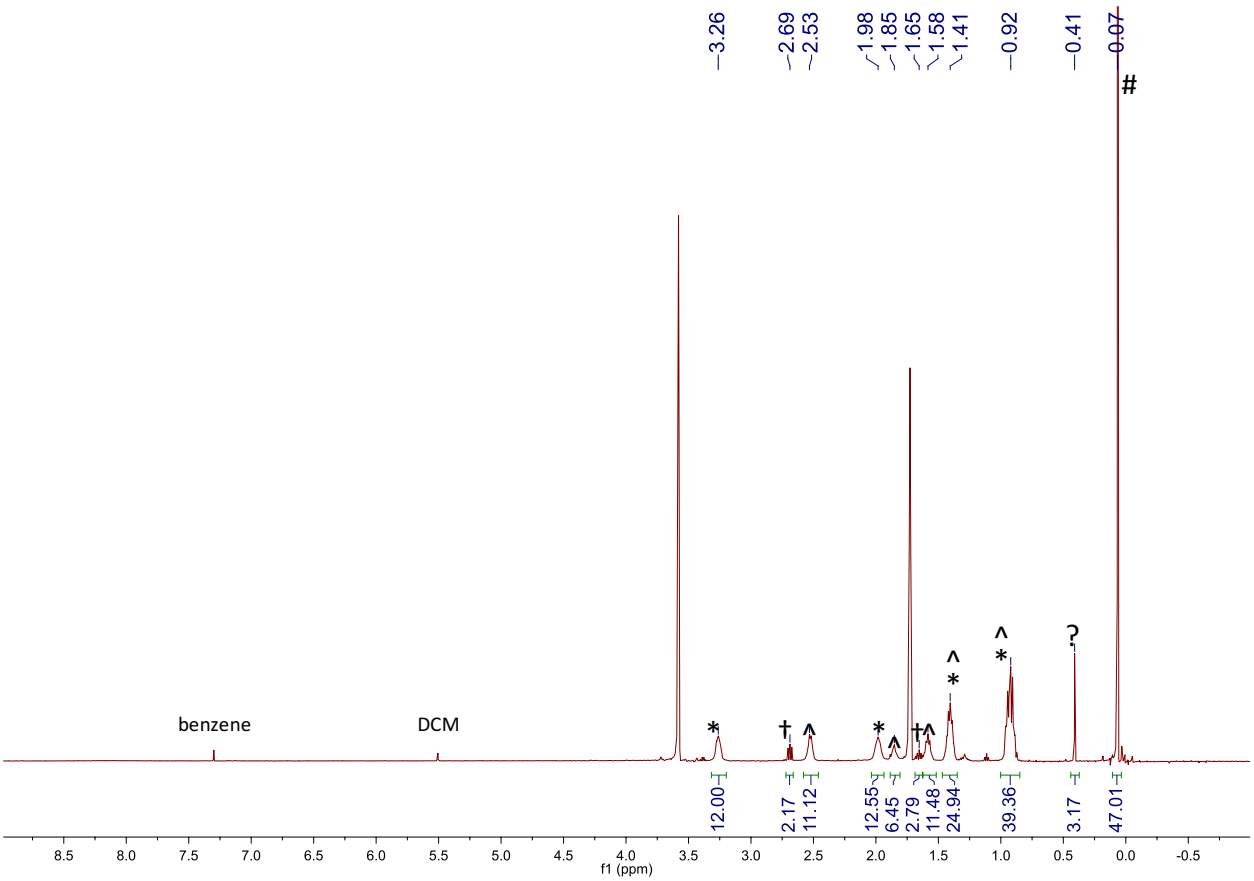

Figure A3.1. ^{1}H NMR spectrum of 3.2 in THF-d_8 with HMDSO added as an internal standard.

Experimental details: Complex 3.2 (8.0 mg, 3.0 µmol) was transferred to a J. Young NMR tube equipped with a rotoflow Teflon valve and dissolved in THF-d_8 (1 mL). HMDSO (1.0 µL, 4.7 µmol) was added via syringe as an internal standard. A ^{1}H NMR spectrum was then collected using a long relaxation delay (d_1 = 60 s) to ensure accurate integrations. (*) indicates a resonance assignable to **3.2**, (^) indicates a resonance assignable to HS^{n}Bu, (†) indicates a resonance assignable to di-*n*-butyl disulfide, (#) indicates a resonance assignable to HMDSO, and (?) indicates a resonance assignable to an unknown impurity.

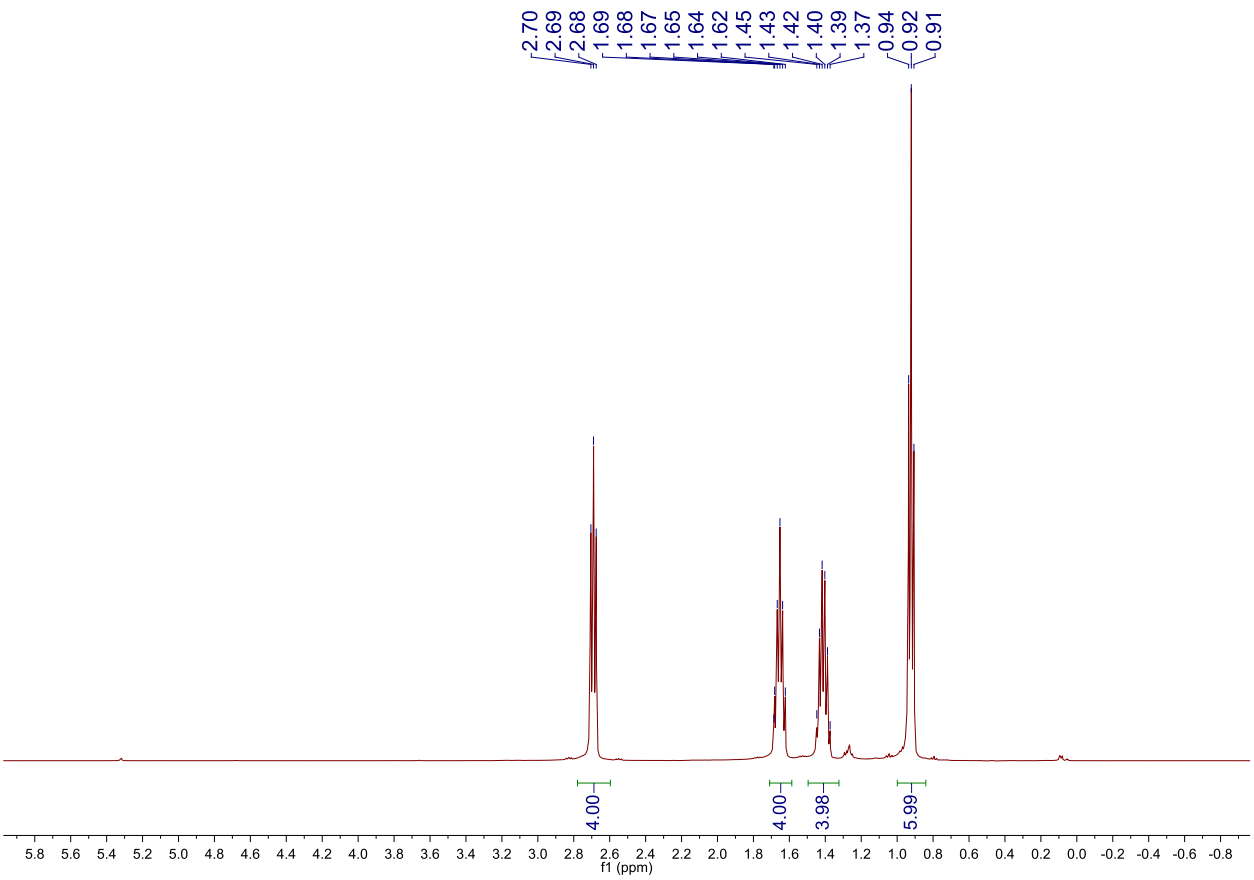

Figure A3.2. ^{1}H NMR spectrum of di-*n*-butyl disulfide in CD_2Cl_2.

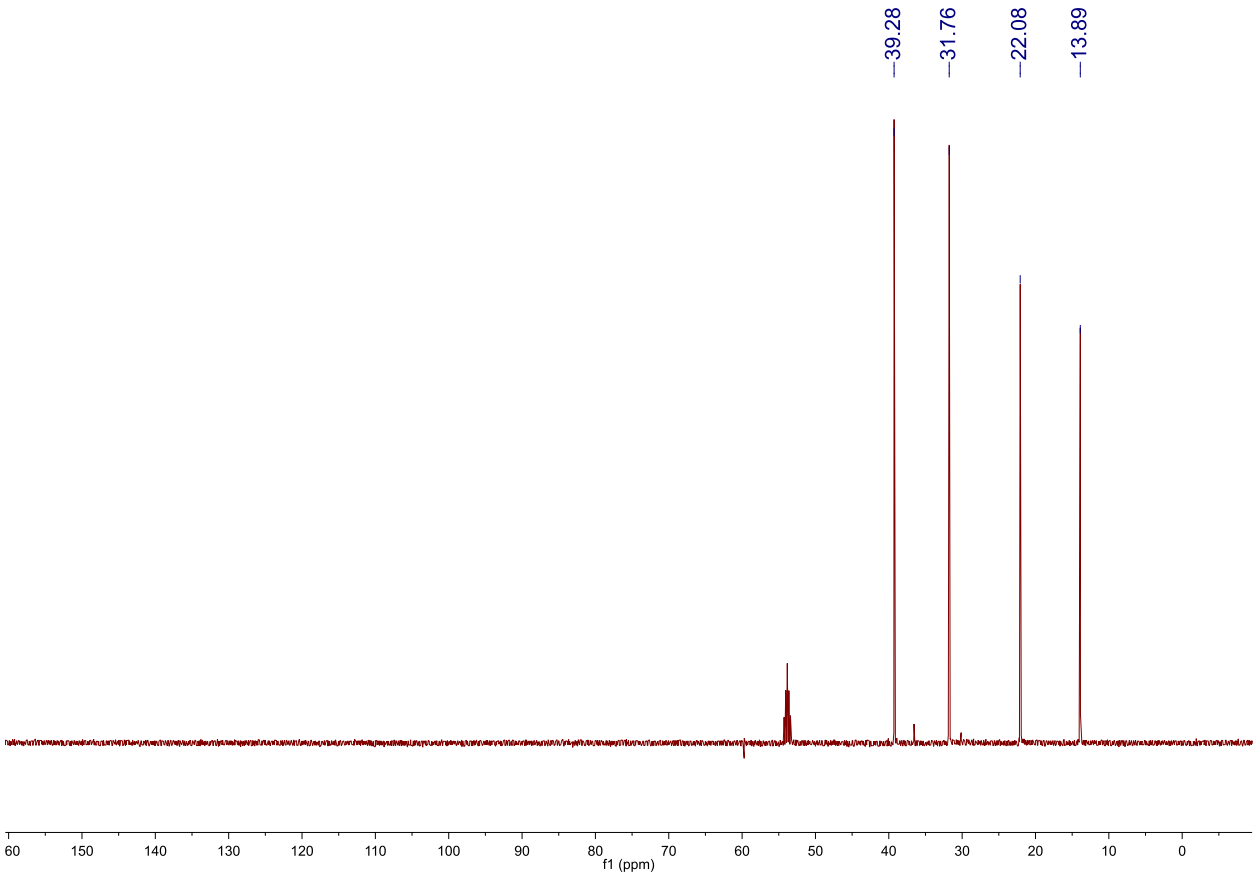

Figure A3.3. ^{13}C NMR spectrum of di-*n*-butyl disulfide in CD_2Cl_2.

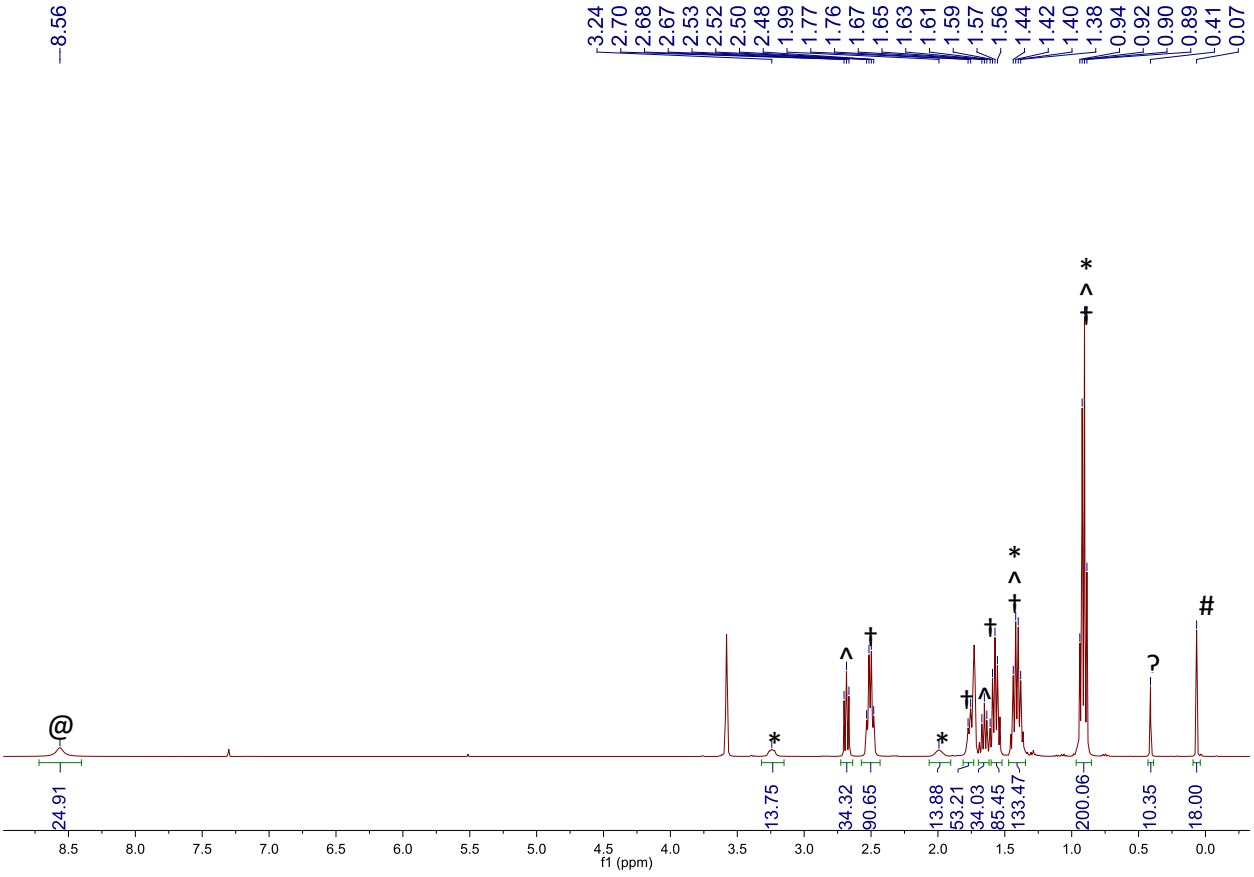

Figure A3.4. *In situ* ^{1}H NMR spectrum in THF-d_8 of the reaction of $CuCl_2$ and HS^{n}Bu after 20 min. **Experimental details**: $CuCl_2$ (6 mg, 0.045 mmol) was added to a J. Young NMR tube equipped with a rotoflow Teflon valve and suspended in THF-d_8 (0.8 mL). To this suspension was added HS^{n}Bu (25 µL, 0.23 mmol) whereupon the brown solids dissolved and a bright yellow solution was formed. To this reaction mixture was added HMDSO (0.5 µL, 2.35 µmol) via syringe as an internal standard. The J. Young tube was allowed to stand for 20 min, whereupon a ^{1}H NMR spectrum was collected with a long relaxation delay (d_1 = 60 s) to ensure accurate integrations. (*) indicates resonances assignable to **3.2**, (^) indicates a resonance assignable to di-*n*-butyl disulfide, (†) indicates a resonance assignable to 1-butanethiol, (@) indicates a resonance assignable to HCl, (#) indicates a resonance assignable to HMDSO, and (?) indicates a resonance assignable to an unidentified side-product.

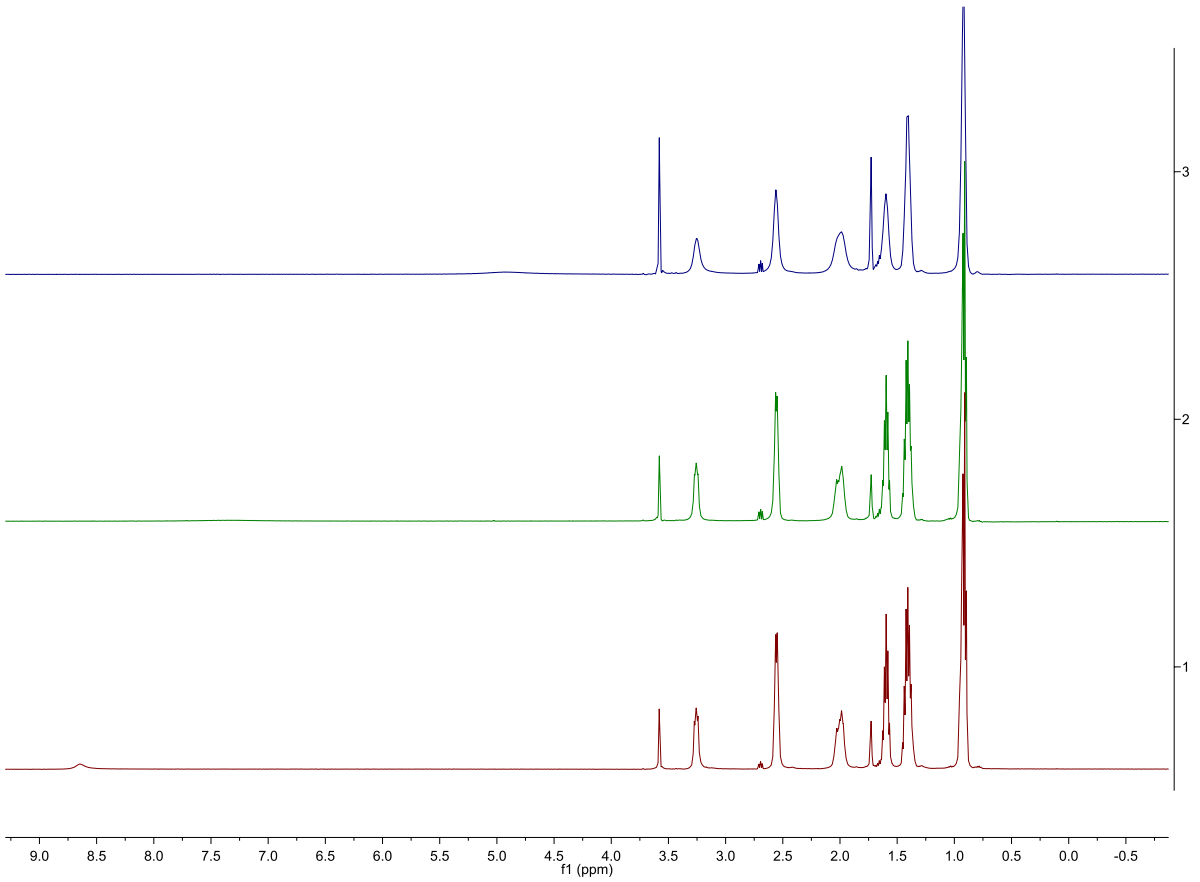

Figure A3.5. ^{1}H NMR spectra of **3.2** in THF-d_8 at 25 °C over a period of 24 h. Bottom = 10 min, middle = 5 h, top = 24 h.

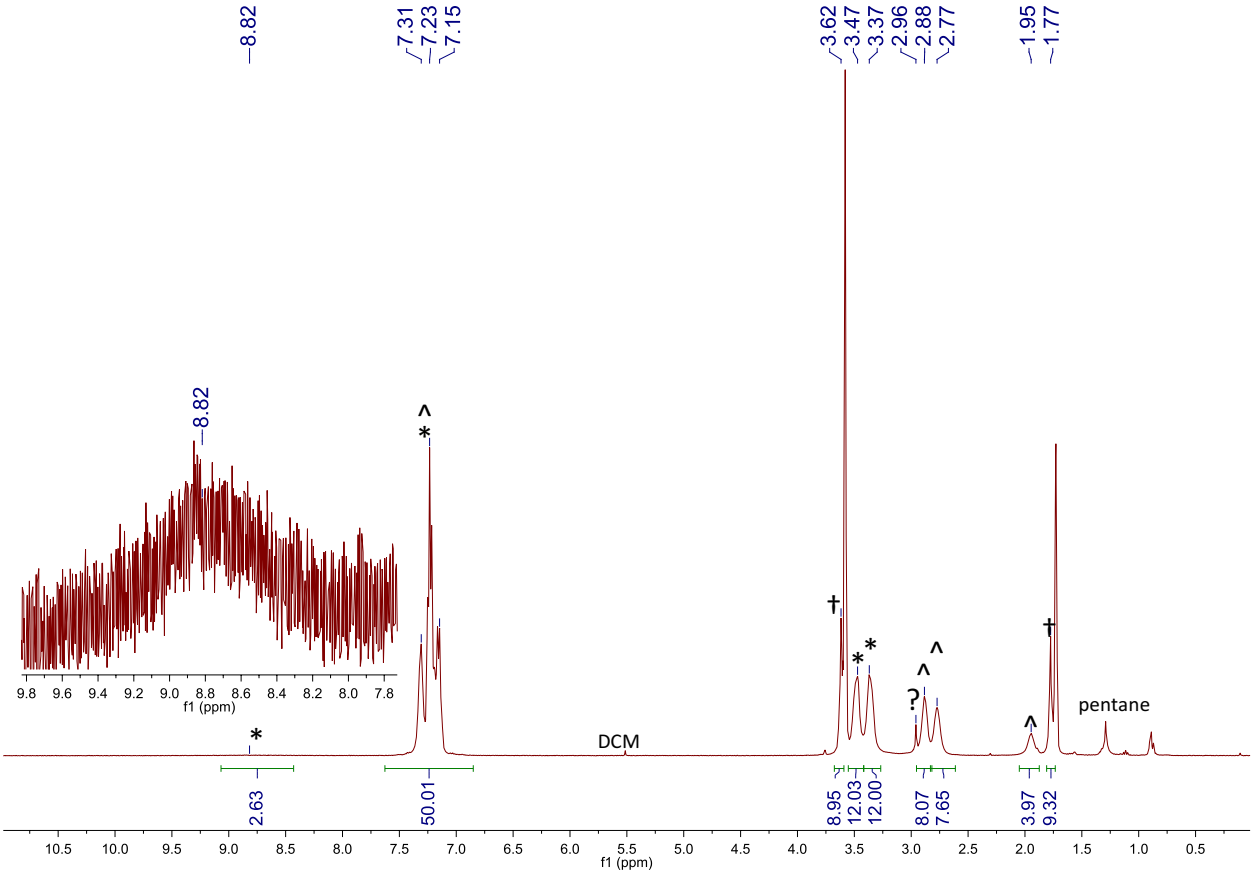

Figure A3.6. ^{1}H NMR spectrum of **3.3** in THF-d_8 with an inset showing the H-bonded proton resonance of the $[H(THF)_2]^+$ cation. (*) indicates resonances assignable to **3.3**, (^) indicates a resonance assignable to $HSCH_2CH_2Ph$, (†) indicates a resonance assignable to THF, and (?) indicates a resonance assignable to an unknown impurity.

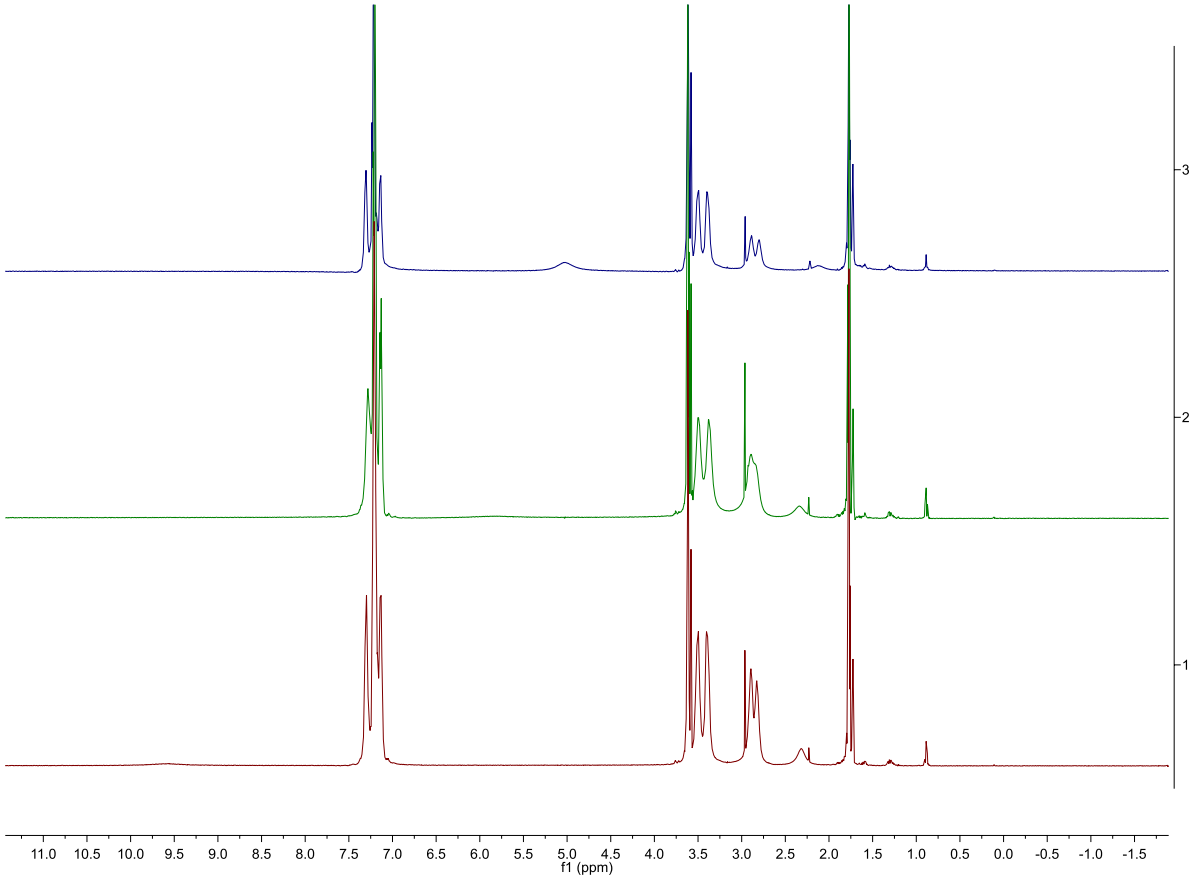

Figure A3.7. ^{1}H NMR spectra of **3.3** in THF-d_8 at 25 °C over a period of 24 h. Bottom = 10 min, middle = 5 h, top = 24 h.

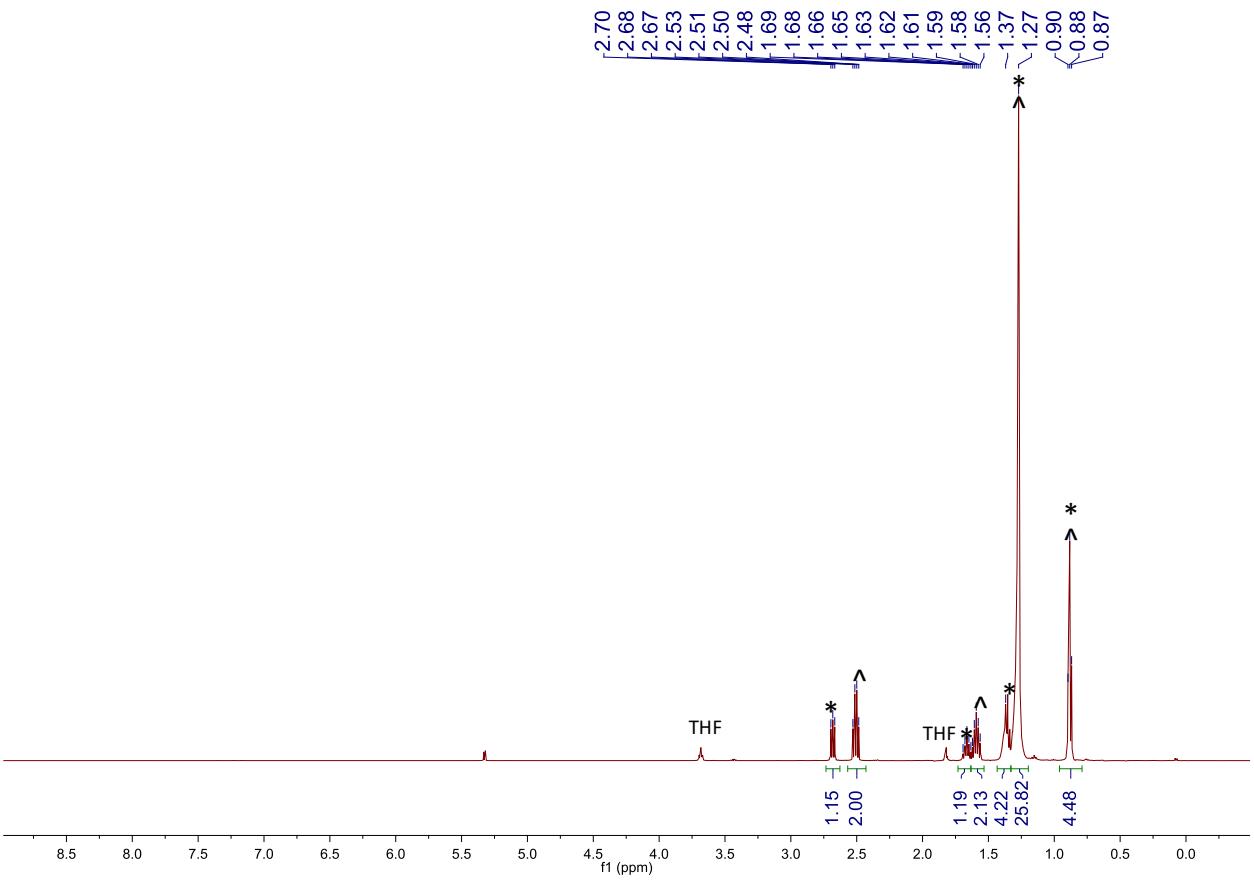

Figure A3.8. ^{1}H NMR spectrum in CD_2Cl_2 of the THF soluble products from the reaction of $CuCl_2$ and 1-dodecanethiol. (*) indicates a resonance assignable to di(1-dodecane)disulfide[31] and (^) indicates a resonance assignable to 1-dodecanethiol.

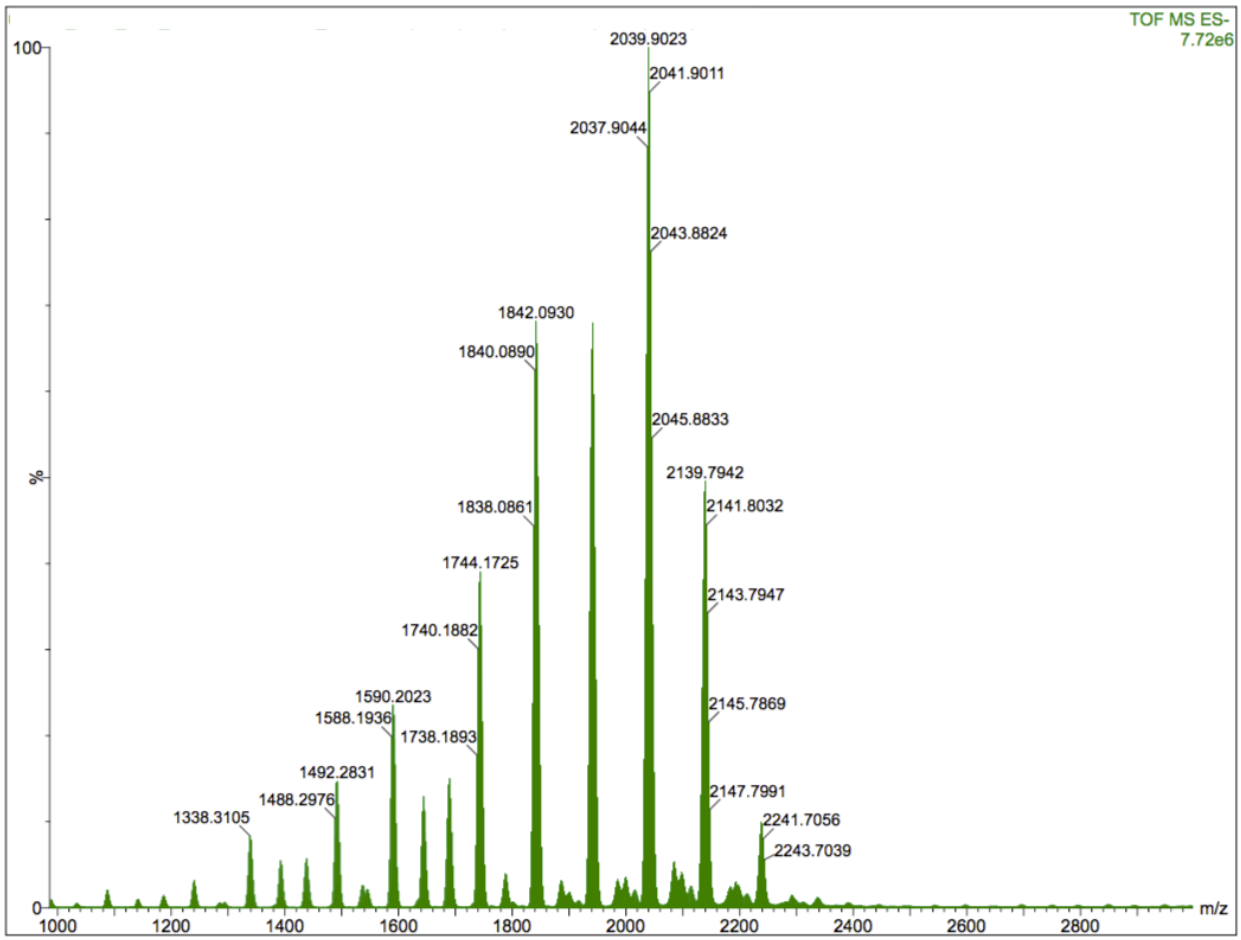

Figure A3.9. Partial ESI-MS (negative mode) of **3.2** in THF with added NEt_4Cl. The parent peak at *m/z* = 2039.9023 represents $[Cu_{17}(SR')_6Cl_{12}]^-$ (R' = ^{n}Bu) and the surrounding peaks represent the parent ion $\pm[CuCl]_n$.

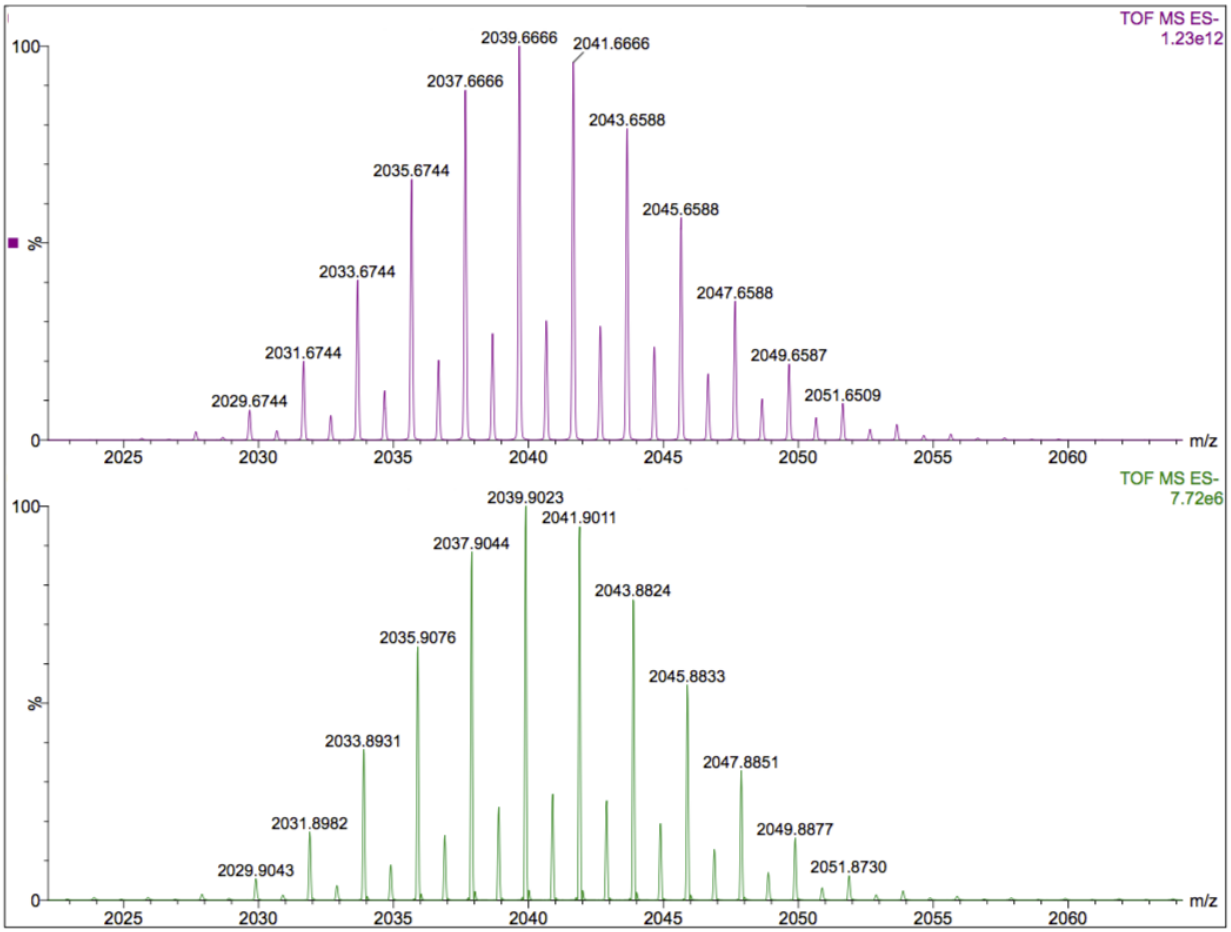

Figure A3.10. Partial ESI-MS (negative mode) of **3.2** in THF with added NEt_4Cl. The experimental (bottom) and calculated (top) peaks assignable to the $[Cu_{17}(SR')_6Cl_{12}]^-$ (R' = ^{n}Bu) ion are shown.

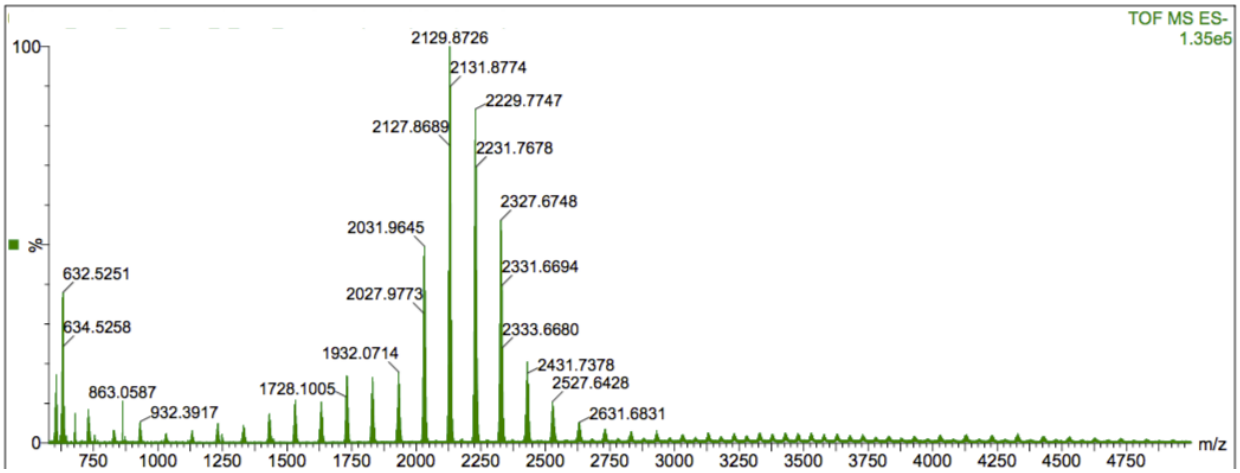

Figure A3.11. Partial ESI-MS (negative mode) of **3.3** in THF with added NEt_4Cl. The parent peak at *m/z* = 2129.8726 represents $[Cu_{15}(SR")_6Cl_{10}]^-$ (R" = CH_2CH_2Ph) and the surrounding peaks represent the parent ion $\pm[CuCl]_n$.

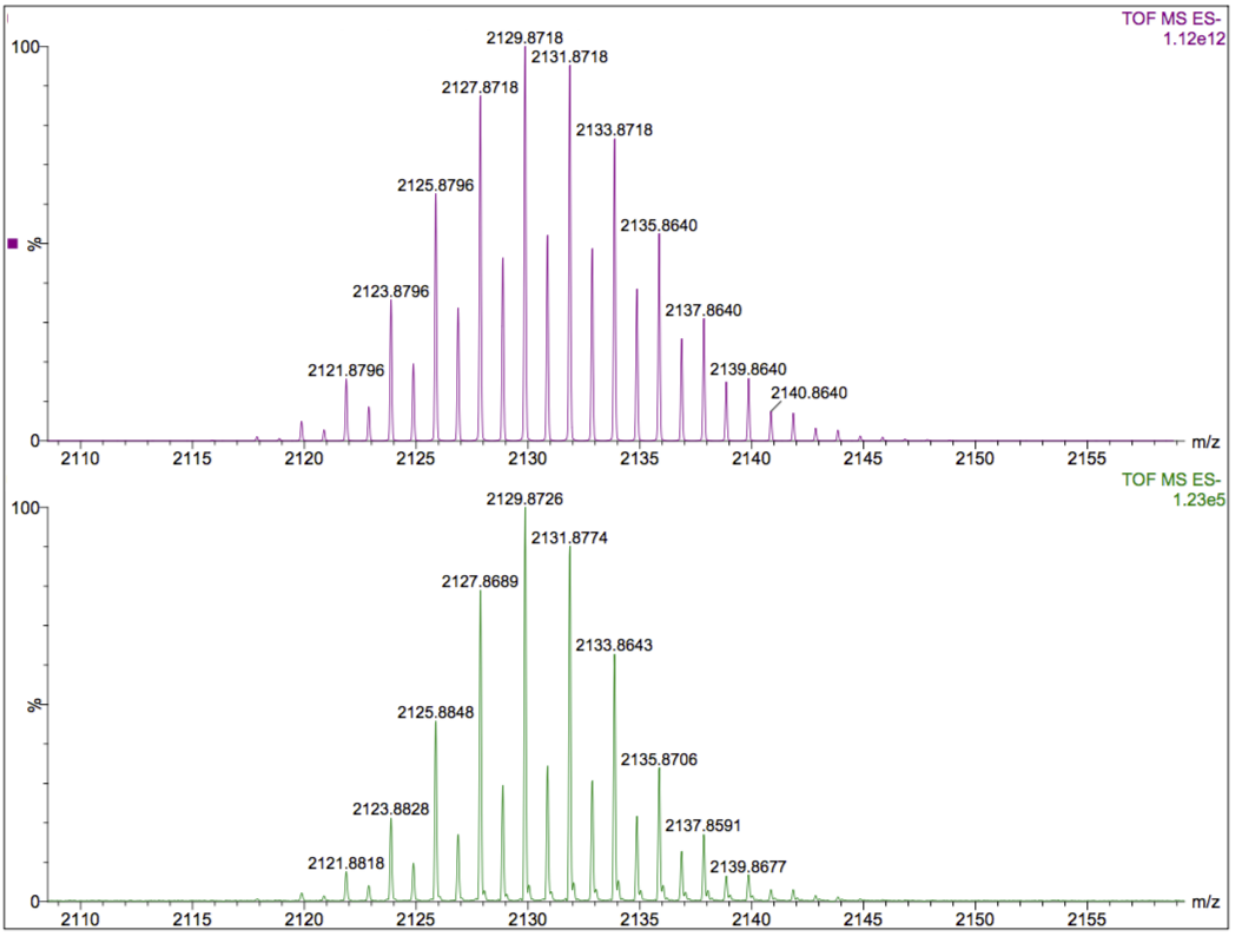

Figure A3.12. Partial ESI-MS (negative mode) of **3.3** in THF with added NEt_4Cl. The experimental (bottom) and calculated (top) peaks assignable to the $[Cu_{15}(SR")_6Cl_{10}]^-$ (R" = CH_2CH_2Ph) ion are shown.

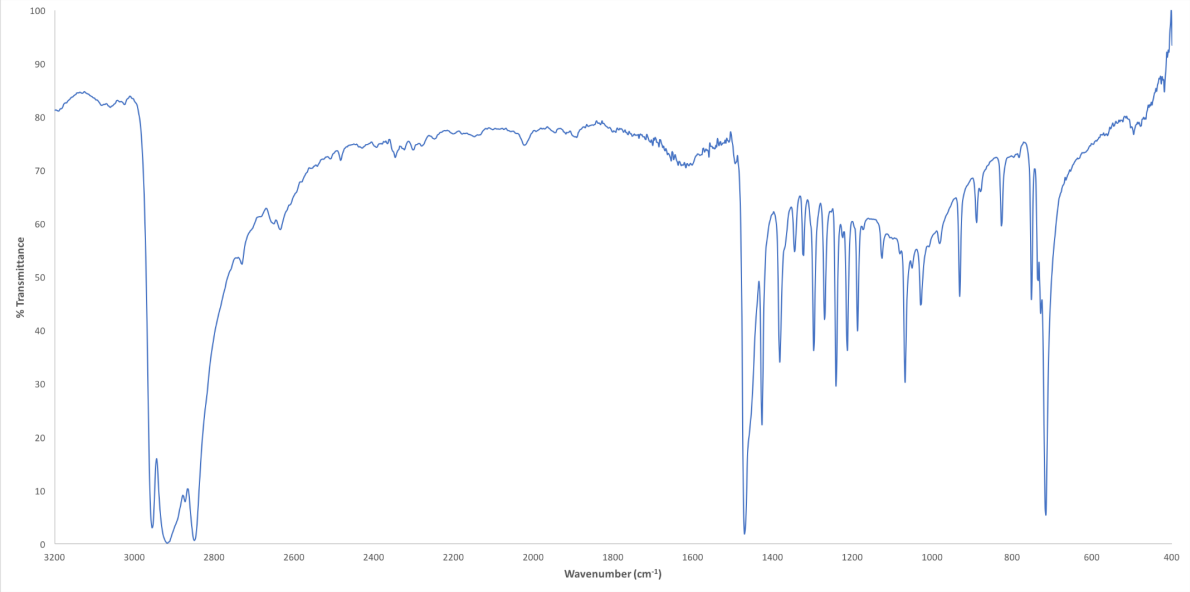

Figure A3.13. Partial IR spectrum of **3.1**, synthesized from THF (KBr pellet).

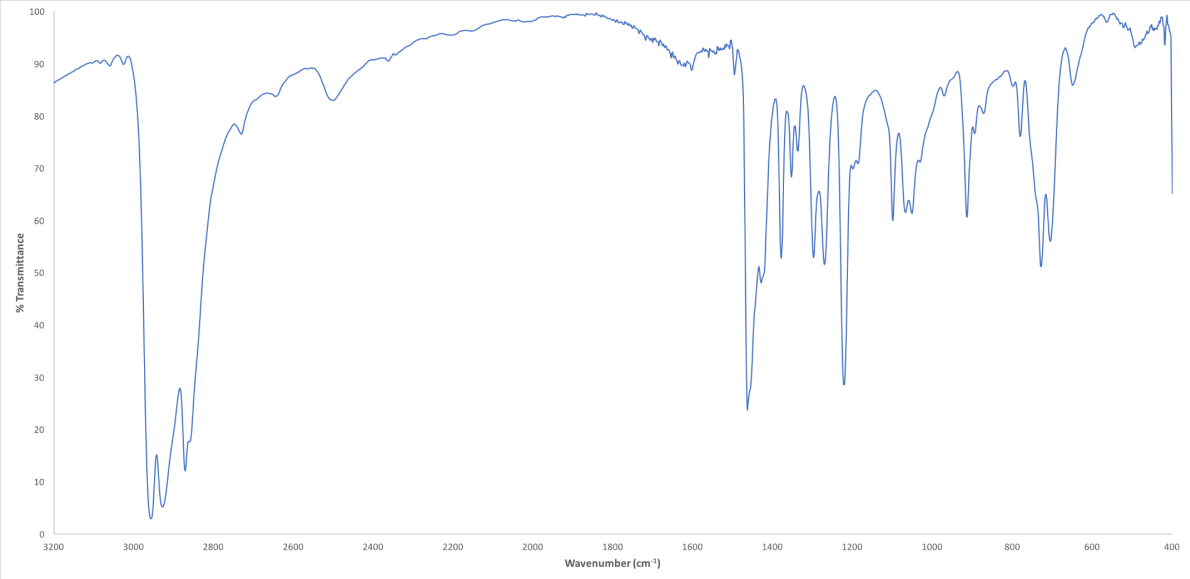

Figure A3.14. Partial IR spectrum of **3.2** (KBr pellet).

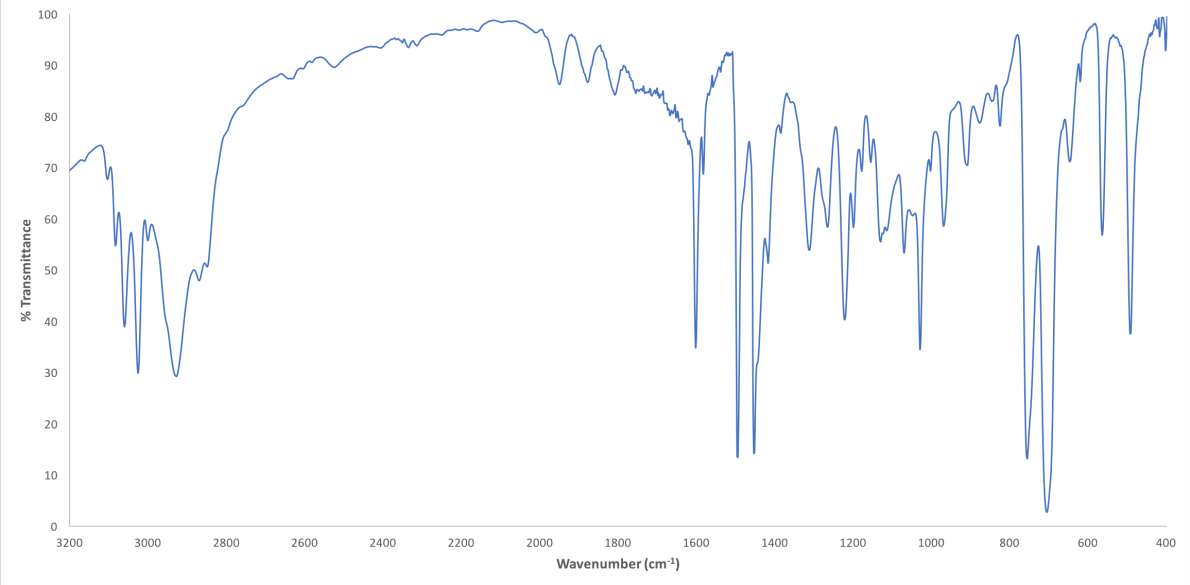

Figure A3.15. Partial IR spectrum of **3.3** (KBr pellet).

Table 3.3. X-ray Photoelectron Spectroscopy data for **3.1**.

Assignment	E_b (eV)
Cu 2p1/2	952.70
Cu 2p3/2	932.70
Cu LMM	575.0
Cu LMM	571.1
Cu LMM	568.3
C 1s	285.20
Cl 2s	269.70
S 2s	227.10
Cl 2p	199.20
S 2p	163.20
Cu 3s	123.10

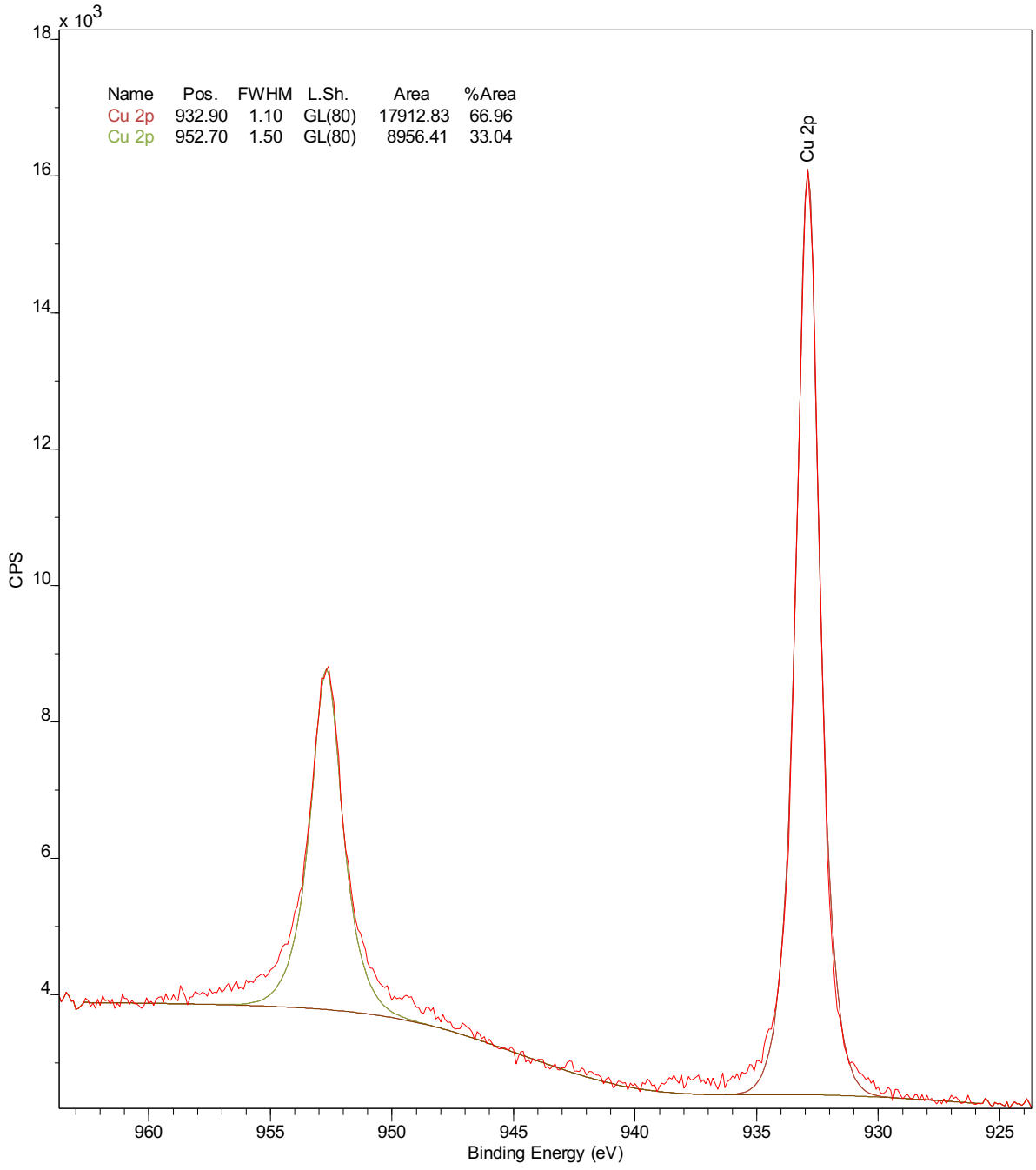

Figure A3.16. Partial XPS spectrum of **3.1** synthesized from THF showing the Cu(I) 2p transitions.

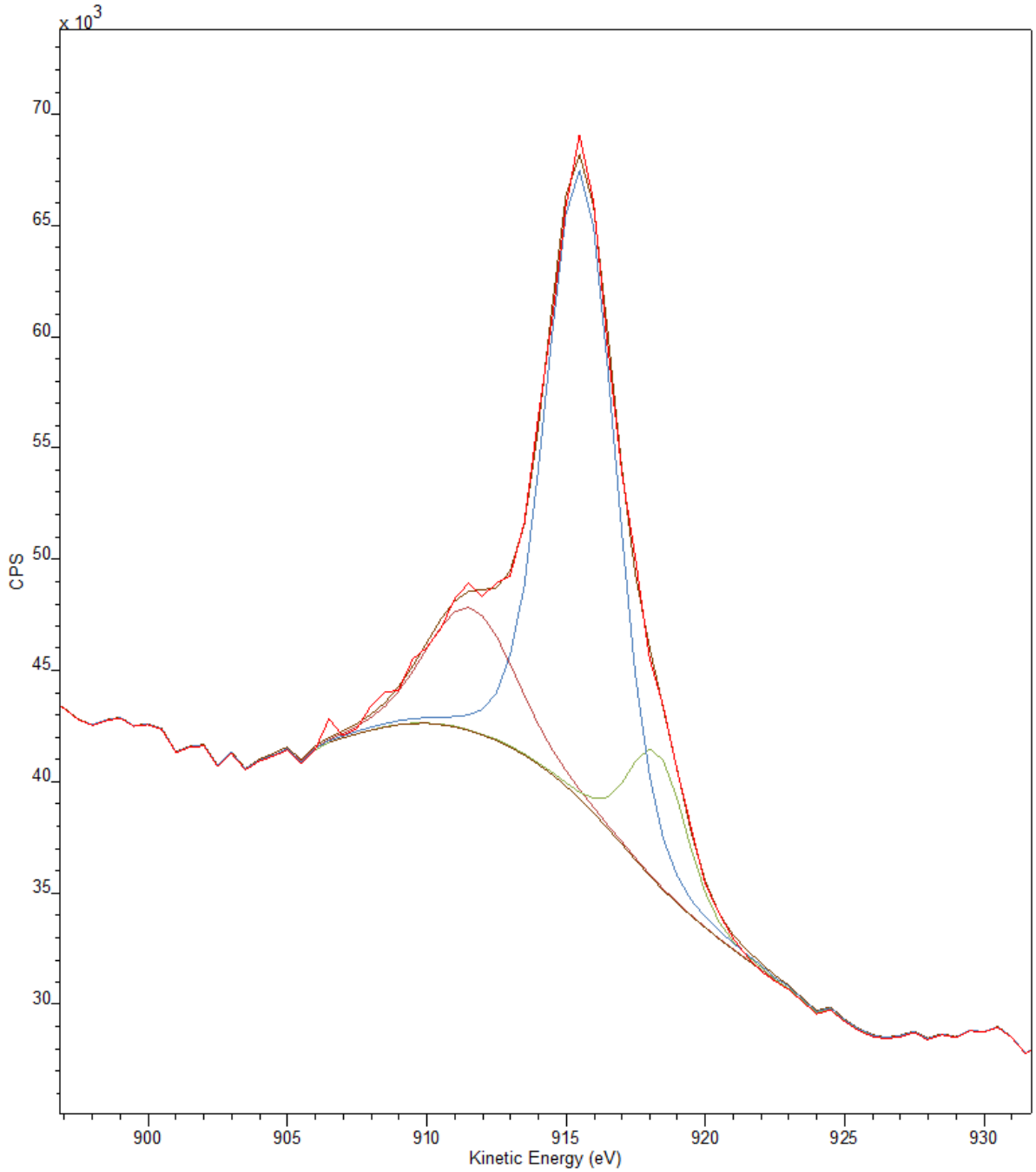

Figure A3.17. Partial XPS spectrum of **3.1** synthesized from THF showing the Cu(I) LMM transitions.

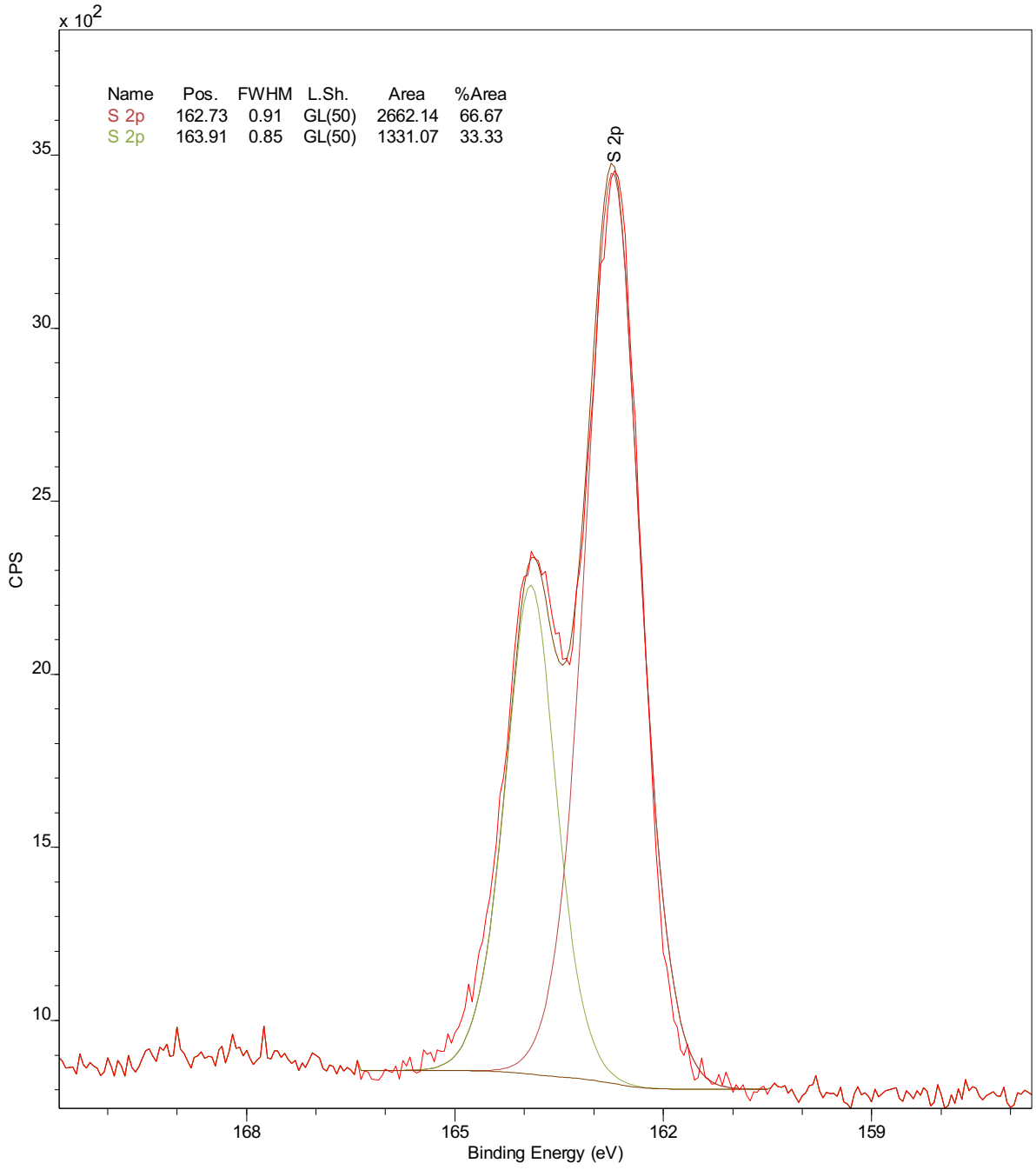

Figure A3.18. Partial XPS spectrum of **3.1** synthesized from THF showing the S 2p transitions.

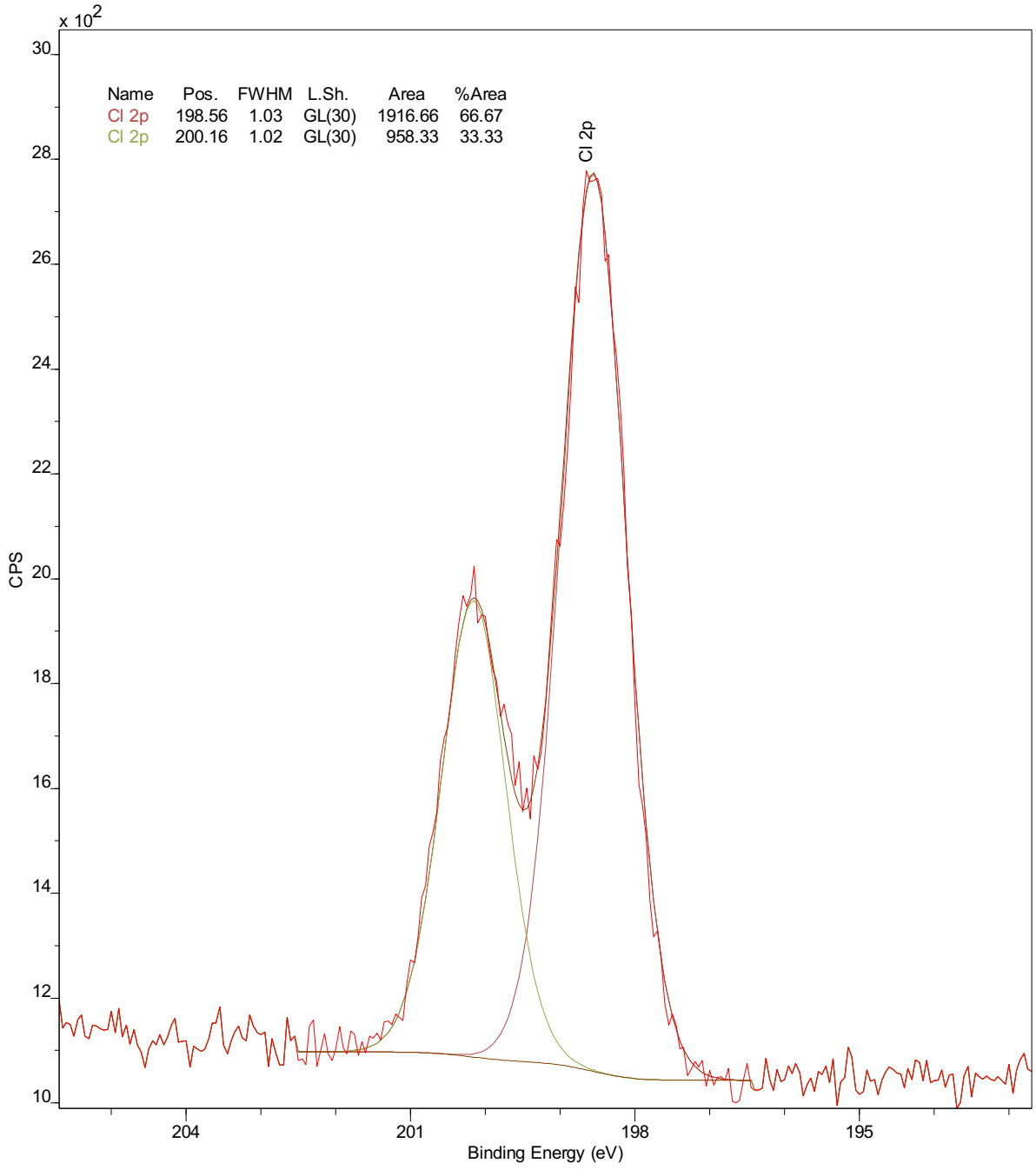

Figure A3.19. Partial XPS spectrum of **3.1** synthesized from THF showing the Cl 2p transitions.

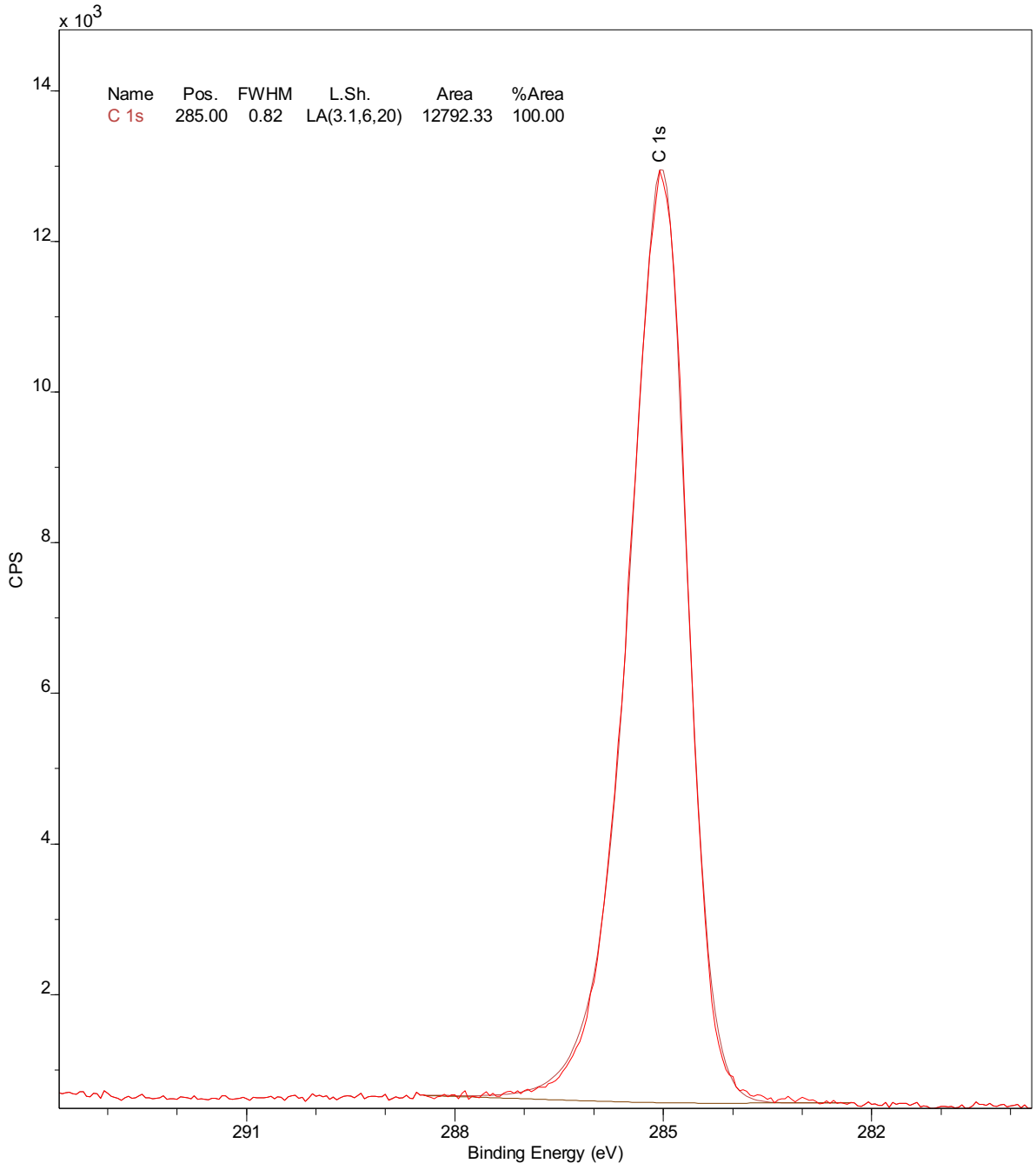

Figure A3.20. Partial XPS spectrum of **3.1** synthesized from THF showing the C 1s transition.

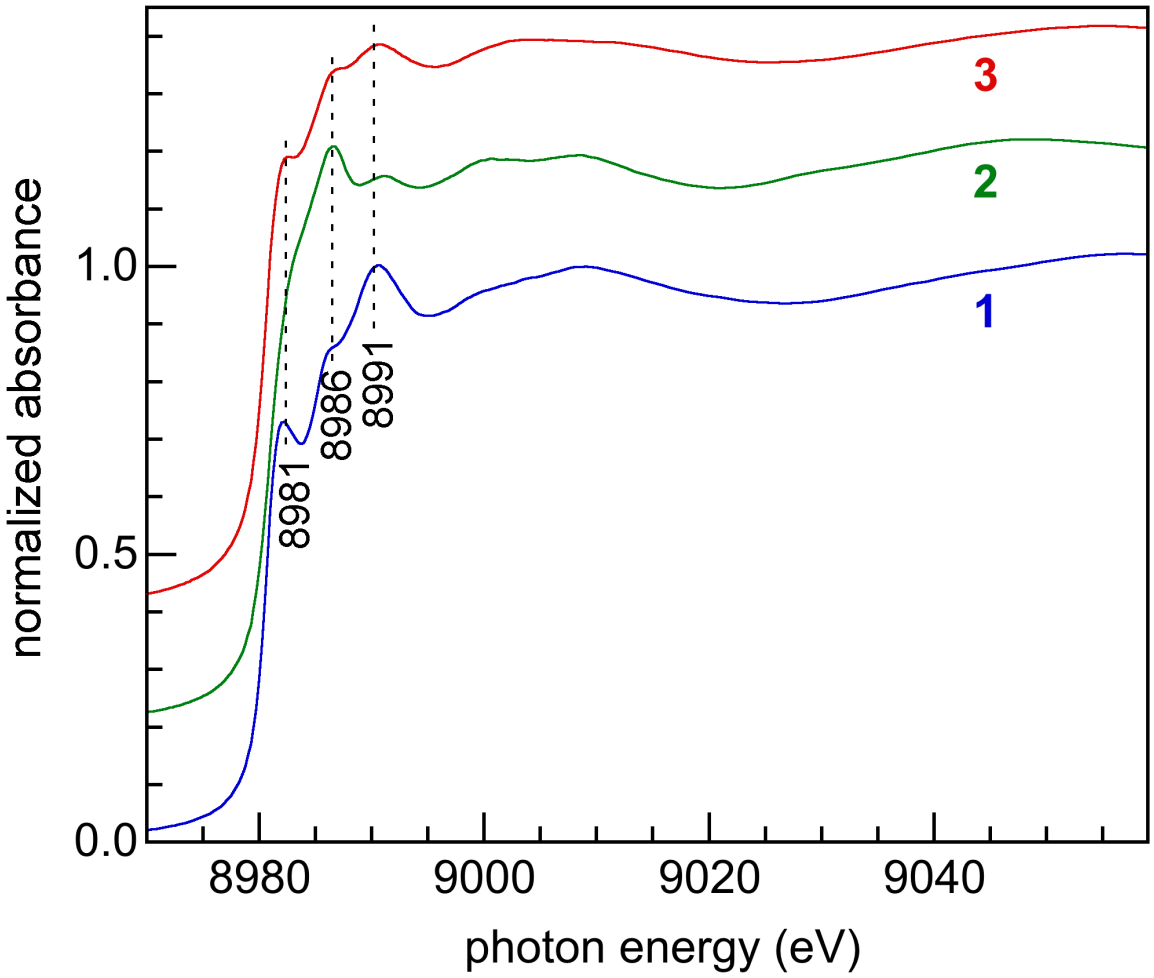

Figure A3.21. Comparison of Cu K-edge XANES of clusters **3.1**, **3.2** and **3.3**. Spectra are offset vertically for clarity. For each cluster, the XANES profile includes three peaks, at 8981.0, 8986.0 and 8991.0 eV. These features arise from dipole-allowed $1s \rightarrow 4p$ transitions. Tetrahedrally-coordinated Cu ions in the "Atlas-sphere" core are expected to show only $1s \rightarrow 4p$ excitations, while the trigonal planar Cu atoms with D_{3h} symmetry will have distinct $1s \rightarrow 4p_{xy}$ and $1s \rightarrow 4p_z$ transitions. The appearance of three peaks in the XANES is consistent with these assignments. However, their relative intensities vary for each cluster, likely due to variability in the number and type of non-core Cu atoms as a result of the different capping thiolate ligands (*n*-butanethiolate, ethylphenylthiolate, or dodecanethiolate).

Additional EXAFS Analysis. Fits of the EXAFS data were initially performed with a single Cu-Cu path (Table 3.4). For all three thiolate clusters, the refined Cu-Cu pathlengths exceed 2.7 Å. This distance is significantly longer than the expected value for metallic bonding (2.55 Å), but is consistent with the long interactions between Cu(I) ions. The results show generally good agreement with the Atlas-sphere model. However, the resulting values of *N*(Cu-Cu) are slightly lower than expected for clusters **3.2** and **3.3**, while the corresponding σ^2 values are larger than expected (Table 3.4). Unlike $[Cu_{14}H_{12}(Ph_2phen)_6(PPh_3)_4][Cl]_2$, the "Atlas sphere" structure does not have near-collinear Cu-Cu-Cu paths to account for the intensity at ca. 4 Å. Triangular multiple-scattering paths involving Cu-S/Cl did not give good results. The long-range peak in the EXAFS of **3.1** is adequately modeled using only a Cu-Cu single-scattering path (represented as Cu-Cu2).

Table 3.4. Comparison of average FEFF-predicted paths for the "Atlas-sphere" core $[Cu_{12}(SR)_6Cl_{12}]^{6-}$ with EXAFS curvefit parameters for the new thiolate clusters, modeled using a single short Cu-Cu path.

Cluster	Path	N	R (Å)	$10^3\ \sigma^2$ (Å^2)	E_0 (eV)
$[Cu_{12}(SR)_6Cl_{12}]^{6-}$	Cu-L1	1.5	2.28(4)		
	Cu-Cu	2.0	2.76(14)		
	Cu-L2	2.9	4.03(15)		
3.1 [a]	Cu-L	1.9(3)	2.280(2)	3.9(3)	5.7(5)
	Cu-Cu1	2.0(3)	2.77(4)	7(1)	
	Cu-Cu2	2.4(4)	4.047(2)	8.9(5)	
3.2 [b]	Cu-L	1.2(2)	2.271(5)	3.0(9)	5.7(2)
	Cu-Cu	1.2(4)	2.76(4)	11(2)	
3.3 [c]	Cu-L	1.5(3)	2.298(6)	4.1(3)	4.7(5)
	Cu-Cu	1.1(2)	2.71(1)	12(4)	

[a] N_{idp} = 23, ΔR = 1.0 – 4.5 Å, Δk = 3.0 – 13.5 Å^{-1}. [b] N_{idp} = 15, ΔR = 1.0 – 3.0 Å, Δk = 3.0 – 14.5 Å^{-1}. [c] N_{idp} =13, ΔR = 1.0 – 3.0 Å, Δk = 3.0 – 13.3 Å^{-1}. In all fits, S_o^2 was fixed at 0.8, in accordance with previous analyses of Cu(I) standards and Cu-based clusters,[26-27] and ΔE_0 was refined as a global fit parameter. Uncertainties are shown in parentheses; values without uncertainties were fixed during curvefitting.

EXAFS data for **3.1**, **3.2**, and **3.3** were also fitted with two difference Cu-Cu pathlengths. The results of the fits are shown in Table 3.1. For all three clusters, refinement of two Cu-Cu paths results in Cu-Cu distances that differ by only ca. 0.2 Å, with the shorter path making a greater contribution to the spectrum due to its larger value of *N*. For **3.1**, the principal effect of two Cu-Cu paths (relative to only one Cu-Cu path; see above for details) is a reduction in the mean-squared displacements, while the combined value of *N*(Cu-Cu) remains unchanged at 2.0(5). For **3.2** and **3.3**, the average *N*(Cu-Cu) values increase significantly, to 1.9(4) and 2.3(5), respectively, while the σ^2 values remain unchanged (See Table 3.1). A second effect of including two short Cu-Cu paths on N_{total}(Cu-Cu) is a dampening of the peak intensity, consequence of destructive interference between the paths, which results in more accurate *N*(Cu-Cu) values. This is illustrated by the individual scattering paths for curvefits with two Cu-Cu paths (Figure A3.22).

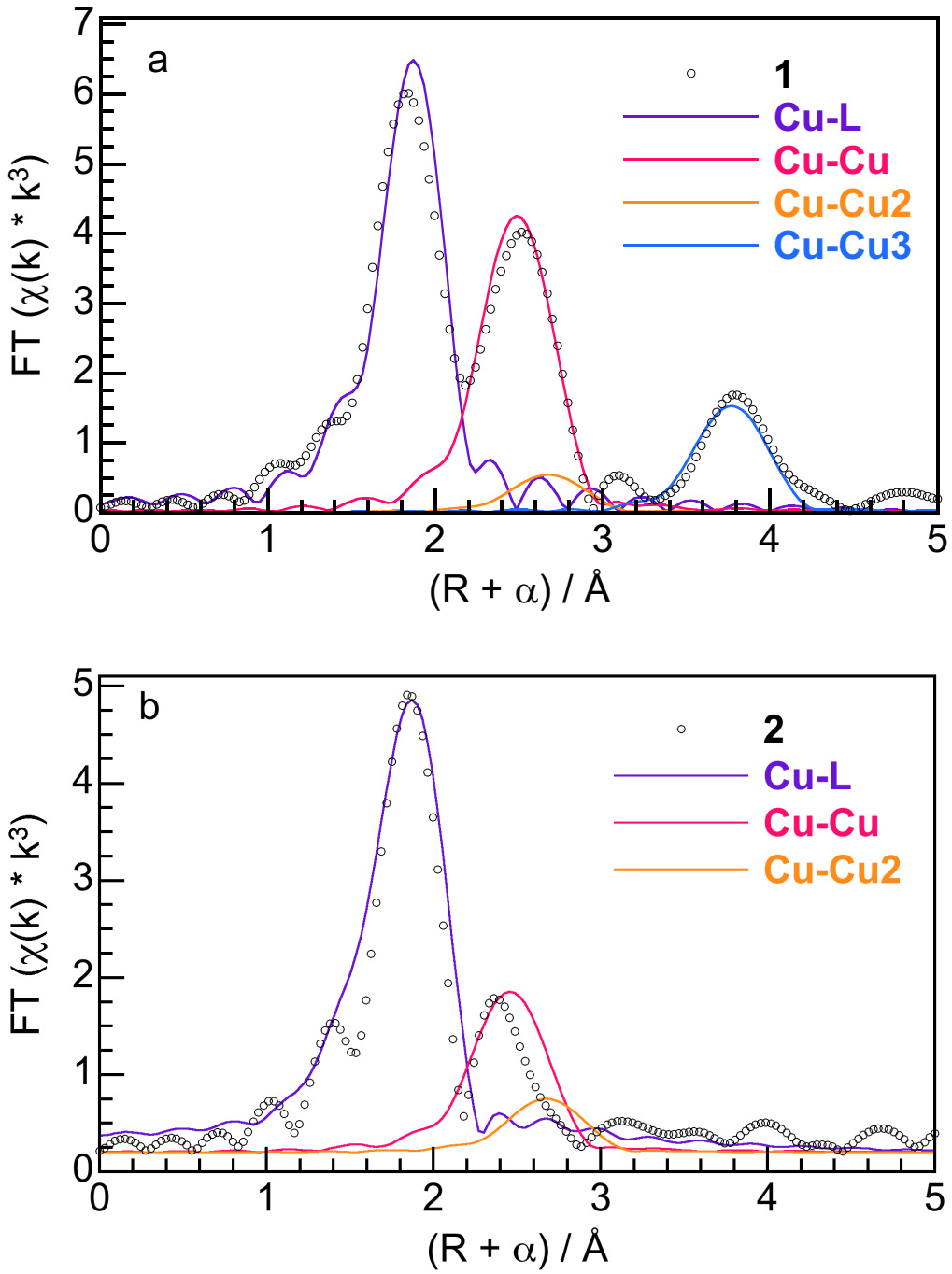

Figure A3.22. Individual scattering paths from the EXAFS curvefits of clusters **3.1** and **3.2**, corresponding to the fits shown in Table 3.1.

Table 3.5. Curvefit parameters for the Cu K-edge EXAFS of $[Cu_{14}H_{12}(phen)_6(PPh_3)_4][Cl]_2$.

Path	Crystal structure [a]		EXAFS		
	N	d (Å)	N	R (Å)	$10^3\ \sigma^2$ (Å^2)
Cu-N	0.86	2.104	0.86	2.067(10)	9(3)
Cu-P	0.3	2.294	0.3	2.300(10)	5(1)
Cu-Cu1	6[b]	2.51	1.7(2)	2.520(4)	6(1)[c]
Cu-Cu2		2.66	2.3(2)	2.658(4)	6(1)[c]
Cu-Cu3		2.90	0.1(1)	2.89(1)	6(1)[c]
Cu-Cu-Cu	6	4.31	2.7(5)	4.310	9(2)

[a] Average values, based on the published single-crystal X-ray diffraction structure.[48] [b] The Cu-Cu paths that occurred at distances with the highest frequency, predicted from the FEFF calculation, were modeled in the curvefit. N_{idp} =21, ΔR = 1.1 – 3.7 Å, Δk = 2.3 – 14.9 Å^{-1}. [c]The σ^2 values were constrained to the same parameter. The value of S_o^2 was fixed at 0.8, in accordance with previous analyses of Cu(I) standards and Cu-based clusters,[26-27] ΔE_0 was refined as a global fit parameter, yielding ΔE_o = 6.0(4) eV. Uncertainties are shown in parentheses; values without uncertainties were fixed during curvefitting.

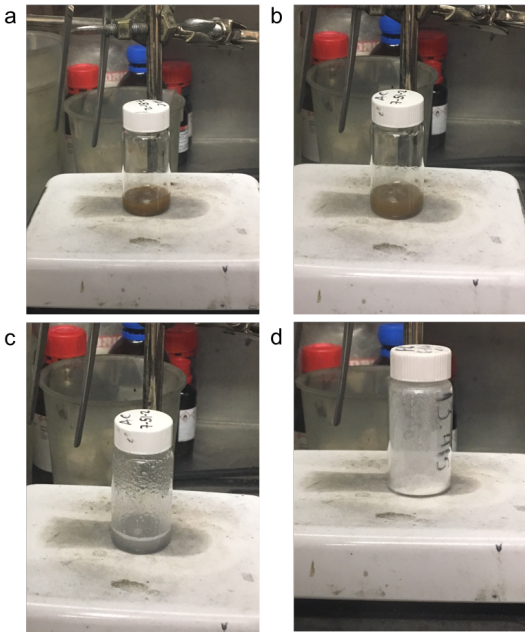

Figure A3.23. Photographs following the progress of the reaction between $CuCl_2$ and $HS(CH_2)_{11}CH_3$ (4 equiv) in dibenzyl ether (2 mL) at various reaction times. (a) $CuCl_2$ in dibenzyl ether, (b) 20 s after addition of thiol, (c) 20 min, (d) isolated powder of **3.1**.

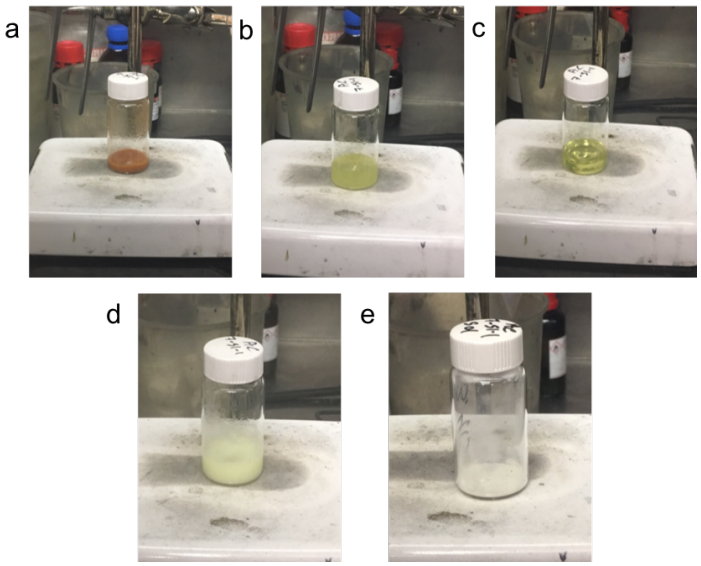

Figure A3.24. Photographs following the progress of the reaction between $CuCl_2$ and $HS(CH_2)_{11}CH_3$ (4 equiv) in THF (2 mL) at various reaction times. (a) $CuCl_2$ in THF, (b) 20 s after addition of thiol, (c) 5 min, (d) 20 min, (e) isolated powder of **3.1**.

3.6 References

(1) Jin, R.; Zeng, C.; Zhou, M.; Chen, Y., Atomically Precise Colloidal Metal Nanoclusters and Nanoparticles: Fundamentals and Opportunities. *Chem. Rev.* **2016**, *116*, 10346-10413.

(2) Heaven, M. W.; Dass, A.; White, P. S.; Holt, K. M.; Murray, R. W., Crystal structure of the gold nanoparticle $[N(C_8H_{17})_4][Au_{25}(SCH_2CH_2Ph)_{18}]$. *J. Am. Chem. Soc.* **2008**, *130*, 3754-5.

(3) Zhu, M.; Aikens, C. M.; Hollander, F. J.; Schatz, G. C.; Jin, R., Correlating the crystal structure of a thiol-protected Au_{25} cluster and optical properties. *J. Am. Chem. Soc.* **2008**, *130*, 5883-5.

(4) Qian, H.; Eckenhoff, W. T.; Zhu, Y.; Pintauer, T.; Jin, R., Total Structure Determination of Thiolate-Protected Au_{38} Nanoparticles. *J. Am. Chem. Soc.* **2010**, *132*, 8280-8281.

(5) Qian, H.; Jin, R., Ambient Synthesis of $Au_{144}(SR)_{60}$ Nanoclusters in Methanol. *Chem. Mater.* **2011**, *23*, 2209-2217.

(6) Zeng, C.; Chen, Y.; Kirschbaum, K.; Lambright, K. J.; Jin, R., Emergence of hierarchical structural complexities in nanoparticles and their assembly. *Science* **2016**, *354*, 1580-1584.

(7) Sakthivel, N. A.; Theivendran, S.; Ganeshraj, V.; Oliver, A. G.; Dass, A., Crystal Structure of Faradaurate-279: $Au_{279}(SPh\text{-}tBu)_{84}$ Plasmonic Nanocrystal Molecules. *J. Am. Chem. Soc.* **2017**, *139*, 15450-15459.

(8) Joshi, C. P.; Bootharaju, M. S.; Alhilaly, M. J.; Bakr, O. M., $[Ag_{25}(SR)_{18}]^-$: The "Golden" Silver Nanoparticle. *J. Am. Chem. Soc.* **2015**, *137*, 11578-11581.

(9) Desireddy, A.; Conn, B. E.; Guo, J.; Yoon, B.; Barnett, R. N.; Monahan, B. M.; Kirschbaum, K.; Griffith, W. P.; Whetten, R. L.; Landman, U.; Bigioni, T. P., Ultrastable silver nanoparticles. *Nature* **2013**, *501*, 399-402.

(10) Yang, H.; Wang, Y.; Huang, H.; Gell, L.; Lehtovaara, L.; Malola, S.; Hakkinen, H.; Zheng, N., All-thiol-stabilized Ag_{44} and $Au_{12}Ag_{32}$ nanoparticles with single-crystal structures. *Nat. Commun.* **2013**, *4*, 2422.

(11) Luo, Y.-R., Bond Dissociation Energies. In *CRC Handbook of Chemistry and Physics*, 89th ed.; Lide, D. R., Ed. CRC Press/Taylor and Francis: Boca Raton, FL, 2009.

(12) Fuhr, O.; Fernandez-Recio, L.; Fenske, D., New Copper Chalcogenide Clusters with a Selenide Core and a Sulfide Shell. *Eur. J. Inorg. Chem.* **2005**, *2005*, 2306-2314.

(13) Langer, R.; Yadav, M.; Weinert, B.; Fenske, D.; Fuhr, O., Luminescence in Functionalized Copper Thiolate Clusters – Synthesis and Structural Effects. *Eur. J. Inorg. Chem.* **2013**, *2013*, 3623-3631.

(14) Wang, Z.; Chen, B.; Rogach, A. L., Synthesis, optical properties and applications of light-emitting copper nanoclusters. *Nanoscale Horiz.* **2017**, *2*, 135-146.

(15) Das, N. K.; Ghosh, S.; Priya, A.; Datta, S.; Mukherjee, S., Luminescent Copper Nanoclusters as a Specific Cell-Imaging Probe and a Selective Metal Ion Sensor. *J. Phys. Chem. C* **2015**, *119*, 24657-24664.

(16) Lin, Y.-J.; Chen, P.-C.; Yuan, Z.; Ma, J.-Y.; Chang, H.-T., The isomeric effect of mercaptobenzoic acids on the preparation and fluorescence properties of copper nanoclusters. *Chem. Commun.* **2015**, *51*, 11983-11986.
(17) Ai, L.; Jiang, W.; Liu, Z.; Liu, J.; Gao, Y.; Zou, H.; Wu, Z.; Wang, Z.; Liu, Y.; Zhang, H.; Yang, B., Engineering a red emission of copper nanocluster self-assembly architectures by employing aromatic thiols as capping ligands. *Nanoscale* **2017**, *9*, 12618-12627.
(18) Wei, W.; Lu, Y.; Chen, W.; Chen, S., One-Pot Synthesis, Photoluminescence, and Electrocatalytic Properties of Subnanometer-Sized Copper Clusters. *J. Am. Chem. Soc.* **2011**, *133*, 2060-2063.
(19) Nguyen, T.-A. D.; Cook, A. W.; Wu, G.; Hayton, T. W., Subnanometer-Sized Copper Clusters: A Critical Re-evaluation of the Synthesis and Characterization of $Cu_8(MPP)_4$ (HMPP = 2-Mercapto-5-*n*-propylpyrimidine). *Inorg. Chem.* **2017**, *56*, 8390-8396.
(20) Wu, Z.; Liu, J.; Gao, Y.; Liu, H.; Li, T.; Zou, H.; Wang, Z.; Zhang, K.; Wang, Y.; Zhang, H.; Yang, B., Assembly-Induced Enhancement of Cu Nanoclusters Luminescence with Mechanochromic Property. *J. Am. Chem. Soc.* **2015**, *137*, 12906-12913.
(21) Wu, Z.; Liu, H.; Li, T.; Liu, J.; Yin, J.; Mohammed, O. F.; Bakr, O. M.; Liu, Y.; Yang, B.; Zhang, H., Contribution of Metal Defects in the Assembly Induced Emission of Cu Nanoclusters. *J. Am. Chem. Soc.* **2017**, *139*, 4318-4321.
(22) Liu, Y.; Yao, D.; Zhang, H., Self-Assembly Driven Aggregation-Induced Emission of Copper Nanoclusters: A Novel Technology for Lighting. *ACS Appl. Mater. Interfaces* **2018**, *10*, 12071-12080.
(23) Wang, Z.; Chen, B.; Rogach, A. L., Synthesis, optical properties and applications of light-emitting copper nanoclusters. *Nanoscale Horiz.* **2017**, *2*, 135-146.
(24) Nguyen, T.-A. D.; Jones, Z. R.; Goldsmith, B. R.; Buratto, W. R.; Wu, G.; Scott, S. L.; Hayton, T. W., A Cu_{25} Nanocluster with Partial Cu(0) Character. *J. Am. Chem. Soc.* **2015**, *137*, 13319-13324.
(25) Cook, A. W.; Nguyen, T.-A. D.; Buratto, W. R.; Wu, G.; Hayton, T. W., Synthesis, Characterization, and Reactivity of the Group 11 Hydrido Clusters $[Ag_6H_4(dppm)_4(OAc)_2]$ and $[Cu_3H(dppm)_3(OAc)_2]$. *Inorg. Chem.* **2016**, *55*, 12435-12440.
(26) Nguyen, T.-A. D.; Jones, Z. R.; Leto, D. F.; Wu, G.; Scott, S. L.; Hayton, T. W., Ligand-Exchange-Induced Growth of an Atomically Precise Cu_{29} Nanocluster from a Smaller Cluster. *Chem. Mater.* **2016**, *28*, 8385-8390.
(27) Cook, A. W.; Jones, Z. R.; Wu, G.; Scott, S. L.; Hayton, T. W., An Organometallic Cu_{20} Nanocluster: Synthesis, Characterization, Immobilization on Silica, and "Click" Chemistry. *J. Am. Chem. Soc.* **2018**, *140*, 394-400.
(28) Chakrahari, K. K.; Liao, J.-H.; Kahlal, S.; Liu, Y.-C.; Chiang, M.-H.; Saillard, J.-Y.; Liu, C. W., $[Cu_{13}\{S_2CN^nBu_2\}_6(acetylide)_4]^+$: A Two-Electron Superatom. *Angew. Chem., Int. Ed.* **2016**, *55*, 14704-14708.
(29) Weßing, J.; Ganesamoorthy, C.; Kahlal, S.; Marchal, R.; Gemel, C.; Cador, O.; Da Silva, A. C. H.; Da Silva, J. L. F.; Saillard, J.-Y.; Fischer, R. A., The Mackay-Type Cluster $[Cu_{43}Al_{12}](Cp^*)_{12}$: Open-Shell 67-Electron Superatom with Emerging Metal-Like Electronic Structure. *Angew. Chem., Int. Ed.* **2018**, *57*, 14630-14634.

(30) Yuan, P.; Chen, R.; Zhang, X.; Chen, F.; Yan, J.; Sun, C.; Ou, D.; Peng, J.; Lin, S.; Tang, Z.; Teo, B. K. K.; Zheng, L.-S.; Zheng, N., Ether-soluble Cu_{53} Nanoclusters as an Effective Precursor of High-quality CuI Films for Optoelectronic Applications. *Angew. Chem., Int. Ed.* **2019**, *58*, 835-839.
(31) Hasan, M.; Bethell, D.; Brust, M., The Fate of Sulfur-Bound Hydrogen on Formation of Self-Assembled Thiol Monolayers on Gold: ^{1}H NMR Spectroscopic Evidence from Solutions of Gold Clusters. *J. Am. Chem. Soc.* **2002**, *124*, 1132-1133.
(32) Biesinger, M. C., Advanced analysis of copper X-ray photoelectron spectra. *Surf. Interface Anal.* **2017**, *49*, 1325-1334.
(33) C. D. Wagner, A. V. N., A. Kraut-Vass, J. W. Allison, C. J. Powell, J. R. Rumble Jr. NIST Standard Reference Database 20, Version 3.4 (web version). http://srdata.nist.gov/xps/.
(34) Janssen, M. D.; Spek, A. L.; Grove, D. M.; van Koten, G., A Mixed (Arenethiolato)copper(I)/Copper Bromide Aggregate: X-ray Structure of Octanuclear $[Cu_8\{SC_6H_3(CH_2NMe_2)_2\text{-}2,6\}_3Br_5]$. *Inorg. Chem.* **1996**, *35*, 4078-4081.
(35) Parish, R. V.; Salehi, Z.; Pritchard, R. G., Five-Coordinate Sulfur in a Polymeric Copper(I) Thiolate Complex. *Angew. Chem., Int. Ed. Engl.* **1997**, *36*, 251-253.
(36) G. Prichard, R.; V. Parish, R.; Salehi, Z., Self-assembling copper(I) clusters involving electron-deficient, quadruply bridging thiolate ligands. *J. Chem. Soc., Dalton Trans.* **1999**, 243-250.
(37) Li, D.; Wu, T.; Zhou, X.-P.; Zhou, R.; Huang, X.-C., Twelve-Connected Net with Face-Centered Cubic Topology: A Coordination Polymer Based on $[Cu_{12}(\mu_4\text{-}SCH_3)_6]^{6+}$ Clusters and CN^- Linkers. *Angew. Chem., Int. Ed.* **2005**, *44*, 4175-4178.
(38) Qian, H.; Zhu, Y.; Jin, R., Atomically precise gold nanocrystal molecules with surface plasmon resonance. *Proc. Natl. Acad. Sci. U.S.A.* **2012**, *109*, 696-700.
(39) Scholz, S.; Lerner, H.-W.; Bolte, M., Chlorotripyridinecopper(I). *Acta Cryst. E.* **2002**, *58*, m72-m73.
(40) Brookhart, M.; Grant, B.; Volpe, A. F., $[(3,5\text{-}(CF_3)_2C_6H_3)_4B]^-[H(OEt_2)_2]^+$: A Convenient Reagent for Generation and Stabilization of Cationic, Highly Electrophilic Organometallic Complexes. *Organometallics* **1992**, *11*, 3920-3922.
(41) Jutzi, P.; Müller, C.; Stammler, A.; Stammler, H.-G., Synthesis, Crystal Structure, and Application of the Oxonium Acid $[H(OEt_2)_2]^+[B(C_6F_5)_4]$. *Organometallics* **2000**, *19*, 1442-1444.
(42) Pietikäinen, J.; Maaninen, A.; Laitinen, R. S.; Oilunkaniemi, R.; Valkonen, J., Halogenation of tellurium by SO_2Cl_2. Formation and crystal structures of $(H_3O)[Te_3Cl_{13}]\cdot 1/2SO_2$, $[(C_4H_8O)_2H][TeCl_5]\cdot(C_4H_8O)$, $[(Me_2SO)_2H]_2[TeCl_6]$, and $[Ni(NCCH_3)_6][Te_2Cl_{10}]$. *Polyhedron* **2002**, *21*, 1089-1095.
(43) Krossing, I.; Reisinger, A., Perfluorinated Alkoxyaluminate Salts of Cationic Brønsted Acids: Synthesis, Structure, and Characterization of $[H(OEt_2)_2][Al\{OC(CF_3)_3\}_4]$ and $[H(THF)_2][Al\{OC(CF_3)_3\}_4]$. *Eur. J. Inorg. Chem.* **2005**, *2005*, 1979-1989.
(44) Schnaars, D. D.; Wu, G.; Hayton, T. W., Reactivity of $UI_4(OEt_2)_2$ with phenols: probing the chemistry of the U–I bond. *Dalton Trans.* **2009**, 3681-3687.

(45) Nachtigall, O.; Pataki, A.; Molski, M.; Lentz, D.; Spandl, J., Solvates of Manganese Trichloride Revisited - Synthesis, Isolation, and Crystal Structure of $MnCl_3(THF)_3$. *Z. Anorg. Allg. Chem.* **2015**, *641*, 1164-1168.
(46) Stasko, D.; Hoffmann, S. P.; Kim, K.-C.; Fackler, N. L. P.; Larsen, A. S.; Drovetskaya, T.; Tham, F. S.; Reed, C. A.; Rickard, C. E. F.; Boyd, P. D. W.; Stoyanov, E. S., Molecular Structure of the Solvated Proton in Isolated Salts. Short, Strong, Low Barrier (SSLB) H-bonds. *J. Am. Chem. Soc.* **2002**, *124*, 13869-13876.
(47) Hazin, K.; Serin, S. C.; Patrick, B. O.; Ezhova, M. B.; Gates, D. P., $[HL_2][P(1,2\text{-}O_2C_6Cl_4)_3]$ (L = THF, DMF): Brønsted acid initiators for the polymerization of n-butyl vinyl ether and p-methoxystyrene. *Dalton Trans.* **2017**, *46*, 5901-5910.
(48) Nguyen, T.-A. D.; Goldsmith, B. R.; Zaman, H. T.; Wu, G.; Peters, B.; Hayton, T. W., Synthesis and Characterization of a Cu_{14} Hydride Cluster Supported by Neutral Donor Ligands. *Chem. – Eur. J.* **2015**, *21*, 5341-5344.
(49) Dehnen, S.; Fenske, D.; Deveson, A. C., $[Cu_{12}S_6(P^nPr_3)_8]$ and $[Cu_{20}S_{10}(P^nBu_1Bu_2)_8]$: Two sulfur bridged copper clusters with Cu-s cluster cores of known compositions but new structures. *J. Cluster Sci.* **1996**, *7*, 351-369.
(50) Yang, X.-X.; Issac, I.; Lebedkin, S.; Kühn, M.; Weigend, F.; Fenske, D.; Fuhr, O.; Eichhöfer, A., Red-luminescent biphosphine stabilized '$Cu_{12}S_6$' cluster molecules. *Chem. Commun.* **2014**, *50*, 11043-11045.
(51) Eichhöfer, A.; Buth, G.; Lebedkin, S.; Kühn, M.; Weigend, F., Luminescence in Phosphine-Stabilized Copper Chalcogenide Cluster Molecules—A Comparative Study. *Inorg. Chem.* **2015**, *54*, 9413-9422.
(52) Salehi, Z.; V. Parish, R.; G. Pritchard, R., A polymeric cationic copper(I) complex involving a quadruply bridging, zwitterionic thiolate ligand: $\{[Cu_8Cl_6(SCH_2CH_2NH_3)_6]Cl_2\}$. *J. Chem. Soc., Dalton Trans.* **1997**, 4241-4246.
(53) Block, E.; Kang, H.; Ofori-Okai, G.; Zubieta, J., The crystal and molecular structure of a tetranuclear copper thiolate cluster, $[Cu\{SC_6H_3\text{-}2,6\text{-}(SiMe_3)_2\}]_4$. *Inorg. Chim. Acta* **1990**, *167*, 147-148.
(54) Schröter-Schmid, I. S., J., Synthese und Struktur von Thiolatokomplexen des einwertigen Kupfers: Tetrameres und Octameres $|CuSC_6H_2(^iPr)_3|$. *Z. Naturforsch.* **1990**, *45b*, 1537 - 1542
(55) Dance, I. G.; Calabrese, J. C., The crystal and molecular structure of the hexa-(μ_2-benzenethiolato)tetracuprate(I) dianion. *Inorg. Chim. Acta* **1976**, *19*, L41-L42.
(56) Coucouvanis, D.; Murphy, C. N.; Kanodia, S. K., Metal-mercaptide chemistry. The synthesis and structural characterization of the $[Cu(SC_6H_5)_3]^{2-}$ anion. A rational synthesis and the structure of the $[Cu_4(SC_6H_5)_6]^{2-}$ cluster. *Inorg. Chem.* **1980**, *19*, 2993-2998.
(57) Dance, I. G.; Bowmaker, G. A.; Clark, G. R.; Seadon, J. K., The formation and crystal and molecular structures of hexa(μ-organothiolato)tetracuprate(I) cage dianions: bis-(tetramethylammonium)hexa-(μ-methanethiolato)tetracuprate(I) and two polymorphs of bis(tetramethylammonium)hexa-(μ-benzenethiolato)-tetracuprate(I). *Polyhedron* **1983**, *2*, 1031-1043.
(58) Baumgartner, M.; Schmalle, H.; Dubler, E., Synthesis, characterization and crystal structure of copper(I) thiolates: $[(C_6H_5)_4P^+]_2[Cu_4(C_2H_5S^-)_6]\cdot 0.5C_2H_6O_2$ and $[(C_6H_5)_4P^+][Cu_7(C_2H_5S^-)_8]$. *Polyhedron* **1990**, *9*, 1155-1164.

(59) Baumgartner, M.; Schmalle, H.; Baerlocher, C., Synthesis, Characterization, and Crystal Structure of Three Homoleptic Copper(I) Thiolates: $(Cu(CH_3S^-))_\infty$, $[(C_6H_5)_4P^+]_2[Cu_5(CH_3S^-)_7] \cdot C_2H_6O_2$, and $[(C_3H_7)_4N^+]_2[Cu_4(CH_3S^-)_6 \cdot CH_4O$. *J. Solid State Chem.* **1993**, *107*, 63-75.

(60) Fujisawa, K.; Imai, S.; Suzuki, S.; Moro-oka, Y.; Miyashita, Y.; Yamada, Y.; Okamoto, K.-i., M–S vibrational study in three-coordinate thiolato compounds $(NEt_4)_2[M(SC_6H_4\text{-}p\text{-}X)_3]$ and $(NEt_4)_2[M_4(\mu\text{-}SC_6H_4\text{-}p\text{-}Cl)_6]$: M=Cu(I) and Ag(I), X=Cl and Br. *J. Inorg. Biochem.* **2000**, *82*, 229-238.

(61) Zeevi, S.; Tshuva, E. Y., Synthesis and X-ray Characterization of Mono- and Polynuclear Thiolatocopper(I) Complexes: The Effect of Steric Bulk on Coordination Number and Nuclearity. *Eur. J. Inorg. Chem.* **2007**, *2007*, 5369-5376.

(62) Kohner-Kerten, A.; Tshuva, E. Y., Preparation and X-ray characterization of two-coordinate Cu(I) complex of aliphatic thiolato ligand: Effect of steric bulk on coordination features. *J. Organomet. Chem.* **2008**, *693*, 2065-2068.

(63) Dance, I. G., Formation and X-ray structure of the hexa(t-butylthiolato)pentacuprate(I) monoanion. *J. Chem. Soc., Chem. Commun.* **1976**, 68-69.

(64) Bowmaker, G. A.; Clark, G. R.; Seadon, J. K.; Dance, I. G., The formation and structural chemistry of the hexa(μ-*t*-butylthiolato) pentacuprate(I) cage anion with triethylammonium and tetraethylammonium cations. *Polyhedron* **1984**, *3*, 535-544.

(65) Fujisawa, K.; Imai, S.; Kitajima, N.; Moro-oka, Y., Preparation, Spectroscopic Characterization, and Molecular Structure of Copper(I) Aliphatic Thiolate Complexes. *Inorg. Chem.* **1998**, *37*, 168-169.

(66) Dance, I. G., The hepta(μ_2-benzenethiolato)pentacuprate(I) dianion; X-ray crystal and molecular structure. *J. Chem. Soc., Chem. Commun.* **1976**, 103b-104.

(67) Dance, I., The Hepta(μ-benzenethiolato)pentametallate(I) dianions of copper and silver: Formation and crystal structures. *Aust. J. Chem.* **1978**, *31*, 2195-2206.

(68) Ferrara, S. J.; Mague, J. T.; Donahue, J. P., Synthesis and Structures of Cuprous Triptycylthiolate Complexes. *Inorg. Chem.* **2012**, *51*, 6567-6576.

(69) Yang, Q.; Tang, K.; Liao, H.; Han, Y.; Chen, Z.; Tang, Y., Synthesis and X-ray crystal structure of $[Cu(SC_6H_2{}^iPr_3)]_8$. *J. Chem. Soc., Chem. Commun.* **1987**, 1076-1077.

(70) Block, E.; Gernon, M.; Kang, H.; Ofori-Okai, G.; Zubieta, J., Coordination chemistry of sterically hindered thiolate ligands. Preparation and structural characterization of the oligomeric homoleptic complexes $[Cu(S_6H_4\text{-}o\text{-}SiMe_3)]_{12}$ and $[\{Ag(SC_6H_4\text{-}o\text{-}SiMe_3)\}_4]_2$ and a comparison to the structure of the cadmium mononuclear species $(Et_4N)_2[Cd(SC_6H_4\text{-}o\text{-}SiMe_3)_4]$. *Inorg. Chem.* **1989**, *28*, 1263-1271.

(71) Blower, P. J.; Dilworth, J. R., Thiolato-complexes of the transition metals. *Coord. Chem. Rev.* **1987**, *76*, 121-185.

(72) Vortisch, V.; Kroneck, P.; Hemmerich, P., Model studies on the coordination of copper in enzymes. IV. Structure and stability of cuprous complexes with sulfur-containing ligands. *J. Am. Chem. Soc.* **1976**, *98*, 2821-2826.

(73) Tang, K.; Aslam, M.; Block, E.; Nicholson, T.; Zubieta, J., Steric control of aggregation in neutral silver(I) thiolates, $[AgSR]_n$. Crystal and molecular structures of $[AgSCH(SiMe_3)_2]_8$, a discrete molecular biscycle of weakly interacting

$[AgSCH(SiMe_3)_2]_4$ units, and of $[AgSC(SiPhMe_2)_3]_3$ and $[AgSC(SiMe_3)_3]_4$, discrete molecular monocycles containing linearly coordinated silver(I) and doubly bridging mercapto sulfur donors from novel sterically hindered thiolate ligands. A comparison with the nonmolecular structure of $[Ag_4\{SCH_2(SiMe_3)\}_3]_n$[1]. *Inorg. Chem.* **1987**, *26*, 1488-1497.

(74) Dance, I. G.; Fisher, K. J.; Banda, R. M. H.; Scudder, M. L., Layered structure of crystalline compounds silver thiolates (AgSR). *Inorg. Chem.* **1991**, *30*, 183-187.

(75) Bratsch, S. G., Standard Electrode Potentials and Temperature Coefficients in Water at 298.15 K. *J. Phys. Chem. Ref. Data* **1989**, *18*, 1-21.

(76) Dance, I. G., Crystallization and structure of bis(tetramethylammonium) octakis(benzenethiolato)hexaargentate(I), extending the series of cages $[M_4(SPh)_6]^{2-}$, $[M_5(SPh)_7]^{2-}$, $[M_6(SPh)_8]^{2-}$, and $[M_{12}(SPh)_{16}]^{4-}$. *Inorg. Chem.* **1981**, *20*, 1487-1492.

(77) Battisti, A.; Bellina, O.; Diversi, P.; Losi, S.; Marchetti, F.; Zanello, P., Preparation, Structure and Reactivity of Polynuclear Gold(I) Phosphanyl Alkanethiolates. *Eur. J. Inorg. Chem.* **2007**, *2007*, 865-875.

(78) Al-Sa'ady, A. K. H.; Moss, K.; McAuliffe, C. A.; Parish, R. V., Mössbauer and nuclear magnetic resonance spectroscopic studies on 'Myocrisin', 'Solganol', 'Auranofin', and related gold(I) thiolates. *J. Chem. Soc., Dalton Trans.* **1984**, 1609-1616.

(79) Kyle, K. R.; Palke, W. E.; Ford, P. C., The photoluminescence properties of the copper(I) clusters $Cu_4I_4A_4$ (A = aromatic amine) in solution. *Coord. Chem. Rev.* **1990**, *97*, 35-46.

(80) Knotter, D. M.; Blasse, G.; Van Vliet, J. P. M.; Van Koten, G., Luminescence of copper(I) arenethiolates and its relation to copper(I) luminescence in other complexes. *Inorg. Chem.* **1992**, *31*, 2196-2201.

(81) Ford, P. C.; Vogler, A., Photochemical and Photophysical Properties of Tetranuclear and Hexanuclear Clusters of Metals with d^{10} and s^2 Electronic Configurations. *Acc. Chem. Res.* **1993**, *26*, 220-226.

(82) Ford, P. C.; Cariati, E.; Bourassa, J., Photoluminescence Properties of Multinuclear Copper(I) Compounds. *Chem. Rev.* **1999**, *99*, 3625-3648.

(83) Wang, X.-L.; Qin, C.; Wang, E.-B.; Su, Z.-M.; Li, Y.-G.; Xu, L., Self-Assembly of Nanometer-Scale $[Cu_{24}I_{10}L_{12}]^{14+}$ Cages and Ball-Shaped Keggin Clusters into a (4,12)-Connected 3D Framework with Photoluminescent and Electrochemical Properties. *Angew. Chem., Int. Ed.* **2006**, *45*, 7411-7414.

(84) Maiti, B. K.; Pal, K.; Sarkar, S., Flexible CuI–Thiolate Clusters with Relevance to Metallothioneins. *Eur. J. Inorg. Chem.* **2007**, *2007*, 5548-5555.

(85) Li, Z.; Li, X.; Lin, P.; Du, S., Self-assembly of 1D Coordination Polymers Containing Copper(I) tert-butylthiolato Clusters: Structural Characterization and Properties. *J. Cluster Sci.* **2008**, *19*, 357-366.

(86) Troyano, J.; Perles, J.; Amo-Ochoa, P.; Martínez, J. I.; Concepción Gimeno, M.; Fernández-Moreira, V.; Zamora, F.; Delgado, S., Luminescent Thermochromism of 2D Coordination Polymers Based on Copper(I) Halides with 4-Hydroxythiophenol. *Chem. – Eur. J.* **2016**, *22*, 18027-18035.

(87) Cook, A. W.; Wu, G.; Hayton, T. W., A Re-examination of the Synthesis of Monolayer-Protected $Co_x(SCH_2CH_2Ph)_m$ Nanoclusters: Unexpected Formation of

a Thiolate-Protected Co(II) T3 Supertetrahedron. *Inorg. Chem.* **2018**, *57*, 8189-8194.
(88) Ravel, B.; Newville, M., ATHENA, ARTEMIS, HEPHAESTUS: data analysis for X-ray absorption spectroscopy using IFEFFIT. *J. Synchrotron Rad.* **2005**, *12*, 537-541.
(89) Higuchi, O.; Tateshita, K.; Nishimura, H., Antioxidative Activity of Sulfur-Containing Compounds in Allium Species for Human Low-Density Lipoprotein (LDL) Oxidation in Vitro. *J. Agric. Food Chem.* **2003**, *51*, 7208-7214.
(90) *SMART Apex II, Version 2.1*. Bruker AXS Inc.: Madison, WI, 2005.
(91) *SAINT Software User's Guide, Version 7.34a*. Bruker AXS Inc.: Madison, WI, 2005.
(92) Sheldrick, G. M., *SADABS*. University of Göttingen: Göttingen, Germany, 2005.
(93) *SHELXTL PC, Version 6.12*. Bruker AXS Inc.: Madison, WI, 2005.

Chapter 4. An Organometallic Cu_{20} Nanocluster: Synthesis, Characterization, Immobilization on Silica, and "Click" Chemistry

Portions of this work were published in:

Andrew W. Cook, Zachary R. Jones, Guang Wu, Susannah L. Scott, and Trevor W. Hayton. An Organometallic Cu_{20} Nanocluster: Synthesis, Characterization, Immobilization on Silica, and "Click" Chemistry. *J. Am. Chem. Soc.* **2018**, *140*, 394-400.

Table of Contents

4.1 Introduction

Atomically-precise nanoclusters (APNCs) have been the subject of intense interest over the past decade for their use in a variety of emerging technological applications, including catalysis.[1-7] Significantly, their perfectly mono-disperse and atomically-precise nature permits their complete structural characterization, facilitating the development of detailed structure/activity relationships (SARs).[8-11] Yet, while the study of APNCs could uncover new insights in catalysis, many APNCs are actually not well-suited for this purpose. For example, the vast majority of the known nanoclusters have been synthesized with a passivating shell of thiolate capping ligands.[12] While such ligands impart significant thermal and chemical stability to APNCs, and are often required to render the APNCs isolable, they block active sites, and must be partially removed before catalysis can occur.[13-15] At the same time, the strength of the metal-sulfur bond often makes it difficult to remove the thiolate ligands efficiently.[16-18] For example, Jin and co-workers reported that pre-treatment of $Au_{25}(SR)_{18}/CeO_2$ (R = C_2H_4Ph) with O_2 at 150 °C was required to activate the material for catalytic CO oxidation.[19] Similarly, pre-treatment of $Au_{25}(SR)_{18}/TiO_2$ at 300 °C was required to activate this material for the catalytic semi-hydrogenation of internal alkynes.[20] The need for harsh conditions is significant because they can cause irreversible changes in the structure and/or nuclearity of the APNCs, which dramatically diminishes the ability to extract robust SARs using APNC catalysts. Notably, in both of the examples described above, the catalyst structure during and/or after activation was not determined.

To address this challenge, several research groups are developing APNCs which are not passivated by thiolate ligands, and which, in principle, should not require harsh pre-treatment for activation.[21] These organometallic APNCs are most commonly stabilized with hydrides

(i.e., H^-) as capping ligands,[22-27] and more recently, acetylides (i.e., $RC{\equiv}C^-$).[28-40] For example, The Hayton group has reported the syntheses of $[Cu_{25}H_{22}(PPh_3)_{12}]Cl$ and $[Cu_{29}Cl_4H_{22}(Ph_2phen)_{12}]Cl$ (Ph_2phen = 4,7-diphenyl-1,10-phenanthroline), both of which are ligated by a mix of hydride and neutral Lewis base ligands.[25, 27] Similarly, Liu and co-workers recently synthesized the copper acetylide nanocluster $[Cu_{13}\{S_2CN^nBu_2\}_6(CCR)_4][PF_6]$ (R = C(O)OMe, C_6H_4F) (Figure 4.1A), Zhang and co-workers generated the silver acetylide cluster $Ag_{74}(CCPh)_{44}$, and Wang and co-workers prepared the gold acetylide APNC $[Au_{19}(CCPh)_9(Hdppa)_3](SbF_6)_2$ (Hdppa = N,N-*bis*(diphenylphosphino)amine) (Figure 4.1B).[28, 33, 39]

Preliminary results suggest that organometallic APNCs are more reactive than their thiolate-capped cousins. For example, $[Au_{24}Ag_{20}(SPy)_4(CCPh)_{20}Cl_2]$ (SPy = 2-pyridylthiolate) was observed to release its phenylacetylide capping ligands at relatively low temperatures (~100 °C), although the cluster was not screened for any catalytic reactivity.[31] Also of note, Zheng and co-workers claimed that $[Au_{34}Ag_{28}(CCPh)_{34}]$ supported on XC-72 carbon was active for catalytic hydrolysis of triethylsilane without any pre-treatment.[41] One drawback of the above-mentioned study, however, is that the structure of the supported cluster was not interrogated. Therefore, it is still an open question whether organometallic APNCs maintain their structural integrity upon deposition onto a support. This concern is especially relevant for organometallic APNCs, given their higher thermal, oxygen, and water sensitivity, relative to thiolate-capped APNCs.[12, 41]

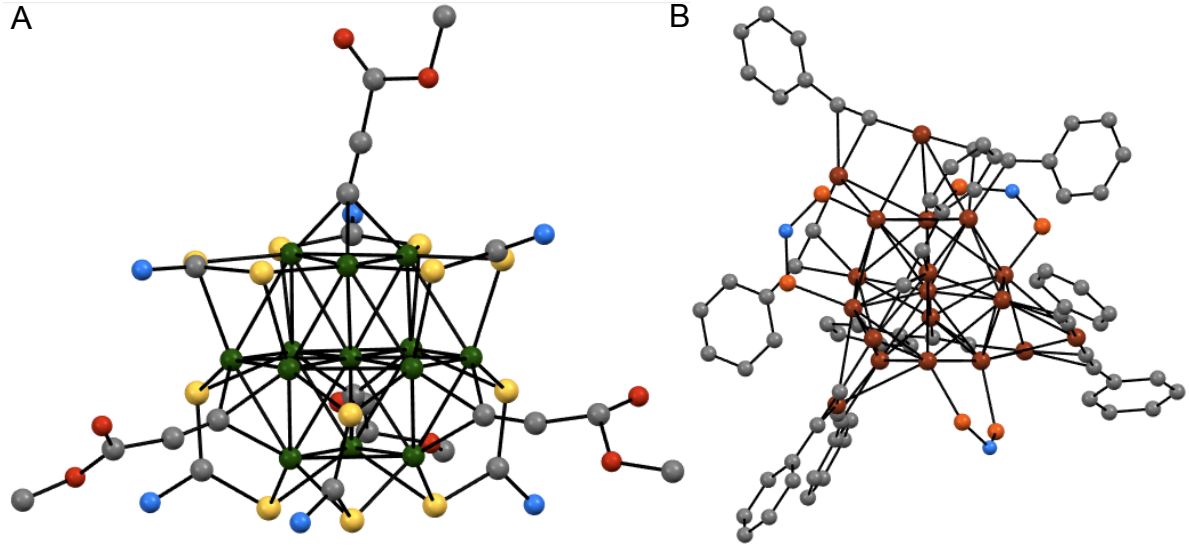

Figure 4.1. Ball and stick diagram of the group 11 acetylide superatoms $[Cu_{13}\{S_2CN^nBu_2\}_6(CCR)_4][PF_6]$ (R = C(O)OMe, C_6H_4F) (A, ref. 33) and $[Au_{19}(CCPh)_9(Hdppa)_3](SbF_6)_2$ (Hdppa = N,N-*bis*(diphenylphosphino)amine) (B, ref. 28). All hydrogen atoms, counter ions, solvate molecules, butyl groups in A, and phenyl groups on the Hdppa ligands in B have been omitted for clarity. Color legend: Cu = green; Au = brown; S = yellow; P = orange; N = blue; O = red; C = gray.

Herein, I report the synthesis and characterization of an unprecedented organometallic copper-based APNC, $[Cu_{20}(CCPh)_{12}(OAc)_6]$, and explore its ability to catalyze Huisgen [3+2] cycloadditions. Significantly, I find that the silica-immobilized cluster is a highly effective catalyst for this transformation. More importantly, the supported cluster is more stable under the "Click" reaction conditions than is the unsupported cluster. I have also confirmed that the supported cluster, both pre- and post-catalysis, has not undergone any major structural and/or nuclearity changes relative to the unsupported cluster. This research demonstrates for the first time that organometallic APNCs can maintain their structural integrity during catalysis, permitting the development of SARs for these unique nanomaterials.

4.2 Results and Discussion

4.2.1 Synthesis and Characterization of $[Cu_{20}(CCPh)_{12}(OAc)_6]$ (4.1)

Addition of 0.6 equiv of phenylacetylene (HCCPh) to a slurry of Cu(OAc) (1 equiv) in THF resulted in a rapid color change from pale green to bright yellow, characteristic of the known Cu(I) coordination polymer, $[Cu(CCPh)]_n$,[42] concomitant with the generation of HOAc.[42-43] Addition of 0.36 equiv of diphenylsilane (Ph_2SiH_2) to this slurry resulted in a gradual color change to dark red-brown, accompanied by the appearance of a dark brown powder. Work-up of the solution after stirring at room temperature for 15 h resulted in the isolation of the mixed-valent copper acetylide nanocluster, $[Cu_{20}(CCPh)_{12}(OAc)_6]$ (**4.1**), as a red-orange, crystalline solid in 49% yield (Scheme 4.1A). Copper metal is also formed during the reaction, and was isolated in 42% yield (based on Cu(OAc)) by filtration of the reaction mixture through a 0.2 μm PTFE filter. The presence of the by-product $Ph_2Si(OAc)_2$ was confirmed by ^1H NMR spectroscopy of the supernatant (Figure A4.2). For comparison, the only other Cu acetylide nanocluster, $[Cu_{13}\{S_2CN^nBu_2\}_6(CCR)_4][PF_6]$ (R = C(O)OMe, C_6H_4F), was formed during semihydrogenation of an alkyne by the Cu(I) hydride nanocluster $[Cu_{28}H_{15}\{S_2CN^nBu_2\}_{12}][PF_6]$.[33]

Scheme 4.1. Syntheses of Complex 4.1

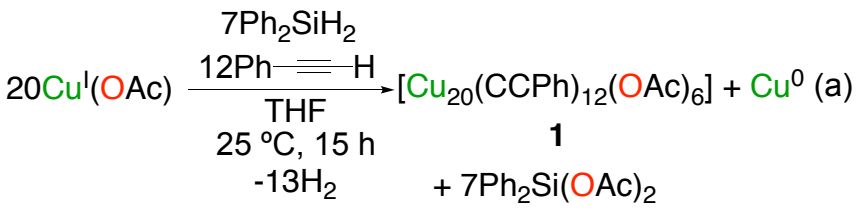

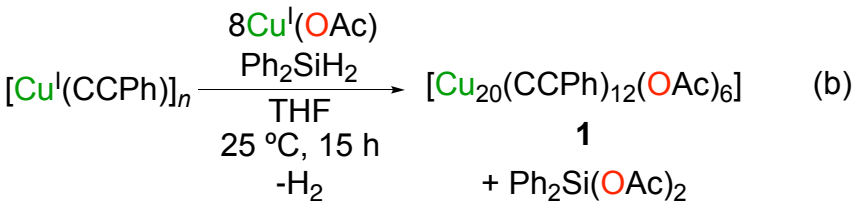

Complex **4.1** crystallizes as the THF adduct, **4.1**·C_4H_8O, as red blocks in the triclinic space group $P\bar{1}$ (Figure 4.2A). Four additional THF molecules are incorporated into the crystal lattice as solvates. In the solid state, **4.1**·C_4H_8O contains a tetrahedral $[Cu_4]^{2+}$ core (Figure 4.2B). Encapsulating the tetrahedral core is a $[Cu_{16}(CCPh)_{12}(OAc)_6]^{2-}$ shell. The Cu-Cu distances within the cluster span a large range (2.463(3) – 2.934(3) Å), similar to other structurally characterized copper nanoclusters.[25, 27, 33, 44-45] The twelve acetylide ligands incorporated into the $[Cu_{16}(CCPh)_{12}(OAc)_6]^{2-}$ shell are arranged in four [*cyclo*-Cu(CCPh)]$_3$ units, which are situated at the vertices of a tetrahedron (Figure 4.2C). One acetylide ligand features a μ_4:η^1,η^1,η^2,η^2 binding mode, four of the acetylide ligands feature a μ_3:η^1,η^1,η^2 binding mode, and seven feature a μ_4:η^1,η^1,η^1,η^2 binding mode. The six acetate ligands are bound in κ^2 fashion, are located on the edges of the tetrahedron, and feature an average Cu-O distance of 1.96(2) Å (Figure 4.2C). To the best of my knowledge, complex **4.1** is the first group 11 nanocluster to incorporate acetate co-ligands.[12] Additionally, a THF molecule is coordinated to Cu18, with a Cu–O bond distance of 2.47(1) Å. Consequently, complex **4.1**·C_4H_8O exhibits no symmetry in the solid state. However, NMR spectroscopic characterization in CD_2Cl_2 demonstrates that complex **4.1** exhibits idealized T_d symmetry in solution (*vide infra*), suggesting that this THF molecule is only weakly bound to the cluster. This observation also suggests that the acetylide ligands interconvert between the three observed binding modes.

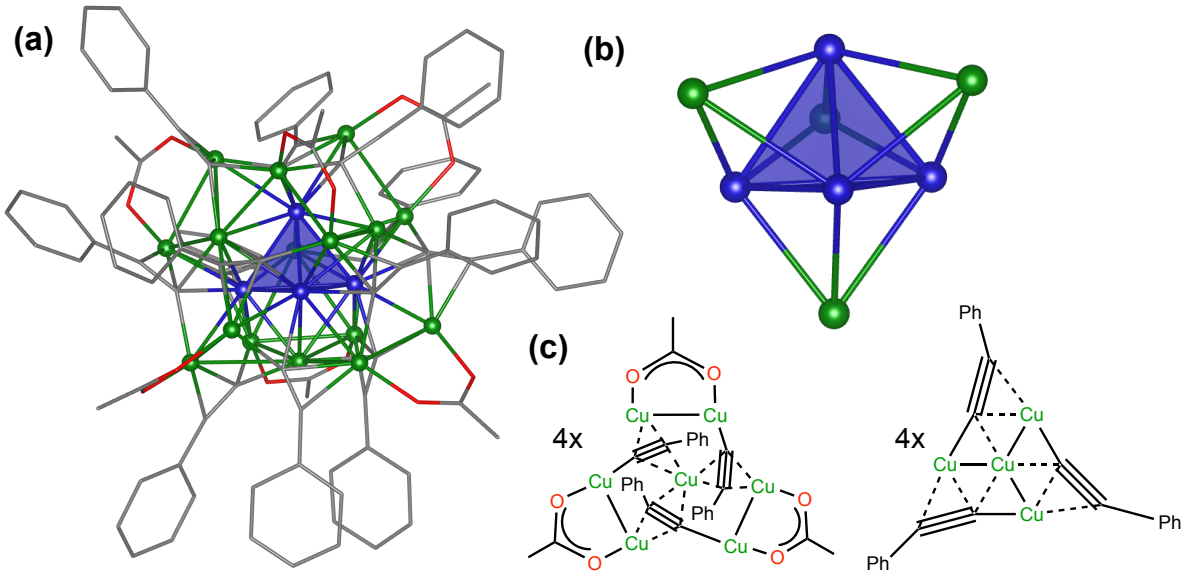

Figure 4.2. Ball and stick diagrams showing (a) complex **4.1**·C_4H_8O; (b) the tetrahedral Cu_4^{2+} core (blue), shown with face-capping copper atoms (green); and (c) illustrations of the ligand binding modes present in **4.1**·C_4H_8O. Hydrogen atoms, four THF solvate molecules and one coordinated THF molecule omitted for clarity. Color legend: Cu = blue, green; C = grey; O = red.

Interestingly, because there are only 18 anionic ligands (12 acetylides and six acetates), two of the 20 Cu atoms in **4.1** must have a formal oxidation state of 0 to maintain charge balance. Accordingly, complex **4.1** can be viewed as a superatom with a magic number N* = 2 and an $[M_4]^{2+}$ core.[1, 25, 27, 33-34, 40, 46-48] This is a relatively uncommon magic number, and a rare core structure, for group 11 superatoms.[39, 41, 44-45, 49-51] Almost all structurally characterized superatoms, such as the related copper acetylide superatom, $[Cu_{13}\{S_2CN^nBu_2\}_6(CCR)_4][PF_6]$,[33] contain metal-centered icosahedral, cuboctahedral, or anti-cuboctahedral cores.[12, 25, 27, 40, 45-51] In complex **4.1**, no such central metal atom is present, therefore the two "extra" electrons most likely occupy the a_1 symmetric bonding molecular orbital formed from the linear combination of the four Cu 4s orbitals within the tetrahedral

$[Cu_4]^{2+}$ core (Figure 4.3). The three t_2 symmetric orbitals remain unoccupied.[52] The unique core structure and incorporation of acetate ligands in **4.1** expands the structural diversity of copper superatoms, and raises the possibility that many more copper superatoms, with a wide variety of ligand types, should be isolable.

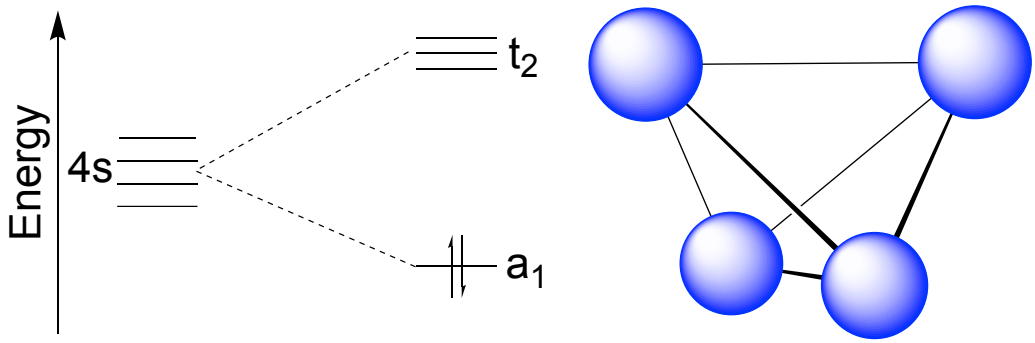

Figure 4.3. Proposed energy level diagram for the tetrahedral core of **4.1**.

Both the ^{1}H and ^{13}C{^{1}H} NMR spectra of **4.1** in CD_2Cl_2 are consistent with a T_d-symmetric structure in solution. For example, the ^{1}H NMR spectrum (Figure 4.4) of **4.1** features a singlet at 2.01 ppm, integrating for 18 protons, assigned to the six magnetically equivalent acetate ligands. In addition, resonances at 7.41, 7.15, and 6.95 ppm, integrating for 24, 12, and 24 protons, respectively, are assigned to the *o*-Ph, *p*-Ph, and *m*-Ph environments of 12 magnetically equivalent phenylacetylide ligands. The ^{13}C{^{1}H} NMR spectrum (Figure A4.1) of **4.1** features a resonance at 23.31 ppm, which is assigned to the methyl groups of the acetate co-ligands, while a resonance at 135.31 ppm is assigned to the Cu-bound acetylide carbons. Electrospray ionization mass spectroscopy (ESI-MS) of isolated complex **4.1** in THF, acquired in positive ion mode, is consistent with my proposed formulation (Figure A4.19). The major features, at *m/z* 2778.1309 and 2902.0662, correspond to $[M - OAc]^+$ (calcd *m/z* 2778.1221) and $[M + Cu]^+$ (calcd *m/z* 2902.0608) ions, respectively.

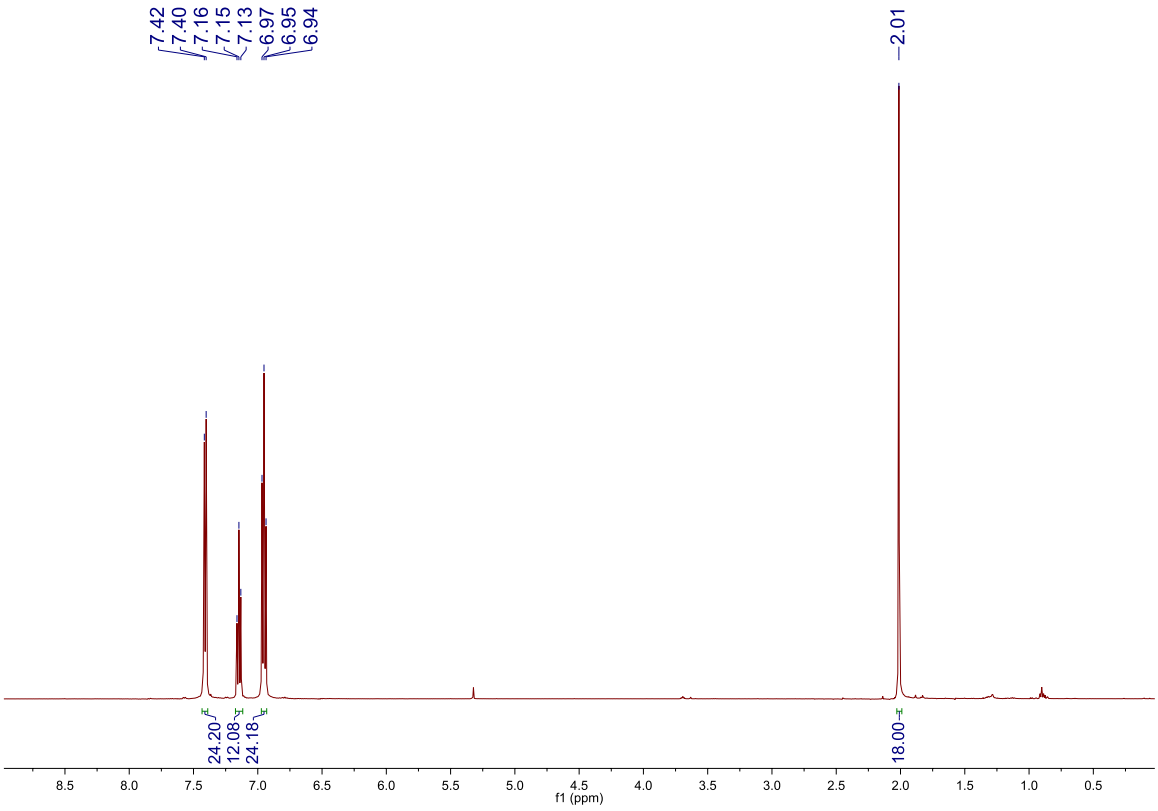

Figure 4.4. ^{1}H NMR spectrum of **4.1** in CD_2Cl_2.

I also briefly examined the chemical properties of **4.1**. It is soluble in benzene, toluene, THF, and CH_2Cl_2, but insoluble in MeCN, MeOH, Et_2O, and nonpolar solvents. It is stable in CD_2Cl_2 for at least 48 h, and stable to air and water (as a CD_2Cl_2 solution) for up to 24 h. As a solid, complex **4.1** shows no signs of decomposition after 2 months of exposure to air and water on the bench top. I also explored the electrochemical properties of complex **4.1** in CH_2Cl_2 at 25 °C. The cyclic voltammogram of **4.1** features two irreversible oxidation events at E = 0.20 and 0.55 V (vs. Fc/Fc^{+}) (Figure A4.26). These features remain irreversible, even at scan rates of up to 2000 mV s^{-1}. I hypothesize that electrons are being removed from the a_1 symmetric bonding orbital, disrupting the Cu-Cu bonding network, and resulting in rapid decomposition of the cluster.[52] For comparison, the related Cu_{13} cluster, $[Cu_{13}\{S_2CN^{n}Bu_2\}_6(CCR)_4][PF_6]$ (R = C(O)OMe), exhibits two comparable quasi-reversible

oxidation features (-0.05 and 0.34 V, vs. Fc/Fc^+), which the authors also ascribe to removal of Cu-Cu bonding electrons.[33] The cyclic voltammogram of **4.1** also features an irreversible reduction event at –1.02 V, which only appears after sampling the two irreversible oxidations. These observations are suggestive of an *ECE*-type process, but the identity of the species responsible for reduction feature is not known at this time.

4.2.2 Mechanistic Considerations

The first step in the formation of complex **4.1** appears to be the generation of the well-known yellow Cu(I) coordination polymer $[Cu(CCPh)]_n$, along with HOAc.[42-43] Ph_2SiH_2 then reacts with HOAc to make H_2 and $Ph_2Si(OAc)_2$. In parallel, I surmise that Ph_2SiH_2 also reacts with unconsumed Cu(OAc) to give Cu(0), which is captured by $[Cu(CCPh)]_n$ to generate the final nanocluster product. This mechanism is consistent with the formation of the yellow solid I observe in the reaction mixture at short reaction times. It is also consistent with the observation of bulk Cu metal in the reaction mixture, which is likely formed when some of the Cu(0) source is not captured by $[Cu(CCPh)]_n$ during the reaction, and eventually precipitates as bulk copper metal.

To test this hypothesis, I attempted the synthesis of **4.1** using a mixture of Cu(OAc) (8 equiv) and independently-synthesized $[Cu(CCPh)]_n$ (12 equiv) as Cu sources (Scheme 4.1B). Reaction of this combination with Ph_2SiH_2 (1 equiv) in THF for 30 h resulted in the formation of a red-orange THF solution and a green-brown solid. Work-up of the THF-soluble fraction resulted in the isolation of **4.1** in 26% yield. While its yield is low, the formation of **4.1** under these conditions is consistent with my proposed mechanism. Additionally, the reaction of Ph_2SiH_2 with 95% HOAc in CD_3CN (Scheme 4.2), in the presence of 10 mol% of Cu(OAc), resulted in rapid formation of H_2, $Ph_2SiH(OAc)$ and $Ph_2Si(OAc)_2$, according to ^1H NMR

spectroscopy (Figure A4.4), confirming my hypothesis regarding the mechanism of formation of $Ph_2Si(OAc)_2$. Interestingly, no reaction between Ph_2SiH_2 and HOAc was observed in the absence of Cu(OAc).

Scheme 4.2. Reaction of Silane with Acetic Acid in the Presence of Cu Catalyst

$$Ph_2SiH_2 + HOAc \xrightarrow[CD_3CN \\ -H_2]{10\ mol\%\ Cu(OAc)} Ph_2SiH(OAc) + Ph_2Si(OAc)_2$$

I also attempted the synthesis of **4.1** in the presence of excess Ph_2SiH_2 (10 equiv total). Under these conditions, I observed almost exclusive formation of Cu^0. Thus, it appears that when **4.1** is formed in the presence of unreacted silane, the cluster rapidly decomposes. Consistent with this observation, reaction of **4.1** with 3 equiv of Ph_2SiH_2 in CD_2Cl_2 resulted in decomposition of **4.1** and formation of Cu metal as the only identifiable Cu-containing material (Figure A4.3).

Several groups,[12] including the Hayton group,[25] have demonstrated that the metal:ligand ratio employed during nanocluster syntheses can affect the final cluster size. In the system described here, however, increasing the Cu(OAc):alkyne ratio to 20:6 (from 20:12 used in Scheme 4.1B), in an attempt to isolate a larger nanocluster, resulted only in formation of copious amounts of Cu metal (and no tractable Cu acetylide clusters). Decreasing the Cu(OAc):alkyne ratio to 20:20 still resulted in the formation of complex **4.1**, but in a lower isolated yield.

4.2.3 Grafting of 4.1 onto Silica

I also explored the reaction of **4.1** with dehydrated and partially-dehydroxylated silica (Sylopol 952, pretreated in vacuum at 200 °C, provided courtesy of Dr. Zach Jones, former member of the Scott group at UCSB). Reaction of a red C_6D_6 solution of **4.1** with 36.0 mg

silica (to give a solid containing ca. 3 wt% Cu) results in gradual transfer of **4.1** from solution to the silica (1 h total reaction time), to provide an orange solid and a colorless solution. A solution-state ^{1}H NMR spectrum of the reaction supernatant after 1 h revealed a complete absence of peaks assignable to **4.1**, as well as formation of 1 equiv of PhCCH (Scheme 4.3 and Figure A4.5). I see no evidence for formation of HOAc in solution, consistent with the relative basicities of $[OAc]^-$ and $[PhCC]^-$. To explain these observations, I suggest that reaction of **4.1** with a surface hydroxyl group (≡SiOH) results in protonation of one acetylide ligand of **4.1** and formation of immobilized cluster **4.2** via a new Cu-O-Si bond.

Scheme 4.3. Reaction of 4.1 with Silica

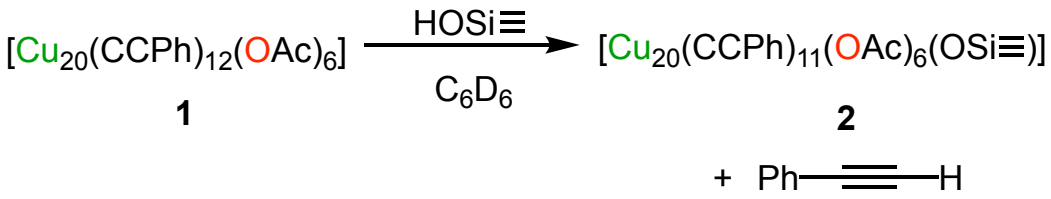

4.2.4 Reactivity of 4.1 with Acidic Proton Sources

Given the reactivity of complex **4.1** towards silica, I wished to explore the stability of the cluster in the presence of acidic protons. Thus, reaction of complex **4.1** with benzyl alcohol (6 equiv) at room temperature was monitored by ^{1}H NMR spectroscopy in CD_2Cl_2 (Figure A4.6). Over the course of 2 h, there appeared to be no reaction. However, upon sitting for 24 h, the red-orange color of complex **4.1** had slightly faded concomitant with the deposition of a small amount of colorless solid. The solid material is likely Cu(OAc) and, in conjunction with the fading color, indicates that **4.1** is likely decomposing slowly. However, the ^{1}H NMR spectra remain unchanged over this period, with the exception of a new acetate resonance at 1.57 ppm, which appears after 24 h. From these data, it appears that complex **4.1** is relatively stable in the presence of alcohols and does not undergo ligand exchange to generate a new

cluster, only decomposition to Cu(OAc). Interestingly, the reactivity is divergent to what was observed with silica as I observed no HCCPh from this reaction. This result is corroborated by monitoring the stability of complex **4.1** by ^{1}H NMR spectroscopy in a mixture of CD_2Cl_2:CD_3OD (3:1, v/v) over 24 h (Figure A4.7). Again, I observed a slight fading of the color of **4.1** with a similar colorless solid forming. The ^{1}H NMR spectra reveal only complex **4.1** and CD_3OD, even after 24 h.

Finally, I monitored the reaction of complex **4.1** with acetic acid (6 equiv) at room temperature by ^{1}H NMR spectroscopy in CD_2Cl_2 (Figure A4.8). After 20 min, a small amount of PhCCH has formed, which was to be expected, and the acetate resonance has broadened slightly. After 2h, more PhCCH has been generated and the acetate resonance has broadened further. There are also several new aryl resonances, suggesting that either acetate ligands had been incorporated into the Cu_{20} motif or an entirely new cluster core was generated. These new aryl resonances, as well as PhCCH continue to grow in over 24 h. Over this period, the color of complex **4.1** fades slightly and there is a large amount of colorless solid that forms. The colorless solid once again is probably Cu(OAc), which likely forms through the decomposition of the proposed transient cluster with additional acetate ligands This result suggests that while complex **4.1** is partially stable to acids over short timeframes, it readily exchanges acetylides for acetates and this new cluster will decompose over extended periods of time.

4.2.5 "Click" Chemistry with 4.1 and 4.2

Copper-catalyzed [3+2] Huisgen cycloadditions of terminal alkynes and organic azides (CuAAC) have been the cornerstone of "Click" chemistry since the seminal reports of Meldal and Sharpless in 2002.[53-54] Recently, Straub and co-workers reported that a small Cu(I)

acetylide cluster was a competent catalyst for the "Click" reaction.[55] Intriguingly, that cluster features acetylide ligands with μ_4:η^1,η^1,η^1,η^2 and μ_3:η^1,η^1,η^2 binding modes, which are nearly identical to those observed in complex **4.1**.[55] Thus, I hypothesized that **4.1** would also be a competent catalyst for the same transformation. Accordingly, I examined the ability of **4.1** to catalyze the [3+2] cycloaddition of several alkynes (HCCR, R = Ph, CO_2Et, and ^{t}Bu) with benzyl azide (Table 4.1). Addition of **4.1** (0.5 mol% Cu_{20} cluster) to a CD_2Cl_2 solution of benzyl azide (1.1 equiv) and HCCPh (1 equiv), at room temperature, generated 1-benzyl-4-phenyl-1*H*-1,2,3-triazole (**4.3**) in good yield (entry 1, Table 4.1). Complex **4.1** is also effective at a much lower catalyst loading (0.05 mol% Cu_{20} cluster, entry 2, Table 4.1).

Comparable yields of triazoles ethyl-1-benzyl-1H-1,2,3-triazole-4-carboxylate (**4.4**) and 1-benzyl-4-tert-butyl-1H-1,2,3-triazole (**4.5**) were observed upon substitution of HCCPh with either HCC(CO_2Et) or HCC^{t}Bu, respectively (entries 3 and 4, Table 4.1). Notably, however, in these two cases I also observe the formation of **4.3** in the reaction mixture (see Figures A4.16 and A4.17), indicating that the phenylacetylide ligands present in **4.1** play a role in the catalytic cycle and can be incorporated into the product. To rationalize this observation, I propose that the first step of the catalytic cycle involves reaction of benzyl azide with a bound phenylacetylide ligand, resulting in formation of a copper-bound triazolate fragment.[56] This fragment undergoes subsequent protonolysis by incoming alkyne to generate **4.3** and a new copper-bound acetylide ligand.

Interestingly, as the homogeneous catalytic reaction proceeds, the red-orange color of **4.1** slowly disappears and a bright yellow solid resembling $[Cu(CCPh)]_n$ begins to precipitate from the reaction mixture.[42] This phenomenon was observed for all three alkyne substrates. Additionally, the ^{1}H NMR signals attributed to complex **4.1** lose > 95% of their intensity

(relative to the internal standard) over the course of the reaction. These data suggest that **4.1** has somewhat limited stability under the reaction conditions, and likely dissociates into smaller clusters and/or discrete Cu^{+} ions, either of which may also be catalytically active.[57] Accordingly, I cannot definitively conclude that complex **4.1** is the active catalyst in this system, and it may simply function as a pre-catalyst. Similar behavior has been observed in other Cu nanoparticle systems.[58-59]

Table 4.1. [3+2] cycloaddition between benzyl azide and various terminal alkynes catalyzed by **4.1** and **4.2**.[a]

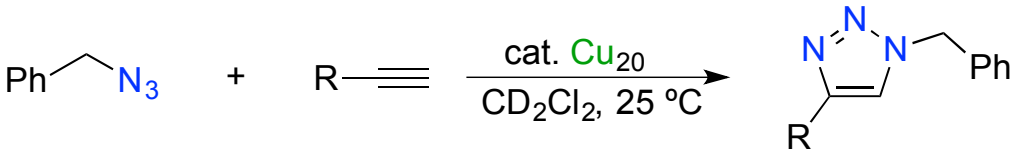

Entry	R	time (h)	loading (mol %)[b]	yield (%)[c]	TON
1	Ph	5	0.5	95	190
2	Ph	7	0.05	85	1700
3	CO_2Et	5	0.5	86	172
4	^{t}Bu	5	0.5	92	184
5	Ph	7	0.5[d]	95	190
6	Ph	7	0.5[e]	94	188
7[f]	Ph	2	0.5	>99	198

[a]For experimental details, see sections 4.4.7 – 4.4.10. [b]Catalyst loading defined as mol% Cu_{20} cluster. [c]Yield of triazole determined by integration of ^{1}H NMR spectra acquired with a 60 s pulse delay, using hexamethyldisiloxane as internal standard. [d]Catalyst immobilized on SiO_2. [e]Recovered catalyst, still immobilized on SiO_2. [f]Reaction performed at 40 °C.

I also examined the ability of heterogeneous **4.2** to catalyze the [3+2] cycloaddition of phenylacetylene and benzyl azide, under conditions identical to those employed in the

homogeneous reaction. Thus, addition of **4.2** (0.5 mol% Cu_{20} cluster) to a CD_2Cl_2 solution of benzyl azide (1.1 equiv) and HCCPh (1 equiv) generated **4.3** in comparable yields to those observed using intact **4.1** (entry 5, Table 4.1). The recycled silica-supported catalyst also generated **4.3** in comparable yield (entry 6, Table 4.1). Notably, I see no evidence for leaching of complex **4.1** from the SiO_2 support into CD_2Cl_2 over 7 h by ^1H NMR spectroscopy, either in the absence or presence of the alkyne and azide substrates (Figures A4.11 and A4.18). Supported cluster **4.2** is also an effective catalyst for the [3+2] cycloaddition reaction at 40 °C (entry 7, Table 4.1). However, at these elevated temperatures, the catalyst undergoes a gradual color change from red-orange to pale yellow over the course of the reaction, suggesting that it may undergo a structural change upon heating.

It is well known that solvated Cu^+ ions can effectively catalyze the "Click" reaction.[43, 57] As a result, it has been a challenge to establish if Cu nanomaterials themselves are the actual catalysts or if leached Cu^+ ions are responsible for the observed reactivity.[60] To probe the stability of **4.2**, I separated the supported catalyst from the supernatant of a reaction between benzyl azide and HCCPh by filtration, then exposed the supernatant to fresh substrate (Figure A4.13). Under these conditions, I observed no conversion of alkyne and benzyl azide to the triazole after 7 h, suggesting that Cu^+ ions were not leached from the supported catalyst into solution over the course of the initial reaction. Overall, this result suggests that **4.2** is more stable than **4.1** under "Click" reaction conditions.

For comparison, several groups have shown that supported copper nanomaterials can catalyze CuAAC chemistry.[58, 61-68] Broadly speaking, these materials exhibit activities and recyclability similar to those observed for **4.2**. However, many of these nanomaterials feature large polydispersities,[69-71] or suffer from ill-defined surface chemistries.[61, 63] As such, it is a

challenge to reliably and predictably deposit these material on a support. Additionally, this polydispersity makes it a significant challenge to extract SARs in an effort to develop better catalyst systems.

4.2.6 Characterization of 4.1 and 4.2 by X-ray Absorption Spectroscopy

Solid samples of **4.1**, **4.2**, and **4.2**$_{\mathbf{post}}$ were given to Dr. Zach Jones, formerly of the Scott group at UCSB, to perform XAS and subsequent data analysis on. Previous studies[25, 27] on Cu-based APNCs revealed remarkable XAS sensitivity to both ligand sets and Cu nuclearity. Therefore, Cu K-edge XAFS was undertaken to compare structural features of complex **4.1** with its silica-supported analog, **4.2**, as well as the recovered post-catalysis material, **4.2**$_{\mathbf{post}}$. The absence of significant differences in the XANES profiles of **4.1** and **4.2** suggests that the nanocluster structure is preserved upon grafting onto SiO_2 (Figure A4.29). In the EXAFS, two prominent features appear at 1.6 and 2.3 Å in the FT magnitude of the EXAFS of **4.1** (Figure 4.5). The first peak represents light atoms directly coordinated to Cu, i.e., the donor atoms of the bidentate acetate and side-on bound acetylide ligands. The second peak represents the contributions of the Cu-Cu paths.

The curvefit of the EXAFS of **4.1** (Figure A4.32) includes a Cu–O path and a Cu–C path, whose distances were fixed at the most commonly observed values in the X-ray crystal structure (1.951 and 2.061 Å, respectively, the latter being the distance corresponding to the Cu-C π-bonds). The fit returned *N*(Cu–O) and *N*(Cu–C) values of 0.6(3) and 1.2(4), respectively (Table 4.2). The number of Cu-O paths agrees with the average number of bidentate acetate ligands per Cu (0.3), while the value for the Cu–C path exceeds the average number of acetylide ligands per Cu (0.6), as expected due to the presence of both σ- and π-interactions involving these ligands. The Cu-Cu paths, which range from 2.471 to 3.085 Å in

the crystal structure, were represented in the curvefit by two paths whose distances were fixed at the most frequent Cu-Cu bond lengths. The resulting fit returned a combined *N*(Cu-Cu) of 2.3(5), similar to the crystallographically-determined value of 2.7.

The EXAFS of silica-supported **4.2** features two similar peaks, at 1.6 and 2.2 Å, with slightly different relative intensities compared to those observed for **4.1** (Figure 4.5). The distances for the Cu-O and Cu-C paths were again fixed using the most common values found in the molecular cluster **4.1**, while both coordination numbers were refined. Minor changes in the fitted values of *N*(Cu–O) and *N*(Cu–C), to 1.0(1) and 0.6(4), respectively, are consistent with a reaction of **4.1** with silica, which results in one acetylide ligand being replaced by a surface silyloxide (likely in a bridging configuration), among other possible interactions (see Figure A4.33 and Table 4.2). Although the intensity of the peak in the FT magnitude corresponding to the Cu-Cu paths decreased slightly upon deposition onto silica, curvefitting returned a similar total value for *N*(Cu–Cu), 2.3(3). I hypothesize that the Cu-Cu distribution becomes less uniform upon deposition, and the number of longer paths increases at the expense of the shorter paths. The resulting destructive interference results in an overall decrease in FT magnitude, without any cluster fragmentation. Thus, the EXAFS analysis suggests that immobilization of **4.1** results in little or no change to the cluster nuclearity, and only minor changes to the cluster structure.

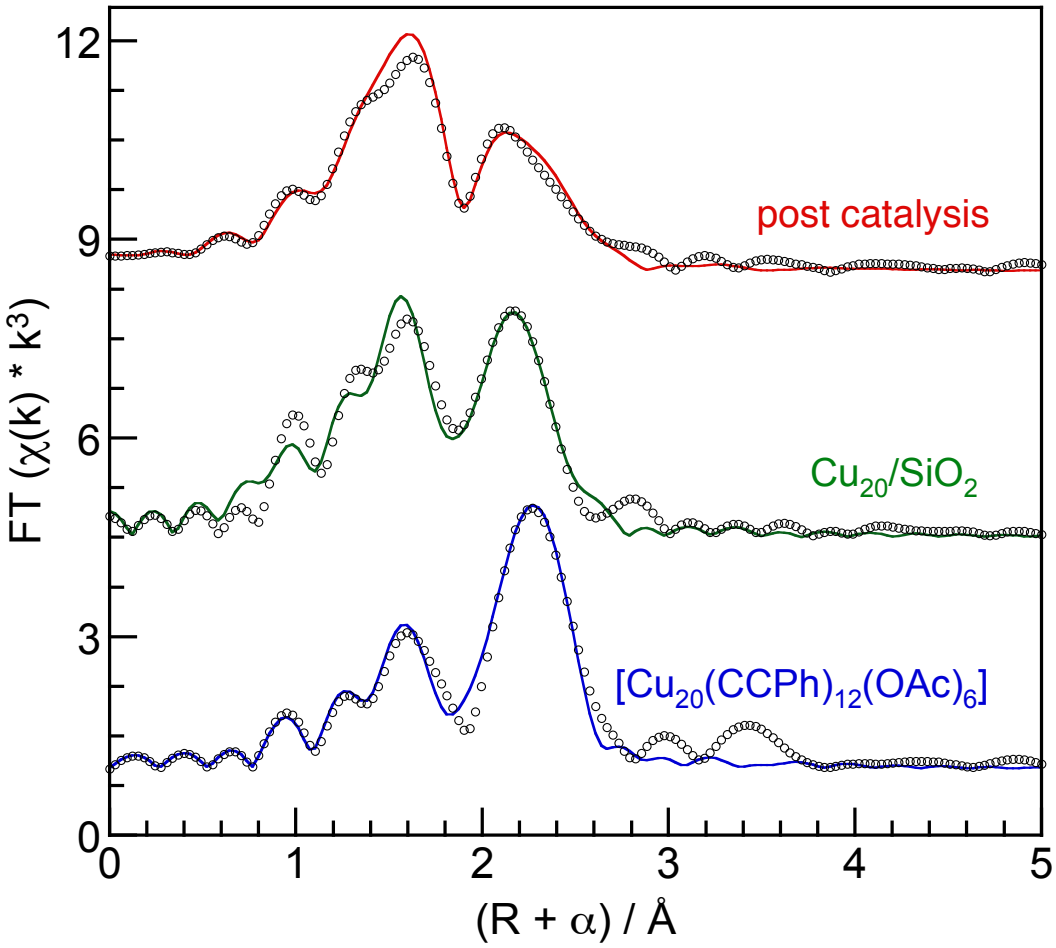

Figure 4.5. Comparison of Cu K-edge EXAFS (displayed as FT magnitude, points, with curvefits, lines) for $[Cu_{20}(CCPh)_{12}(OAc)_6]$ (**4.1**, blue), freshly-prepared Cu_{20}/SiO_2 (**4.2**, green), and post-catalysis Cu_{20}/SiO_2 (**4.2**$_{\mathbf{post}}$, red).

The supported cluster material was recovered after use as a catalyst for the cycloaddition of benzyl azide and HCCPh. The EXAFS of the recovered post-catalysis material, **4.2**$_{\mathbf{post}}$, is again similar to that of the immobilized cluster **4.2** (Figure 4.5). The curvefit reveals an increase in *N*(Cu-O), to 1.7(3), while the value for *N*(Cu-C) remains essentially unchanged at 0.7(3) (Figure A4.34 and Table 4.2). The peak arising from the Cu-Cu paths broadened, while the total value of *N*(Cu-Cu) decreased to 1.7(5). Although these values are slightly different than those found for **4.2**, qualitative inspection of the spectrum for **4.2**$_{\mathbf{post}}$ suggests that the

supported cluster's ligand complement is largely preserved, i.e., there has been minimal rearrangement of the Cu-Cu skeleton. More importantly, these changes are not consistent with extensive cluster fragmentation or aggregation. The qualitative similarities in the EXAFS are also consistent with the XANES profiles of **4.2** and **4.2$_{post}$**, which show nearly indistinguishable, superimposable edges and absorbance maxima (Figure A4.29, Table 4.5).

There are only a handful of prior reports describing the characterization of APNCs before and after deposition onto a solid support. For example, Spivey and co-workers demonstrated by EXAFS that deposition of a thiolate-capped Au_{38} cluster on TiO_2 resulted in aggregation.[72] In contrast, Wu and co-workers concluded that deposition of a Au_{22} nanocluster onto TiO_2 resulted in no agglomeration, on the basis of HAADF–STEM imaging.[73] While this cluster was competent for CO oxidation, the post-catalysis cluster was not characterized, so its nuclearity is unknown. Similarly, Scott and co-workers demonstrated that thiolate-protected Au_{25}(11-MUA)$_{18}$ (11-MUA = mercaptoundecanoic acid) maintained its structure after deposition onto SiO_2, but agglomerated upon calcination at 250 °C.[18] Thus, the nanocluster series **4.1**, **4.2**, and **4.2$_{post}$** represents an exceptionally rare example of retention of cluster structure after deposition on a solid support, and after use in a catalytic reaction.

Table 4.2. Curvefit parameters for the Cu K-edge EXAFS[a]

		EXAFS curvefit		
Material	Path	N	*R*(Å)	σ^2 ($\times 10^3$ Å^{-1})
4.1[b]	Cu-O	0.6(3)	1.951[c]	5(3)[d]
	Cu-C	1.2(4)	2.061[c]	5(3)[d]
	Cu-Cu1	2.1(5)	2.563[c]	6(2)[e]
	Cu-Cu2	0.2(1)	2.671[c]	6(2)[e]
4.2[f]	Cu-O	1.0(1)	1.951[c]	7(2)[d]
	Cu-C	0.6(4)	2.061[c]	7(2)[d]
	Cu-Cu1	1.7(2)	2.505(6)	7(2)[e]
	Cu-Cu2	0.6(2)	2.62(2)	7(2)[e]
4.2$_{\mathbf{post}}$[g]	Cu-O	1.7(3)	1.951[c]	7(1)[d]
	Cu-C	0.7(3)	2.061[c]	7(1)[d]
	Cu-Cu1	1.2(3)	2.53(4)	6(1)[e]
	Cu-Cu2	0.5(3)	2.66(1)	6(1)[e]

[a]Uncertainties in the last significant figure are shown in parentheses. Values without uncertainties were fixed at values determined by X-ray crystallography. [b]Global fit parameters: $S_o^2 = 0.8(1)$; $\Delta E_o = 5(1)$ eV. [c]Fixed at values determined by single crystal X-ray diffraction (this work). [d]Constrained to have the same mean-squared displacement. [e]Constrained to have the same mean-squared displacement. [f]Global fit parameters: $S_o^2 = 0.8(2)$; $\Delta E_o = 8(2)$ eV. [g]Global fit parameters: $S_o^2 = 0.8(1)$; $\Delta E_o = 9(1)$ eV.

4.3 Summary

In summary, I have synthesized and characterized the novel organometallic nanocluster $[Cu_{20}(CCPh)_{12}(OAc)_6]$ (**4.1**). Complex **4.1** is a rare example a 2-electron copper superatom, and the first copper superatom to feature a $[Cu_4]^{2+}$ core. Complex **4.1** can be readily immobilized on dry, partially-dehydroxylated silica, a process that results in release of 1 equiv of phenylacetylene per Cu_{20} cluster. According to qualitative and quantitative EXAFS analysis, the immobilized cluster **4.2** is structurally similar to **4.1**. In addition, both **4.1** and **4.2** are effective catalysts for [3+2] cycloaddition of alkynes and azide at room temperature. Intriguingly, supported cluster **4.2** appears to be substantially more stable than **4.1** under the reaction conditions. More importantly, however, neither **4.1** nor **4.2** require harsh pre-treatment for activation, demonstrating the innate promise of organometallic APNCs for development of SARs in the field of supported catalysis.

4.4 Experimental

4.4.1 General Procedures

All reactions and subsequent manipulations were performed under anaerobic and anhydrous conditions under an atmosphere of nitrogen. Hexanes, toluene and tetrahydrofuran were dried using a Vacuum Atmospheres DRI-SOLV Solvent Purification system and stored over 3 Å sieves for 24 h prior to use. Dichloromethane (CH_2Cl_2) was degassed and stored over 3 Å sieves for 72 h prior to use. CD_2Cl_2 and diphenylsilane were stored over 3 Å molecular sieves for 24 h prior to use. $[Cu(CCPh)]_n$ was synthesized according to the literature procedure.[42] Anhydrous Cu(OAc) (97%) was purchased from Strem Chemicals. All other reagents were purchased from commercial suppliers and used as received.

All NMR spectra were collected at room temperature. ^{1}H and $^{13}C\{^{1}H\}$ NMR spectra were recorded on an Agilent Technologies 400-MR DD2 400 MHz spectrometer or Varian Unity Inova 500 MHz spectrometer. The chemical shifts of all nuclei were referenced by using the residual solvent peaks (^{1}H NMR experiments) or the characteristic resonances of the solvent nuclei as internal standards ($^{13}C\{^{1}H\}$ NMR experiments). IR spectra were recorded on a Nicolet 6700 FT-IR spectrometer with a NXR FT Raman Module. Electronic absorption spectra were recorded on a UV-2401 PC Shimadzu UV-NIR spectrophotometer. Mass spectra were collected at the Materials Research Laboratory Shared Experimental Facilities at UCSB, using an electrospray ionization (ESI) source on positive ion mode with a Waters Xevo G2-XS TOF Time-of-Flight mass spectrometer. Mass spectra were smoothed 3 times using the mean algorithm with a smooth window of 2 channels. Elemental analyses were performed by the Micro-Mass Facility at the University of California, Berkeley.

4.4.2 Cyclic Voltammetry Measurements

Cyclic voltammetry experiments were performed with a CH Instruments 600c potentiostat, and the data were processed using CHI software (version 6.29). All experiments were performed in a glovebox using a 20 mL glass vial as a cell. The working electrode consisted of a platinum disk embedded in glass (2 mm diameter), the counter electrode and reference electrode were platinum wires. Solutions employed for CV studies were typically 1 mM in analyte and 0.1 M in $[NBu_4][PF_6]$. All potentials are reported versus the $[Cp_2Fe]^{0/+}$ couple.

4.4.3 X-ray Absorption Spectroscopy

All spectra and subsequent data analyses were performed by Dr. Zach Jones, formerly of the Scott Group at UCSB. X-ray absorption near-edge spectra (XANES) and extended X-ray

absorption fine structure (EXAFS) were recorded at the Cu *K*-edge (8979 eV) on Beamline 7-3 (bend) at the Stanford Synchrotron Radiation Lightsource (SSRL), which operates at 3.0 GeV with a ring current of 500 mA. X-rays were monochromatized via reflection from a Si(220) double crystal monochromator, φ = 0 °, and passed through a 1 × 6.5 mm entrance slit. The beam was detuned 40 % to reject harmonics. Data were collected with step size of 0.35 eV over the region 40 eV before the edge, and 20 eV after the edge. This results in a near-edge resolution of ca. 0.1 eV. X-ray absorption data were acquired up to $k = 15$ Å^{-1}. N_2-filled ionization detectors were mounted in the beam before and after the sample to collect data in transmission mode. The spectrum of a Cu foil was recorded using a third ionization detector, for simultaneous energy calibration.

Complexes **4.1**, $[Cu_2(OAc)_2]_n$ (represented as a dimer here to better reflect its molecular structure),[74] and $[Cu(CCPh)]_n$ were diluted with boron nitride (99.5 %, Fisher Scientific) in a N_2-filled glovebox, to produce samples containing ca. 3 wt% Cu in order to minimize self-absorption effects. Silica-supported cluster **4.2** was packed undiluted. Each material was loaded into a slotted Al sample plate (slot size 12 x 3 x 0.5 mm) and sealed under N_2, using Kapton tape (8 μm, DuPont). The plates were pre-cooled in liquid N_2 before being transferred to a liquid He flow cryostat (Oxford Instruments) and cooled to <15 K. Six scans were recorded and averaged for each sample. Subsequent scans showed no changes, confirming the integrity of each sample under the measurement conditions.

Data processing and analysis were performed using the Demeter software package (v. 0.9.20).[75] The single-scan spectra were aligned using the edge energy of the Cu foil spectrum, then averaged. The absorption edge was assigned as the first maximum in the first derivative of the spectrum. A linear pre-edge function was subtracted, then the data were normalized by

edge height using Athena software. A smooth, third-order polynomial approximating the absorption background of an isolated atom was subtracted to yield $\chi(k)$. The data were then k^3-weighted and Fourier-transformed. EXAFS curvefitting was conducted with paths generated by FEFF6 from the crystallographic data for the Cu_{20} cluster obtained by single-crystal X-ray diffraction (this work). Coordination numbers (N), distances of scattering atoms (R) and their mean-squared displacements (σ^2) were obtained by non-linear least-squares refinement in R-space, using the standard EXAFS equation. The amplitude reduction factor (S_0^2) and the energy shift parameter (ΔE_0) were refined as global fit parameters. Their values were then fixed while the values of R and σ^2 were refined. Finally, the values of N were refined while holding previously obtained values for R and σ^2 fixed.

4.4.4 Synthesis of $[Cu_{20}(CCPh)_{12}(OAc)_6]$ (4.1)

To a stirring pale green suspension of Cu(OAc) (55.5 mg, 0.453 mmol) in tetrahydrofuran (10 mL) was added phenylacetylene (30 μL, 0.273 mmol) via micropipette. The addition of PhCCH resulted in the immediate deposition of a bright yellow powder, suggestive of the formation of $[Cu(CCPh)]_n$.[42] To this suspension was then added Ph_2SiH_2 (30 μL, 0.162 mmol). The reaction mixture was allowed to stir for 15 h, during which time the solution became dark red-brown, concomitant with the deposition of a brown solid, suggestive of the formation of Cu metal. The mixture was concentrated *in vacuo* to 5 mL and filtered through a pre-weighed 0.2 μm PTFE membrane syringe filter to remove the brown solid. The filter was rinsed with tetrahydrofuran until the washings were colorless (2 × 1 mL). The washings were added to the filtrate. The PTFE filter was then allowed to dry under an N_2 atmosphere for 24 h, whereupon its weight was measured (12.0 mg of Cu^0 powder, 42% yield). Subsequent dissolution of this solid in 12M HNO_3 (1 mL) resulted in the formation of a blue-green solution, consistent with

the presence of Cu^{2+}(aq). Separately, the red THF filtrate was layered with hexanes (9 mL) and stored at -25 °C for 48 h. This resulted in the deposition of red-orange crystals, which were isolated by decanting off the supernatant. The red-orange solid was rinsed with hexanes (3 × 1 mL) until the washings were colorless. The washings were subsequently discarded. The remaining red-orange powder was dried *in vacuo* to yield **4.1** (31.1 mg, 49% yield). Anal. Calcd for $C_{108}H_{78}O_{12}Cu_{20}$: C, 45.70; H, 2.77. Found: C, 45.59; H, 2.78. ^{1}H NMR (400 MHz, 25 °C, CD_2Cl_2): δ 2.01 (s, 18H, *C*H_3), 6.95 (t, J_{HH} = 7.5 Hz, 24H, *m*-Ph), 7.15 (t, J_{HH} = 7.5 Hz, 12H, *p*-Ph), 7.41 (d, J_{HH} = 10 Hz, 24H, *o*-Ph). ^{13}C{^{1}H} NMR (125 MHz, 25 °C, CD_2Cl_2): δ 23.21 (*C*H_3), 89.80 (*C*CCu), 124.08 (*ipso*-Ph), 128.35 (*m*-Ph), 129.13 (*p*-Ph), 132.76 (*o*-Ph), 135.31 (C*C*Cu), 180.05 (*C*(O)CH_3). ESI-MS: *m/z* 2410.3008 $[M - 3Cu - 4OAc]^+$ (Calcd *m/z* 2410.2903), *m/z* 2534.2314 $[M - 2Cu - 3OAc]^+$ (Calcd *m/z* 2534.2332), m/z 2656.1831 $[M - Cu - 2OAc]^+$ (Calcd *m/z* 2656.1760), *m/z* 2778.1309 $[M\text{-}OAc]^+$ (Calcd *m/z* 2778.1221), *m/z* 2902.0662 $[M+Cu]^+$ (Calcd *m/z* 2902.0608). UV-Vis / NIR (CH_2Cl_2, 3.5 μM, 25 °C, $L \cdot mol^{-1} \cdot cm^{-1}$) 315 nm (sh, ε = 8600), 480 nm (sh, ε = 1200). IR (KBr pellet, cm^{-1}): 525 (s), 620 (m), 672 (s), 686 (s), 752 (s), 839(w), 916 (w), 998 (w), 1025 (m), 1045 (w), 1069 (m), 1097 (w), 1156 (w), 1173 (w), 1185 (w) 1237 (w), 1281 (w), 1344 (m), 1421 (s), 1440 (s), 1482 (s), 1557 (s), 1591 (m), 1667 (w), 1841 (w), 1893 (w), 1954 (w), 2925 (w), 2958 (w), 3013 (w), 3027 (w), 3056 (m). Note: the synthesis of **4.1** was also performed with Ph_2SiD_2 as the reducing agent, which generated material that was identical to that formed with Ph_2SiH_2, according to ^{1}H NMR spectroscopy and ESI mass spectrometry, demonstrating that no inclusion of H^-/D^- into the isolated product has occurred.

4.4.5 Synthesis of 4.1 from Cu(OAc) and $[Cu(CCPh)]_n$

To a 20 mL scintillation vial equipped with a magnetic stir bar was added $[Cu(CCPh)]_n$ (53.0 mg, 0.345 mmol) and Cu(OAc) (28.0 mg, 0.228 mmol) in tetrahydrofuran (6 mL). To this brown-yellow slurry was added Ph_2SiH_2 (6.0 µl, 0.032 mmol) via micropipette, and the reaction mixture was allowed to stir. After 30 h, the solution had turned dark red and the yellow solid was consumed. Some of the dark brown solid (Cu(OAc)) remained unreacted, and a small amount of Cu metal (as a mirror) was observed on the walls of the vial. The solution was concentrated *in vacuo* to 4 mL and filtered through a Celite column (0.5 × 3 cm). The Celite pad was then washed with THF (2 × 1 mL). The washings were added to the filtrate. The red filtrate was layered with hexanes (9 mL) and stored at -25 °C for 48 h. This resulted in the deposition of red-orange crystals, which were isolated by decanting off the supernatant. The red-orange solid was rinsed with hexanes (3 × 1 mL) until the washings were colorless. The washings were subsequently discarded. The remaining red-orange powder was dried *in vacuo* to yield **4.1** (21.0 mg, 26% yield). This material was identical to the material synthesized from Cu(OAc), Ph_2SiH_2, and phenylacetylene, according to ^1H NMR spectroscopy.

4.4.6 Immobilization of 4.1 onto silica

This material was provided to me by Dr. Zach Jones, formerly of the Scott Group at UCSB. In a typical synthesis, Sylopol 952 silica (BET surface area of 300 ± 18 m^2/g and pore volume of 1.61 mL/g, ca. 1 g, W. R. Grace), was dehydrated overnight at room temperature under dynamic vacuum (< 0.1 mTorr) then at 200 °C for 6 h. In a N_2-filled glovebox, **4.1** (25 mg) was dissolved in 10 mL anhydrous toluene and transferred to a 50-mL round bottom flask containing dry SiO_2 (225 mg) suspended in an additional 10 mL of toluene. The mixture was

stirred at room temperature for 45 min before **4.2** was recovered by filtration. The resulting orange powder was dried under dynamic vacuum in a 20-mL scintillation vial for 30 min prior to characterization and catalytic testing.

4.4.7 Representative procedure for azide-alkyne cycloaddition catalyzed by 4.1

A J. Young NMR tube was charged with phenylacetylene (9.0 μL, 0.082 mmol), benzyl azide (11.0 μL, 0.088 mmol), and CD_2Cl_2 (1.0 mL). Hexamethyldisiloxane (1.0 μL, 0.0047 mmol) was added as an internal standard. To this solution was added complex **4.1** as a 10 mM solution in CD_2Cl_2 (40 μL, 0.4 μmol). The reaction mixture was allowed to stand at room temperature. After 5 h, a ^{1}H NMR spectrum was recorded, revealing the formation of 1-benzyl-4-phenyl-1*H*-1,2,3-triazole (**4.3**), which was confirmed by comparison to previously reported NMR data.[76] The percent conversion was determined by integration of the resonance assigned to the benzylic protons at 5.57 ppm versus the internal standard. ^{1}H NMR (400 MHz, 25 °C, CD_2Cl_2): δ 5.57 (s, 2H, 1-benzyl C*H*$_2$), 7.33-7.43 (m, 8H, 1-benzyl aryl protons overlapping *m*-Ph and *p*-Ph protons of 4-phenyl), 7.76 (s, 1H, triazole), 7.81 (d, J_{HH} = 7.2 Hz, 2H, *o*-Ph protons of 4-phenyl).

4.4.8 Synthesis of ethyl 1-benzyl-1H-1,2,3-triazole-4-carboxylate (4.4)

A procedure similar to that described for the synthesis of **4.3** was applied for the reaction of ethyl acetylenecarboxylate (8.3 μL, 0.082 mmol) and benzyl azide (11.0 μL, 0.088 mmol). The presence of **4.4** in the reaction mixture was confirmed by comparison to previously reported NMR data.[76] The percent conversion was determined by integration of the resonance assigned to the benzylic protons at 5.57 ppm versus the internal standard. ^{1}H NMR (400 MHz, 25 °C, CD_2Cl_2): δ 1.35 (t, J_{HH} = 7.2 Hz, 3H, CH_2CH_3), 4.34 (q, J_{HH} = 7.3 Hz, 2H, CH_2CH_3),

5.57 (s, 2H, 1-benzyl CH_2), 7.29-7.41 (m, 5H, 1-benzyl aryl protons), 8.01 (s, 1H, triazole 5-H).

4.4.9 Synthesis of 1-benzyl-4-tert-butyl-1H-1,2,3-triazole (4.5)

A procedure similar to that described for the synthesis of **4.3** was applied for the reaction of 3,3-dimethyl-1-butyne (10.1 μL, 0.082 mmol) and benzyl azide (11.0 μL, 0.088 mmol). The presence of **4.5** in the reaction mixture was confirmed by comparison to previously reported NMR data.[77] The percent conversion was determined by integration of the resonance assigned to the benzylic protons at 5.47 ppm versus the internal standard. ^{1}H NMR (400 MHz, 25 °C, CD_2Cl_2): δ 1.31 (s, 9H, ^{t}Bu), 5.47 (s, 2H, CH_2), 7.24 (s, 1H, triazole 5-H), 7.26-7.40 (m, 5H, 1-benzyl aryl protons).

4.4.10 Representative procedure for azide-alkyne cycloaddition catalyzed by 4.2

A J. Young NMR tube was charged with phenylacetylene (4.0 μL, 0.036 mmol), benzyl azide (5.0 μL, 0.040 mmol), and CD_2Cl_2 (1.0 mL). Hexamethyldisiloxane (1.0 μL, 0.0047 mmol) was added as an internal standard. To this solution was added **4.2** as a solid (11.1 mg, 0.20 μmol of **4.1**). The reaction mixture was allowed to stand at room temperature. After 7 h, a ^{1}H NMR spectrum was recorded, revealing the formation of 1-benzyl-4-phenyl-1*H*-1,2,3-triazole, whose presence was confirmed by comparison to previously reported NMR data.[76] The percent conversion was determined by integration of the resonance assigned to the benzylic protons at 5.57 ppm versus the internal standard. ^{1}H NMR (400 MHz, 25 °C, CD_2Cl_2): δ 5.57 (s, 2H, 1-benzyl CH_2), 7.33-7.43 (m, 8H, 1-benzyl aryl protons overlapping *m*-Ph and *p*-Ph protons of 4-phenyl), 7.76 (s, 1H, triazole), 7.81 (d, J_{HH} = 7.2 Hz, 2H, *o*-Ph protons of 4-phenyl).

4.4.11 X-ray Crystallography

Data for **4.1**·$5C_4H_8O$ were collected on a Bruker KAPPA APEX II diffractometer equipped with an APEX II CCD detector using a TRIUMPH monochromater with a MoKα X-ray source (α = 0.71073 Å). Crystals were mounted on a cryoloop under Paratone-N oil, and all data were collected at 100(2) K using an Oxford nitrogen gas cryostream system. X-ray data for **4.1**·$5C_4H_8O$ were collected utilizing frame exposures of 10 s. Data collection and cell parameter determination were conducted using the SMART program.[78] Integration of the data frames and final cell parameter refinement were performed using SAINT software.[79] Absorption correction of the data was carried out using the multi-scan method SADABS.[80] Subsequent calculations were carried out using SHELXTL.[81] Structure determination was done using direct methods and difference Fourier techniques. All hydrogen atom positions were idealized, and rode on the atom of attachment. Structure solution, refinement, graphics, and creation of publication materials were performed using SHELXTL.[81]

Further crystallographic details can be found in Table 4.3.

Table 4.3. X-ray Crystallographic Data for **4.1**·$5C_4H_8O$.

	4.1·$5C_4H_8O$
empirical formula	$C_{128}H_{118}Cu_{20}O_{17}$
crystal habit, color	block, red
crystal size (mm)	0.15 × 0.15 × 0.05
crystal system	triclinic
space group	$P\bar{1}$
volume (Å^3)	5800(4)
a (Å)	14.279(6)
b (Å)	14.958(6)
c (Å)	28.802(12)
α (deg)	93.368(7)
β (deg)	102.082(7)
γ (deg)	103.927(7)
Z	2
formula weight (g/mol)	3199.02
density (calculated) (Mg/m^3)	1.832
absorption coefficient (mm^{-1})	3.645
F_{000}	3204
total no. reflections	72768
unique reflections	24541
final R indices [I>2σ(I)]	R_1 = 0.1191
	wR_2 = 0.3018
largest diff. peak and hole (e$^-$A^{-3})	2.367 and -1.904
GOF	1.056

4.5 Appendix

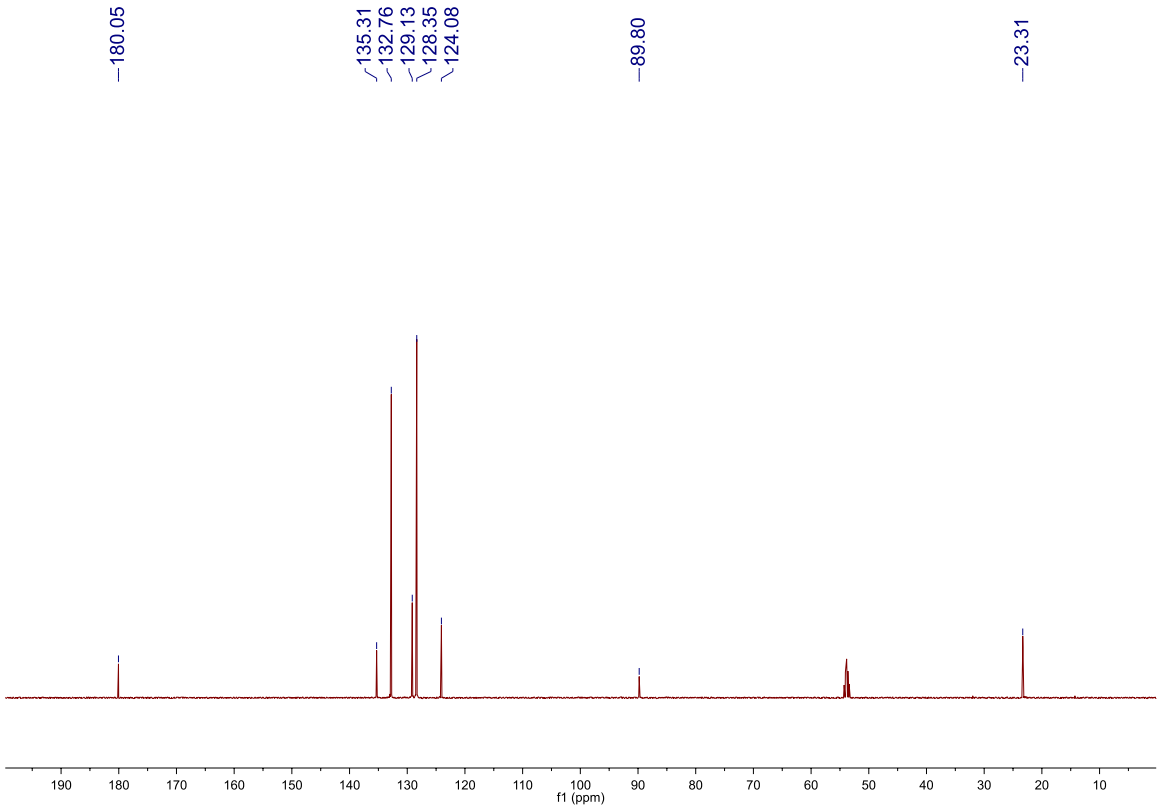

Figure A4.1. $^{13}C\{^{1}H\}$ NMR spectrum of **4.1** in CD_2Cl_2.

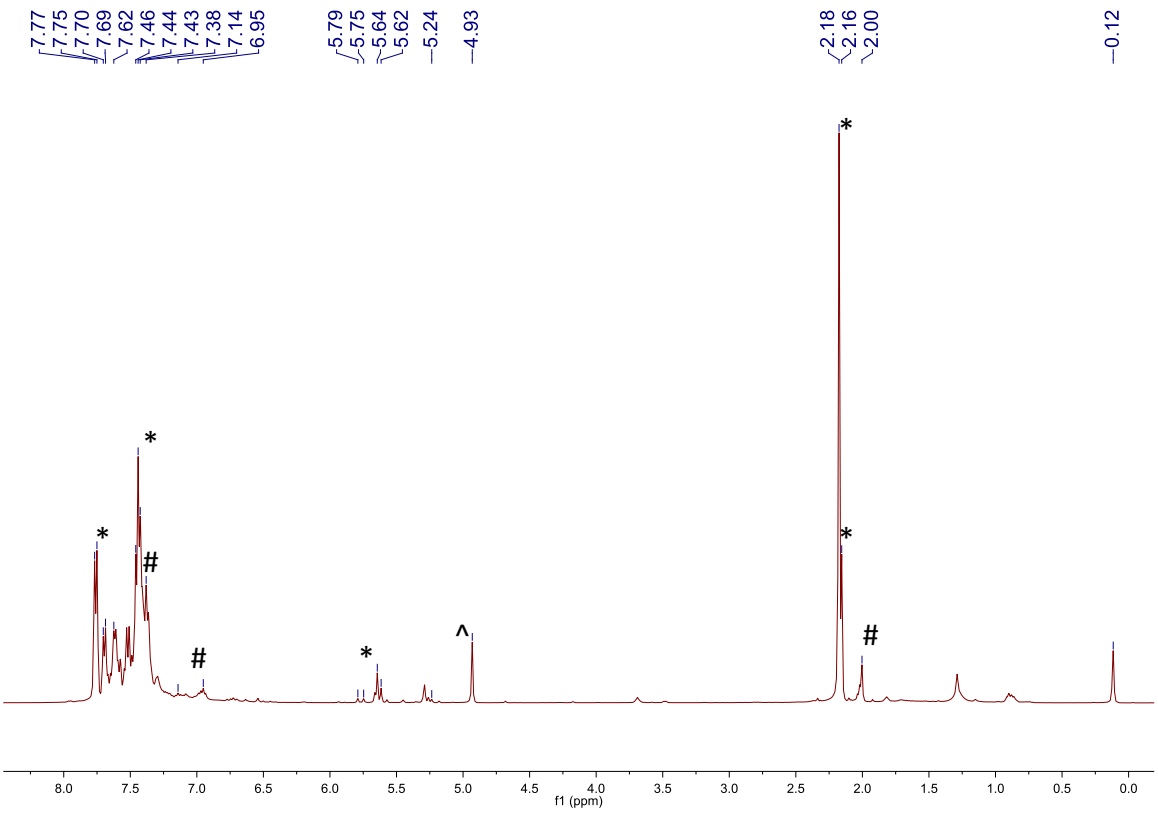

Figure A4.2. ^{1}H NMR spectrum in CD_2Cl_2 of the supernatant obtained after the removal of **4.1** by crystallization. **Experimental details:** The supernatant from the crystallization of **4.1** was decanted away from the red-orange solid and stored in a 20 mL scintillation vial. The red-orange solid was rinsed with hexanes (3 × 1 mL) until the washings were colorless. The washings were subsequently added to the supernatant. The pale orange supernatant was then dried *in vacuo*, redissolved in CD_2Cl_2 (1 mL), and a ^{1}H NMR spectrum was recorded. (*) indicates a resonance assignable to $Ph_2Si(OAc)_2$ and $Ph_2SiH(OAc)$, (#) indicates a resonance assignable to complex **4.1** and (^) indicates a resonance assignable to unreacted Ph_2SiH_2.

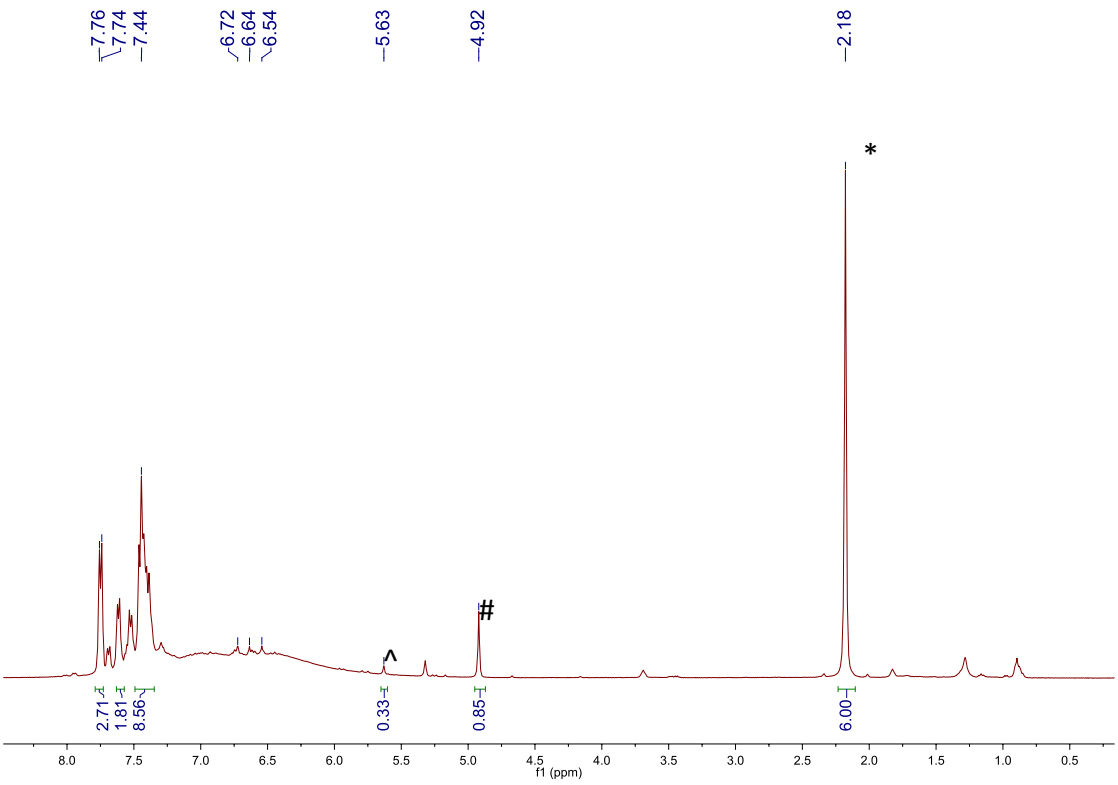

Figure A4.3. ^{1}H NMR spectrum of the *in situ* reaction of **4.1** with Ph_2SiH_2 (3 equiv) in CD_2Cl_2 after 5h. **Experimental details:** A J. Young NMR tube equipped with a Teflon rotoflow valve was charged with **4.1** (28.0 mg, 9.86 μmol) and CD_2Cl_2 (1 mL). This resulted in the formation of a dark red-orange solution. A ^{1}H NMR spectrum was then recorded. The sample was brought back into the glovebox, whereupon Ph_2SiH_2 (6.0 μL, 32.5 μmol) was added via micropipette. This resulted in a slight darkening of the solution to red-brown. The reaction was monitored intermittently by ^{1}H NMR spectroscopy over the course of 5 h. Over this period, the solution slowly became dark brown-black, concomitant with the deposition of a dark brown solid and formation of a Cu^0 mirror on the walls of the J. Young NMR tube. The (*) indicates a resonance assignable to $Ph_2Si(OAc)_2$, (^) indicates a resonance assignable to $Ph_2SiH(OAc)$, and (#) indicates a resonance assignable to unreacted Ph_2SiH_2.

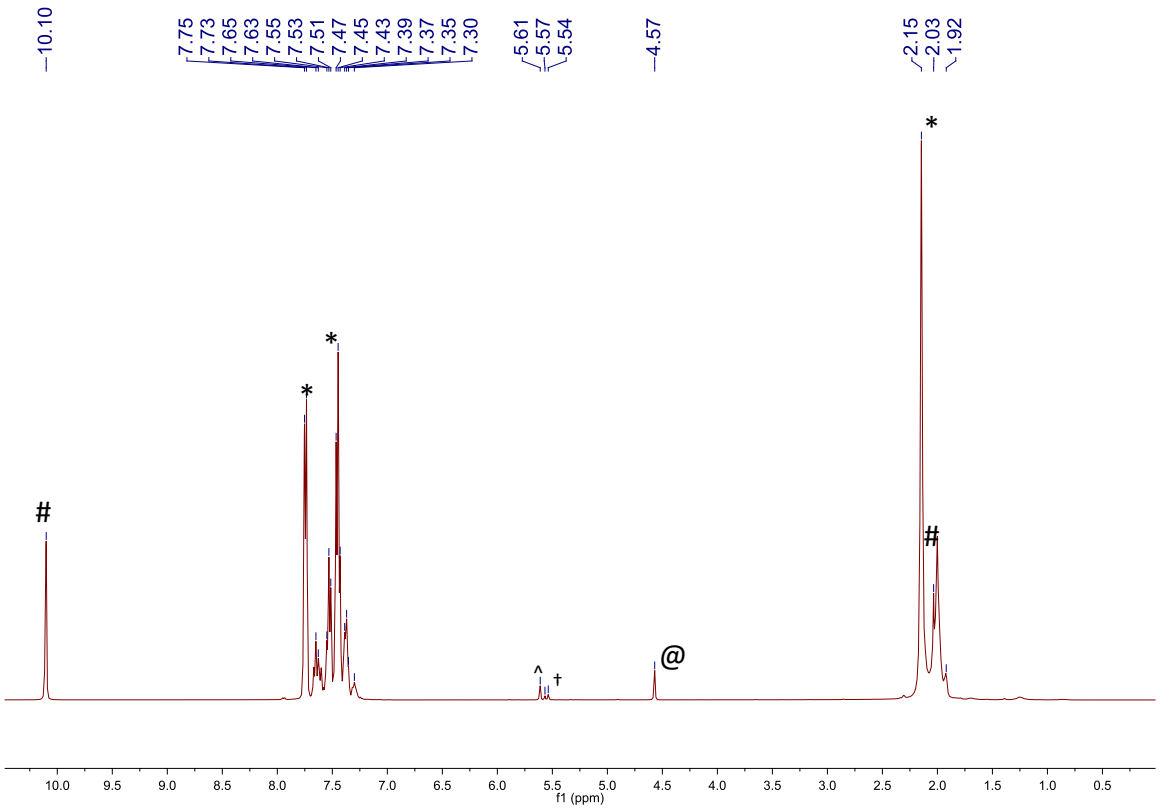

Figure A4.4. ^{1}H NMR spectrum of the reaction of HOAc (2 equiv) with Ph_2SiH_2 (1 equiv) in the presence of Cu(OAc) (0.167 equiv, 16.7 mol% Cu) in CD_3CN after 1 h. **Experimental details:** A J. Young NMR tube equipped with a Teflon rotoflow valve was charged with Cu(OAc) (4.4 mg, 0.036 mmol). A CD_3CN solution (1 mL) of Ph_2SiH_2 (40.0 µL, 0.216 mmol) and HOAc (24.76 µg, 0.433 mmol) was then added to the NMR tube, which resulted in formation of a pale brown solution, along with vigorous effervescence. A small amount of a fine brown powder remained undissolved at this point. The reaction mixture was allowed to stand for 1 h. Over this period, the solution continued to bubble, while a small amount of a dark brown solid precipitated from the reaction mixture. The (*) indicates a resonance assignable to $Ph_2Si(OAc)_2$, (^) indicates a resonance assignable to $Ph_2SiH(OAc)$, (#) indicates a resonance assignable to unreacted HOAc, (†) indicates a resonance assignable to CH_2Cl_2, and (@) indicates a resonance assignable to H_2.

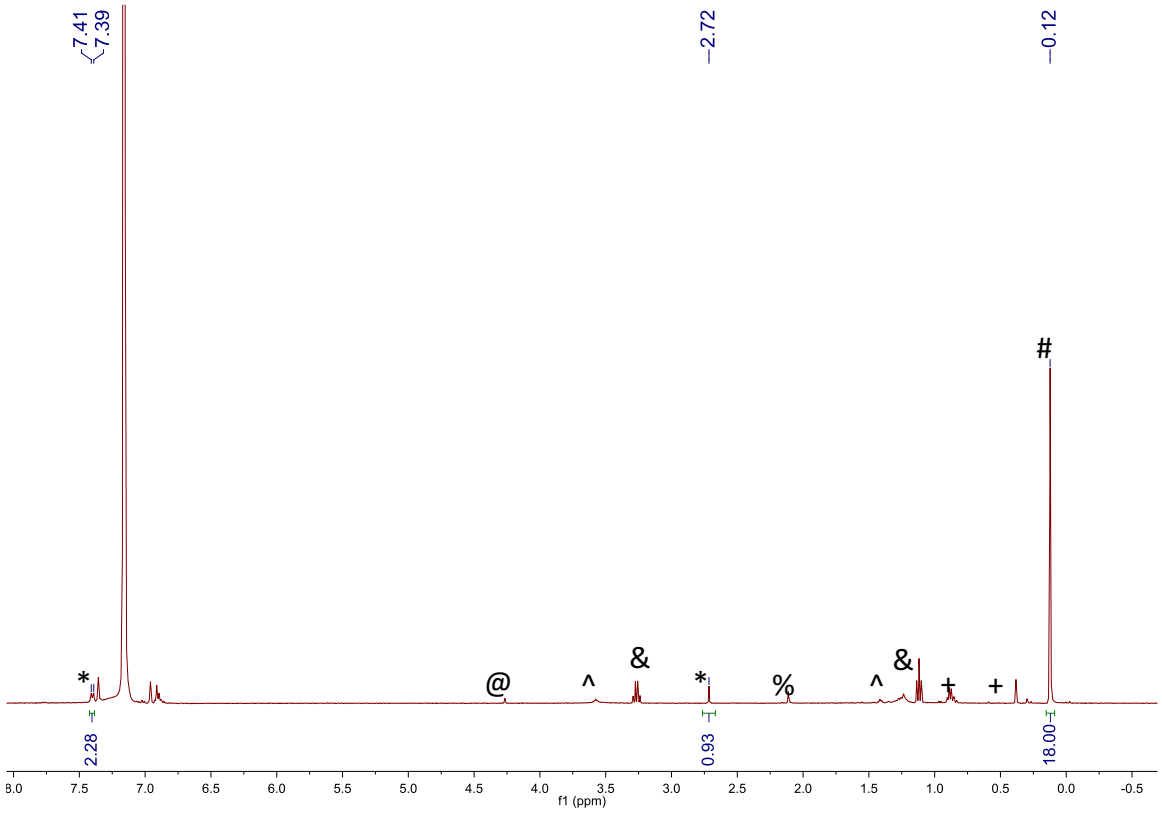

Figure A4.5. ^{1}H NMR spectrum of the *in situ* immobilization of **4.1** on SiO_2 in C_6D_6 after 1 h. **Experimental details:** A J. Young NMR tube equipped with a Teflon rotoflow valve was charged with **4.1** (2.0 mg, 0.705 μmol) and dissolved in C_6D_6 (1 mL). Hexamethyldisiloxane (0.15 μL, 0.705 μmol) was added as an internal standard. To this red solution was added dry SiO_2 (36.0 mg, which would give ca. 3% Cu by mass) as a solid. The mixture was shaken vigorously for 5 minutes and then allowed to stand for 1 h, which resulted in the gradual transfer of **4.1** from solution to the silica, to provide an orange solid and colorless solution. A ^{1}H NMR spectrum was then recorded. No signals attributable to **4.1** were observed in this spectrum. (*) indicates a resonance assignable to HCCPh, (#) indicates a resonance assignable to hexamethyldisiloxane, (@) indicates a resonance assignable to CH_2Cl_2, (^) indicates a resonance assignable to tetrahydrofuran, (&) indicates a resonance assignable to diethyl ether, (%) indicates a resonance assignable to toluene, and (+) indicates a resonance assignable to hexanes. Integration of the HCCPh acetylinic proton resonance at 2.72 ppm against the internal standard indicated that 1 equiv of HCCPh per **4.1** was formed upon immobilization of **4.1** on SiO_2.

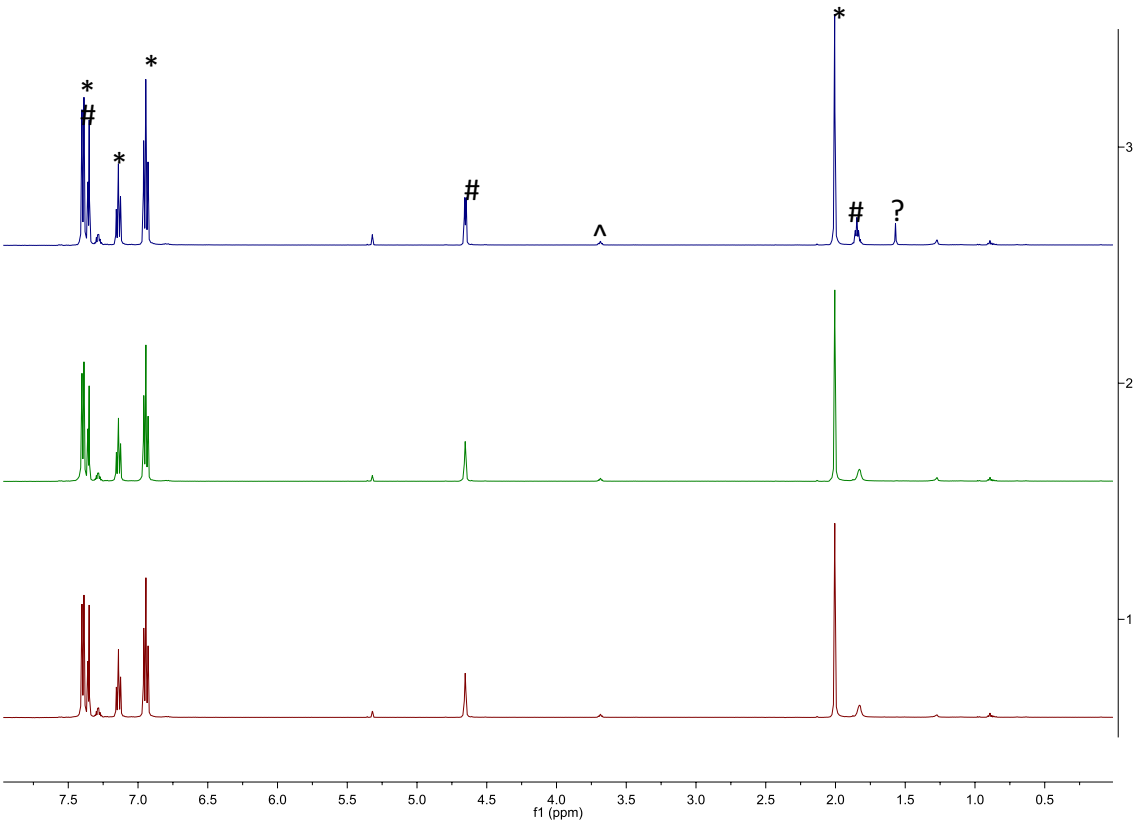

Figure A4.6. ^{1}H NMR spectra of the reaction of **4.1** with benzyl alcohol in CD_2Cl_2 over 24 h. **Experimental details:** A J. Young NMR tube equipped with a Teflon rotoflow valve was charged with **4.1** (16 mg, 5.6 μmol) and dissolved in CD_2Cl_2 (1 mL). To the NMR tube was added benzyl alcohol (3.5 μL, 34 μmol) with a micropipette. The reaction mixture was allowed to stand at room temperature for 24 h, over which time the progress of the reaction was monitored by ^{1}H NMR spectroscopy (bottom = 20 min, middle = 2 h, top = 24 h). (*) indicates a resonance assignable to **4.1**, (#) indicates a resonance assignable to benzyl alcohol, (?) indicates a resonance assignable to a new acetate containing product, and (^) indicates a resonance assignable to THF.

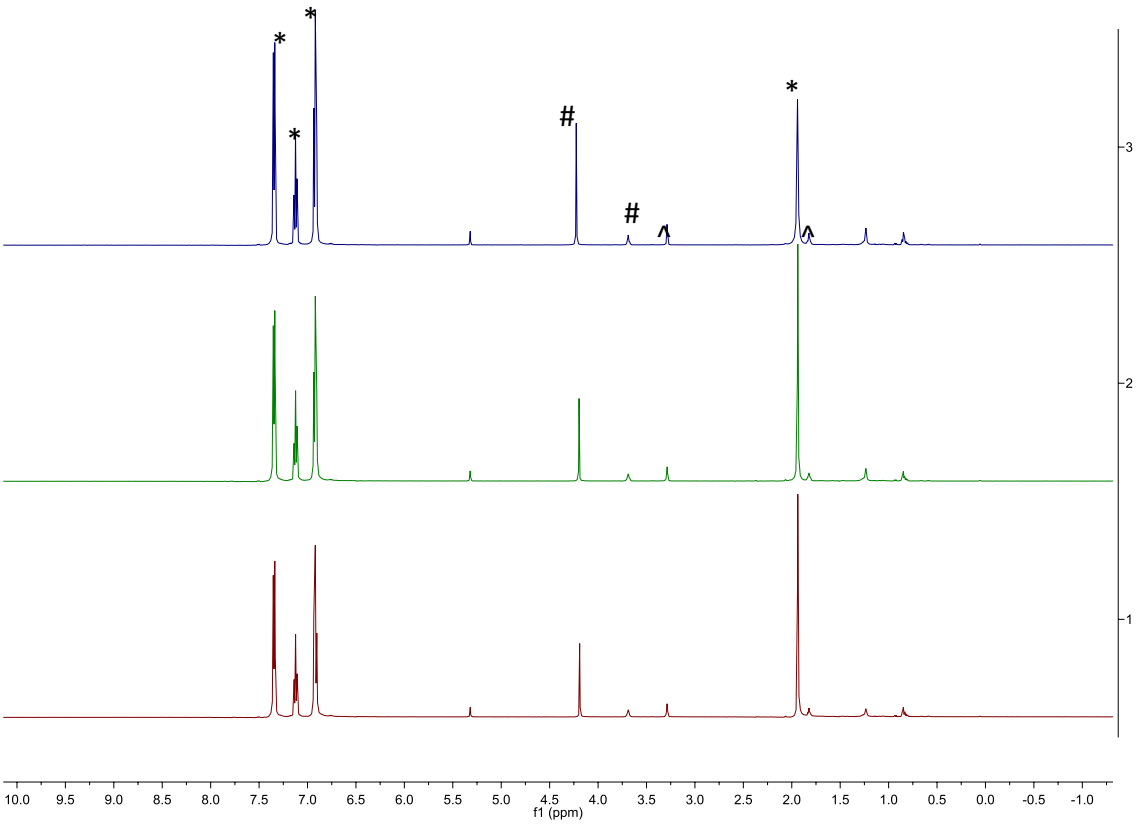

Figure A4.7. ^{1}H NMR spectra of **4.1** in a mixture of CD_2Cl_2 and CD_3OD (3:1, v/v) over 24 h. **Experimental details:** A J. Young NMR tube equipped with a Teflon rotoflow valve was charged with **4.1** (11 mg, 3.9 μmol) and dissolved in CD_2Cl_2 (0.6 mL). To the NMR tube was added CD_3OD (0.2 μL). The reaction mixture was allowed to stand at room temperature for 24 h, over which time the progress of the reaction was monitored by ^{1}H NMR spectroscopy (bottom = 20 min, middle = 2 h, top = 24 h). (*) indicates a resonance assignable to **4.1**, (#) indicates a resonance assignable to CD_3OD, and (^) indicates a resonance assignable to THF.

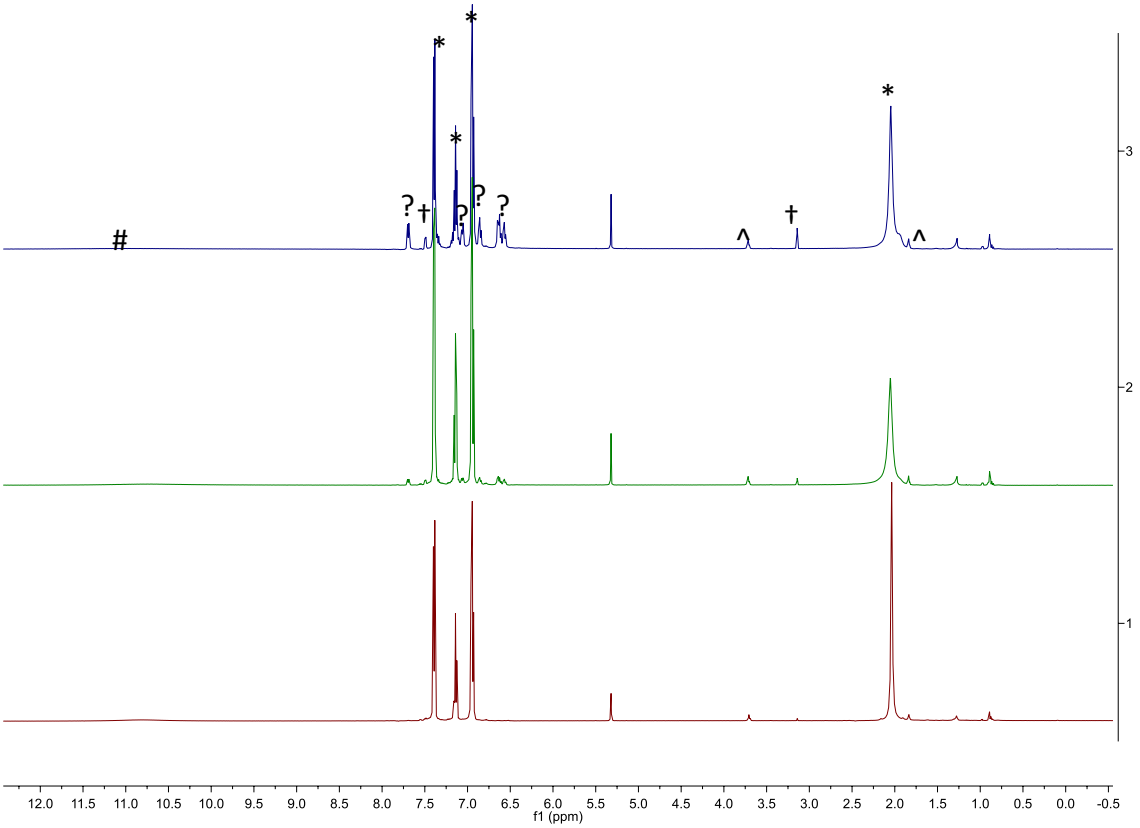

Figure A4.8. ^{1}H NMR spectra of the reaction of **4.1** with acetic acid in CD_2Cl_2 over 24 h. **Experimental details:** A J. Young NMR tube equipped with a Teflon rotoflow valve was charged with **4.1** (25 mg, 8.8 μmol) and dissolved in CD_2Cl_2 (1 mL). To the NMR tube was added acetic acid (3.0 μL, 48 μmol) with a micropipette. The reaction mixture was allowed to stand at room temperature for 24 h, over which time the progress of the reaction was monitored by ^{1}H NMR spectroscopy (bottom = 20 min, middle = 2 h, top = 24 h). (*) indicates a resonance assignable to **4.1**, (#) indicates a resonance assignable to acetic acid, (?) indicates a resonance assignable to an unidentified product, (†) indicates a resonance assignable to PhCCH, and (^) indicates a resonance assignable to THF.

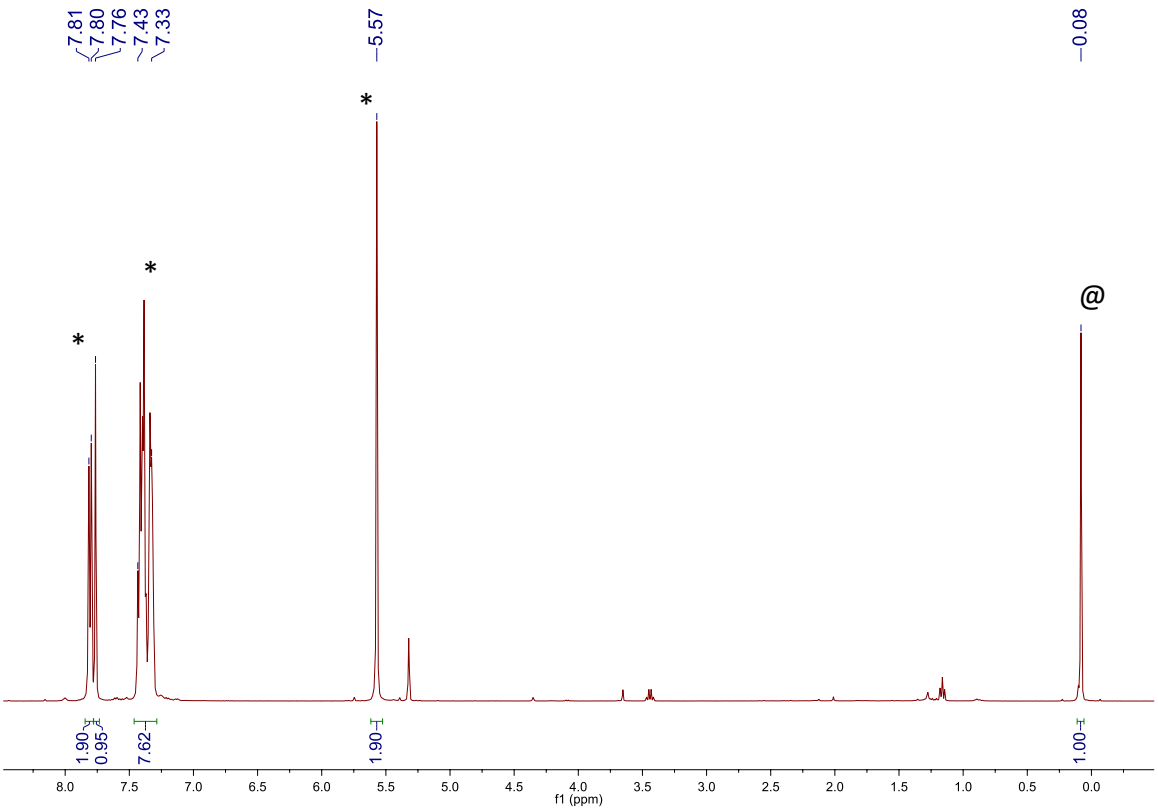

Figure A4.9. ^{1}H NMR spectrum in CD_2Cl_2 of the reaction of phenylacetylene and benzyl azide with **4.1** (0.5 mol% of Cu_{20} cluster) after 5 h. (*) indicates a resonance assignable to 1-benzyl-4-phenyl-1*H*-1,2,3-triazole (**4.3**) and (@) indicates a resonance assignable to hexamethyldisiloxane. No resonances assignable to **4.1** are present in the spectrum.

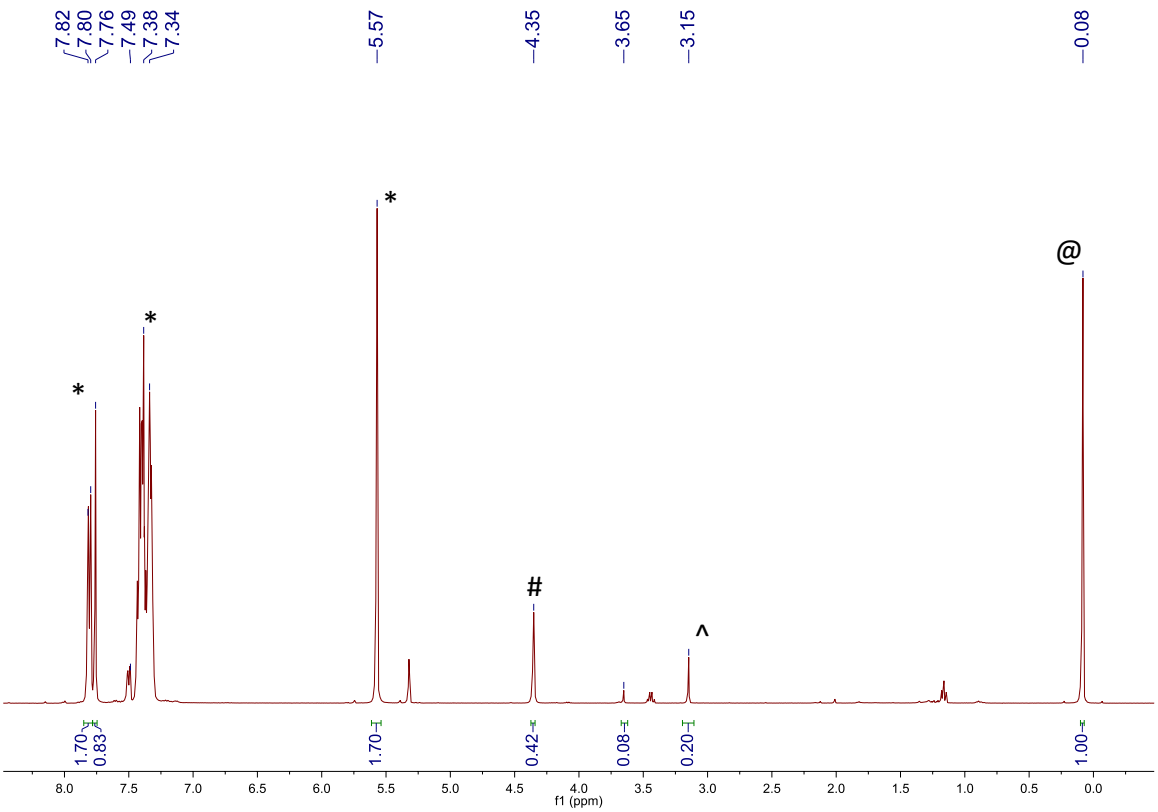

Figure A4.10. ^{1}H NMR spectrum in CD_2Cl_2 of the reaction of phenylacetylene and benzyl azide with **4.1** (0.05 mol% of Cu_{20} cluster) after 7 h. (*) indicates a resonance assignable to 1-benzyl-4-phenyl-1*H*-1,2,3-triazole (**4.3**), (#) indicates a resonance assignable to unreacted benzyl azide, (^) indicates a resonance assignable to unreacted phenylacetylene, and (@) indicates a resonance assignable to hexamethyldisiloxane.

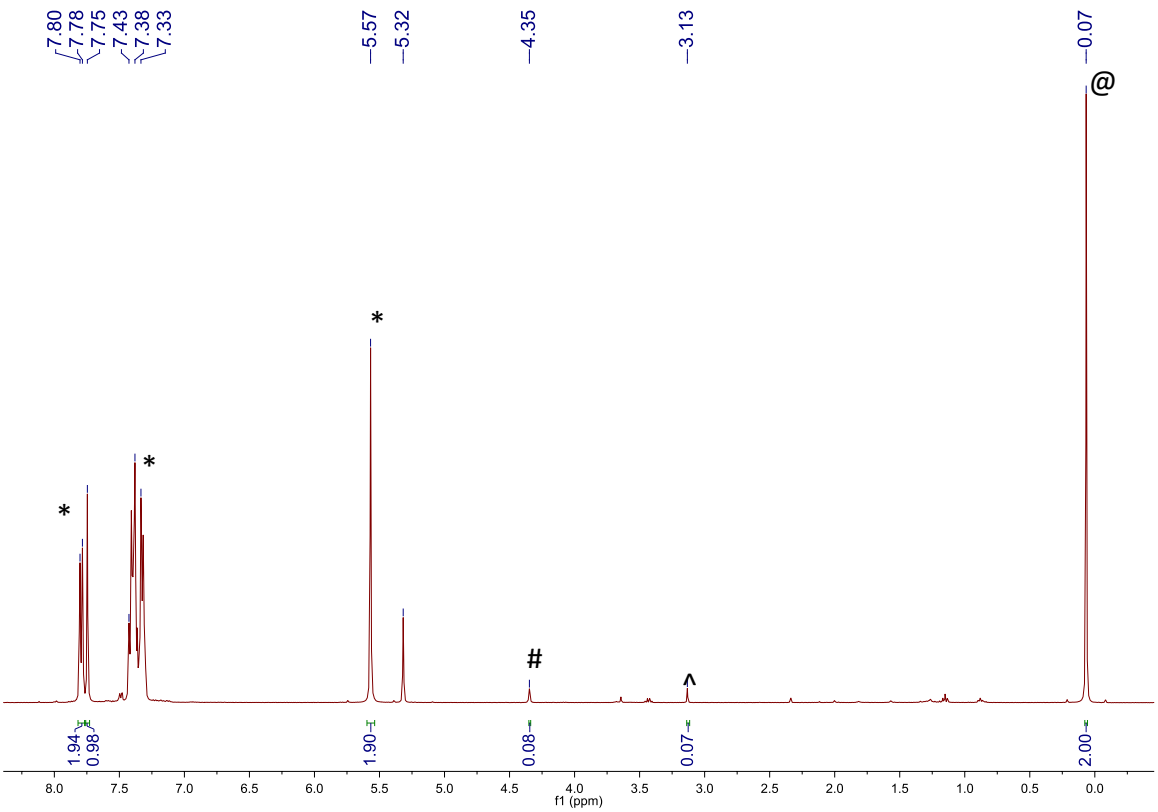

Figure A4.11. ^{1}H NMR spectrum in CD_2Cl_2 of the reaction of phenylacetylene and benzyl azide with **4.2** (0.5 mol% of Cu_{20} cluster) after 7 h. (*) indicates a resonance assignable to 1-benzyl-4-phenyl-1*H*-1,2,3-triazole (**4.3**), (#) indicates a resonance assignable to unreacted benzyl azide, (^) indicates a resonance assignable to unreacted phenylacetylene, and (@) indicates a resonance assignable to hexamethyldisiloxane. No resonances assignable to **4.1** or HOAc are present in the spectrum.

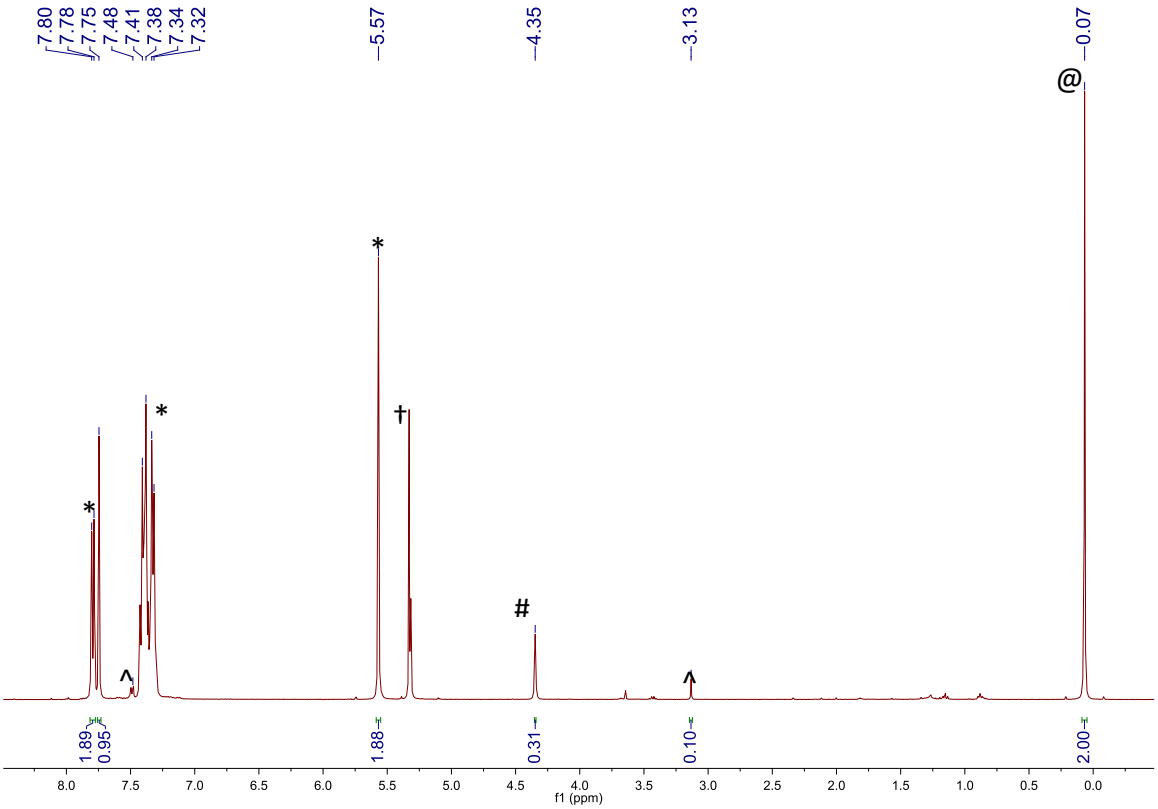

Figure A4.12. ^{1}H NMR spectrum in CD_2Cl_2 of phenylacetylene, benzyl azide, and **4.2** (0.5 mol% of Cu_{20} cluster, recovered from a previous catalytic cycle) after 7 h. **Experimental details:** A J. Young NMR tube equipped with a Teflon rotoflow valve was charged with phenylacetylene (4.0 µL, 0.036 mmol), benzyl azide (5.0 µL, 0.040 mmol), hexamethyldisiloxane (1.0 µL, 0.0047 mmol) and **4.2** (11.1 mg, 0.2 µmol, 0.5 mol% of Cu_{20} cluster), and the sample was monitored by ^{1}H NMR spectroscopy over the course of 7h (Figure A4.8). The J. Young NMR tube was then brought into the glovebox and its contents transferred to a 20 mL scintillation vial. The colorless supernatant was decanted off of the red-orange solid **4.2**, the solids were rinsed with DCM (3 × 1 mL), and then dried *in vacuo*. The recovered solid **4.2** was then transferred to a J. Young NMR tube equipped with a Teflon rotoflow valve. To this tube was then added phenylacetylene (4.0 µL, 0.036 mmol) and benzyl azide (5.0 µL, 0.040 mmol) and hexamethyldisiloxane (1.0 µL, 0.0047 mmol). The sample was monitored intermittently by ^{1}H NMR spectroscopy over the course of 7h. (*) indicates a resonance assignable to 1-benzyl-4-phenyl-1*H*-1,2,3-triazole (**4.3**), (#) indicates a resonance assignable to unreacted benzyl azide, (^) indicates a resonance assignable to unreacted phenylacetylene, (@) indicates a resonance assignable to hexamethyldisiloxane and (†) indicates a resonance assignable to CH_2Cl_2.

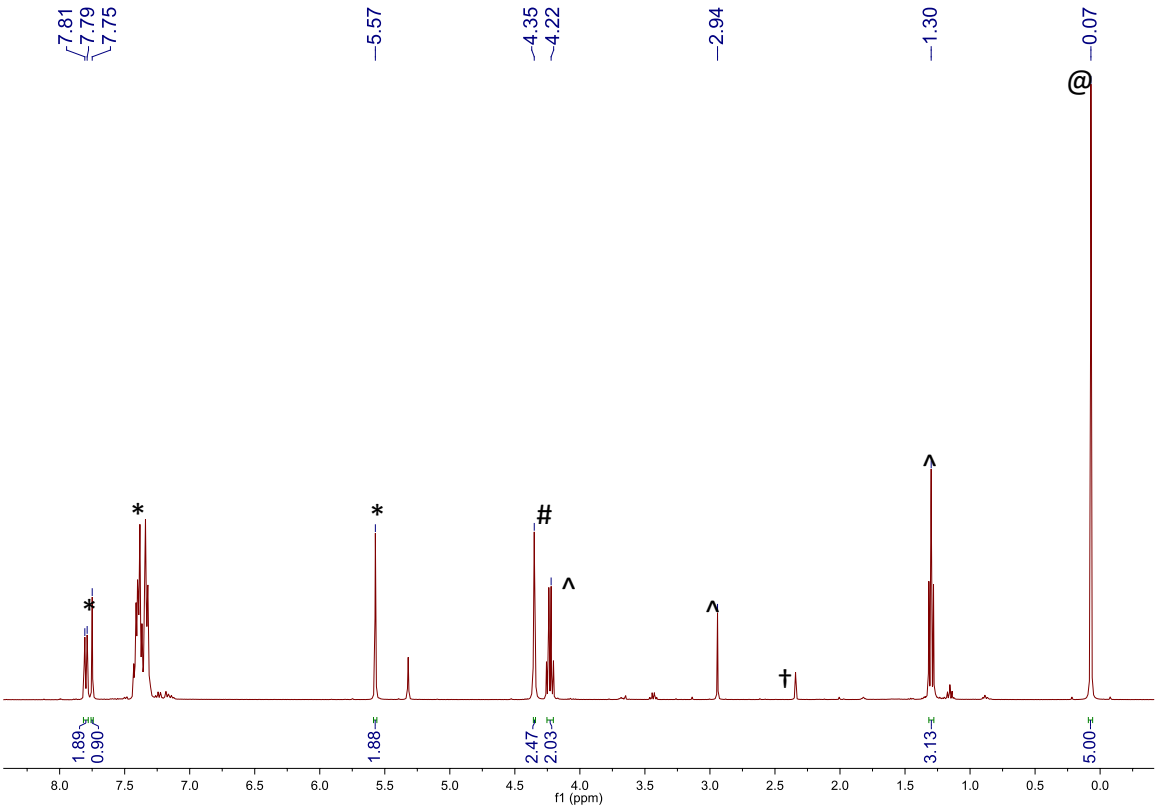

Figure A4.13. ^{1}H NMR spectrum in CD_2Cl_2 of ethyl propiolate, benzyl azide, and the post-catalysis supernatant generated upon reaction of phenylacetylene, benzyl azide, and **4.2** (0.5 mol% of Cu_{20} cluster), after 7 h. **Experimental details:** A J. Young NMR tube equipped with a Teflon rotoflow valve was charged with phenylacetylene (4.0 µL, 0.036 mmol), benzyl azide (5.0 µL, 0.040 mmol), hexamethyldisiloxane (2.5 µL, 0.0118 mmol), and **4.2** (11.1 mg, 0.2 µmol, 0.5 mol% of Cu_{20} cluster), and the sample was monitored by ^{1}H NMR spectroscopy over the course of 7h. The J. Young NMR tube was then brought into the glovebox and its contents transferred to a 20 mL scintillation vial. The colorless solution was filtered through a Celite column (1 × 0.5 cm) supported on glass wool, leaving behind the red-orange solid. The colorless solution was transferred to a second J. Young NMR tube equipped with a Teflon rotoflow valve. To this NMR tube was added ethyl propiolate (3.7 µL, 0.036 mmol), and benzyl azide (5.0 µL, 0.040 mmol). The sample was monitored intermittently by ^{1}H NMR spectroscopy over the course of 7h. (*) indicates a resonance assignable to 1-benzyl-4-phenyl-1*H*-1,2,3-triazole (**4.3**), (#) indicates a resonance assignable to unreacted benzyl azide, (^) indicates a resonance assignable to unreacted ethyl propiolate, (@) indicates a resonance assignable to hexamethyldisiloxane, and (†) indicates a resonance assignable to toluene. No resonances assignable to **4.4** were observed in the spectrum.

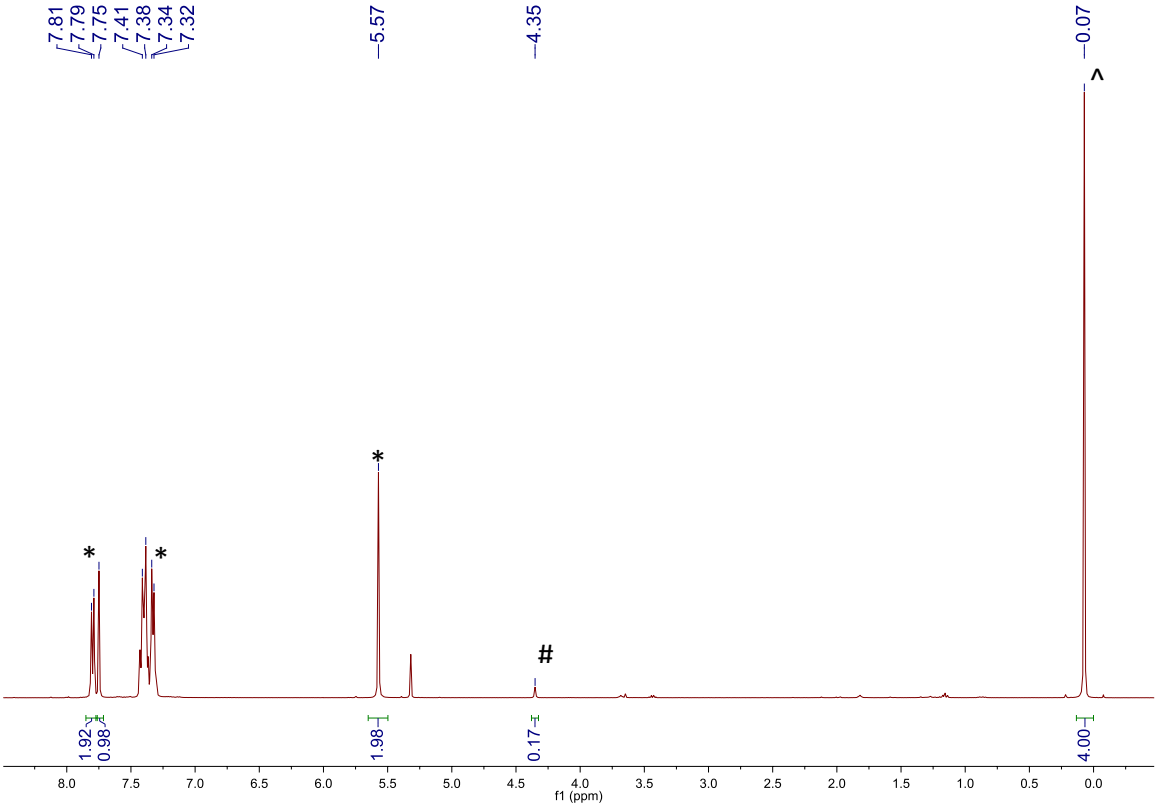

Figure A4.14. ^{1}H NMR spectrum in CD_2Cl_2 of the reaction of phenylacetylene and benzyl azide with **4.2** (0.5 mol% of Cu_{20} cluster) after 2 h at 40 °C. (*) indicates a resonance assignable to 1-benzyl-4-phenyl-1*H*-1,2,3-triazole (**4.3**), (#) indicates a resonance assignable to unreacted benzyl azide, and (^) indicates a resonance assignable to hexamethyldisiloxane. No resonances assignable to **4.1** or HOAc are observed in the spectrum. However, during the course of the reaction the catalyst undergoes a gradual color change from red-orange to pale yellow over the course of the reaction, suggesting that it may undergo a structural change upon heating.

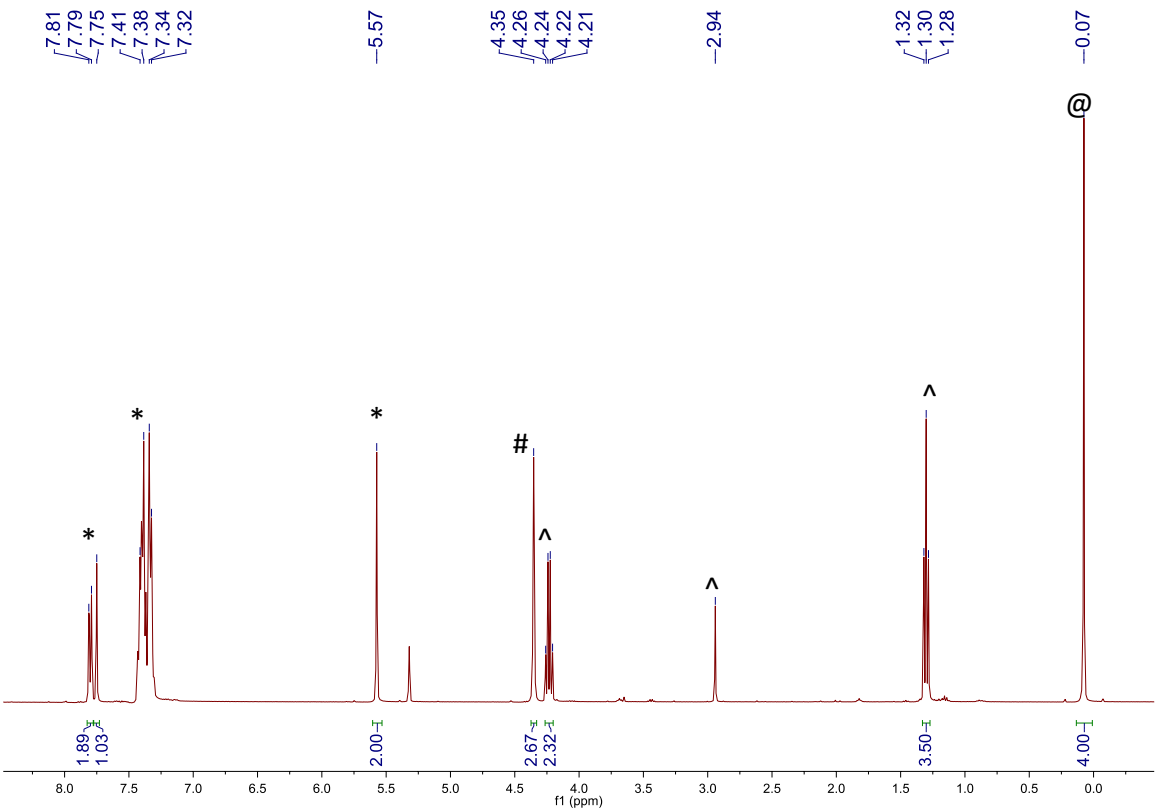

Figure A4.15. ^{1}H NMR spectrum in CD_2Cl_2 of ethyl propiolate, benzyl azide, and the post-catalysis supernatant generated upon reaction of phenylacetylene, benzyl azide, and **4.2** (0.5 mol% of Cu_{20} cluster) at 40 °C, after 7 h. **Experimental details:** A J. Young NMR tube equipped with a Teflon rotoflow valve was charged with phenylacetylene (4.0 µL, 0.036 mmol), benzyl azide (5.0 µL, 0.040 mmol), hexamethyldisiloxane (2 µL, 0.0118 mmol), and **4.2** (11.1 mg, 0.2 µmol, 0.5 mol% of Cu_{20} cluster), and the sample was monitored by ^{1}H NMR spectroscopy over the course of 2h at 40 °C (Figure A4.11). The J. Young NMR tube was then brought into the glovebox and its contents transferred to a 20 mL scintillation vial. The colorless solution was filtered through a Celite column (1 × 0.5 cm) supported on glass wool, leaving behind a pale yellow solid. The colorless solution was transferred to a second J. Young NMR tube equipped with a Teflon rotoflow valve. To this NMR tube was added ethyl propiolate (3.7 µL, 0.036 mmol), and benzyl azide (5.0 µL, 0.040 mmol). The sample was monitored intermittently by ^{1}H NMR spectroscopy over the course of 7h. (*) indicates a resonance assignable to 1-benzyl-4-phenyl-1*H*-1,2,3-triazole (**4.3**), (#) indicates a resonance assignable to unreacted benzyl azide, (^) indicates a resonance assignable to unreacted ethyl propiolate, and (@) indicates a resonance assignable to hexamethyldisiloxane. No resonances assignable to **4.4** were observed in the spectrum.

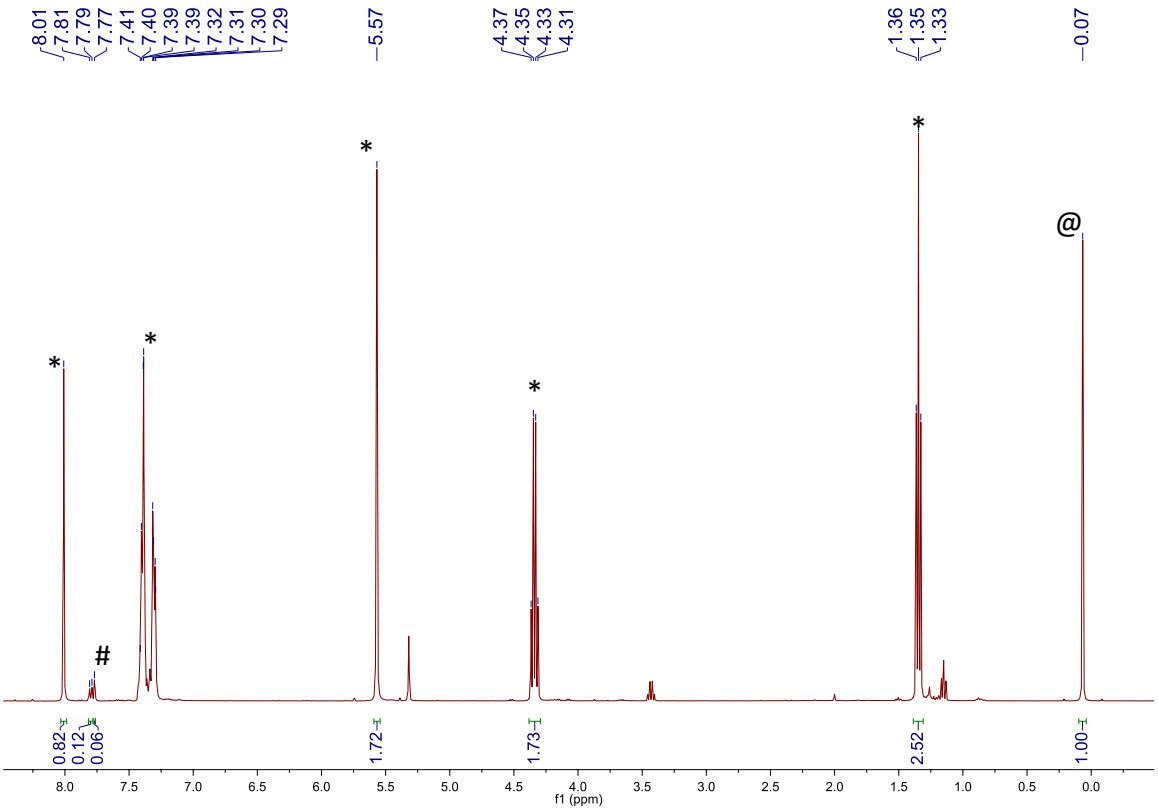

Figure A4.16. ^{1}H NMR spectrum in CD_2Cl_2 of ethyl propiolate, benzyl azide, and **4.1** (0.5 mol% of Cu_{20} cluster) after 5 h. (*) indicates a resonance assignable to ethyl 1-benzyl-1*H*-1,2,3-triazole-4-carboxylate (**4.4**), (#) indicates a resonance assignable to 1-benzyl-4-phenyl-1*H*-1,2,3-triazole (**4.3**), and (@) indicates a resonance assignable to hexamethyldisiloxane.

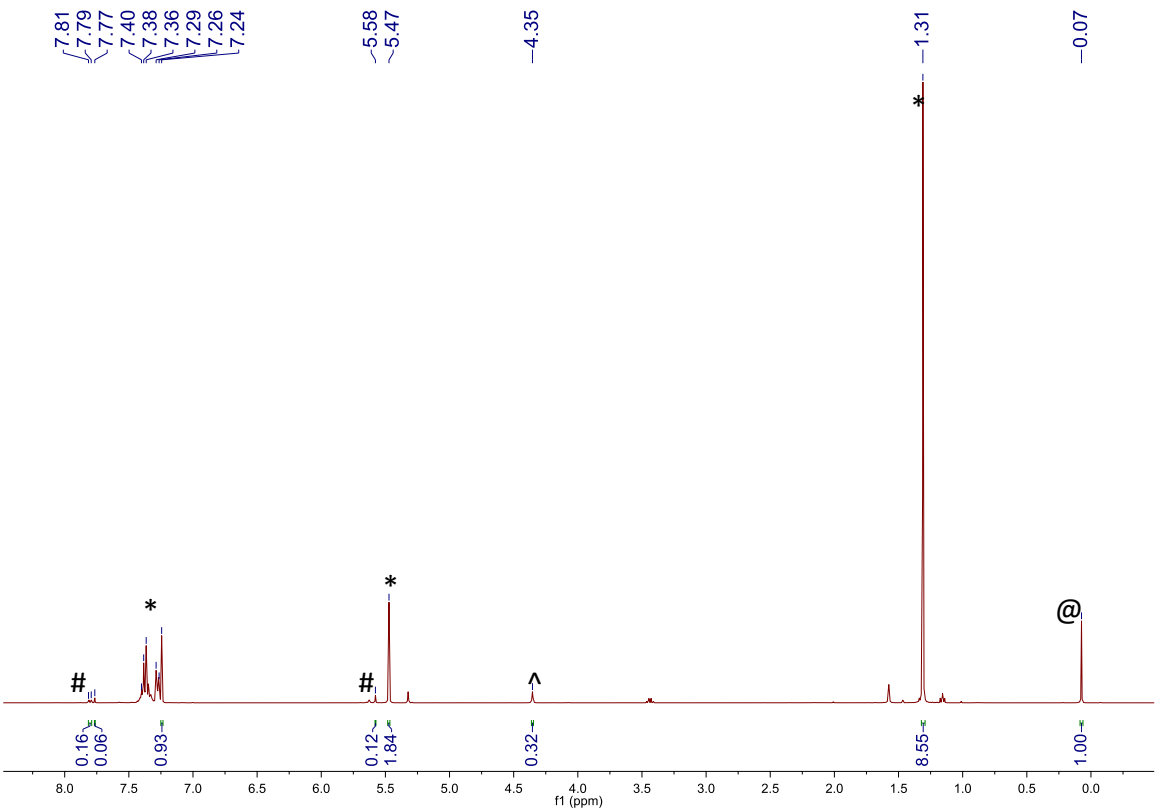

Figure A4.17. ^{1}H NMR spectrum in CD_2Cl_2 of 3,3-dimethyl-1-butyne, benzyl azide, and **4.1** (0.5 mol% of Cu_{20} cluster) after 5 h. (*) indicates a resonance assignable to 1-benzyl-4-*tert*-butyl-1*H*-1,2,3-triazole (**4.5**), (#) indicates a resonance assignable to 1-benzyl-4-phenyl-1*H*-1,2,3-triazole (**4.3**), (^) indicates a resonance assignable to unreacted benzyl azide, and (@) indicates a resonance assignable to hexamethyldisiloxane.

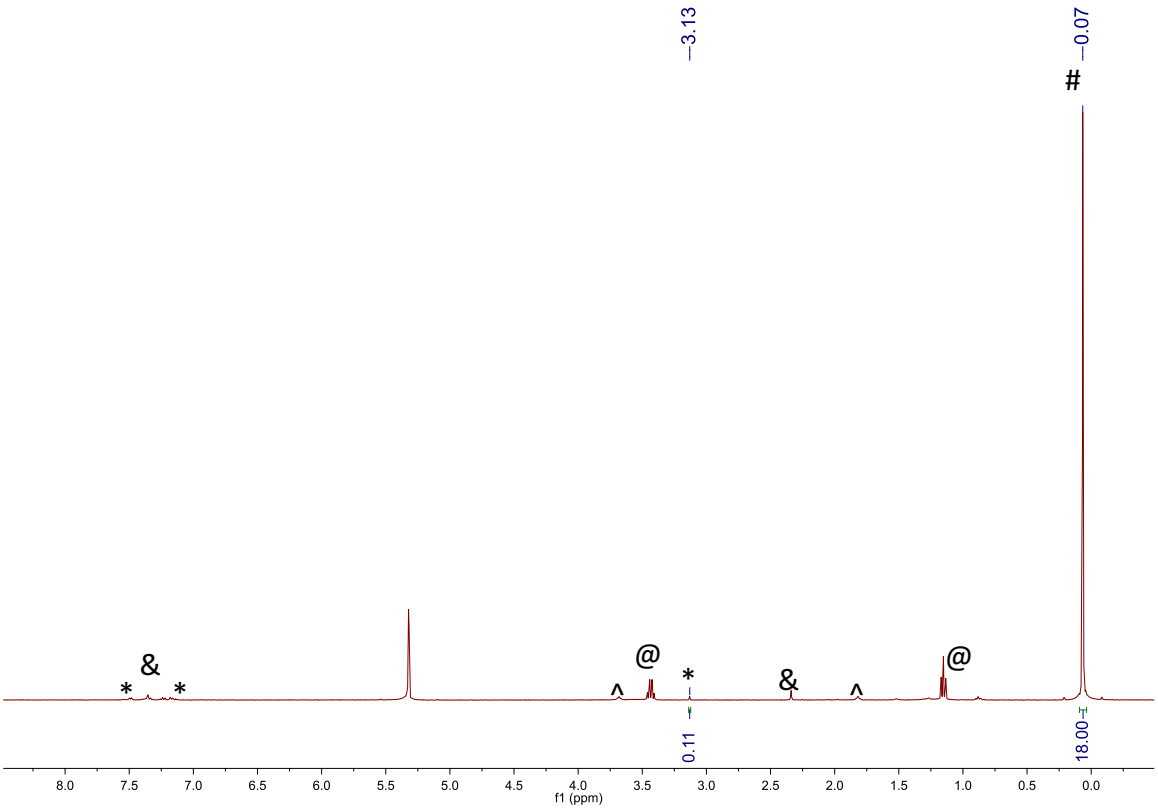

Figure A4.18. ^{1}H NMR spectrum of a sample of **4.2** that was allowed to stand in CD_2Cl_2 for 7h. **Experimental details:** A J. Young NMR tube equipped with a Teflon rotoflow valve was charged with **4.2** (41.0 mg, 0.722 μmol of Cu_{20} cluster) and suspended in CD_2Cl_2 (1.2 mL). Hexamethyldisiloxane (2.5 μL, 0.0118 mmol) was added as an internal standard. The sample was then monitored intermittently by ^{1}H NMR spectroscopy over the course of 7h. Over the course of the spectroscopic monitoring of this sample, the solution remained colorless. (*) indicates a resonance assignable to a small amount of phenylacetylene, (#) indicates a resonance assignable to hexamethyldisiloxane, (@) indicates a resonance assignable to diethyl ether, (^) indicates a resonance assignable to tetrahydrofuran, and (&) indicates a resonance assignable to toluene. No resonances assignable to **4.1** or HOAc are present in the spectrum.

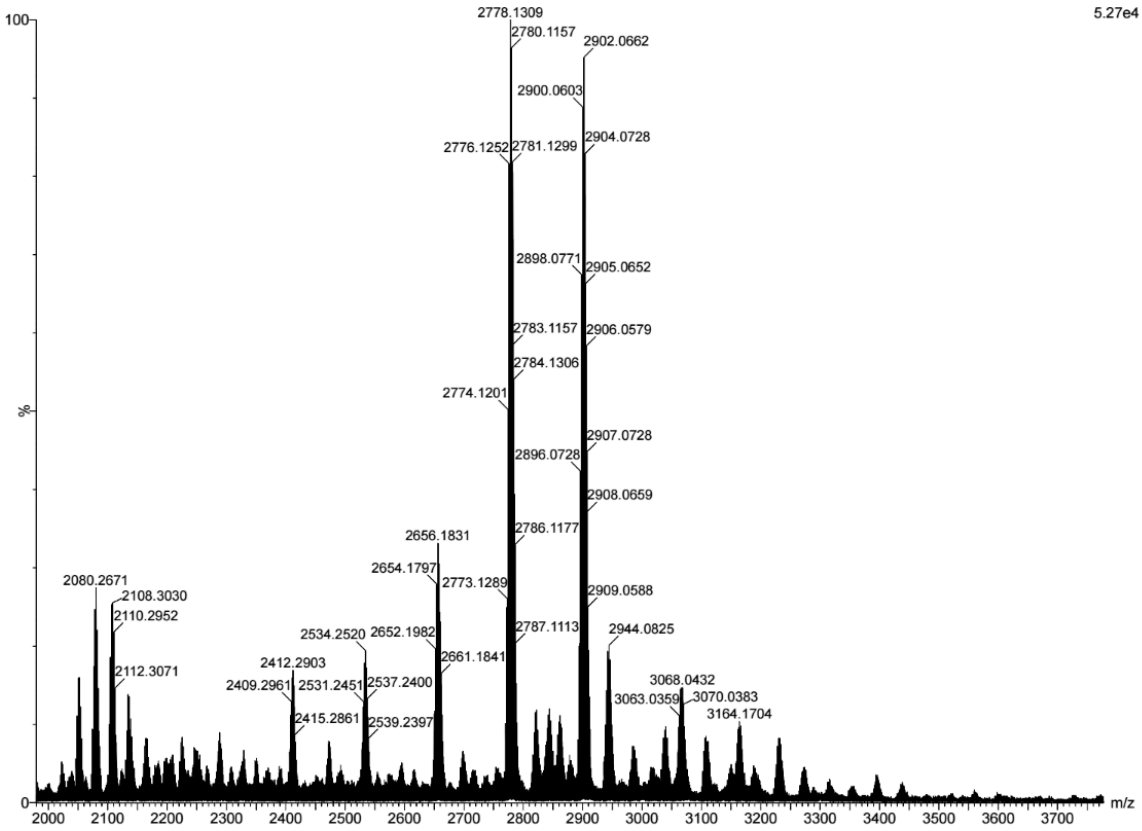

Figure A4.19. Partial ESI-MS (positive mode) of $[Cu_{20}(CCPh)_{12}(OAc)_6]$ (**4.1**).

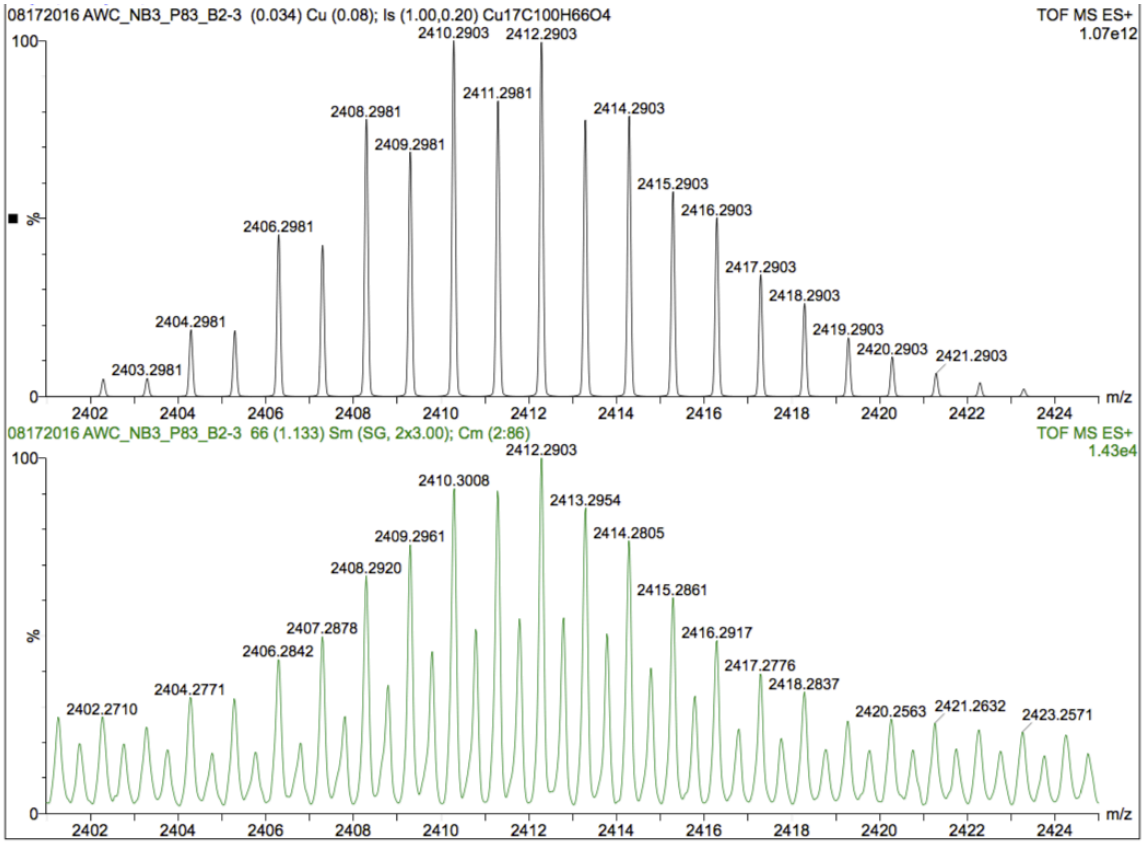

Figure A4.20. Partial ESI-MS (positive mode) of $[Cu_{20}(CCPh)_{12}(OAc)_6]$ (**4.1**). The experimental (bottom) and calculated (top) peaks assignable to the $[M - 3Cu - 4OAc]^+$ ion are shown.

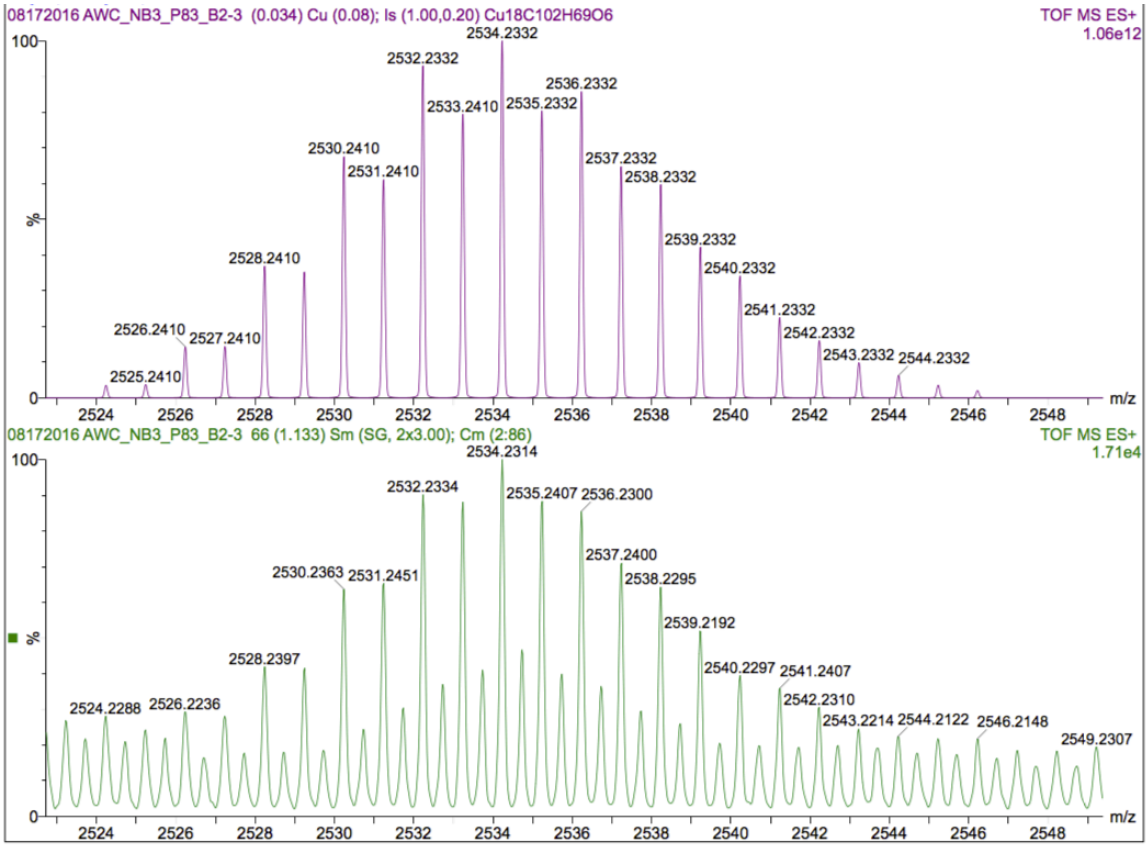

Figure A4.21. Partial ESI-MS (positive mode) of $[Cu_{20}(CCPh)_{12}(OAc)_6]$ (**4.1**). The experimental (bottom) and calculated (top) peaks assignable to the $[M - 2Cu - 3OAc]^+$ ion are shown.

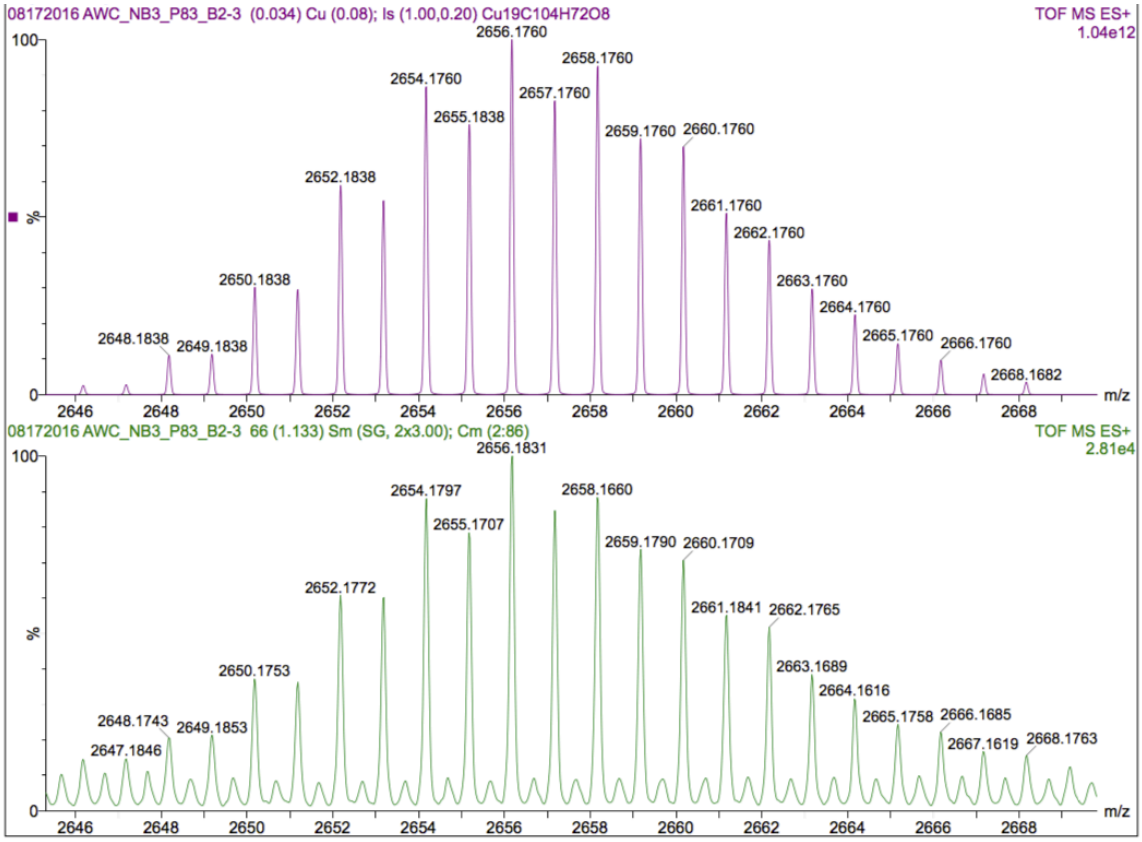

Figure A4.22. Partial ESI-MS (positive mode) of $[Cu_{20}(CCPh)_{12}(OAc)_6]$ (**4.1**). The experimental (bottom) and calculated (top) peaks assignable to the $[M - Cu - 2OAc]^+$ ion are shown.

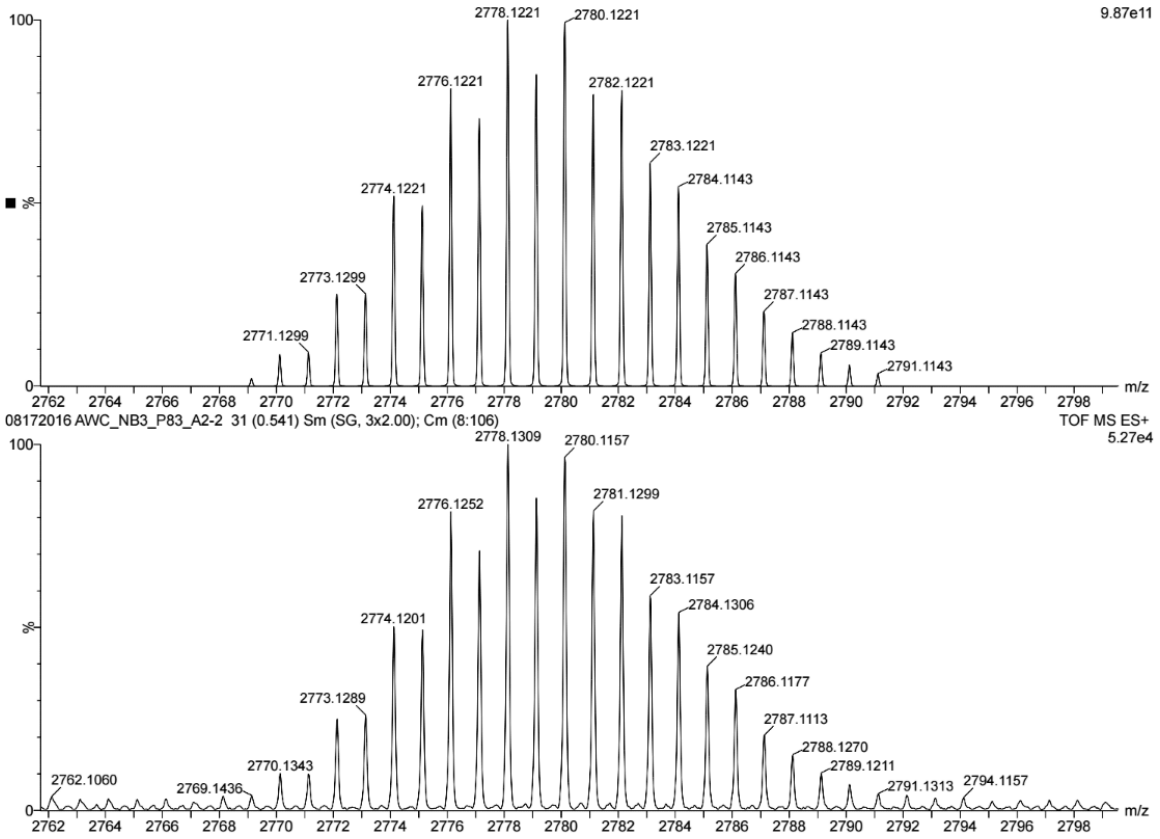

Figure A4.23. Partial ESI-MS (positive mode) of $[Cu_{20}(CCPh)_{12}(OAc)_6]$ (**4.1**). The experimental (bottom) and calculated (top) peaks assignable to the $[M - OAc]^+$ ion are shown.

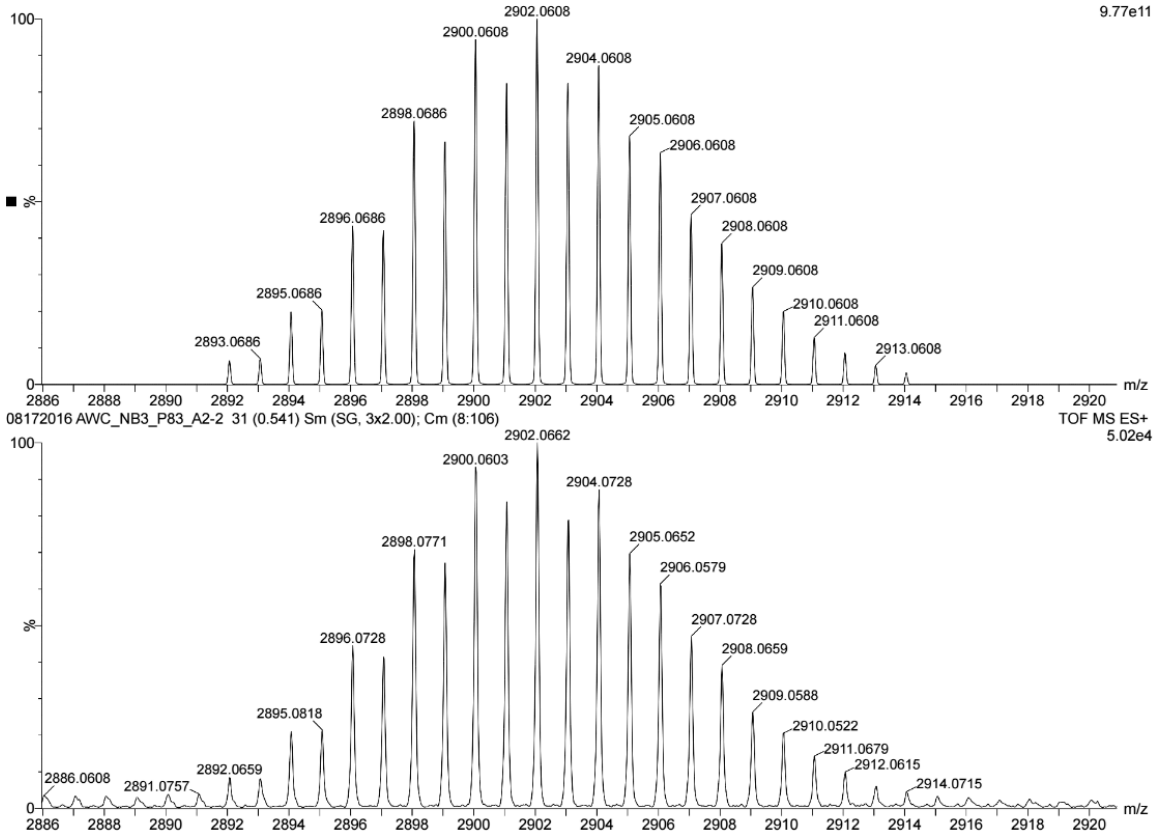

Figure A4.24. Partial ESI-MS (positive mode) of $[Cu_{20}(CCPh)_{12}(OAc)_6]$ (**4.1**). The experimental (bottom) and calculated (top) peaks assignable to the $[M + Cu]^+$ ion are shown.

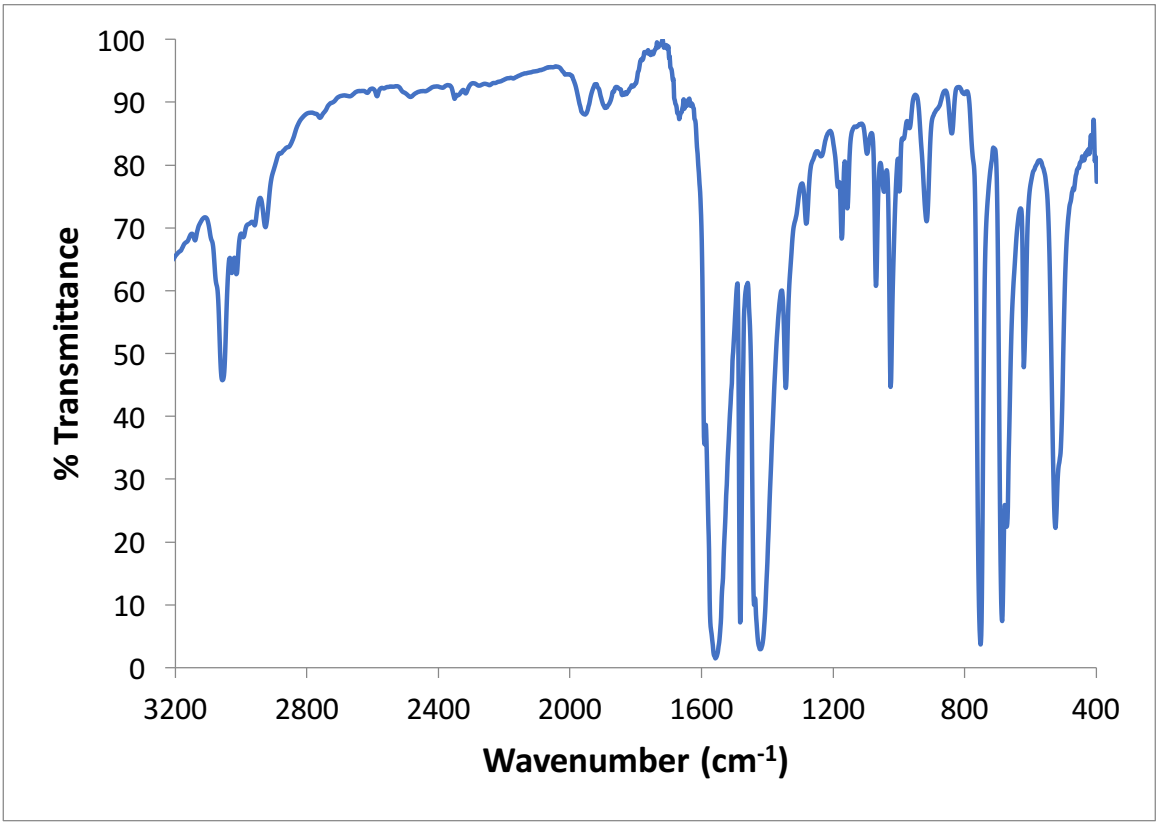

Figure A4.25. Partial IR spectrum of **4.1** (KBr pellet)

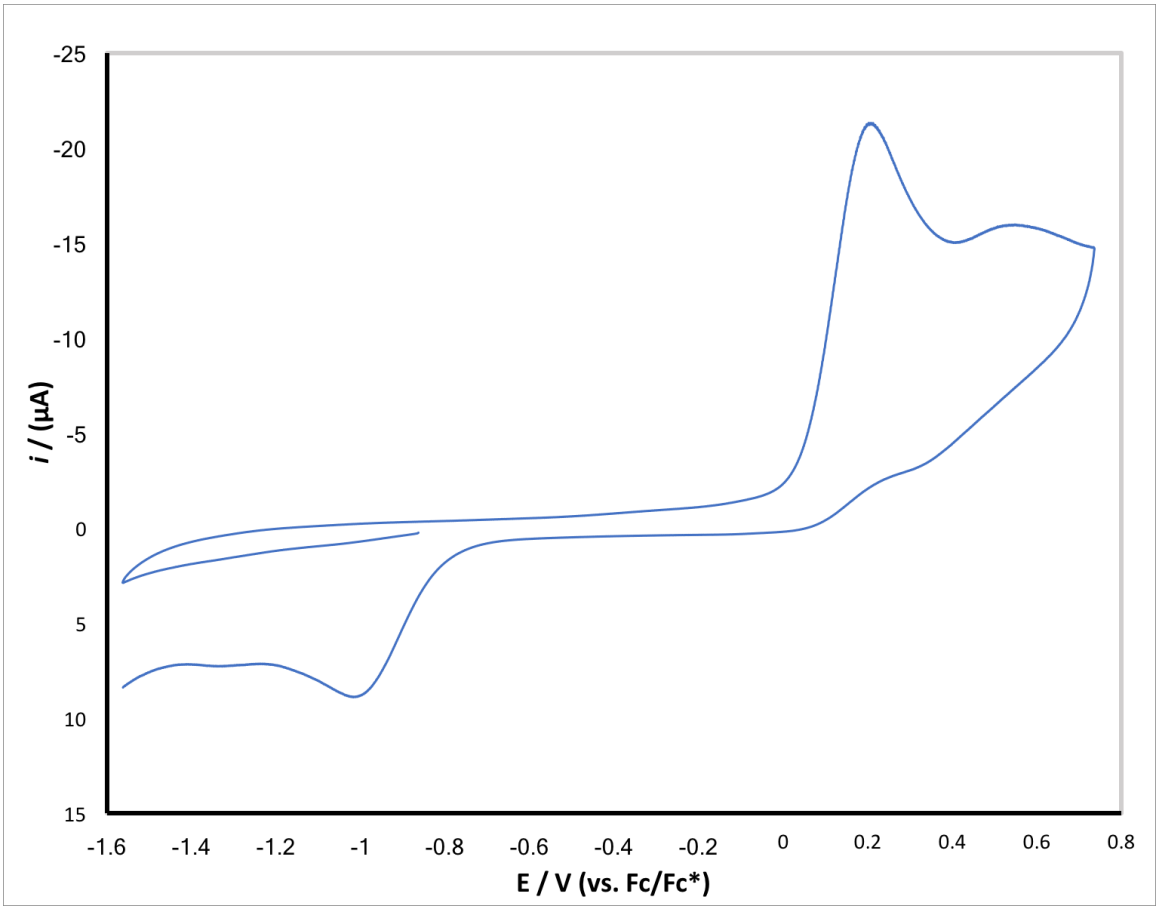

Figure A4.26. Cyclic voltammogram of complex **4.1** (100 mV/s, vs. Fc/Fc^{+}), measured in CH_2Cl_2 with 0.1 M $[NBu_4][PF_6]$ as the supporting electrolyte.

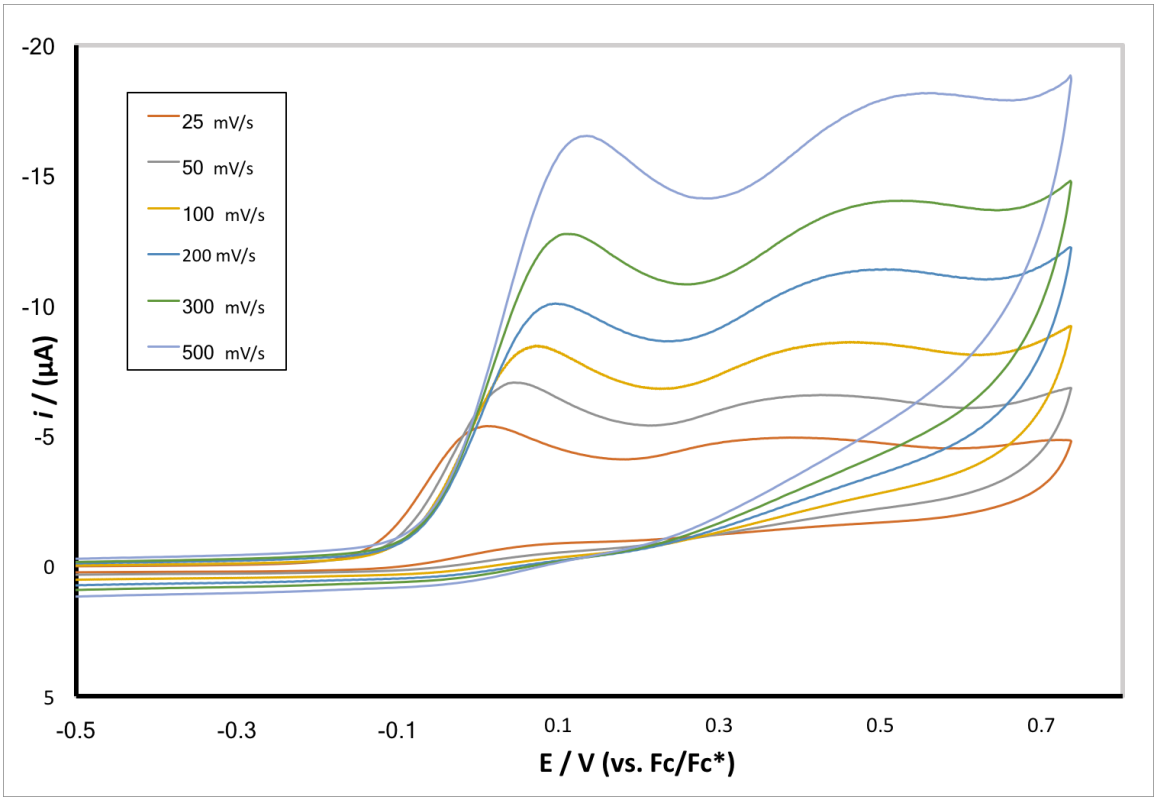

Figure A4.27. Cyclic voltammogram of the oxidation features of complex **4.1** measured in CH_2Cl_2 with 0.1 M $[NBu_4][PF_6]$ as the supporting electrolyte (vs. Fc/Fc^+).

Table 4.4. Electrochemical parameters for **4.1** in CH_2Cl_2 (vs. Fc/Fc^+, $[NBu_4][PF_6]$ as the supporting electrolyte).

Oxidation Feature 1	**Scan Rate, V/s**	**$E_{p,c}$, V**
	0.025	0.013
	0.050	0.046
	0.100	0.068
	0.200	0.097
	0.300	0.109
	0.500	0.136

Oxidation Feature 2	**Scan Rate, V/s**	**$E_{p,c}$, V**
	0.025	0.378
	0.050	0.419
	0.100	0.443
	0.200	0.474
	0.300	0.508
	0.500	0.544

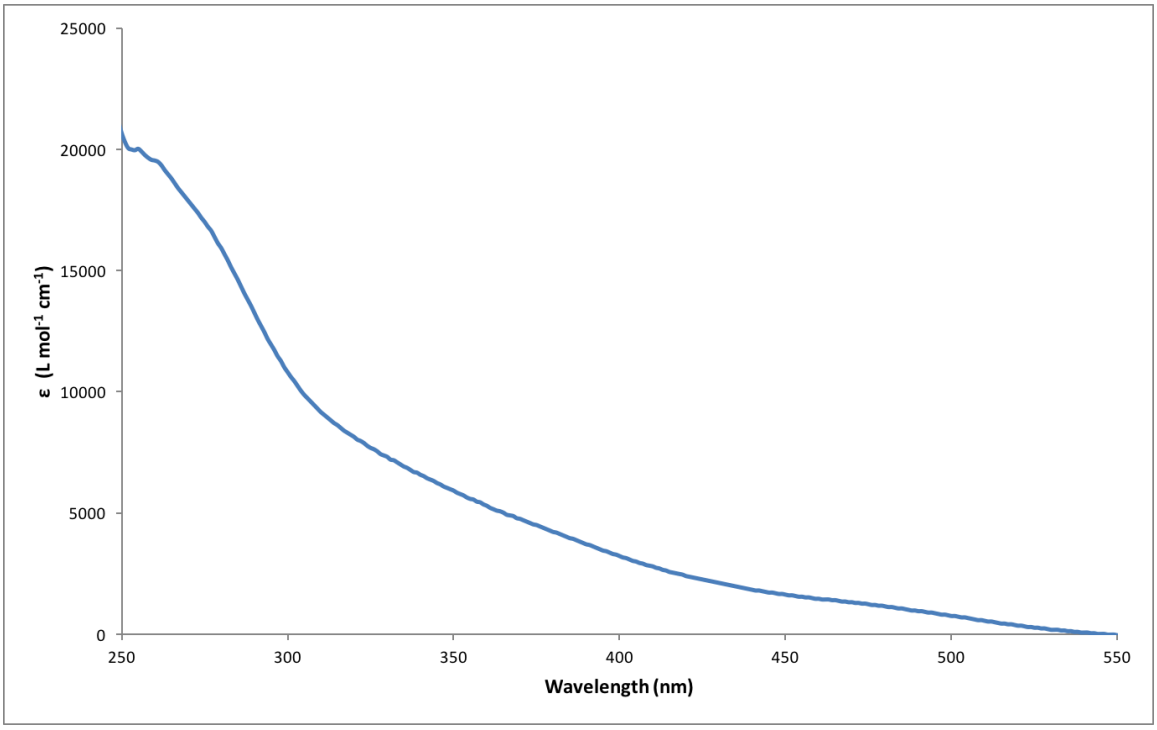

Figure A4.28. UV-vis spectrum of complex **4.1** (3.5 μM) in CH_2Cl_2

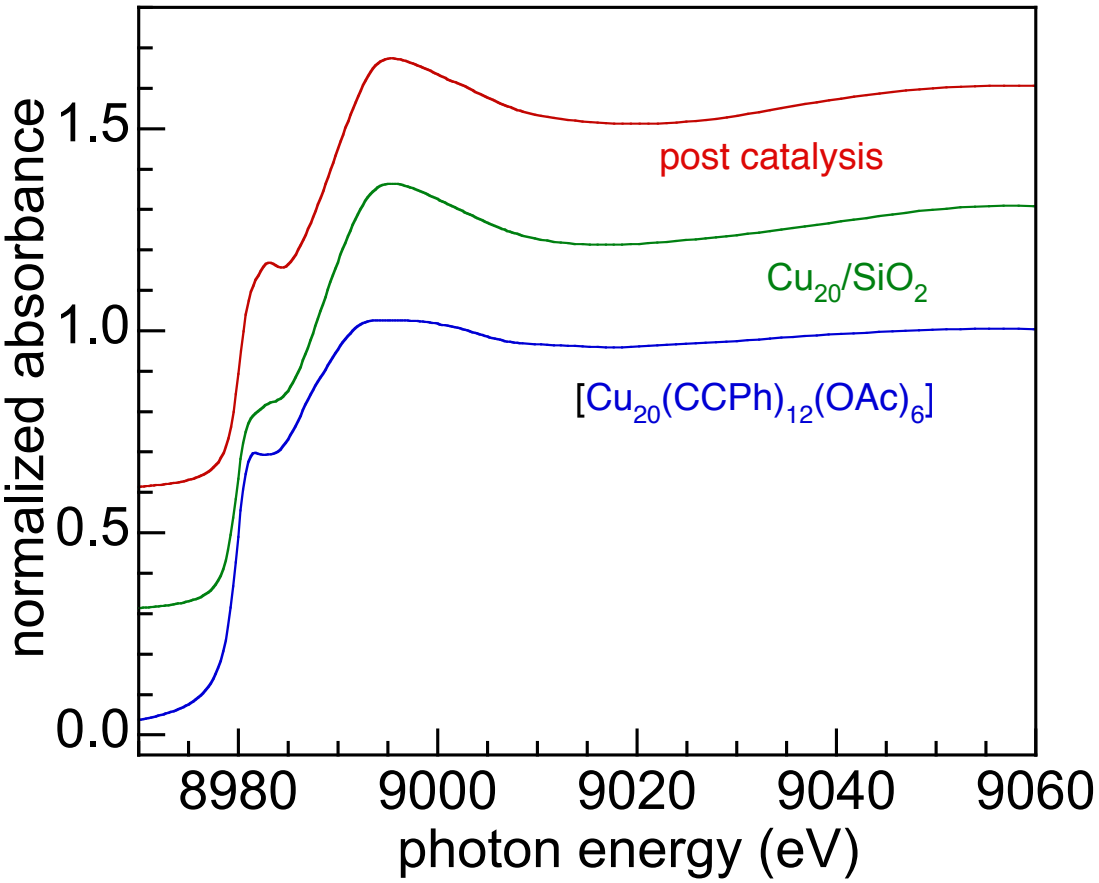

Figure A4.29. Comparison of Cu K-edge XANES of (**4.1**) $[Cu_{20}(CCPh)_{12}(OAc)_6]$ (blue), (**4.2**) Cu_{20}/SiO_2 (green), and (**4.2$_{post}$**) Cu_{20}/SiO_2, post catalysis (red).

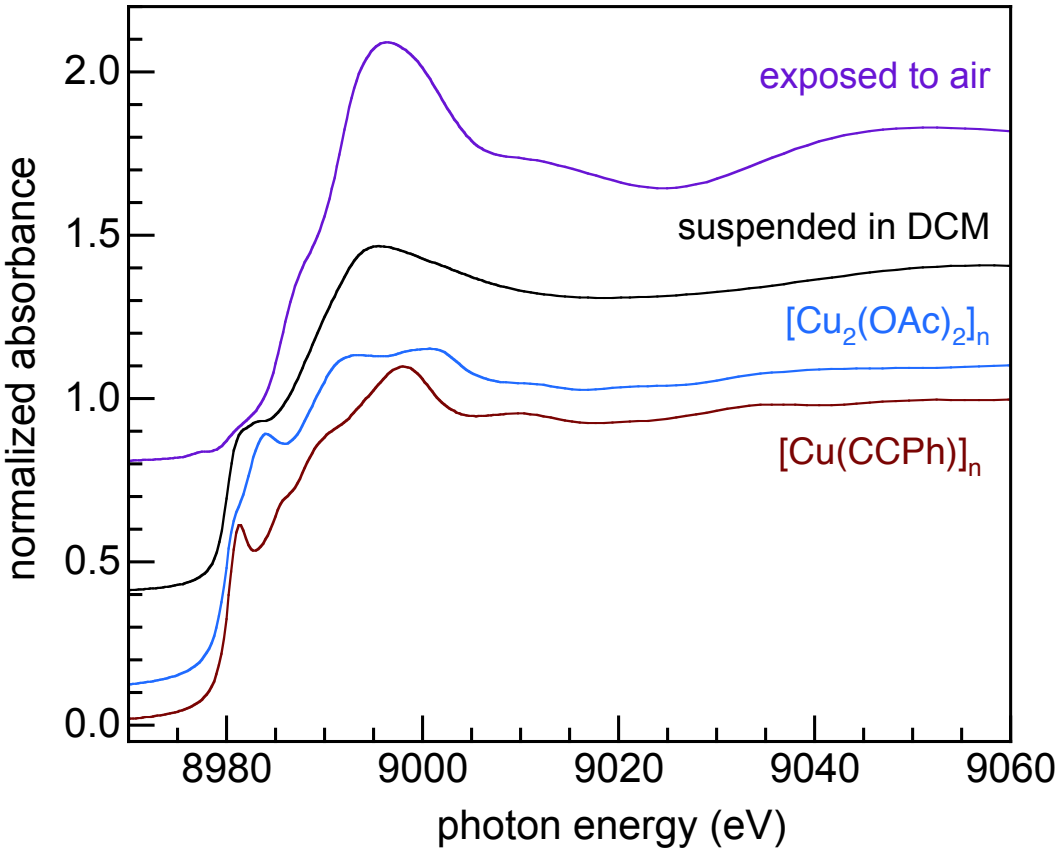

Figure A4.30. Comparison of Cu K-edge XANES for $[Cu(CCPh)]_n$ (burgundy), $[Cu_2(OAc)_2]_n$ (blue),[74] **4.2** after suspension in CH_2Cl_2 at room temperature (black), and **4.2** after deliberate exposure to air for 1 week (purple).

Table 4.5. Comparison of Cu K-edge absorption edges

Compound	Edge (eV)
Cu_{20}/SiO_2, **4.2** in air	8991.0
Cu_2O	8980.5
$[Cu(CCPh)]_n$	8980.5
$[Cu_2(OAc)_2]_n$	8980.1
Cu_{20}/SiO_2, **4.2** in DCM	8980.3
Cu_{20}/SiO_2, $\mathbf{4.2_{post}}$	8980.3
Cu_{20}/SiO_2, **4.2**	8980.3
$[Cu_{20}(CCPh)_{12}(OAc)_6]$, **4.1**	8979.9
Cu foil	8979.0

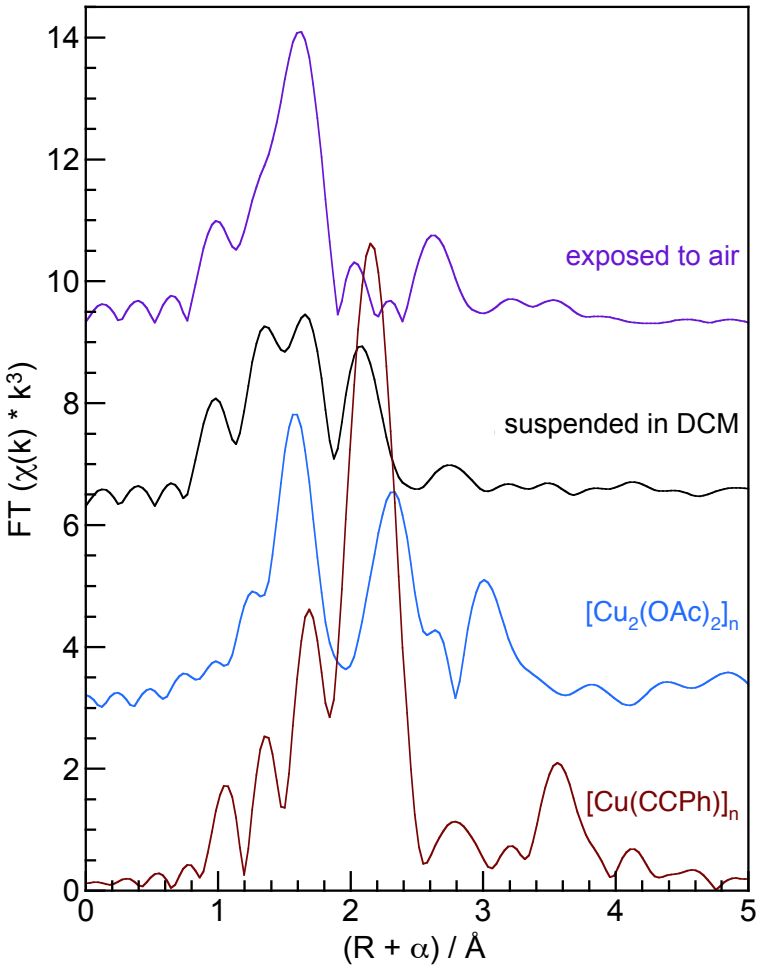

Figure A4.31. Comparison of Cu K-edge EXAFS (displayed as FT magnitude) for $[Cu(CCPh)]_n$ (burgundy), $[Cu_2(OAc)_2]_n$(blue),[74] **4.2** suspended in CH_2Cl_2 at room temperature (black), and **4.2** after deliberate exposure to air for 1 week (purple).

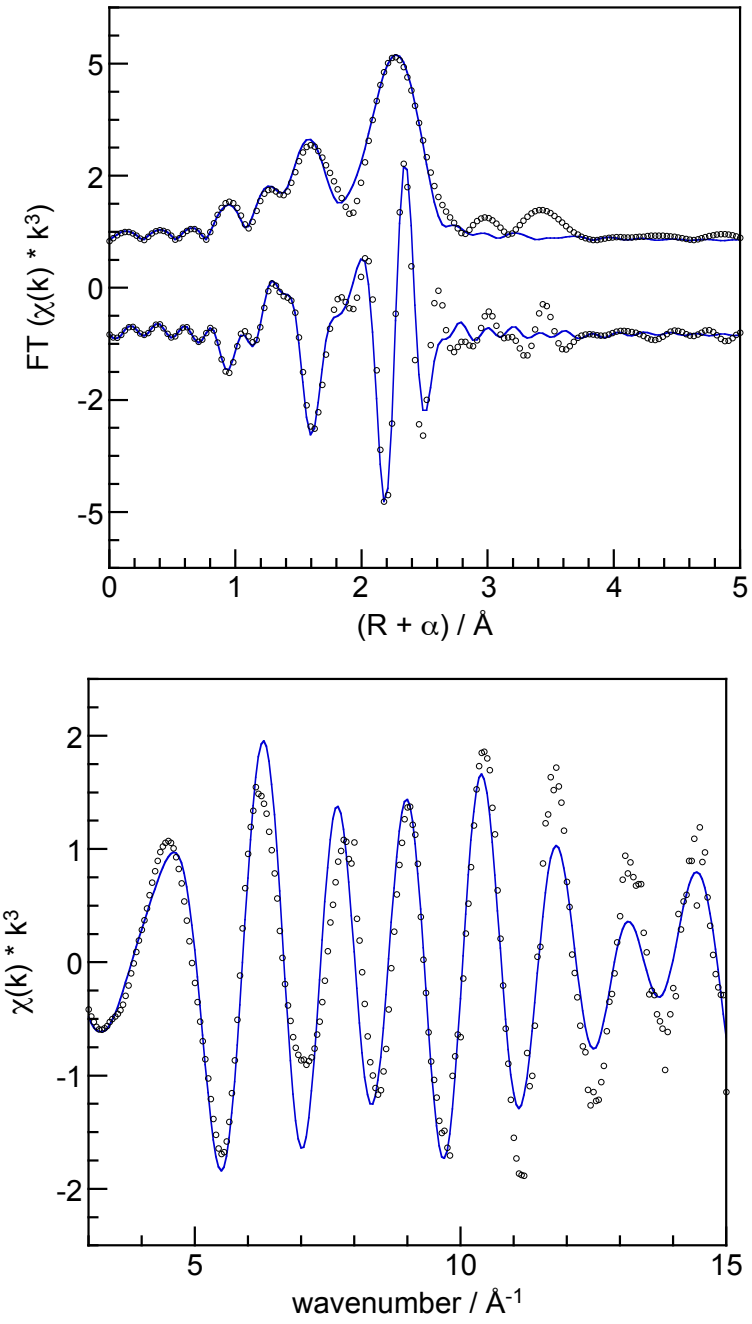

Figure A4.32. Cu K-edge EXAFS of $[Cu_{20}(CCPh)_{12}(OAc)_6]$ (**4.1**) (in k^3-weighted *R*-space, as FT magnitude and imaginary component, circles, top; and in *k*-space, bottom), showing curvefit (lines) to the standard EXAFS equation. Curvefit parameters are given in Table 4.2.

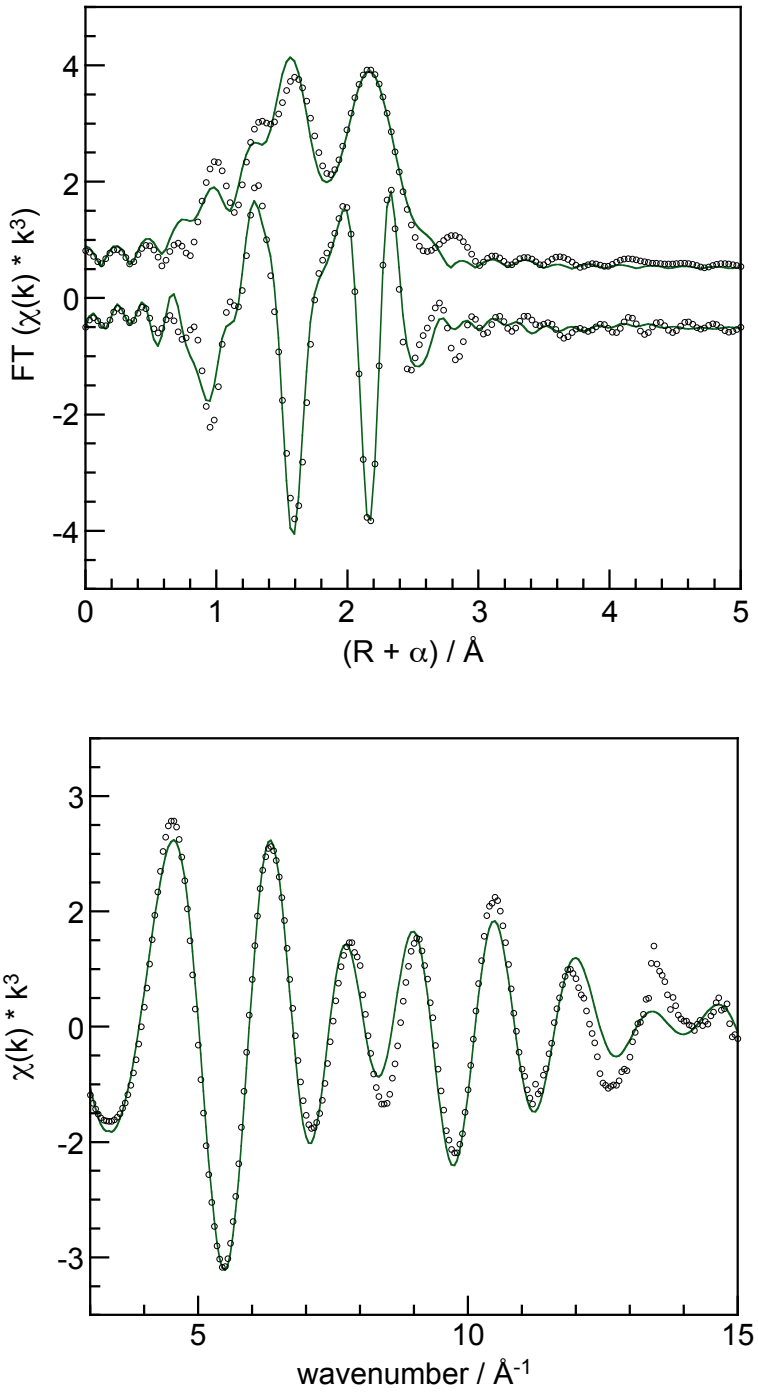

Figure A4.33. Cu K-edge EXAFS of Cu_{20}/SiO_2 (**4.2**) (in k^3-weighted *R*-space, as FT magnitude and imaginary component, circles, top; and in *k*-space, bottom), showing curvefit (lines) to the standard EXAFS equation. Curvefit parameters are given in Table 4.2.

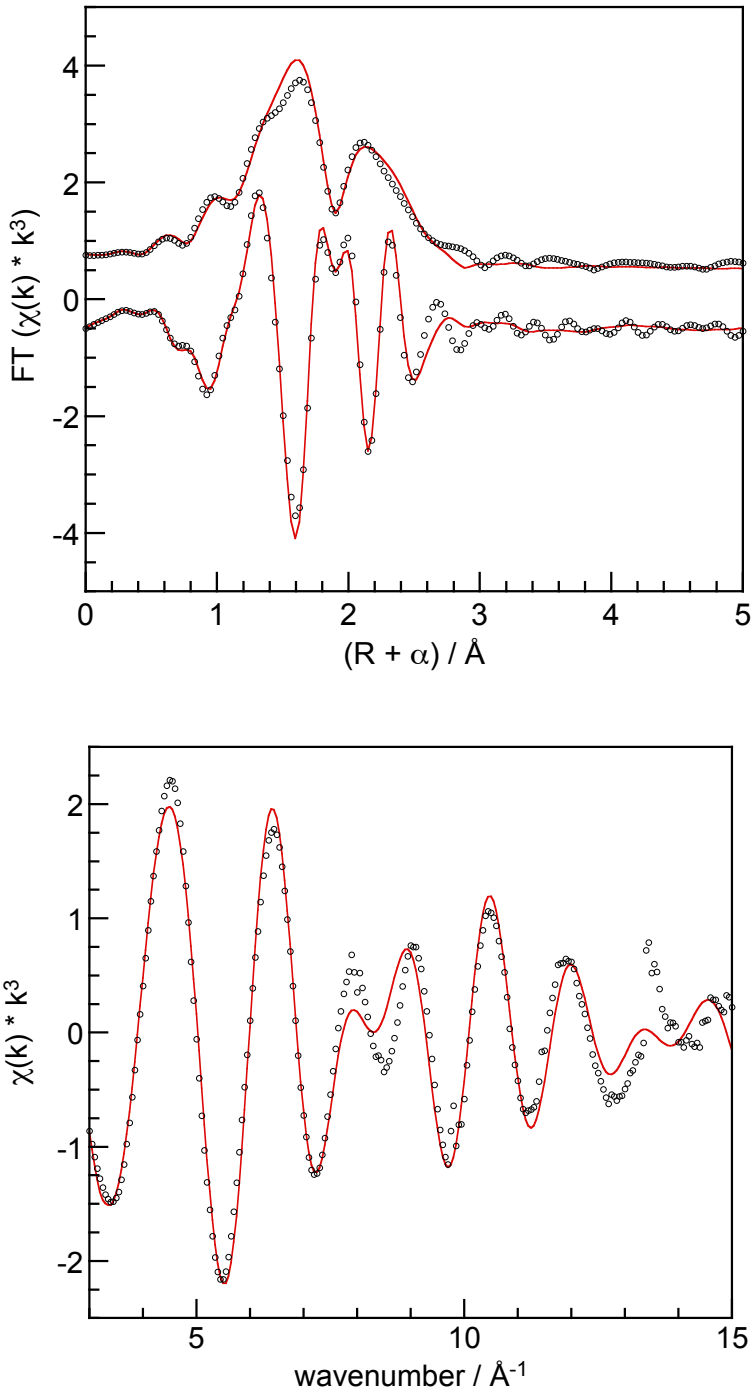

Figure A4.34. Cu K-edge EXAFS of Cu_{20}/SiO_2 (**4.2$_{post}$**) post catalysis (in k^3-weighted *R*-space, as FT magnitude and imaginary component, circles, top; and in *k*-space, bottom), showing curvefit (lines) to the standard EXAFS equation. Curvefit parameters are given in Table 4.2.

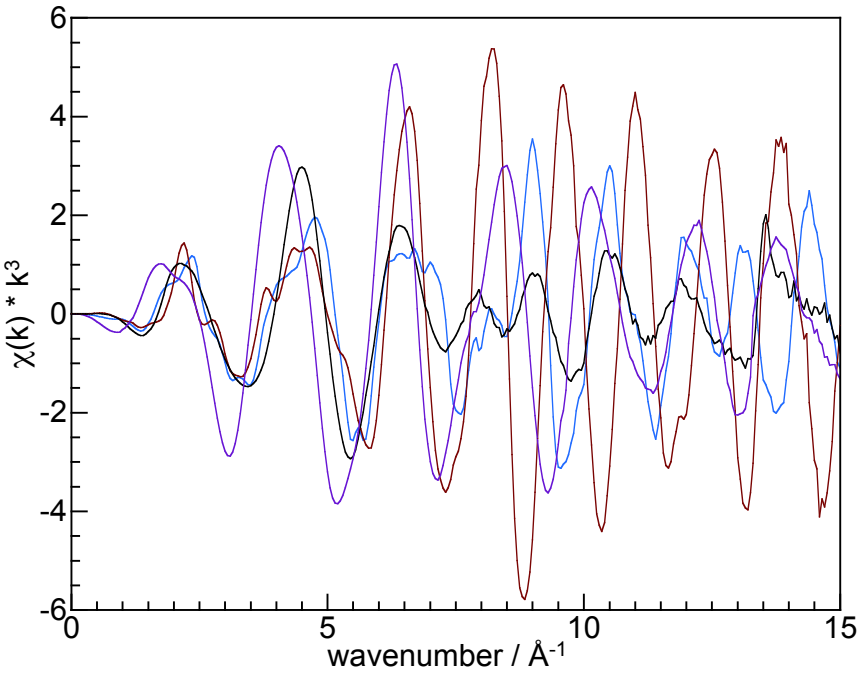

Figure A4.35. Comparison of Cu K-edge EXAFS (in *k*-space) for $[Cu(CCPh)]_n$ (burgundy), $[Cu_2(OAc)_2]_n$ (blue), **4.2** after suspension in CH_2Cl_2 at room temperature (black), and **4.2** after deliberate exposure to air for 1 week (purple).

4.6 References

(1) Hakkinen, H., Atomic and electronic structure of gold clusters: understanding flakes, cages and superatoms from simple concepts. *Chem. Soc. Rev.* **2008**, *37*, 1847-1859.

(2) Schmid, G., The relevance of shape and size of Au_{55} clusters. *Chem. Soc. Rev.* **2008**, *37*, 1909-1930.

(3) Li, G.; Jin, R., Atomically Precise Gold Nanoclusters as New Model Catalysts. *Acc. Chem. Res.* **2013**, *46*, 1749-1758.

(4) Yamazoe, S.; Koyasu, K.; Tsukuda, T., Nonscalable Oxidation Catalysis of Gold Clusters. *Acc. Chem. Res.* **2014**, *47*, 816-824.

(5) Daniel, M.-C.; Astruc, D., Gold Nanoparticles: Assembly, Supramolecular Chemistry, Quantum-Size-Related Properties, and Applications toward Biology, Catalysis, and Nanotechnology. *Chem. Rev.* **2004**, *104*, 293-346.

(6) Parker, J. F.; Fields-Zinna, C. A.; Murray, R. W., The Story of a Monodisperse Gold Nanoparticle: $Au_{25}L_{18}$. *Acc. Chem. Res.* **2010**, *43*, 1289-1296.

(7) Harkness, K. M.; Tang, Y.; Dass, A.; Pan, J.; Kothalawala, N.; Reddy, V. J.; Cliffel, D. E.; Demeler, B.; Stellacci, F.; Bakr, O. M.; McLean, J. A., $Ag_{44}(SR)_{30}^{4-}$: a silver-thiolate superatom complex. *Nanoscale* **2012**, *4*, 4269-4274.

(8) Yan, N.; Yuan, Y.; Dyson, P. J., Nanometallic chemistry: deciphering nanoparticle catalysis from the perspective of organometallic chemistry and homogeneous catalysis. *Dalton Trans.* **2013**, *42*, 13294-13304.

(9) Zhu, Y.; Qian, H.; Drake, B. A.; Jin, R., Atomically Precise $Au_{25}(SR)_{18}$ Nanoparticles as Catalysts for the Selective Hydrogenation of α,β-Unsaturated Ketones and Aldehydes. *Angew. Chem. Int. Ed.* **2010**, *49*, 1295-1298.

(10) Zhu, Y.; Qian, H.; Jin, R., An Atomic-Level Strategy for Unraveling Gold Nanocatalysis from the Perspective of $Au_n(SR)_m$ Nanoclusters. *Chem. Eur. J.* **2010**, *16*, 11455-11462.

(11) Zhu, Y.; Qian, H.; Jin, R., Catalysis opportunities of atomically precise gold nanoclusters. *J. Mater. Chem.* **2011**, *21*, 6793-6799.

(12) Jin, R.; Zeng, C.; Zhou, M.; Chen, Y., Atomically Precise Colloidal Metal Nanoclusters and Nanoparticles: Fundamentals and Opportunities. *Chem. Rev.* **2016**, *116*, 10346-10413.

(13) Das, S.; Goswami, A.; Hesari, M.; Al-Sharab, J. F.; Mikmeková, E.; Maran, F.; Asefa, T., Reductive Deprotection of Monolayer Protected Nanoclusters: An Efficient Route to Supported Ultrasmall Au Nanocatalysts for Selective Oxidation. *Small* **2014**, *10*, 1473-1478.

(14) Elliott, E. W.; Glover, R. D.; Hutchison, J. E., Removal of Thiol Ligands from Surface-Confined Nanoparticles without Particle Growth or Desorption. *ACS Nano* **2015**, *9*, 3050-3059.

(15) Wang, L.; Tang, Z.; Yan, W.; Yang, H.; Wang, Q.; Chen, S., Porous Carbon-Supported Gold Nanoparticles for Oxygen Reduction Reaction: Effects of Nanoparticle Size. *ACS Appl. Mater. Interfaces* **2016**, *8*, 20635-20641.

(16) Ma, G.; Binder, A.; Chi, M.; Liu, C.; Jin, R.; Jiang, D.-e.; Fan, J.; Dai, S., Stabilizing gold clusters by heterostructured transition-metal oxide-mesoporous silica supports

for enhanced catalytic activities for CO oxidation. *Chem. Commun.* **2012**, *48*, 11413-11415.
(17) Fang, J.; Li, J.; Zhang, B.; Yuan, X.; Asakura, H.; Tanaka, T.; Teramura, K.; Xie, J.; Yan, N., The support effect on the size and catalytic activity of thiolated Au_{25} nanoclusters as precatalysts. *Nanoscale* **2015**, *7*, 6325-6333.
(18) Sudheeshkumar, V.; Shivhare, A.; Scott, R. W. J., Synthesis of sinter-resistant Au@silica catalysts derived from Au_{25} clusters. *Catal. Sci. Tech.* **2017**, *7*, 272-280.
(19) Nie, X.; Qian, H.; Ge, Q.; Xu, H.; Jin, R., CO Oxidation Catalyzed by Oxide-Supported $Au_{25}(SR)_{18}$ Nanoclusters and Identification of Perimeter Sites as Active Centers. *ACS Nano* **2012**, *6*, 6014-6022.
(20) Li, G.; Jin, R., Gold Nanocluster-Catalyzed Semihydrogenation: A Unique Activation Pathway for Terminal Alkynes. *J. Am. Chem. Soc.* **2014**, *136*, 11347-11354.
(21) Liu, P.; Qin, R.; Fu, G.; Zheng, N., Surface Coordination Chemistry of Metal Nanomaterials. *J. Am. Chem. Soc.* **2017**, *139*, 2122-2131.
(22) Edwards, A. J.; Dhayal, R. S.; Liao, P.-K.; Liao, J.-H.; Chiang, M.-H.; Piltz, R. O.; Kahlal, S.; Saillard, J.-Y.; Liu, C. W., Chinese Puzzle Molecule: A 15 Hydride, 28 Copper Atom Nanoball. *Angew. Chem. Int. Ed.* **2014**, *53*, 7214-7218.
(23) Dhayal, R. S.; Liao, J.-H.; Kahlal, S.; Wang, X.; Liu, Y.-C.; Chiang, M.-H.; van Zyl, W. E.; Saillard, J.-Y.; Liu, C. W., $[Cu_{32}(H)_{20}\{S_2P(OiPr)_2\}_{12}]$: The Largest Number of Hydrides Recorded in a Molecular Nanocluster by Neutron Diffraction. *Chem. – Eur. J.* **2015**, *21*, 8369-8374.
(24) Nguyen, T.-A. D.; Goldsmith, B. R.; Zaman, H. T.; Wu, G.; Peters, B.; Hayton, T. W., Synthesis and Characterization of a Cu_{14} Hydride Cluster Supported by Neutral Donor Ligands. *Chem. Eur. J.* **2015**, *21*, 5341-5344.
(25) Nguyen, T.-A. D.; Jones, Z. R.; Goldsmith, B. R.; Buratto, W. R.; Wu, G.; Scott, S. L.; Hayton, T. W., A Cu_{25} Nanocluster with Partial Cu(0) Character. *J. Am. Chem. Soc.* **2015**, *137*, 13319-13324.
(26) Dhayal, R. S.; van Zyl, W. E.; Liu, C. W., Polyhydrido Copper Clusters: Synthetic Advances, Structural Diversity, and Nanocluster-to-Nanoparticle Conversion. *Acc. Chem. Res.* **2016**, *49*, 86-95.
(27) Nguyen, T.-A. D.; Jones, Z. R.; Leto, D. F.; Wu, G.; Scott, S. L.; Hayton, T. W., Ligand-Exchange-Induced Growth of an Atomically Precise Cu_{29} Nanocluster from a Smaller Cluster. *Chem. Mater.* **2016**, *28*, 8385-8390.
(28) Wan, X.-K.; Tang, Q.; Yuan, S.-F.; Jiang, D.-e.; Wang, Q.-M., Au_{19} Nanocluster Featuring a V-Shaped Alkynyl–Gold Motif. *J. Am. Chem. Soc.* **2015**, *137*, 652-655.
(29) Wan, X.-K.; Yuan, S.-F.; Tang, Q.; Jiang, D.-e.; Wang, Q.-M., Alkynyl-Protected Au_{23} Nanocluster: A 12-Electron System. *Angew. Chem., Int. Ed.* **2015**, *54*, 5977-5980.
(30) Wan, X.-K.; Xu, W. W.; Yuan, S.-F.; Gao, Y.; Zeng, X.-C.; Wang, Q.-M., A Near-Infrared-Emissive Alkynyl-Protected Au_{24} Nanocluster. *Angew. Chem., Int. Ed.* **2015**, *54*, 9683-9686.
(31) Wang, Y.; Su, H.; Xu, C.; Li, G.; Gell, L.; Lin, S.; Tang, Z.; Häkkinen, H.; Zheng, N., An Intermetallic $Au_{24}Ag_{20}$ Superatom Nanocluster Stabilized by Labile Ligands. *J. Am. Chem. Soc.* **2015**, *137*, 4324-4327.

(32) Zhang, R.; Hao, X.; Li, X.; Zhou, Z.; Sun, J.; Cao, R., Soluble Silver Acetylide for the Construction and Structural Conversion of All-Alkynyl-Stabilized High-Nuclearity Homoleptic Silver Clusters. *Cryst. Growth Des.* **2015**, *15*, 2505-2513.
(33) Chakrahari, K. K.; Liao, J.-H.; Kahlal, S.; Liu, Y.-C.; Chiang, M.-H.; Saillard, J.-Y.; Liu, C. W., $[Cu_{13}\{S_2CN^nBu_2\}_6(acetylide)_4]^+$: A Two-Electron Superatom. *Angew. Chem., Int. Ed.* **2016**, *55*, 14704-14708.
(34) Wang, Y.; Su, H.; Ren, L.; Malola, S.; Lin, S.; Teo, B. K.; Häkkinen, H.; Zheng, N., Site Preference in Multimetallic Nanoclusters: Incorporation of Alkali Metal Ions or Copper Atoms into the Alkynyl-Protected Body-Centered Cubic Cluster $[Au_7Ag_8(C{\equiv}C^tBu)_{12}]^+$. *Angew. Chem. Int. Ed.* **2016**, *55*, 15152-15156.
(35) Lei, Z.; Wan, X.-K.; Yuan, S.-F.; Wang, J.-Q.; Wang, Q.-M., Alkynyl-protected gold and gold-silver nanoclusters. *Dalton Trans.* **2017**, *46*, 3427-3434.
(36) Wan, X.-K.; Cheng, X.-L.; Tang, Q.; Han, Y.-Z.; Hu, G.; Jiang, D.-e.; Wang, Q.-M., Atomically Precise Bimetallic $Au_{19}Cu_{30}$ Nanocluster with an Icosidodecahedral Cu_{30} Shell and an Alkynyl–Cu Interface. *J. Am. Chem. Soc.* **2017**, *139*, 9451-9454.
(37) Jin, J.-L.; Xie, Y.-P.; Cui, H.; Duan, G.-X.; Lu, X.; Mak, T. C. W., Structure-Directing Role of Phosphonate in the Synthesis of High-Nuclearity Silver(I) Sulfide-Ethynide-Thiolate Clusters. *Inorg. Chem.* **2017**, *56*, 10412-10417.
(38) Wan, X. K.; Guan, Z. J.; Wang, Q. M., Homoleptic Alkynyl-Protected Gold Nanoclusters: Au_{44} $(PhC{\equiv}C)_{28}$ and Au_{36} $(PhC{\equiv}C)_{24}$. *Angew. Chem. Int. Ed.* **2017**, *56*, 11494–11497.
(39) Qu, M.; Li, H.; Xie, L.-H.; Yan, S.-T.; Li, J.-R.; Wang, J.-H.; Wei, C.-Y.; Wu, Y.-W.; Zhang, X.-M., Bidentate Phosphine-Assisted Synthesis of an All-Alkynyl-Protected Ag_{74} Nanocluster. *J. Am. Chem. Soc.* **2017**, *139*, 14346-12349.
(40) Yuan, S.-F.; Li, P.; Tang, Q.; Wan, X.-K.; Nan, Z.-A.; Jiang, D.-e.; Wang, Q.-M., Alkynyl-protected silver nanoclusters featuring an anticuboctahedral kernel. *Nanoscale* **2017**, *9*, 11405-11409.
(41) Wang, Y.; Wan, X.-K.; Ren, L.; Su, H.; Li, G.; Malola, S.; Lin, S.; Tang, Z.; Häkkinen, H.; Teo, B. K.; Wang, Q.-M.; Zheng, N., Atomically Precise Alkynyl-Protected Metal Nanoclusters as a Model Catalyst: Observation of Promoting Effect of Surface Ligands on Catalysis by Metal Nanoparticles. *J. Am. Chem. Soc.* **2016**, *138*, 3278-3281.
(42) Chui, S. S. Y.; Ng, M. F. Y.; Che, C.-M., Structure Determination of Homoleptic AuI, AgI, and CuI Aryl/Alkylethynyl Coordination Polymers by X-ray Powder Diffraction. *Chem. – Eur. J.* **2005**, *11*, 1739-1749.
(43) Shao, C.; Cheng, G.; Su, D.; Xu, J.; Wang, X.; Hu, Y., Copper(I) Acetate: A Structurally Simple but Highly Efficient Dinuclear Catalyst for Copper-Catalyzed Azide-Alkyne Cycloaddition. *Adv. Synth. Catal.* **2010**, *352*, 1587-1592.
(44) Freitag, K.; Banh, H.; Gemel, C.; Seidel, R. W.; Kahlal, S.; Saillard, J.-Y.; Fischer, R. A., Molecular brass: Cu_4Zn_4, a ligand protected superatom cluster. *Chem. Commun.* **2014**, *50*, 8681-8684.
(45) Ganesamoorthy, C.; Weßing, J.; Kroll, C.; Seidel, R. W.; Gemel, C.; Fischer, R. A., The Intermetalloid Cluster $[(Cp^*AlCu)_6H_4]$, Embedding a Cu_6 Core Inside an Octahedral Al_6 Shell: Molecular Models of Hume–Rothery Nanophases. *Angew. Chem. Int. Ed.* **2014**, *53*, 7943-7947.

(46) Yang, H.; Lei, J.; Wu, B.; Wang, Y.; Zhou, M.; Xia, A.; Zheng, L.; Zheng, N., Crystal structure of a luminescent thiolated Ag nanocluster with an octahedral Ag_6^{4+} core. *Chem. Commun.* **2013**, *49*, 300-302.
(47) Yang, H.; Wang, Y.; Zheng, N., Stabilizing subnanometer Ag(0) nanoclusters by thiolate and diphosphine ligands and their crystal structures. *Nanoscale* **2013**, *5*, 2674-2677.
(48) Kang, X.; Wang, S.; Song, Y.; Jin, S.; Sun, G.; Yu, H.; Zhu, M., Bimetallic Au_2Cu_6 Nanoclusters: Strong Luminescence Induced by the Aggregation of Copper(I) Complexes with Gold(0) Species. *Angew. Chem., Int. Ed.* **2016**, *55*, 3611-3614.
(49) van der Velden, J. W. A.; Bour, J. J.; Vollenbroek, F. A.; Beurskens, P. T.; Smits, J. M. M., Synthesis of a new pentanuclear gold cluster by metal evaporation. Preparation and X-ray structure determination of [tris{bis(diphenylphosphino)methane}][bis(diphenylphosphino)methanido]pentagold dinitrate. *J. Chem. Soc., Chem. Commun.* **1979**, 1162-1163.
(50) Demartin, F.; Manassero, M.; Naldini, L.; Ruggeri, R.; Sansoni, M., Synthesis and X-ray characterization of an iodine-bridged tetranuclear gold cluster, di-μ-iodo-tetrakis(triphenylphosphine)-tetrahedro-tetragold. *J. Chem. Soc., Chem. Commun.* **1981**, 222-223.
(51) Zeller, E.; Beruda, H.; Schmidbaur, H., Tetrahedral gold cluster $[Au_4]^{2+}$: crystal structure of $\{[(tert\text{-}Bu)_3PAu]_4\}^{2+}(BF_4^-)_2.2CHCl_3$. *Inorg. Chem.* **1993**, *32*, 3203-3204.
(52) Saillard, J.-Y.; Halet, J.-F., Structure and Bonding Patterns in Large Molecular Ligated Metal Clusters. In *The Chemical Bond I: 100 Years Old and Getting Stronger*, Mingos, D. M. P., Ed. Springer International Publishing: Cham, 2016; pp 157-179.
(53) Tornøe, C. W.; Christensen, C.; Meldal, M., Peptidotriazoles on Solid Phase: [1,2,3]-Triazoles by Regiospecific Copper(I)-Catalyzed 1,3-Dipolar Cycloadditions of Terminal Alkynes to Azides. *J. Org. Chem.* **2002**, *67*, 3057-3064.
(54) Rostovtsev, V. V.; Green, L. G.; Fokin, V. V.; Sharpless, K. B., A Stepwise Huisgen Cycloaddition Process: Copper(I)-Catalyzed Regioselective "Ligation" of Azides and Terminal Alkynes. *Angew. Chem., Int. Ed.* **2002**, *41*, 2596-2599.
(55) Makarem, A.; Berg, R.; Rominger, F.; Straub, B. F., A Fluxional Copper Acetylide Cluster in CuAAC Catalysis. *Angew. Chem. Int. Ed.* **2015**, *54*, 7431-7435.
(56) Jin, L.; Tolentino, D. R.; Melaimi, M.; Bertrand, G., Isolation of bis(copper) key intermediates in Cu-catalyzed azide-alkyne "click reaction". *Sci. Adv.* **2015**, *1*, e1500304.
(57) Meldal, M.; Tornøe, C. W., Cu-Catalyzed Azide−Alkyne Cycloaddition. *Chem. Rev.* **2008**, *108*, 2952-3015.
(58) Alonso, F.; Moglie, Y.; Radivoy, G., Copper Nanoparticles in Click Chemistry. *Acc. Chem. Res.* **2015**, *48*, 2516-2528.
(59) Lee, B.-H.; Wu, C.-C.; Fang, X.; Liu, C. W.; Zhu, J.-L., $[Cu_8(\mu_4\text{-}H)\{S_2P(OEt)_2\}_6](PF_6)$: A Novel Catalytic Hydride-Centered Copper Cluster for Azide-Alkyne Cycloaddtion. *Catal. Lett.* **2013**, *143*, 572-577.
(60) Decan, M. R.; Impellizzeri, S.; Marin, M. L.; Scaiano, J. C., Copper nanoparticle heterogeneous catalytic 'click' cycloaddition confirmed by single-molecule spectroscopy. *Nat. Commun.* **2014**, *5*, 4612.

(61) Lipshutz, B. H.; Taft, B. R., Heterogeneous Copper-in-Charcoal-Catalyzed Click Chemistry. *Angew. Chem. Int. Ed.* **2006**, *45*, 8235-8238.
(62) Sharghi, H.; Khalifeh, R.; Doroodmand, M. M., Copper Nanoparticles on Charcoal for Multicomponent Catalytic Synthesis of 1,2,3-Triazole Derivatives from Benzyl Halides or Alkyl Halides, Terminal Alkynes and Sodium Azide in Water as a "Green" Solvent. *Adv. Synth. Catal.* **2009**, *351*, 207-218.
(63) Alonso, F.; Moglie, Y.; Radivoy, G.; Yus, M., Multicomponent Synthesis of 1,2,3-Triazoles in Water Catalyzed by Copper Nanoparticles on Activated Carbon. *Adv. Synth. Catal.* **2010**, *352*, 3208-3214.
(64) Lee, B. S.; Yi, M.; Chu, S. Y.; Lee, J. Y.; Kwon, H. R.; Lee, K. R.; Kang, D.; Kim, W. S.; Lim, H. B.; Lee, J.; Youn, H.-J.; Chi, D. Y.; Hur, N. H., Copper nitride nanoparticles supported on a superparamagnetic mesoporous microsphere for toxic-free click chemistry. *Chem. Commun.* **2010**, *46*, 3935-3937.
(65) Alonso, F.; Moglie, Y.; Radivoy, G.; Yus, M., Click chemistry from organic halides, diazonium salts and anilines in water catalysed by copper nanoparticles on activated carbon. *Org. Biomol. Chem.* **2011**, *9*, 6385-6395.
(66) Nador, F.; Volpe, M. a. A.; Alonso, F.; Feldhoff, A.; Kirschning, A.; Radivoy, G., Copper nanoparticles supported on silica coated maghemite as versatile, magnetically recoverable and reusable catalyst for alkyne coupling and cycloaddition reactions. *Appl. Catal., A* **2013**, *455*, 39–45.
(67) Rance, G. A.; Solomonsz, W. A.; Khlobystov, A. N., Click chemistry in carbon nanoreactors. *Chem. Commun.* **2013**, *49*, 1067-1069.
(68) Sarmah, B.; Satpati, B.; Srivastava, R., Cu ion-exchanged and Cu nanoparticles decorated mesoporous ZSM-5 catalysts for the activation and utilization of phenylacetylene in a sustainable chemical synthesis. *RSC Adv.* **2016**, *6*, 87066-87081.
(69) Molteni, G.; Bianchi, C. L.; Marinoni, G.; Santo, N.; Ponti, A., Cu/Cu-oxide nanoparticles as catalyst in the "click" azide-alkyne cycloaddition. *New J. Chem.* **2006**, *30*, 1137-1139.
(70) Abdulkin, P.; Moglie, Y.; Knappett, B. R.; Jefferson, D. A.; Yus, M.; Alonso, F.; Wheatley, A. E. H., New routes to Cu(i)/Cu nanocatalysts for the multicomponent click synthesis of 1,2,3-triazoles. *Nanoscale* **2013**, *5*, 342-350.
(71) Fu, F.; Martinez, A.; Wang, C.; Ciganda, R.; Yate, L.; Escobar, A.; Moya, S.; Fouquet, E.; Ruiz, J.; Astruc, D., Exposure to air boosts CuAAC reactions catalyzed by PEG-stabilized Cu nanoparticles. *Chem. Commun.* **2017**, *53*, 5384-5387.
(72) Gaur, S.; Miller, J. T.; Stellwagen, D.; Sanampudi, A.; Kumar, C. S. S. R.; Spivey, J. J., Synthesis, characterization, and testing of supported Au catalysts prepared from atomically-tailored $Au_{38}(SC_{12}H_{25})_{24}$ clusters. *Phys. Chem. Chem. Phys.* **2012**, *14*, 1627-1634.
(73) Wu, Z.; Hu, G.; Jiang, D.-e.; Mullins, D. R.; Zhang, Q.-F.; Allard, L. F.; Wang, L.-S.; Overbury, S. H., Diphosphine-Protected Au_{22} Nanoclusters on Oxide Supports Are Active for Gas-Phase Catalysis without Ligand Removal. *Nano Lett.* **2016**, *16*, 6560-6567.
(74) Mounts, R. D.; Ogura, T.; Fernando, Q., Crystal structure of copper(I) acetate. *Inorg. Chem.* **1974**, *13*, 802-805.

(75) Ravel, B.; Newville, M., ATHENA, ARTEMIS, HEPHAESTUS: data analysis for X-ray absorption spectroscopy using IFEFFIT. *J. Synchrontron Radiat.* **2005**, *12*, 537-541.
(76) Appukkuttan, P.; Dehaen, W.; Fokin, V. V.; Van der Eycken, E., A Microwave-Assisted Click Chemistry Synthesis of 1,4-Disubstituted 1,2,3-Triazoles via a Copper(I)-Catalyzed Three-Component Reaction. *Org. Lett.* **2004**, *6*, 4223-4225.
(77) Candelon, N.; Lastecoueres, D.; Diallo, A. K.; Ruiz Aranzaes, J.; Astruc, D.; Vincent, J.-M., A highly active and reusable copper(i)-tren catalyst for the "click" 1,3-dipolar cycloaddition of azides and alkynes. *Chem. Commun.* **2008**, 741-743.
(78) *SMART Apex II, Version 2.1*. Bruker AXS Inc.: Madison, WI, 2005.
(79) *SAINT Software User's Guide, Version 7.34a*. Bruker AXS Inc.: Madison, WI, 2005.
(80) Sheldrick, G. M., *SADABS*. University of Göttingen: Göttingen, Germany, 2005.
(81) *SHELXTL PC, Version 6.12*. Bruker AXS Inc.: Madison, WI, 2005.

Chapter 5. A Re-examination of the Synthesis of Monolayer-Protected $Co_x(SCH_2CH_2Ph)_m$ Nanoclusters: Unexpected Formation of a Thiolate-Protected Co(II) T3 Supertetrahedron

Portions of this work were published in:

Andrew W. Cook, Guang Wu, and Trevor W. Hayton. A Re-examination of the Synthesis of Monolayer-Protected $Co_x(SCH_2CH_2Ph)_m$ Nanoclusters: Unexpected Formation of a Thiolate-Protected Co(II) T3 Supertetrahedron. *Inorg. Chem.* **2018**, *57*, 8189-8194.

Table of Contents

5.1 Introduction

Recent advances in the synthesis of APNCs have resulted in a remarkable increase in the number of structurally-characterized clusters.[1-6] Despite this wealth of work, however, structurally characterized APNCs exist for only a handful of transition metal (Cu,[7-13] Ag,[5, 14-16] Au,[5, 14, 17] Pd,[18-19] and Zn[20]) and main group elements (Al,[21-24] Ga,[23, 25] Ge,[26-30] In,[31-32] and Sn[26, 28, 33-36]). Expansion to the other transition metals, such as Co, could lead to novel magnetic materials, which could have applications in catalysis, imaging, and quantum computing.[37-39] However, metallic cobalt nanomaterials are highly air-sensitive, which renders them a challenge to isolate and characterize. Several different strategies have been employed to protect these nanomaterials from unwanted oxidation, including reductive annealing to improve Co crystallinity,[40] dispersion in polymer,[41-44] coating with gold,[45-46] or embedding on a support, such as graphite[47-48] or silica.[49-50] Passivation of nanomaterials with a protective "shell" comprised of anionic and/or neutral donor ligands is another viable strategy for imparting air stability. The most common passivating ligands for APNCs are thiolates (RS^-);[2, 5] however, carbon monoxide,[18-19] hydrides[7, 9-10, 12] and acetylides[11, 13-17] have also been employed.

In 2017, Barrabés and co-workers reported the synthesis of the thiolate-protected cobalt APNCs, $Co_x(SR)_m$ (R = CH_2CH_2Ph), via reaction of $CoCl_2$ with RSH and $NaBH_4$ in THF/H_2O.[51] This material was characterized by UV-vis spectroscopy, X-ray photoelectron spectroscopy (XPS), scanning transmission electron microscopy (STEM), and X-ray absorption near edge spectroscopy (XANES); however, single crystals for X-ray diffraction were not forthcoming. On the basis of matrix assisted laser desorption/ionization-mass spectrometry (MALDI-MS) analysis, the authors suggested the "formation of cobalt clusters

in a range of 25-30 cobalt atoms"[51] and offered $Co_{25}(SR)_{18}$ and $Co_{30}(SR)_{16}$ as two potential formulations to fit this criterion. Given the rarity of atomically-precise cobalt nanoclusters, I endeavored to reproduce the reported synthesis and further study these unique materials. Herein, I report that the major product of this reaction is actually the thiolate-protected Co(II) T3 supertetrahedron, $[Co_{10}(SR)_{16}Cl_4]$, and not a Co(0)-containing APNC, as originally reported.

5.2 Results and Discussion

5.2.1 Re-examination of the Original Synthetic Procedure as Reported by Barrabés and Co-workers

The 2017 synthesis of $Co_x(SR)_m$ followed a modified Brust protocol (Scheme 5.1).[51-52] $CoCl_2 \cdot 6H_2O$ (1 equiv) was dehydrated at 150 °C and then dissolved in tetrahydrofuran (10 mL). $PhCH_2CH_2SH$ (3 equiv) was added to the blue solution and stirred for 30 minutes, resulting in a color change to dark blue. $NaBH_4$ (9 equiv), dissolved in H_2O (2 mL) and chilled to 0 °C, was then quickly added to the reaction mixture. The solution was stirred for 1 h and subsequently filtered and washed with methanol. The solid was then extracted with CH_2Cl_2, resulting in a pink solution containing the proposed $Co_x(SR)_m$ clusters. A yield was not reported.

Scheme 5.1. Original Synthetic Procedure Used to Prepare $Co_x(SCH_2CH_2Ph)_m$ Nanoclusters

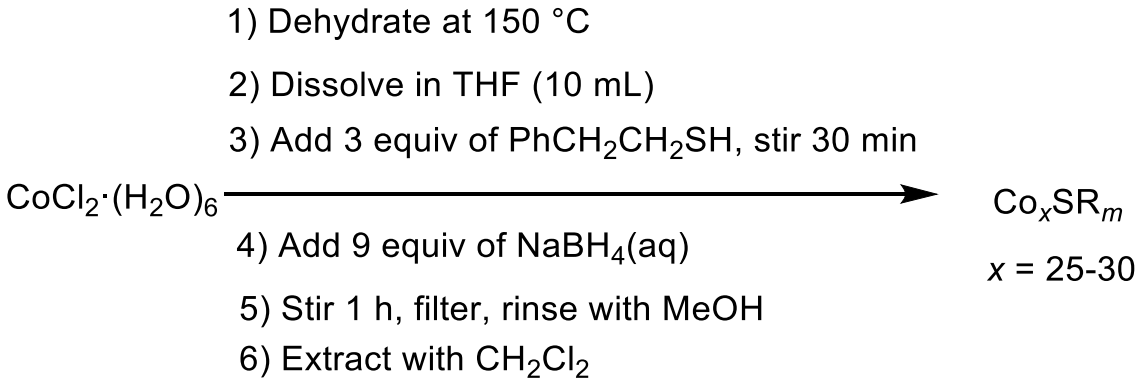

I attempted to repeat the original synthesis as closely as possible; however, I made a few minor changes to the procedure to allow for *in situ* spectroscopic monitoring. Specifically, I replaced the THF and H_2O with THF-d_8 and D_2O, respectively, and I performed the reaction in a J. Young NMR tube under an inert gas atmosphere (Figures A5.2 and A5.3). Under these conditions, I was able to successfully reproduce the deep blue solution previously reported to form upon addition of $PhCH_2CH_2SH$ to $CoCl_2$. Interestingly, upon addition of a D_2O solution of $NaBH_4$ (9 equiv) I observe a color change to dark green. This solution then slowly turned dark brown, concomitant with the deposition of a grey-brown solid. A ^1H NMR spectrum of the reaction mixture after 30 min reveals the presence of three diagnostic resonances at -10.02, 103.22, and 120.11 ppm (Figure A5.2), which are assignable to the cobalt(II)-thiolate cluster, $[Co_{10}(SR)_{16}Cl_4]$ (**5.1**) (*vide infra*). Complex **5.1** is the only major product observed in the reaction mixture, demonstrating that the transformation is remarkably chemoselective.

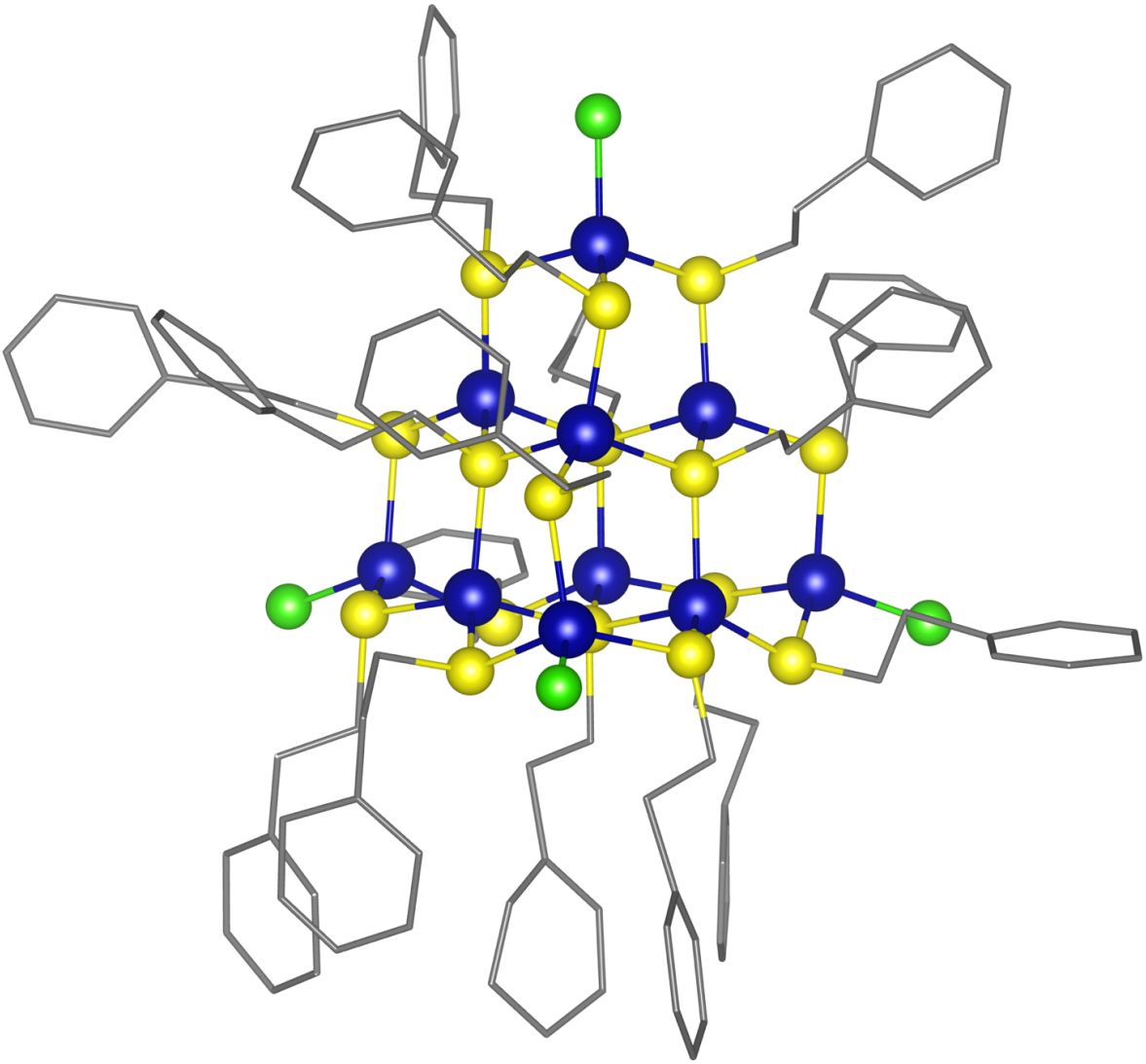

Figure 5.1. Ball-and-stick diagram showing **5.1**·2CH_2Cl_2. Hydrogen atoms and CH_2Cl_2 solvate molecules omitted for clarity. Color legend: Co = blue; S = yellow; C = grey; Cl = green

5.2.2 Rational Synthesis of Complex 5.1 and Characterization of the Complex

To facilitate the isolation of **5.1** I repeated the above procedure in the absence of water and in an inert atmosphere glove box (Scheme 5.2). Work-up of this reaction mixture resulted in the isolation of dark brown crystals of the cobalt-thiolate cluster $[Co_{10}(SR)_{16}Cl_4]$ (**5.1**) in 37% yield. Also formed in this reaction is a grey-brown solid, whose appearance is consistent

with that of NaCl, but which is contaminated with small amounts of a Co-containing product. I believe the modest yield of this reaction is due to the presence of excess thiol (see below), which impedes the crystallization process.

Scheme 5.2. Syntheses of Complex 5.2

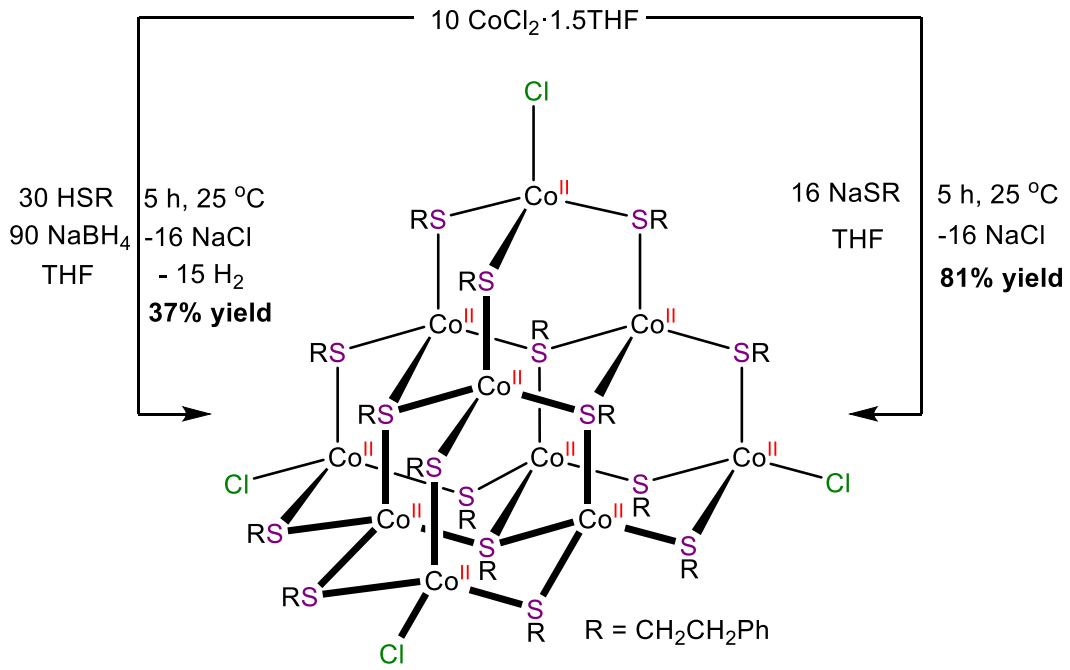

5.1

Complex **5.1** crystallizes in the monoclinic space group C*c* as the CH_2Cl_2 solvate, **5.1**·$2CH_2Cl_2$ (Figure 5.1). It features a $[Co_6S_{16}Cl_4]$ core with idealized T_d symmetry. Each of the ten Co centers features a pseudo-tetrahedral geometry and the four Cl^- ligands occupy the corners of the tetrahedron. Twelve of the 16 thiolate ligands feature a μ_2 binding mode. These are situated along the edges of the tetrahedron in six groups of two. Four of the thiolate ligands feature a μ_3 binding mode. These are situated at the centers of each triangular face. The average Co-Cl distance is 2.21 Å, which is consistent with the values reported for the related cluster, $[NBu_4]_2[Co_4(SPh)_6Cl_4]$.[53] Similarly, the Co-S distances for the μ_2 thiolate ligands (range: 2.24-2.32 Å) are within the reported range for the related Co thiolate clusters,

$[NBu_4]_2[Co_4(SPh)_6Cl_4]$ and $M_2[Co_4(SPh)_{10}]$ (M = Me_4N^+, Et_4N^+,$hexyl_2NH_2^+$).[53-54] The Co-S distances for the μ_3 thiolate ligands (range: 2.30-2.35 Å) are generally longer, but overlap somewhat with those observed for the μ_2 thiolate ligands. Finally, the long Co-Co distances (range: 3.66-3.97 Å) in **5.1** precludes the presence of any direct Co–Co bonds. Similar Co–Co distances were also observed for $[NBu_4]_2[Co_4(SPh)_6Cl_4]$ and $M_2[Co_4(SPh)_{10}]$.[53-54]

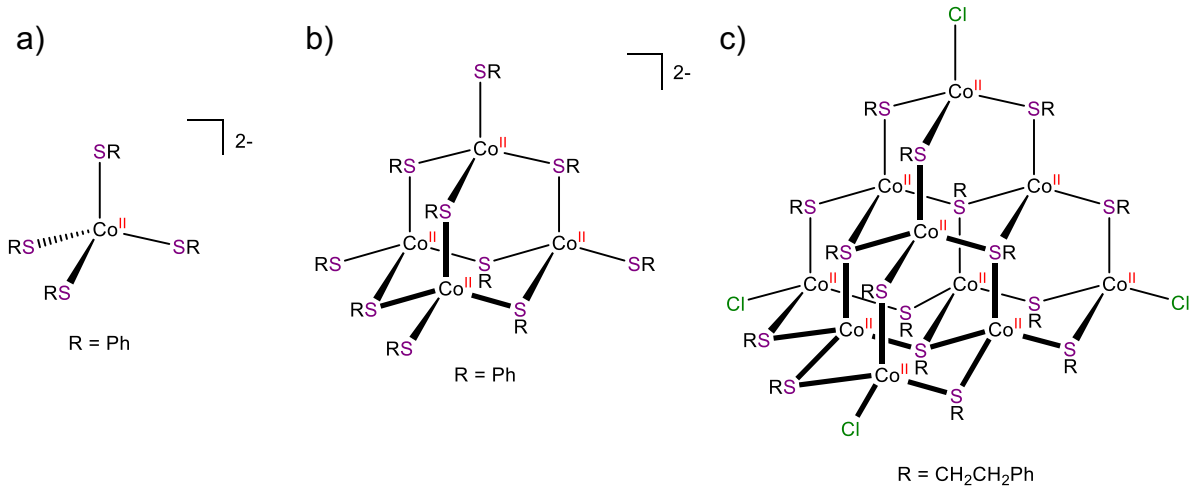

Figure 5.2. Comparison of the related Co(II) complexes $M_2[Co(SPh)_4]$ (M = PPh_4^+, Et_4N^+) (a, ref. 64-65), the T2 supertetrahedron $M_2[Co_4(SPh)_{10}]$ (M = (Me_4N^+, Et_4N^+, $hexyl_2NH_2^+$) (b, ref. 53), and the T3 supertetrahedron complex **5.1**.

Complex **5.1** is a rare example of an open-shell, chalcogenide-stabilized T3 supertetrahedral cluster.[55-56] Comparable chalcogenide-stabilized supertetrahedra, such as $[Cd_{10}(SCH_2CH_2OH)_{16}][X]_4$ (X = ClO_4^-, NO_3^-, SO_4^{2-})[57-59] and $[Me_4N]_2[E_4M_{10}(SPh)_{16}]$ (E = S, Se; M = Zn, Cd),[60] feature the diamagnetic Zn^{2+} and Cd^{2+} ions. Other open-shell supertetrahedra, such as $[M_{10}O(tmp)_4(diketonate)_4]$ (M = Ni, Co; H_3tmp = 1,1,1-tris(hydroxymethyl)propane) and $[Mn_{10}O_4(N_3)_4(hmp)_{12}][ClO_4]_2$ (Hhmp = 2-(hydroxylmethyl)pyridine) feature alkoxide co-ligands.[61-63] Complex **5.1** can also be viewed as the T3 analogue of known T2 supertetrahedral clusters, $M_2[Co_4(SPh)_{10}]$ (M = (Me_4N^+,

Et_4N^+, $hexyl_2NH_2^+$) and $[NBu_4]_2[Co_4(SPh)_6Cl_4]$,[53-54] which are themselves closely related to the classic monometallic cobalt-thiolate complexes, $M_2[Co(SPh)_4]$ ($M = PPh_4^+$, Et_4N^+) (Figure 5.2).[64-65]

I next endeavored to synthesize complex **5.1** via a rational route (Scheme 5.2). Given that $NaBH_4$ appears to be acting solely as a base during the formation of **5.1**, I rationalized that the reaction protocol could be simplified by substitution of $PhCH_2CH_2SH/NaBH_4$ with $NaSCH_2CH_2Ph$. Thus, reaction of $CoCl_2 \cdot 1.5THF$ with 1.6 equiv of $NaSCH_2CH_2Ph$ in THF resulted in the formation of a green solution, which gradually turned dark brown over the course of 5 h, concomitant with the deposition of a grey powder. Work-up of the reaction mixture allowed for the isolation of **5.1** as a dark brown crystalline solid. When synthesized in this fashion complex **5.1** can be isolated in 81% yield.

A ^1H NMR spectrum (Figure 5.3 and 5.4) of **5.1** in CD_2Cl_2 features 10 resonances, ranging from 115.7 to -19.6 ppm. The number of resonances, and their integrations, are consistent with the presence of two magnetically inequivalent thiolate environments in a 12:4 ratio, as predicted by the solid-state molecular structure. More significantly, the resonances at 115.7, 57.2, and -19.6 ppm feature very similar chemical shifts to the diagnostic resonances observed in the ^1H NMR spectrum of the *in situ* reaction mixture (*vide supra*). This further confirms that **5.1** is being formed in the reaction of $CoCl_2$ with $PhCH_2CH_2SH$ and $NaBH_4$ in THF/H_2O.

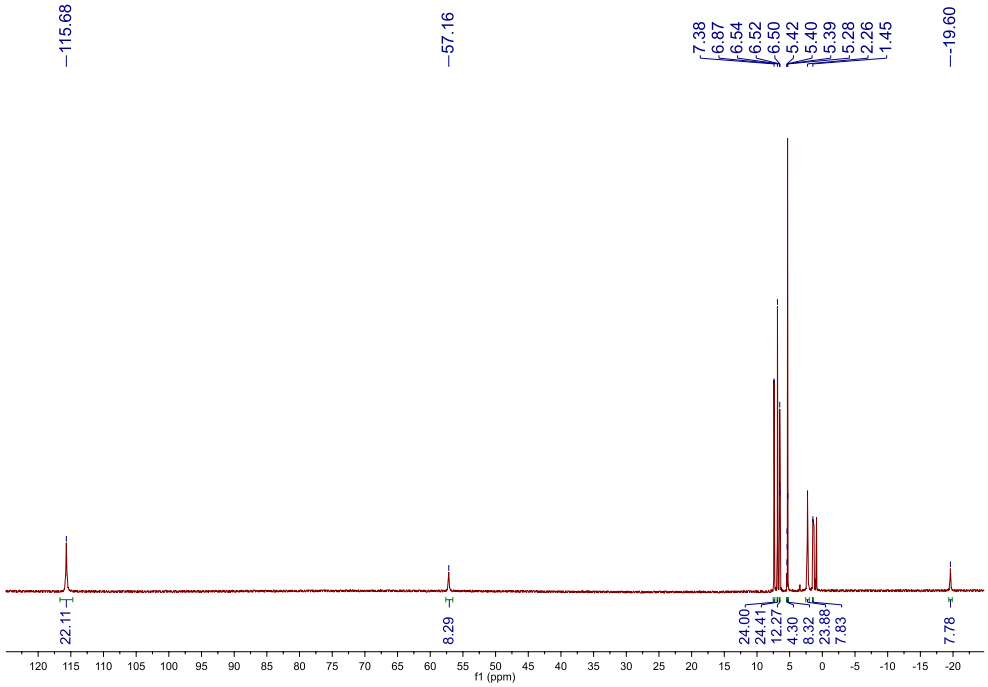

Figure 5.3. ^{1}H NMR spectrum of **5.1** in CD_2Cl_2.

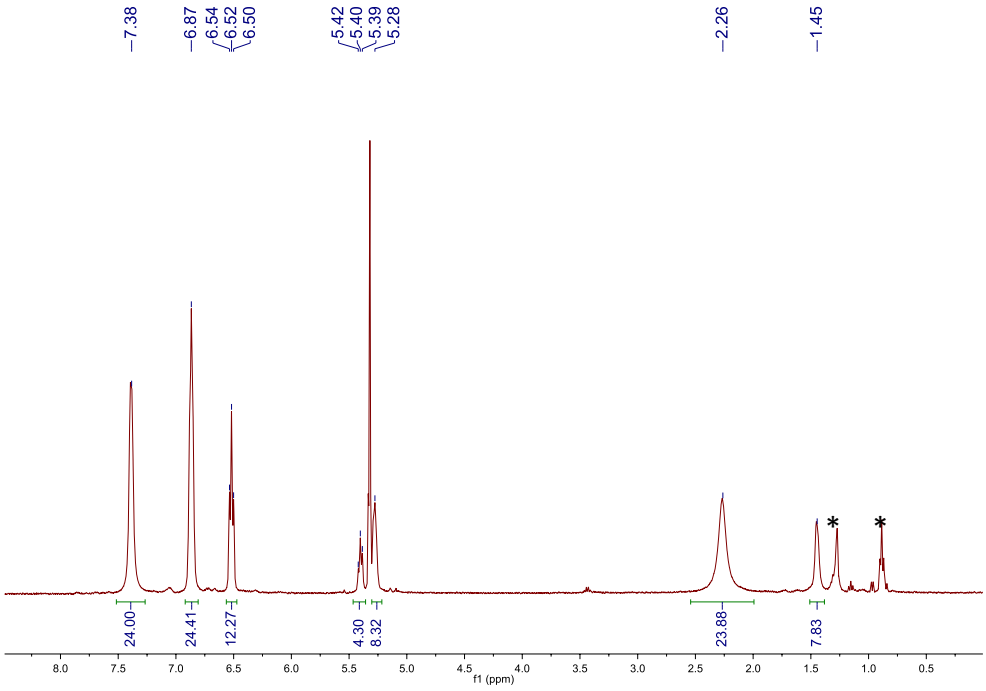

Figure 5.4. Partial ^{1}H NMR spectrum of **5.1** in CD_2Cl_2. (*) indicates a resonance assignable to hexanes.

The electrospray ionization (ESI) mass spectrum of complex **5.1** in CH_2Cl_2, acquired in negative ion mode, is also consistent with my proposed formulation (Figure 5.5). The major feature at *m/z* = 2929.9475 is assignable to two overlapping ions: the parent peak $[M]^-$ and the fragment $[Co_9(SR)_{16}Cl_4 + Cu]^-$. Additionally, a peak at *m/z* = 2962.9119 is assignable to $[M + Cl]^-$.

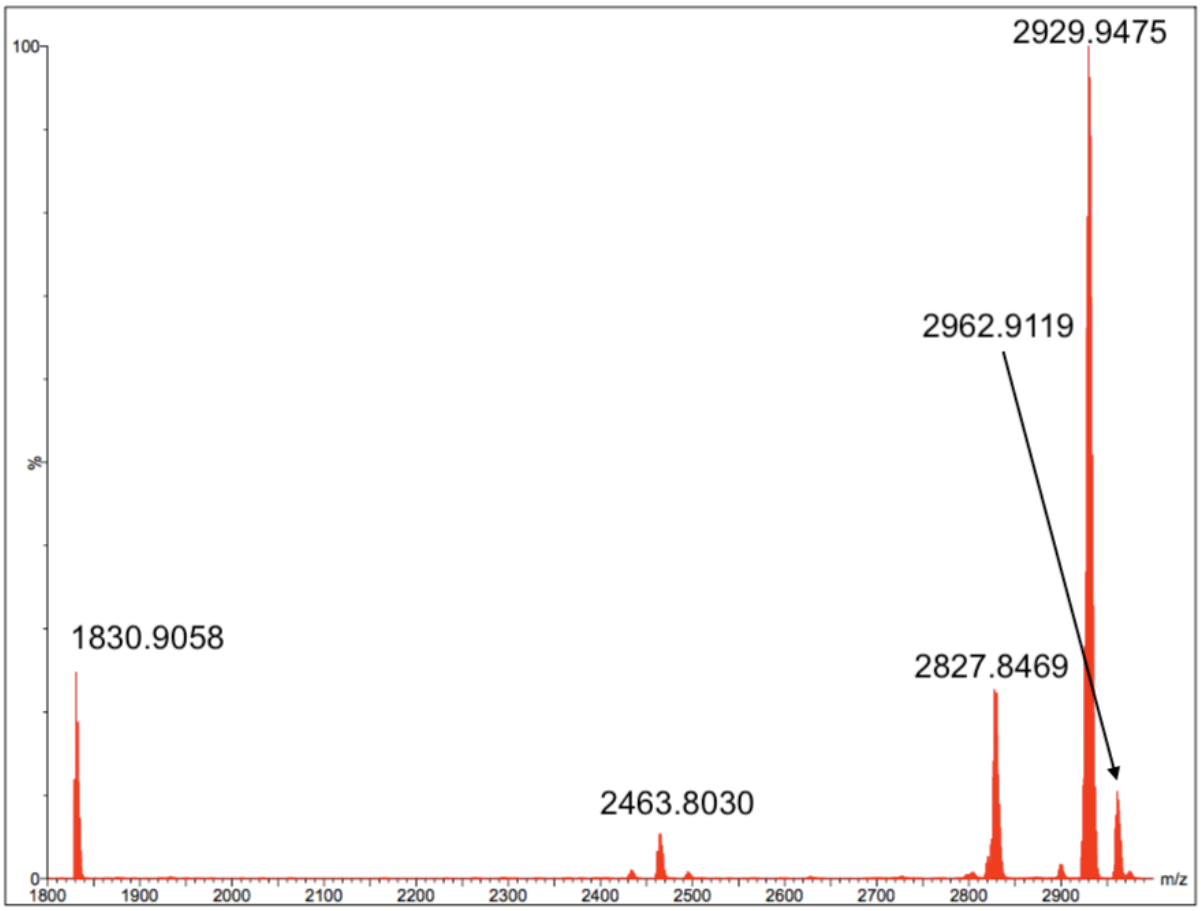

Figure 5.5. ESI-MS of complex **5.1** in negative mode.

5.2.3 Magnetic Susceptibility of Complex 5.1

Magnetic susceptibility data were also collected on a microcrystalline sample of **5.1** (Figure 5.6, bottom) with the help of Josh Bocarsly of the Seshadri group at UCSB. At 300 K, complex **5.1** exhibits an effective magnetic moment of 7.36 B.M., lower than the anticipated spin-only effective magnetic moment (12.25 B.M.), and indicative of moderate

antiferromagnetic coupling between cobalt centers. Dance also reported antiferromagnetic coupling between the Co centers in $[NMe_4]_2[Co_4(SPh)_{10}]$ (average $J = -17$ cm^{-1}).[54] Finally, the magnetization curve M vs. H is linear, implying that complex **5.1** is a simple paramagnet (Figure 5.6, top), and shows no hysteresis at any temperature.

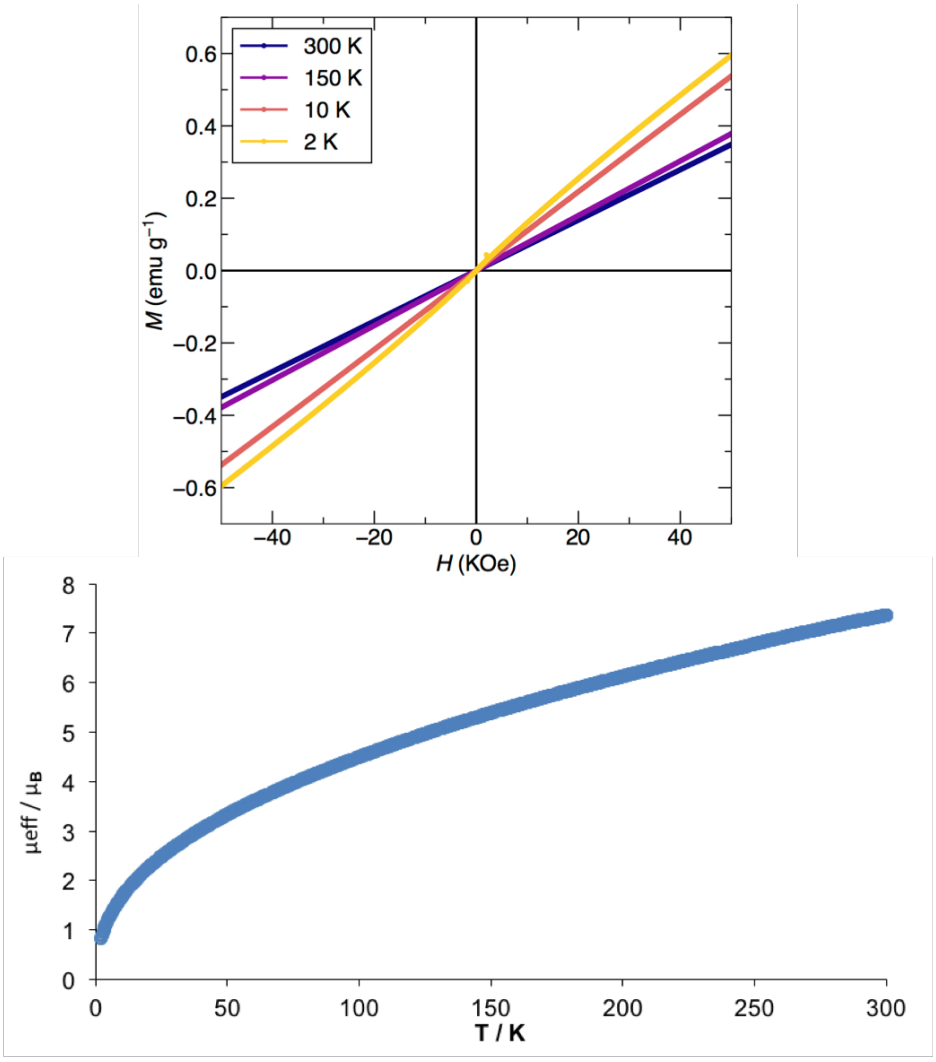

Figure 5.6. Solid-state magnetic susceptibility data M vs. H (top) and and μ_{eff} vs. T (bottom) for **5.1** measured from 2 to 300 K.

5.2.4 Effects of Reaction Stoichiometry on the Formation of Complex 5.1

I also endeavored to examine the effect of reaction stoichiometry on the formation of **5.1**. The reaction of $CoCl_2 \cdot 1.5$THF with 1 equiv of NaSR still results in the formation of **5.1**, but

with a significantly reduced yield (ca. 16%). Similarly, reaction of $CoCl_2 \cdot 1.5THF$ with 2 equiv of NaSR (Figure A5.5) resulted in the formation of large number of paramagnetic, Co-containing products, including complex **5.1** (but in insignificant amounts). Not surprisingly, I was unsuccessful in my attempts to isolate any products from this reaction mixture. From these experiments, I hypothesize that Cl^- must play an important role in directing the self-assembly of **5.1**. Presumably, the use of greater than 1.6 equiv of thiolate per Co results in a deficiency of Cl^-, which prevents the assembly of **5.1** and results in formation of a broad distribution of clusters. Previous workers have also noticed that the speciation of Co(II)-thiolates is highly dependent on reaction stoichiometry.[53-54]

5.2.5 Chemical Properties of Complex 5.1

I also briefly examined the chemical properties of complex **5.1**. It is soluble in benzene, toluene, and CH_2Cl_2, but insoluble in MeCN, Et_2O, and alkanes. Complex **5.1** is soluble in THF, but partially decomposes over the course of 5 h, as evidenced by the deposition of a brown solid on standing in this solvent (Figure A5.4). Attempted dissolution of **5.1** in py-d_5 results in immediate formation of a green solution that contains no resonances assignable to **5.1**, concomitant with deposition of a brown solid (Figure A5.6). While **5.1** clearly reacts with pyridine, I have been unable to determine the identity of the product(s) formed. I also explored the reactivity of complex **5.1** with other neutral donor ligands. Monitoring the reaction of the cluster with phenanthroline (4 equiv) by ^1H NMR spectroscopy in CD_2Cl_2 (Figure A5.8) results in the immediate formation of a similar green solution, concomitant with the deposition of red and green solids. Over the course of 3 h, the green color of the solution took on a brown tint and further green and red solids crashed out of solution. The ^1H NMR spectra of this reaction show a myriad of products forming 10 min after the addition of phenathroline, as well

as no resonances assignable to complex **5.1**. Resonances at 222 and 171 ppm grow in over 3 h and seem to be the dominant product(s) from this reaction. All attempts at isolating material from this reaction have thus far failed. I also attempted the reaction of **5.1** with 4,4'-bipyridine (4 equiv) in dichloromethane. Immediately upon addition of solid 4,4'-bipyridine to a dichloromethane solution of **5.1** a brick-red solid formed. This product was collected on a fritted glass filter; however, its characterization was not forthcoming due to its complete insolubility in all organic solvents.

I also explored the chemical reduction and oxidations of complex **5.1**. Reaction of complex **5.1** with the reducing again diphenylsilane (Ph_2SiH_2, 5 equiv) in dichloromethane resulted in no color change after 20 h. A ^{1}H NMR spectrum of an aliquot of the reaction mixture was taken in CD_2Cl_2 (Figure A5.9), which revealed resonances assignable to unreacted **5.1** and Ph_2SiH_2. Reaction of **5.1** with a more potent reducing agent, KC_8 (4 equiv), in THF resulted in a rapid color change from brown to black concomitant with the deposition of a gray and brown solids over the course of 1 h. A ^{1}H NMR spectrum of an aliquot of the reaction mixture was taken in C_6D_6 (Figure A5.10) revealed no resonances assignable to **5.1** and no tractable material could be isolated. In an attempt to oxidize or exchange the anions of the cluster, **5.1** was exposed to AgOTf (OTf = trifluoromethanesulfonate, 8 equiv) in CD_2Cl_2 at room temperature and was monitored by ^{1}H NMR spectroscopy over 20 h (Figure A5.11 and A5.12). Immediately after addition of AgOTf, the reaction mixture turned green-brown concomitant with a small amount of brown powder. After 1 h, a ^{1}H NMR spectrum reveals several new paramagnetic resonances as well as unreacted **5.1**. Similarly, a ^{19}F NMR spectrum revealed the presence of several new resonances. After 4 h, the reaction mixture remained the same green-brown color and the ^{1}H NMR spectrum revealed no change. However, after 20 h

the reaction mixture had turned a dark green color and more brown powder had crashed out of solution. A ^{1}H NMR spectrum showed no resonances aside from broad solvent signals. Attempts at isolating the products from this reaction have thus far been unsuccessful. As noted in my studies into the reaction stoichiometry, it would appear that post-synthetic perturbation also disrupts the delicate balance of the Co:thiolate:chloride ratio that stabilizes complex **5.1**. This ratio of metal to ligand is important not only to the formation of **5.1**, but also the preservation of its structure. Further studies into the self-assembly of Co-thiolate clusters would necessarily have to take this into account if odd speciation is observed.

5.2.6 Analysis of the Likely Products Generated by Barrabés and Co-workers

The reaction of $CoCl_2$ by $NaBH_4$, both in the presence or absence of a passivating ligand, has been studied extensively.[49-50, 66-70] In the absence of a passivating ligand, these reductions result in the formation of finely-divided Co(0) (in non-aqueous solvents) or Co_2B (under aqueous conditions).[66] In the presence of a passivating ligand, or in the presence of surfactant, the results are more complicated. In one instance, this reaction resulted in the formation of simple Co(II) thiolate complexes,[69-70] while in other cases authentic Co(0) nanoparticles were generated.[49-50, 66-68] Given this past precedent, as well as my own experiments, I believe that the 2017 synthesis initially resulted in formation of **5.1**, and not $Co_x(SCH_2CH_2Ph)_m$-type nanoclusters, as originally suggested. However, complex **5.1** then decomposed upon exposure to air and water during work-up, likely generating a mixture of $Co_xO_y(SCH_2CH_2Ph)_m$–type clusters. Consistent with this hypothesis, exposure of complex **5.1** to air, as a CH_2Cl_2 solution, results in a color change from deep brown to coral. A UV-vis spectrum of this solution features absorptions at 404, 493, and 611 nm (Figure 5.7 and A5.22). These values are very similar to those reported in 2017 for $Co_x(SCH_2CH_2Ph)_m$ (Figure 5.7, inset), demonstrating that the

original material requires O_2 for its formation, and is therefore unlikely to contain any Co(0) character.

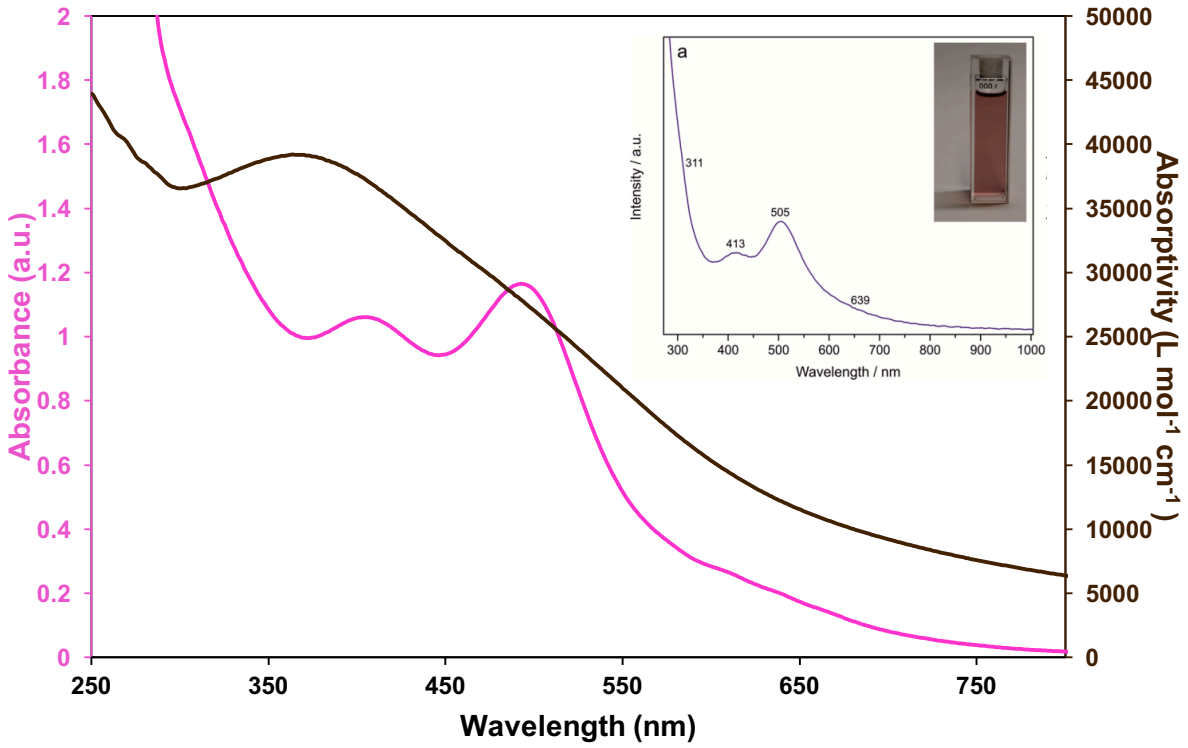

Figure 5.7. UV-Vis spectra of **5.1** in dichloromethane (37.5 μM) before (brown trace) and after (pink trace) exposure to air. Inset shows UV-Vis spectra originally reported by Barrabés and co-workers.[51]

5.2.7 Using Bond Dissociation Energy (BDE) to Predict Nanocluster Formation

As mentioned previously, all current known thiolate-protected nanoclusters are limited to clusters of Au and Ag.[5] While there are examples of Cu nanoclusters, the supporting ligands for these complexes are either acetylides[11, 13] or a mix of hydrides and phosphines.[10, 12] Attempted syntheses of low-valent Cu-thiolate compounds have thus far resulted in the isolation of simple Cu(I) coordination clusters.[71-72] Similarly, several groups synthesized the Ni(II)-thiolate oligomers $[Ni(SCH_2CH_2Ph)_2]_x$ (x = 4, 6) under nearly identical reaction

conditions.[72-76] In an effort to understand why the chemistry of Ag and Au differs from that of Cu and Ni (and Co, as demonstrated in this chapter), I propose a simple thermochemical model. Namely, the difference in the bond dissociation energies (BDE)[77] between M-S and M-M bonds for a given metal can be used to predict nanocluster stability (Figure 5.8). As this difference decreases, the formation of a M-M bond at the expense of breaking a M-S bond should require significantly less energy input. Therefore, it is of critical importance to minimize this difference and find metals and ligands with compatible BDEs in order to successfully isolate a nanocluster. For example, for M = Ag, Au, the difference in BDE between a M-M and a M-S bond is relatively small (<60 kJ/mol). Therefore, formation of a M-M bond from metal-thiolate oligomers is thermochemically accessible through addition of an external reducing agent, such as $NaBH_4$, and cluster growth can be promoted. On the other hand, for M = Cu, Ni, and Co, the BDE difference is much larger (93 – 204 kJ/mol), which favors generation of metal-thiolate oligomers and disfavors formation of M-M bonds, in good agreement with experimental results. Therefore, to isolate nanoclusters of these metals, it may be necessary to eschew traditional synthetic methods and to develop new ligands whose BDEs more closely match those of the metal-metal bonds and fall below this empirically derived 60 kJ/mol threshold. For example, isolation of low-valent copper-selenoate or copper-telluroate clusters, which have BDE differences of 54 kJ/mol and 30 kJ/mol, respectively,[77] should be possible.

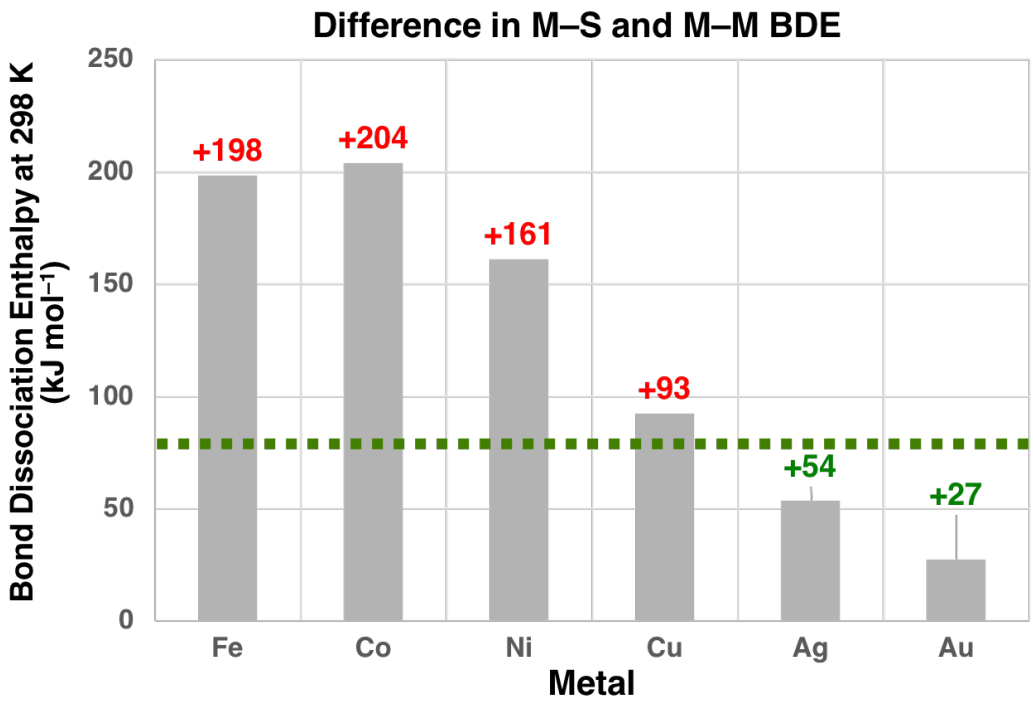

Figure 5.8. Difference in BDE of metal-thiolate and metal-metal bonds for iron, cobalt, nickel, copper, silver and gold.[77] Numbers shown in green represent BDE differences that are small enough to promote nanocluster growth whereas numbers shown in red have BDE differences that promote metal-thiolate oligomers. The green dashed line at 60 kJ/mol highlights the empirical BDE difference threshold under which metal-metal bond formation is favored.

5.3 Summary

I have re-examined the synthesis of thiolate-protected cobalt APNCs by reaction of $CoCl_2$ with $NaBH_4$ and $PhCH_2CH_2SH$. Despite efforts to faithfully reproduce the reported procedure, I am unable to detect the presence of a cobalt(0)-containing APNC. Instead, I isolated the intriguing Co(II) cluster, $[Co_{10}(SR)_{16}Cl_4]$. This complex represents the first example of a thiolate-protected Co(II) T3 supertetrahedron. These results are in good agreement with other attempts to generate copper- and nickel-thiolate APNCs using synthetic protocols developed

for gold and silver. That is, the formation of metal-metal bonds is thermodynamically disfavored and metal-thiolate oligomers are too stable to reduction to produce APNCs in this manner. I believe that $[Co_{10}(SR)_{16}Cl_4]$ was also being formed in the original synthesis; however, the cluster likely reacted with oxygen and water during work-up, giving a mix of $Co_xO_y(SCH_2CH_2Ph)_m$-type clusters. This result highlights the challenges inherent in the generation of low-valent cobalt nanoclusters, including the need for rigorous exclusion of air during their synthesis, work-up, and characterization.

5.4 Experimental

5.4.1 General Procedures

All reactions and subsequent manipulations were performed under anaerobic and anhydrous conditions under an atmosphere of nitrogen. Tetrahydrofuran, diethyl ether, and hexanes were dried using a Vacuum Atmospheres DRI-SOLV Solvent Purification system and stored over 3Å sieves for 24 h prior to use. Pentane, acetonitrile (MeCN), pyridine, benzene and dichloromethane (CH_2Cl_2), were degassed and dried over 3Å molecular sieves for 72 h prior to use. Ph_2SiH_2, CD_2Cl_2, THF-d_8, and C_5D_5N (py-d_5) were dried over 3Å molecular sieves for 24 h prior to use. $CoCl_2 \cdot 1.5THF$ was prepared according to previous reports.[78] All other reagents were purchased from commercial suppliers and used as received.

All NMR spectra were collected at room temperature. ^1H NMR spectra were recorded on an Agilent Technologies 400-MR DD2 400 MHz spectrometer or a Varian Unity Inova 600 MHz spectrometer. The chemical shifts of all nuclei were referenced by using the residual solvent peaks. IR spectra were recorded on a Nicolet 6700 FT-IR spectrometer with a NXR FT Raman Module. Electronic absorption spectra were recorded on a UV-2401 PC Shimadzu UV-NIR spectrophotometer. Mass spectra were collected at the Materials Research

Laboratory Shared Experimental Facilities at UCSB, using an electrospray ion (ESI) source in negative ion mode with a Waters Xevo G2-XS TOF mass spectrometer. Mass spectra were smoothed 3 times using the mean algorithm with a smooth window of 2 channels. Elemental analyses were performed by the Micro-Mass Facility at the University of California, Berkeley.

5.4.2 Magnetism Measurements

Magnetic properties were recorded using a Quantum Design Physical Property Measurement System (PPMS DynaCool) outfitted with a vibrating sample magnetometer with the assistance of Josh Bocarsly of the Seshadri group at UCSB. Complex **5.1** was analyzed using 10-15 mg of powdered crystalline material loaded into a polypropylene capsule under inert atmosphere, which was subsequently sealed with vacuum grease to prevent exposure to air and quickly transferred to the magnetometer under a He or vacuum environment. The experiments for complex **5.1** were performed between 2 and 300 K. Diamagnetic corrections ($\chi_{dia} = -1.937 \times 10^{-3}$ $cm^3 \cdot mol^{-1}$) were made using Pascal's constants.[79]

5.4.3 Attempted Synthesis of Monolayer-Protected $Co_x(SCH_2CH_2Ph)_m$ Nanoclusters[51]

To a solution of $CoCl_2 \cdot 1.5THF$ (55.0 mg, 0.231 mmol) in THF (10 mL) was added 2-phenylethanethiol (0.10 mL, 0.75 mmol) with a syringe. The blue solution was allowed to stir for 30 minutes, during which time no visible color change occurred. The solution was then cooled to -25 °C and $NaBH_4$ (80.0 mg, 2.11 mmol) was added quickly as a solid. The solution immediately turned dark green, and some effervescence was observed. The reaction mixture was allowed to warm to 25 °C and was then stirred for 5 h, gradually turning dark brown in color, concomitant with the deposition of a grey-brown solid. The mixture was then dried *in vacuo* and triturated with pentane (2 × 1 mL). The resultant heterogeneous mixture of dark

brown and grey solid was dissolved in CH_2Cl_2 (2 mL) and filtered through a Celite column supported on glass wool (0.5 × 4 cm). The column was washed with dichloromethane (2 × 0.5 mL) until the washings were colorless. A grey-brown plug (presumably NaCl) remained on the column. The washings were added to the filtrate. The filtrate was then layered with hexanes (12 mL) and stored at -25 °C for 3 d, which resulted in the deposition of dark brown crystals. The crystals were isolated by decanting the supernatant and were then washed with hexanes (2 × 1 mL). The washings were subsequently discarded. The dark brown crystals were dried *in vacuo* to yield **5.1** (26.5 mg, 37%).

5.4.4 Synthesis of $Na(SCH_2CH_2Ph)$

To a stirring solution of sodium bis(trimethylsilyl)amide (400 mg, 2.2 mmol) in diethyl ether (15 mL) was added 2-phenylethanethiol (300 μL, 2.2 mmol) via syringe. A thick white solid formed instantly. The reaction mixture was permitted to stir at 25 °C for 24 h, whereupon the mixture was filtered through a medium porosity frit. The frit and its contents were then rinsed with diethyl ether (3 × 2 mL). The resulting white powder was collected and dried *in vacuo* to yield $Na(SCH_2CH_2Ph)$ (329 mg, 93% yield). Anal. Calcd for $NaSC_8H_9$: C, 59.97; H, 5.66. Found C, 59.25; H, 5.48. ^{1}H NMR (400 MHz, 25 °C, py-d_5) δ 3.39 (m, 4H), 7.22 (br s, 5H). IR (KBr pellet, cm^{-1}): 492 (s), 569 (m), 615 (m), 695 (s), 718 (s), 757 (s), 825 (w), 903 (w), 961 (w), 1002 (w), 1026 (m), 1069 (w), 1126 (m), 1157 (w), 1196 (m), 1220 (s), 1307 (m), 1452 (s), 1496 (s), 1583 (w), 1603 (m), 1748 (w), 1805 (w), 1947 (w), 2264 (m), 2284 (s), 2909 (s), 2934 (s), 3027 (s), 3062 (s), 3084 (s).

5.4.5 Rational Synthesis of $[Co_{10}(SCH_2CH_2Ph)_{16}Cl_4]$ (5.1)

To a 20 mL scintillation vial equipped with a magnetic stir bar was added $CoCl_2 \cdot 1.5THF$ (58 mg, 0.24 mmol), $Na(SCH_2CH_2Ph)$ (61 mg, 0.38 mmol), and tetrahydrofuran (5 mL). The

reaction mixture was allowed to stir for 5 h at 25 °C, changing color from dark green to dark brown over this time, concomitant with the deposition of a grey-brown solid. The reaction mixture was then dried *in vacuo* and triturated with pentane (2 × 1 mL). The resulting dark brown solid was subsequently dissolved in CH_2Cl_2 (2 mL) and filtered through a Celite column supported on glass wool (0.5 × 4 cm). The column was washed with dichloromethane (2 × 0.5 mL) until the washings were colorless. The washings were added to the filtrate. The filtrate was then layered with hexanes (12 mL) and stored at -25 °C for 3 d, which resulted in the deposition of dark brown crystals. The crystals were isolated by decanting the supernatant and were then washed with hexanes (2 × 1 mL). The washings were subsequently discarded. The dark brown crystals were dried *in vacuo* to yield **5.1** (58 mg, 81%). Anal. Calcd for $C_{128}H_{144}S_{16}Cl_4Co_{10}$: C, 52.53; H, 4.96. Found: C, 52.40; H, 4.71. ^{1}H NMR (400 MHz, 25 °C, CD_2Cl_2): δ -19.60 (s, μ_3-SC*H*$_2$CH$_2$ or μ_3-thiolate *o*-Ph, 8H), 1.45 (s, μ_3-SC*H*$_2$CH$_2$ or μ_3-thiolate *o*-Ph, 8H), 2.26(br s, μ_2-SCH$_2$C*H*$_2$, 24H), 5.28 (br s, μ_3-thiolate *m*-Ph, 8H), 5.40 (t, J_{HH} = 8 Hz, μ_3-thiolate *p*-Ph, 4H), 6.52 (t, J_{HH} = 8 Hz, μ_2-thiolate *p*-Ph, 12H), 6.87 (s, μ_2-thiolate *m*-Ph, 24H), 7.38 (s, μ_2-thiolate *o*-Ph, 24H), 57.16 (s, μ_3-SCH$_2$C*H*$_2$, 8H), 115.68 (s, μ_2-SC*H*$_2$CH$_2$, 24H). ESI-MS: *m/z* 1830.9058 $[Co_6(SR)_{10}Cl_3]^-$ (Calcd *m/z* 1830.9307), *m/*z 2463.8030 $[Co_7(SR)_{13}Cl_4 + 2Cu]^-$ (Calcd *m/z* 2463.8196), *m/z* 2827.8469 $[Co_9(SR)_{15}Cl_4 + CuCl]^-$ (Calcd *m/z* 2827.8101) *m/z* 2929.9475 $[M]^-$ and $[Co_9(SR)_{16}Cl_4 + Cu]^-$ (Calcd *m/z* 2925.8875 and 2929.8838), *m/z* 2960.9270 $[M + Cl]^-$ (Calcd *m/z* 2960.8562). UV-Vis / NIR (CH_2Cl_2, 37.6 μM, 25 °C, $L \cdot mol^{-1} \cdot cm^{-1}$): 307 nm (ε = 39000), 678 nm (ε = 4900), 743 nm (ε = 4300), 887 nm (ε = 2000). IR (KBr pellet, cm^{-1}): 524 (m), 620 (w), 672 (m), 687 (s), 752 (s), 840 (w), 881 (w), 917 (w), 1025 (w), 1070 (w), 1099 (w), 1157 (w), 1173 (w), 1282 (w),

1344 (m), 1422 (s), 1440 (m), 1482 (s), 1558 (s), 1592 (w), 1669 (w), 1842 (w), 1894 (w), 1957 (w), 2927 (w), 3013 (w), 3055 (w).

5.4.6 Reaction of $CoCl_2 \cdot 1.5THF$ with 1 equiv of $NaSCH_2CH_2Ph$

To a 20 mL vial equipped with a magnetic stir bar was added $CoCl_2 \cdot 1.5THF$ (58 mg, 0.24 mmol), $Na(SCH_2CH_2Ph)$ (39 mg, 0.24 mmol), and tetrahydrofuran (5 mL). The reaction mixture was allowed to stir for 5 h at 25 °C, changing color from dark green to dark brown over this time, concomitant with the deposition of a grey-brown solid. The reaction mixture was dried *in vacuo* and triturated with pentane (2 × 1 mL). The resultant dark brown solid was subsequently dissolved in CH_2Cl_2 (2 mL) and filtered through a Celite column supported on glass wool (0.5 × 4 cm). The column was washed with dichloromethane (2 × 0.5 mL) until the washings were colorless. The washings were added to the filtrate. A mixture of grey-brown (presumably NaCl) and blue solids (presumably unreacted $CoCl_2 \cdot 1.5THF$) remained on the Celite plug. The filtrate was then layered with hexanes (12 mL) and stored at -25 °C for 3 d, which resulted in the deposition of dark brown crystals. The crystals were isolated by decanting the supernatant and were then washed with hexanes (2 × 1 mL). The washings were subsequently discarded. The dark brown crystals were dried *in vacuo* to yield **5.1** (7 mg, 16%). The identity of this material was confirmed by comparison of its ^1H NMR spectrum in CD_2Cl_2 to that of authentic **5.1**.

5.4.7 X-ray Crystallography

Data for **5.1**$\cdot 2CH_2Cl_2$ were collected on a Bruker KAPPA APEX II diffractometer equipped with an APEX II CCD detector using a TRIUMPH monochromater with a MoKα X-ray source (α = 0.71073 Å). Crystals were mounted on a cryoloop under Paratone-N oil, and all data were collected at 100(2) K using an Oxford nitrogen gas cryostream system. X-

ray data for **5.1**·$2CH_2Cl_2$ were collected utilizing frame exposures of 10 s. Data collection and cell parameter determination was conducted using the SMART program.[80] Integration of the data frames and final cell parameter refinement were performed using SAINT software.[81] Absorption correction of the data was carried out using the multi-scan method SADABS.[82] Subsequent calculations were carried out using SHELXTL.[83] Structure determination was done using direct methods and difference Fourier techniques. All hydrogen atom positions were idealized, and rode on the atom of attachment. Structure solution, refinement, graphics, and creation of publication materials were performed using SHELXTL.[83]

Complex **5.1**·$2CH_2Cl_2$ contains positional disorder in several of the SCH_2CH_2Ph ligands. In many cases, the positional disorder of these ligands was addressed by modeling the carbon atoms of over 2 positions, each with half occupancy. However, in one instance (S16) alternative positions were not found. Hydrogen atoms were not assigned to disordered carbon atoms. The C–C bonds of these ligands were fixed with the DFIX command, and the phenyl rings were constrained with the FLAT command. Additionally, one of the CH_2Cl_2 solvate molecules was modelled over three positions, in a 0.5:0.25:0.25 ratio. The positions of the carbon and chlorine atoms were fixed with the SADI command. Hydrogen atoms were not assigned to this solvate.

Further crystallographic details can be found in Table 5.1.

Table 5.1. X-ray Crystallographic Data for **5.1**·$2CH_2Cl_2$.

	5.1·$2CH_2Cl_2$
empirical formula	$C_{130}H_{148}Cl_8Co_{10}S_{16}$
crystal habit, color	block, brown
crystal size (mm)	0.15 × 0.1 × 0.1
crystal system	monoclinic
space group	C*c*
volume (Å^3)	14247.7(15)
a (Å)	25.0171(14)
b (Å)	26.8758(16)
c (Å)	21.4593(13)
α (deg)	90
β (deg)	99.075(3)
γ (deg)	90
Z	4
formula weight (g/mol)	3096.34
density (calculated) (Mg/m^3)	1.443
absorption coefficient (mm^{-1})	1.562
F_{000}	6360
total no. reflections	28916
unique reflections	16107
final R indices [I>2σ(I)]	R_1 = 0.0878
	wR_2 = 0.2770
largest diff. peak and hole (e$^-$A^{-3})	1.259 and -0.867
GOF	1.025

5.5 Appendix

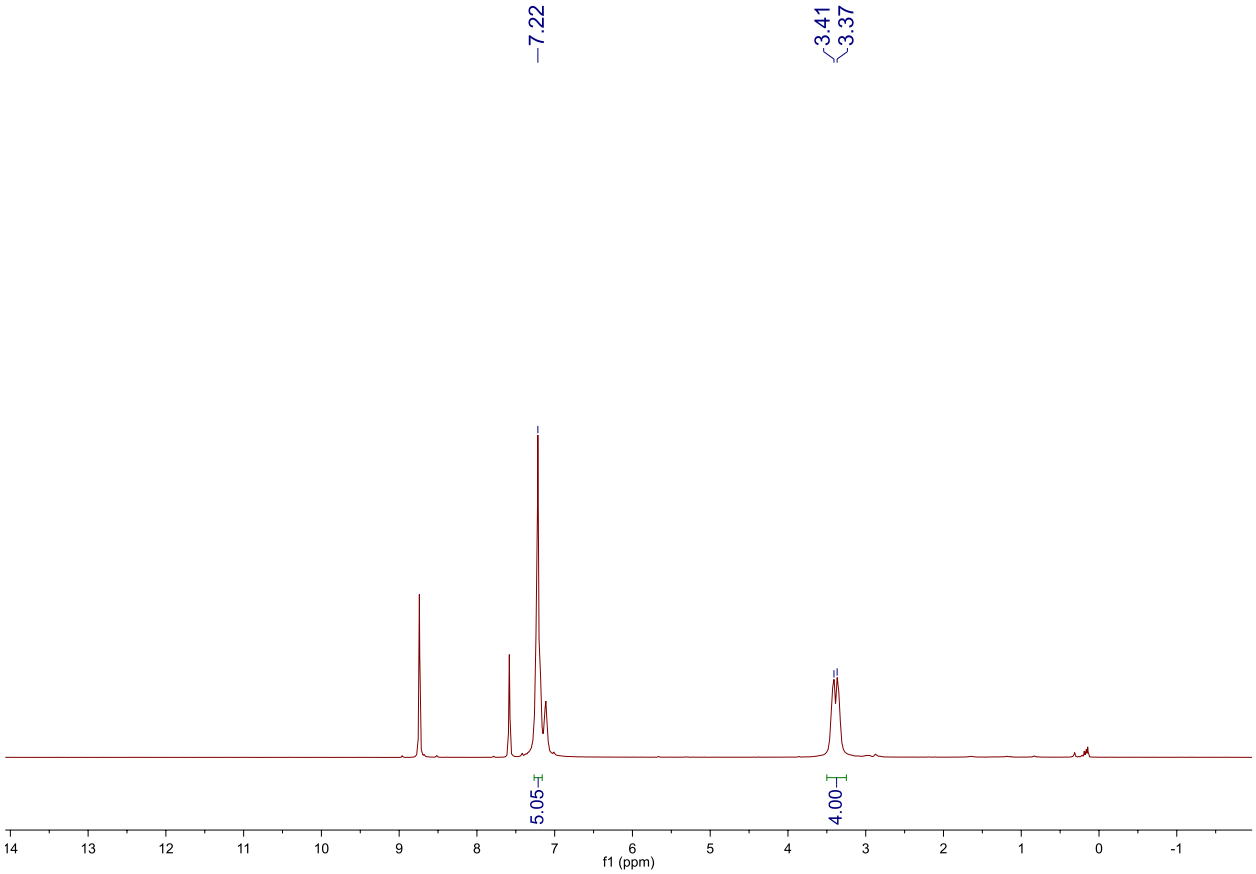

Figure A5.1. ^{1}H NMR spectrum of $NaSCH_2CH_2Ph$ in py-d_5.

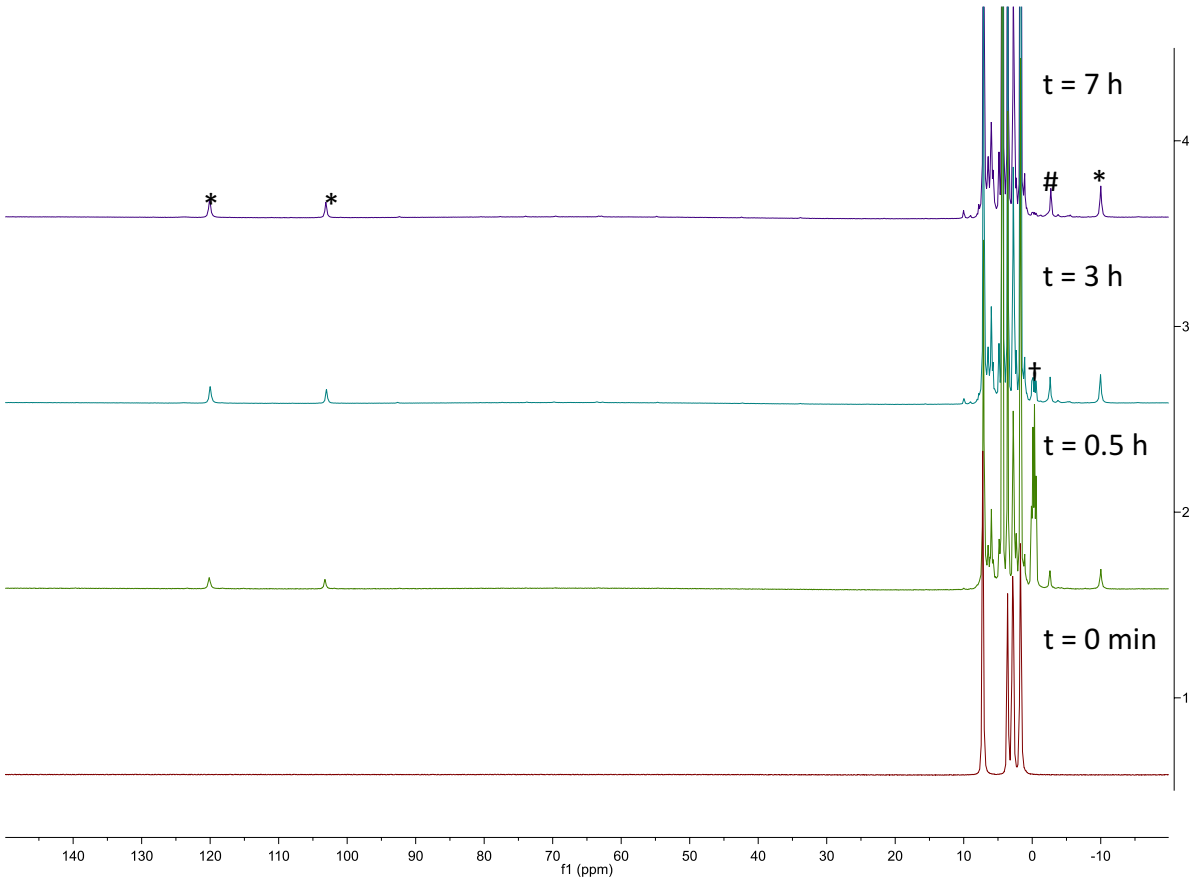

Figure A5.2. *In situ* ^{1}H NMR spectra of the reaction of $CoCl_2$·1.5THF (1 equiv), 2-phenylethanethiol (3 equiv), and $NaBH_4$ (9 equiv) in THF-d_8 and D_2O (5:1, v:v). **Experimental details:** A J. Young NMR tube equipped with a Teflon rotoflow valve was charged with $CoCl_2$·1.5THF (6.0 mg, 0.025 mmol), 2-phenylethanethiol (10 µL, 0.075 mmol), and THF-d_8 (1.0 mL), and a ^{1}H NMR spectrum of the blue solution was recorded after 30 min. A solution of $NaBH_4$ (9.0 mg, 0.24 mmol) in D_2O (0.2 mL), cooled to 0 °C, was quickly added to the NMR tube under a flow of N_2. After addition, the NMR tube was sealed and the headspace was placed under vacuum. The solution quickly turned dark brown-green, concomitant with vigorous bubbling. The reaction was allowed to stand at 25 °C and was intermittently monitored by ^{1}H NMR spectroscopy over the course of 7 h, during which time the solution gradually turned dark brown, concomitant with the deposition of a thick grey-brown solid and a colorless viscous oil. (*) indicates a resonance assignable to **5.1**, (#) indicates a resonance assignable to an unknown paramagnetic product, and (†) indicates a resonance assignable to $NaBH_4$.

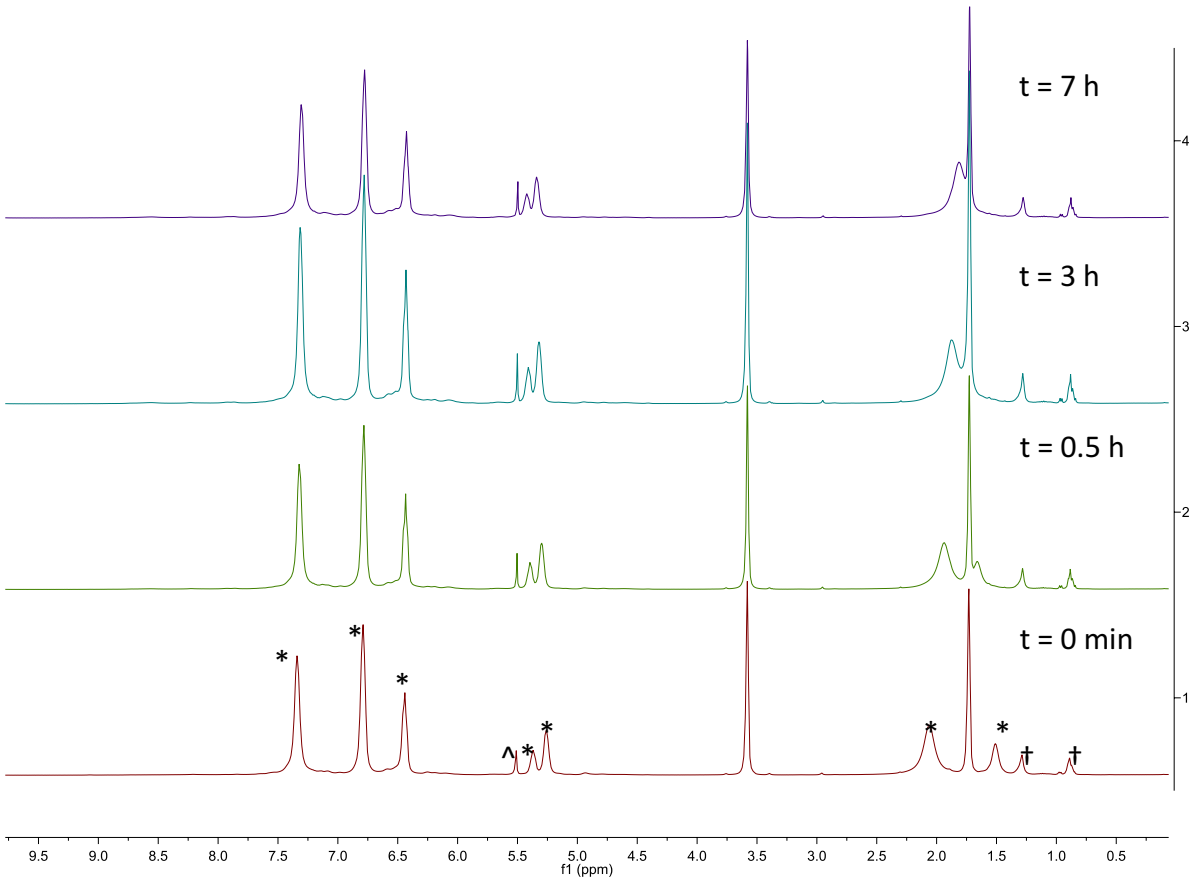

Figure A5.3. Partial *in situ* ^{1}H NMR spectra of the reaction of $CoCl_2$·1.5THF (1 equiv), 2-phenylethanethiol (3 equiv), and $NaBH_4$ (9 equiv) in THF-d_8 and D_2O (5:1, v:v)**.** (*) indicates a resonance assignable to **5.1**, (^) CH_2Cl_2, and (†) indicates a resonance assignable to hexanes.

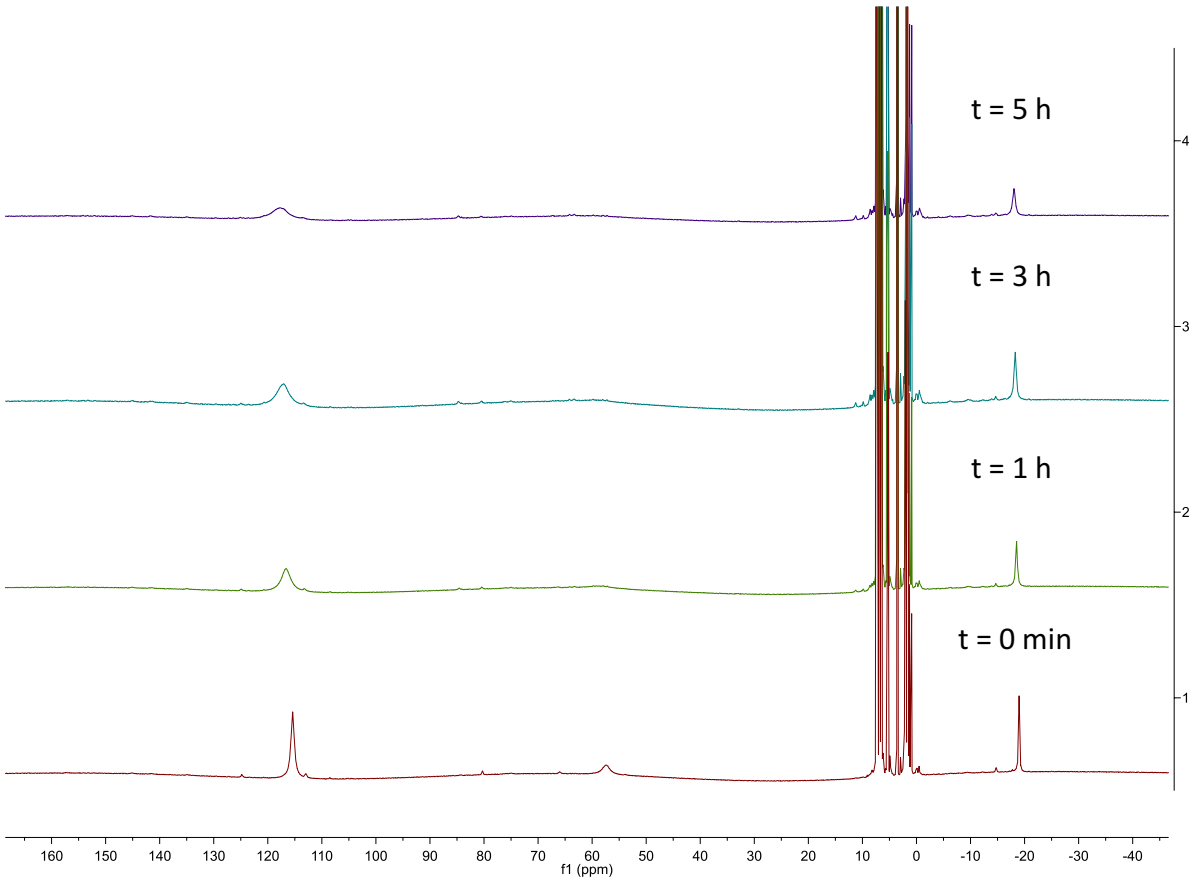

Figure A5.4. ^{1}H NMR spectra of **5.1** in THF-d_8. **Experimental details:** A J. Young NMR tube equipped with a Teflon rotoflow valve was charged with **5.1** (25.0 mg, 8.54 μmol) and THF-d_8 (0.8 mL) and a ^{1}H NMR spectrum of the brown solution was recorded. The sample was allowed to stand at 25 °C and was intermittently monitored by ^{1}H NMR spectroscopy over the course of 5 h, during which time a small amount of deep brown precipitate formed, concomitant with the formation of a red film on the walls of the J. Young NMR tube.

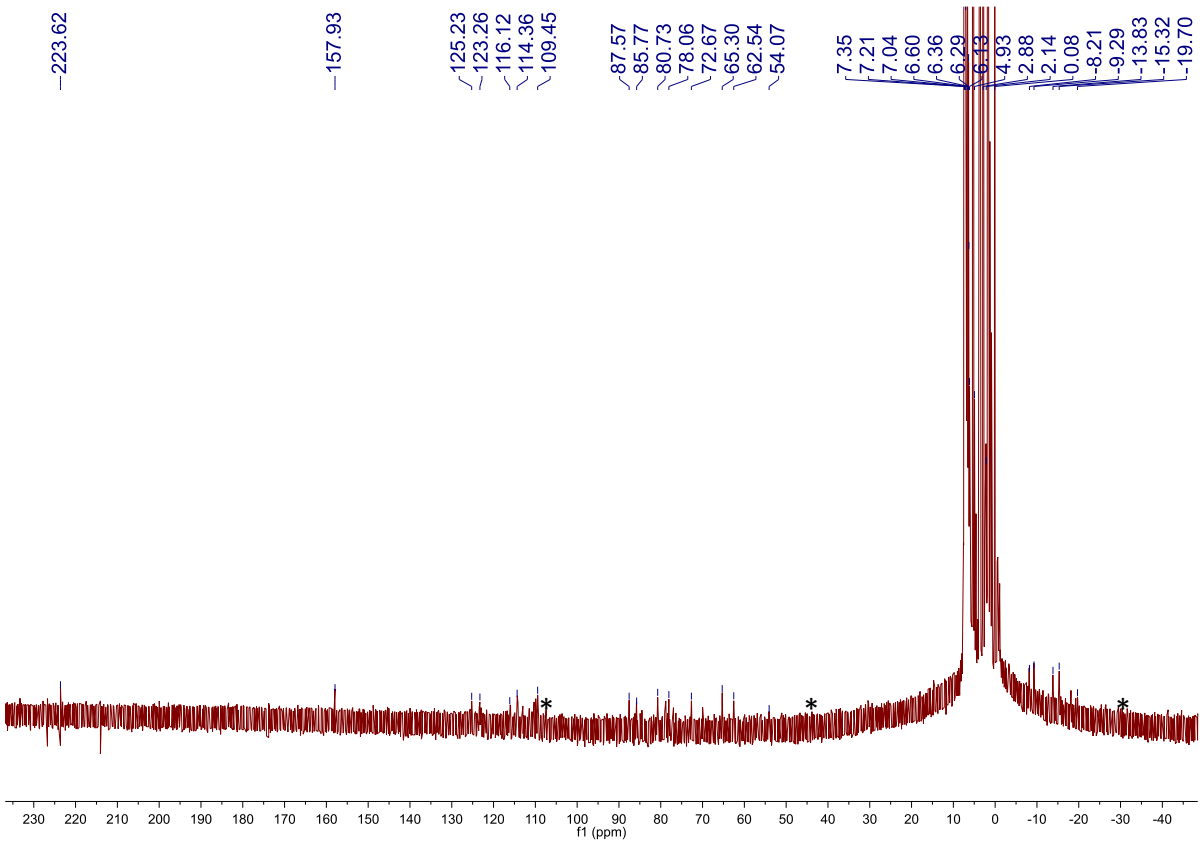

Figure A5.5. ^{1}H NMR spectrum (in CD_2Cl_2) of the solid formed upon reaction of $CoCl_2$·1.5THF (1 equiv) and NaSR (2 equiv). **Experimental details:** To a 20 mL vial equipped with a magnetic stir bar was added $CoCl_2$·1.5THF (58 mg, 0.24 mmol), $NaCH_2CH_2Ph$ (78 mg, 0.48 mmol), and tetrahydrofuran (6 mL). The reaction mixture was allowed to stir for 5 h at 25 °C, changing color from dark green to dark brown over this time, concomitant with the deposition of a grey-brown solid. The reaction mixture was dried *in vacuo* and triturated with pentane (2 × 1 mL). The resultant dark brown solid was subsequently dissolved in CH_2Cl_2 (2 mL) and filtered through a Celite column supported on glass wool (0.5 × 4 cm). The column was washed with dichloromethane (2 × 0.5 mL) until the washings were colorless. The washings were added to the filtrate. The filtrate was then layered with hexanes (12 mL) and stored at -25 °C for 3 d, which resulted in the deposition of dark brown powder. The powder was isolated by decanting the supernatant and was washed with hexanes (2 × 1 mL). A ^{1}H NMR spectrum of the solid was then recorded in CD_2Cl_2, which revealed the presence of a complex mixture of products. (*) indicates a resonance assignable to complex **5.1**.

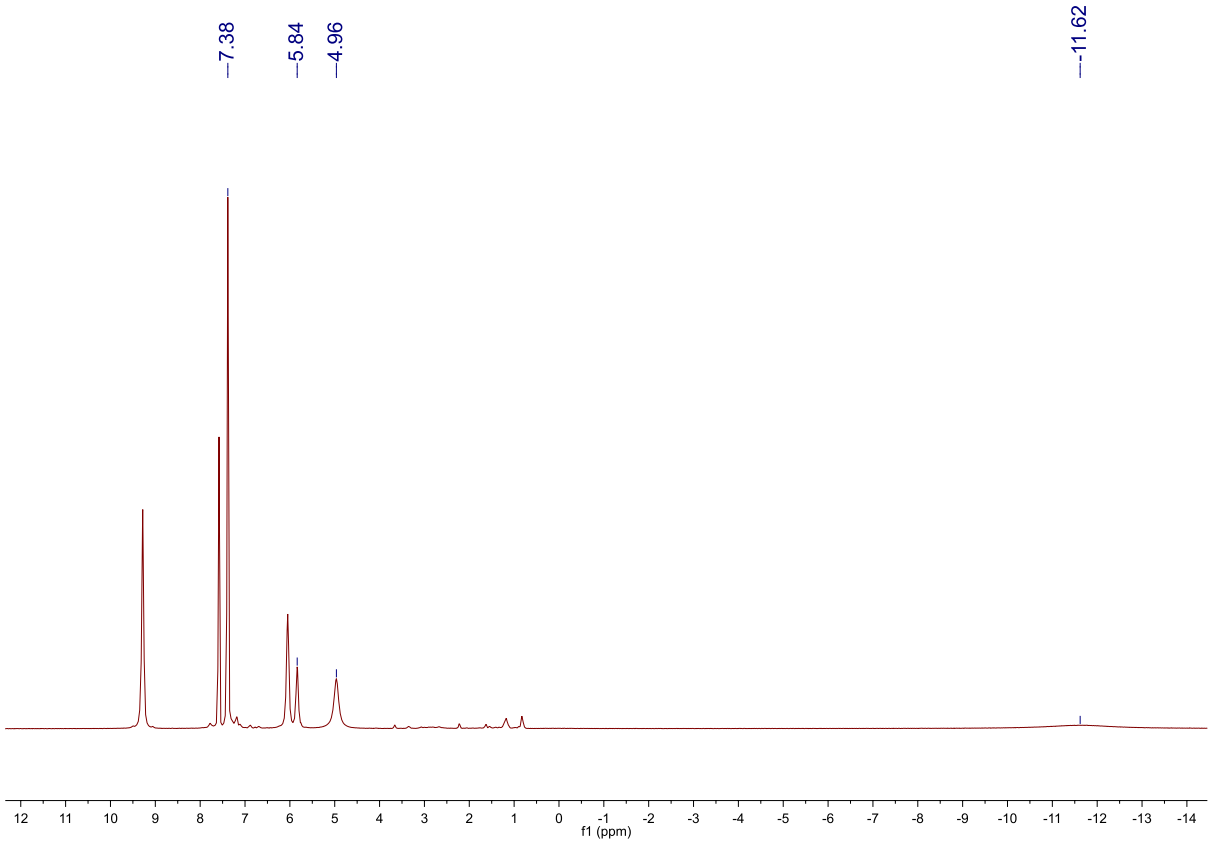

Figure A5.6. ^{1}H NMR spectrum of **5.1** in py-d_5. There are no resonances assignable to **5.1** in the spectrum, suggesting **5.1** is unstable in this strongly coordinating solvent.

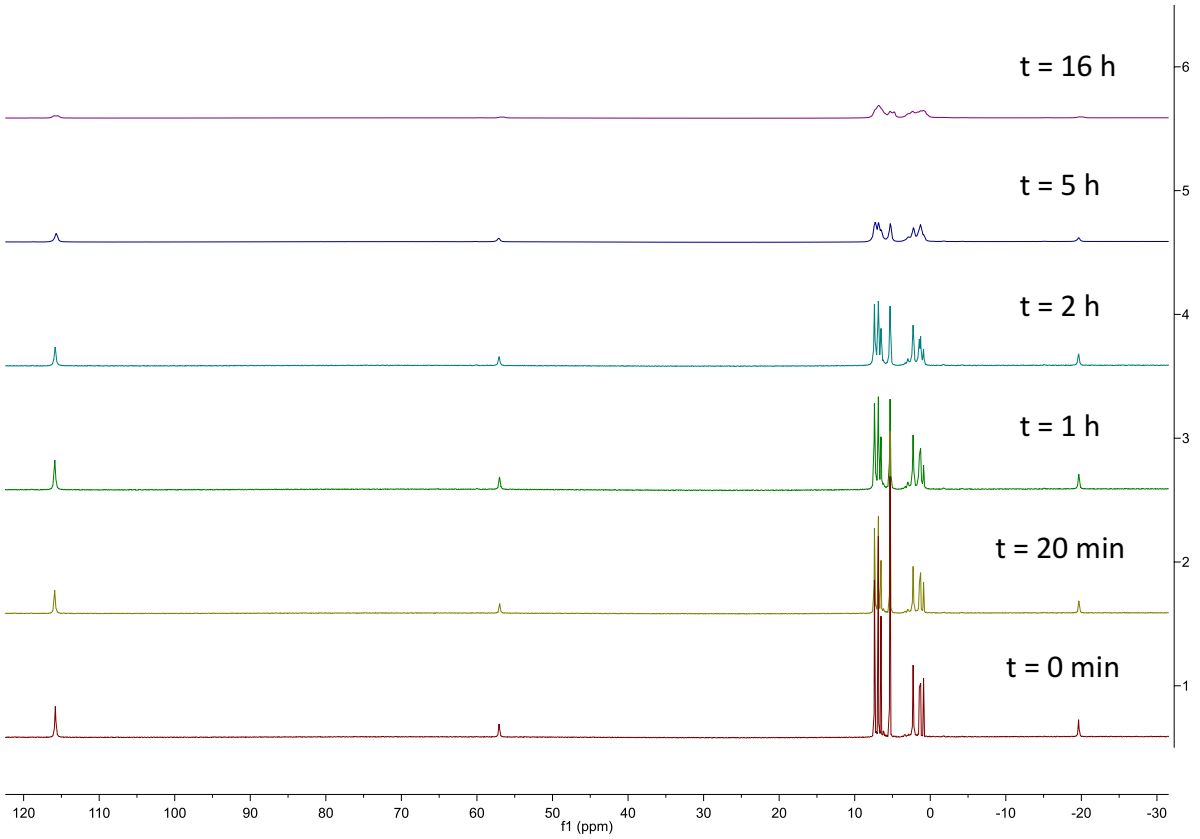

Figure A5.7. ^{1}H NMR spectra of **5.1** in CD_2Cl_2 after exposure to air. **Experimental details:** A J. Young NMR tube equipped with a Teflon rotoflow valve was charged with **5.1** (5.0 mg, 1.7 μmol) and CD_2Cl_2 (1.0 mL) and a ^{1}H NMR spectrum was recorded. The rotoflow valve was then removed from the J. Young tube for 10 minutes, whereupon the J. Young tube was resealed and a ^{1}H NMR spectrum was recorded. The sample was allowed to stand at 25 °C and was monitored intermittently by ^{1}H NMR spectroscopy over the course of 16h.

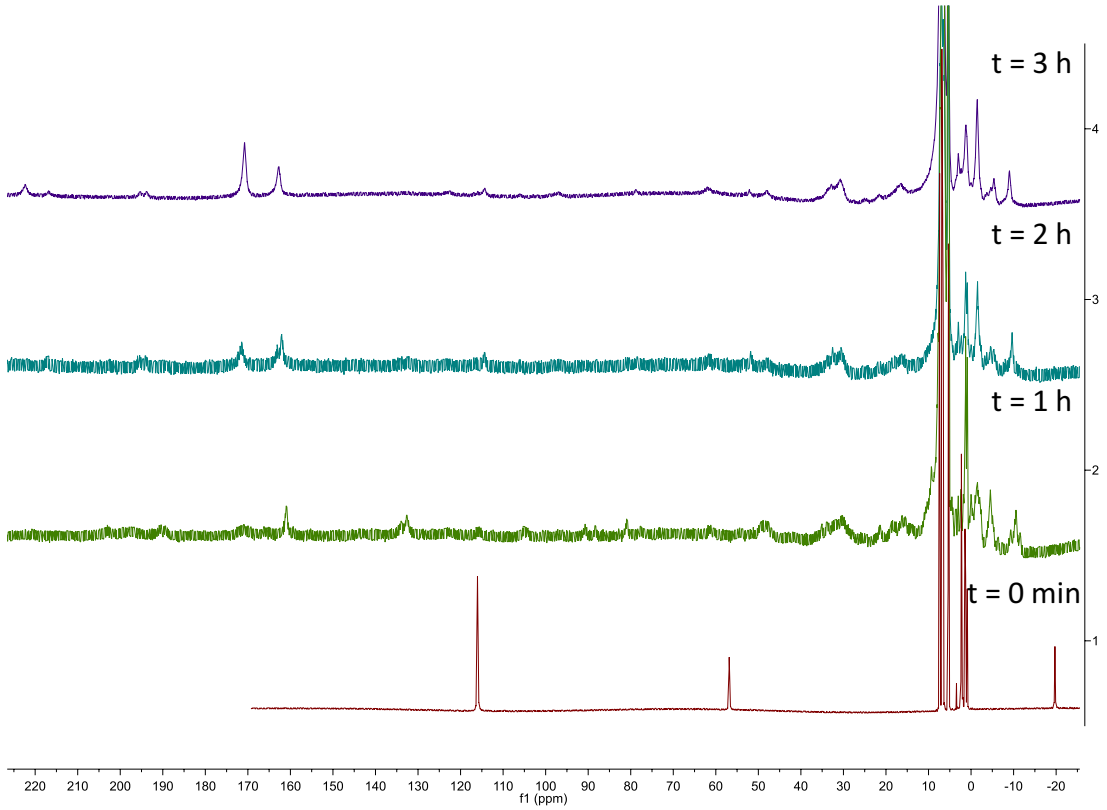

Figure A5.8. ^{1}H NMR spectra of the reaction of **5.1** with phenanthroline in CD_2Cl_2. **Experimental Details:** A J. Young NMR tube equipped with a Teflon rotoflow valve was charged with **5.1** (12.0 mg, 4.1 μmol) and CD_2Cl_2 (1.0 mL) and a ^{1}H NMR spectrum was recorded. To the NMR tube was added phenanthroline (3.0 mg, 16 μmol) which resulted in a color change from brown to green and the deposition of green and red solids. The sample was allowed to stand at 25 °C and was monitored intermittently by ^{1}H NMR spectroscopy over the course of 3 h.

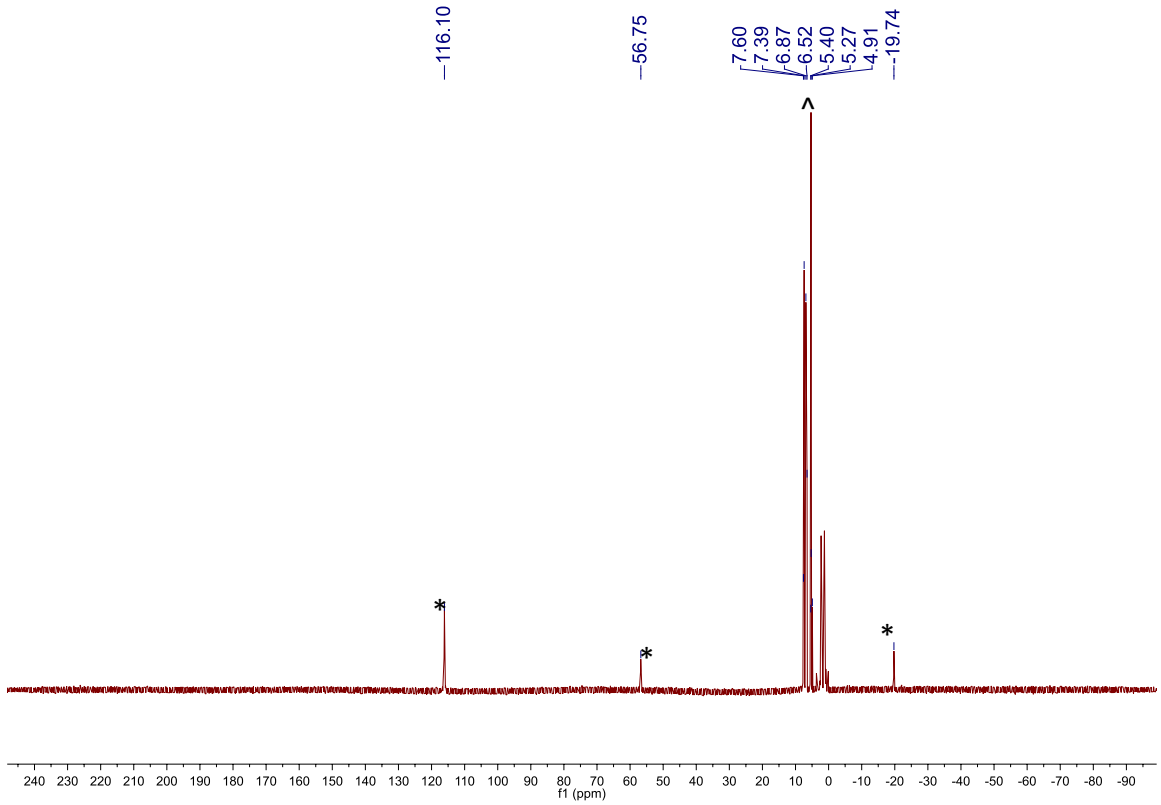

Figure A5.9. ^{1}H NMR spectrum of an aliquot the reaction of **5.1** with Ph_2SiH_2 in CD_2Cl_2. **Experimental Details:** A 20 mL scintillation vial equipped with a magnetic stir bar was charged with **5.1** (15.0 mg, 5.1 μmol) and CH_2Cl_2 (2.0 mL). To this stirring solution was added Ph_2SiH_2 (5 μL, 27 μmol). The reaction was allowed to stir at room temperature for 20 h whereupon an aliquot of the reaction mixture was taken and the solvents removed *in vacuo*. A ^{1}H NMR spectrum was then recorded in CD_2Cl_2. (*) indicated a resonance assignable to **5.1** and (^) indicates a resonance assignable to Ph_2SiH_2.

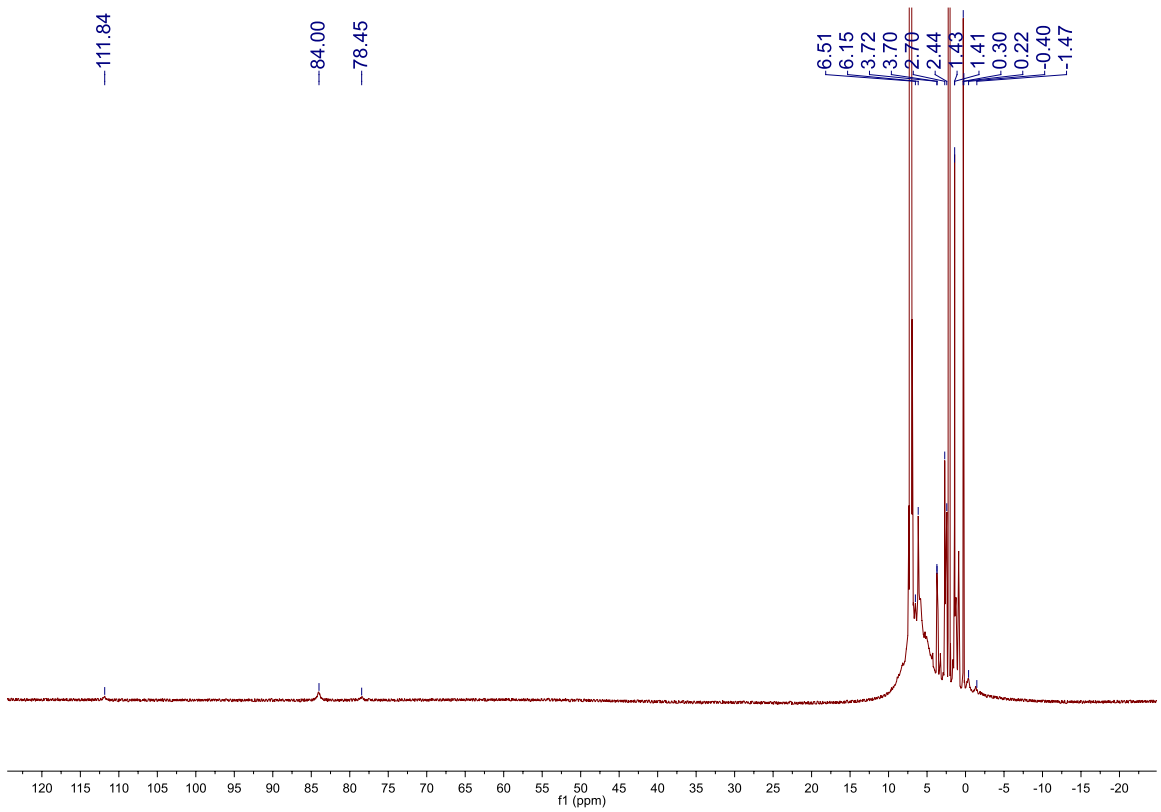

Figure A5.10. ^{1}H NMR spectrum of an aliquot the reaction of **5.1** with KC_8 in THF. **Experimental Details:** A 20 mL scintillation vial equipped with a magnetic stir bar was charged with **5.1** (20.0 mg, 6.83 μmol) and THF (2.0 mL). To this stirring solution was added KC_8 (3.7 mg, 27.4 μmol). The reaction was allowed to stir at room temperature for 1 h whereupon an aliquot of the reaction mixture was taken and the solvents removed *in vacuo*. A ^{1}H NMR spectrum was then recorded in C_6D_6.

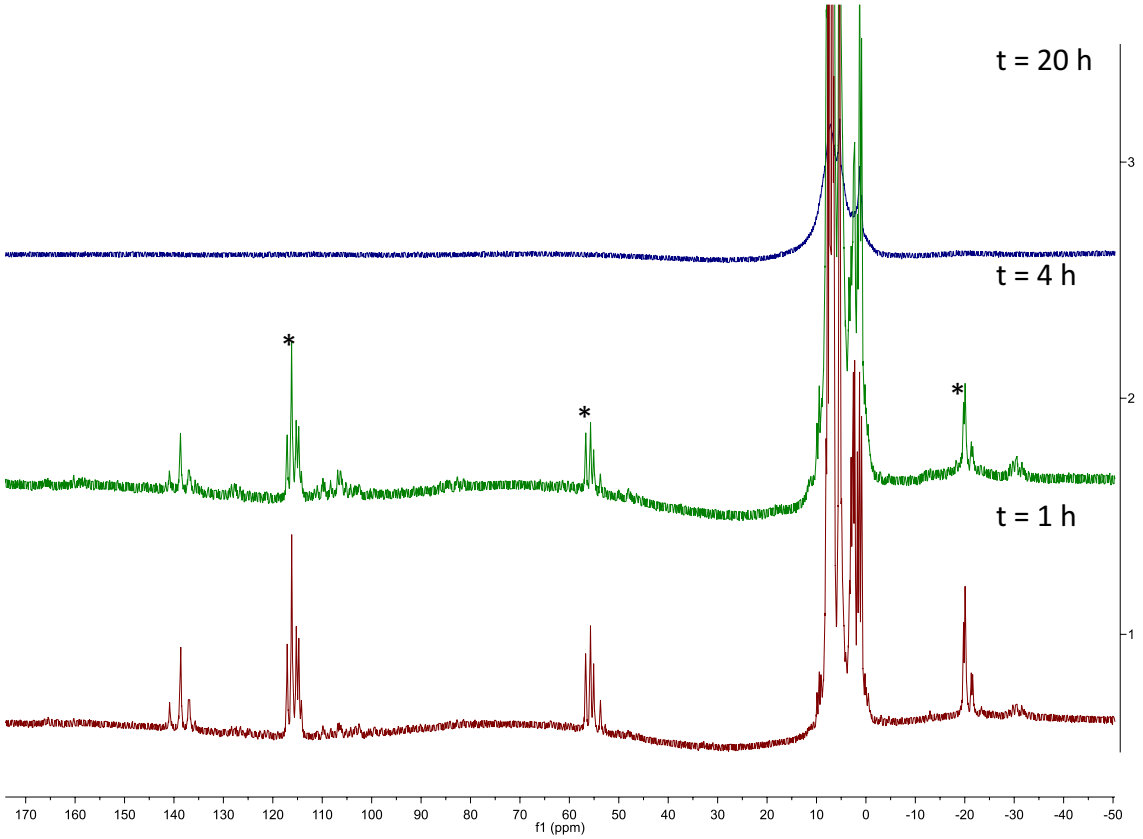

Figure A5.11. ^{1}H NMR spectra of the reaction of **5.1** with AgOTf in CD_2Cl_2. **Experimental Details:** A 20 mL scintillation vial equipped with a magnetic stir bar was charged with **5.1** (68.0 mg, 26 μmol) and CD_2Cl_2 (1.5 mL). To the vial was added AgOTf (48.0 mg, 0.19 mmol) which resulted in a color change from brown to brown-green and the deposition of a small amount of brown powder. After 30 min of stirring, the solution was transferred a J. Young NMR tube equipped with a Teflon rotoflow valve. The sample was allowed to stand at 25 °C and was monitored intermittently by ^{1}H NMR spectroscopy over the course of 20 h over which time the reaction mixture became dark green and more brown powder formed. (*) indicates a resonance assignable to **5.1**, all other resonances are thus far unassigned.

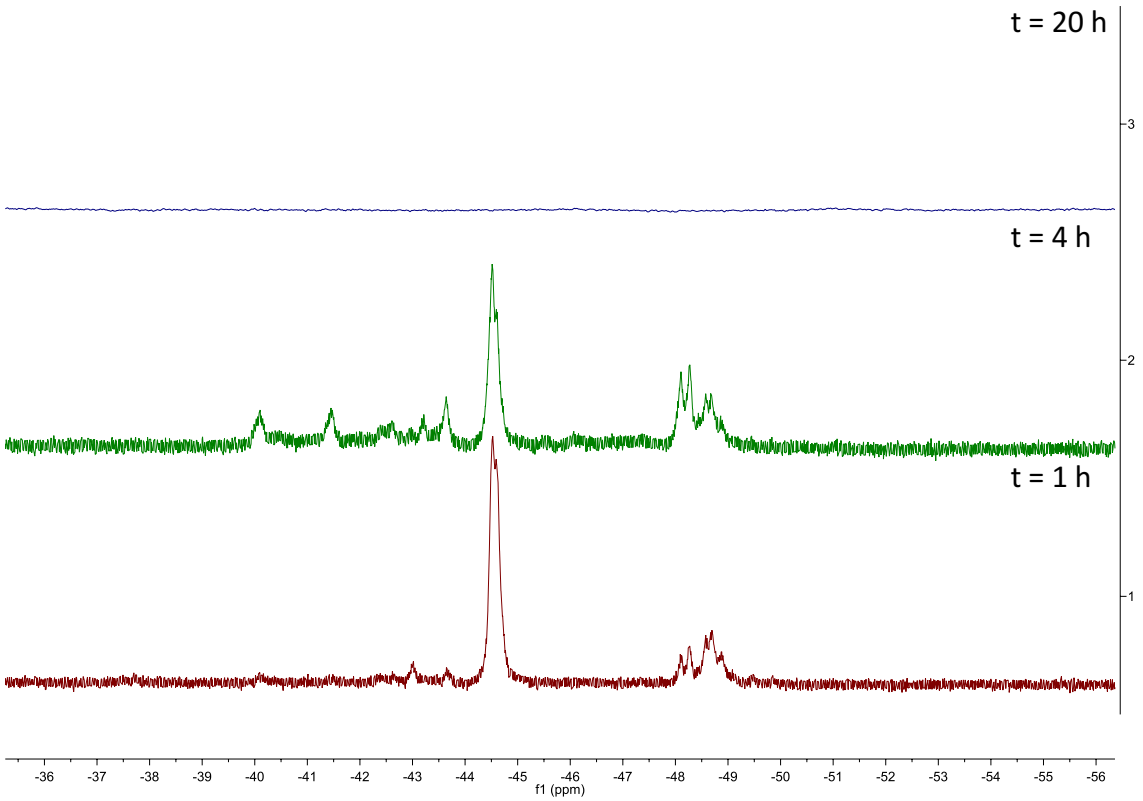

Figure A5.12. ^{19}F NMR spectra of the reaction of **5.1** with AgOTf in CD_2Cl_2.

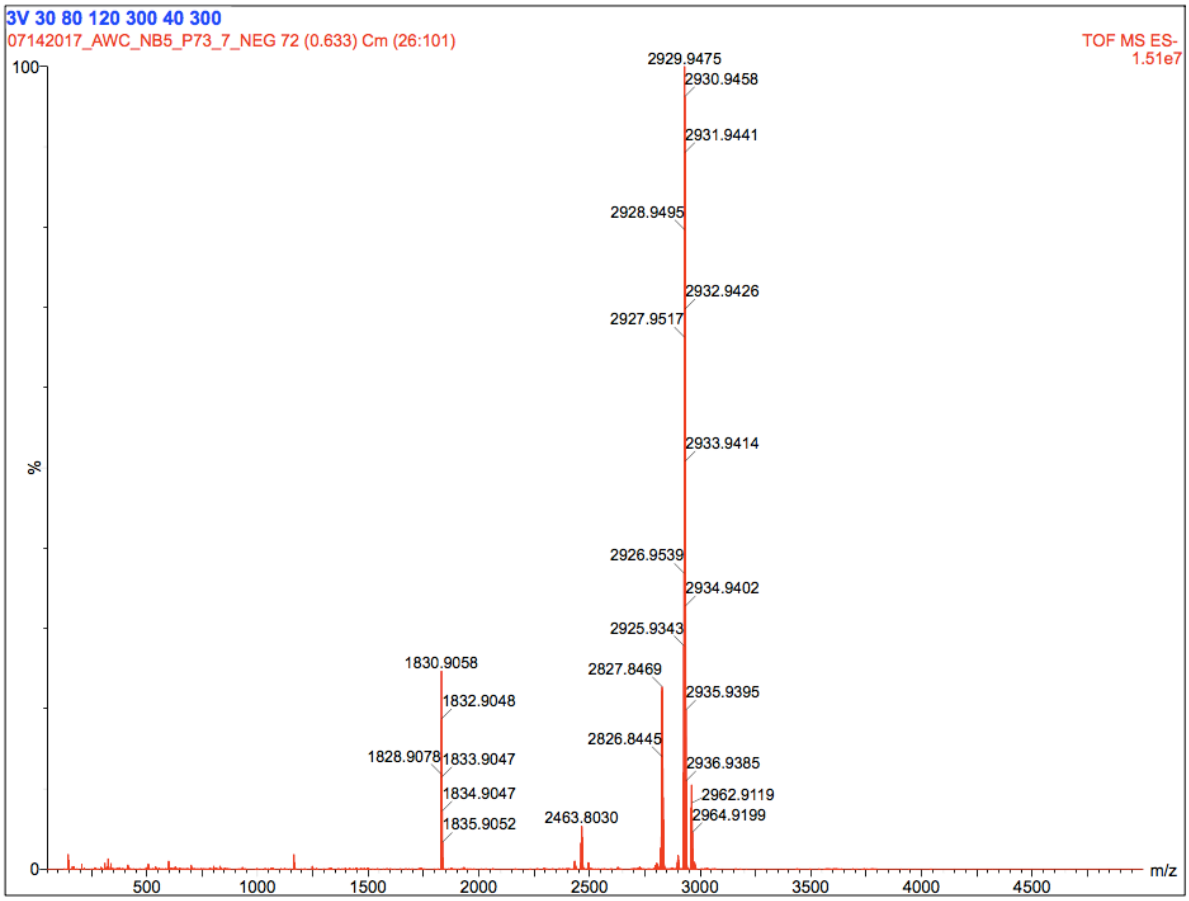

Figure A5.13. ESI-MS (negative mode) of $[Co_{10}(SR)_{16}Cl_4]$ (**5.1**).

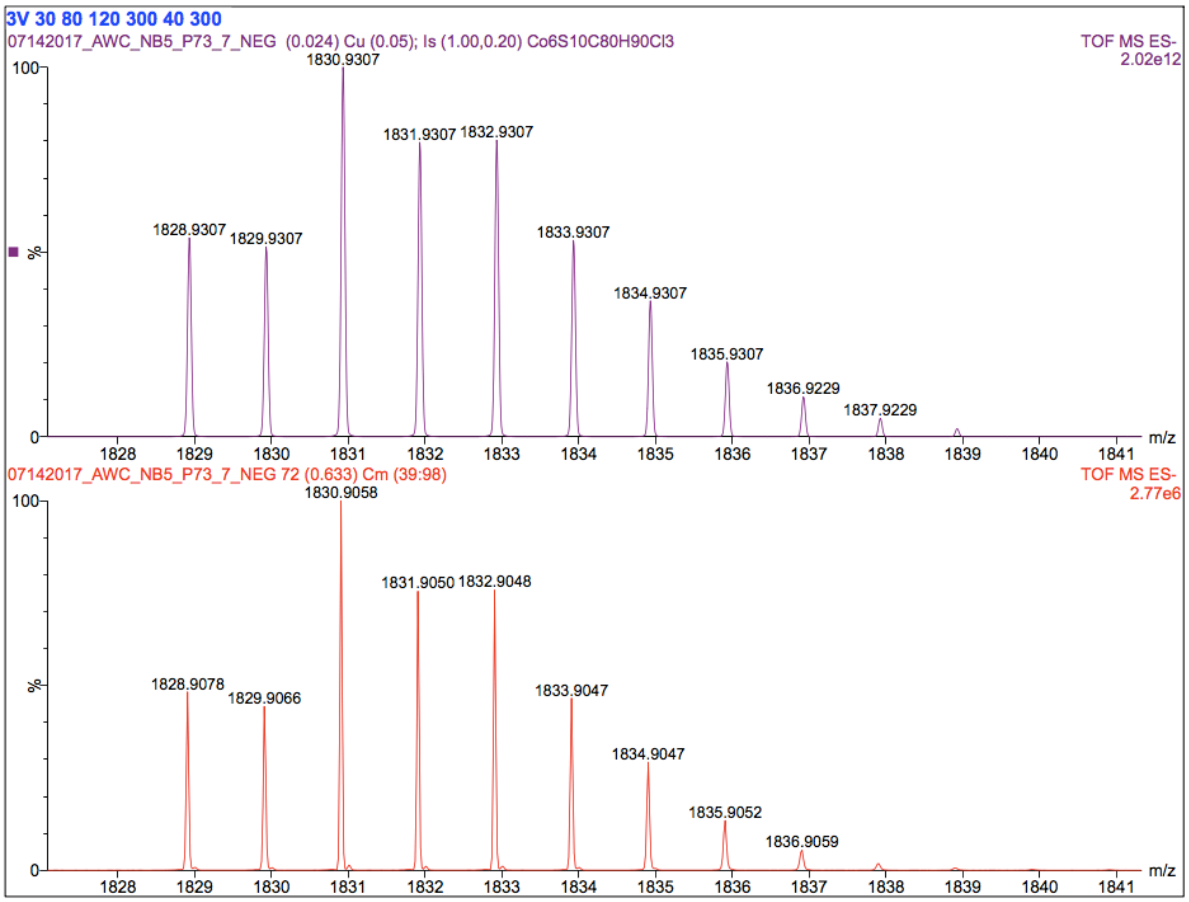

Figure A5.14. Partial ESI-MS (negative mode) of $[Co_{10}(SR)_{16}Cl_4]$ (**5.1**). The experimental (bottom) and calculated (top) peaks assignable to the $[Co_6(SR)_{10}Cl_3]^-$ ion are shown.

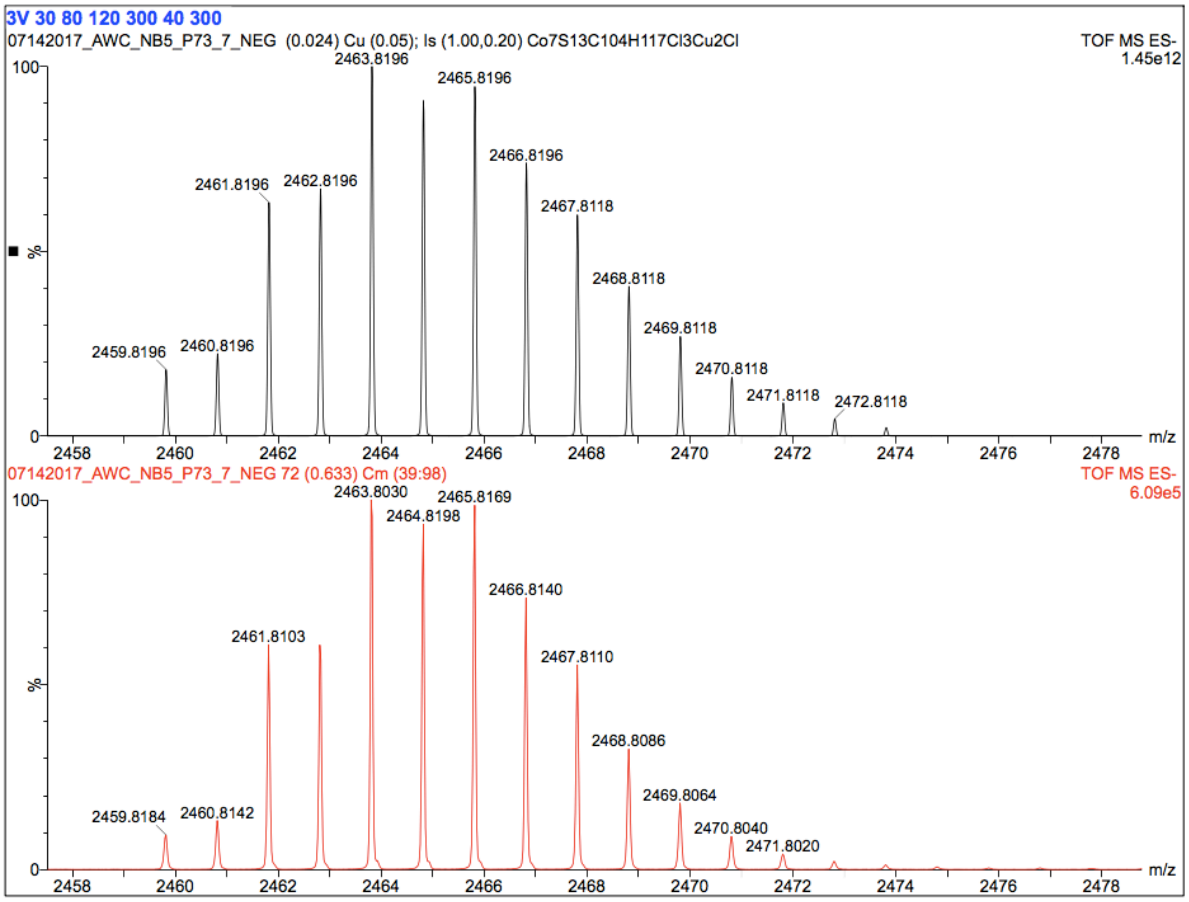

Figure A5.15. Partial ESI-MS (negative mode) of $[Co_{10}(SR)_{16}Cl_4]$ (**5.1**). The experimental (bottom) and calculated (top) peaks assignable to the $[Co_7(SR)_{13}Cl_4 + 2Cu]^-$ ion are shown.

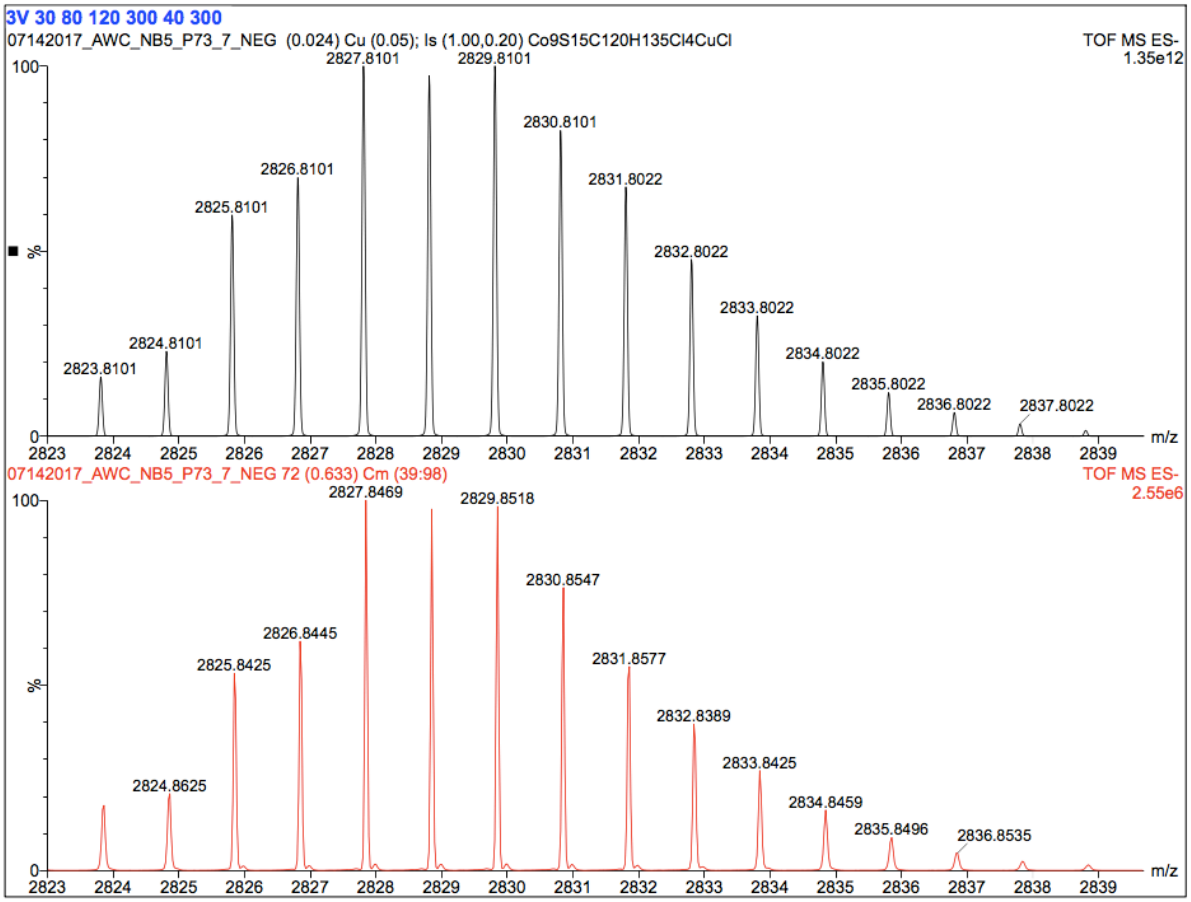

Figure A5.16. Partial ESI-MS (negative mode) of $[Co_{10}(SR)_{16}Cl_4]$ (**5.1**). The experimental (bottom) and calculated (top) peaks assignable to the $[Co_9(SR)_{15}Cl_4 + CuCl]^-$ ion are shown.

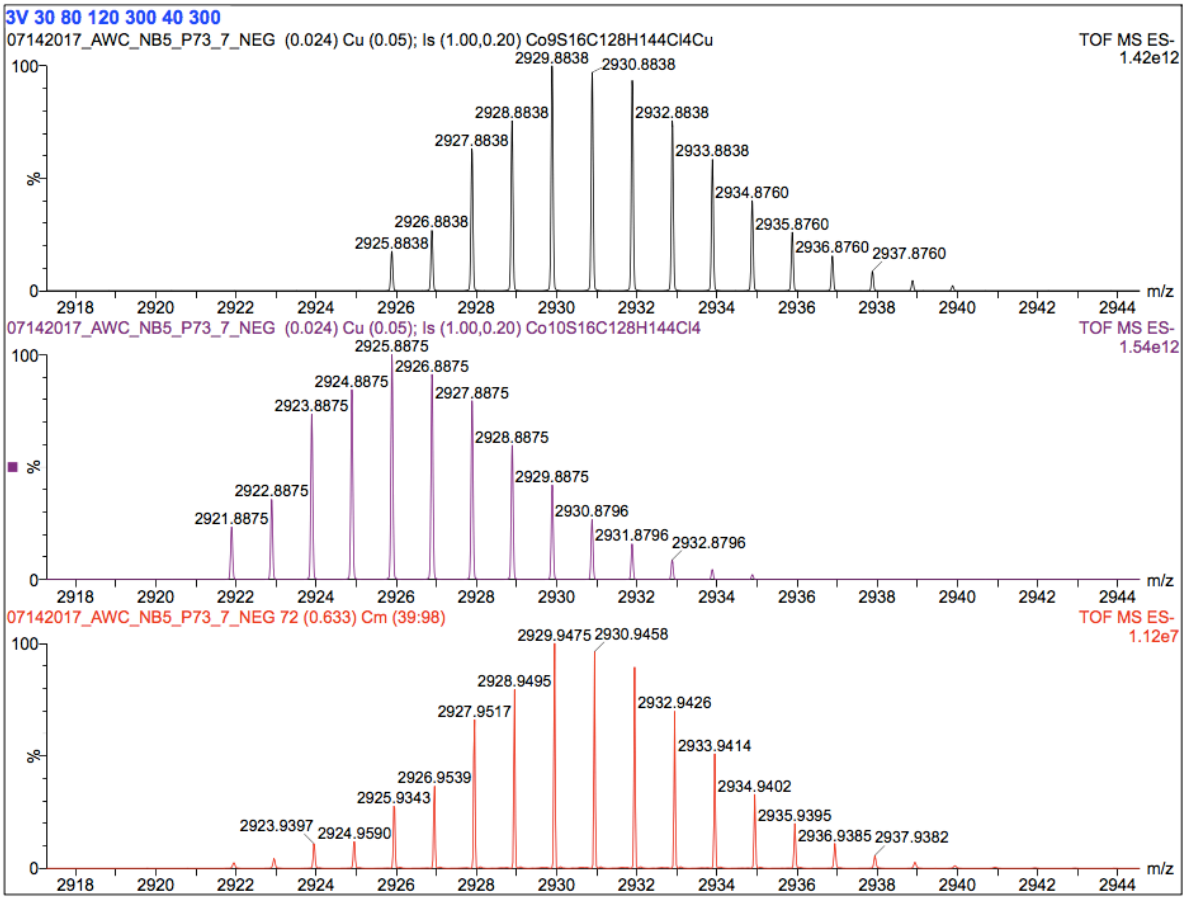

Figure A5.17. Partial ESI-MS (negative mode) of $[Co_{10}(SR)_{16}Cl_4]$ (**5.1**). The experimental (bottom) peak is assignable to the $[M]^-$ ion (calculated, middle) and the $[Co_9(SR)_{16}Cl_4 + Cu]^-$ ion (calculated, top).

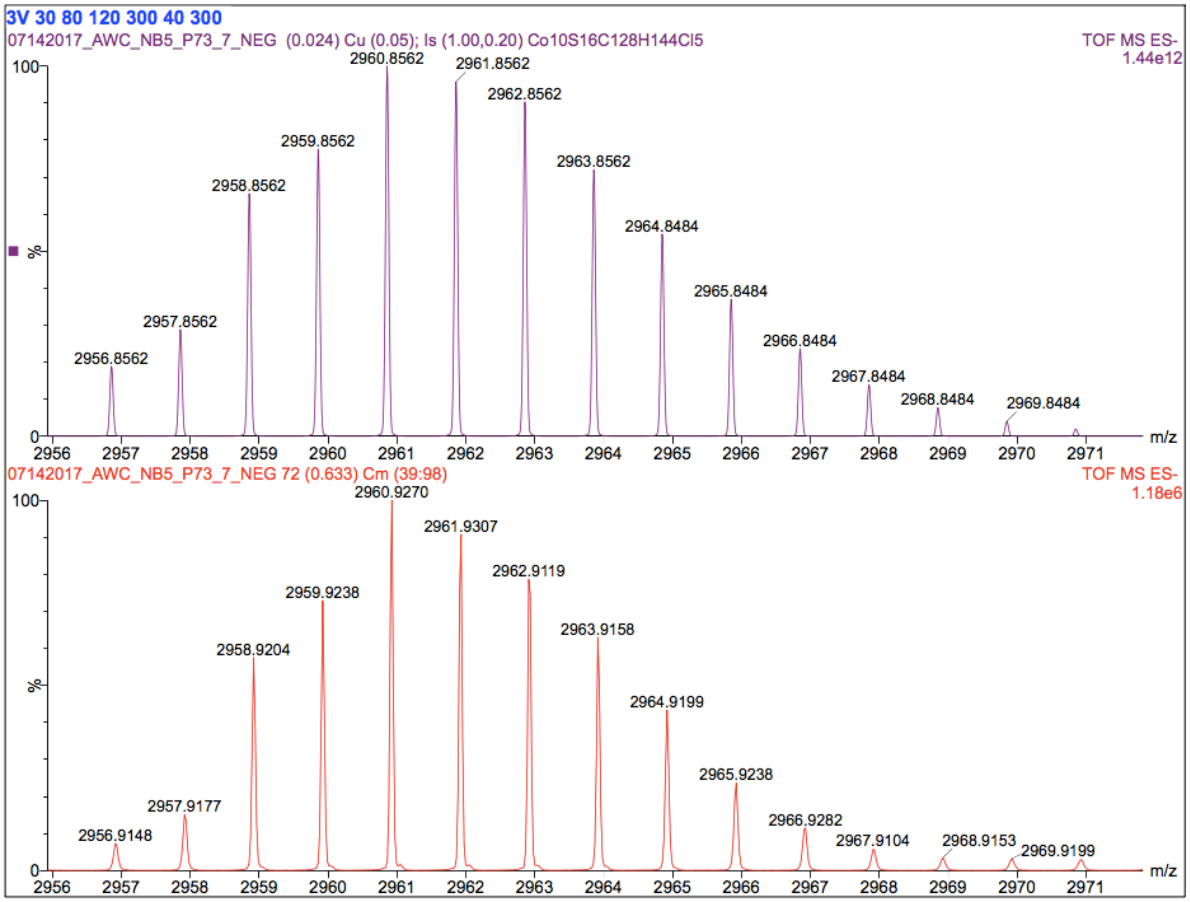

Figure A5.18. Partial ESI-MS (negative mode) of $[Co_{10}(SR)_{16}Cl_4]$ (**5.1**). The experimental (bottom) and calculated (top) peaks assignable to the $[M+Cl]^-$ ion are shown.

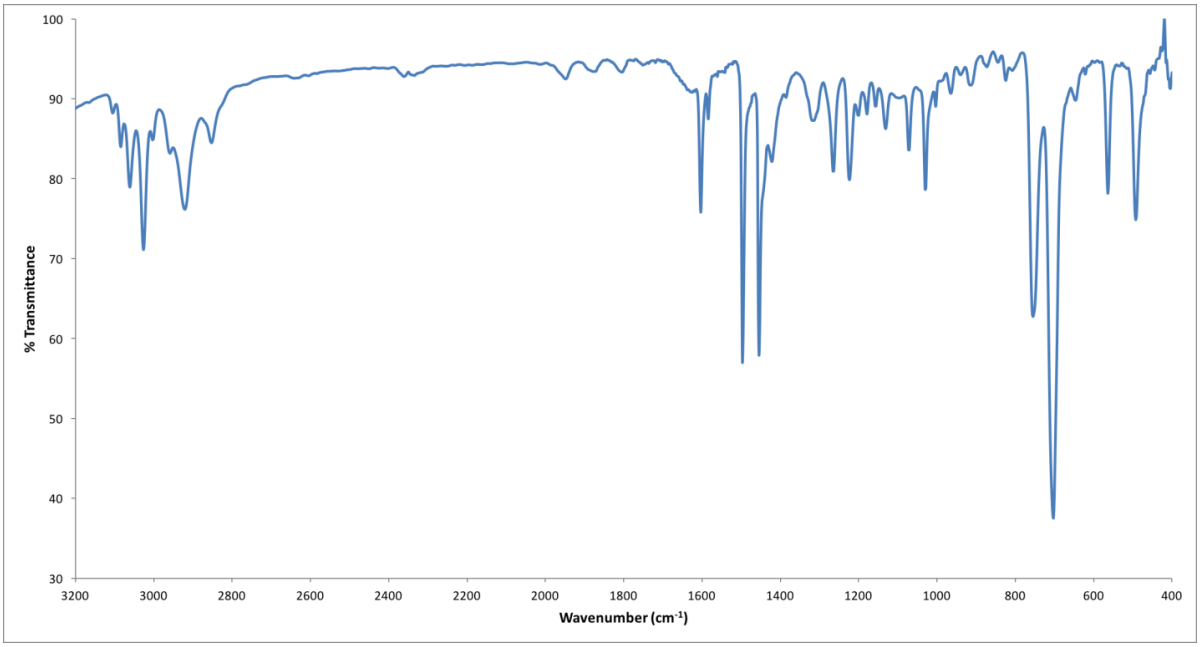

Figure A5.19. IR spectrum of **5.1**.

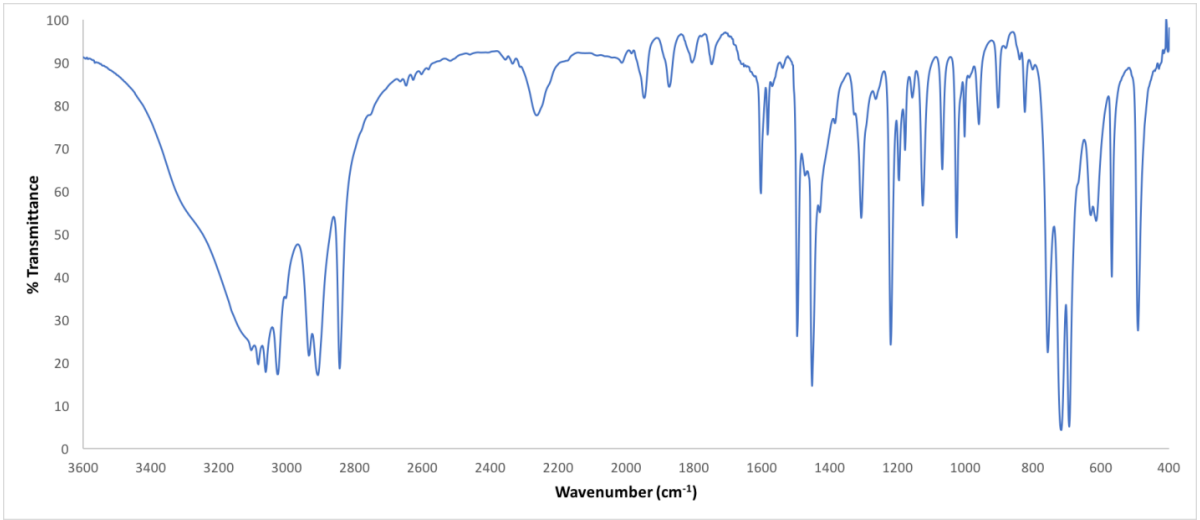

Figure A5.20. IR spectrum of NaSR.

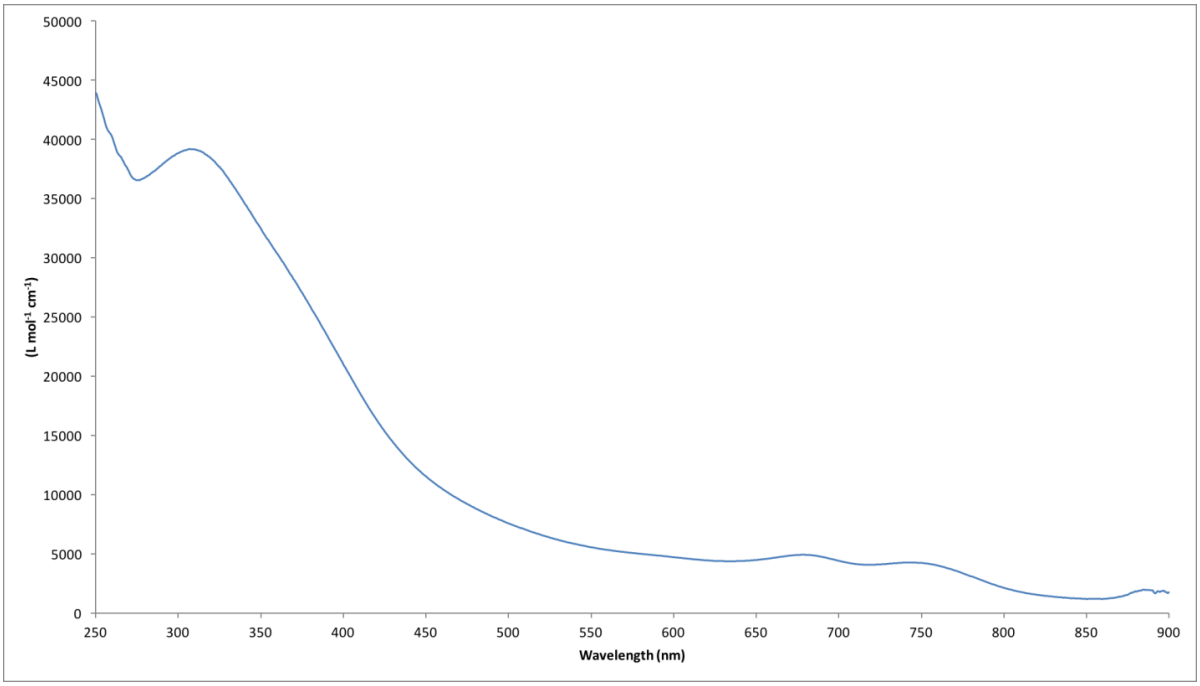

Figure A5.21. UV-Vis spectrum of complex **5.1** (37.6 μM) in CH_2Cl_2.

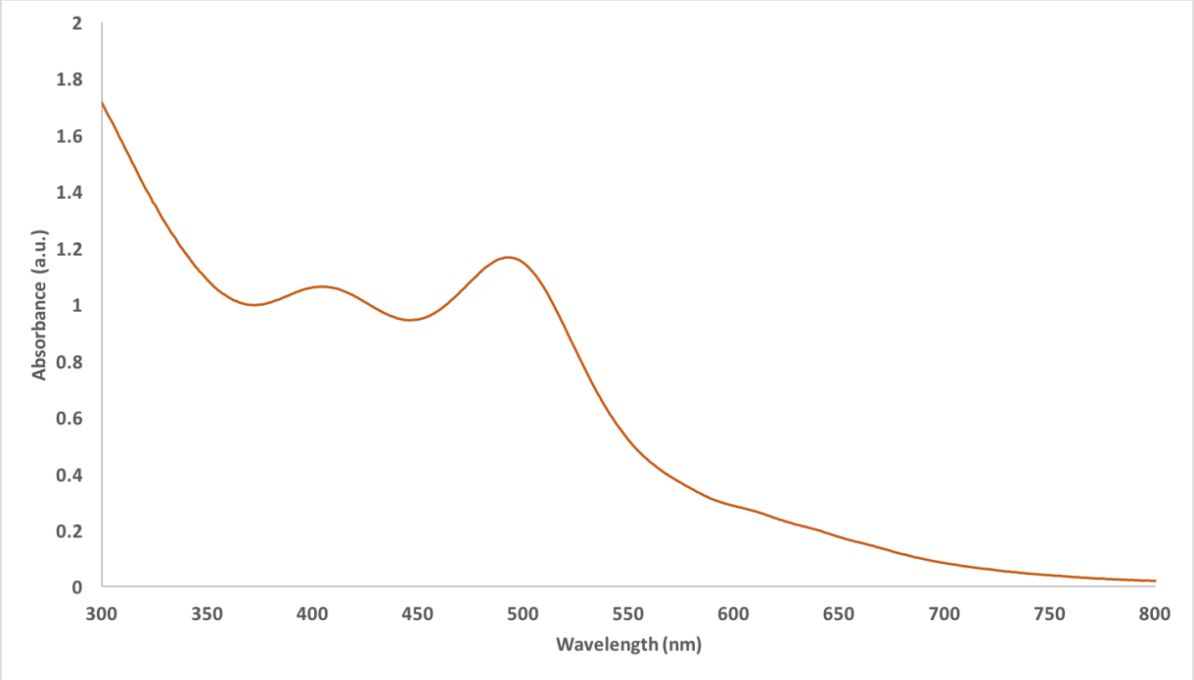

Figure A5.22. UV-Vis spectrum of complex **5.1** (37.6 μM) in CH_2Cl_2, after exposure to air for 20 h. **Experimental details:** A quartz UV-Vis cell equipped with an air-tight screw cap was charged with a CH_2Cl_2 solution (4 mL, 37.5 μM) of complex **5.1** and a spectrum was recorded. The screw cap was then removed and the solution was exposed to air for 5 min before the cell was resealed. The solution was allowed to stand at 25 °C for 20 h and another spectrum was recorded. During this time, the color of the solution slowly turned from deep brown to coral. UV-Vis / NIR (CH_2Cl_2, 25 °C): 404 nm, 493 nm, 611 nm.

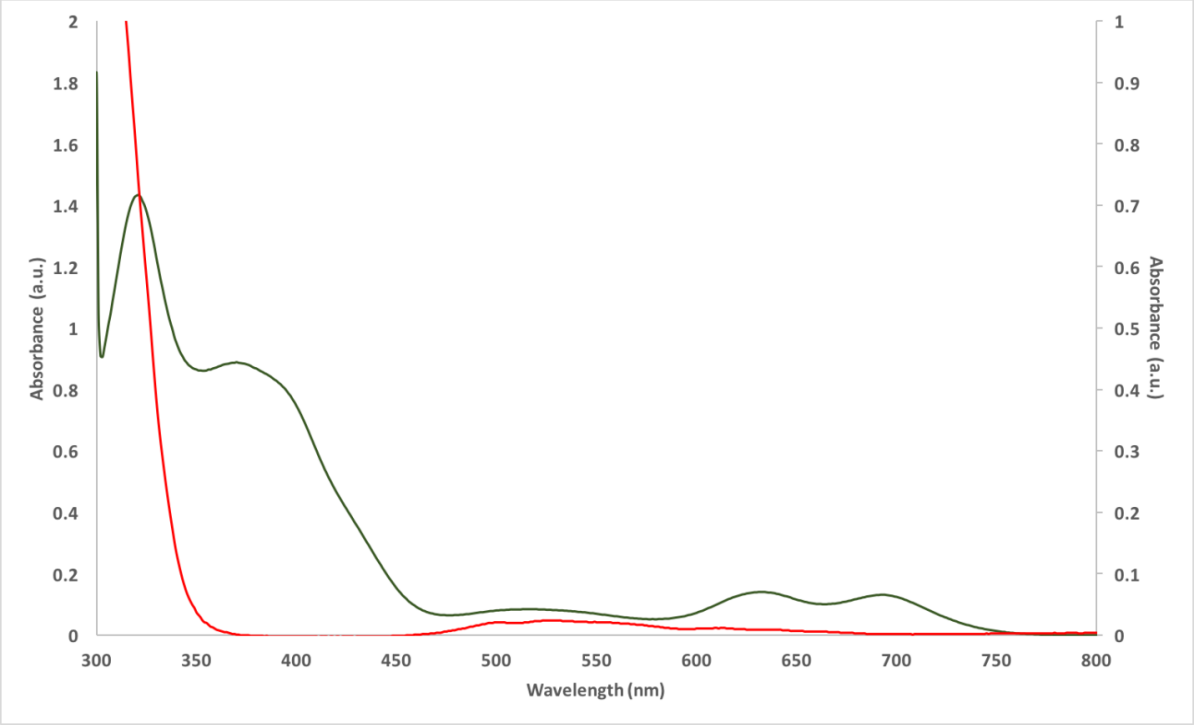

Figure A5.23. UV-Vis spectrum of complex **5.1** (green, left axis) and $CoCl_2 \cdot 1.5THF$ (red, right axis) in pyridine. Complex **5.1** undergoes a reaction with pyridine, which results in formation of a green solution, along with deposition of a brown solid. As a result, the concentration is an estimate. Complex **5.1**: UV-Vis / NIR (py, 37.6 µM 25 °C): 321 nm, 370 nm, 394 nm, 520 nm, 634 nm. 695 nm. $CoCl_2$: UV-Vis / NIR (py, 1.81 mM, 25 °C): 503, 542, 608 nm.

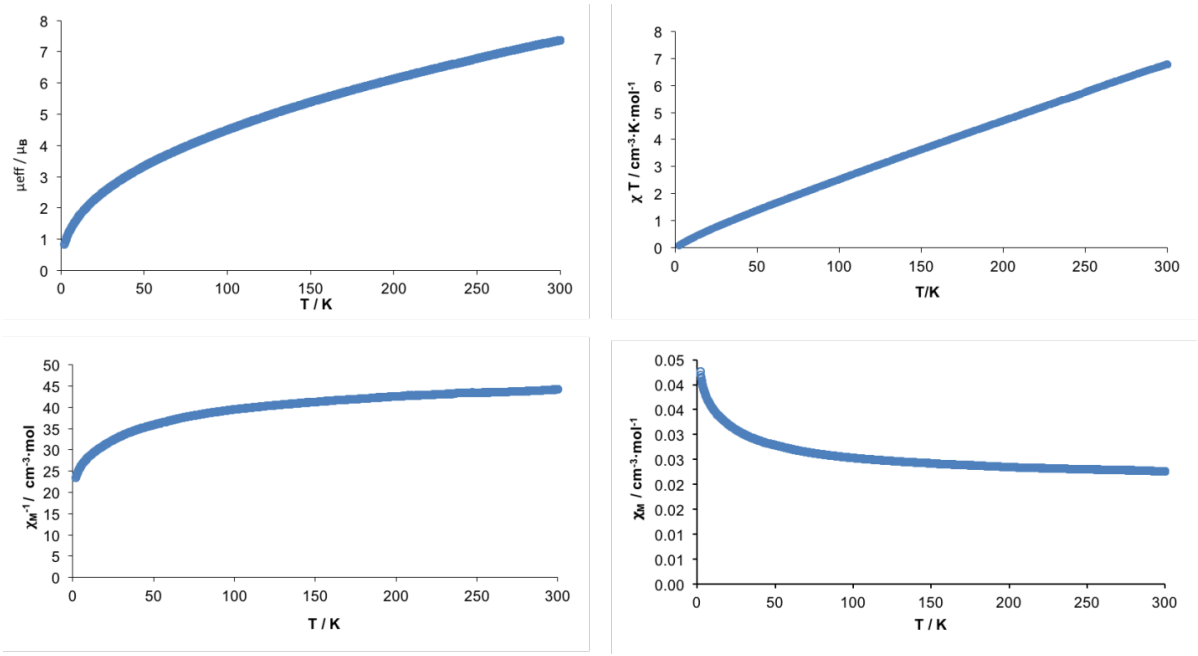

Figure A5.24. Temperature dependent, solid state magnetic susceptibility for $[Co_{10}(SR)_{16}Cl_4]$ (**5.1**). $\chi_{dia} = -1.937 \times 10^{-3}$ $cm^3 \cdot mol^{-1}$, mass = 11.8 mg, M = 2926.69 g/mol.

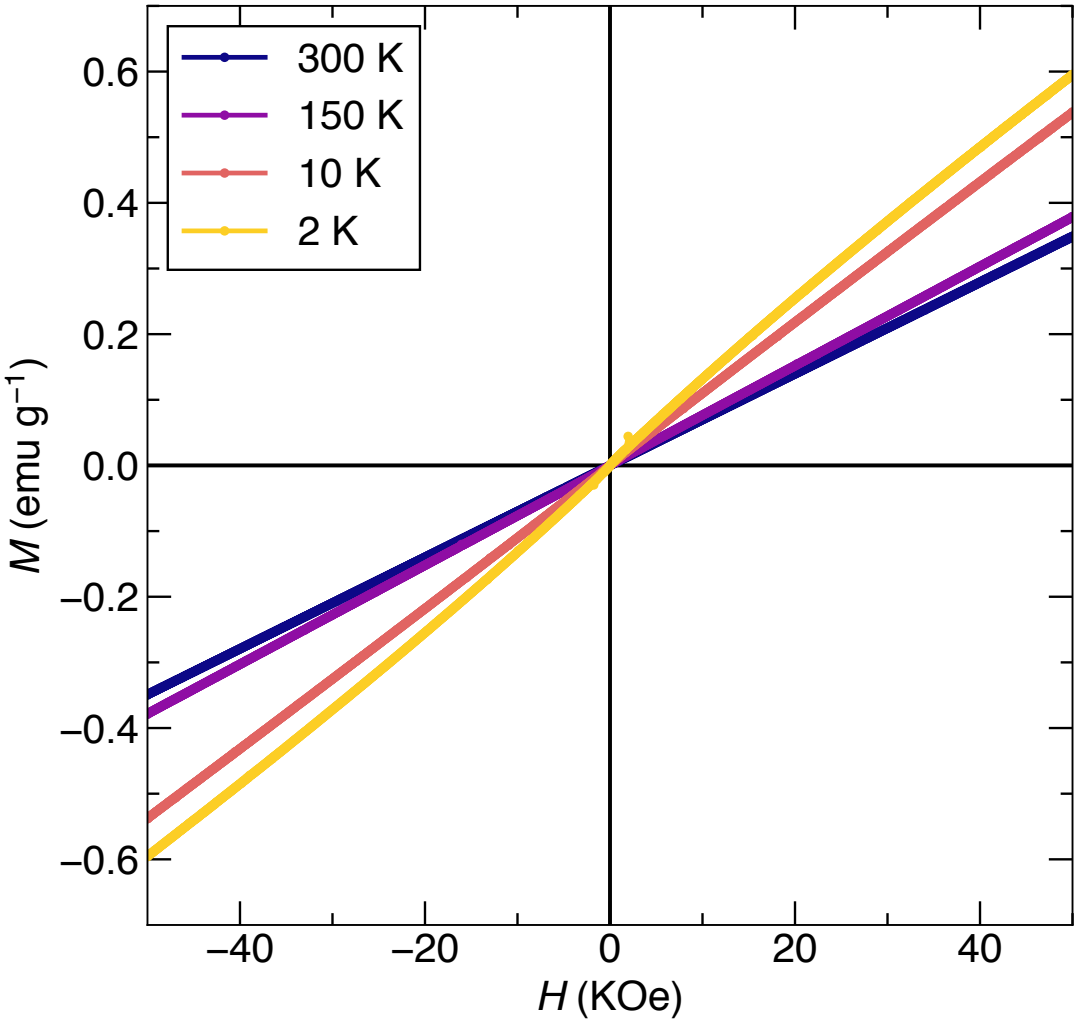

Figure A5.25. Temperature dependent, solid state magnetic susceptibility for $[Co_{10}(SR)_{16}Cl_4]$ (**5.1**) showing magnetization vs. applied field at constant temperature.

5.6 References

(1) Templeton, A. C.; Wuelfing, W. P.; Murray, R. W., Monolayer-Protected Cluster Molecules. *Acc. Chem. Res.* **2000**, *33*, 27-36.

(2) Jin, R., Quantum sized, thiolate-protected gold nanoclusters. *Nanoscale* **2010**, *2*, 343-362.

(3) Li, G.; Jin, R., Atomically Precise Gold Nanoclusters as New Model Catalysts. *Acc. Chem. Res.* **2013**, *46*, 1749-1758.

(4) Kim, B. H.; Hackett, M. J.; Park, J.; Hyeon, T., Synthesis, Characterization, and Application of Ultrasmall Nanoparticles. *Chem. Mater.* **2014**, *26*, 59-71.

(5) Jin, R.; Zeng, C.; Zhou, M.; Chen, Y., Atomically Precise Colloidal Metal Nanoclusters and Nanoparticles: Fundamentals and Opportunities. *Chem. Rev.* **2016**, *116*, 10346-10413.

(6) Luo, Z.; Castleman, A. W.; Khanna, S. N., Reactivity of Metal Clusters. *Chem. Rev.* **2016**, *116*, 14456-14492.

(7) Edwards, A. J.; Dhayal, R. S.; Liao, P.-K.; Liao, J.-H.; Chiang, M.-H.; Piltz, R. O.; Kahlal, S.; Saillard, J.-Y.; Liu, C. W., Chinese Puzzle Molecule: A 15 Hydride, 28 Copper Atom Nanoball. *Angew. Chem., Int. Ed.* **2014**, *53*, 7214-7218.

(8) Freitag, K.; Banh, H.; Gemel, C.; Seidel, R. W.; Kahlal, S.; Saillard, J.-Y.; Fischer, R. A., Molecular brass: Cu_4Zn_4, a ligand protected superatom cluster. *Chem. Commun.* **2014**, *50*, 8681-8684.

(9) Ganesamoorthy, C.; Weßing, J.; Kroll, C.; Seidel, R. W.; Gemel, C.; Fischer, R. A., The Intermetalloid Cluster $[(Cp^*AlCu)_6H_4]$, Embedding a Cu_6 Core Inside an Octahedral Al_6 Shell: Molecular Models of Hume–Rothery Nanophases. *Angew. Chem., Int. Ed.* **2014**, *53*, 7943-7947.

(10) Nguyen, T.-A. D.; Jones, Z. R.; Goldsmith, B. R.; Buratto, W. R.; Wu, G.; Scott, S. L.; Hayton, T. W., A Cu_{25} Nanocluster with Partial Cu(0) Character. *J. Am. Chem. Soc.* **2015**, *137*, 13319-13324.

(11) Chakrahari, K. K.; Liao, J.-H.; Kahlal, S.; Liu, Y.-C.; Chiang, M.-H.; Saillard, J.-Y.; Liu, C. W., $[Cu_{13}\{S_2CN^nBu_2\}_6(acetylide)_4]^+$: A Two-Electron Superatom. *Angew. Chem., Int. Ed.* **2016**, *55*, 14704-14708.

(12) Nguyen, T.-A. D.; Jones, Z. R.; Leto, D. F.; Wu, G.; Scott, S. L.; Hayton, T. W., Ligand-Exchange-Induced Growth of an Atomically Precise Cu_{29} Nanocluster from a Smaller Cluster. *Chem. Mater.* **2016**, *28*, 8385-8390.

(13) Cook, A. W.; Jones, Z. R.; Wu, G.; Scott, S. L.; Hayton, T. W., An Organometallic Cu_{20} Nanocluster: Synthesis, Characterization, Immobilization on Silica, and "Click" Chemistry. *J. Am. Chem. Soc.* **2018**, *140*, 394-400.

(14) Lei, Z.; Wan, X.-K.; Yuan, S.-F.; Wang, J.-Q.; Wang, Q.-M., Alkynyl-protected gold and gold-silver nanoclusters. *Dalton Trans.* **2017**, *46*, 3427-3434.

(15) Qu, M.; Li, H.; Xie, L.-H.; Yan, S.-T.; Li, J.-R.; Wang, J.-H.; Wei, C.-Y.; Wu, Y.-W.; Zhang, X.-M., Bidentate Phosphine-Assisted Synthesis of an All-Alkynyl-Protected Ag_{74} Nanocluster. *J. Am. Chem. Soc.* **2017**, 12346-12349.

(16) Yuan, S.-F.; Li, P.; Tang, Q.; Wan, X.-K.; Nan, Z.-A.; Jiang, D.-e.; Wang, Q.-M., Alkynyl-protected silver nanoclusters featuring an anticuboctahedral kernel. *Nanoscale* **2017**, 11405-11409.

(17) Wan, X.-K.; Cheng, X.-L.; Tang, Q.; Han, Y.-Z.; Hu, G.; Jiang, D.-e.; Wang, Q.-M., Atomically Precise Bimetallic $Au_{19}Cu_{30}$ Nanocluster with an Icosidodecahedral Cu_{30} Shell and an Alkynyl–Cu Interface. *J. Am. Chem. Soc.* **2017**, 9451-9454.
(18) Mednikov, E. G.; Jewell, M. C.; Dahl, L. F., Nanosized $(\mu_{12}\text{-Pt})Pd_{164-x}Pt_x(CO)_{72}(PPh_3)_{20}$ ($x \approx 7$) Containing Pt-Centered Four-Shell 165-Atom Pd−Pt Core with Unprecedented Intershell Bridging Carbonyl Ligands: Comparative Analysis of Icosahedral Shell-Growth Patterns with Geometrically Related $Pd_{145}(CO)_x(PEt_3)_{30}$ ($x \approx 60$) Containing Capped Three-Shell Pd_{145} Core. *J. Am. Chem. Soc.* **2007**, *129*, 11619-11630.
(19) Erickson, J. D.; Mednikov, E. G.; Ivanov, S. A.; Dahl, L. F., Isolation and Structural Characterization of a Mackay 55-Metal-Atom Two-Shell Icosahedron of Pseudo-Ih Symmetry, $Pd_{55}L_{12}(\mu_3\text{-CO})_{20}$ (L = PR_3, R = Isopropyl): Comparative Analysis with Interior Two-Shell Icosahedral Geometries in Capped Three-Shell Pd_{145}, Pt-Centered Four-Shell Pd–Pt M_{165}, and Four-Shell Au_{133} Nanoclusters. *J. Am. Chem. Soc.* **2016**, *138*, 1502-1505.
(20) Banh, H.; Dilchert, K.; Schulz, C.; Gemel, C.; Seidel, R. W.; Gautier, R.; Kahlal, S.; Saillard, J. Y.; Fischer, R. A., Atom-Precise Organometallic Zinc Clusters. *Angew. Chem., Int. Ed.* **2016**, *55*, 3285-3289.
(21) Ecker, A.; Weckert, E.; Schnöckel, H., Synthesis and structural characterization of an Al_{77} cluster. *Nature* **1997**, *387*, 379-381.
(22) Huber, M.; Schnepf, A.; Anson, C. E.; Schnöckel, H., $Si@Al_{56}[N(2,6\text{-}{}^{i}Pr_2C_6H_3)SiMe_3]_{12}$: The Largest Neutral Metalloid Aluminum Cluster, a Molecular Model for a Silicon-Poor Aluminum–Silicon Alloy? *Angew. Chem., Int. Ed.* **2008**, *47*, 8201-8206.
(23) Schnockel, H., Formation, structure and bonding of metalloid Al and Ga clusters. A challenge for chemical efforts in nanosciences. *Dalton Trans.* **2008**, 4344-4362.
(24) Henke, P.; Trapp, N.; Anson, C. E.; Schnöckel, H., $Al_{12}K_8[OC(CH_3)_3]_{18}$: A Wade, Zintl, or Metalloid Cluster, or a Hybrid of All Three? *Angew. Chem., Int. Ed.* **2010**, *49*, 3146-3150.
(25) Wolf, R.; Uhl, W., Main-Group-Metal Clusters Stabilized by N-Heterocyclic Carbenes. *Angew. Chem., Int. Ed.* **2009**, *48*, 6774-6776.
(26) Schnepf, A., Metalloid group 14 cluster compounds: An introduction and perspectives to this novel group of cluster compounds. *Chem. Soc. Rev.* **2007**, *36*, 745-758.
(27) Schenk, C.; Schnepf, A., $Ge_{14}[Ge(SiMe_3)_3]_5Li_3(THF)_6$: the largest metalloid cluster compound of germanium: on the way to fullerene-like compounds? *Chem. Commun.* **2008**, 4643-4645.
(28) Scharfe, S.; Kraus, F.; Stegmaier, S.; Schier, A.; Fässler, T. F., Zintl Ions, Cage Compounds, and Intermetalloid Clusters of Group 14 and Group 15 Elements. *Angew. Chem., Int. Ed.* **2011**, *50*, 3630-3670.
(29) Schenk, C.; Kracke, A.; Fink, K.; Kubas, A.; Klopper, W.; Neumaier, M.; Schnöckel, H.; Schnepf, A., The Formal Combination of Three Singlet Biradicaloid Entities to a Singlet Hexaradicaloid Metalloid $Ge_{14}[Si(SiMe_3)_3]_5[Li(THF)_2]_3$ Cluster. *J. Am. Chem. Soc.* **2011**, *133*, 2518-2524.

(30) Kysliak, O.; Schrenk, C.; Schnepf, A., The Largest Metalloid Group 14 Cluster, $Ge_{18}[Si(SiMe_3)_3]_6$: An Intermediate on the Way to Elemental Germanium. *Angew. Chem., Int. Ed.* **2016**, *55*, 3216-3219.
(31) Protchenko, A. V.; Dange, D.; Blake, M. P.; Schwarz, A. D.; Jones, C.; Mountford, P.; Aldridge, S., Oxidative Bond Formation and Reductive Bond Cleavage at Main Group Metal Centers: Reactivity of Five-Valence-Electron MX_2 Radicals. *J. Am. Chem. Soc.* **2014**, *136*, 10902-10905.
(32) Aldridge, S.; Protchenko, A.; Urbano, J.; Abdalla, J.; Campos, J.; Vidovic, D.; Schwarz, A.; Blake, M.; Mountford, P.; Jones, C., Electronic Delocalization in Two and Three Dimensions: Differential Aggregation in Indium 'Metalloid' Clusters. *Angew. Chem., Int. Ed.* **2017**, 15098-15102.
(33) Brynda, M.; Herber, R.; Hitchcock, P. B.; Lappert, M. F.; Nowik, I.; Power, P. P.; Protchenko, A. V.; Růžička, A.; Steiner, J., Higher-Nuclearity Group 14 Metalloid Clusters: $[Sn_9\{Sn(NRR')\}_6]$. *Angew. Chem., Int. Ed.* **2006**, *45*, 4333-4337.
(34) Schrenk, C.; Winter, F.; Pöttgen, R.; Schnepf, A., $\{Sn_9[Si(SiMe_3)_3]_2\}^{2-}$: A Metalloid Tin Cluster Compound With a Sn_9 Core of Oxidation State Zero. *Inorg. Chem.* **2012**, *51*, 8583-8588.
(35) Schrenk, C.; Winter, F.; Pöttgen, R.; Schnepf, A., $\{Sn_{10}[Si(SiMe_3)_3]_4\}^{2-}$: A Highly Reactive Metalloid Tin Cluster with an Open Ligand Shell. *Chem. – Eur. J.* **2015**, *21*, 2992-2997.
(36) Wiederkehr, J.; Wolper, C.; Schulz, S., Synthesis and solid state structure of a metalloid tin cluster $[Sn_{10}(trip_8)]$. *Chem. Commun.* **2016**, *52*, 12282-12285.
(37) Schätz, A.; Reiser, O.; Stark, W. J., Nanoparticles as Semi-Heterogeneous Catalyst Supports. *Chem. – Eur. J.* **2010**, *16*, 8950-8967.
(38) Colombo, M.; Carregal-Romero, S.; Casula, M. F.; Gutierrez, L.; Morales, M. P.; Bohm, I. B.; Heverhagen, J. T.; Prosperi, D.; Parak, W. J., Biological applications of magnetic nanoparticles. *Chem. Soc. Rev.* **2012**, *41*, 4306-4334.
(39) Tejada, J.; Chudnovsky, E. M.; Barco, E. d.; Hernandez, J. M.; Spiller, T. P., Magnetic qubits as hardware for quantum computers. *Nanotechnology* **2001**, *12*, 181.
(40) Wu, L.; Li, Q.; Wu, C. H.; Zhu, H.; Mendoza-Garcia, A.; Shen, B.; Guo, J.; Sun, S., Stable Cobalt Nanoparticles and Their Monolayer Array as an Efficient Electrocatalyst for Oxygen Evolution Reaction. *J. Am. Chem. Soc.* **2015**, *137*, 7071-7074.
(41) Osuna, J.; de Caro, D.; Amiens, C.; Chaudret, B.; Snoeck, E.; Respaud, M.; Broto, J.-M.; Fert, A., Synthesis, Characterization, and Magnetic Properties of Cobalt Nanoparticles from an Organometallic Precursor. *J. Chem. Phys.* **1996**, *100*, 14571-14574.
(42) Verelst, M.; Ely, T. O.; Amiens, C.; Snoeck, E.; Lecante, P.; Mosset, A.; Respaud, M.; Broto, J. M.; Chaudret, B., Synthesis and Characterization of CoO, Co_3O_4, and Mixed Co/CoO Nanoparticules. *Chem. Mater.* **1999**, *11*, 2702-2708.
(43) Puntes, V. F.; Krishnan, K. M.; Alivisatos, A. P., Colloidal Nanocrystal Shape and Size Control: The Case of Cobalt. *Science* **2001**, *291*, 2115-2117.
(44) Keng, P. Y.; Shim, I.; Korth, B. D.; Douglas, J. F.; Pyun, J., Synthesis and Self-Assembly of Polymer-Coated Ferromagnetic Nanoparticles. *ACS Nano* **2007**, *1*, 279-292.

(45) Bao, Y.; Calderon, H.; Krishnan, K. M., Synthesis and Characterization of Magnetic-Optical Co−Au Core−Shell Nanoparticles. *J. Phys. Chem. C* **2007**, *111*, 1941-1944.
(46) Song, Y.; Ding, J.; Wang, Y., Shell-Dependent Evolution of Optical and Magnetic Properties of Co@Au Core–Shell Nanoparticles. *J. Phys. Chem. C* **2012**, *116*, 11343-11350.
(47) Lu, A.-H.; Li, W.-C.; Matoussevitch, N.; Spliethoff, B.; Bonnemann, H.; Schuth, F., Highly stable carbon-protected cobalt nanoparticles and graphite shells. *Chem. Commun.* **2005**, 98-100.
(48) Grass, R. N.; Athanassiou, E. K.; Stark, W. J., Covalently Functionalized Cobalt Nanoparticles as a Platform for Magnetic Separations in Organic Synthesis. *Angew. Chem., Int. Ed.* **2007**, *46*, 4909-4912.
(49) Kobayashi, Y.; Horie, M.; Konno, M.; Rodríguez-González, B.; Liz-Marzán, L. M., Preparation and Properties of Silica-Coated Cobalt Nanoparticles. *J. Phys. Chem. B* **2003**, *107*, 7420-7425.
(50) Salgueirino-Maceira, V.; Correa-Duarte, M. A., Cobalt and silica based core-shell structured nanospheres. *J. Mater. Chem.* **2006**, *16*, 3593-3597.
(51) Pollitt, S.; Pittenauer, E.; Rameshan, C.; Schachinger, T.; Safonova, O. V.; Truttmann, V.; Bera, A.; Allmaier, G.; Barrabés, N.; Rupprechter, G., Synthesis and Properties of Monolayer-Protected $Co_x(SC_2H_4Ph)_m$ Nanoclusters. *J. Phys. Chem. C* **2017**, *121*, 10948-10956.
(52) Goulet, P. J. G.; Lennox, R. B., New Insights into Brust−Schiffrin Metal Nanoparticle Synthesis. *J. Am. Chem. Soc.* **2010**, *132*, 9582-9584.
(53) Fenske, D.; Meyer, J.; Merzweiler, K., Zur Reaktion von $PhSSiMe_3$ mit $[CoCl_2(PPh_3)_2]$ und $(NBu_4)[CoCl_3(PPh_3)]$. Die Kristallstrukturen von $(NBu_4)_2[Co_4(SPh)_6Cl_4]$, $[Co_4(SPh)_6Cl_2(POPh_3)(PPh_3)]$ und $(NBu_4)[Mn_2(SPh)_3(CO)_6]$. *Z. Naturforsch* **1987**, *42b*, 1207–1211.
(54) Dance, I. G., Synthesis, Crystal Structure, and Properties of the Hexa(μ-benzenethiolato)tetra(benzenethiolatocobaltate(II)) Dianion, the Prototype Cobalt(II)-Thiolate Molecular Cluster. *J. Am. Chem. Soc.* **1979**, *101*, 6264-6273.
(55) Feng, P.; Bu, X.; Zheng, N., The Interface Chemistry between Chalcogenide Clusters and Open Framework Chalcogenides. *Acc. Chem. Res.* **2005**, *38*, 293-303.
(56) Levchenko, T. I.; Huang, Y.; Corrigan, J. F., Large Metal Chalcogenide Clusters and Their Ordered Superstructures via Solvothermal and Ionothermal Syntheses. In *Clusters – Contemporary Insight in Structure and Bonding*, Dehnen, S., Ed. Springer International Publishing: Cham, 2017; pp 269-319.
(57) Strickler, P., The structure of a novel polynuclear complex related to the sphalerite lattice. *J. Chem. Soc., Chem. Comm.* **1969**, 655b-656.
(58) Bürgi, H.-B., Stereochemistry of Polynuclear Cadmium(II) Thioglycolates: Crystal structure of cadmium(II) bisthioglycolate. *Helv. Chim. Acta* **1974**, *57*, 513-519.
(59) Lacelle, S.; Stevens, W. C.; Kurtz, D. M.; Richardson, J. W.; Jacobson, R. A., Crystal and Molecular Structure of $[Cd_{10}(SCH_2CH_2OH)_{16}](ClO_4)_4 \cdot 8H_2O$. Correlations with Cadmium-113 NMR Spectra of the Solid and Implications for Cadmium-Thiolate Ligation in Proteins. *Inorg. Chem.* **1984**, *23*, 930-935.
(60) Dance, I. G.; Choy, A.; Scudder, M. L., Syntheses, Properties, and Molecular and Crystal Structures of $(Me_2N)_4[E_4M_{10}(SPh)_{16}]$ (E = Sulfur or Selenium; M = Zinc or

Cadmium): Molecular Supertetrahedral Fragments of the Cubic Metal Chalcogenide Lattice. *J. Am. Chem. Soc.* **1984**, *106*, 6285-6295.
(61) Lisnard, L.; Tuna, F.; Candini, A.; Affronte, M.; Winpenny, R. E. P.; McInnes, E. J. L., Supertetrahedral and Bi-supertetrahedral Cages: Synthesis, Structures, and Magnetic Properties of Deca- and Enneadecametallic Cobalt(II) Clusters. *Angew. Chem., Int. Ed.* **2008**, *47*, 9695-9699.
(62) Shaw, R.; Tidmarsh, I. S.; Laye, R. H.; Breeze, B.; Helliwell, M.; Brechin, E. K.; Heath, S. L.; Murrie, M.; Ochsenbein, S.; Gudel, H.-U.; McInnes, E. J. L., Supertetrahedral decametallic Ni(II) clusters directed by μ_6-*tris*-alkoxides. *Chem. Commun.* **2004**, 1418-1419.
(63) Stamatatos, T. C.; Abboud, K. A.; Wernsdorfer, W.; Christou, G., Ferromagnetically-coupled decanuclear, mixed-valence $[Mn_{10}O_4(N_3)_4(hmp)_{12}]^{2+}$ [hmpH = 2-(hydroxymethyl)pyridine] clusters with rare *T* symmetry and an $S = 22$ ground state. *Polyhedron* **2007**, *26*, 2042-2046.
(64) Swenson, D.; Baenziger, N. C.; Coucouvanis, D., Tetrahedral mercaptide complexes. Crystal and molecular structures of $[(C_6H_5)_4P]_2M(SC_6H_5)_4$ complexes (M = cadmium(II), zinc(II), nickel(II), cobalt(II), and manganese(II)). *J. Am. Chem. Soc.* **1978**, *100*, 1932-1934.
(65) Suturina, E. A.; Nehrkorn, J.; Zadrozny, J. M.; Liu, J.; Atanasov, M.; Weyhermüller, T.; Maganas, D.; Hill, S.; Schnegg, A.; Bill, E.; Long, J. R.; Neese, F., Magneto-Structural Correlations in Pseudotetrahedral Forms of the $[Co(SPh)_4]^{2-}$ Complex Probed by Magnetometry, MCD Spectroscopy, Advanced EPR Techniques, and ab Initio Electronic Structure Calculations. *Inorg. Chem.* **2017**, *56*, 3102-3118.
(66) Glavee, G. N.; Klabunde, K. J.; Sorensen, C. M.; Hadjipanayis, G. C., Sodium borohydride reduction of cobalt ions in nonaqueous media. Formation of ultrafine particles (nanoscale) of cobalt metal. *Inorg. Chem.* **1993**, *32*, 474-477.
(67) Lin, X. M.; Sorensen, C. M.; Klabunde, K. J.; Hadjipanayis, G. C., Temperature Dependence of Morphology and Magnetic Properties of Cobalt Nanoparticles Prepared by an Inverse Micelle Technique. *Langmuir* **1998**, *14*, 7140-7146.
(68) Salgueiriño-Maceira, V.; Correa-Duarte, M. A.; Farle, M.; López-Quintela, M. A.; Sieradzki, K.; Diaz, R., Synthesis and Characterization of Large Colloidal Cobalt Particles. *Langmuir* **2006**, *22*, 1455-1458.
(69) Sanghamitra, N. J. M.; Mazumdar, S., Effect of Polar Solvents on the Optical Properties of Water-Dispersible Thiol-Capped Cobalt Nanoparticles. *Langmuir* **2008**, *24*, 3439-3445.
(70) Kitaev, V., Comment on Effect of Polar Solvents on the Optical Properties of Water-Dispersible Thiol-Capped Cobalt Nanoparticles. *Langmuir* **2008**, *24*, 7623-7624.
(71) Nguyen, T.-A. D.; Cook, A. W.; Wu, G.; Hayton, T. W., Subnanometer-Sized Copper Clusters: A Critical Re-evaluation of the Synthesis and Characterization of $Cu_8(MPP)_4$ (HMPP = 2-Mercapto-5-*n*-propylpyrimidine). *Inorg. Chem.* **2017**, *56*, 8390-8396.
(72) Cook, A. W.; Hayton, T. W., Case Studies in Nanocluster Synthesis and Characterization: Challenges and Opportunities. *Acc. Chem. Res.* **2018**, *51*, 2456-2464.

(73) Kagalwala, H. N.; Gottlieb, E.; Li, G.; Li, T.; Jin, R.; Bernhard, S., Photocatalytic Hydrogen Generation System Using a Nickel-Thiolate Hexameric Cluster. *Inorg. Chem.* **2013**, *52*, 9094-9101.
(74) Ji, J.; Wang, G.; Wang, T.; You, X.; Xu, X., Thiolate-protected Ni_{39} and Ni_{41} nanoclusters: synthesis, self-assembly and magnetic properties. *Nanoscale* **2014**, *6*, 9185-9191.
(75) Zhu, M.; Zhou, S.; Yao, C.; Liao, L.; Wu, Z., Reduction-resistant and reduction-catalytic double-crown nickel nanoclusters. *Nanoscale* **2014**, *6*, 14195-14199.
(76) Joya, K. S.; Sinatra, L.; AbdulHalim, L. G.; Joshi, C. P.; Hedhili, M. N.; Bakr, O. M.; Hussain, I., Atomically monodisperse nickel nanoclusters as highly active electrocatalysts for water oxidation. *Nanoscale* **2016**, *8*, 9695-9703.
(77) Luo, Y.-R., Bond Dissociation Energies. In *CRC Handbook of Chemistry and Physics*, 89th ed.; Lide, D. R., Ed. CRC Press/Taylor and Francis: Boca Raton, FL, 2009.
(78) Kern, R. J., Tetrahydrofuran complexes of Transition metal chlorides. *Journal of Inorganic and Nuclear Chemistry* **1962**, *24*, 1105–1109.
(79) Bain, G. A.; Berry, J. F., Diamagnetic Corrections and Pascal's Constants. *J. Chem. Educ.* **2008**, *85*, 532.
(80) *SMART Apex II, Version 2.1*. Bruker AXS Inc.: Madison, WI, 2005.
(81) *SAINT Software User's Guide, Version 7.34a*. Bruker AXS Inc.: Madison, WI, 2005.
(82) Sheldrick, G. M., *SADABS*. University of Göttingen: Göttingen, Germany, 2005.
(83) *SHELXTL PC, Version 6.12*. Bruker AXS Inc.: Madison, WI, 2005.

Chapter 6. Homoleptic Ketimide Complexes of Platinum, Palladium, and Iron: Isolation of a Two-Coordinate Pt(II) Complex, a Hexagonal Pd_7 Nanocluster, and a Tetrahedral Fe_4 Nanocluster

Table of Contents

6.1 Introduction

Two-coordinate complexes have come under increased scrutiny for their high reactivity and unique magnetic properties.[1] Their low coordination number renders them highly reactive, owing to the ease of substrate access to the metal ion. Consequently, these materials are of interest for catalysis, small molecule activation, and as precursors to nanomaterials, as perhaps best exemplified by the $M(N\{SiMe_3\}_2)_2$-type complexes (M = Mn, Fe, Co). [1-6] With respect to magnetism, the highly anisotropic ligand field and unquenched orbital angular momentum extant in two-coordinate complexes leads to large magnetic moments and high barriers to magnetic reversal, which make these complexes promising single molecule magnets.[7-8] For example, the two-coordinate Fe(II) amide complex, $Fe(N^tBu_2)_2$, features a high magnetic moment and a large internal magnetic field.[9] Similar results are observed for $[Fe(C(SiMe_3))_2]^{0/-}$.[10-11] For the lanthanides, $[(Cp^{ttt})_2Dy][B(C_6F_5)_4]$ (Cp^{ttt} = 1,2,4-tri(*tert*-butyl) cyclopentadienyl) and $[(Cp^{iPr5})DyCp^*][B(C_6F_5)_4]$, which, while not truly two-coordinate, do feature an axial fields imposed by the trans arrangement of their two bulky Cp ligands, exhibit the highest energy barriers for magnetic reversal yet recorded.[12-14] Similarly, $[Dy(O^tBu)_2(py)_5][BPh_4]$, which contains two axial alkoxide ligands, features a remarkably high barrier to magnetic relaxation.[15]

As catalysts, low-coordinate transition metal complexes are rather potent.[1, 16] For example, Tilley and co-workers also examined the ability for the low-coordinate iron complex, $Fe\{N(SiMe_3)_2\}_2$, to catalyze the hydrosilylation of carbonyl compounds.[17] Notably, this catalyst far more active than other iron-based systems and tolerates a wide-variety of functional groups. The same iron precursor was also found to be an effective catalyst for N_2 reduction and the hydrogenation of alkenes, likely through a mixed valent Fe-hydride cluster

which is generated *in situ*.[18-19] These results highlight the need to develop additional low-coordinate iron complexes and iron clusters for use in catalysis, potentially as replacements for more expensive noble metal catalysts.

While these examples reveal the inherent promise in low-coordinate, low-valent complexes for catalysis and magnetic materials, the search for better new low-coordination complexes would benefit from identification of new ligands that can enforce the desired 2-coordinate geometry. In this regard, the ketimide ligand, $[R_2C=N]^-$, may be a suitable candidate. Like amides and alkoxides, ketimides are strong donors, and should be able to generate the required anisotropic ligand field as well as enforce a coordinatively unsaturated coordination geometry. And like amides and alkoxides, ketmides can feature a range of steric profiles and donor abilities.[20-23]

The Hayton research group and others have been exploring the chemistry of the ketimide ligand with a variety of transition metals.[24-33] For example, the Hayton group recently reported the syntheses of the homoleptic transition metal ketimides, $M(N=C^tBu_2)_4$ (M = Fe, Co), which both feature the relatively rare +4 formal oxidation state for these metals.[34] They also both possess squashed tetrahedral geometries.[26, 30] These unusual properties are thought to be a consequence of the interplay between the strong π-donating and π-accepting abilities of the linear ketimide ligand.[32] These strong donor properties suggested to us that ketimides could enforce a low-coordinate geometry and generate a strong axial ligand field. Furthermore, the strong accepting ability of these ligands may be able to promote cluster formation, as they can stabilize low-valent oxidation states and have been shown to promote metal-metal bonding, as seen in the dimeric complexes $[Li(12\text{-crown-}4)_2]]M_2(N=C^tBu_2)_5]$ (M = Mn, Fe, Co).[28].

Several other M(N=C^{t}Bu$_2$)$_4$-type complexes are also known, including examples containing M = Ti, Nb, Ta, Cr, Mo, W, and Mn.[26-27, 30-32, 35-36] Homoleptic ketimide complexes are also know for copper, boron, aluminum, and uranium.[29, 37-39] In this context, the absence of a homoleptic group 10 ketimide is notable, especially given the foundational role that Pd and Pt have played in the development of organometallic chemistry.[40] To rectify this oversight, a previous graduate student in the Hayton group, Dr. Peter Damon, explored the reactivity of a series of Pd and Pt salts with Li(N=C^{t}Bu$_2$) and was able to isolate the homoleptic group 10 ketimide complexes Pt(N=C^{t}Bu)$_2$ (**6.1**) and Pd$_7$(N=C^{t}Bu)$_6$ (**6.5**). Unfortunately, the full characterization of these complexes and mechanistic insights into their formation were not completed by the time Dr. Damon graduated.[41] Similarly, another previous graduate student of the Hayton group, Dr. Richard Lewis, used the aryl ketimide Li(N=Ph$_2$) in the synthesis of the Fe nanocluster Fe$_4$(N=CPh$_2$)$_6$ (**6.7**), though isolation of the complex proved troublesome and the yields poor.[42] However, the isolation of these complexes gives credence to the hypothesis that ketimides can be used to stabilize low-valent, low-coordination number complexes, as well as clusters.

Herein, I describe the characterization of the side products formed during the synthesis of the linear Pt(II) coordination complex **6.1**, namely [(^{t}Bu$_2$C=N)Pt(μ-N,C-*N*=C(^{t}Bu)C(Me)$_2$*C*H$_2$)Pt(N=C^{t}Bu$_2$)] (**6.2**) and [Pt(N=C^{t}Bu$_2$)$_2$(μ-η^4:η^1-C$_8$H$_{11}$)Pt(N=C^{t}Bu$_2$)(1,5-COD)] (**6.4**). I also synthesized and characterized the key intermediate in the formation of **6.1**, [Pt(1,5-COD)(N=C^{t}Bu$_2$)Cl] (**6.3**). I also improved the synthesis of the Pd$_7$ nanocluster **6.5**, as well as completed its characterization and gleaned insights into the mechanism of its formation. Significantly, the isolation of **6.1** confirms that ketimides are suitable for the stabilization of linear, two-coordinate metal complexes. Finally,

I describe my improvements to the synthesis of **6.7** as well as its full characterization via NMR and Mössbauer spectroscopy as well as spin quantum interference device (SQUID) magnetometry.

6.2 Results and Discussion

6.2.1 Characterization of [(^{t}Bu$_2$C=N)Pt(μ-N,C-*N*=C(^{t}Bu)C(Me)$_2$*C*H$_2$)Pt(N=C^{t}Bu$_2$)] (6.2) and [Pt(N=C^{t}Bu$_2$)$_2$(μ-η^4:η^1-C$_8$H$_{11}$)Pt(N=C^{t}Bu$_2$)(1,5-COD)] (6.4)

The reaction of $PtCl_2$(1,5-COD) with 2 equiv of Li(N=C^{t}Bu$_2$) in THF results in immediate formation of yellow-orange solution, which gradually changes to red-brown over 90 min. Work-up and crystallization from pentane resulted in the deposition of a mixture of small red-brown blocks of Pt(N=C^{t}Bu$_2$)$_2$ (**6.1**), which has been structurally characterized by Dr. Damon, and dark brown blocks of [(^{t}Bu$_2$C=N)Pt(μ-N,C-*N*=C(^{t}Bu)C(Me)$_2$*C*H$_2$)Pt(N=C^{t}Bu$_2$)] (**6.2**) on the vial walls. ^{1}H NMR analysis of this mixture revealed the presence of **6.1** and **6.2** in an approximate 1:1 molar ratio, which corresponds to yields of 22% and 32%, respectively. (Scheme 6.1). Because of their similar solubilities, complexes **6.1** and **6.2** could not be fully separated, and they were characterized as a mixture. They are both highly soluble in pentane, hexanes, Et_2O, benzene, toluene, and THF, and somewhat soluble in MeCN. Attempts to perform the reaction of Li(N=C^{t}Bu$_2$) with other Pt(II) salts (such as $PtCl_2$ or $PtCl_2(PhCN)_2$) or with other ketimide precursors (e.g., NaN=C^{t}Bu$_2$), in an effort to improve the chemoselectivity of the transformation, resulted in formation of intractable mixtures.

Scheme 6.1. Syntheses of Complexes 6.1 – 6.4

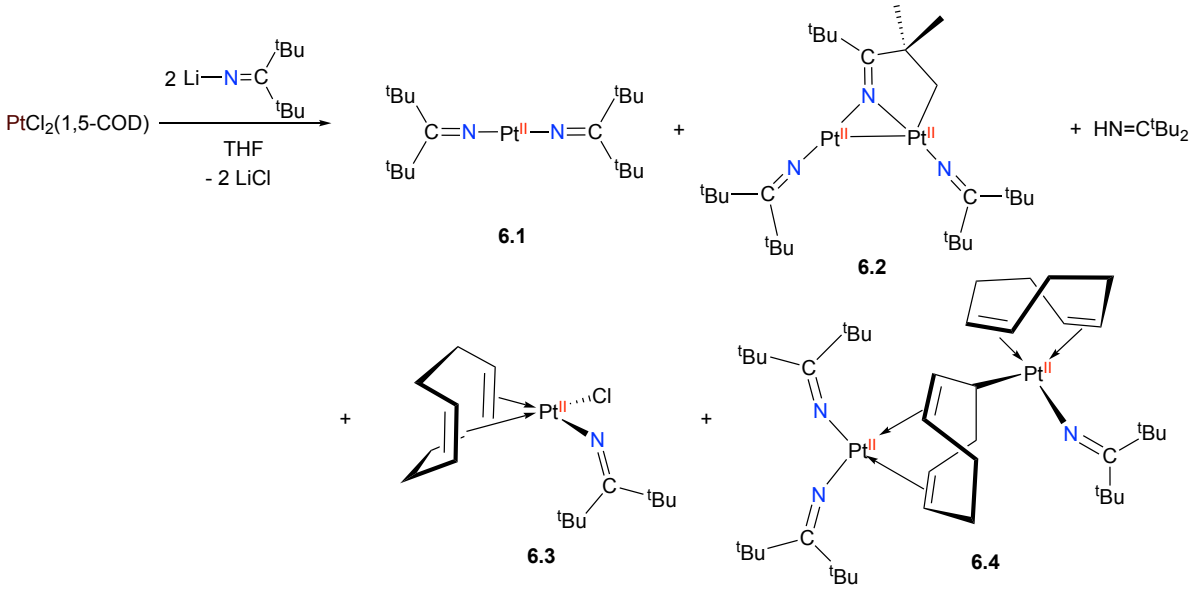

Complex **6.1** (Figure 6.1) has already been crystallographically characterized by Dr. Damon,[41] but further examination of the structure has been carried out. It is noted that many two-coordinate Pt(0) and Pt(I) complexes are known,[2-6] **6.1** is the first two-coordinate Pt(II) complex to be reported.[1] Several two-coordinate Ni(II) complexes, such as $[Ni\{N(H)Ar^{iPr6}\}_2]$ ($Ar^{iPr6} = C_6H_3$-2,6(C_6H_2-2,4,6-$^iPr_3$)$_2$),[43] are known as well, but these tend to be paramagnetic. This change in the electronic ground-state is caused by two factors: first, the greater spatial extent of the 5d vs. 3d orbitals, and thus their better overlap with donor atoms on the ligands; and, second, the strong π-donating and π-accepting properties of the linear ketimide ligand, which produces a larger crystal field than that provided by an amide ligand.

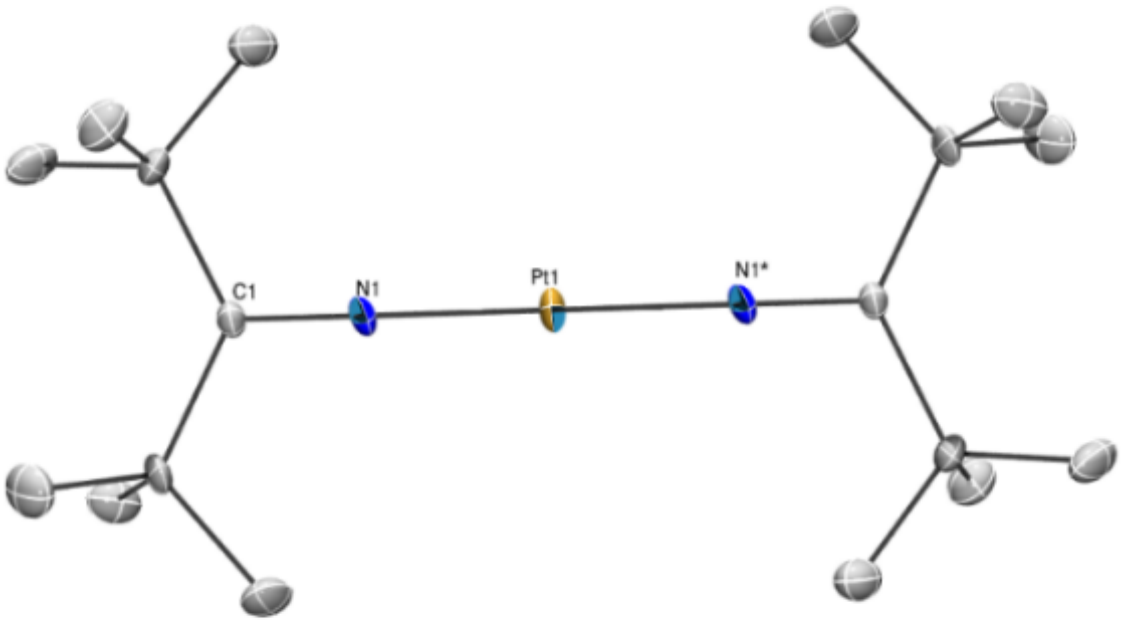

Figure 6.1. ORTEP diagram of one independent molecule of **6.1** shown with 50% probability ellipsoids. Hydrogen atoms and a second molecule of **6.1** are omitted for clarity.

Complex **6.2** crystallizes in the monoclinic space group $P2_1/n$ (Figure 6.2). It features two Pt(II) centers, each ligated by a terminal ketimide ligand, and each bridged by a ketimide ligand that has been deprotonated at a methyl carbon. The nitrogen of the modified ketimide ligand is ligated to both Pt centers, while its methylene group is only ligated to Pt2. Similar to **6.1**, all three ketimide ligands in **6.2** are co-planar and the N-Pt-N angles (166.1(4) and 170.6(3)°) approach linearity. The Pt-N distances for the terminal ketimide ligands (1.825(8) and 1.85(1) Å) are similar to those observed in **6.1**. For comparison, the Pt(II) amides, *cis*-$Pt(Cl)(NPh_2)(PEt_3)_2$ and *trans*-$Pt(H)(NHPh)(PEt_3)_2$, feature much longer Pt-N bond lengths of 2.09(2) Å and 2.125(5) Å, respectively,[44-47] while the Pt(II) ketimide, [Pt(bpy)Me(N=CMe{C(C(Me)=O)(=C(Me)OH})], features a Pt-N bond length of 2.01(2)

Å.[48] The N=C bond lengths of the ketimide ligands (1.256(6), 1.258(2) Å) are typical of carbon-nitrogen distances in other ketimide complexes.[26, 28, 30, 32]

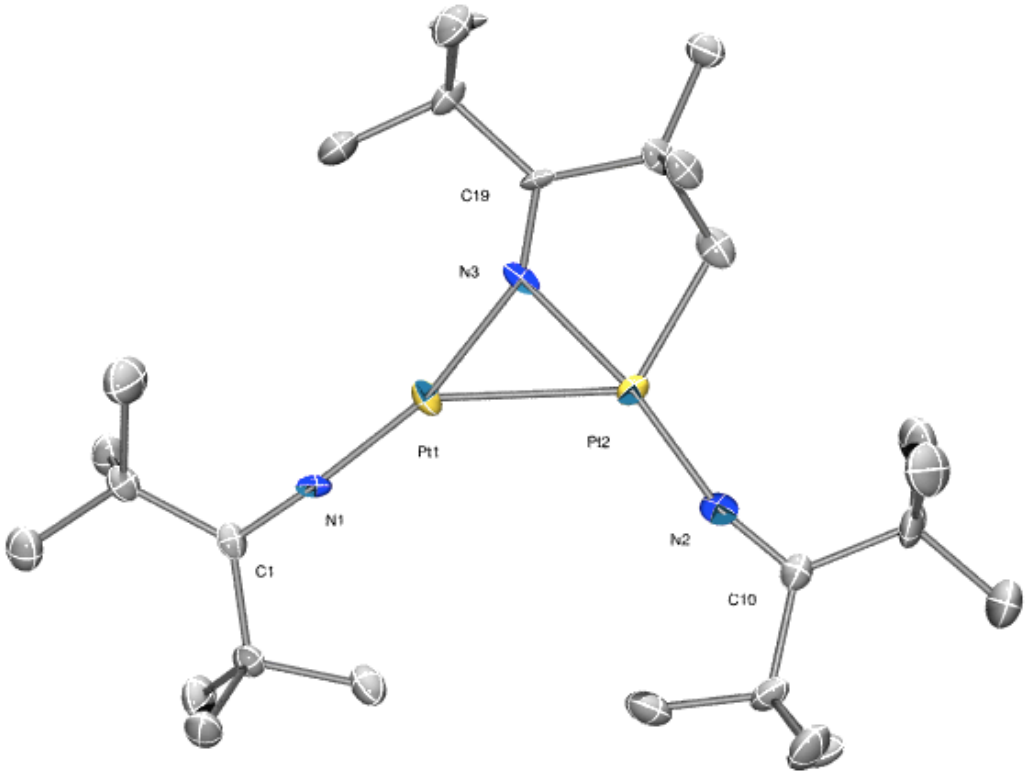

Figure 6.2. ORTEP diagram of **6.2** shown with 50% probability ellipsoids. Hydrogen atoms are omitted for clarity. Selected bond distances (Å) and angles (°): Pt1-N1 = 1.825(8), Pt2-N2 = 1.85(1), Pt1-Pt2 = 2.5951(6), Pt1-N3 = 1.934(7), Pt2-N3 = 1.989(9), Pt2-C27 = 2.08(1), N1-Pt1-N3 = 166.1(4), N2-Pt2-N3 = 170.6(3), C1-N1-Pt1 = 175.8(8), C10-N2-Pt2 = 164.7(8), C19-N3-Pt1 = 151.6(8), C19-N3-Pt2 = 125.4(7).

The Pt-N-C bond angles in **6.2** (175.8(8) °, 164.7(8)°, and 151.6(8)°) are also consistent with sp hybridization of the N atom.[26, 28, 30, 32] Both features are suggestive of a strong degree of π-donation and/or π-backdonation from/to the ketimide ligand. The Pt-Pt distance (2.5951(6) Å) is much shorter than those reported for other platinum(II) complexes with bridging amido ligands,[49-50] and is more in line with those seen in Pt(II) acetate.[51] Finally, the

Pt-C distance (2.08(1) Å) is similar to those of other structurally characterized Pt(II) complexes with C-H activated ^{t}Bu groups.[52-55]

A few bright yellow crystals of a third product were also isolated from this reaction. Analysis by X-ray crystallography revealed these to be [Pt(N=C^{t}Bu$_2$)$_2$(μ-η^4:η^1-C$_8$H$_{11}$)Pt(N=C^{t}Bu$_2$)(1,5-COD)] (**6.4**) (Figure 6.3). This material was isolated in minute quantities and could not be further characterized.

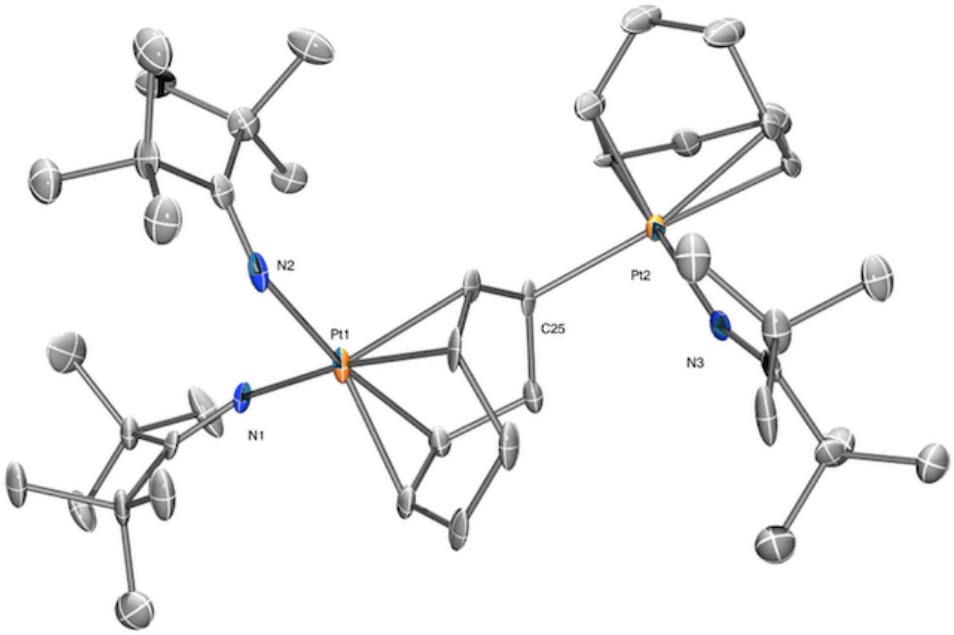

Figure 6.3. ORTEP diagram of [Pt(N=C^{t}Bu$_2$)$_2$(μ-η^4:η^1-C$_8$H$_{11}$)Pt(N=C^{t}Bu$_2$)(1,5-COD)]·0.5C$_5$H$_{12}$ (**6.4**·0.5C$_5$H$_{12}$). Hydrogen atoms are omitted for clarity. Selected bond distances (Å) and angles (°): Pt1–N1 1.977(4); Pt1–N2 1.976(5); Pt2–N3 1.928(5); Pt2–C25 2.102(7); N1–C1 1.253(9); N2–C10 1.250(8); N3–C35 1.245(7); N1-Pt1-N2 91.1(2); N3-Pt2-C25 92.4(2); Pt1-N1-C1 142.8(4); Pt1-N2-C10 143.1(5); Pt2-N3-C35 158.9(5).

While I was unable to isolate pure samples of **6.1** or **6.2** (they always co-crystallized), I was able to assign their ^{1}H NMR spectrum (Figure 6.4). The spectrum in C$_6$D$_6$ consists of a sharp singlet at 1.11 ppm, which is assignable to **6.1**. Additionally, there are 3 singlets, at 1.46,

1.30, and 1.28 ppm, each integrating for 9 protons, and one singlet at 1.22 ppm, integrating for 18 protons, which are assignable to the 5 magnetically inequivalent ^{t}Bu groups (with two overlapping) of **6.2**. Additionally, the spectrum features a singlet at 1.18 ppm, which integrates for 6 protons, and a singlet at 3.25 ppm, which integrates for 2 protons (and features Pt satellites with $^{2}J_{PtH}$ = 88 Hz).

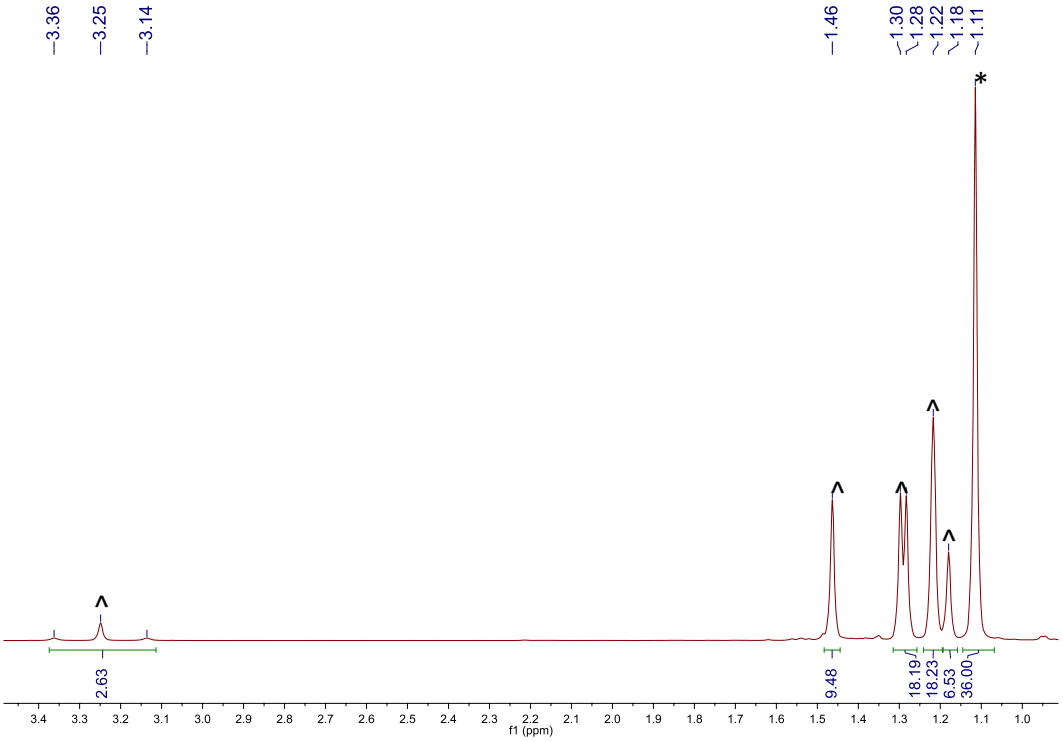

Figure 6.4. Portion of a ^{1}H NMR spectrum of an isolated mixture of **6.1** (*) and **6.2** (^), in an approximately 1:1 molar ratio, in C_6D_6.

An ESI-MS of the isolated crystals (dissolved in THF) features a signal at *m/z* 476.2674 (Figures A6.23), which corresponds to the [**6.1** + H]$^{+}$ ion (calcd *m/z* 476.2645). This spectrum features a second prominent signal at *m/z* 810.3602 (Figure A6.24), which corresponds to [**6.2** + H]$^{+}$ (Calcd *m/z* 810.3633).

More interestingly, for a mixture of **6.1** and **6.2** that was slightly enriched with **6.1**, I detected in C_6D_6 at 25 °C a ^{195}Pt NMR (^{195}Pt NMR spectra were recorded with the assistance

of Prof. Peter Hrobárik and Dr. Branislav Horváth) resonance at -663 ppm that is assignable to **6.1** (Figure 6.5). Upon increasing the temperature to 50 °C, the signal shifted downfield (δ_{Pt} = -629 ppm) and became a well-resolved quintet due to couplings with two equivalent ^{14}N nuclei (I = 1), with $^{1}J(^{195}Pt, ^{14}N)$ coupling constant of 537 Hz (Figure 6.6). The ^{195}Pt nucleus in **6.1** is remarkably deshielded as compared to other Pt(II) complexes with nitrogen-based ligands, which normally feature δ_{Pt} within the range -2700 to -1700 ppm (Table 6.4); in addition, the $^{1}J(^{195}Pt, ^{14}N)$ value is the largest coupling constant reported to date for a Pt-N bond, consistent with its shortest distance and multiple bond character in **6.1**.

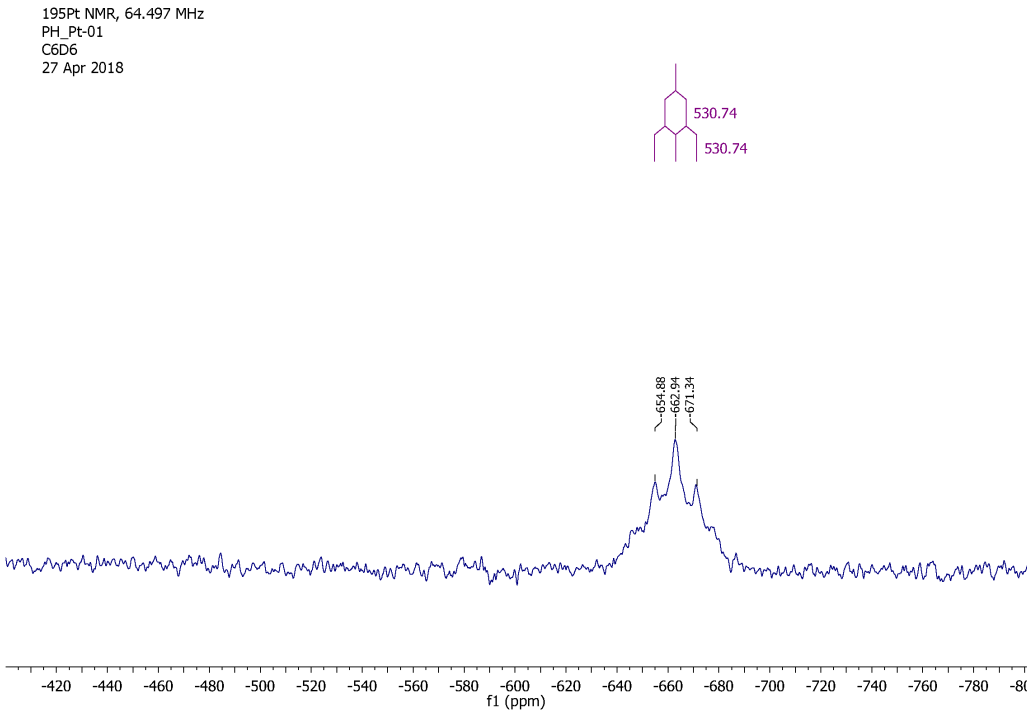

Figure 6.5. ^{195}Pt NMR spectrum of a mixture of **6.1** and **6.2** in C_6D_6, recorded at 25 °C.

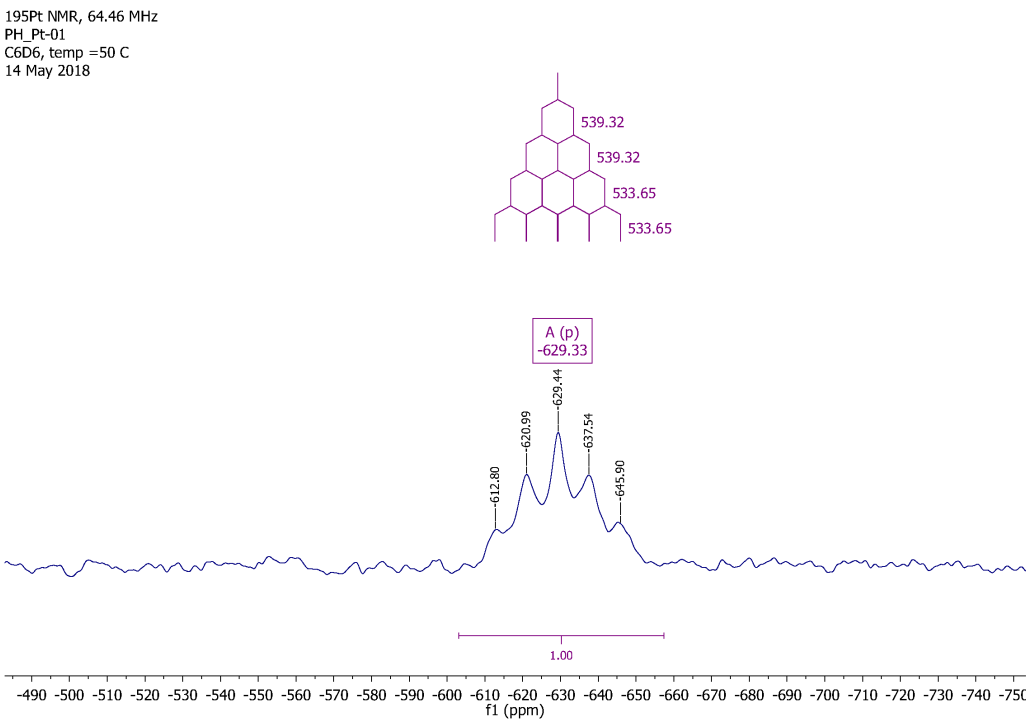

Figure 6.6. ^{195}Pt NMR spectrum of a mixture of **6.1** and **6.2** in C_6D_6, recorded at 50 °C.

6.2.2 Mechanistic Insights into the Formation of 6.1 and 6.2

To better understand the formation of **6.1** and **6.2**, and identify the origin of poor chemoselectivity, I monitored the reaction of $PtCl_2$(1,5-COD) with 2 equiv of Li(N=C^{t}Bu$_2$) by ^{1}H NMR spectroscopy. A ^{1}H NMR spectrum of an aliquot of the crude reaction mixture, taken after 20 min of reaction time, reveals the presence of the complexes **6.1**, **6.2**, and the mono(ketimide) complex, [Pt(1,5-COD)(N=C^{t}Bu$_2$)Cl] (**6.3**), in an approximately 1:2:10 ratio, respectively (Figures A6.1 and A6.2). In contrast, a ^{1}H NMR spectrum of an aliquot, taken after 90 min of reaction time, reveals the presence of the complexes **6.1**, **6.2**, and **6.3** in an approximately 1:1:1 ratio, respectively (Figures A6.3 and A6.4). Given these data, I hypothesize that **6.3** is the initial Pt-containing product formed during the reaction of $PtCl_2$(1,5-COD) with Li(N=C^{t}Bu$_2$), and that it is responsible for the bright orange color of the mixture at short reaction times. Also present in the 90 min spectrum is a small amount of

$HN{=}C^tBu_2$, as well as signals that that I have tentatively assigned to complex **6.4**. According to the ^1H NMR spectrum, **6.4** is not formed in significant quantities, but its presence can partially rationalize the relatively low yields of **6.1** and **6.2**. Moreover, given the decrease in the amount of **6.2** relative to **6.1** with longer reaction times, it appears that **6.1** is not a precursor to **6.2**.

6.2.3 Synthesis and Characterization of [Pt(1,5-COD)(N=C^{t}Bu$_2$)Cl] (6.3)

Scheme 6.2. Synthesis of 6.3

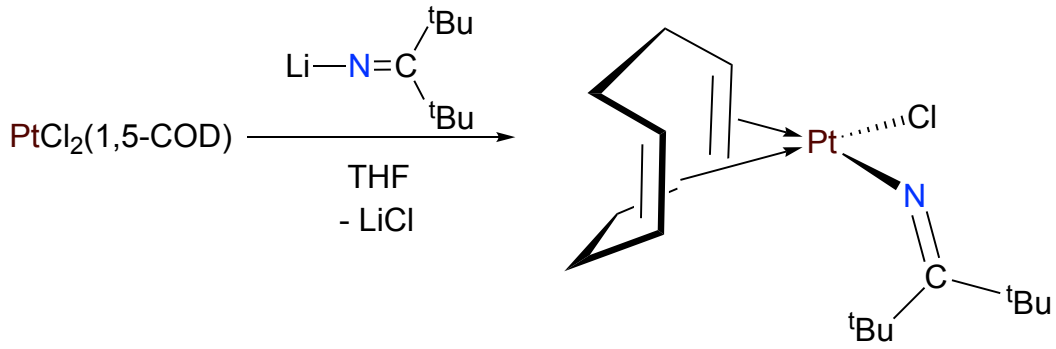

6.3

Complex **6.3** can be independently synthesized by reaction of $PtCl_2$(1,5-COD) with 1 equiv of Li(N=C^{t}Bu$_2$) in THF (Scheme 6.2). When generated in this fashion it can be isolated as an orange powder in 46% yield. Complex **6.3** has been characterized by X-ray crystallography (Figure 6.7) and by ^1H and $^{13}C\{^1H\}$ NMR spectroscopy (Figures A6.6 and A6.7). In the solid state, it features a Pt-N bond length of 1.961(4) Å, which is notably longer than those of **6.1**, and is suggestive of a significantly lesser degree of π-donation and π-backdonation between the Pt center and ketimide ligand. Consistent with this hypothesis, the Pt-N-C angle in **6.3** (143.8(4)°) deviates significantly from linearity.

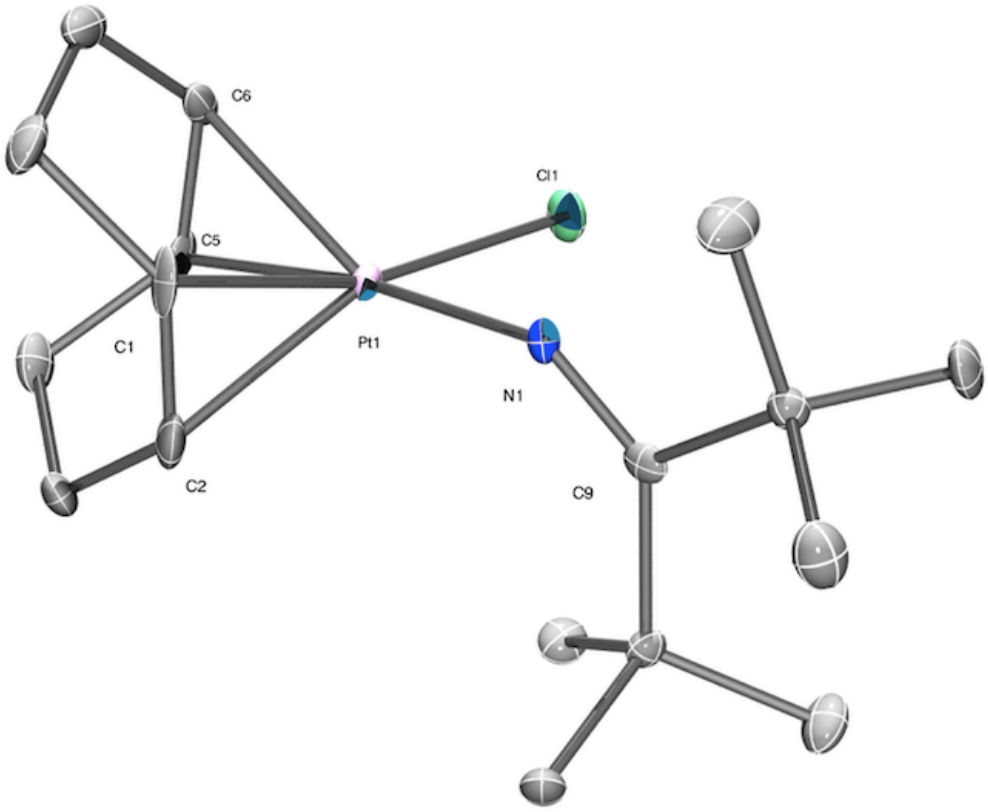

Figure 6.7. ORTEP diagram of [Pt(1,5-COD)(N=C^{t}Bu$_2$)Cl] (**6.3**). Hydrogen atoms are omitted for clarity. Selected bond distances (Å) and angles (°): Pt1–N1 1.961(4); N1–C9 1.255(8); Pt1–C1 2.150(5); Pt1–C2 2.153(7); Pt1–C5 2.184(5); Pt–C6 2.212(6); C1–C2 1.39(1); C5–C6 1.399(8); Cl1-Pt1-N1 90.1(1); Pt1-N1-C9 143.8(4).

6.2.4 Using 6.3 as a Precursor for the Synthesis of 6.1 and 6.2

I also explored the suitability of **6.3** as a precursor to **6.1** and **6.2**. Thus, reaction of **6.3** with 1 equiv of Li(N=C^{t}Bu$_2$) in THF, results formation of both **6.1** and **6.2** in an approximately 1:1 ratio, according to a ^{1}H NMR spectrum of the crude reaction mixture (Figure A6.8). Several other minor resonances are also present in the reaction mixture, which I have tentatively assigned to complex **6.4**. A small amount of HN=C^{t}Bu$_2$ is also present in the

sample. Given that this route did not appear to offer any advantages over the initial method of preparation, it was not pursued further.

6.2.5 Improved Synthesis and Characterization of $Pd_7(N{=}C^tBu_2)_6$ (6.5)

Reaction of $PdCl_2(PhCN)_2$ with 2 equiv of $Li(N{=}C^tBu_2)$ in THF results in the formation of a dark green solution. Work-up of the reaction mixture results in the isolation of $Pd_7(N{=}C^tBu_2)_6$ (**6.5**), in a 40% yield as dark green blocks (Scheme 6.3). Complex **6.5** is soluble in pentane, hexanes, Et_2O, benzene, toluene, and THF, and somewhat soluble in MeCN, but quickly decomposes in the presence of CH_2Cl_2. It is stable as a solid under inert atmosphere at -25 °C for at least several months.

Scheme 6.3. Syntheses of Complexes 6.5 and 6.6

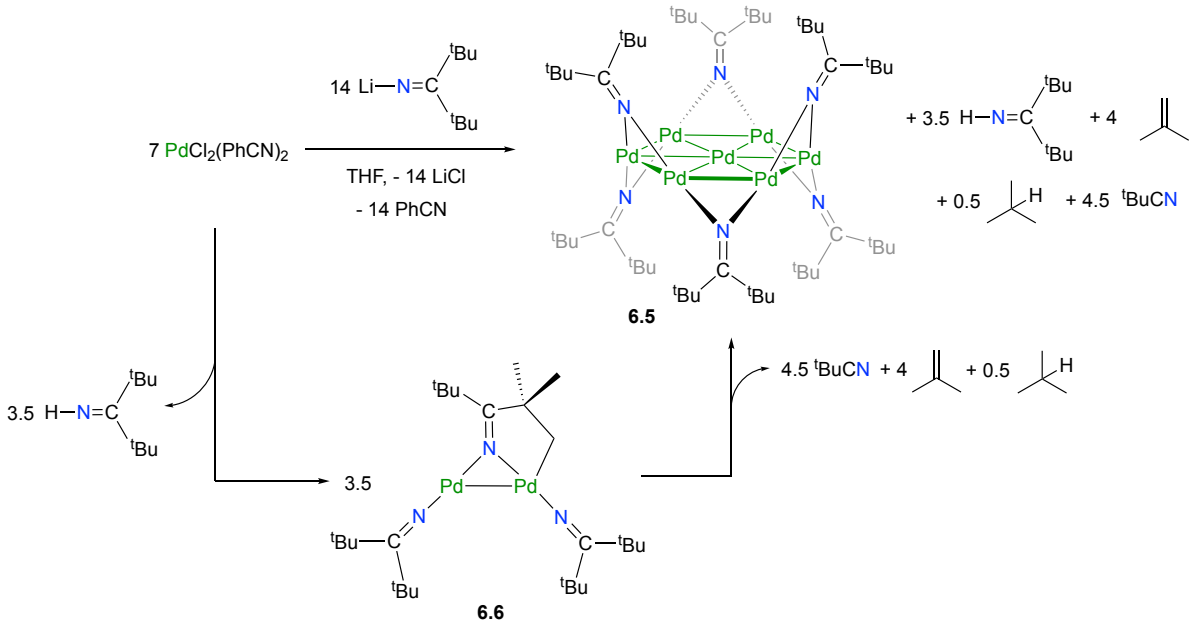

The structural characterization of complex **6.5** was originally been carried out by Dr. Damon,[41] however the solid state molecular structure is shown in Figure 6.8.

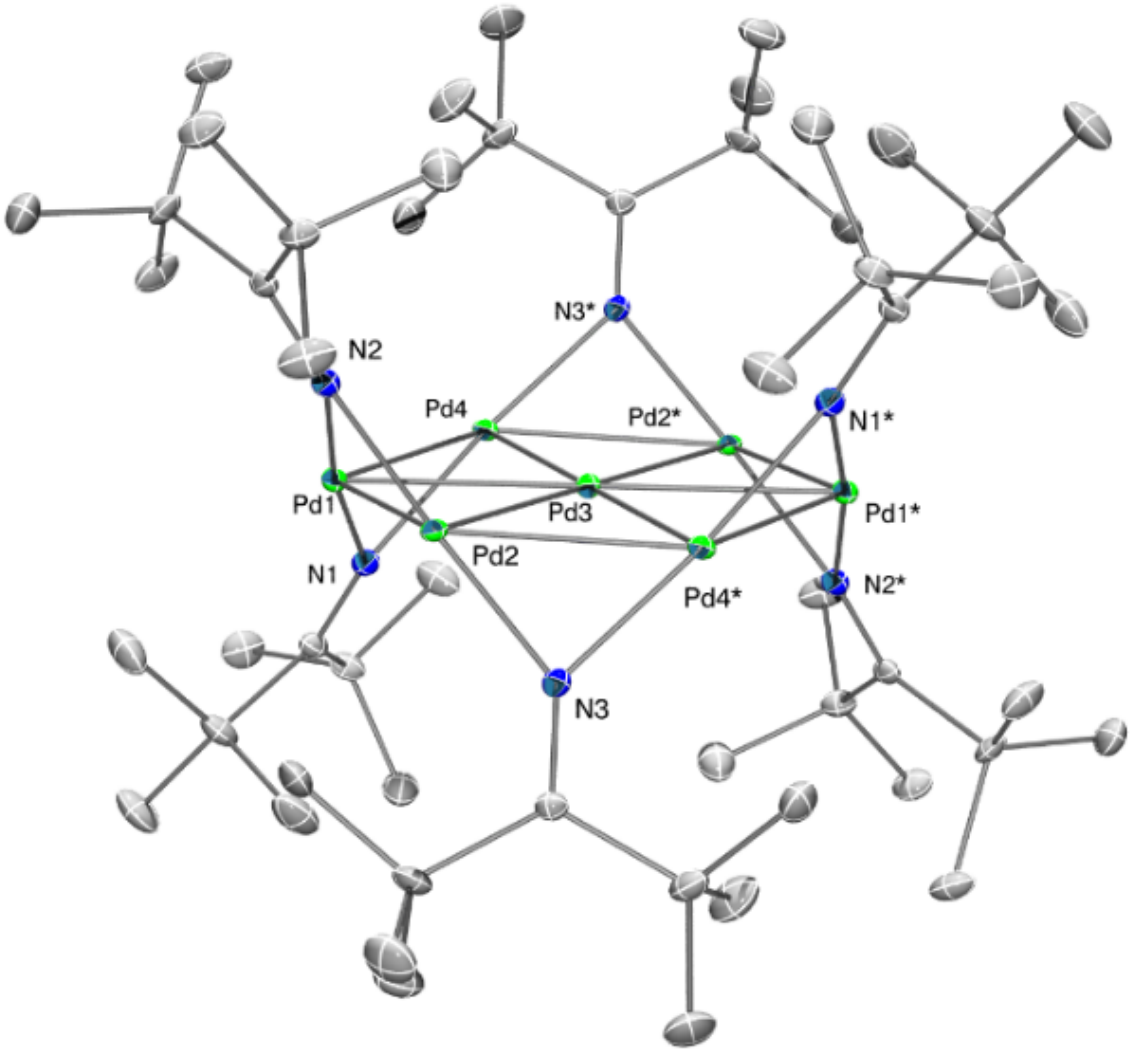

Figure 6.8. ORTEP diagram of **6.5**. Hydrogen atoms are omitted for clarity.

The ^{1}H NMR spectrum of **6.5** in C_6D_6 features a sharp singlet at 1.65 ppm (Figure 6.9), consistent with high-symmetry structure observed in the solid-state. Also present are resonances at 2.38, 1.66, 1.60, and 1.54, 1.30, 1.24, and 1.18 ppm, which I have assigned to the Pd analogue of complex **6.2**, [(^{t}Bu$_2$C=N)Pd(μ-N,C-*N*=C(^{t}Bu)C(Me)$_2$*C*H$_2$)Pd(N=C^{t}Bu$_2$)] (**6.6**) (Scheme 6.3). These resonances are observed in a 2:9:9:9:6:9:9 ratio. Both the chemical shifts and relative intensities of these peaks are essentially identical to those observed for **6.2**, supporting this assignment.

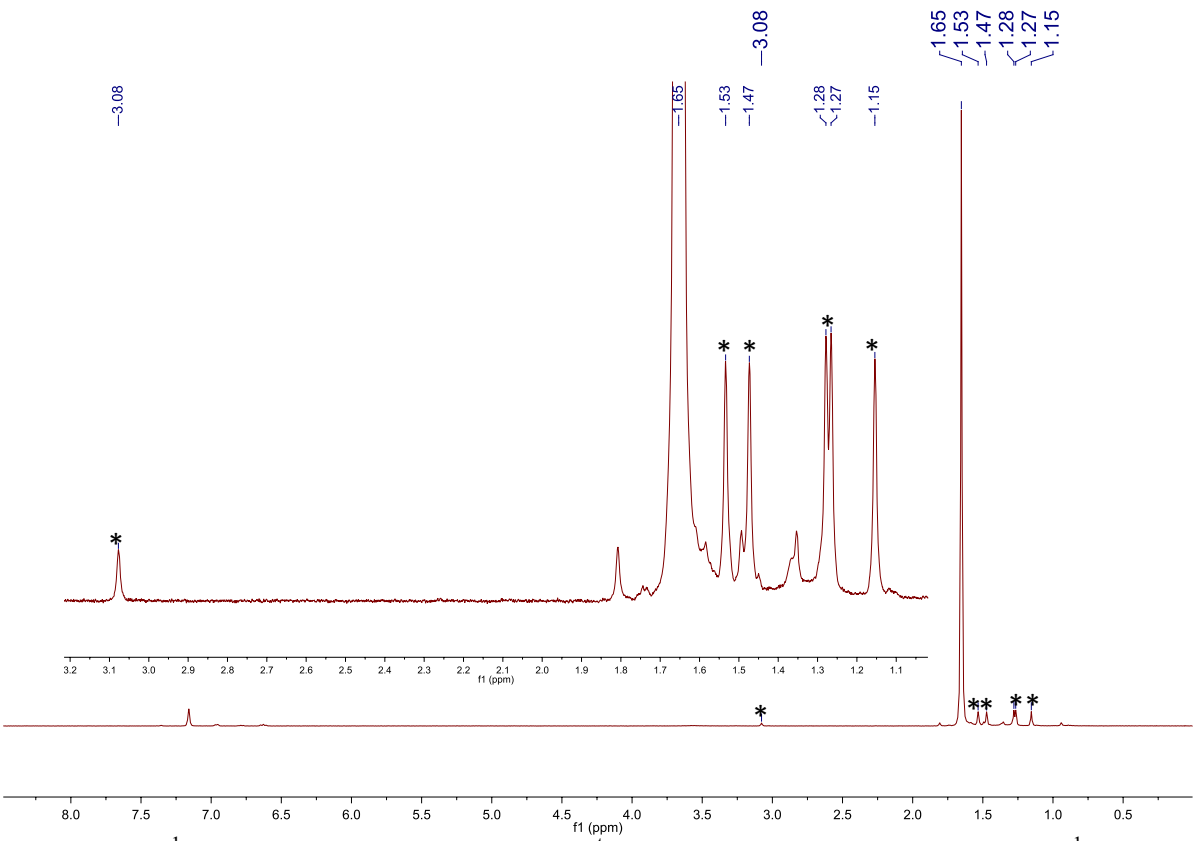

Figure 6.9. ^{1}H NMR spectrum of $Pd_7(N{=}C^tBu_2)_6$ (**6.5**) in C_6D_6. Inset: partial ^{1}H NMR spectrum of complex **6.5** showing the resonances assignable to complex **6.6**. (*) denotes resonances assignable to small amounts of [(^{t}Bu$_2$C=N)Pd(μ-N,C-*N*=C(^{t}Bu)C(Me)$_2$*C*H$_2$)Pd(N=C^{t}Bu$_2$)] (**6.6**).

The ^{13}C{^{1}H} NMR spectrum displays a diagnostic resonance at 181.0 ppm (Figure A6.10), assignable to the ketimide N=C carbon. A similar chemical shift (188.5 ppm) was observed for the copper ketimide cluster, $[Cu(N{=}C^tBu_2)]_4$.[25] The ESI mass spectrum of **6.5** features a signal at m/z 1586.2362 (Figure A6.26), corresponding to the parent $[M]^+$ ion (calcd *m/z* 1586.1953). A second prominent peak at *m/z* 740.1635 is assigned to the fragmentation product, $[Pd_3(N{=}C^tBu_2)_3]^+$ (calcd *m/z* 740.1459). Excellent agreement between the observed and calculated isotope distributions for both signals (Figure A6.27) supports the absence of bridging hydride ligands in this complex.

6.2.6 Mechanistic Insights into the Formation of 6.5

To better understand the formation of **6.5**, and identify the stoichiometry of the transformation, I monitored the reaction of $PdCl_2(PhCN)_2$ with 2 equiv of $Li(N=C^tBu_2)$ in THF-d_8, in the presence of an internal standard, by ^{1}H NMR spectroscopy (Figures A6.11 and A6.12). A ^{1}H NMR spectrum of this sample after 5 h reveals the presence resonances assignable to **6.5**, $HN=C^tBu_2$, ^{t}BuCN, isobutylene, and isobutane. Also present are resonances assignable to **6.6**. Given the distribution of products in the reaction mixture, I hypothesize that the formation of **6.5** proceeds via the intermediacy of **6.6**. Specifically, I propose that reaction of $PdCl_2(PhCN)_2$ with $Li(N=C^tBu_2)$ results in formation of **6.6** and $HN=C^tBu_2$. Complex **6.6** then converts to low-valent **6.5** via oxidation of its ketimide ligands, concomitant with formation of ^{t}BuCN, isobutylene, and isobutene (Scheme 6.3). Previously, the Hayton group demonstrated that $M(N=C^tBu_2)_4$ (M = Mn, Fe) decompose upon thermolysis via ketimide oxidation, forming $Mn_3(N=C^tBu_2)_6$ and $Fe_2(N=C^tBu_2)_5$, respectively, along with ^{t}BuCN, isobutane and isobutylene.[27, 31] A similar redox process is apparently occurring during the formation of **6.5**.

6.2.7 Electrochemistry of 6.5

I also, recorded the cyclic voltammogram of complex **6.5** in THF (Figure 6.10). The cyclic voltammogram of **6.5** features an irreversible oxidation at $E_{p,a}$ = -0.166 V (vs. Fc/Fc^+) with an onset potential $E_{onset,a}$ = -0.385 V (vs. Fc/Fc^+) and a reversible reduction at $E_{1/2}$ = -2.204 V (vs. Fc/Fc^+) with an onset potential $E_{onset,c}$ = -2.124 V (vs. Fc/Fc^+) (Figures A6.35 – A6.38 and Table 6.3). These potentials correspond to HOMO and LUMO energies of approximately -4.71 eV and -2.98 eV, respectively,[56] and a HOMO-LUMO gap of 1.73 eV. The reversibility of the reduction feature also suggests that **[6.5]**$^-$ could be isolable.

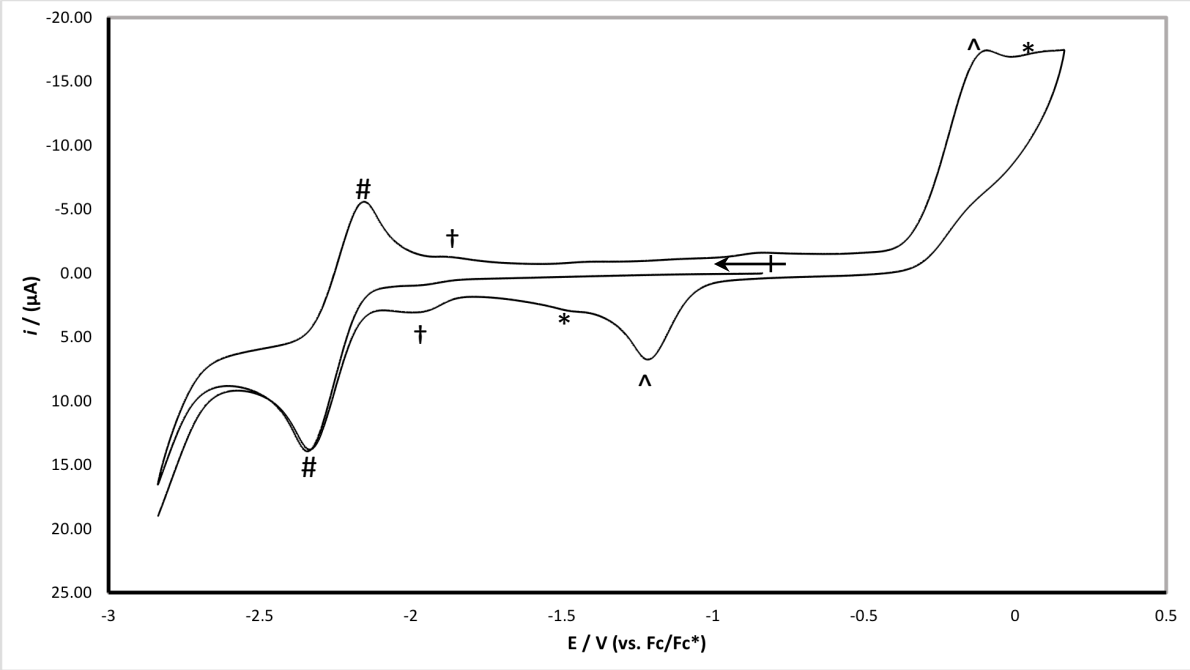

Figure 6.10. Cyclic voltammogram of complex **6.5** (200 mV/s, vs. Fc/Fc^{+}), measured in THF with 0.1 M $[NBu_4][PF_6]$ as supporting electrolyte. The electrochemical feature indicated by (#) is assigned to the $[\mathbf{6.5}]^{0/-}$ couple; the electrochemical feature indicated by (^) is due to the irreversible oxidation of **6.5** via an ECE-type mechanism, which gives rise to the reduction feature at -1.4 V; the electrochemical feature indicated by (*) is likely due to a decomposition product, as it grows in intensity during the course of the experiment; the electrochemical feature indicated by (†) is likely due to a trace amount of **6.6**.

6.2.8 Synthesis and Characterization of $Fe_4(N{=}CPh_2)_6$ (6.7)

Expansion of this ketimide nanocluster chemistry to other transition metals, namely Co, Fe, and Ni, may produce magnetic nanomaterials, with applications as single molecule magnets or qubits.[57-59] However, the preparation of such nanoclusters has proved challenging as typical synthetic protocols for group 11 nanoclusters call for the *in situ* reduction of metal salts with $NaBH_4$ in the presence of thiols, which exclusively generates M(II)-thiolate oligomers rather than the desired mixed-valent species for M = Co, Fe, and Ni.[60] However,

recent studies have shown that low-valent Fe clusters are isolable through reaction of Fe salts with Grignard reagents or chemical reduction of pre-assembled all-ferrous clusters.[18-19, 61-68]

For example, Neidig and co-workers reported the reduction of Fe^{3+} with 4-R-C_6H_4MgBr or MeMgBr yielded the mixed-valent, Fe(II)/Fe(I) clusters, [Fe_4(μ-4-R-C_6H_4)$_6$(THF)$_x$] (R = H, x = 4; R = Me, x= 3, 4; R = F, x = 4) and [$MgCl(THF)_5$][Fe_8Me_{12}], with average Fe oxidation states of 3/2 and 13/8, respectively.[62-63] While the magnetism of these complexes was not explored, they were found to be reactive intermediates for C-C cross coupling with aryl and alkyl halides.[62-63] Similarly, Betley and co-workers isolated [(18-crown-6)K(THF)$_2$][(^{tbs}L)Fe_3] (^{tbs}LH_6 = 1,3,5-(^{t}BuMe$_2$SiNH-*o*-$C_6H_4NH)_3C_6H_9$), [M][(^{tren}L)$_2Fe_8$(PMe$_2$Ph)$_2$] (M = $[Bu_4N]^+$, $[(15\text{-crown-}5)Na(THF)]^+$; ^{tren}L$H_9$ = [*o*-$H_2NC_6H_4NH(CH_2)_2]_3N$), and [NBu_4]$_2$[(^{H}L)$_2Fe_6$] (^{H}LH_6 = MeC(CH_2NHPh-*o*-NH_2)$_3$), with average Fe oxidation states of 4/3, 15/8 and 11/6 respectively, via reduction of their parent clusters with either KC_8 or sodium naphthalide.[64, 66-67] Notably. the latter complex has a room temperature electronic ground-state of S = 11, the highest thermally persistent spin reported to date.[68]

Herein I expand upon the synthesis and characterization of the mixed-valent, tetrahedral iron-ketimide cluster $Fe_4(N{=}CPh_2)_6$, which was originally isolated by Dr. Richard Lewis.[42] Significantly, I find that this cluster is thermally robust and has a room temperature ground spin-state approaching S = 7. Further, this cluster showcases the unique ability for the ketimide ligand to stabilize both high-valent and low-valent metal centers. Thus, addition of lithium diphenylketimide (LiN=CPh_2) (1.5 equiv) to a slurry of $FeBr_2$ (1 equiv) in THF resulted in the formation of a red-brown solution. Addition of Zn powder (2 equiv) to the reaction mixture resulted in the gradual color change to dark-brown, concomitant with the deposition of a dark

brown solid. Work-up of this brown solution after stirring at room temperature for 18 h resulted in the isolation of the mixed-valent, iron-ketimide cluster $Fe_4(NC{=}Ph_2)_6$ (**6.7**) as a brown, crystalline solid in 44% yield (Scheme 6.4). Formally, two Fe centers in **6.7** have been reduced by Zn to Fe(I).

Scheme 6.4. Synthesis of complex 6.7

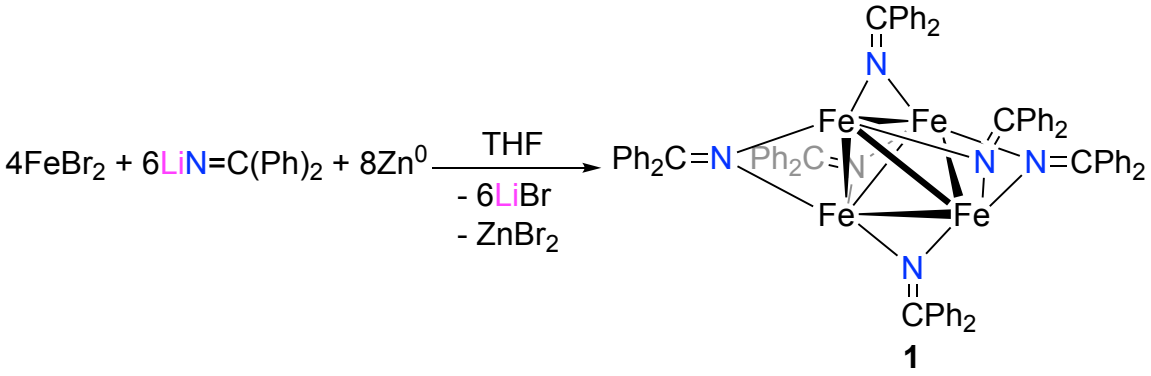

1

Complex **6.7** crystallizes as brown plates in the triclinic space group $P\bar{1}$ with two independent molecules of **6.7** per unit cell (Figure 6.11). 7.5 equivalents of toluene are also incorporated in the unit cell. Each independent molecule of **6.7** features a tetrahedral $[Fe_4]^{6+}$ core with each edge of the tetrahedron bridged by a ketimide ligand. Ignoring the Fe-Fe bonds, each Fe center has trigonal planar (D_{3h}) geometry with the average ∑N-Fe-N = 357.1°. The Fe-Fe distances range from 2.504(4) to 2.621(4) Å (average = 2.56 Å), which are within the range of Fe-Fe bonds.[69-70] Overall, complex **6.7** exhibits T_d symmetry in the solid state.

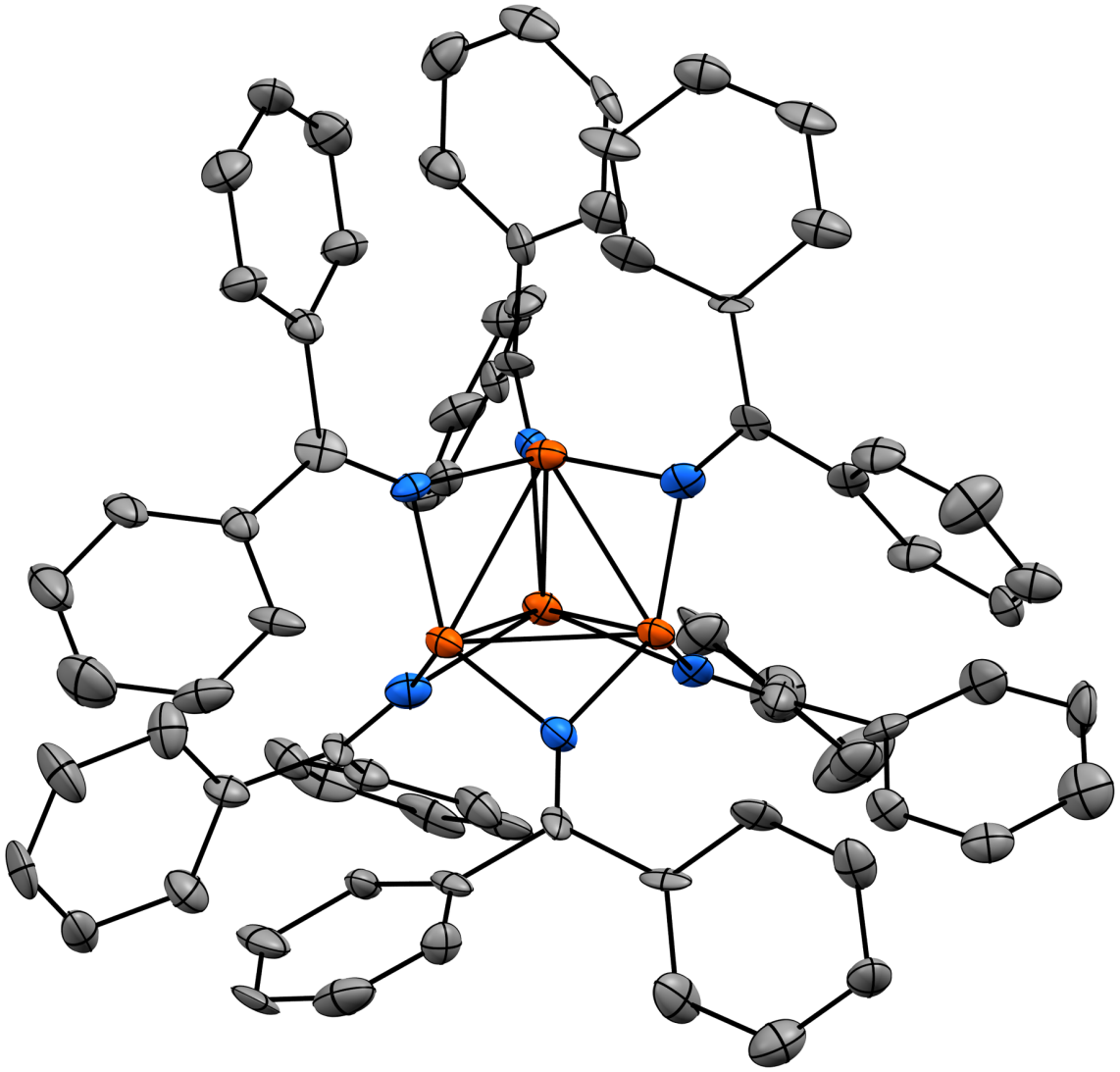

Figure 6.11. ORTEP diagram of one independent molecule of **6.7** with 50% probability ellipsoids. Hydrogen atoms, toluene solvates, and a second molecule of **6.7** are omitted for clarity. Color legend: Fe = orange; N = blue; C = gray.

To determine the extent of metal-metal bonding in complex **6.7**, the formal shortness ratio, *r*,[71] was calculated by taking the ratio of the Fe-Fe bond distance and the sum of single-bond radii.[72] The *r* value for complex **6.7** is 1.10, indicative of weak single bonds between Fe centers. Comparatively, the $[Fe_4(\mu\text{-}4\text{-}MeC_6H_4)_6(THF)_x]$ clusters reported by Neidig and co-workers[62] have average Fe-Fe bond distances of 2.47 Å and 2.45 Å with *r* = 1.06 and 1.05,

for x = 4 and 3, respectively. Similarly, the $[MgCl(THF)_5][Fe_8Me_{12}]$ cluster has average Fe-Fe bond distances of 2.433 Å and r = 1.05.[63] Finally, the only other reported Fe-ketimide complex with Fe-Fe bonds, $[Li(12\text{-crown-}4)_2][Fe_2(N{=}C^tBu_2)]_5$, was found to have a Fe-Fe bond distance of 2.433(1) Å with r = 1.05.[28] The Fe-Fe bond distances for the mixed valent Fe(II)/Fe(I) clusters reported by Betley and co-workers[12-19] are in good agreement with complex **6.7**, with Fe-Fe bond distances and r values ranging from 2.46 to 2.65 Å and 1.05 to 1.14, respectively. The slight elongation of the Fe-Fe distances in **6.7** may be due to the steric profile of the ketimide ligand as well as the population of Fe-Fe antibonding orbitals (*vide infra*). Conversely, Betley and co-workers reported that the average Fe-Fe distances for the more oxidized clusters, $[(^HL)_2Fe_6]^{n+}$ (n = 0-4),[64, 73] were consistently longer (2.597(1) to 2.757(3) Å) than those found in **6.7**, supporting my assessment of that this complex is low-valent. The average Fe-N bond distance (1.95 Å) is slightly shorter than those reported for the Fe-ketimide dimers with bridging ketimide moieties $[Li(12\text{-crown-}4)_2][Fe_2(N{=}C^tBu_2)]_5$ (average $Fe\text{-}N_{bridging}$ = 2.06 Å) and $[Fe(Mes)(N{=}C(Mes)Ph)(NCMe)]_2$ (Mes = 2,4,6-Me_3C_6H2) (average Fe-N = 2.05 Å), but is in line with the iron-carbonyl dimer $[Fe(CO)_3(N{=}C(p\text{-}MeC_6H_4)_2]_2$ (average Fe-N = 1.94 Å), indicative of the monoanionic nature of the ketimide.[28, 74-75]

The ^1H NMR spectrum of **6.7** in C_6D_6 (Figure 6.12) consists of three, broad paramagnetic resonances at 57.29, 30.88, and 8.56 ppm, assignable to the *o*-Ph, *m*-Ph, and *p*-Ph environments, respectively, which suggests that the high symmetry of the cluster is maintained in solution. Monitoring the reaction of $FeBr_2$ (1 equiv), $LiN{=}CPh_2$ (1.5 equiv), and Zn (2 equiv) in THF-d_8 (Figure A6.15) indicates that **6.7** is generated quickly, as well as other intermediates. Over the course of 24 h, however, **6.7** becomes the major product in the reaction

mixture. Attempts to carry out this reaction in the absence of Zn results in the formation of only a small amount of **6.7** as a mixture of other products (Figure A6.17). ESI-MS of complex **6.7** in THF, acquired in negative ion mode, is consistent with the proposed formulation (Figure A6.29). A single major feature at *m/z* = 1304.2397 corresponds to [M^-] (calcd *m/z* = 1304.2262).

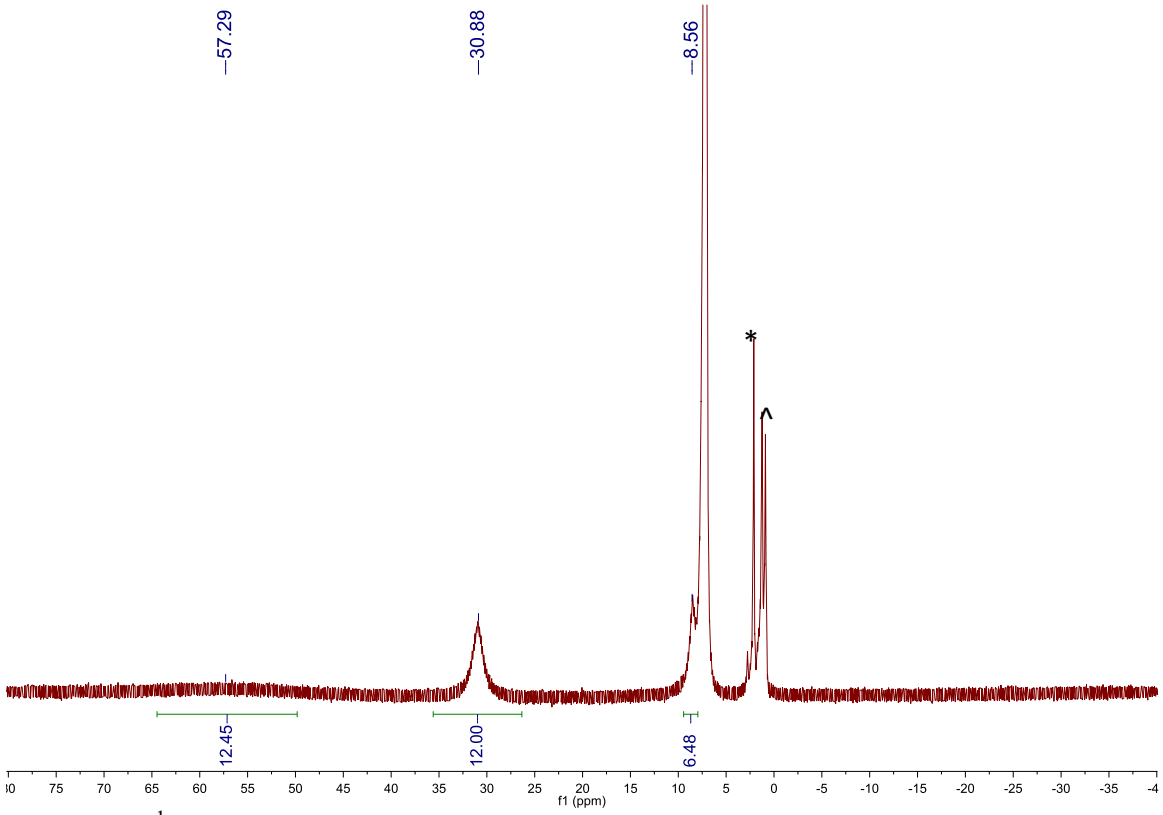

Figure 6.12. ^{1}H NMR spectrum of **6.7** in C_6D_6. (*) indicates a resonance assignable to toluene and (^) indicates a resonance assignable to pentane.

I also briefly explored the chemical properties of complex **6.7**. To probe the thermal stability of the cluster, a C_6D_6 solution of **6.7** was allowed to stand at room temperature for 3 d, over which time no changes were observed in the ^{1}H NMR spectrum. Similarly, a toluene-d_8 solution was gradually heated and monitored by ^{1}H NMR spectroscopy (Figure A6.20) and complex **6.7** again showed no signs of decomposition up to 80 ºC and only begins to degrade at 100 ºC. This is in contrast to the Fe_4 cluster reported by Neidig and co-workers, which

rapidly decomposed even at 0 ºC.[62] Consistent with its low formal oxidation state, a C_6D_6 solution of complex **6.7** rapidly reacts with air, with no resonances assignable to the cluster present 10 minutes after exposure to oxygen and water (Figure A6.21). Complex **6.7** is very sparingly soluble in Et_2O, partially soluble in benzene and toluene, and very soluble in THF. However, the cluster is insoluble in pentane and acetonitrile and rapidly decomposes in dichloromethane (Figure A6.19).

6.2.9 Magnetic Susceptibility of $[Fe_4(N{=}CPh_2)_6]$

I then endeavored to explore the solution and solid state magnetism of complex **6.7** via Evans' method[76] and superconducting quantum interference device (SQUID) magnetometry (Figure 6.13). Significantly, I found that complex **6.7** exhibits a solution-state effective magnetic moment of 13.21 B.M. at 298 K in toluene-d_8. Comparatively, at 300 K, the solid state magnetic moment was found to be 14.64 B.M ($\chi_M T$ = 26.56 cm^3 K/mol), which persists until 20 K. Upon cooling to 1.8 K, the moment drops precipitously to 6.59 B.M. ($\chi_M T$ = 5.43 cm^3 K/mol). These data are consistent with the expected spin-only value for $S = 7$ (14.97 B.M., $g = 2.0$), and is among the highest reported for iron clusters to date.[64, 68] The $\chi_M T$ values were fit using PHI[77] according to the spin Hamiltonian $\hat{H} = D\hat{S}_z^2 + g_{iso}\mu_B S \cdot H$, where $S = 7$, $D = 2.7$ cm^{-1}, and $g = 1.98$.

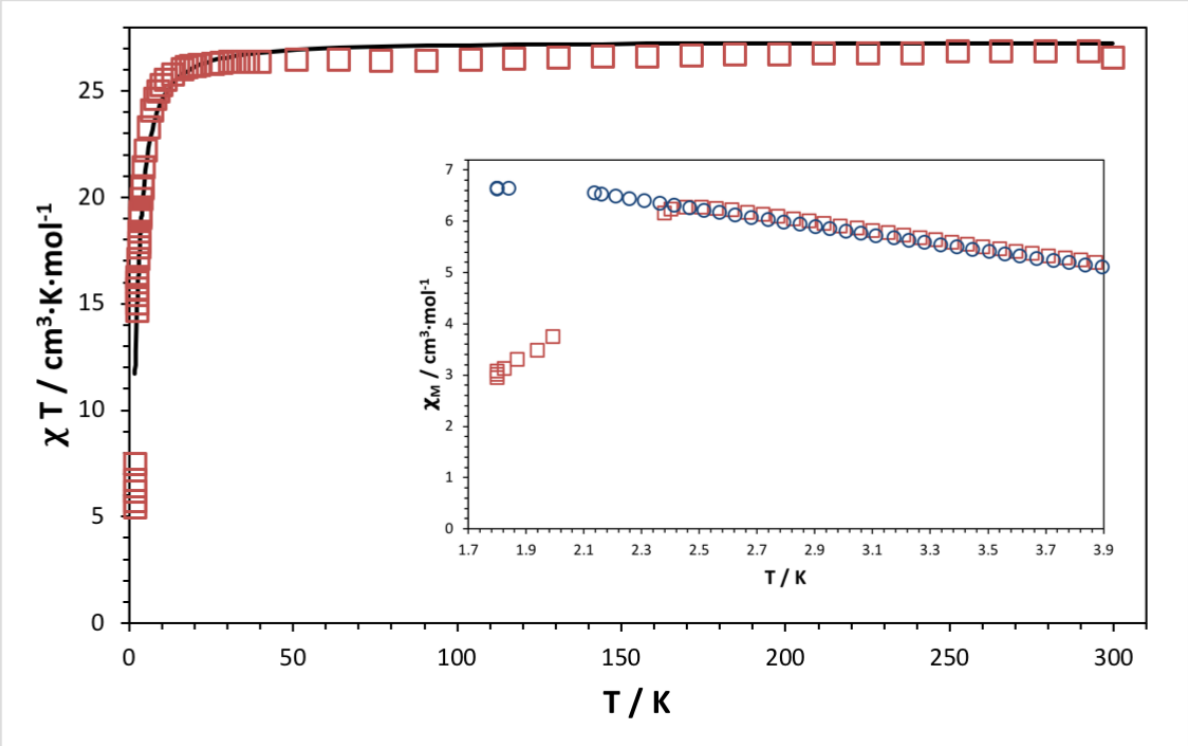

Figure 6.13. Variable temperature solid-state magnetic susceptibility of **6.7** (red squares) collected under a 0.5 T field from 1.8 to 300 K. The continuous black trace corresponds to the fit of the data as described in the text. Inset: ZFC (red squares) and FC (blue circles) magnetization data collected for **6.7**.

To probe the SMM behavior of complex **6.7**, zero-field-cooled (ZFC) and field-cooled (FC) data were collected at 0.5 T (Figure 6.13, inset). The ZFC and FC data diverge at $T < 2.4$ K, indicative of magnetic blocking below these temperatures. This magnetic ordering was probed by collecting magnetization data between ±7 T at 1.8 K (Figure 6.14). Magnetic saturation was observed at ±7.7 μ_B and displayed remnant magnetization of ±3.3 μ_B with a coercive field of 0.3 T. Further studies into the relaxation dynamics, especially alternating current experiments, will be necessary to further elucidate the SMM behavior of complex **6.7**.

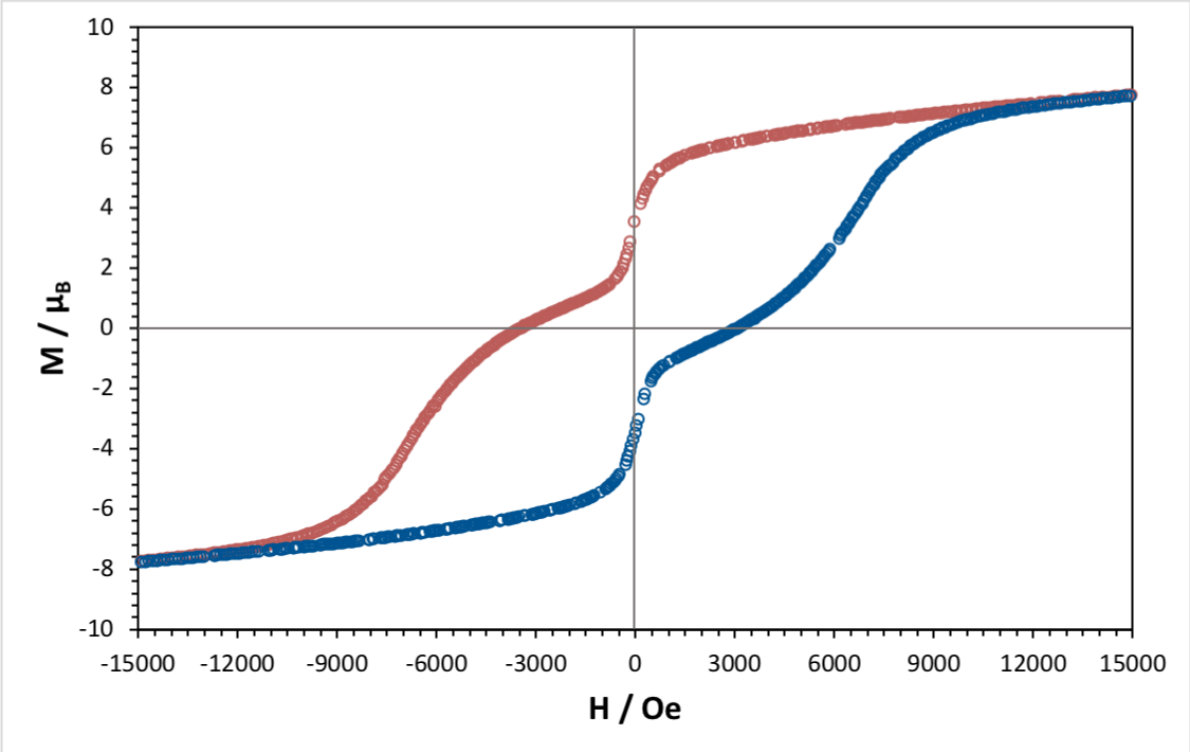

Figure 6.14. Partial magnetization data at 1.8 K for $Fe_4(N{=}CPh_2)_6$ (**6.7**) showing magnetization vs. applied field cycling from ±7 T.

6.2.10 Zero-field ^{57}Fe Mössbauer Spectroscopy of $[Fe_4(N{=}CPh_2)_6]$

A zero-field ^{57}Fe Mössbauer spectrum of complex **6.7** taken at 90 K (Figure 6.14) reveals a sharp quadrupole doublet with isomer shift δ = 0.34 mm/s and quadrupole splitting ΔE_Q = 0.79 mm/s, in line with other mixed-valent Fe(II)/Fe(I) clusters.[18, 61-68] For comparison, the mixed-valent Fe clusters reported by Neidig and co-workers, $[Fe_4(C_6H_5)_6(THF)_4]$ and $[MgCl(THF)_5][Fe_8Me_{12}]$, showed broad doublets with isomer shifts δ = 0.60 and 0.30 and quadrupole couplings ΔE_Q = 0.84 and 0.85 mm/s, respectively.[62-63] These data are consistent with the formulation of **6.7** as a complex with oxidation state intermediate between Fe(II) and Fe(I) with high symmetry in the solid state.[78] Additionally, the presence of a single Fe quadrupole doublet suggests that the iron valence electrons are fully delocalized across the Fe_4 unit on the Mössbauer time scale (10^7 s^{-1}); as such complex **6.7** should be considered as

$[Fe^{1.5+}]_4$ as opposed to $[Fe^{1+}]_2[Fe^{2+}]_2$, in good agreement with the magnetic susceptibility measurements. This delocalization has been observed for other mixed-valent Fe complexes, as well.[79-81]

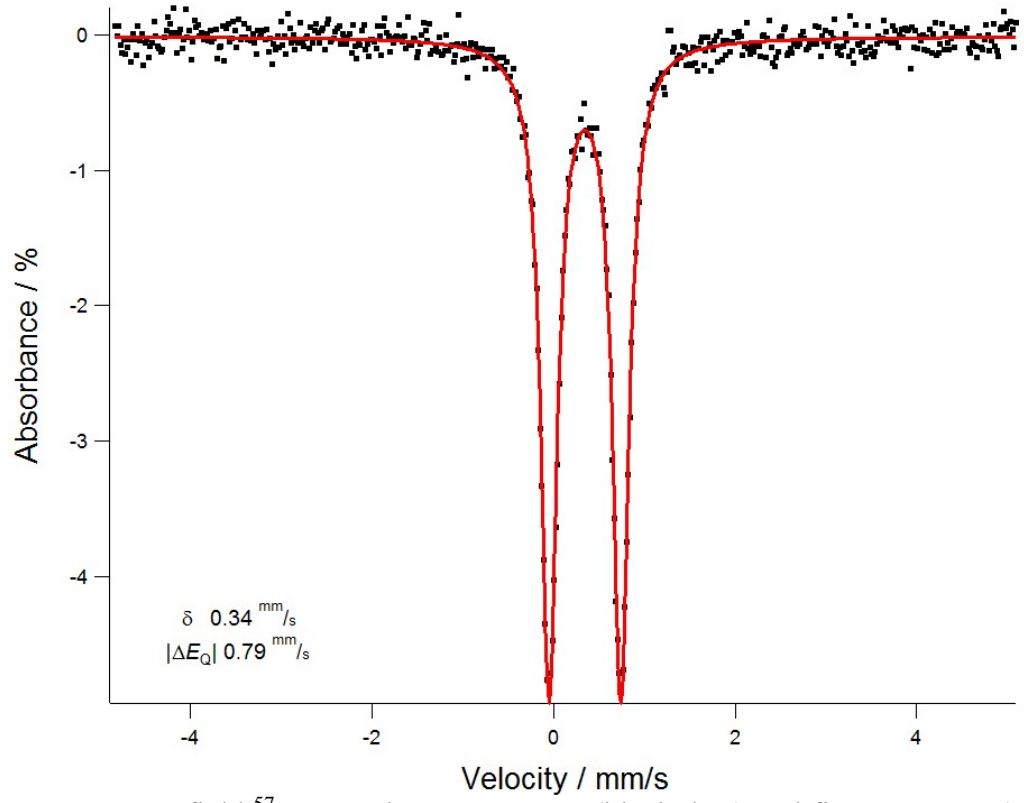

Figure 6.15. Zero-field ^{57}Fe Mössbauer spectrum (black dots) and fit parameters (red trace) of $Fe_4(N{=}CPh_2)_6$ (**6.7**) at 90 K.

6.2.11 Electronic Structure of 6.7

The delocalization of the Fe–Fe bonding electrons and $S = 7$ ground state can be described using group theory (Figure 6.16), as previously reported by Holm and co-workers for Fe_4S_4 clusters.[82-83] The ligand $2p_x$ and $2p_y$ orbitals transform as $(a_1 + e + t_1 + 2t_2)$, which interact with the Fe-based 4s $(a_1 + t_2)$ and 4p $(e + t_1 + t_2)$ orbitals to give 12 σ-bonding orbitals. The Fe 3d orbitals transform as the bonding set $(a_1 + e + t_2)$, the non-bonding set $(e + t_1 + t_2)$, and the antibonding set $(t_1 + t_2)$. The 6 ketimide ligands and 4 Fe enters contribute 18 and 32

valence electrons, respectively, 24 of which completely fill the Fe–N σ-bonding orbitals. The remaining 26 electrons populate the Fe-Fe orbitals in a high-spin configuration $(a_1)^2(e)^4(t_2)^6(e)^2(t_1)^3(t_2)^3(t_1)^3(t_2)^3$, which is consistent with the assignment of an $S = 7$ ground state. Additionally, the overall Fe-Fe bond order of ¾ per Fe is consistent with the observed formal shortness ratio of 1.10.

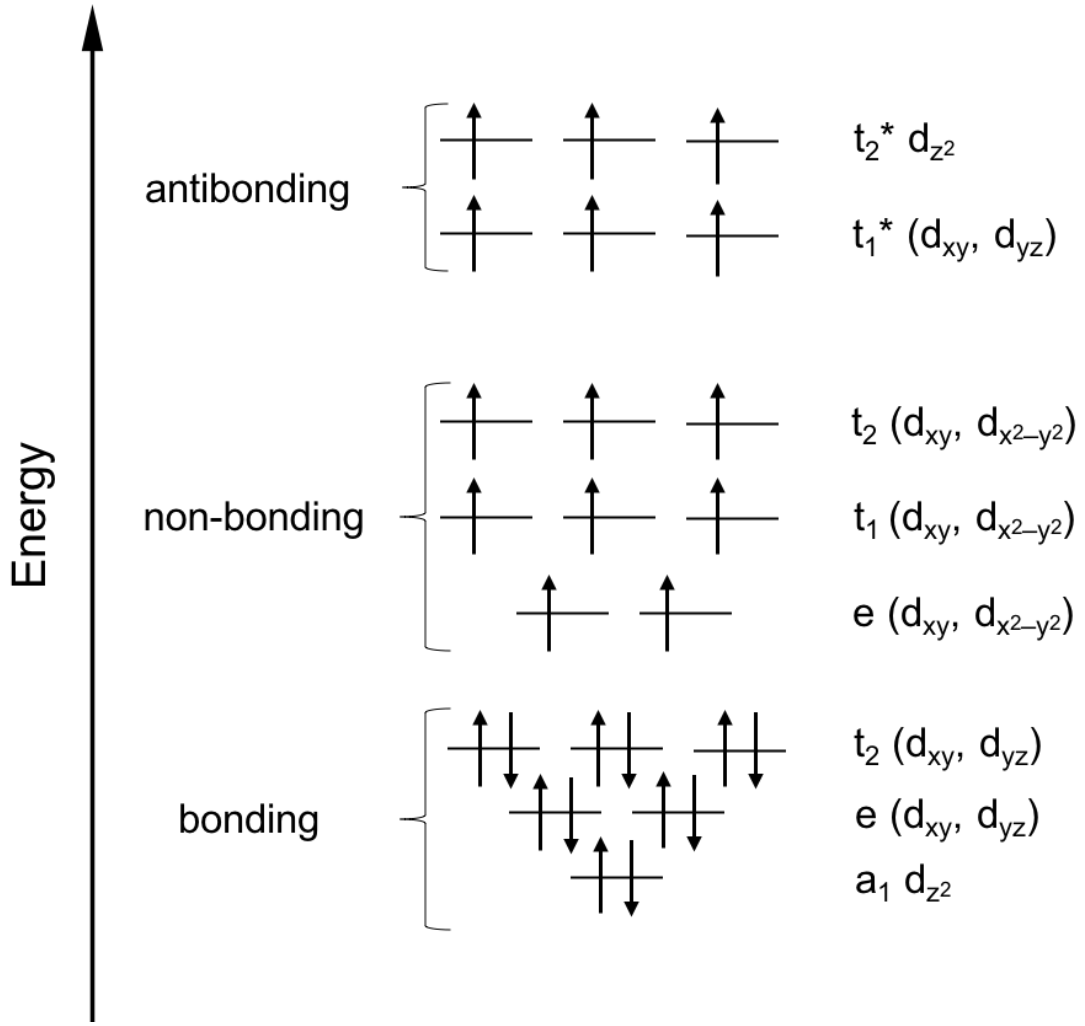

Figure 6.16. Qualitative molecular orbital diagram describing the delocalized Fe d-orbitals. The Fe–N σ-bonding orbitals have been omitted for clarity.

6.3 Summary

I have improved the synthesis of and fully characterized the ketimide complexes of group 10, $Pt(N=C^tBu_2)_2$ (**6.1**) and $Pd_7(N=C^tBu_2)_6$ (**6.5**), as well as investigated the mechanism oftheir formation. I have also expanded on the synthesis of the tetrahedral, mixed-valent iron ketimide cluster $[Fe_4(N=CPh_2)_6]$ (**6.7**) and explored its magnetic susceptibility. Complex **6.1** represents the first linear Pt(II) complex to be reported, expanding the scope of Pt(II) coordination chemistry beyond the more common square planar and T-shaped geometries. Its unusual coordination geometry can be rationalized by its exceptionally covalent M-N interactions, a consequence of the strong π-donor and π-acceptor properties of the linear ketimide ligand. These interactions result in short, highly covalent Pt-N bonds, which stabilize this formally unsaturated, $16e^-$ species. This covalency is also evident in its highly deshielded ^{195}Pt chemical shift and large ^{195}Pt-^{14}N nuclear spin-spin coupling constant. The unsual electronic properties imparted to Pt (as revealed by the unusual ^{195}Pt chemical shift) suggest that other linear $[M(ketimide)_2]^{n+}$ complexes (M = TM and Ln) would also feature interesting electronic strucutres and could potentially possess unique magnetic properites. The generationof species of this type will likely require the use of substantially bulkier ketimide ligands, but because of their relatively straight forward synthesis, this should be easy to achieve.

The isolation of complex **6.5** is also notable. Its isolation demonstrates that ketimides are effective at stabilizing low valent group 10 nanoclusters. This is significant because most nanoclusters of Pd are stabilized with carbonyl co-ligands,[84-90] which significantly tempers their reactivity and limits their utility as catalysts. In contrast, the ketimide co-ligands in complex **6.5** may not hamper the reactivity its Pd centers. In this regard, I have begun to

explore the small molecule reactivity of $Pd_7(N{=}C^tBu_2)_6$ to test this possibility and to study properties of this unique nanocluster.

Complex **6.7** exhibits a fully delocalized electronic ground-state, which results in a room temperature spin ground-state approaching $S = 7$. Mössbauer spectroscopy and SQUID magnetometry confirm the intermediate oxidation state iron centers and delocalization of the charge throughout the cluster. Magnetization data also suggest complex **6.7** acts as a SMM and further studies into this behavior are forthcoming. Previously, the ketimide ligand had been used to stabilize high-valent transition metal complexes and complexes **6.5** and **6.7** represent the first examples of a homoleptic, low-valent ketimide complex. Therefore, I hope to explore the reactivity of **6.7**, especially as its role as a precursor or template to larger clusters. Overall, these complexes provide excellent demonstrations of the unique electronic properties that the ketimide ligand can impart to a metal center.

6.4 Experimental

6.4.1 General Procedures

All reactions and subsequent manipulations were performed under anaerobic and anhydrous conditions in the glovebox under an atmosphere of dinitrogen. Hexanes, diethyl ether (Et_2O), and tetrahydrofuran (THF) were dried by passage over activated molecular sieves using a Vacuum Atmospheres DRI-SOLV solvent purification system. Pentane, toluene, dichloromethane, and benzene were dried on an MBraun solvent purification system. Isooctane and acetonitrile were degassed and stored over activated 3 Å molecular sieves for 72 h prior to use. C_6D_6, dichloromethane-d_2 (CD_2Cl_2), toluene-d_8, THF-d_8, and hexamethyldisiloxane (HMDSO) were dried over activated 3 Å molecular sieves for 24 h prior to use. $Li(N{=}C^tBu_2)$,[91-93] $Na(N{=}C^tBu_2)$,[94] $Li(N{=}CPh_2)$,[95] $PdCl_2(PhCN)_2$[96] and $PtCl_2(PhCN)_2$[97]

were prepared by literature procedures. All other reagents were purchased from commercial suppliers and used as received.

^{1}H, ^{7}Li, and $^{13}C\{^{1}H\}$ NMR spectra were recorded on an Agilent Technologies 400-MR DD2 400 MHz spectrometer or Varian Unity Inova 500 MHz spectrometer at 25 ºC. The chemical shifts of ^{1}H and ^{13}C nuclei were referenced by using the residual solvent peaks (^{1}H NMR experiments) or the characteristic resonances of the solvent nuclei as internal standards ($^{13}C\{^{1}H\}$ NMR experiments).

^{195}Pt NMR spectra were recorded on Varian Mercury Plus 300 MHz spectrometer operating at 64.46 MHz with a 5 mm broad-band probe with the help of Prof. Peter Hrobárik and Dr. Branislav Hvoráth. The ^{195}Pt spectra were measured directly, without ^{1}H decoupling, with spectral widths of 25 kHz, using a 45° excitation pulse and acquisition time of 0.1 s, resulting in 50000 scans. The 2k data sets were zero filled to 8k and an exponential multiplication corresponding to 100 Hz of line broadening was applied to the FIDs prior to Fourier transformation. In view of the ^{195}Pt chemical shift sensitivity and peak broadening to the temperature, the spectra were measured at 25 °C and 50 °C, the latter providing a better resolved multiplet. Unified chemical shift scale was used for ^{195}Pt with 0.1 M aqueous solution of $Na_2[PtCl_6]$ as the external reference [$\delta(^{195}Pt) = 0.0$ ppm].

IR spectra were recorded on a Nicolet 6700 FT-IR spectrometer. UV-Vis/NIR spectra were recorded on a Shimadzu UV3600 UV-NIR spectrometer. Mass spectra were collected by the Mass Spectrometry Facility at the University of California, Santa Barbara, using an electrospray ion (ESI) source on positive ion mode with a Waters Micromass QTOF2 Quadrupole/Time-of-Flight Tandem mass spectrometer. Elemental analyses were performed by the Microanalytical Laboratory at University of California (Berkeley, CA).

6.4.2 Cyclic Voltammetry Measurements

CV experiments were performed with a CH Instruments 600c Potentiostat, and the data were processed using CHI software (version 6.29). All experiments were performed in a glove box using a 5 mL glass vial as the cell. The working electrode consisted of a platinum disk embedded in glass (2 mm diameter), the counter electrode was a platinum wire, and the reference electrode consisted of AgCl plated on Ag wire. Solutions employed during CV studies were typically 1 mM in complex **6.5** and 0.1 M in $[Bu_4N][PF_6]$. All potentials are reported versus the $[Cp_2Fe]^{0/+}$ couple. For all trials, $i_{p,a}/i_{p,c} = 1$ for the $[Cp_2Fe]^{0/+}$ couple, while $i_{p,c}$ increased linearly with the square root of the scan rate (i.e., $\sqrt{v}$). Redox couples which exhibited behavior similar to the $[Cp_2Fe]^{0/+}$ couple were considered reversible.

6.4.3 Zero-Field ^{57}Fe Mössbauer Spectroscopy

Data were collected on a SEECo Model W304 resonant gamma-ray spectrometer (activity = 50 mCi ± 10%), ^{57}Co/Rh source (manufactured by Ritverc) equipped with a Janis Research Model SVT-400 cryostat system. The source linewidth is <0.12 mm/s for the outermost lines of a 25 micron α-Fe foil standard. Isomer shifts are referenced to α-Fe foil at room temperature. All ^{57}Fe Mössbauer samples were prepared using 25 mg of powdered **6.7** suspended in Paratone-N oil and measured at 90 K unless otherwise noted. The sample was loaded into a polypropylene capsule under inert atmosphere, which was subsequently sealed with vacuum grease to prevent exposure to air. The data were fit using a custom Igor Pro (Wavemetrics) macro package developed by the Betley group at Harvard University.

6.4.4 Magnetism Measurements

Magnetic properties were recorded using a Quantum Design Magnetic Property Measurement 5XL Super Conducting Quantum Interference Device (MPMS 5XL SQUID)

magnetometer. Complex **6.7** was analyzed using 11.5 mg of powdered crystalline material loaded into a polypropylene capsule under inert atmosphere, which was subsequently sealed with vacuum grease to prevent exposure to air. The experiments for complex **6.7** were performed between 1.8 and 300 K. Diamagnetic corrections (χ_{dia} = -7.447 × 10^{-4} $cm^3 \cdot mol^{-1}$) were made using Pascal's constants.[98]

6.4.5 Synthesis of Pt(N=C^{t}Bu$_2$)$_2$ (6.1) and [(^{t}Bu$_2$C=N)Pt(μ-*N*,*C*-N=C(^{t}Bu)C(Me)$_2$CH$_2$)-Pt(N=C^{t}Bu$_2$)] (6.2)

In a 20 mL scintillation vial equipped with a magnetic stir bar, $PtCl_2$(1,5-COD) (107.0 mg, 0.286 mmol) was slurried in THF (2 mL) to give white suspension, which was subsequently cooled to -25 ºC. Concurrently, 2 equiv of Li(NC=^{t}Bu$_2$) (88.8 mg, 0.589 mmol) was dissolved in THF (2 mL) to give a colorless solution, which was also cooled to -25 ºC. Over the course of 1 minute, the Li(N=C^{t}Bu$_2$) solution was added dropwise to the stirring suspension of $PtCl_2$(1,5-COD). The reaction mixture immediately became bright yellow, then orange, then gradually dark brown. The reaction mixture was allowed to stir at room temperature for 90 min, whereupon the volatiles were removed *in vacuo* to give an orange-brown oily solid. This solid was triturated with pentane (1 × 1 mL) and then dissolved in pentane (2 mL) and filtered through a Celite column supported on glass wool (0.5 cm × 2 cm) to give a clear orange-brown filtrate, while leaving a white precipitate on the Celite. The filter pad was washed with pentane (2 × 1 mL) and added to the filtrate. The filtrate (in a 5 mL vial) was placed inside of a 20 mL scintillation vial containing 4 mL of isooctane. Storage of this two vial system at -25 °C for 6 d resulted in the deposition of a mixture of red-brown blocks and dark brown blocks (40.4 mg), which were isolated by decanting the supernatant. ^{1}H NMR analysis of this solid (*vide infra*) revealed the presence of **6.1** and **6.2** in an approximately 1:1

molar ratio, corresponding to 22% and 32% yields of **6.1** and **6.2**, respectively. It should be noted that, in my hands, **6.1** and **6.2** could only be isolated as a mixture. In a few instances, I also isolated minute quantities of complex **6.4** as a bright yellow crystalline solid, which was characterized by X-ray crystallography. ^{1}H NMR (C_6D_6, 25 °C, 400 MHz): δ 1.11 (**6.1**, s, 36H, C(C*H*$_3$)$_3$), 1.18 (**6.2**, s, 6H, C(C*H*$_3$)$_2$(CH$_2$)), 1.22 (**6.2**, s, 18H, overlapping C(C*H*$_3$)$_3$), 1.28 (**6.2**, s, 9H, C(C*H*$_3$)$_3$), 1.30 (**6.2**, s, 9H, C(C*H*$_3$)$_3$), 1.46 (**6.2**, s, 9H, C(C*H*$_3$)$_3$), 3.25 (**6.2**, s, 2H, C(CH$_3$)$_2$(C*H*$_2$), $^{2}J_{PtH}$ = 88 Hz). ^{195}Pt NMR (C_6D_6, 25 °C, 66.46 MHz): δ -663 (**6.1**, m, $^{1}J_{PtN}$ = 531 Hz). ^{195}Pt NMR (C_6D_6, 50 °C, 66.46 MHz): δ -629 (**6.1**, quintet, $^{1}J_{PtN}$ = 537 Hz). ESI-MS: *m/z* 476.2674 $[M+H]^+$ (Calcd *m/z* 476.2645), 810.3602 $[Pt_2(N{=}C^tBu_2)_3]^+$ (Calcd *m/z* 810.3633).

6.4.6 Synthesis of [Pt(1,5-COD)(N=C^{t}Bu$_2$)Cl] (6.3)

In a 20 mL scintillation vial equipped with a magnetic stir bar, PtCl2(1,5-COD) (101.0 mg, 0.270 mmol) was slurried in THF (2 mL) to give a white suspension. Then, 1 equiv of Li(NC=tBu2) (40.1 mg, 0.273 mmol) was quickly added as a solid to the PtCl2(1,5-COD) suspension. The reaction mixture immediately turned bright orange. The mixture was allowed to stir at room temperature for 90 min, whereupon the volatiles were removed in vacuo to give an orange oily solid. This solid was triturated with pentane (2 × 1 mL), dissolved in diethyl ether (3 mL), and filtered through a Celite column supported on glass wool (0.5 cm × 2 cm) to give a clear orange filtrate, while leaving a white precipitate on the Celite. The filter pad was washed with diethyl ether (2 × 1 mL) and the washings were added to the filtrate. The filtrate was concentrated in vacuo to 3 mL. Storage of this solution at -25 °C for 1 d resulted in the deposition of orange blocks of **6.3** (59.8 mg, 46% yield), which were isolated by decanting off the supernatant. 1H NMR (C6D6, 25 °C, 400 MHz): δ 1.20 (m, 2H, methylene

CH), 1.44 (m, 2H, methylene CH), 1.50 (s, 18H, C(CH3)3), 1.84 (overlapping m, 4H, methylene CH), 4.22 (m, 2H, CH, 2JPtH = 48 Hz), 4.90 (m, 2H, CH, 2JPtH = 72 Hz). 13C{1H} NMR (C6D6, 25 °C, 100 MHz): δ 29.94 (s, CH2, 2JPtC = 15 Hz), 30.33 (s, CH2, 2JPtC = 13 Hz), 32.45 (s, C(CH3)3), 43.45 (s, C(CH3)3), 91.27 (s, CH, 1JPtC = 208 Hz), 94.48 (s, CH, 1JPtC = 107 Hz), 176.41 (s, N=C). Anal. Calcd. for PtC17H30NCl: C, 42.63; H, 6.31; N, 2.92. Found: C, 42.56; H, 6.13; N, 2.77. IR (KBr pellet, cm-1): 2987 (m), 2951 (s), 2900 (s), 1627 (s), 1604 (m), 1480 (s), 1457 (m), 1430 (w), 1386 (m), 1360 (m), 1335 (w), 1213 (m), 1076 (w), 1029 (w), 1005 (m), 991 (m), 948 (m), 870 (m), 840 (w), 778 (m), 697 (w), 475 (m).

6.4.7 Synthesis of $Pd_7(N{=}C^tBu_2)_6$ (6.5)

In a 20 mL scintillation vial equipped with a magnetic stir bar, $PdCl_2(PhCN)_2$ (106.9 mg, 0.28 mmol) was dissolved in THF (2 mL) to give an orange solution, which was subsequently cooled to -25 ºC. Concurrently, 2 equiv of $Li(N{=}C^tBu_2)$ (82.4 mg, 0.56 mmol) was dissolved in THF (2 mL) to give a colorless solution, which was also cooled to -25 ºC. Over the course of 1 minute, the $Li(N{=}C^tBu_2)$ solution was added dropwise to a stirring solution of $PdCl_2(PhCN)_2$. The resulting mixture immediately turned to a dark forest green color. The reaction mixture was stirred for 5 h, whereupon the volatiles were removed *in vacuo* to give a dark green oily solid. This solid was triturated with pentane (1 × 1 mL) and then was dissolved in pentane (2 mL) and filtered through a Celite column supported on glass wool (0.5 cm × 2 cm) to give a clear dark green filtrate, while leaving a white precipitate on the Celite. The filter pad was washed with pentane (2 × 1 mL) and added to the filtrate. The filtrate (in a 5 mL vial) was placed inside of a 20 mL scintillation vial containing 4 mL of isooctane. Storage of this two-vial system at -25 °C for 7 d resulted in the deposition of dark green blocks

of **6.5**, which were isolated by decanting the supernatant (25.5 mg, 40% yield). The ^{1}H NMR data for this sample also reveals the presence of a small amount of [(^{t}Bu$_2$C=N)Pd(μ-N,C-*N*=C(^{t}Bu)C(Me)$_2$*C*H$_2$)Pd(N=C^{t}Bu$_2$)] (**6.6**). Complexes **6.5** and **6.6** were present in a 6:1 ratio. All attempts to isolate **6.6** have thus far been unsuccessful. ^{1}H NMR (C_6D_6, 25°C, 400 MHz): δ 1.15 (**6.6**, s, 9H, C(C*H*$_3$)$_3$), 1.27 (**6.6**, s, 9H, C(C*H*$_3$)), 1.28 (**6.6**, s, 9H, C(C*H*$_3$)$_3$), 1.47 (**6.6**, s, 9H, C(C*H*$_3$)$_3$), 1.49 (**6.6**, s, 6H, C(C*H*$_3$)$_2$(CH$_2$)), 1.53 (**6.6**, s, 9H, C(C*H*$_3$)$_3$), 1.65 (**6.5**, s, 108H, C(C*H*$_3$)$_3$), 3.08 (**6.6**, s, 2H, C(CH$_3$)$_2$(C*H*$_2$)). ^{13}C{^{1}H} NMR (C_6D_6, 25 °C, 126 MHz): δ 32.97 (s, C(*C*H$_3$)$_3$), 42.83 (s, *C*(CH$_3$)$_3$), 180.97 (s, N=*C*). Anal. Calcd. for $C_{54}H_{108}N_6Pd_7$: C, 40.88; H, 6.86; N, 5.30. Found: C, 40.75; H, 6.66; N, 5.04. IR (KBr pellet, cm^{-1}): 3003 (m), 2946 (s), 2922 (s), 1579 (ν(C=N), s), 1566 (ν(C=N), s), 1477 (s), 1443 (s), 1383 (m), 1360 (s), 1260 (vw), 1214 (s), 1103 (w), 1042 (w), 973 (w), 925 (w), 840 (w), 688 (w), 668 (w). UV-Vis / NIR (pentane, 18.9 μM, 25 °C, L·mol^{-1}·cm^{-1}) 251 nm (ε = 99,900), 290 nm (sh, ε = 69,500), 369 nm (ε = 56,200), 420 nm (sh, ε = 33,400), 604 nm (ε = 17,100), 771 nm (ε = 16,300). ESI-MS: *m/z* 1586.2362 [M]$^{+}$ (Calcd *m/z* 1586.1953), 740.1635 [Pd$_3$(N=C^{t}Bu$_2$)$_3$]$^{+}$ (Calcd *m/z* 740.1459).

6.4.8 Synthesis of $Fe_4(N=CPh_2)_6$ (6.7)

In a 20 mL scintillation vial equipped with a magnetic stir bar, $FeBr_2$ (322.0 mg, 1.49 mmol) was slurried in THF (10 mL) to give an orange-brown suspension, which was subsequently cooled to -25 °C. Concurrently, LiN=CPh$_2$ (421.0 mg, 2.25 mmol) was dissolved in THF (6 mL) to give a red solution, which was also cooled to -25 °C. Over the course of 5 min, the LiN=CPh$_2$ was added dropwise to the stirring suspension of $FeBr_2$. The reaction mixture immediately became red-brown and was allowed to stir at room temperature for 10 min over which time all of the $FeBr_2$ had dissolved. At this point Zn powder (200 mg, 3.06

mmol) was added to the reaction mixture with no immediate change. The reaction mixture was allowed to stir for 18 h at room temperature over which time the solution became dark brown and a brown-black precipitate had formed. Also present in the reaction mixture was a gray powder of unreacted Zn. The solvents were removed *in vacuo* to give a brown oily solid. This solid was triturated with pentane (3 × 2 mL) to give a tacky brown powder. This solid was then dissolved in Et_2O (2 mL) and filtered through a Celite column supported on glass wool (0.5 cm × 5 cm) to give a light brown filtrate, while leaving behind a dark brown solid. The filter pad was washed with Et_2O (5 × 2 mL) until the washings were nearly colorless and the washings were added to the filtrate. The Et_2O filtrate was then discarded. The remaining brown solids were washed with warm (ca. 80 °C) toluene (15 × 2 mL) until the washings were colorless and mixture of gray, brown, and white powders remained on the filter pad. The brown toluene solution was then concentrated i*n vacuo* to 6 mL and layered with pentane (12 mL). Storage of this system at -25 °C for 48 h yielded a brown microcrystalline powder. These solids were isolated by decanting the brown supernatant and were then washed with pentane (3 × 2 mL). The washings were subsequently discarded. The brown powder was dried *in vacuo* to yield **6.7** (213.0 mg, 44%). Crystals suitable for X-ray crystallography were obtained from a solution of **6.7** (10.0 mg) in toluene (1 mL) stored at -25 °C for 24 h. Anal. Calcd for $C_{78}H_{60}Fe_4N_6$: C, 71.80; H, 4.64; N, 6.44. Found: C, 71.49; H, 5.01; N, 6.52. ^{1}H NMR (400 MHz, 25 °C, C_6D_6): δ 8.56 (br s, *p*-Ph, 6H), 30.88 (br s, *m*-Ph, 12H), 57.29 (br s, *o*-Ph, 12H). ^{1}H NMR (400 MHz, 25 °C, THF-d_8): δ 8.46 (br s, *p*-Ph, 6H), 31.22 (br s, *m*-Ph, 12H). ^{1}H NMR (500 MHz, 25 °C, toluene-d_8): δ 8.50 (br s, *p*-Ph, 6H), 30.35 (br s, *m*-Ph, 12H), 55.65 (br s, *o*-Ph, 12H). ESI-MS: *m/z* 1304.2397 [M^-] (Calcd *m/z* 1304.2262). UV-Vis/NIR (toluene, 76.7 μM, 25 C, $L \cdot mol^{-1} \cdot cm^{-1}$): 400 nm (sh, ε = 7700), 540 nm (ε = 5300). IR (KBr pellet, cm^-

[1]): 479 (m), 623 (m), 644 (m), 670 (m), 696 (s), 731 (m), 787 (s), 846 (w), 899 (w), 932 (w), 972 (w), 1000 (w), 1027 (m), 1075 (m), 1156 (w), 1178 (w), 1242 (m), 1308 (w), 1394 (w), 1444 (m), 1489 (w), 1567 (s), 1593 (s), 1619 (s), 2852 (w), 2920 (m), 2956 (w), 3025 (m), 3054 (m). Zero-field ^{57}Fe Mössbauer [(90 K), δ, $|\Delta E_Q|$ (mm/s)]: 0.34, *0.79*.

6.4.9 X-ray Crystallography

Data for **6.2** – **6.7**·7.5C_7H_8 were collected on a Bruker KAPPA APEX II diffractometer equipped with an APEX II CCD detector using a TRIUMPH monochromater with a Mo Kα X-ray source (α = 0.71073 Å). The crystals of **6.2** – **6.7**·7.5C_7H_8 were mounted on a cryoloop under Paratone-N oil, and all data were collected at 100(2) K using an Oxford nitrogen gas cryostream system. X-ray data for **6.2 – 6.4**·0.5C_5H_{12} and **6.7**·7.5C_7H_8 were collected utilizing frame exposures of 10 seconds and 30 seconds, respectively. Data collection and cell parameter determination were conducted using the SMART program.[99] Integration of the data frames and final cell parameter refinement were performed using SAINT software.[100] Absorption corrections of the data for **6.2 – 6.7**·7.5C_7H_8 were carried out using the multi-scan method SADABS.[101] Subsequent calculations were carried out using SHELXTL.[102] Structure determination was done using direct or Patterson methods and difference Fourier techniques. All hydrogen atom positions were idealized, and rode on the atom of attachment.

The 1,5-COD ligand in complex **6.4**·0.5C_5H_{12} contained some minor positional disorder. As a result, the temperature factors of C31 and C32 were constrained with the EADP command. In addition, the pentane solvate in complex **6.4**·0.5C_5H_{12} was found to be disordered over two positions in a 50:50 ratio. Complex **6.7**·7.5C_7H_8 contains positional disorder in several atoms of the N=CPh_2 ligands. In all instances, the anisotropic temperature factors for these atoms were constrained using the EADP command. Due to positional

disorder, all of the C_7H_8 solvate molecules were refined isotropically. In one instance (C301 – C304), the C–C bond distances of the C_7H_8 solvate were fixed using the SADI command. In this solvate molecule, the methyl group (C304) was modelled over two positions and the other half of the molecule was generated using the eqiv command. As such, the hydrogen atom was not assigned to C302.

Further crystallographic details for complexes **6.2 – 6.7**·7.5C_7H_8 can be found in Table 6.1 and Table 6.2.

Table 6.1. Crystallographic details for complexes **6.2** – **6.4**·0.5C_5H_{12}.

	6.2	**6.3**	**6.4**·0.5C_5H_{12}
Formula	$Pt_2C_{27}H_{53}N_3$	$PtC_{17}H_{30}NCl$	$Pt_2C_{40.5}H_{83}N_3$
Crystal Habit, Color	Block, Brown	Block, Orange	Block, Yellow
Crystal Size (mm)	0.20 × 0.20 × 0.05	0.20 × 0.10 × 0.10	0.15× 0.15 × 0.05
MW (g/mol)	809.90	478.96	1062.32
Crystal System	Monoclinic	Orthorhombic	Triclinic
Space Group	$P2_1/n$	$Pna2_1$	P-1
a (Å)	12.581(3)	29.276(3)	11.016(3)
b (Å)	12.315(3)	8.0362(9)	13.921(4)
c (Å)	20.571(5)	7.4414(8)	15.334(4)
α (°)	90	90	83.268(7)
β (°)	104.566(6)	90	72.405(7)
γ (°)	90	90	83.753(7)
V ($Å^3$)	3084.8(12)	1750.7(3)	2219.4(10)
Z	4	4	2
T (K)	100(2)	100(2)	100(2)
λ (Å)	0.71073	0.71073	0.71073
GOF	1.339	0.993	0.995
Density (calcd) (Mg/m^3)	1.744	1.817	1.590
Absorption Coefficient (mm^{-1})	9.077	8.159	6.329
F_{000}	1568	936	1066
Total no Reflections	11666	7415	19279
Unique Reflections	6481	3036	9793
Final R indices*	$R_1 = 0.0535$	$R_1 = 0.0190$	$R_1 = 0.0403$
	$wR_2 = 0.0977$	$wR_2 = 0.0405$	$wR_2 = 0.0672$
Largest Diff. peak and hole ($e^- A^{-3}$)	6.497, -3.069	1.426, -0.964	1.459, -2.142

* For [I > 2σ(I)]

Table 6.2. Crystallographic details for complex **6.7**·7.5C_7H_8

	6.7·7.5C_7H_8
Formula	$Fe_8N_{12}C_{208.5}H_{180}$
Crystal Habit, Color	Plate, brown
Crystal Size (mm)	0.20 × 0.15 × 0.10
MW (g/mol)	3300.43
Crystal System	Triclinic
Space Group	$P\bar{1}$
a (Å)	19.2992(9)
b (Å)	19.3512(13)
c (Å)	27.2060(12)
α (°)	105.998(4)
β (°)	90.079(3)
γ (°)	119.907(3)
V ($Å^3$)	8348.0(8)
Z	2
T (K)	100(2)
λ (Å)	0.71073
GOF	0.770
Density (calcd) (Mg/m^3)	1.313
Absorption Coefficient (mm^{-1})	0.735
F_{000}	3446.0
Total no Reflections	26427
Unique Reflections	17842
Final R indices*	R_1 = 0.1596
	wR_2 = 0.3992
Largest Diff. peak and hole ($e^- A^{-3}$)	1.524 and -0.980

6.5 Appendix

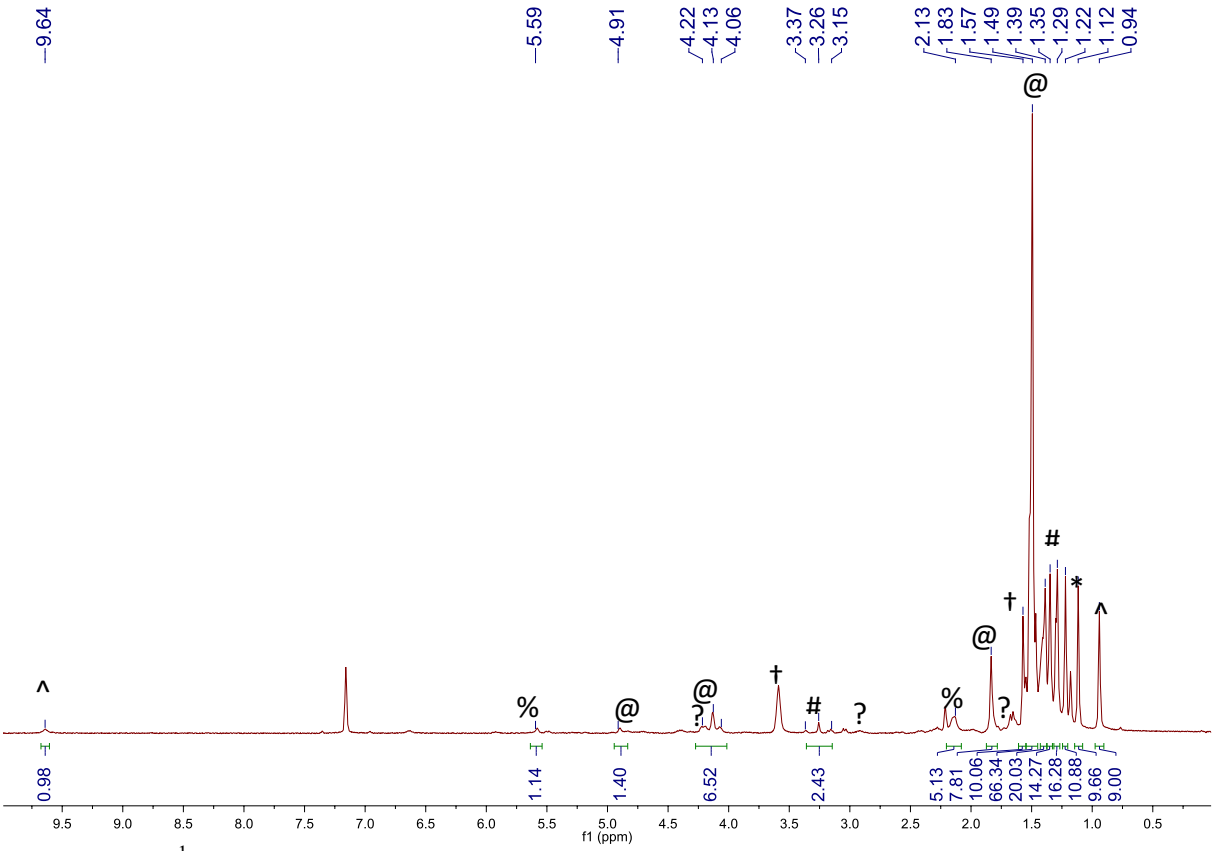

Figure A6.1. ^{1}H NMR spectrum taken in C_6D_6 of an aliquot of the reaction between $PtCl_2$(1,5-COD) with 2 equiv of Li(N=C^{t}Bu$_2$) after 20 minutes. (*) denotes resonance assignable to Pt(N=C^{t}Bu$_2$)$_2$ (**6.1**), (#) denotes resonances assignable to [(^{t}Bu$_2$C=N)Pt(μ-*N*,*C*-N=C(^{t}Bu)C(Me)$_2$CH$_2$)Pt(N=C^{t}Bu$_2$)] (**6.2**), (^) denotes resonances assignable to H(N=C^{t}Bu$_2$), and (†) denotes a resonance assignable to THF. (%) denotes resonances tentatively assigned to [Pt(N=C^{t}Bu$_2$)$_2$(μ-η^4:η^1-C$_8$H$_{11}$)Pt(N=C^{t}Bu$_2$)(1,5-COD)] (**6.4**) and (@) denotes resonances assignable to [Pt(1,5-COD)(N=C^{t}Bu$_2$)Cl] (**6.3**). (?) denotes resonances that are thus far unassigned.

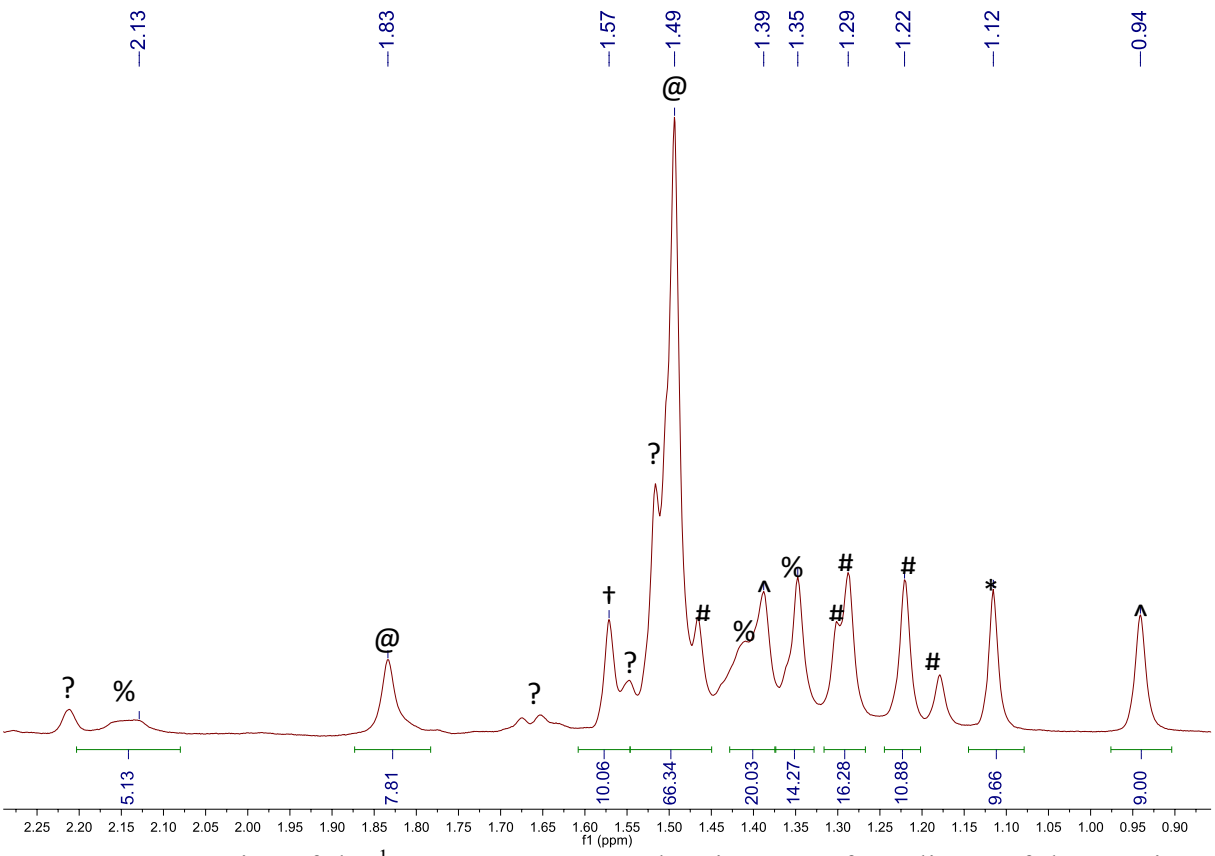

Figure A6.2. Portion of the ^{1}H NMR spectrum taken in C_6D_6 of an aliquot of the reaction between $PtCl_2$(1,5-COD) with 2 equiv of Li(N=C^{t}Bu$_2$) after 20 minutes. (*) denotes resonance assignable to Pt(N=C^{t}Bu$_2$)$_2$ (**6.1**), (#) denotes resonances assignable to [(^{t}Bu$_2$C=N)Pt(μ-*N*,*C*-N=C(^{t}Bu)C(Me)$_2$CH$_2$)Pt(N=C^{t}Bu$_2$)] (**6.2**), (^) denotes resonances assignable to H(N=C^{t}Bu$_2$), and (†) denotes a resonance assignable to THF. (%) denotes resonances tentatively assigned to [Pt(N=C^{t}Bu$_2$)$_2$(μ-η^4:η^1-C$_8$H$_{11}$)Pt(N=C^{t}Bu$_2$)(1,5-COD)] (**6.4**) and (@) denotes resonances assignable to [Pt(1,5-COD)(N=C^{t}Bu$_2$)Cl] (**6.3**). (?) denotes resonances that are thus far unassigned.

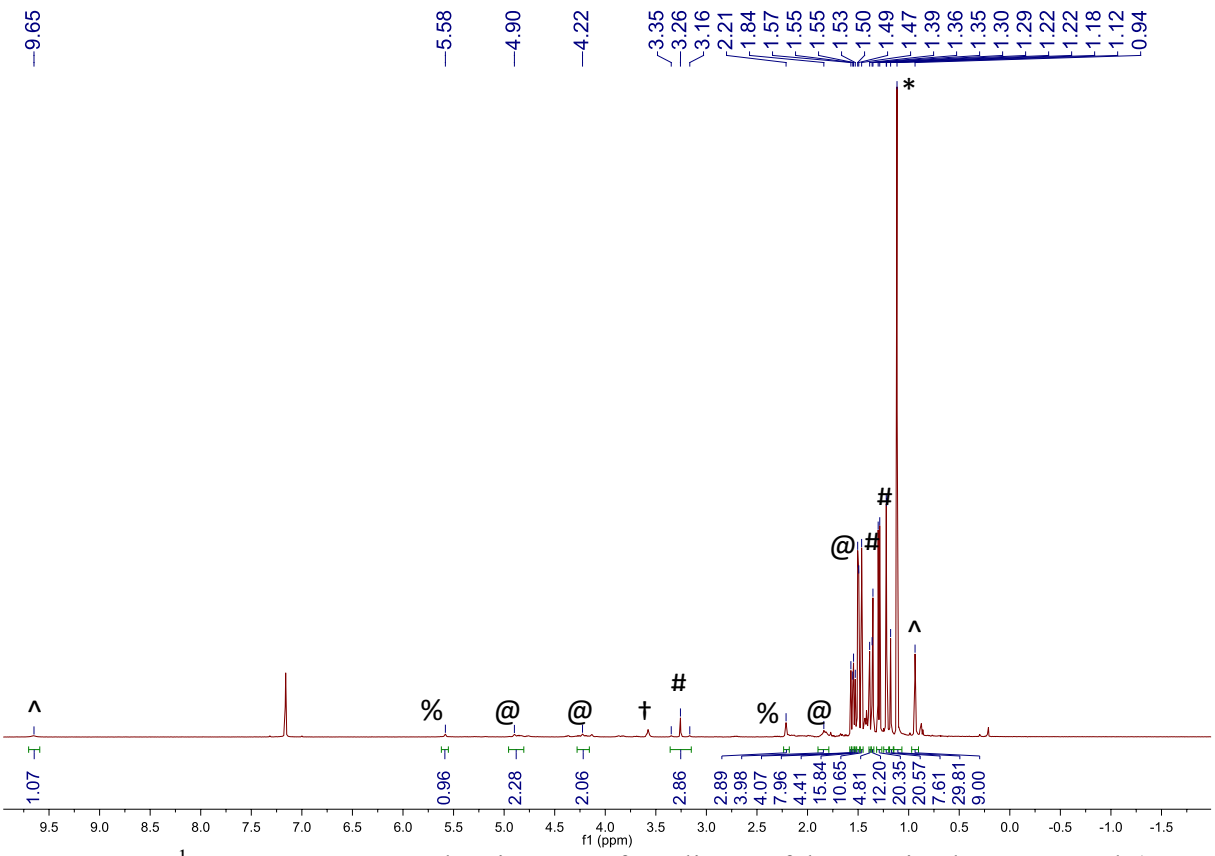

Figure A6.3. ^{1}H NMR spectrum taken in C_6D_6 of an aliquot of the reaction between $PtCl_2$(1,5-COD) with 2 equiv of Li(N=C^{t}Bu$_2$) after 90 minutes. (*) denotes resonance assignable to Pt(N=C^{t}Bu$_2$)$_2$ (**6.1**), (#) denotes resonances assignable to [(^{t}Bu$_2$C=N)Pt(μ-*N*,*C*-N=C(^{t}Bu)C(Me)$_2$CH$_2$)Pt(N=C^{t}Bu$_2$)] (**6.2**), (^) denotes resonances assignable to H(N=C^{t}Bu$_2$), and (†) denotes a resonance assignable to THF. (@) denotes resonances assignable to [Pt(1,5-COD)(N=C^{t}Bu$_2$)Cl] (**6.3**) and (%) denotes resonances tentatively assignable to [Pt(N=C^{t}Bu$_2$)$_2$(μ-η^4:η^1-C$_8$H$_{11}$)Pt(N=C^{t}Bu$_2$)(1,5-COD)] (**6.4**). All other resonances are thus far unassigned.

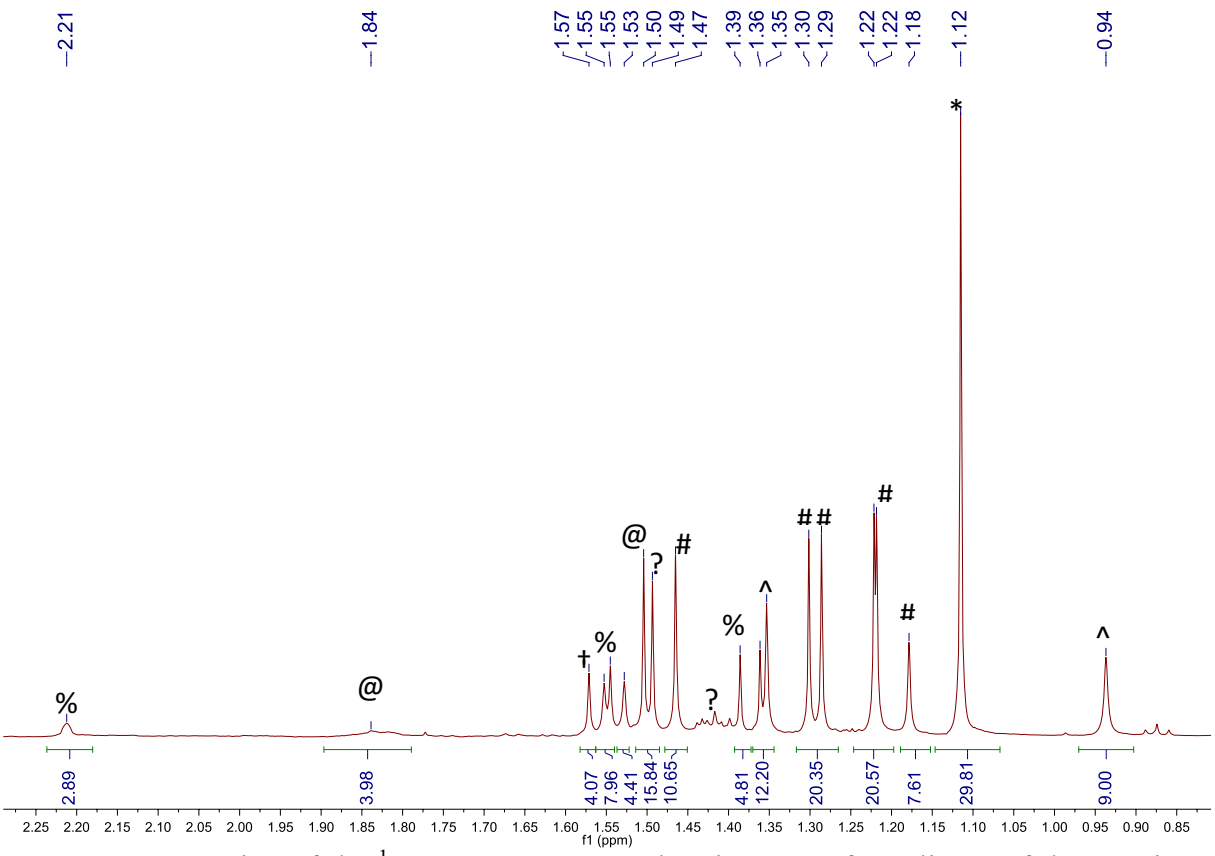

Figure A6.4. Portion of the ^{1}H NMR spectrum taken in C_6D_6 of an aliquot of the reaction between $PtCl_2$(1,5-COD) with 2 equiv of Li(N=C^{t}Bu$_2$) after 90 minutes. (*) denotes resonance assignable to Pt(N=C^{t}Bu$_2$)$_2$ (**6.1**), (#) denotes resonances assignable to [(^{t}Bu$_2$C=N)Pt(μ-*N*,*C*-N=C(^{t}Bu)C(Me)$_2$CH$_2$)Pt(N=C^{t}Bu$_2$)] (**6.2**), (^) denotes resonances assignable to H(N=C^{t}Bu$_2$), and (†) denotes a resonance assignable to THF. (@) denotes resonances assignable to [Pt(1,5-COD)(N=C^{t}Bu$_2$)Cl] (**6.3**) and (%) denotes resonances tentatively assignable to [Pt(N=C^{t}Bu$_2$)$_2$(μ-η^4:η^1-C$_8$H$_{11}$)Pt(N=C^{t}Bu$_2$)(1,5-COD)] (**6.4**). (?) denotes resonances that are thus far unassigned.

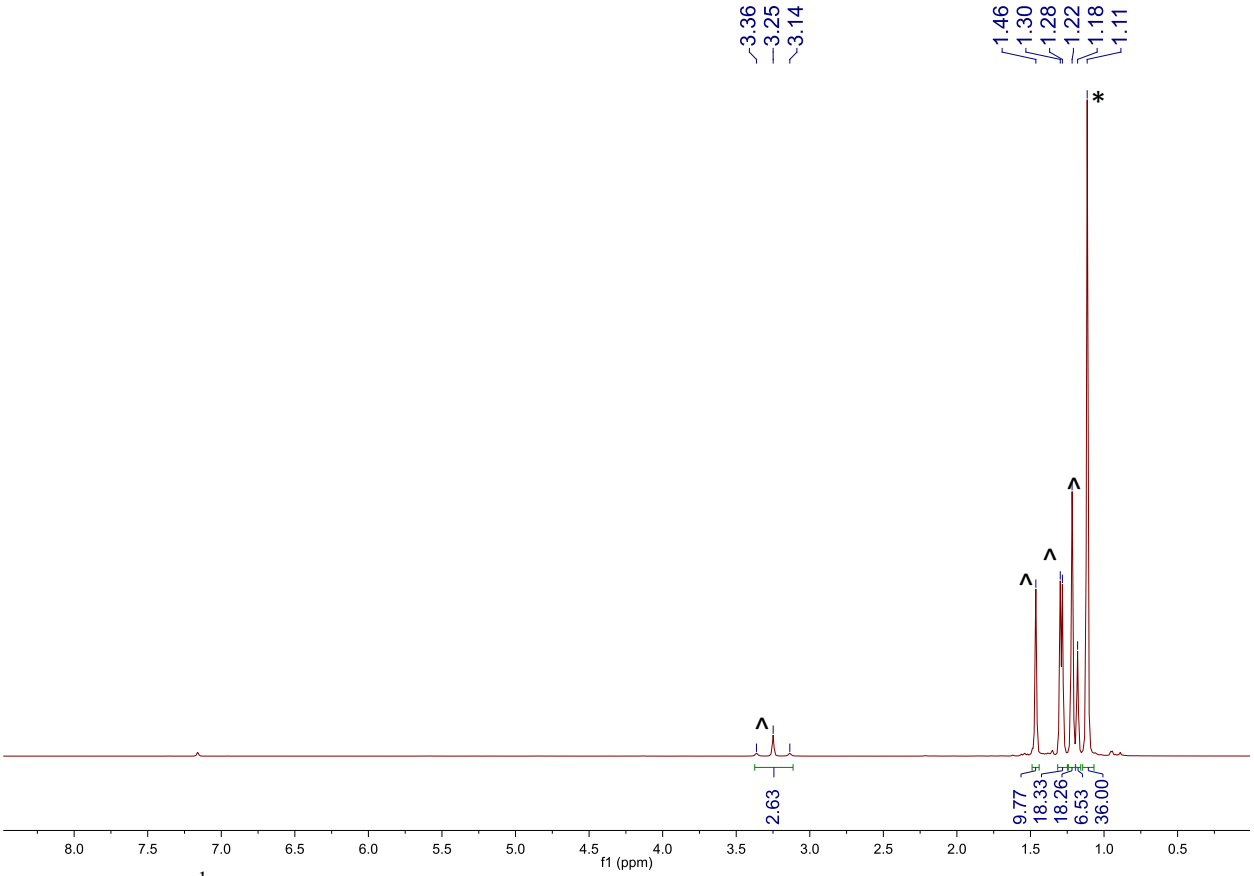

Figure A6.5. ^{1}H NMR spectrum of an isolated mixture of **6.1** (*) and **6.2** (^), in an approximately 1:1 molar ratio, in C_6D_6.

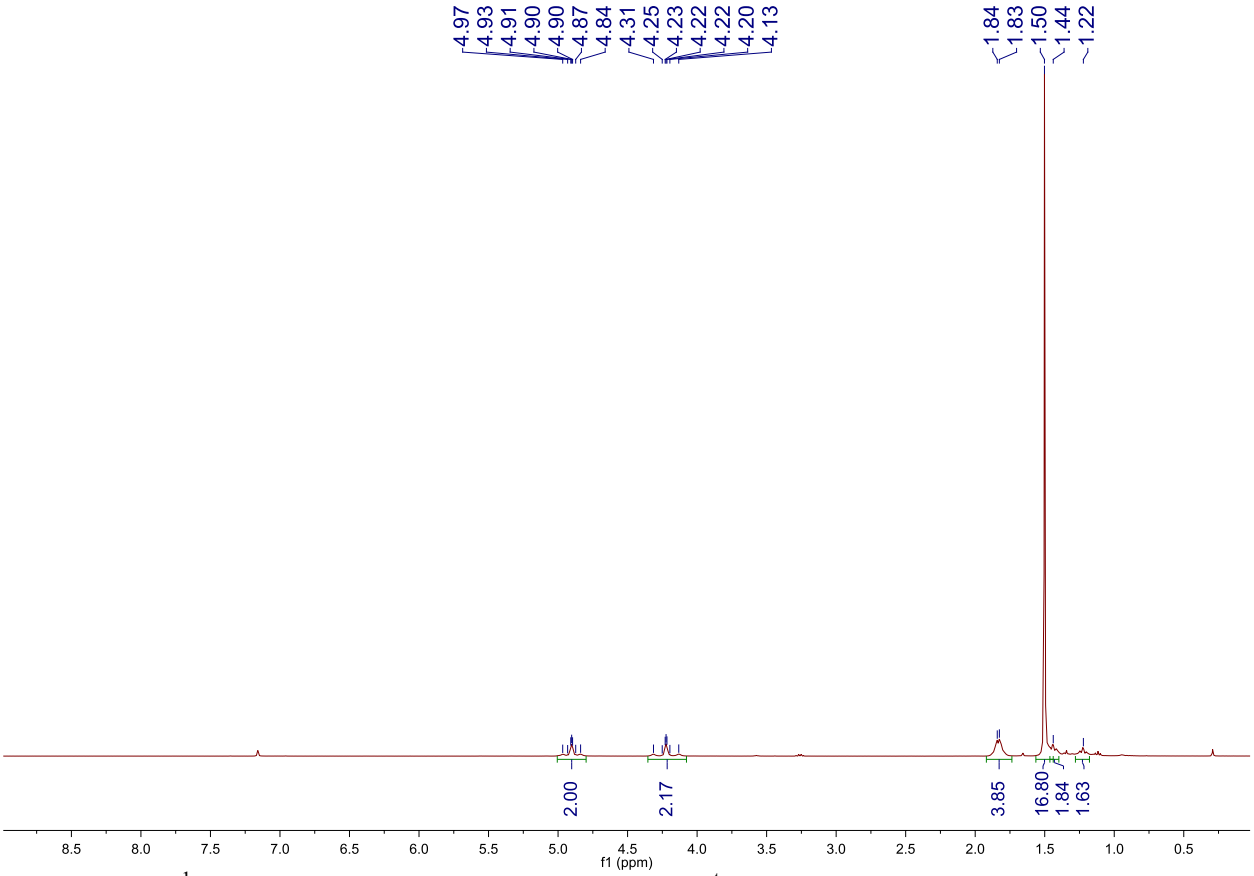

Figure A6.6. ^{1}H NMR spectrum of [Pt(1,5-COD)(N=C^{t}Bu$_2$)Cl] (**6.3**) in C_6D_6.

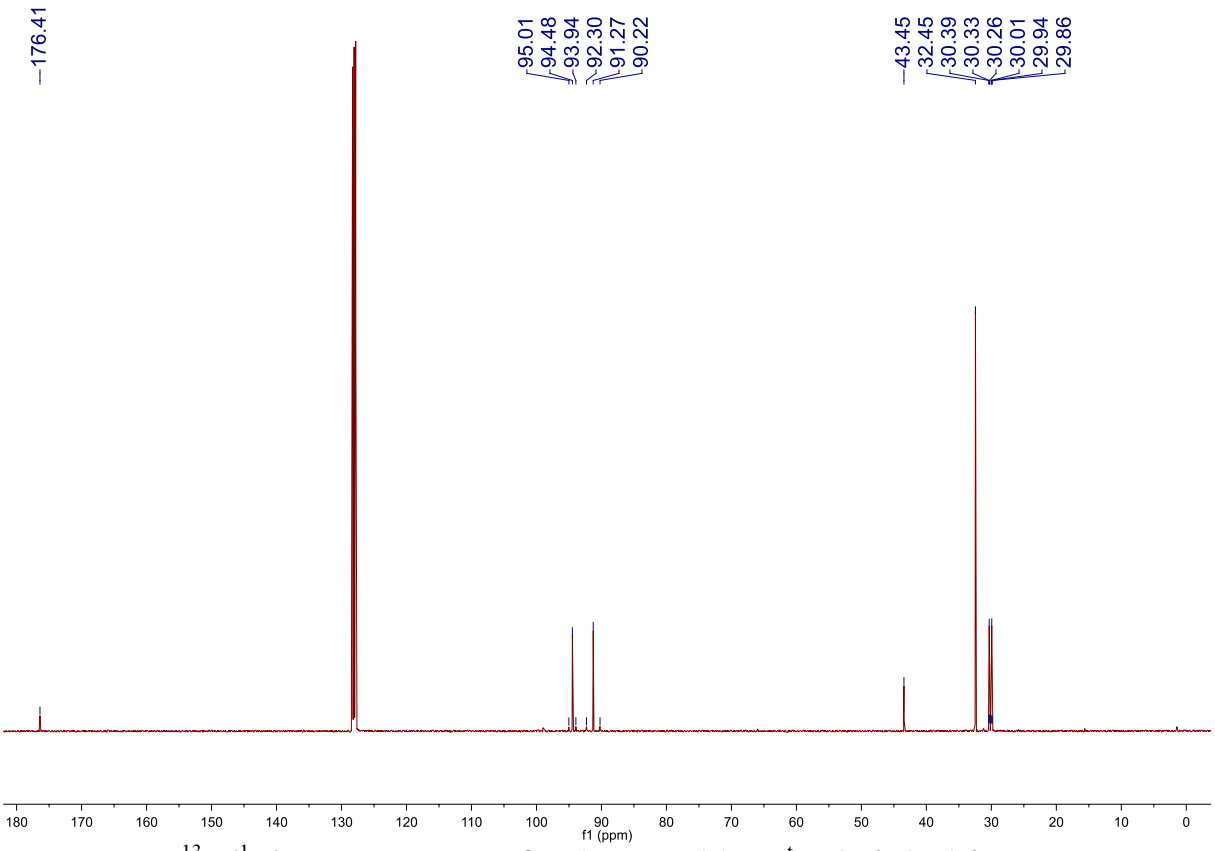

Figure A6.7. $^{13}C\{^{1}H\}$ NMR spectrum of [Pt(1,5-COD)(N=C^{t}Bu$_2$)Cl] (**6.3**) in C_6D_6.

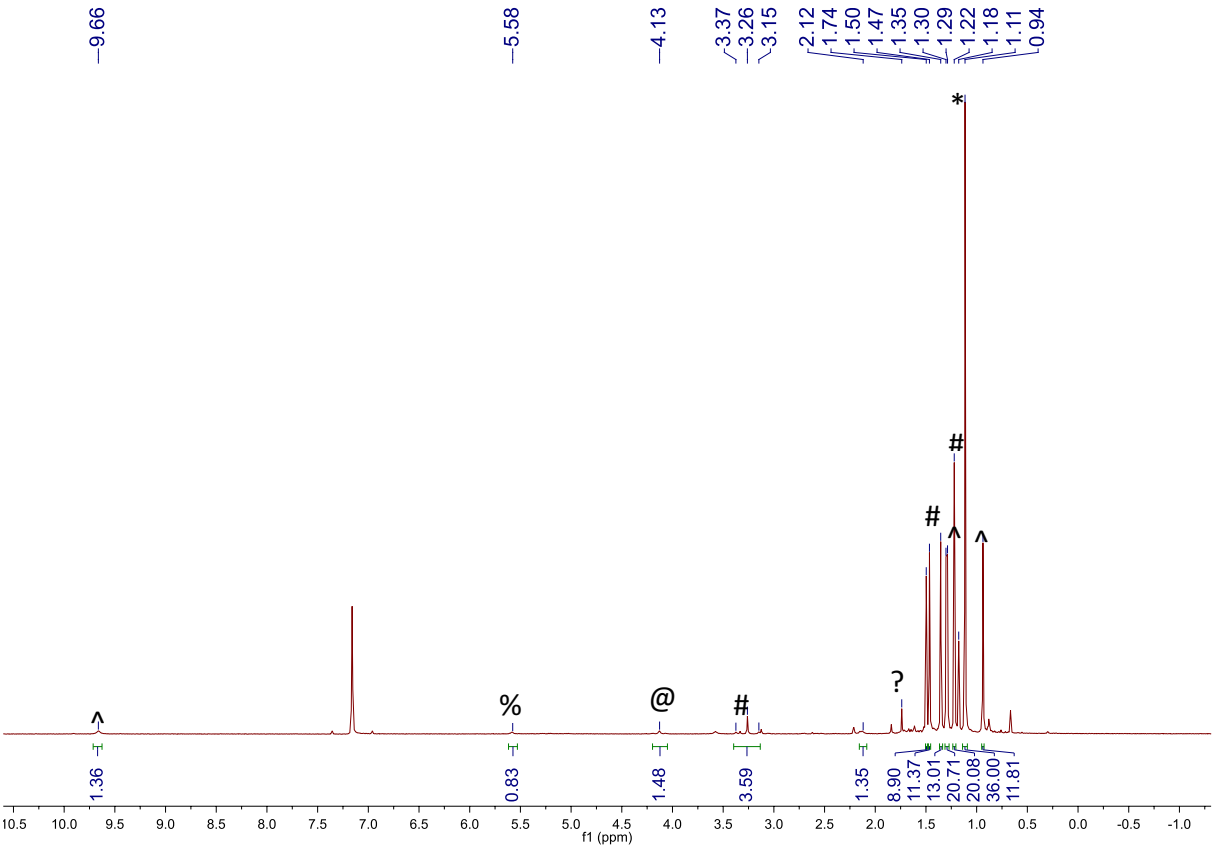

Figure A6.8. ^{1}H NMR spectrum, taken in C_6D_6, of an aliquot taken after 90 min from the reaction between **6.3** and 1 equiv of Li(N=C^{t}Bu$_2$). **Experimental details:** To a stirring, orange solution of 6.3 (39.0 mg, 0.0815 mmol) in THF (1 mL), chilled to -25 ºC, was added dropwise a cold (-25 °C) slurry of Li(N=C^{t}Bu$_2$) (12 mg, 0.0816 mmol) in THF (3 mL). After 90 min, an aliquot (0.5 mL) of the reaction mixture was removed from the reaction vial and the volatiles were removed *in vacuo*. The resulting brown oil was then dissolved in C_6D_6 (1 mL) and a ^{1}H NMR spectrum was collected. (*) denotes a resonance assignable to Pt(N=C^{t}Bu$_2$)$_2$ (**6.1**), (#) denotes resonance assignable to [(^{t}Bu$_2$C=N)Pt(μ-*N*,*C*-N=C(^{t}Bu)C(Me)$_2$CH$_2$)Pt(N=C^{t}Bu$_2$)] (**6.2**), and (^) denotes resonances assignable to H(N=C^{t}Bu$_2$). (%) denotes a resonance tentatively assignable to [Pt(N=C^{t}Bu$_2$)$_2$(μ-η^4:η^1-C$_8$H$_{11}$)Pt(N=C^{t}Bu$_2$)(1,5-COD)] (**6.4**). The molar ratio of **6.1** to **6.2** in this aliquot was approximately 1:1. (?) denotes resonances that are thus far unassigned.

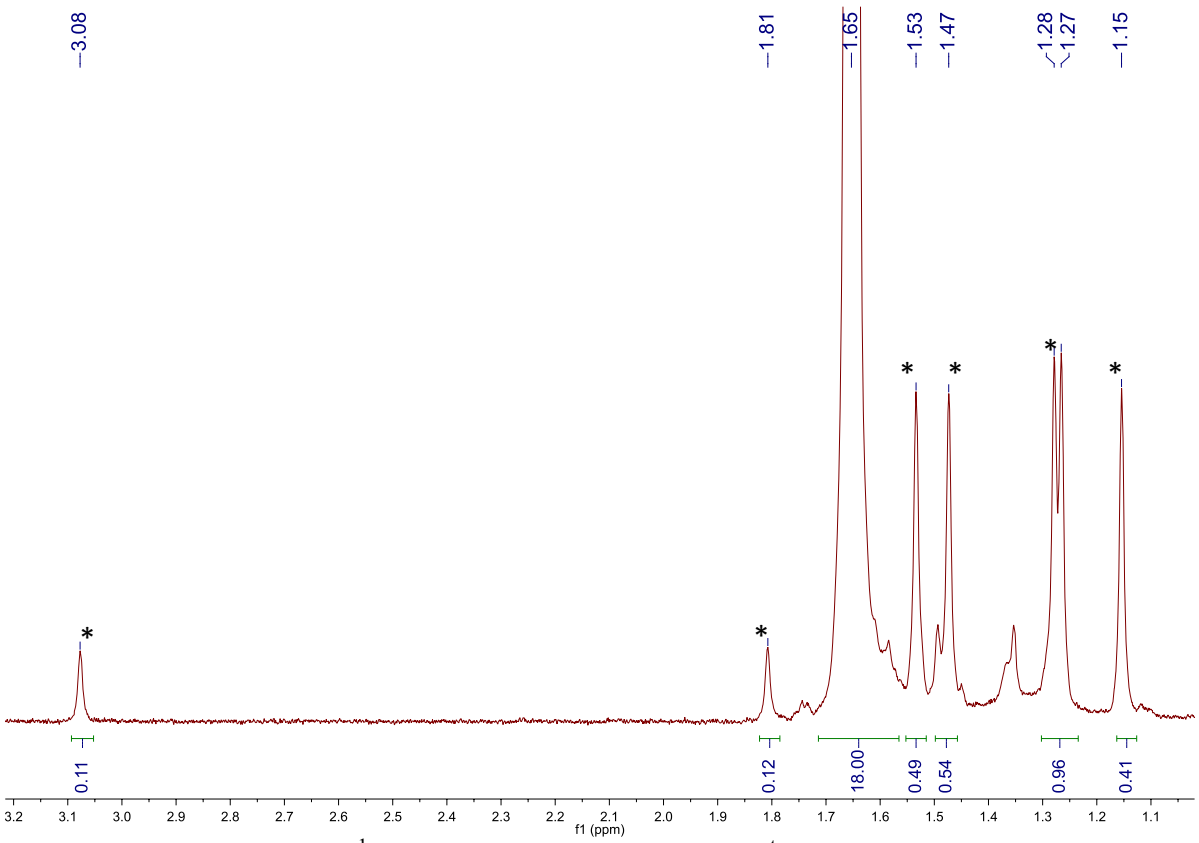

Figure A6.9. Portion of a ^{1}H NMR spectrum of $Pd_7(N{=}C^tBu_2)_6$ (**6.5**) in C_6D_6. (*) denotes resonances assignable to complex **6.6**.

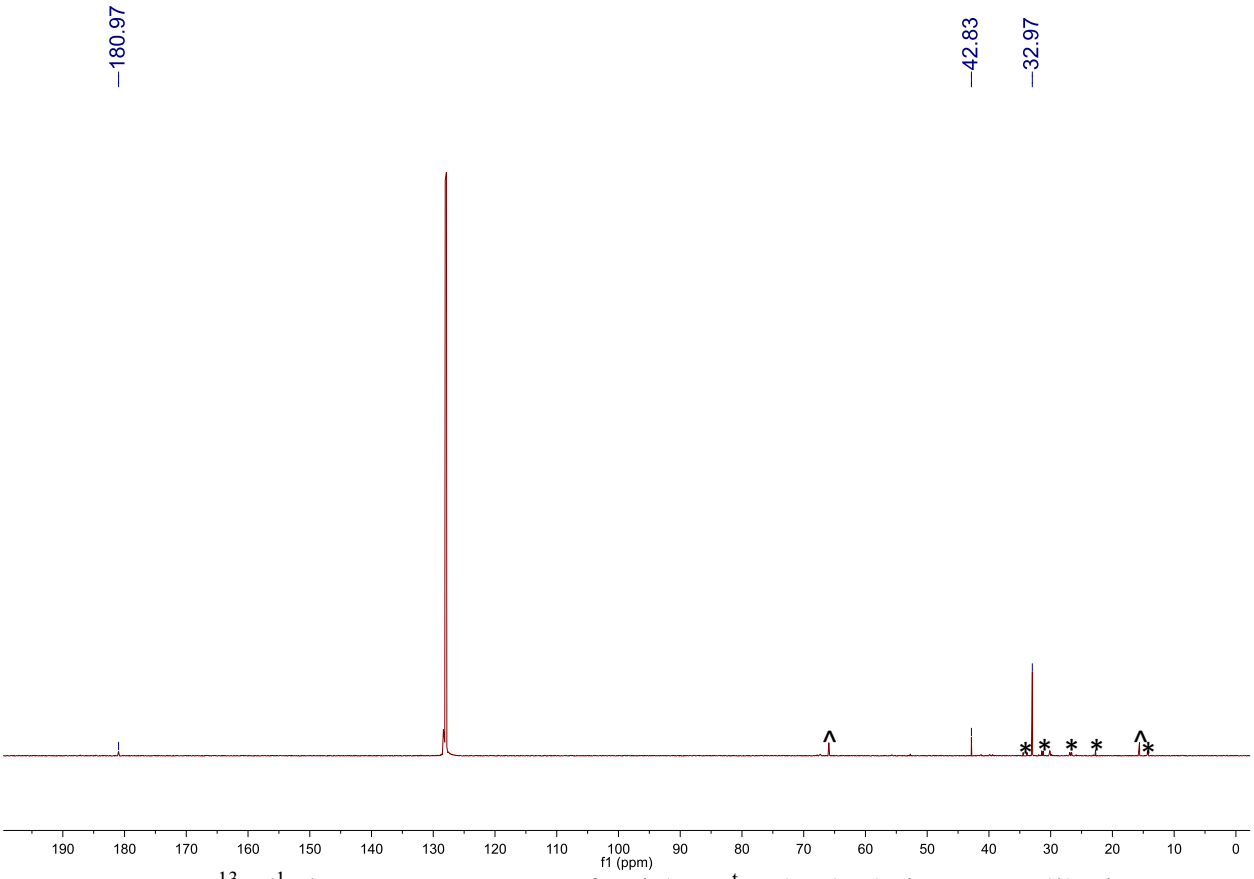

Figure A6.10. $^{13}C\{^{1}H\}$ NMR spectrum of $Pd_7(N{=}C^tBu_2)_6$ (**6.5**) in C_6D_6. (*) denotes resonances assignable to complex **6.6** and (^) denotes a resonance assignable to diethyl ether.

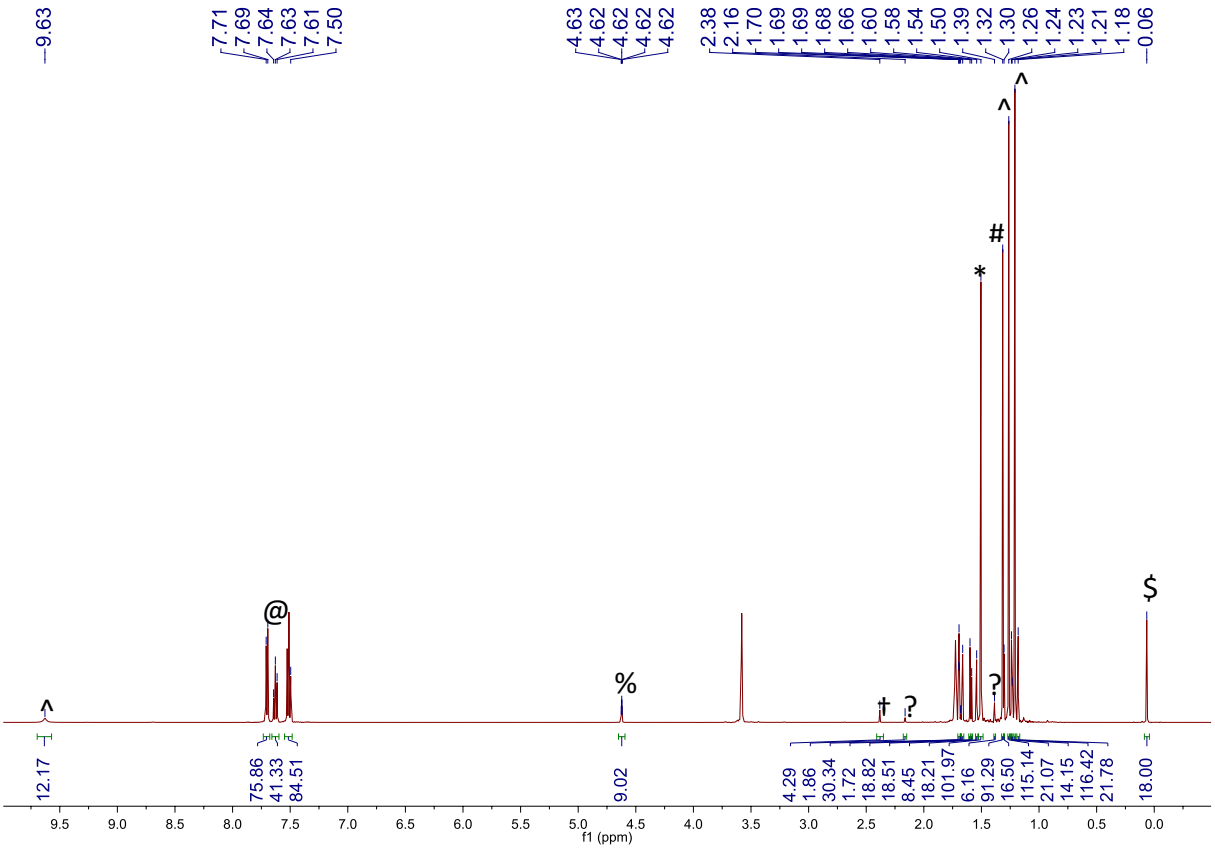

Figure A6.11. ^{1}H NMR spectrum taken in THF-d_8 of the reaction between $PdCl_2(PhCN)_2$ and 2 equiv of Li(N=C^{t}Bu$_2$) after 5 h. **Experimental details:** A J. Young NMR tube equipped with a Teflon rotoflow valve was charged with $PdCl_2(PhCN)_2$ (18.1 mg, 0.0472 mmol), and Li(N=C^{t}Bu$_2$) (17.0 mg, 0.115 mmol), and THF-d_8 (1.0 mL) to give a brown solution. HMDSO (0.50 μL, 2.4 mmol) was then added via syringe as an internal standard. The reaction mixture was allowed to stand for 5 h. During this time, the solution slowly became dark green, indicative of the formation of **6.5**. A 1H NMR spectrum was then recorded. The spectral assignments were further confirmed using COSY and HSQC spectroscopies. (*) indicates a resonance assignable to **6.5**, (†) indicates a resonance assignable to **6.6**, (^) indicates a resonance assignable to HN=C^{t}Bu$_2$, (#) indicates a resonance assignable to ^{t}BuCN, (@) indicates a resonance assignable to PhCN, (%) indicates a resonance assignable to isobutylene, (&) indicates a resonance assignable to isobutane, ($) indicates a resonance assignable to HMDSO, and (?) indicates a resonance assignable to an unidentified Pd-containing product. These assignments were confirmed by comparison with the reported literature spectra[30, 103] or by comparison with authentic material. ^{1}H NMR (THF-d_8, 25 °C, 500 MHz): δ 0.06 (HMDSO, s, 18H, CH_3), 1.18 (6.6, s, 9H, C(CH_3)$_3$), 1.21 (HN=C^{t}Bu$_2$, s, 9H, C(CH_3)$_3$), 1.23 (isobutane, s, 9H, CH(CH_3)$_3$), 1.24 (6.6, s, 9H, C(CH_3)$_3$), 1.26 (HN=C^{t}Bu$_2$, s, 1H, C(CH_3)$_3$), 1.30 (6.6, s, 6H, C(CH_3)$_2$(CH$_2$)), 1.32 (^{t}BuCN, s, 9H, C(CH_3)$_3$), 1.50 (5, s, 108H, C(CH_3)$_3$), 1.54 (6.6, s, 9H, C(CH_3)$_3$), 1.60 (6.6, s, 9H, C(CH_3)$_3$), 1.66 (6.6, s, 9H, C(CH_3)$_3$), 1.68 (isobutane, m, 1H, CH(CH$_3$)$_3$), 1.69 (isobutylene, sept, 6H, H$_2$C=C(CH_3)$_2$, J_{HH} = 2 Hz), 2.38 (6.6, s, 2H, C(CH$_3$)$_2$(CH_2)), 4.62 (isobutylene, sept, 2H, H_2C=C(CH$_3$)$_2$, J_{HH} = 2 Hz), 7.50 (PhCN, m, 2H, *m*-Ph), 7.63 (PhCN, m, 1H, *p*-Ph), 7.70 (PhCN, m, 2H, *o*-Ph), 9.63 (HN=C^{t}Bu$_2$, s, 1H, NH).

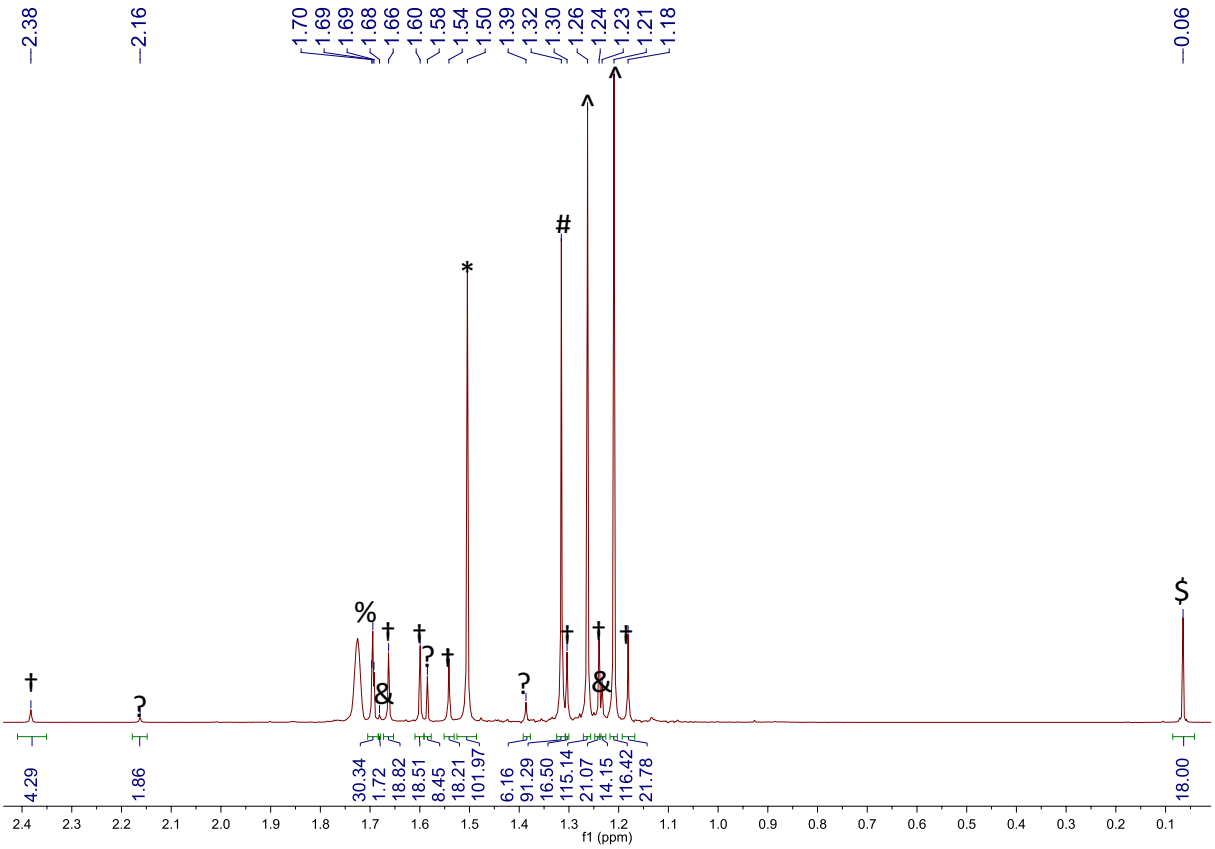

Figure A6.12. Portion of a ^{1}H NMR spectrum taken in THF-d_8 of the reaction between $PdCl_2(PhCN)_2$ and 2 equiv of $Li(N{=}C^tBu_2)$ after 5 h. (*) indicates a resonance assignable to **6.5**, (†) indicates a resonance assignable to **6.6**, (^) indicates a resonance assignable to $HN{=}C^tBu_2$, (#) indicates a resonance assignable to ^{t}BuCN, (@) indicates a resonance assignable to PhCN, (%) indicates a resonance assignable to isobutylene, (&) indicates a resonance assignable to isobutane, ($) indicates a resonance assignable to HMDSO, and (?) indicates a resonance assignable to an unidentified Pd-containing product.

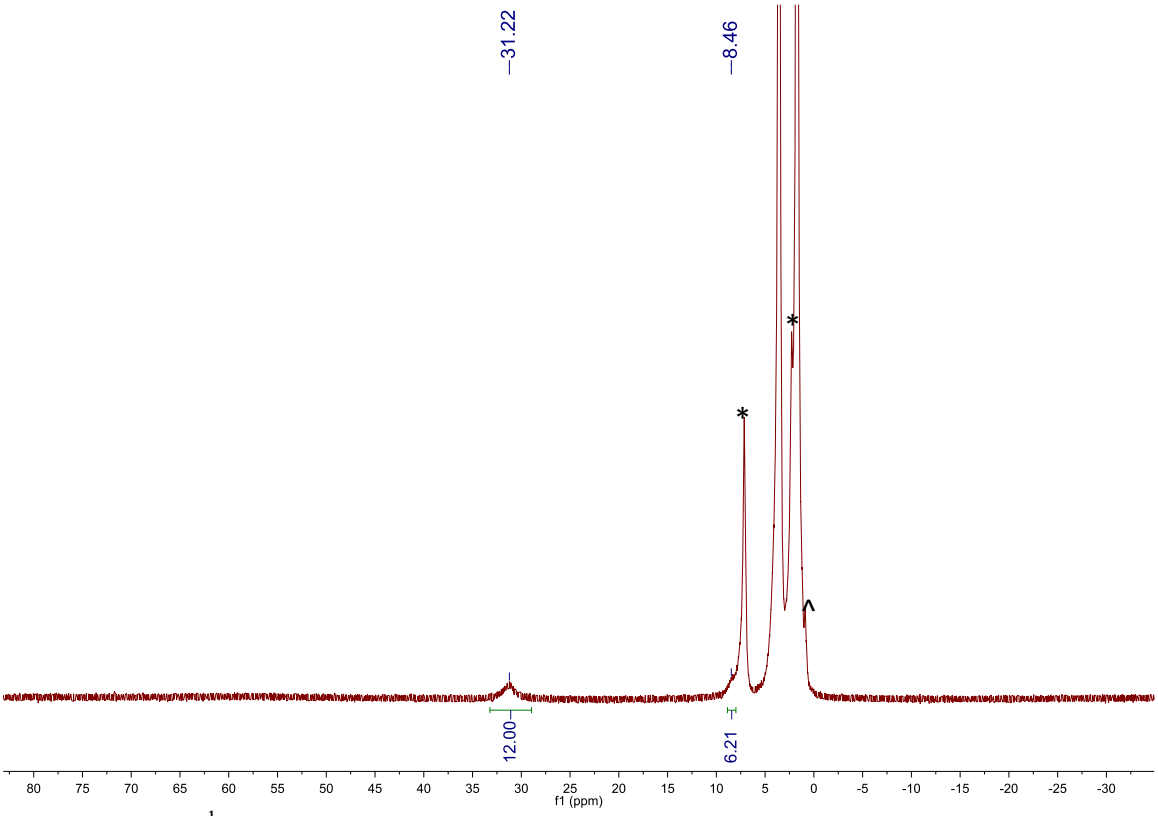

Figure A6.13. ^{1}H NMR spectrum of **6.7** in THF-d_8. (*) indicates a resonance assignable toluene and (^) indicates a resonance assignable to pentane. The *o*-Ph resonance was too broad to be located in this spectrum.

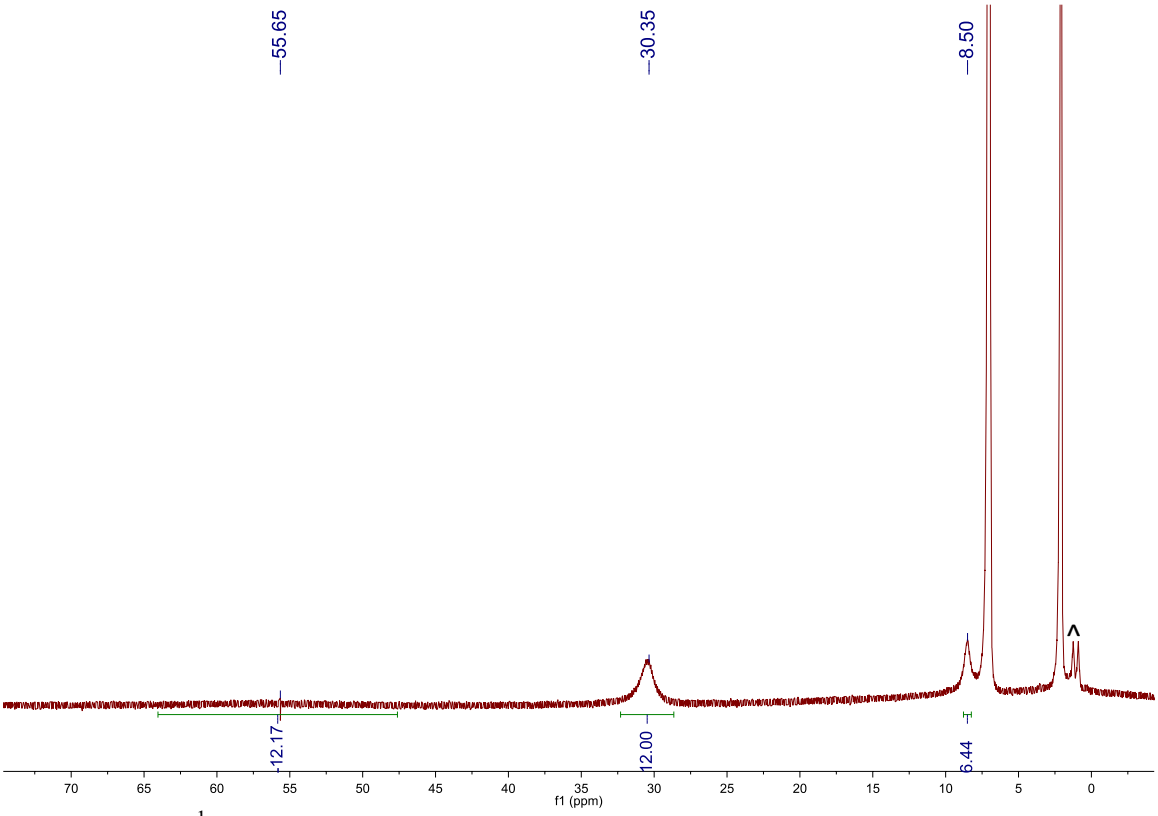

Figure A6.14. ^{1}H NMR spectrum of **6.7** in toluene-d_8. (*) indicates a resonance assignable to pentane.

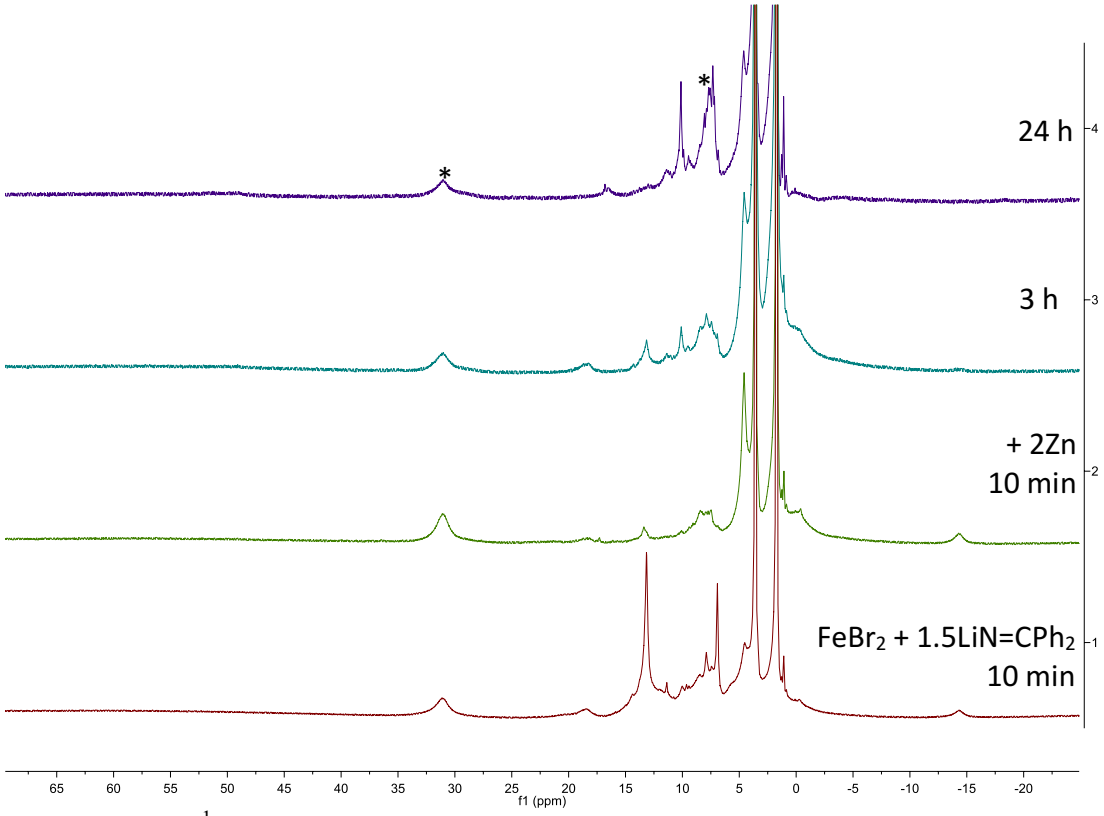

Figure A6.15. ^{1}H NMR spectra of the reaction of $FeBr_2$ with $LiN{=}CPh_2$ (1.5 equiv) and Zn (2 equiv) in THF-d_8. **Experimental details:** $FeBr_2$ (7.7 mg, 36 μ mol) was added to a J. Young NMR tube equipped with a Teflon rotoflow valve. To this solid was added a red solution of $LiN{=}CPh_2$ (10.0 mg, 53 μmol) dissolved in THF-d_8 (1.0 mL). The solution immediately turned brown and ^{1}H and ^{7}Li NMR spectra were recorded after 10 min. The NMR tube was then brought back inside a glovebox at which time Zn powder (5.0 mg, 76 μmol) was added as a solid. The NMR tube was allowed to shake at room temperature and the reaction was monitored intermittently by ^{1}H and ^{7}Li NMR spectroscopy. (*) indicates a resonance assignable to **6.7**, all other resonances are thus far unassigned.

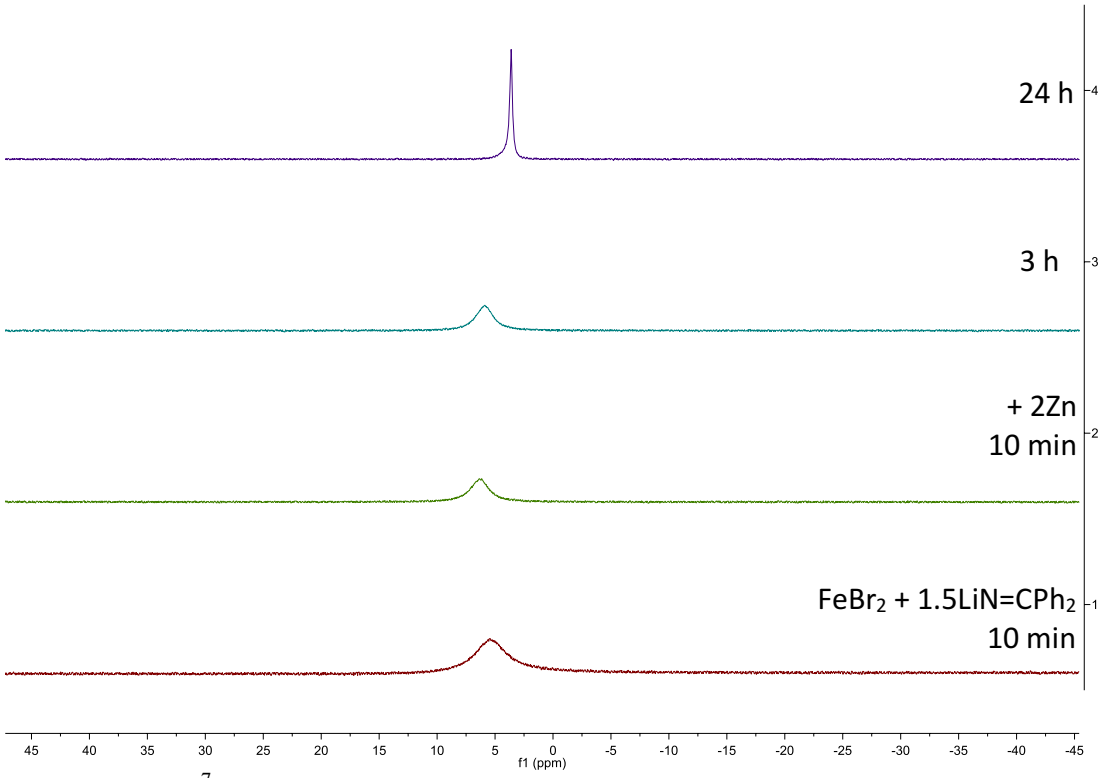

Figure A6.16. ^{7}Li NMR spectra of the reaction of $FeBr_2$ with $LiN{=}CPh_2$ (1.5 equiv) and Zn (2 equiv) in THF-d_8.

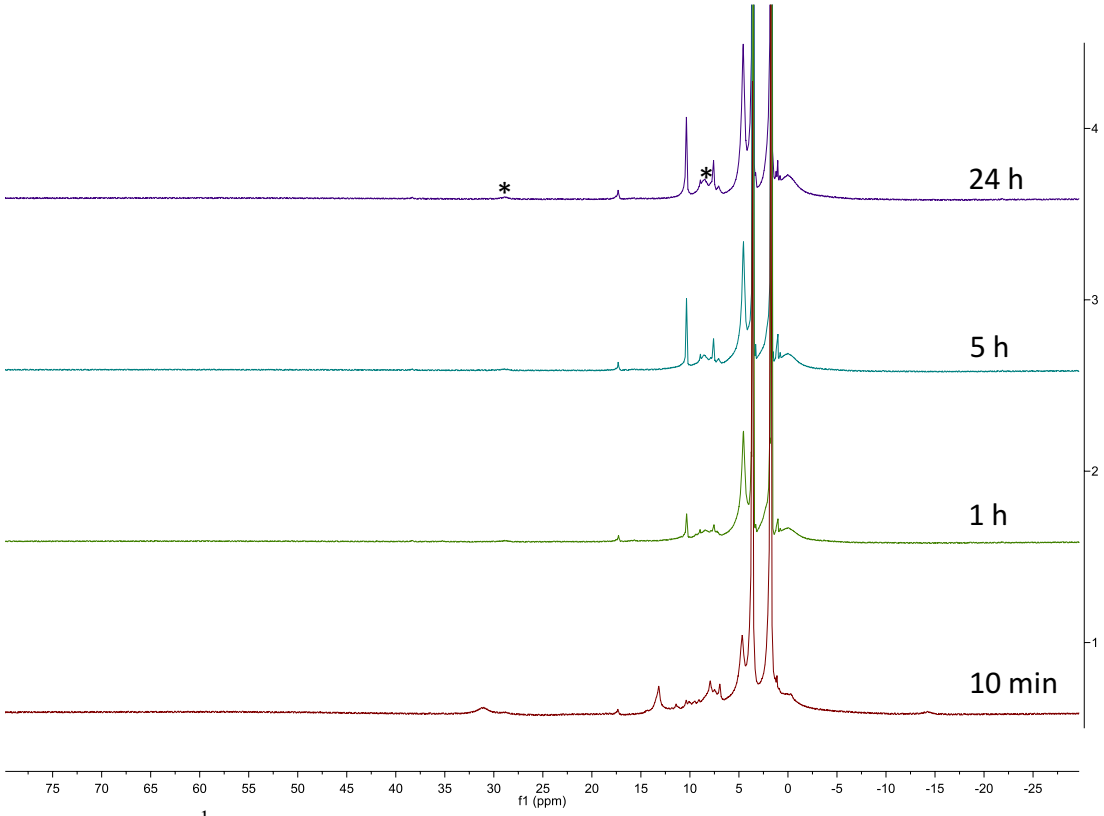

Figure A6.17. ^{1}H NMR spectra of the reaction of $FeBr_2$ with $LiN{=}CPh_2$ (1.5 equiv) in THF-d_8. **Experimental details:** $FeBr_2$ (7.7 mg, 36 μmol) was added to a J. Young NMR tube equipped with a Teflon rotoflow valve. To this solid was added a red solution of $LiN{=}CPh_2$ (10.0 mg, 53 μmol) dissolved in THF-d_8 (1.0 mL). The solution immediately turned brown and ^{1}H and ^{7}Li NMR spectra were recorded after 10 min. The NMR tube was allowed to shake at room temperature and the reaction was monitored intermittently by ^{1}H and ^{7}Li NMR spectroscopy. (*) indicates a resonance assignable to **6.7**, all other resonances are thus far unassigned.

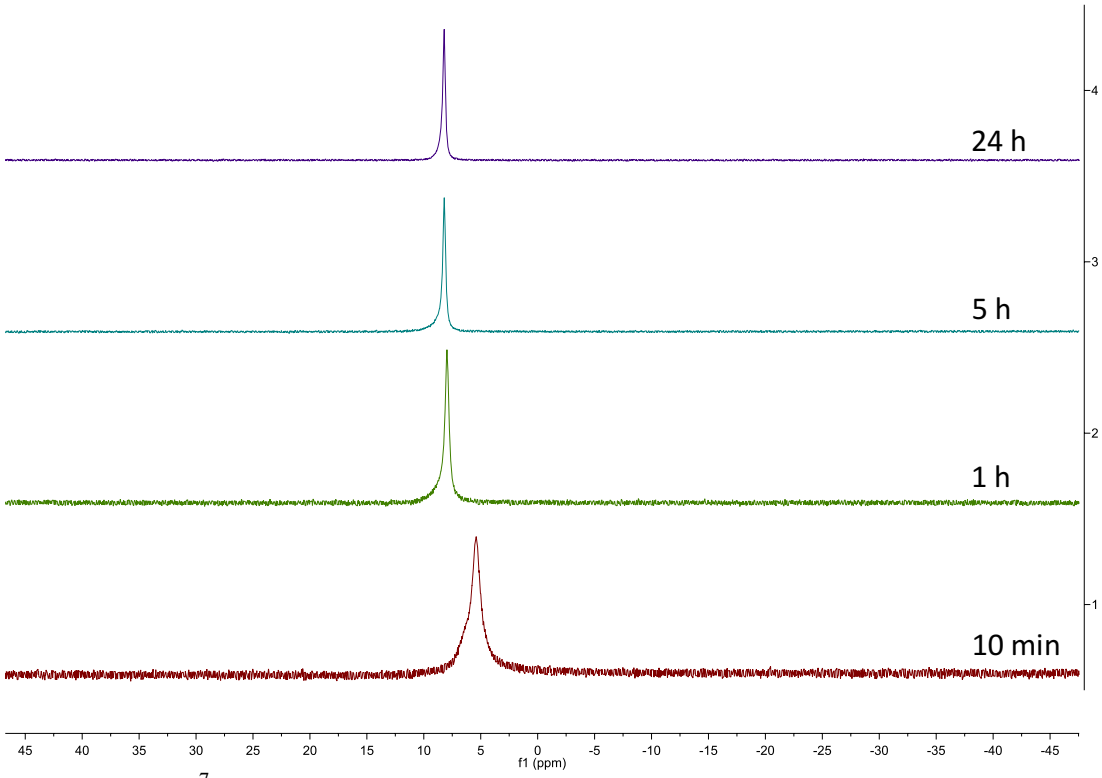

Figure A6.18. ^{7}Li NMR spectra of the reaction of $FeBr_2$ with $LiN{=}CPh_2$ (1.5 equiv) in THF-d_8.

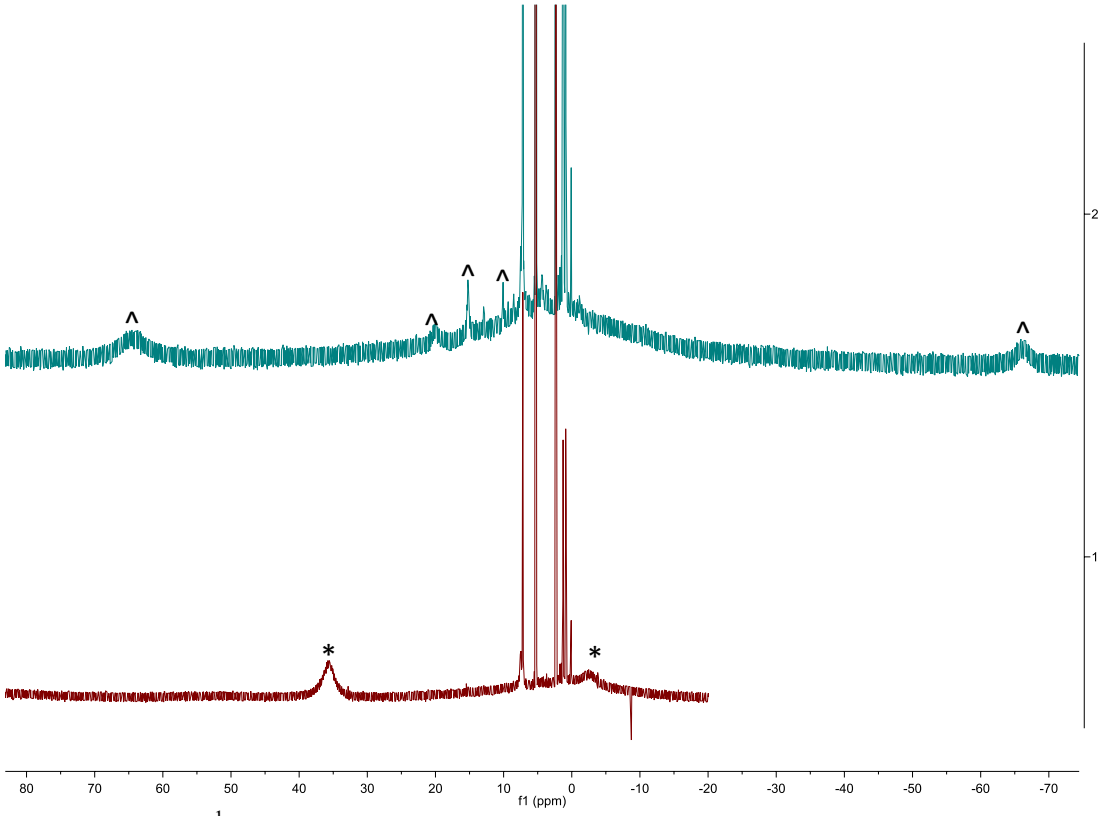

Figure A6.19. ^{1}H NMR spectra showing the decomposition of **6.7** in CD_2Cl_2 at room temperature. **Experimental details:** Solid **6.7** (2.0 mg, 1.5 μmol) was added to a J. Young NMR tube equipped with a Teflon rotoflow valve and dissolved in CD_2Cl_2 (1.0 mL). A ^{1}H NMR of the brown solution was recorded (bottom spectrum). The solution was allowed to stand at room temperature for 3h over which time the solution turned a red-brown color concomitant with the deposition of a dark brown solid and a ^{1}H NMR spectrum was recorded (top spectrum). (*) indicates a resonance assignable to **6.7** and (^) indicates a resonance assignable to a decomposition product.

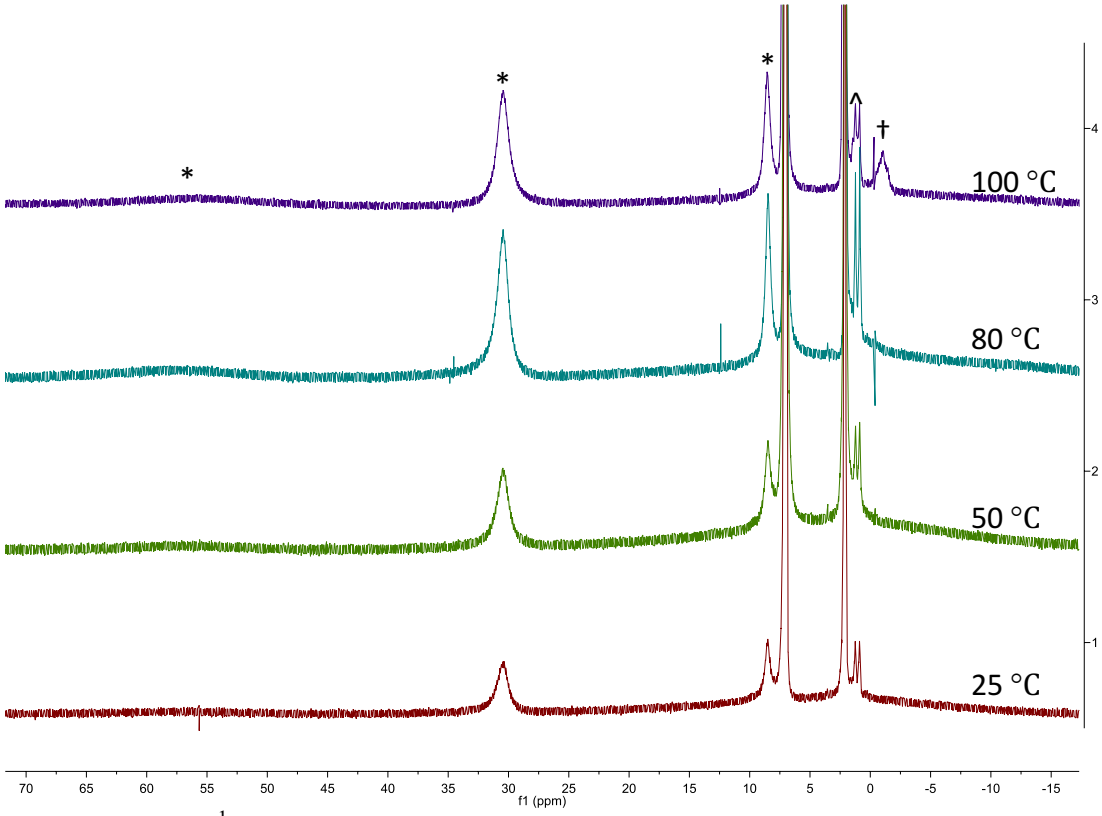

Figure A6.20. ^{1}H NMR spectra showing the stability of **6.7** in toluene-d_8 at various temperatures. **Experimental details:** Solid **6.7** (15.0 mg, 11.5 μmol) was added to a J. Young NMR tube equipped with a Teflon rotoflow valve and partially dissolved in toluene-d_8 (1.0 mL). A ^{1}H NMR spectrum was recorded. The solution was then gradually heated to 50, 80, and 100 °C and allowed to stand at each temperature for 1h before a ^{1}H NMR spectrum was recorded. At 50 °C approximately 60% of **6.7** had dissolved; at 80 °C approximately 90% if **6.7** had dissolved; at 100 °C **6.7** became to decompose and a fine black powder had deposited in the NMR tube. (*) indicates a resonance assignable to **6.7**, (†) indicates a resonance assignable to a decomposition product, and (^) indicates a resonance assignable to pentane.

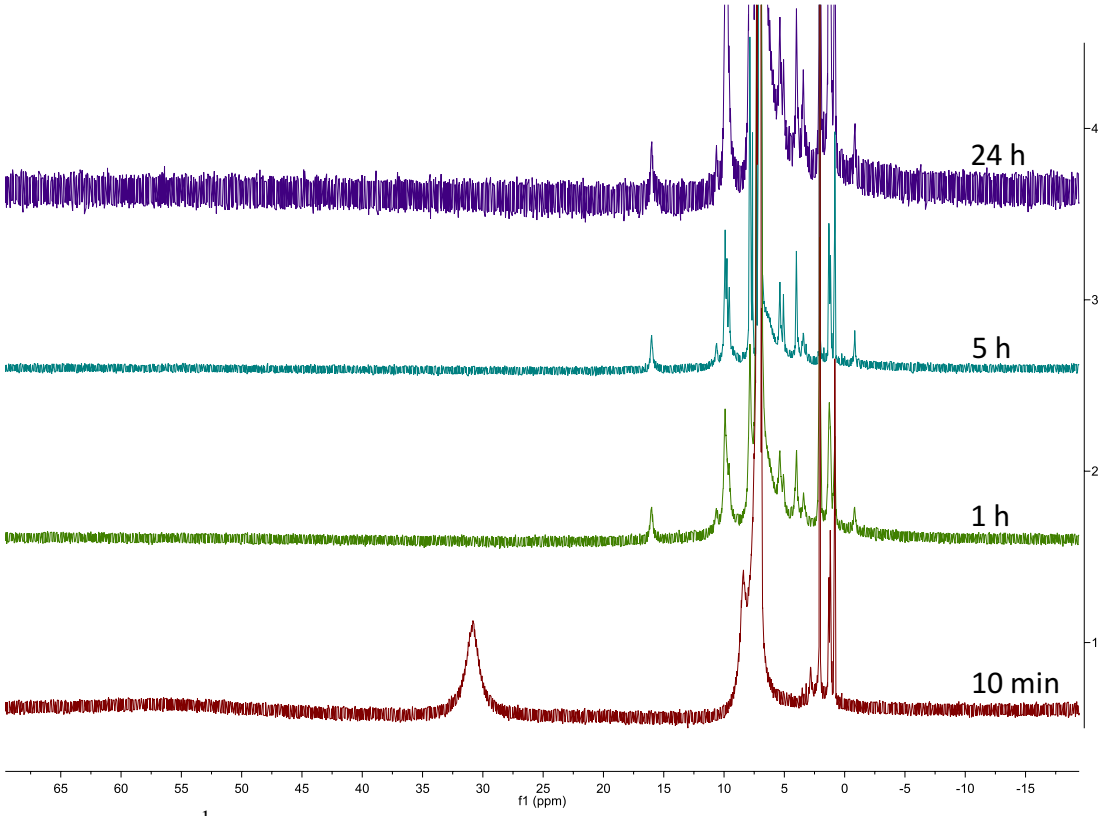

Figure A6.21. ^{1}H NMR spectra in C_6D_6 showing the decomposition of **6.7** after exposure to air. **Experimental details:** Solid **6.7** (4.0 mg, 3.1 μmol) was added to a NMR tube and dissolved in C_6D_6 (1.0 mL). A ^{1}H NMR spectrum was recorded (bottom). The NMR tube cap was then removed and the solution was exposed to air for 5 minutes. The reaction was monitored intermittently by ^{1}H NMR spectroscopy. After 10 min, no resonances assignable to **6.7** are present. Over the course of 24h, the solution turns an orange-brown color and a dark brown precipitate forms. The identity of the decomposition product(s) has not been determined.

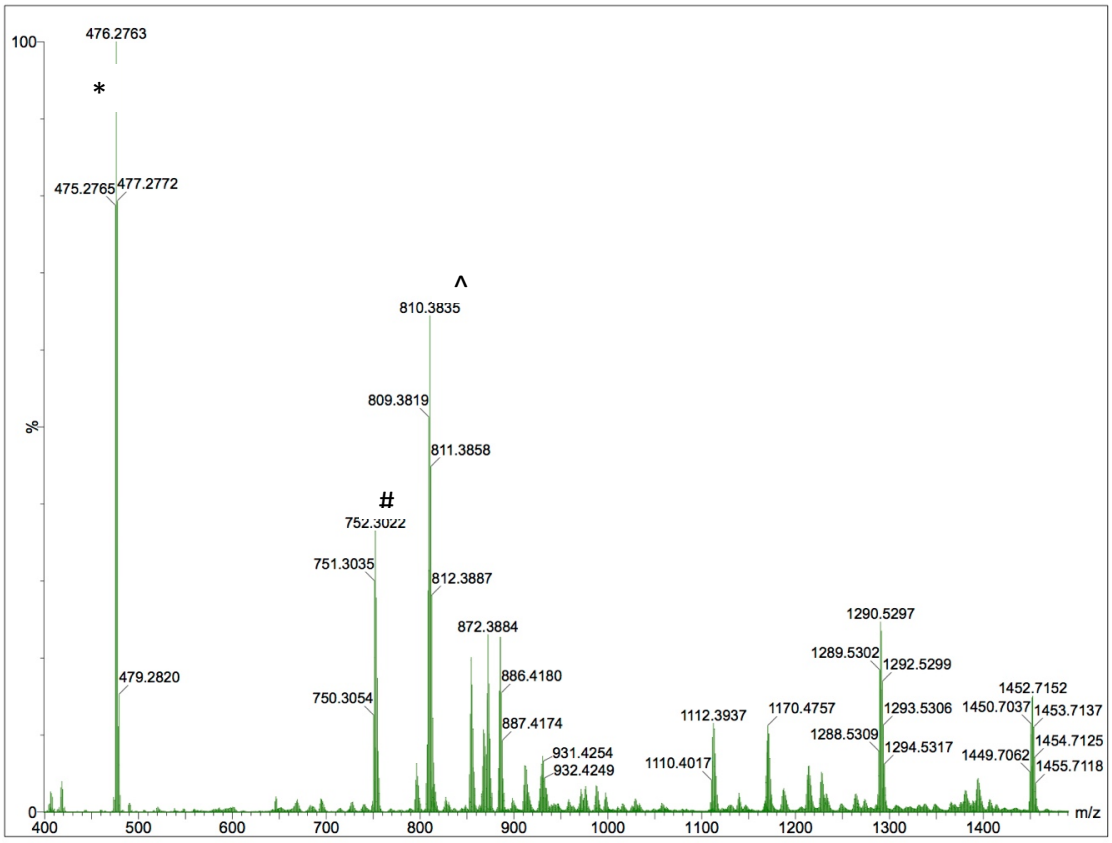

Figure A6.22. ESI-MS (positive mode) of an isolated mixture of **6.1** and **6.2** in THF. (*) denotes the presence of a peak assignable to the [**6.1** + H]$^+$ ion, (^) denotes the presence of a peak assignable to the [**6.2** + H]$^+$ ion, (#) denotes the presence of a peak assignable to the [**6.2** – ^{t}Bu]$^+$ ion. The other peaks remain unassigned.

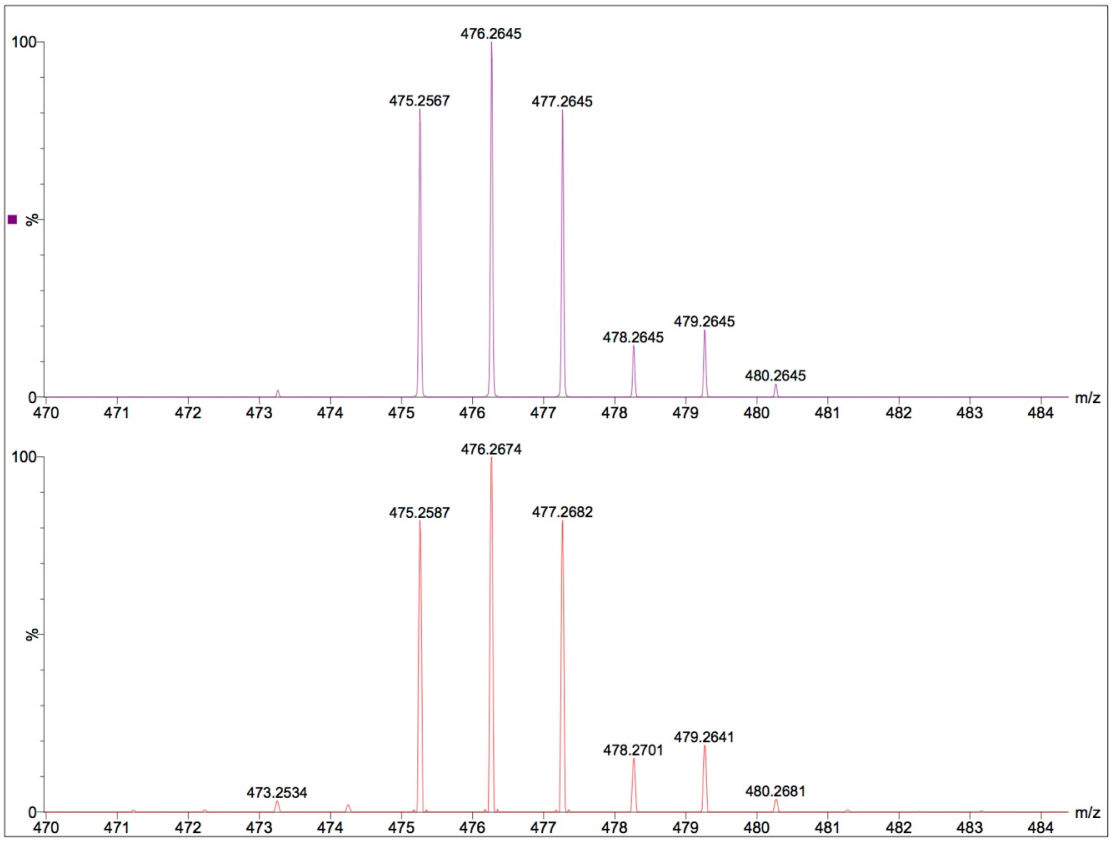

Figure A6.23. Partial ESI-MS (positive mode) of the isolated mixture of **6.1** and **6.2**, dissolved in THF. The experimental (bottom) and calculated peaks assignable to the [**6.3** + H]$^+$ ion are shown.

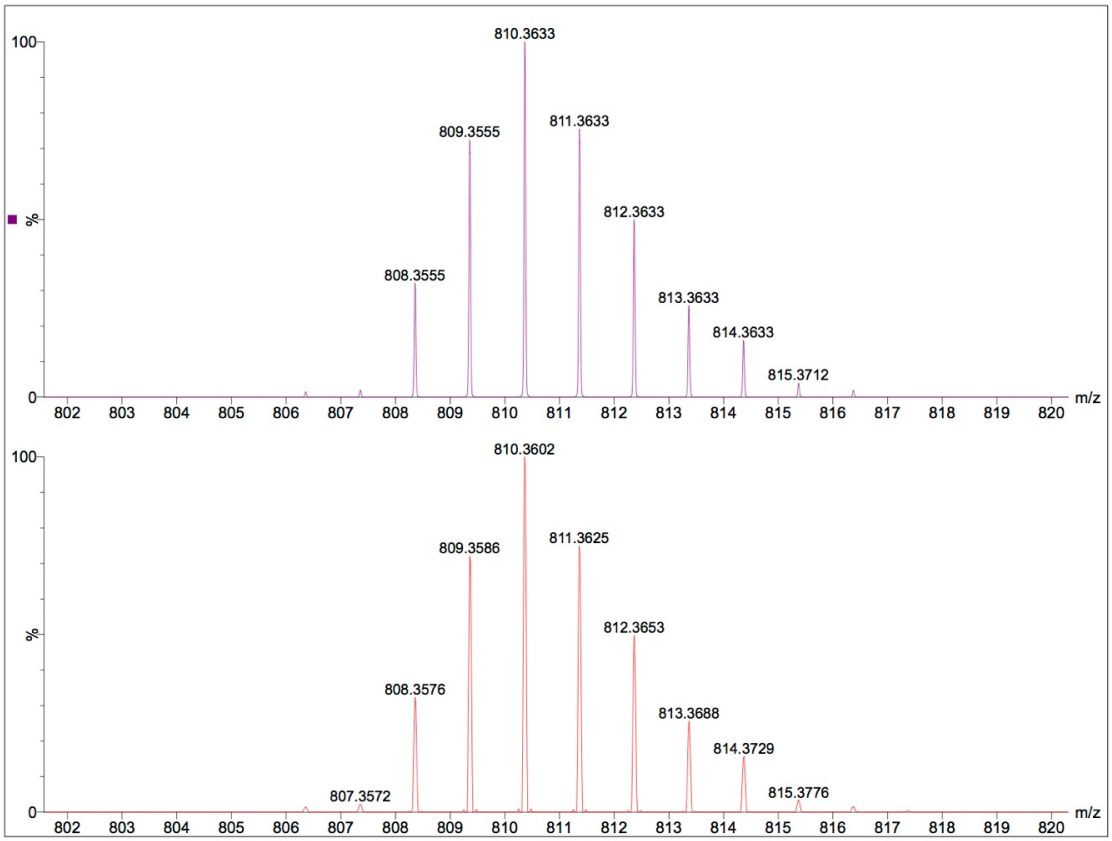

Figure A6.24. Partial ESI-MS (positive mode) of the isolated mixture of **6.1** and **6.2**, dissolved in THF. The experimental (bottom) and calculated peaks assignable to the [**6.2** + H]$^+$ ion are shown.

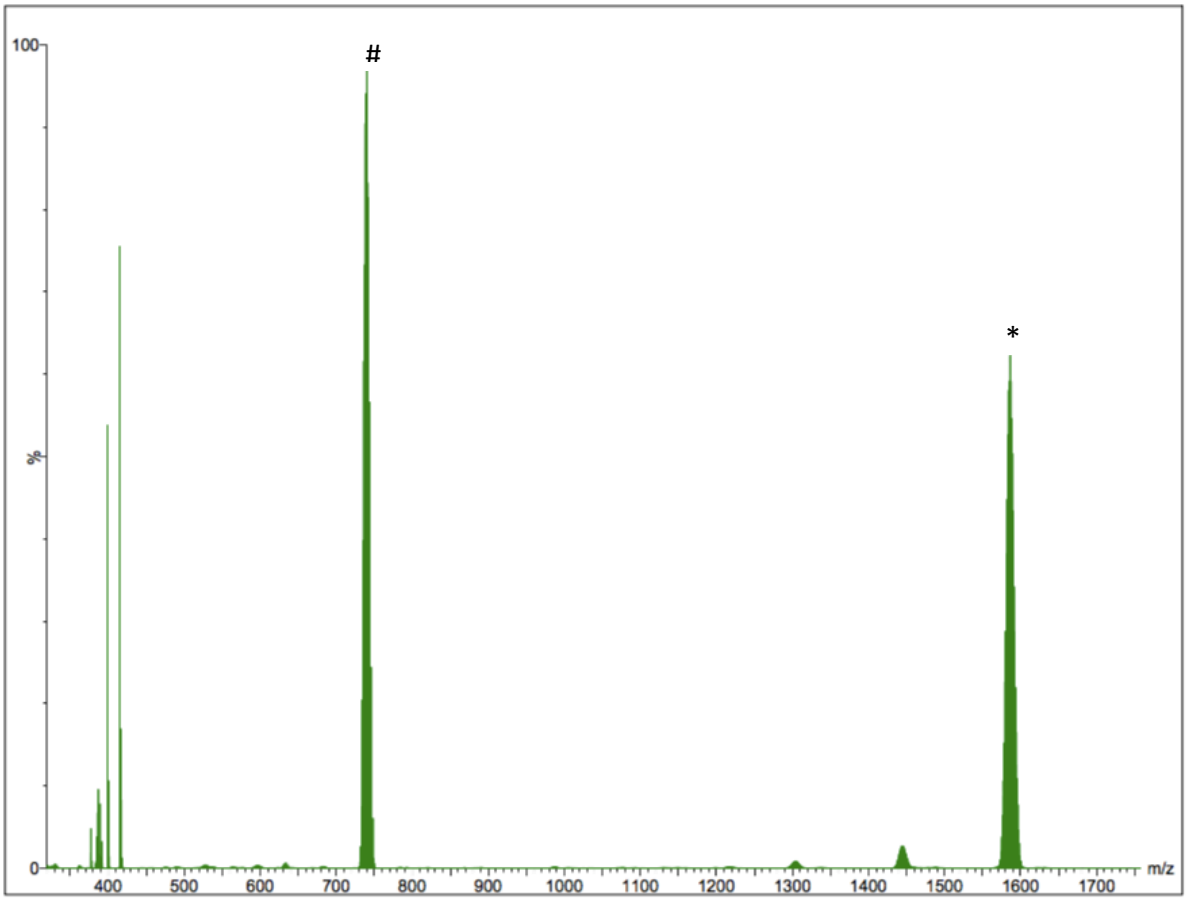

Figure A 6.25. ESI-MS of $Pd_7(N{=}C^tBu_2)_6$ (**6.5**) in THF. (*) denotes the peak assignable to the $[M]^+$ ion and (#) denotes the peak assignable to the $[Pd_3(N{=}C^tBu_2)_3]^+$ fragment.

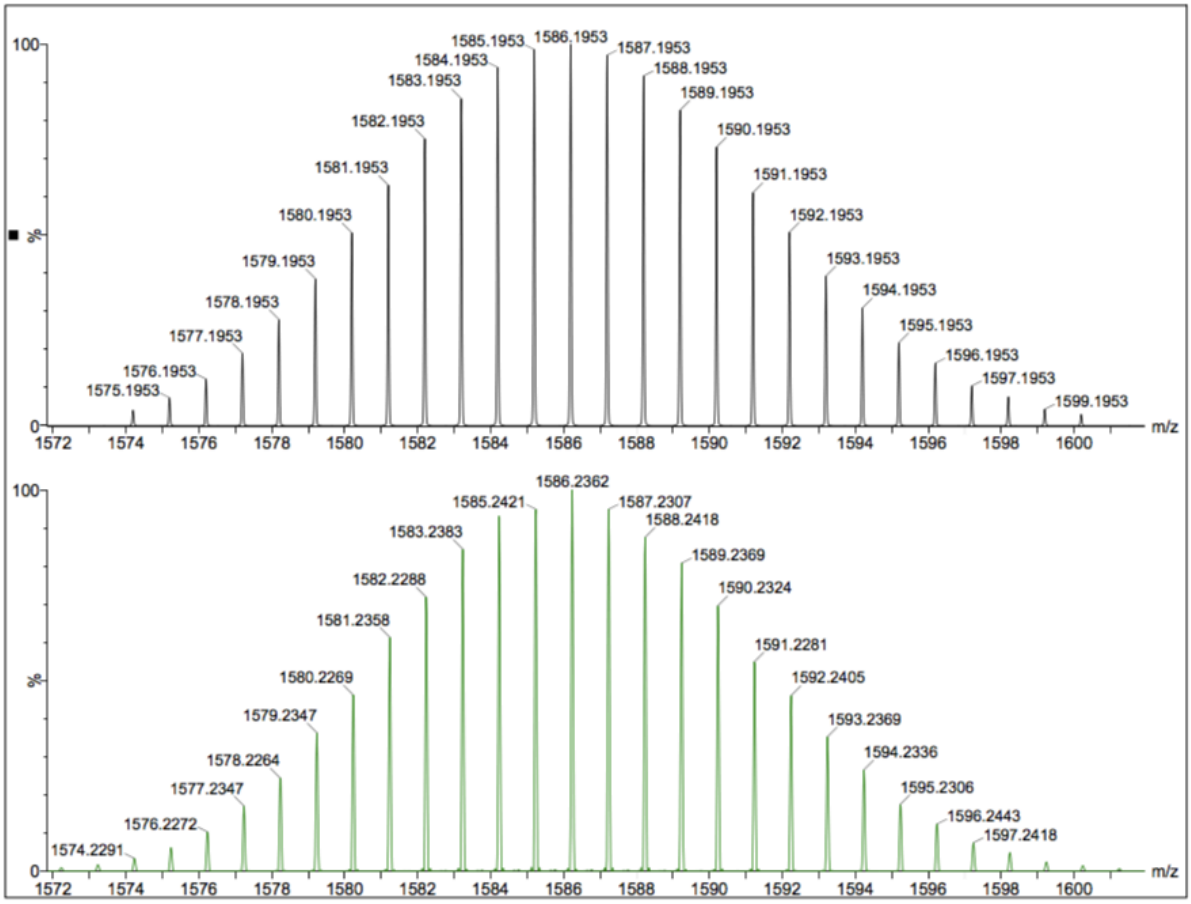

Figure A6.26. Partial ESI-MS of $Pd_7(N{=}C^tBu_2)_6$ (**6.5**) in THF. The experimental (bottom) and calculated (top) peaks assignable to the $[M]^+$ ion are shown.

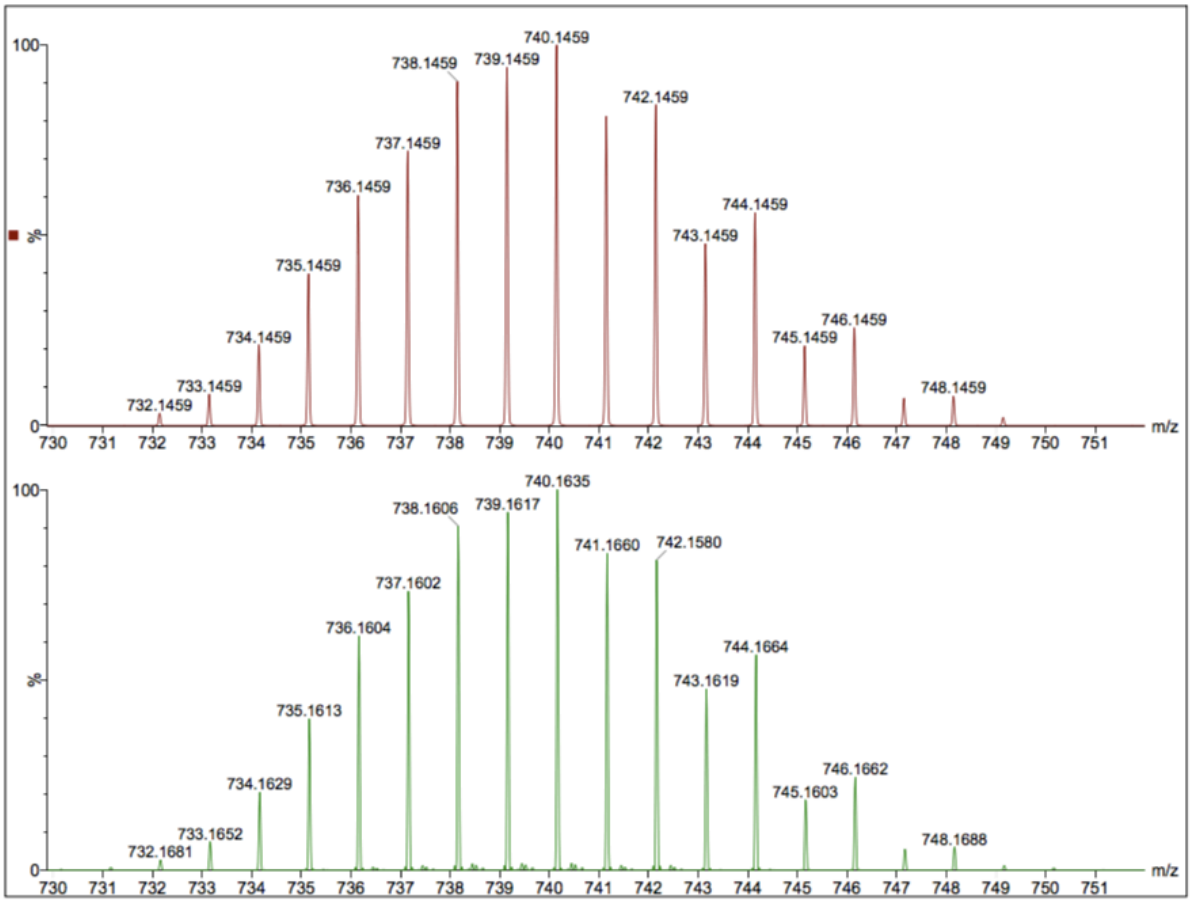

Figure A6.27. Partial ESI-MS of $Pd_7(N{=}C^tBu_2)_6$ (**6.5**) in THF. The experimental (bottom) and calculated (top) peaks assignable to the $[Pd_3(N{=}C^tBu_2)_3]^+$ fragment are shown.

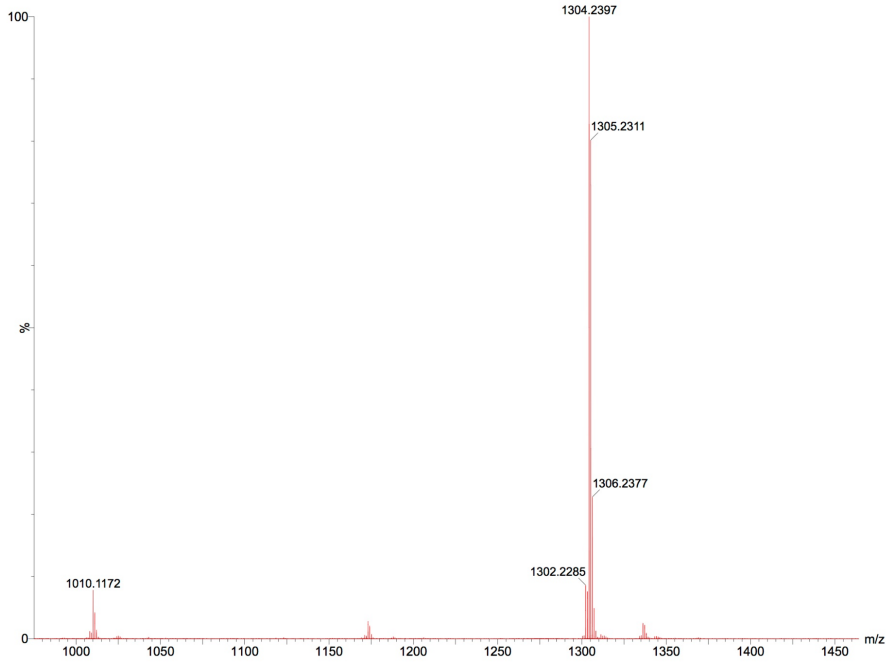

Figure A6.28. ESI-MS (negative mode) of $Fe_4(N{=}CPh_2)_6$ (**6.7**) taken in THF.

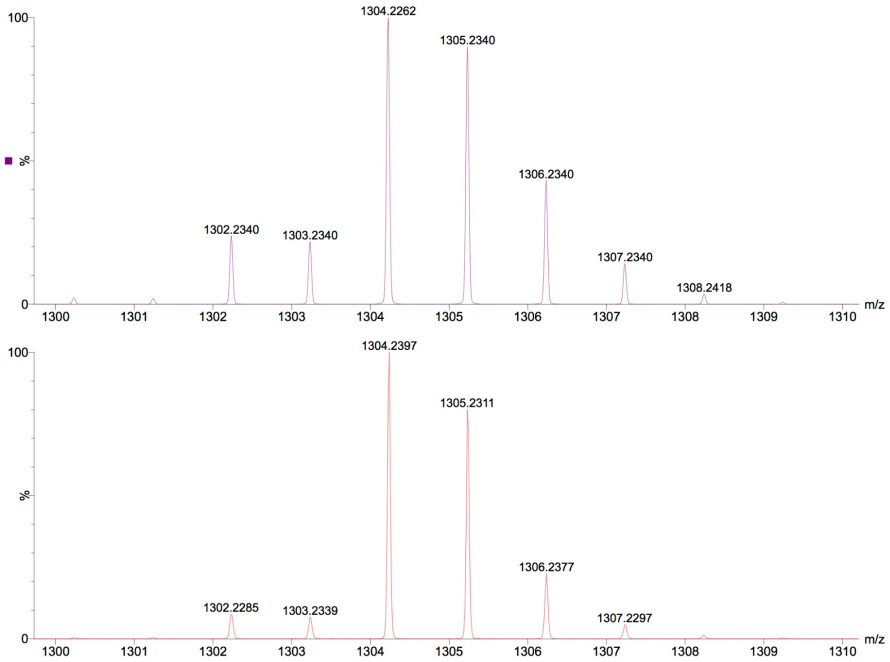

Figure A6.29. Partial ESI-MS (negative mode) of $Fe_4(N{=}CPh_2)_6$ (**6.7**) taken in THF. The experimental (bottom) and calculated (top) peaks assignable to the $[M^-]$ ion are shown.

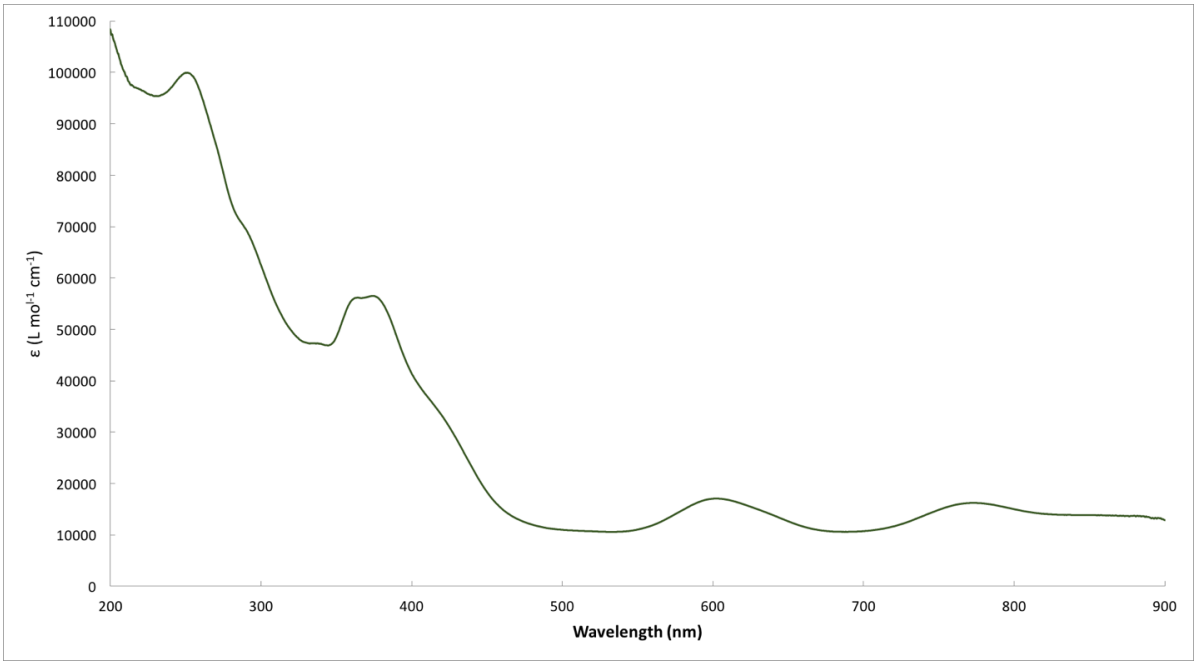

Figure A6.30. UV-Vis spectrum of **6.5** (18.9 μM) in pentane.

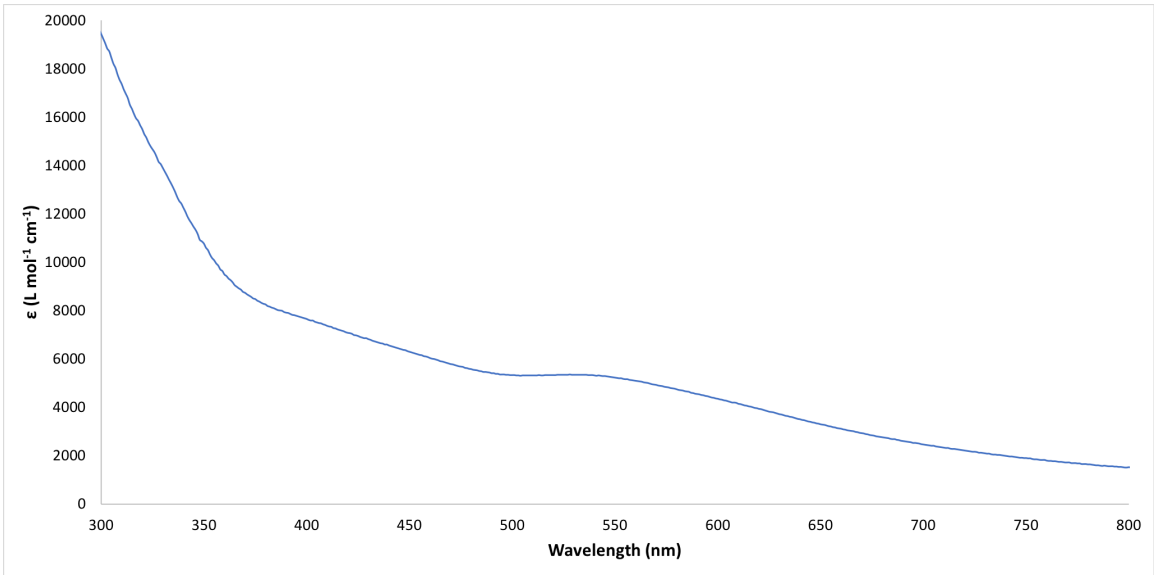

Figure A6.31. UV-Vis/NIR spectrum of **6.7** (76.7 μM) in toluene.

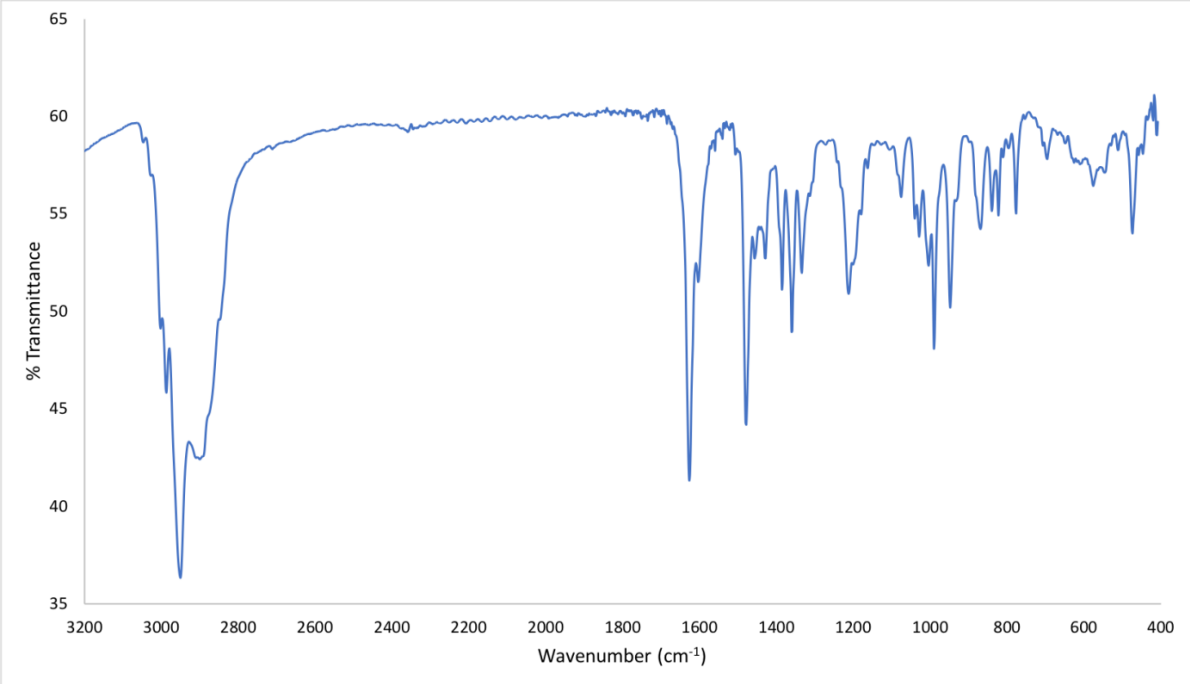

Figure A6.32. Partial IR spectrum of Pt(1,5-COD)(N=C^{t}Bu$_2$)Cl (**6.3**) as a KBr pellet.

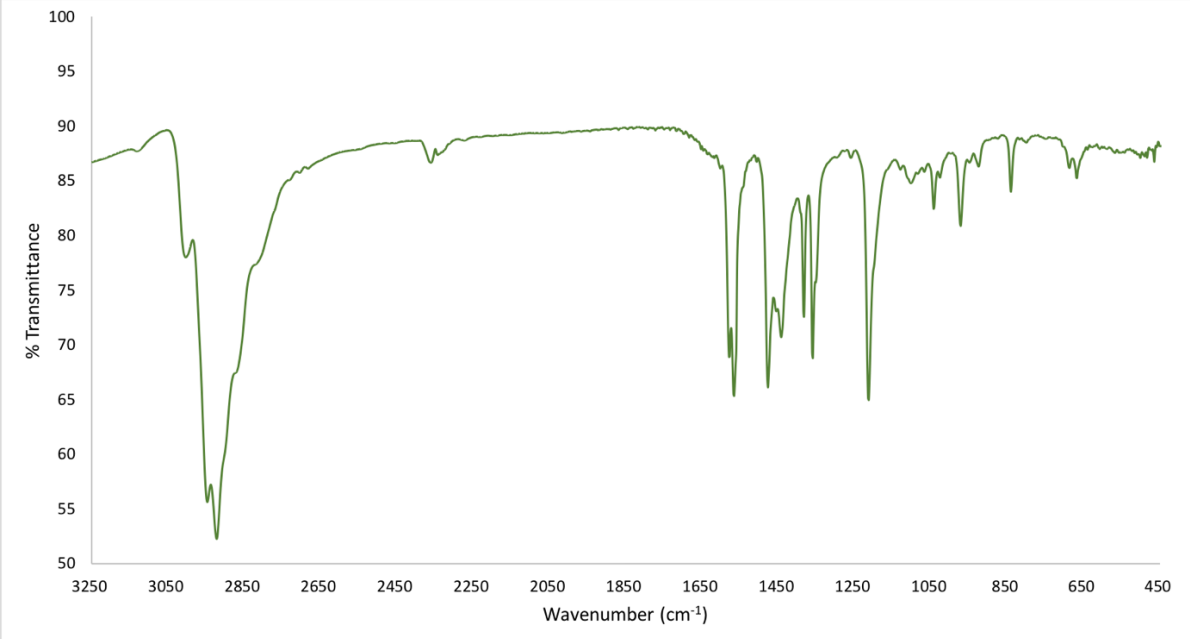

Figure A6.33. Partial IR spectrum of Pd$_7$(N=C^{t}Bu$_2$)$_6$ (**6.5**) as a KBr pellet.

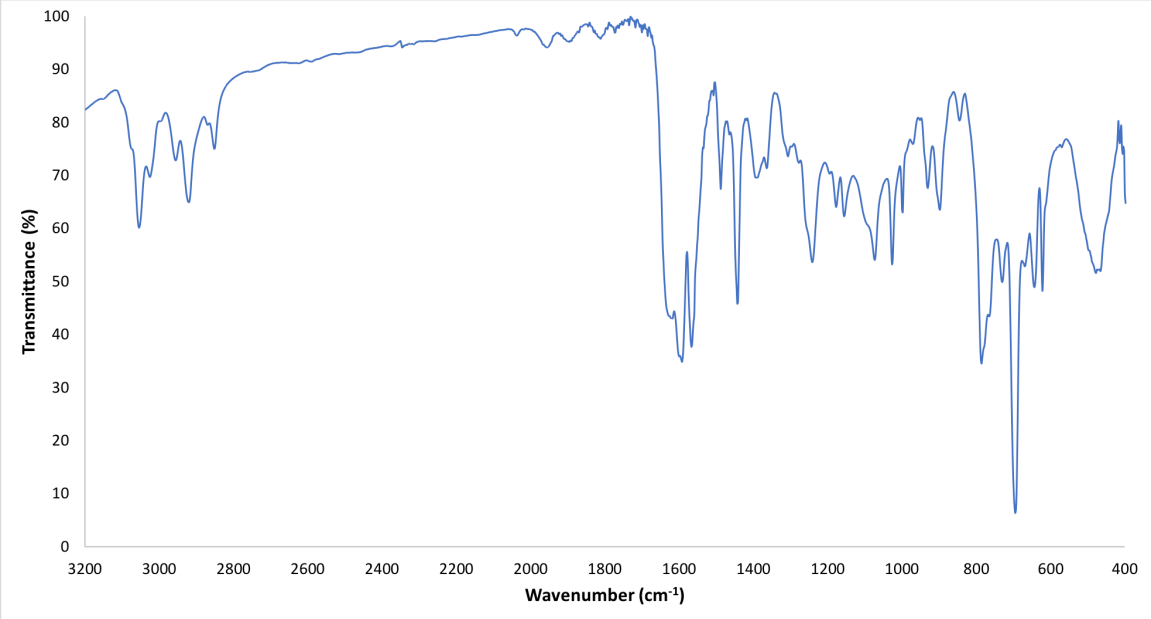

Figure A6.34. Partial IR spectrum of $Fe_4(N{=}CPh_2)_6$ (**6.7**) as a KBr pellet.

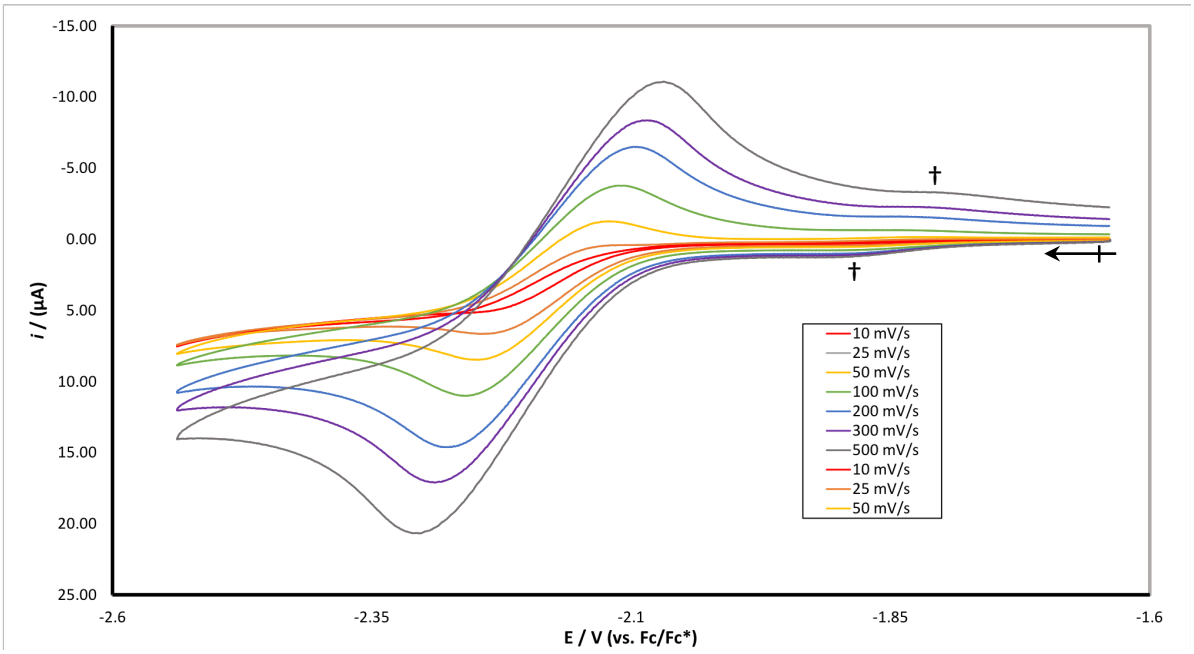

Figure A6.35. Partial cyclic voltammogram of the reduction feature of complex **6.5**, measured in THF with 0.1 M $[NBu_4][PF_6]$ as supporting electrolyte (vs. Fc/Fc^+). The electrochemical feature indicated by (†) is likely due to a trace amount of **6.6**.

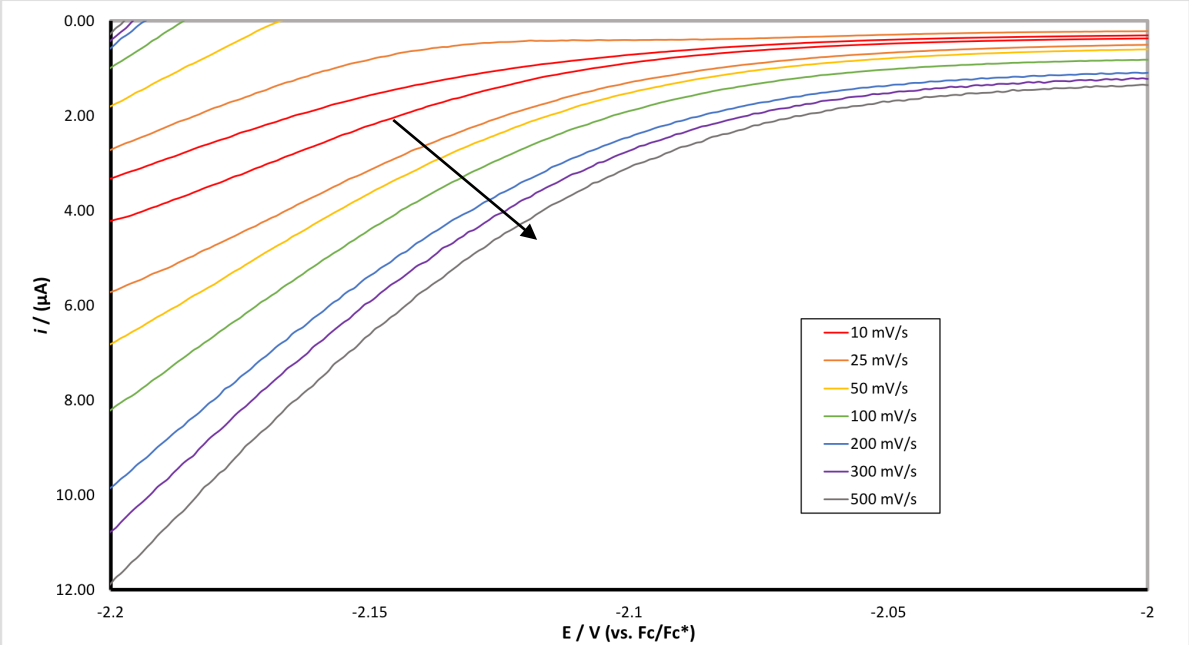

Figure A6.36. Partial cyclic voltammogram showing the onset of the reduction feature of complex **6.5**, measured in THF with 0.1 M $[NBu_4][PF_6]$ as supporting electrolyte (vs. Fc/Fc^+). The arrow indicates the approximate position of the onset potential at each scan rate.

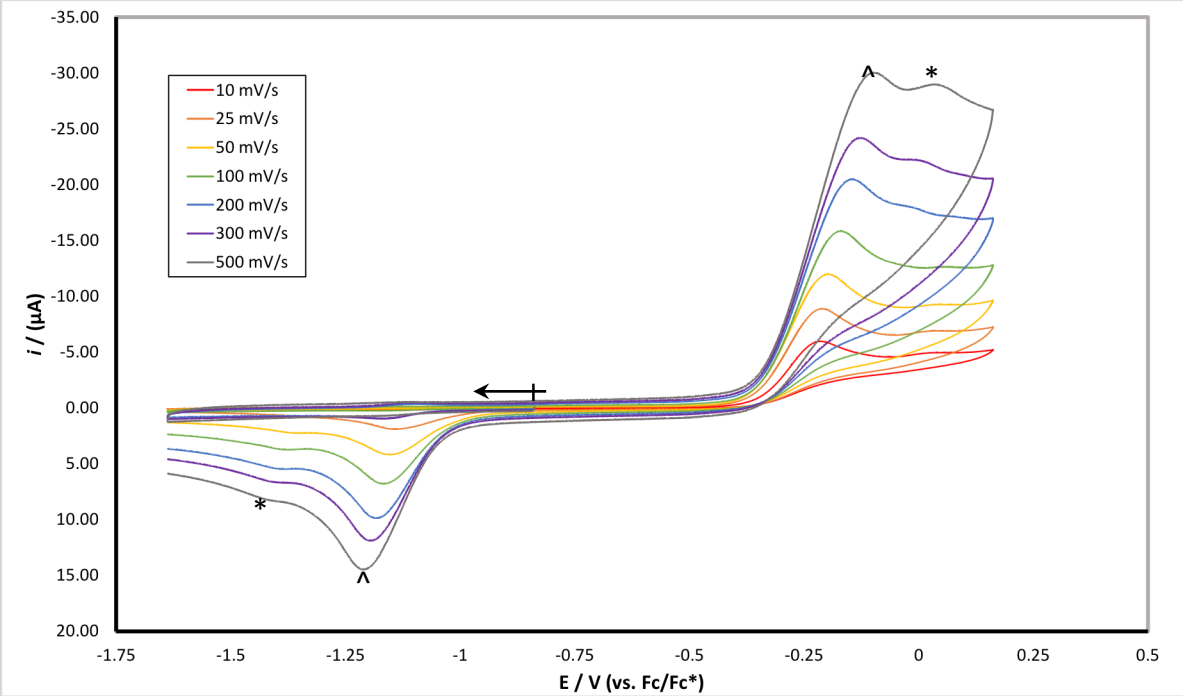

Figure A6.37. Partial cyclic voltammogram of the oxidation feature of complex **6.5**, measured in THF with 0.1 M $[NBu_4][PF_6]$ as supporting electrolyte (vs. Fc/Fc^+). The electrochemical feature indicated by (*) is likely due to a decomposition product, as it grows in intensity during the course of the experiment; the electrochemical feature indicated by (^) is due to the irreversible oxidation of **6.5**. This feature remains irreversible even at fast scan rates (2 V/s).

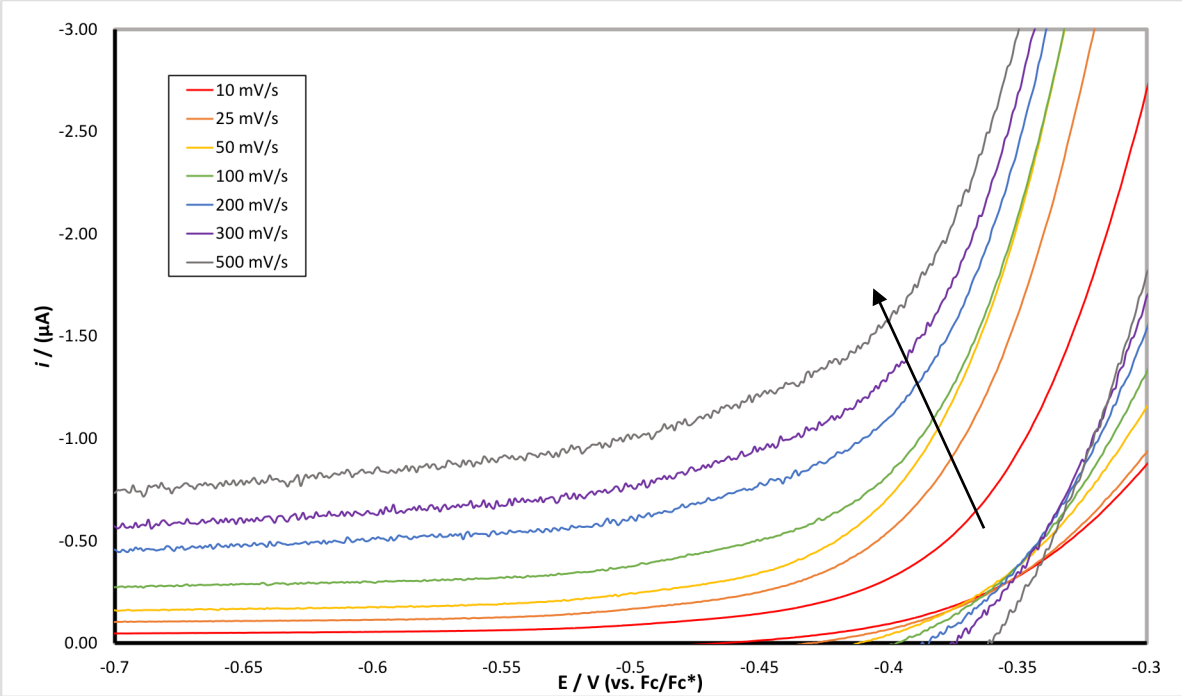

Figure A6.38. Partial cyclic voltammogram showing the onset of the oxidation feature of complex **6.5**, measured in THF with 0.1 M $[NBu_4][PF_6]$ as supporting electrolyte (vs. Fc/Fc^+). The arrow indicates the approximate position of the onset potential at each scan rate.

Table 6.3. Electrochemical parameters for **6.5** in THF (vs. Fc/Fc^+, $[NBu_4][PF_6]$ as the supporting electrolyte).

Reduction Feature	Scan Rate, V/s	$E_{onset,c}$ V	$E_{p,c}$, V	$E_{p,a}$, V	ΔE_p, V	$E_{1/2}$ V	$i_{p,c}/i_{p,a}$
	0.010	-2.135	-2.241	-2.135	0.106	-2.188	1.032
	0.025	-2.129	-2.244	-2.130	0.114	-2.187	1.054
	0.050	-2.127	-2.249	-2.122	0.127	-2.186	1.025
	0.100	-2.124	-2.260	-2.107	0.153	-2.184	1.033
	0.200	-2.120	-2.301	-2.122	0.179	-2.212	1.031
	0.300	-2.117	-2.389	-2.085	0.304	-2.237	1.106
	0.500	-2.115	-2.394	-2.069	0.325	-2.231	1.082

Oxidation Feature	Scan Rate, V/s	$E_{onset,a}$ V	$E_{p,a}$, V
	0.010	-0.368	-0.213
	0.025	-0.377	-0.212
	0.050	-0.382	-0.199
	0.100	-0.384	-0.169
	0.200	-0.390	-0.146
	0.300	-0.394	-0.125
	0.500	-0.402	-0.097

Table 6.4. Experimental ^{195}Pt NMR shifts [in ppm vs. $Na_2PtCl_6(aq)$] for a series of neutral platinum(II) complexes in non-aqueous solution.

Complex	$\delta(^{195}Pt)$ [ppm]	Solvent	Ref.
trans-$PtCl_2(py)_2$	-1944	$CDCl_3$	[104]
$Pt(C_2O_4)$(dach)	-1997	DMSO-d_6	[105]
trans-$PtCl_2\{NH{=}C(Me)ON{=}CMe_2\}_2$	-2040	$CDCl_3$	[104]
$PtCl_2$(dach)	-2281	DMSO-d_6	[105]
cis-$PtCl_2$(bpy)	-2315	DMSO-d_6	[106]
$PtCl_2$(COD)	-3330	$CDCl_3$	[106]
Pt(bpy)(edt)	-3506	$CDCl_3$	[106]
Pt(COD)(dt)	-4070	$CDCl_3$	[106]
cis-$PtCl_2(PPh_3)_2$	-4429	$CDCl_3$	[106]
PtH(PCP)	-4776	THF-d_8	[107]
$Pt(N{=}C^tBu_2)_2$ (**6.1**)	-629	C_6D_6/50°C	This work
	-663	C_6D_6/25°C	This work
[(^{t}Bu$_2$C=N)Pt(μ-*N*,*C*-NC(^{t}Bu)C(Me)$_2$CH$_2$)Pt(N=C^{t}Bu$_2$)] (**6.2**)	N/A	C_6D_6	

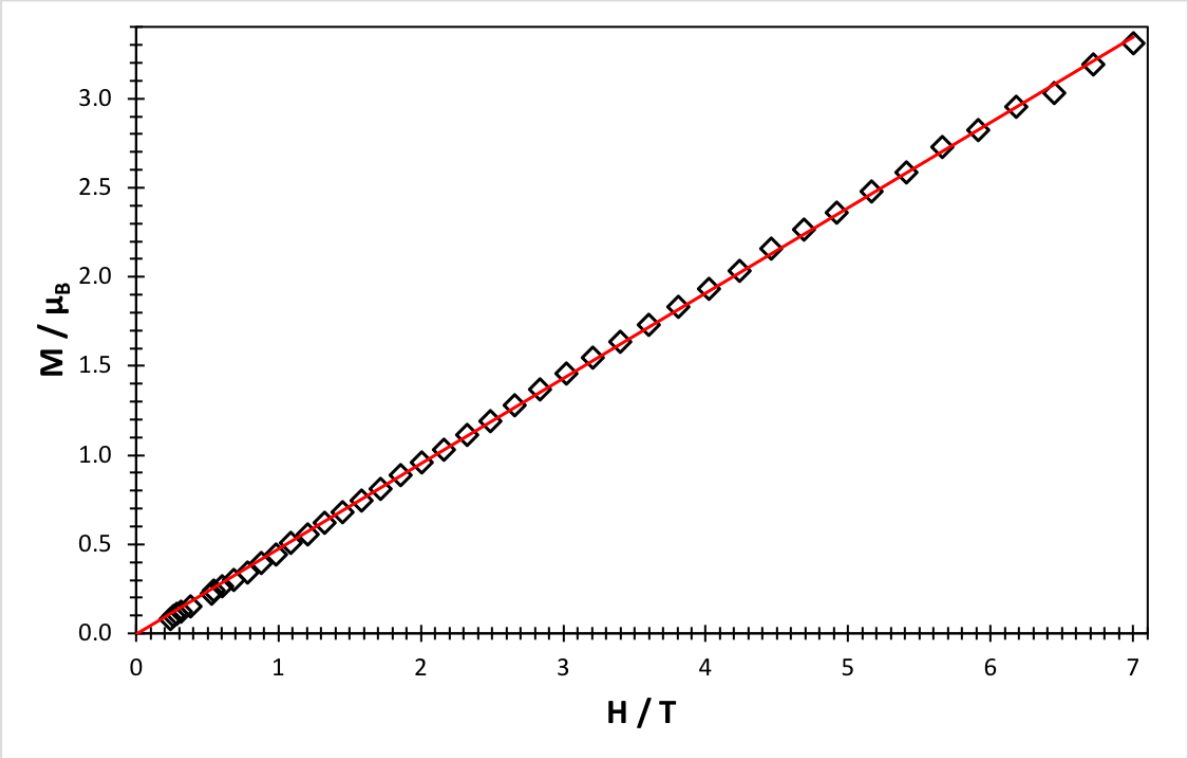

Figure A6.39. Magnetization data at 100 K for $Fe_4(N{=}CPh_2)_6$ (**6.7**) showing magnetization vs. applied field from 0 to 7 T. Used to check for ferromagnetic impurities.

6.6 References

(1) Power, P. P., Stable Two-Coordinate, Open-Shell (d^1–d^9) Transition Metal Complexes. *Chem. Rev.* **2012**, *112*, 3482-3507.

(2) Immirzi, A.; Musco, A.; Zambelli, P.; Carturan, G., Nucleophilic attack on {(π-allyl)Pt[$P(C_6H_{11})_3$]$_2$}PF_6. Preparation and x-ray structure of Pt[$P(C_6H_{11})_3$]$_2$. *Inorg. Chim. Acta* **1975**, *13*, L13-L14.

(3) MacInnis, M. C.; DeMott, J. C.; Zolnhofer, E. M.; Zhou, J.; Meyer, K.; Hughes, R. P.; Ozerov, O. V., Cationic Two-Coordinate Complexes of Pd(I) and Pt(I) Have Longer Metal-Ligand Bonds Than Their Neutral Counterparts. *Chem* **2016**, *1*, 902-920.

(4) Roy, S.; Mondal, K. C.; Meyer, J.; Niepötter, B.; Köhler, C.; Herbst-Irmer, R.; Stalke, D.; Dittrich, B.; Andrada, D. M.; Frenking, G.; Roesky, H. W., Synthesis, Characterization, and Theoretical Investigation of Two-Coordinate Palladium(0) and Platinum(0) Complexes Utilizing π-Accepting Carbenes. *Chem. Eur. J.* **2015**, *21*, 9312-9318.

(5) Barnett, B. R.; Moore, C. E.; Rheingold, A. L.; Figueroa, J. S., Cooperative Transition Metal/Lewis Acid Bond-Activation Reactions by a Bidentate (Boryl)iminomethane Complex: A Significant Metal–Borane Interaction Promoted by a Small Bite-Angle LZ Chelate. *J. Am. Chem. Soc.* **2014**, *136*, 10262-10265.

(6) Bauer, J.; Braunschweig, H.; Brenner, P.; Kraft, K.; Radacki, K.; Schwab, K., Late-Transition-Metal Complexes as Tunable Lewis Bases. *Chem. Eur. J.* **2010**, *16*, 11985-11992.

(7) Zadrozny, J. M.; Atanasov, M.; Bryan, A. M.; Lin, C.-Y.; Rekken, B. D.; Power, P. P.; Neese, F.; Long, J. R., Slow magnetization dynamics in a series of two-coordinate iron(ii) complexes. *Chem. Sci.* **2013**, *4*, 125-138.

(8) Atanasov, M.; Zadrozny, J. M.; Long, J. R.; Neese, F., A theoretical analysis of chemical bonding, vibronic coupling, and magnetic anisotropy in linear iron(ii) complexes with single-molecule magnet behavior. *Chem. Sci.* **2013**, *4*, 139-156.

(9) Reiff, W. M.; Schulz, C. E.; Whangbo, M.-H.; Seo, J. I.; Lee, Y. S.; Potratz, G. R.; Spicer, C. W.; Girolami, G. S., Consequences of a Linear Two-Coordinate Geometry for the Orbital Magnetism and Jahn−Teller Distortion Behavior of the High Spin Iron(II) Complex Fe[N(*t*-Bu)$_2$]$_2$. *J. Am. Chem. Soc.* **2009**, *131*, 404-405.

(10) Zadrozny, J. M.; Xiao, D. J.; Atanasov, M.; Long, G. J.; Grandjean, F.; Neese, F.; Long, J. R., Magnetic blocking in a linear iron(I) complex. *Nature Chem.* **2013**, *5*, 577.

(11) Zadrozny, J. M.; Xiao, D. J.; Long, J. R.; Atanasov, M.; Neese, F.; Grandjean, F.; Long, G. J., Mössbauer Spectroscopy as a Probe of Magnetization Dynamics in the Linear Iron(I) and Iron(II) Complexes $[Fe(C(SiMe_3)_3)_2]^{1-/0}$. *Inorg. Chem.* **2013**, *52*, 13123-13131.

(12) Guo, F.-S.; Day, B. M.; Chen, Y.-C.; Tong, M.-L.; Mansikkamäki, A.; Layfield, R. A., A Dysprosium Metallocene Single-Molecule Magnet Functioning at the Axial Limit. **2017**, *56*, 11445-11449.

(13) Goodwin, C. A. P.; Ortu, F.; Reta, D.; Chilton, N. F.; Mills, D. P., Molecular magnetic hysteresis at 60 kelvin in dysprosocenium. *Nature* **2017**, *548*, 439.

(14) Guo, F.-S.; Day, B. M.; Chen, Y.-C.; Tong, M.-L.; Mansikkamäki, A.; Layfield, R. A., Magnetic hysteresis up to 80 kelvin in a dysprosium metallocene single-molecule magnet. **2018**, eaav0652.
(15) Ding, Y.-S.; Chilton, N. F.; Winpenny, R. E. P.; Zheng, Y.-Z., On Approaching the Limit of Molecular Magnetic Anisotropy: A Near-Perfect Pentagonal Bipyramidal Dysprosium(III) Single-Molecule Magnet. **2016**, *55*, 16071-16074.
(16) Beaumier, E. P.; Pearce, A. J.; See, X. Y.; Tonks, I. A., Modern applications of low-valent early transition metals in synthesis and catalysis. *Nat. Rev. Chem.* **2019**, *3*, 15-34.
(17) Yang, J.; Tilley, T. D., Efficient Hydrosilylation of Carbonyl Compounds with the Simple Amide Catalyst [Fe{N(SiMe$_3$)$_2$}$_2$]. *Angew. Chem., Int. Ed.* **2010**, *49*, 10186-10188.
(18) Araake, R.; Sakadani, K.; Tada, M.; Sakai, Y.; Ohki, Y., [Fe$_4$] and [Fe$_6$] Hydride Clusters Supported by Phosphines: Synthesis, Characterization, and Application in N_2 Reduction. *J. Am. Chem. Soc.* **2017**, *139*, 5596-5606.
(19) Gieshoff, T. N.; Chakraborty, U.; Villa, M.; Jacobi von Wangelin, A., Alkene Hydrogenations by Soluble Iron Nanocluster Catalysts. *Angew. Chem., Int. Ed.* **2017**, *56*, 3585-3589.
(20) Clegg, W.; Snaith, R.; Shearer, H. M. M.; Wade, K.; Whitehead, G., Azomethine derivatives. Part 20. Crystal and molecular structures of the lithioketimine [{Li(N=CBu$^t_2$)}$_6$] and lithioguanidine [{Li[N=C(NMe$_2$)$_2$]}$_6$]; electron-deficient bridging of Li_3 triangles by methyleneamino-nitrogen atoms. *Dalton Trans.* **1983**, 1309-1317.
(21) Chan, L.-H.; Rochow, E. G., Syntheses and ultraviolet spectra of *N*-organosilyl ketimines. *J. Organomet. Chem.* **1967**, *9*, 231-250.
(22) Barr, D.; Clegg, W.; Mulvey, R. E.; Snaith, R.; Wade, K., Bonding implications of interatomic distances and ligand orientations in the iminolithium hexamers [LiN=C(Ph)Bu^t]$_6$ and [LiN=C(Ph)NMe$_2$]$_6$: a stacked-ring approach to these and related oligomeric organolithium systems. *J. Chem. Soc. Chem. Commun.* **1986**, 295-297.
(23) Avent, A. G.; Antolini, F.; Hitchcock, P. B.; Khvostov, A. V.; Lappert, M. F.; Protchenko, A. V., Reactions between a sodium amide Na[N(SiMe$_3$)R$_1$] (R$_1$ = SiMe$_3$, SiMe$_2$Ph or Bu^t) and a cyanoalkane RCN (R = Ad or Bu^t). *Dalton Trans.* **2006**, 919-927.
(24) Kiplinger, J. L.; Morris, D. E.; Scott, B. L.; Burns, C. J., The First f-Element Ketimido Complex: Synthesis and Characterization of (C$_5$Me$_5$)$_2$U(−NCPh$_2$)$_2$. *Organometallics* **2002**, *21*, 3073-3075.
(25) Jantunen, K. C.; Burns, C. J.; Castro-Rodriguez, I.; Da Re, R. E.; Golden, J. T.; Morris, D. E.; Scott, B. L.; Taw, F. L.; Kiplinger, J. L., Thorium(IV) and Uranium(IV) Ketimide Complexes Prepared by Nitrile Insertion into Actinide−Alkyl and −Aryl Bonds. *Organometallics* **2004**, *23*, 4682-4692.
(26) Lewis, R. A.; Wu, G.; Hayton, T. W., Synthesis and Characterization of an Iron(IV) Ketimide Complex. *J. Am. Chem. Soc.* **2010**, *132*, 12814-12816.
(27) Lewis, R. A.; Wu, G.; Hayton, T. W., Stabilizing High-Valent Metal Ions with a Ketimide Ligand Set: Synthesis of Mn(N═C^{t}Bu$_2$)$_4$. *Inorg. Chem.* **2011**, *50*, 4660-4668.

(28) Lewis, R. A.; Morochnik, S.; Chapovetsky, A.; Wu, G.; Hayton, T. W., Synthesis and Characterization of $[M_2(N)C^tBu_2)_5]^-$ (M = Mn, Fe, Co): Metal Ketimide Complexes with Strong Metal–Metal Interactions. *Angew. Chem., Int. Ed.* **2012**, *51*, 12772-12775.
(29) Seaman, L. A.; Wu, G.; Edelstein, N.; Lukens, W. W.; Magnani, N.; Hayton, T. W., Probing the 5f Orbital Contribution to the Bonding in a U(V) Ketimide Complex. *J. Am. Chem. Soc.* **2012**, *134*, 4931-4940.
(30) Lewis, R. A.; George, S. P.; Chapovetsky, A.; Wu, G.; Figueroa, J. S.; Hayton, T. W., Synthesis of a cobalt(iv) ketimide with a squashed tetrahedral geometry. *Chem. Commun.* **2013**, *49*, 2888-2890.
(31) Lewis, R. A.; Smiles, D. E.; Darmon, J. M.; Stieber, S. C. E.; Wu, G.; Hayton, T. W., Reactivity and Mössbauer Spectroscopic Characterization of an Fe(IV) Ketimide Complex and Reinvestigation of an Fe(IV) Norbornyl Complex. *Inorg. Chem.* **2013**, *52*, 8218-8227.
(32) Damon, P. L.; Liss, C. J.; Lewis, R. A.; Morochnik, S.; Szpunar, D. E.; Telser, J.; Hayton, T. W., Quantifying the Electron Donor and Acceptor Abilities of the Ketimide Ligands in $M(N{=}C^tBu_2)_4$ (M = V, Nb, Ta). *Inorg. Chem.* **2015**, *54*, 10081-10095.
(33) Seaman, L. A.; Pedrick, E. A.; Wu, G.; Hayton, T. W., Promoting oxo functionalization in the uranyl ion by ligation to ketimides. *J. Organomet. Chem.* **2018**, *857*, 34-37.
(34) Nam, W., High-Valent Iron(IV) Oxo Complexes of Heme and Non-Heme Ligands in Oxygenation Reactions. *Acc. Chem. Res.* **2007**, *40*, 522-531.
(35) Soriaga, R. A. D.; Nguyen, J. M.; Albright, T. A.; Hoffman, D. M., Diamagnetic Group 6 Tetrakis(di-tert-butylketimido)metal(IV) Complexes. *J. Am. Chem. Soc.* **2010**, *132*, 18014-18016.
(36) Martins, A. M.; Marques, M. M.; Ascenso, J. R.; Dias, A. R.; Duarte, M. T.; Fernandes, A. C.; Fernandes, S.; Ferreira, M. J.; Matos, I.; Conceição Oliveira, M.; Rodrigues, S. S.; Wilson, C., Titanium and zirconium ketimide complexes: synthesis and ethylene polymerisation catalysis. *J. Organomet. Chem.* **2005**, *690*, 874-884.
(37) Soriaga, R. A. D.; Javed, S.; Hoffman, D. M., Synthesis of Copper(I) Complexes with Ketimide and Hydrazide Ligands. *J. Cluster Sci.* **2010**, *21*, 567-575.
(38) Shearer, H. M. M.; Snaith, R.; Sowerby, J. D.; Wade, K., Lithium tetrakis(di-t-butylmethyleneamino)aluminate. *J. Chem. Soc., Chem. Commun.* **1971**, 1275-1276.
(39) Pattison, I.; Wade, K.; Wyatt, B. K., Azomethine derivatives. Part V. Reactions between organolithium compounds and diphenylketimine, some cyanides, and NNN'N'-tetramethylguanidine. *J. Chem. Soc. A* **1968**, 837-842.
(40) Crabtree, R. H., The Organometallic Chemistry of the Transition Metals. 5th ed.; Wiley: 2011.
(41) Damon, P. L. Exploring Metal Complexes in Unusual Oxidation States: Group V & Group X Ketimides and High Valent Cerium. University of California, Santa Barbara, Santa Barbara, CA, 2017.

(42) Lewis, R. A. High Valent First Row Metals and Metal-Metal Bonds Supported by a Ketimide Ligand. University of California, Santa Barbara, Santa Barbara, CA, 2013.
(43) Bryan, A. M.; Merrill, W. A.; Reiff, W. M.; Fettinger, J. C.; Power, P. P., Synthesis, Structural, and Magnetic Characterization of Linear and Bent Geometry Cobalt(II) and Nickel(II) Amido Complexes: Evidence of Very Large Spin–Orbit Coupling Effects in Rigorously Linear Coordinated Co^{2+}. *Inorg. Chem.* **2012**, *51*, 3366-3373.
(44) Eadie, D. T.; Pidcock, A.; Stobart, S. R.; Brennan, E. T.; Cameron, T. S., Amido-complexes of platinum(II). An X-ray crystal structure determination of cis-$[PtCl(NPh_2)(PEt_3)_2]$. *Inorg. Chim. Acta* **1982**, *65*, L111-L112.
(45) Bryndza, H. E.; Fultz, W. C.; Tam, W., Preparation and chemistry of novel platinum(II) amide complexes containing β-hydrogens. *Organometallics* **1985**, *4*, 939-940.
(46) Cowan, R. L.; Trogler, W. C., Syntheses, reactions, and molecular structures of trans-hydrido(phenylamido)bis(triethylphosphine)platinum(II) and trans-hydridophenoxobis(triethylphosphine)platinum(II). *J. Am. Chem. Soc.* **1989**, *111*, 4750-4761.
(47) Sundquist, W. I.; Bancroft, D. P.; Lippard, S. J., Synthesis, characterization, and biological activity of cis-diammineplatinum(II) complexes of the DNA intercalators 9-aminoacridine and chloroquine. *J. Am. Chem. Soc.* **1990**, *112*, 1590-1596.
(48) Cucciolito, M. E.; De Felice, V.; Giordano, F.; Orabona, I.; Ruffo, F., Nucleophilic Attack of Carbanions on Cationic Platinum(II) Nitrile Complexes Affording Stable η^1-Imine Enol and η^1-Enamine Coordinated Fragments. *Eur. J. Inorg. Chem.* **2001**, *2001*, 3095-3100.
(49) Park, S.; Roundhill, D. M.; Rheingold, A. L., New monomeric and binuclear hydride- and alkyl-substituted platinum(II) complexes having unsubstituted terminal or bridging amide ligands. *Inorg. Chem.* **1987**, *26*, 3972-3974.
(50) Henderson, W.; Oliver, A. G., An investigation of the mixed-bridge dinuclear complex $[Pt_2(\mu\text{-}S)(\mu\text{-}NH_2)(PPh_3)_4]^+$. *Inorg. Chim. Acta* **2014**, *416*, 49-56.
(51) de C. T. Carrondo, M. A. A. F.; Skapski, A. C., X-Ray crystal structure of tetrameric platinum(II) acetate: a square-cluster complex with short Pt–Pt bonds and octahedral co-ordination geometry. *J. Chem. Soc. Chem. Commun.* **1976**, 410-411.
(52) Simms, B. L.; Shang, M.; Lu, J.; Youngs, W. J.; Ibers, J. A., Preferential activation of a tert-butyl group over a cyclopropyl group in the intramolecular reaction of trans-dichlorobis(di-tert-butylcyclopropylphosphine)platinum(II) to form a platinaphosphacyclobutane. Synthesis and structure of [cyclic] $PtCl_2[P(tert\text{-}Bu)_2cyclopropyl]_2$ and its derivatives. *Organometallics* **1987**, *6*, 1118-1126.
(53) Troadec, T.; Tan, S.-y.; Wedge, C. J.; Rourke, J. P.; Unwin, P. R.; Chaplin, A. B., One-Electron Oxidation of $[M(P^tBu_3)_2]$ (M=Pd, Pt): Isolation of Monomeric $[Pd(P^tBu_3)_2]^+$ and Redox-Promoted C−H Bond Cyclometalation. *Angew. Chem. Int. Ed.* **2016**, *55*, 3754-3757.
(54) Crosby, S. H.; Clarkson, G. J.; Rourke, J. P., Reactions of a Platinum(II) Agostic Complex: Decyclometalation, Dicyclometalation, and Solvent-Switchable Formation of a Rollover Complex. *Organometallics* **2011**, *30*, 3603-3609.

(55) Roselló-Merino, M.; Rama, R. J.; Díez, J.; Conejero, S., Catalytic dehydrocoupling of amine-boranes and amines into diaminoboranes: isolation of a Pt(ii), Shimoi-type, η^1-BH complex. *Chem. Commun.* **2016**, *52*, 8389-8392.
(56) Cardona, C. M.; Li, W.; Kaifer, A. E.; Stockdale, D.; Bazan, G. C., Electrochemical Considerations for Determining Absolute Frontier Orbital Energy Levels of Conjugated Polymers for Solar Cell Applications. *Adv. Mater.* **2011**, *23*, 2367-2371.
(57) Tejada, J.; Chudnovsky, E. M.; Barco, E. d.; Hernandez, J. M.; Spiller, T. P., Magnetic qubits as hardware for quantum computers. *Nanotechnology* **2001**, *12*, 181.
(58) Christou, G.; Gatteschi, D.; Hendrickson, D. N.; Sessoli, R., Single-Molecule Magnets. *MRS Bull* **2011**, *25*, 66-71.
(59) Pedersen, K. S.; Bendix, J.; Clérac, R., Single-molecule magnet engineering: building-block approaches. *Chem. Commun.* **2014**, *50*, 4396-4415.
(60) Cook, A. W.; Hayton, T. W., Case Studies in Nanocluster Synthesis and Characterization: Challenges and Opportunities. *Acc. Chem. Res.* **2018**, *51*, 2456-2464.
(61) Lichtenberg, C.; Garcia Rubio, I.; Viciu, L.; Adelhardt, M.; Meyer, K.; Jeschke, G.; Grützmacher, H., A Low-Valent Iron Imido Heterocubane Cluster: Reversible Electron Transfer and Catalysis of Selective C–C Couplings. *Angew. Chem., Int. Ed.* **2015**, *54*, 13012-13017.
(62) Carpenter, S. H.; Baker, T. M.; Muñoz, S. B.; Brennessel, W. W.; Neidig, M. L., Multinuclear iron–phenyl species in reactions of simple iron salts with PhMgBr: identification of $Fe_4(\mu\text{-}Ph)_6(THF)_4$ as a key reactive species for cross-coupling catalysis. *Chem. Sci.* **2018**, *9*, 7931-7939.
(63) Muñoz III, S. B.; Daifuku, S. L.; Brennessel, W. W.; Neidig, M. L., Isolation, Characterization, and Reactivity of $Fe_8Me_{12}^-$: Kochi's S = 1/2 Species in Iron-Catalyzed Cross-Couplings with MeMgBr and Ferric Salts. *J. Am. Chem. Soc.* **2016**, *138*, 7492-7495.
(64) Zhao, Q.; Harris, T. D.; Betley, T. A., $[(^{H}L)_2Fe_6(NCMe)_m]^{n+}$ (m = 0, 2, 4, 6; n = −1, 0, 1, 2, 3, 4, 6): An Electron-Transfer Series Featuring Octahedral Fe6 Clusters Supported by a Hexaamide Ligand Platform. *J. Am. Chem. Soc.* **2011**, *133*, 8293-8306.
(65) Hernández Sánchez, R.; Betley, T. A., Meta-Atom Behavior in Clusters Revealing Large Spin Ground States. *J. Am. Chem. Soc.* **2015**, *137*, 13949-13956.
(66) Sánchez, R. H.; Willis, A. M.; Zheng, S.-L.; Betley, T. A., Synthesis of Well-Defined Bicapped Octahedral Iron Clusters $[(trenL)_2Fe_8(PMe_2Ph)_2]^n$ (n = 0, −1). *Angew. Chem., Int. Ed.* **2015**, *54*, 12009-12013.
(67) Hernández Sánchez, R.; Bartholomew, A. K.; Powers, T. M.; Ménard, G.; Betley, T. A., Maximizing Electron Exchange in a $[Fe_3]$ Cluster. *J. Am. Chem. Soc.* **2016**, *138*, 2235-2243.
(68) Sánchez, R. H.; Betley, T. A., Thermally Persistent High-Spin Ground States in Octahedral Iron Clusters. *J. Am. Chem. Soc.* **2018**, *140*, 16792-16806.
(69) Tereniak, S. J. L., Connie, Group 8 Metal–Metal Bonds. In *Molecular Metal-Metal Bonds*, Liddle, S. T., Ed. 2015.

(70) Duncan Lyngdoh, R. H.; Schaefer, H. F.; King, R. B., Metal–Metal (MM) Bond Distances and Bond Orders in Binuclear Metal Complexes of the First Row Transition Metals Titanium Through Zinc. *Chem. Rev.* **2018**, *118*, 11626-11706.
(71) Eisenhart, R. J.; Rudd, P. A.; Planas, N.; Boyce, D. W.; Carlson, R. K.; Tolman, W. B.; Bill, E.; Gagliardi, L.; Lu, C. C., Pushing the Limits of Delta Bonding in Metal–Chromium Complexes with Redox Changes and Metal Swapping. *Inorg. Chem.* **2015**, *54*, 7579-7592.
(72) Pauling, L., Atomic Radii and Interatomic Distances in Metals. *J. Am. Chem. Soc.* **1947**, *69*, 542-553.
(73) Hernández Sánchez, R.; Zheng, S.-L.; Betley, T. A., Ligand Field Strength Mediates Electron Delocalization in Octahedral $[(^{H}L)_2Fe_6(L')_m]^{n+}$ Clusters. *J. Am. Chem. Soc.* **2015**, *137*, 11126-11143.
(74) Bright, D.; Mills, O. S., The structure of di-μ-(4,4′-dimethylbenzophenoniminato)bis(tricarbonyliron). *Chem. Commun.* **1967**, 245-246.
(75) Klose, A.; Solari, E.; Ferguson, R.; Floriani, C.; Chiesi-Villa, A.; Rizzoli, C., Insertion Reactions of Isocyanides and Nitriles into Unsupported Iron-Aryl Bonds: The Synthesis of a Dimeric Iron(II) Homoleptic Iminoacyl Complex. *Organometallics* **1993**, *12*, 2414-2416.
(76) Schubert, E. M., Utilizing the Evans Method with a Superconducting NMR Spectrometer in the Undergraduate Laboratory. *J. Chem. Educ.* **1992**, *69*, 62.
(77) Chilton, N. F.; Anderson, R. P.; Turner, L. D.; Soncini, A.; Murray, K. S., PHI: A powerful new program for the analysis of anisotropic monomeric and exchange-coupled polynuclear d- and f-block complexes. *J. Comput. Chem.* **2013**, *34*, 1164-1175.
(78) Gütlich, P.; Bill, E.; Trautwein, A. X., Hyperfine Interactions. In *Mössbauer Spectroscopy and Transition Metal Chemistry: Fundamentals and Applications*, Springer Berlin Heidelberg: Berlin, Heidelberg, 2011; pp 73-135.
(79) Drüeke, S.; Chaudhuri, P.; Pohl, K.; Wieghardt, K.; Ding, X. Q.; Bill, E.; Sawaryn, A.; Trautwein, A. X.; Winkler, H.; Gurman, S. J., The novel mixed-valence, exchange-coupled, class III dimer $[L_2Fe_2(\mu\text{-}OH)_3]^{2+}$(L =N,N′,N″-trimethyl-1,4,7-triazacyclononane). *J. Chem. Soc., Chem. Commun.* **1989**, 59-62.
(80) Ding, X. Q.; Bominaar, E. L.; Bill, E.; Winkler, H.; Trautwein, A. X.; Drüeke, S.; Chaudhuri, P.; Wieghardt, K., Mössbauer and electron paramagnetic resonance study of the double-exchange and Heisenberg-exchange interactions in a novel binuclear Fe(II/III) delocalized-valence compound. *J. Chem. Phys.* **1990**, *92*, 178-186.
(81) Zall, C. M.; Zherebetskyy, D.; Dzubak, A. L.; Bill, E.; Gagliardi, L.; Lu, C. C., A Combined Spectroscopic and Computational Study of a High-Spin S = 7/2 Diiron Complex with a Short Iron–Iron Bond. *Inorg. Chem.* **2012**, *51*, 728-736.
(82) Simon, G. L.; Dahl, L. F., Organometallic chalcogen complexes. XXVI. Synthesis, structure, and bonding of cubane-like tetra-μ_3-sulfido-tetra-π-pentahaptocyclopentadienyl tetracobalt(III) $[Co_4(h^5\text{-}C_5H_5)_4S_4]$ tetramers (n = 0, +1). Stereochemical influence due to oxidation of completely nonbonding tetrahedral metal system. *J. Am. Chem. Soc.* **1973**, *95*, 2164-2174.

(83) Gall, R. S.; Chu, C. T. W.; Dahl, L. F., Preparation, structure, and bonding of two cubane-like iron-nitrosyl complexes, $Fe_4(NO)_4(\mu_3\text{-}S)_4$ and $Fe_4(NO)_4(\mu_3\text{-}S_2)(\mu_3\text{-}NC(CH_3)_3)_2$. Stereochemical consequences of bridging ligand substitution on a completely bonding tetrametal cluster unit and of different terminal ligands on cubane-like FeS_4 core. *J. Am. Chem. Soc.* **1974**, *96*, 4019-4023.

(84) Mednikov, E. G.; Jewell, M. C.; Dahl, L. F., Nanosized $(\mu_{12}\text{-}Pt)Pd_{164-x}Pt_x(CO)_{72}(PPh_3)_{20}$ ($x \approx 7$) Containing Pt-Centered Four-Shell 165-Atom Pd−Pt Core with Unprecedented Intershell Bridging Carbonyl Ligands: Comparative Analysis of Icosahedral Shell-Growth Patterns with Geometrically Related $Pd_{145}(CO)_x(PEt_3)_{30}$ ($x \approx 60$) Containing Capped Three-Shell Pd_{145} Core. *J. Am. Chem. Soc.* **2007**, *129*, 11619-11630.

(85) Mednikov, E. G.; Dahl, L. F., Nanosized $Pd_{37}(CO)_{28}\{P(p\text{-Tolyl})_3\}_{12}$ Containing Geometrically Unprecedented Central 23-Atom Interpenetrating Tri-icosahedral Palladium Kernel of Double Icosahedral Units: Its Postulated Metal-Core Evolution and Resulting Stereochemical Implications. *J. Am. Chem. Soc.* **2008**, *130*, 14813-14821.

(86) Mednikov, E. G.; Ivanov, S. A.; Dahl, L. F., CO-Induced Formation of an Interpenetrating Bicuboctahedral Au_2Pd_{18} Kernel in Nanosized $Au_2Pd_{28}(CO)_{26}(PEt_3)_{10}$: Formal Replacement of an Interior $(\mu_{12}\text{-}Pd)_2$ Fragment in the Corresponding Known Isostructural Homopalladium $Pd_{30}(CO)_{26}(PEt_3)_{10}$ with Nonisovalent $(\mu_{12}\text{-}Au)_2$ and Resulting Experimental/Theoretical Implications. *Inorg. Chem.* **2011**, *50*, 11795-11806.

(87) Mednikov, E. G.; Vo, N.; Fry, C. G.; Dahl, L. F., High-Yield Synthesis of PPh_3-Ligated Decanuclear Tl–Pd Cluster, $Pd_9[Tl(acac)](CO)_9(PPh_3)_6$: Comparative Analysis of Tl(I)–Pd(0) Bonding Connectivities with Known Tl–Pd Clusters and Resulting Insight Concerning Their Dissimilar Dynamic Solution Behavior. *Organometallics* **2012**, *31*, 2878-2886.

(88) Mednikov, E. G.; Dahl, L. F., Acid/Base-Controlled Au^I/Au^0 Reductive Transformations of the Monogold $[(\mu_{14}\text{-}Au)Pd_{22}(CO)_{20}(PEt_3)_8]^+$ Monocation into Three Different Neutral Digold Nanoclusters: $Au_2Pd_{21}(CO)_{20}(PEt_3)_{10}$, $Au_2Pd_{28}(CO)_{26}(PEt_3)_{10}$, and New Five-Layer Hexagonal Close-Packed $(\mu_{12}\text{-}Au)_2Pd_{42}(CO)_{30}(PEt_3)_{12}$ with a Trigonal-Bipyramidal $AuPd_3Au$ Kernel. *Inorg. Chem.* **2015**, *54*, 1145-1151.

(89) Mednikov, E. G.; Ivanov, S. A.; Dahl, L. F., Nanosized $\{Pd_4(\mu_4\text{-}C)\}Pd_{32}(CO)_{28}(PMe_3)_{14}$ Containing Tetrahedrally Deformed Pd_4 Cage with Encapsulated Carbide Atom: Formal Substitution of Geometrically Analogous Interior Au4 Entity in Isostructural $Au_4Pd_{32}(CO)_{28}(PMe_3)_{14}$ by Electronically Equivalent $Pd_4(\mu_4\text{-}C)$ and Computational/Catalytic Implications. *Inorg. Chem.* **2015**, *54*, 6157-6168.

(90) Erickson, J. D.; Mednikov, E. G.; Ivanov, S. A.; Dahl, L. F., Isolation and Structural Characterization of a Mackay 55-Metal-Atom Two-Shell Icosahedron of Pseudo-Ih Symmetry, $Pd_{55}L_{12}(\mu_3\text{-}CO)_{20}$ (L = PR_3, R = Isopropyl): Comparative Analysis with Interior Two-Shell Icosahedral Geometries in Capped Three-Shell Pd_{145}, Pt-Centered Four-Shell Pd–Pt M_{165}, and Four-Shell Au_{133} Nanoclusters. *J. Am. Chem. Soc.* **2016**, *138*, 1502-1505.

(91) Shearer, H. M. M.; Wade, K.; Whitehead, G., X-Ray crystal and molecular structure of hexameric di-t-butylmethyleneaminolithium, $(LiN{=}CBu^t_2)_6$: electron-deficient bridging of Li_3 triangles by methyleneamino nitrogen atoms. *J. Chem. Soc. Chem. Commun.* **1979**, 943-945.
(92) Clegg, W.; Snaith, R.; Shearer, H. M. M.; Wade, K.; Whitehead, G., Azomethine derivatives. Part 20. Crystal and molecular structures of the lithioketimine $[\{Li(N{=}CBu^t_2)\}_6]$ and lithioguanidine $[\{Li[N{=}C(NMe_2)_2]\}_6]$; electron-deficient bridging of Li_3 triangles by methyleneamino-nitrogen atoms. *Dalton Trans.* **1983**, 1309-1317.
(93) Jennings, J. R.; Snaith, R.; Mahmoud, M. M.; Wallwork, S. C.; Bryan, S. J.; Halfpenny, J.; Petch, E. P.; Wade, K., Preparation and X-ray crystal structures of the dimeric aldiminoborane $(PhCH{=}NBMe_2)_2$ and monomeric paddle-wheel shaped tris(ketimino)borane $B(N{=}CBu^t_2)_3$. *J. Organomet. Chem.* **1983**, *249*, c1-c5.
(94) Clegg, W.; MacGregor, M.; Mulvey, R. E.; O'Neil, P. A., Crystal and Solution Structures of the Novel Complex of Sodium Ketimide with Two Ketimine Ligands $[(^tBu_2C{=}NNa)_4(HN{=}C^tBu_2)_2]$: Stacking of Complexed and Uncomplexed $(NNa)_2$ Rings to give a Highly Distorted $(NNa)_4$ Cubane. *Angew. Chem. Int. Ed.* **1992**, *31*, 93-95.
(95) Pattison, I.; Wade, K.; Wyatt, B. K., Azomethine Derivatives. Part V. Reactions Between Organolithium Compounds and Diphenylketimine, Some Cyanides, and NNN'N'-Tetramethylguanidine. *J. Chem. Soc. A* **1968**, 837-842.
(96) Anderson, G. K. M., L., Reagents for Transition Metal Complex and Organometallic Syntheses. *Inorg. Synth.* **1990**, *28*, 61.
(97) Cheney, A. J.; Shaw, B. L., Transition metal–carbon bonds. Part XXX. Internal metallations of platinum(II)-t-butyldi-o-tolylphosphine and -di-t-butyl-o-tolyphosphine complexes. *J. Chem. Soc., Dalton Trans.* **1972**, 754-763.
(98) Bain, G. A.; Berry, J. F., Diamagnetic Corrections and Pascal's Constants. *J. Chem. Educ.* **2008**, *85*, 532.
(99) *SMART Apex II*, Version 2.1; Bruker AXS Inc.: Madison, WI, 2005.
(100) *SAINT Software User's Guide*, Version 7.34a; Bruker AXS Inc.: Madison, WI, 2005.
(101) Sheldrick, G. M. *SADABS*, University of Gottingen, Germany: 2005.
(102) *SHELXTL PC*, Version 6.12; Bruker AXS Inc.: Madison, WI, 2005.
(103) Guziec Jr, F. S.; Russo, J. M., A Convenient Conversion of Sterically Hindered Ketones into Imines. *Synthesis* **1984**, *1984*, 479-481.
(104) Wagner, G.; Pakhomova, T. B.; Bokach, N. A.; Fraústo da Silva, J. J. R.; Vicente, J.; Pombeiro, A. J. L.; Kukushkin, V. Y., Reduction of (imine)Pt(IV) to (imine)Pt(II) Complexes with Carbonyl-Stabilized Phosphorus Ylides. *Inorg. Chem.* **2001**, *40*, 1683-1689.
(105) Höfer, D.; Galanski, M.; Keppler, B. K., Synthesis, Characterization, and Time-Dependent NMR Spectroscopy Studies of (SP-4-2)-[(trans-1R,2R/1S,2S-$^{15}N_2$)-Cyclohexane-1,2-diamine][($^{13}C_2$)oxalato]platinum(II). *Eur. J. Inorg. Chem.* **2017**, *2017*, 2347-2354.
(106) Keefer, C. E.; Bereman, R. D.; Purrington, S. T.; Knight, B. W.; Boyle, P. D., The ^{195}Pt NMR of L_2Pt(1,2-dithiolene) Complexes. *Inorg. Chem.* **1999**, *38*, 2294-2302.

(107) Schwartsburd, L.; Cohen, R.; Konstantinovski, L.; Milstein, D., A Pincer-Type Anionic Platinum(0) Complex. *Angew. Chem., Int. Ed.* **2008**, *47*, 3603-3606.